UNIVERSITÀ
DEGLI STUDI
DI BRESCIA

DOTTORATO DI RICERCA IN
INGEGNERIA CIVILE, AMBIENTALE, DELLA COOPERAZIONE
INTERNAZIONALE E DI MATEMATICA

Settore Scientifico Disciplinare: ICAR/09

Riabilitazione Strutturale Di Edifici Storici E Contemporanei

XXXIII CICLO

SHEAR STRENGTHENING OF RC ELEMENTS WITH ULTRA HIGH PERFORMANCE FIBRE REINFORCED CONCRETE

DOTTORANDO:
Fabiola Iavarone

RELATORE:
Prof. Fausto MINELLI

CO-RELATORE:
Prof. Giovanni A. PLIZZARI

SYNOPSIS

In this work, the use of Ultra-High Performance Fibre Reinforced Concrete (UHPFRC) for strengthening and repairing reinforced concrete (RC) structures is discussed. The present thesis is intend to better understand the positive effects that retrofitting has on the structural behaviour of reinforced concrete members, focusing primarily on a shear strengthening of existing RC and prestressed concrete beams by means of thin jackets made of UHPFRC.

An experimental program concentrating on the investigation and evaluation of shear bond strength at the interface between substrate and overlay was undertaken. Seventy-two specimens, having three different substrate compressive strength and three different roughnesses at the interface, were tested. The objectives of this test were to study the influence of the substrate strength and of the substrate surface roughness on the interface bond strength between a substrate and overlay concrete.

The test results showed that the influence of the substrate compressive strength is a significant parameter that affects the interface shear stress between concretes with different ages; while, the influence of the substrate surface roughness is not particularly important in the interface bond strength. The data obtained by the experimental program were used for the modelling of bond-slip relationship for the numerical analyses.

A second component of the experimental program examined the behaviour of composite square slab panels. Twenty-four square slab panels repaired with UHPFRC were constructed and tested to failure under monotonically-increases load.

The numerical program involved the modelling of square slab panels, RC and prestressed concrete beams strengthened with a UHPFRC jacket. Particular attention was paid to the RC beams. A parametric study was conducted in order to determine the effect of a UHPFRC jacket, investigating the influence of geometric parameters, concrete compressive strength, longitudinal reinforcement ratio, and thickness of the UHPFRC layer.

The finite element analyses demonstrated the effect that the UHPFRC jackets have on the failure mode, as well as on the post-cracking behaviour, and on the formation and evolution of cracks.

Additionally, this research proposes an analytical formulation to predict the shear strength of beams strengthened with UHPFRC jacketing based on the actual draft of *fib* Model Code 2020.

SOMMARIO

In questo lavoro viene discusso l'uso di materiali Ultra High Performance Fiber Reinforced Concrete (UHPFRC) per il rinforzo e il ripristino di strutture in calcestruzzo armato.

La presente tesi intende comprendere gli effetti benefici che il rinforzo ha sul comportamento degli elementi in c.a., concentrandosi principalmente sul rinforzo a taglio di travi esistenti in calcestruzzo armato e calcestruzzo armato precompresso mediante un'incamiciatura in UHPFRC.

È stato intrapreso un programma sperimentale incentrato sulla valutazione della forza di adesione di interfaccia tra calcestruzzo esistente e calcestruzzo di ripristino. Settantadue campioni, aventi tre diverse resistenze a compressione del substrato e tre diverse rugosità di interfaccia, sono stati testati. Gli obiettivi di questo programma sperimentale erano studiare l'influenza della resistenza a compressione del calcestruzzo esistente e della rugosità della superficie sulla forza di adesione di interfaccia. I risultati del test hanno mostrato che l'influenza della resistenza a compressione del calcestruzzo esistente è un parametro significativo che influenza la forza di adesione di interfaccia; mentre, l'influenza della rugosità superficiale non è particolarmente importante. I dati raccolti sono stati utilizzati per la modellazione del legame di bond nelle analisi numeriche.

Una seconda componente del programma sperimentale ha esaminato il comportamento di pannelli quadrati riparati con UHPFRC. Ventiquattro pannelli sono stati costruiti e testati fino a rottura sotto carico monotono.

Il programma numerico prevede la modellazione di pannelli quadrati, travi in c.a. e travi in calcestruzzo armato precompresso rinforzate con un'incamiciatura di UHPFRC. In particolare, l'attenzione è stata posta alle travi in calcestruzzo armato. È stato condotto uno studio parametrico per determinare l'effetto del rivestimento in UHPFRC, indagando l'influenza dei parametri geometrici, della resistenza a compressione del calcestruzzo, della percentuale di armatura longitudinale e dello spessore dello strato di UHPFRC. Le analisi agli elementi finiti hanno dimostrato l'effetto che le camicie in UHPFRC hanno sulla modalità di rottura, sul comportamento post-fessurazione e sulla formazione ed evoluzione delle fessure.

Inoltre, questa ricerca propone una formulazione analitica per calcolare la resistenza a taglio di travi rinforzate con un'incamiciatura in UHPFRC, sulla base del *fib* Model Code 2020.

ACKNOWLEDGMENTS

The experience of this thesis has been challenging, labour and intensive, but pleasant and rewarding at the same time.
This work would not have been possible without the knowledge and leaderships of Professors Fausto Minelli and Giovanni Plizzari, to whom I would like to express my sincere acknowledgement.
Thank you to my main supervisor, Professor Fausto Minelli, who offered me this PhD project and believed in my capacity to accomplish it. I am very grateful for his scientific advice, constant optimism, and encouragement throughout all this path full of "ups and downs".
I would like to express my special gratitude to Professor Frank J. Vecchio, who welcomed me at the University of Toronto. Thanks for his moderation and kind assistance, for his thoughtfulness, and dedication.

I would like to acknowledge my research group ICAR 09, the staff of the DICATAM, and the Lab "Pietro Pisa" of the University of Brescia.
Once again, I would like to express my sincere gratitude to Mapei for the Financial support provided.

Finally, thank you to my colleagues for their sincerity and friendship: Nico, Enri, Stefano, Simone, Lucia, Sara, Francesca, Mud, Ivan, Bruno, Monica, and especially to my partner in misfortune and satisfaction, Anthony. You have made this experience so valuable and amusing. I could not have chosen a better place for my PhD, I'm incredibly thankful to all of you.

Thank you to my special person Cri for always being there for me.
Thank you to my friends Ale, Anna, Fede, Sari, and Donato for their love and understanding.
Thank you to Lau for her encouragement, optimism, affection, and closeness even if we have been living in different countries.
A special thanks to my Italian friends in Toronto Marta, Sara, Irina, and all others I cannot mention (because of the limited space) who made my internship in Canada the most memorable and pleasant experience ever.

Last but not least, I want to thank my family. Thank you to my wonderful parents and awesome brother for their endless love, and trust.

CONTENTS

LIST OF NOTATIONS

Latin lower case symbols

a	aggregate size
a/d	shear span-to-effective depth ratio
b	width of the specimen
d	diameter
d	effective depth
d	measured maximum deflection
d_r	measured maximum residual deflection
d_f	diameter of the fibre
d_{net}	net mid-span deflection at midspan
$d_{net,F}$	net front mid-span deflection at midspan
$d_{net,C}$	net centre mid-span deflection at midspan
$d_{net,B}$	net back mid-span deflection at midspan
f'_c	concrete cylinder compressive strength
f_{cx}	average concrete axial stress in the x-direction
f_{cy}	average concrete axial stress in the y-direction
f_{c1}	principal tensile stress
f_{c2}	principal compressive stress
f_{ct}	splitting tensile strength
f_{cuf}	cube compressive strength
$f_{ct.L}{}^f$	limit Of Proportionality (LOP)
f_{Lk}	highest stress value in the interval of 0.05 mm of CMOD
$f_{R,j}$	residual flexural tensile strength, j = 1, 2, 3 or 4
$f_{R,jk}$	characteristic flexural residual strength, j = 1, 2, 3 or 4
f_{sx}	average stress of reinforcement parallel to the x-direction
f_{sy}	average stress of reinforcement parallel to the y-direction
f_{scrx}	average stress of reinforcement parallel to the x-direction
f_{scry}	average stress of reinforcement parallel to the y-direction
$f_{sxyield}$	yield stress of the reinforcement in the x-direction
$f_{syyield}$	yield stress of the reinforcement in the y-direction
f'_t	concrete cracking strength
f_{uf}	ultimate tensile strength of the fibre
f_y	steel tensile strength
h_{sp}	distance between the tip of the notch and the top of the specimen
l_f	length of the fibre
l_z	length of the ICD zone
m_U	bending resistance

n	modular ratio
s	average crack spacings
s_b	bottom thickness of UHPFRC jacketing
s_f	spacing of the fibres
s_l	lateral thickness of UHPFRC jacketing
s_{mx}	average crack spacing in the x-direction
s_{my}	average crack spacing in the y-direction
v_b	bond stress of all fibres crossing a 45-degree diagonal
v_c	shear contribution of the compression region
v_{fr}	shear contribution of fibres
v_u	shear strength
v_{Rd}	shear resistance of the composite element
v_{Rc}	shear concrete contribution
v_{Rs}	shear steel reinforcement contribution
v_{RU}	shear UHP-FRC contribution
w	crack opening displacement
w_{lim}	crack width limit

Latin upper case symbols

A_{sw}	area of the transverse reinforcement
CMOD	crack mouth opening displacement
CTOD	crack tip opening displacement
CV	coefficient of variation
E_c	initial tangent stiffness of the concrete
E_s	initial tangent stiffness of reinforcement
ICD	crack induced debonding zone
G_f	fracture energy parameter
J_{tr}	moment of inertia from the transformed section
L	span of the concrete member
LVDTs	linear variable differential transformers
F	fibre factor
F_L	load corresponding to the LOP
F_j	load value, j = 1, 2, 3 or 4
MC2010	fib Model Code for Concrete Structures 2010
MPD	displacement in mid-span
P	peak load
PC	prestressed concrete
PHF	planitop HPC Floor
PHF46	planitop HPC Floor 46
PH	planitop HPC

Q	statical moment of area
R_{cm}	cube compressive strength
RC	reinforced concrete
R_t	roughness
$SDEM$	Simplified Diverse Embedment Model
$UHPFRC$	Ultra-High Performance Fibre Reinforced Concrete
ULS	Ultimate Limit States
V	volume
V	maximum shear force
V_{FEA}	numerical shear strength
V_{model}	analytical shear strength
VEM	Variable Engagement Model
V_f	volume content of the fibre

Greek Symbols

β	shape bond factor
δ'_L	left support displacements
δ'_R	right support displacements
γ_{cxy}	average net concrete shear strain
γ_{xy}	total shear strain
ε_0	concrete compressive strain corresponding to f'_c
ε_c	strain in the concrete
ε_{c1}	average net concrete axial strain, in the principal tensile 1-direction
ε_{c2}	average net concrete axial strain, in the principal compressive 2-direction
ε_{cr}	concrete cracking strain
ε_{cx}	average net concrete axial strain, in the x-direction
ε_{cy}	average net concrete axial strain, in the y-direction
ε_{sx}	average strain of reinforcement parallel to the x-direction
ε_{sy}	average strain of reinforcement parallel to the y-direction
ε_{syield}	yield strain of reinforcement
θ_ε	orientations of principal tensile strain axis
θ_σ	orientations of principal tensile stress axis
θ_n	angles between the normal to the crack and the reinforcement
σ_x	applied axial stress in the x-direction
σy	applied axial stress in the y-direction
σ_{pc}	post-cracking stress
σ_{cc}	cracking stress
υ_{ci}	local shear stress on the crack surface

v_{cxy}	average concrete shear stress
ρ_{sx}	longitudinal reinforcement ratio in x-direction
ρ_{sy}	longitudinal reinforcement ratio in y-direction
ρ_w	shear reinforcement ratio
τ	shear bond stress

SHEAR STRENGTHENING OF RC ELEMENTS WITH ULTRA HIGH PERFORMANCE FIBRE REINFORCED CONCRETE

1 INTRODUCTION

1.1 Background and motivation

Over the last few years, the interest for strengthening and repairing reinforced concrete (RC) structures has increased. RC structures frequently manifest inadequate performance in terms of structural resistance and durability when exposed to severe environmental influences and high mechanical loading.
Various techniques are proposed for the retrofitting of RC structures [*fib* Report, 1991; *fib* Bulletin n. 14, 2001; *fib* Bulletin n. 24, 2003; *fib* Bulletin n. 35, 2006;]. Nevertheless, traditional retrofitting using concrete and repair mortar is often inadequate; therefore, new techniques for the strengthening of existing RC structures have been developed.
In recent years, attempts to improve the performance of cementitious materials by incorporating fibres have led to the emergence of Ultra-High Performance Fibre Reinforced Concrete (UHPFRC). The UHPFRC materials are characterized by a strain-hardening behaviour in tension and high compressive strength as well. These materials possess excellent mechanical properties like high flexural and tensile strength, high fracture toughness, and ductility [Schmidt and Fehling, 2005]. Furthermore, the UHPFRC materials has a high durability, crucial topic as far the use of this material for structural purposes [Ferrara *et al.*, 2005].
The research carried out in the area of strengthening using UHPFRC as retrofitting material combines efficiently the protection and resistance properties of UHPFRC. These characteristics make UHPFRC eligible for the seismic retrofitting and the strengthening of RC elements. The purpose of a concrete repair is to extend the service life of the structure restoring the load-carrying capacity and the stiffness of a concrete member. This can be accomplished by providing a protective layer to a damaged substrate. The UHPFRC is applied on existing reinforced concrete elements as thin reinforcement layer and often combined with reinforcement bars.
The interface between new concrete (overlay) and old concrete (substrate) is a key factor in the success of repair and rehabilitation works. Good adhesion is crucial for providing monolithic action in bonded concrete overlays. It is important that the interface between differently aged concrete has to withstand significant and durable bond.
In the concrete repairs, the overlay has to contribute to both the stiffness and load carrying capacity of the element. Some experiment studies [Alaee and Karihaloo, 2003; Martinola *et al.*, 2007; Brühwiler and Denarié, 2008; Martinola *et al.*; 2010; Beschi *et al.*, 2011; Massicotte *et al.*, 2013; Noshiravani and Brühwiler, 2013; Ruano *et al.*, 2014; Brühwiler *et al.*, 2015; Meda *et al.*, 2016; Lampropoulos *et al.*, 2016; Al-Osta *et al.*, 2017; Reggia *et al.*, 2018] have shown that the UHPFRC composite elements have a

significantly higher stiffness and ultimate resistance than corresponding RC elements alone. The additional UHPFRC reinforcement improves the strength and structural efficiency.
Another important contribution due to the UHPFRC retrofit in beams is that the jacketing of UHPFRC might modify the failure mode from brittle shear failure to a ductile flexural failure mode. In fact, some researchers have evaluated the efficiency of the UHPFRC jacketing as a retrofitting method for shear strengthening of reinforced concrete elements.
Currently, in design codes, there is no equation to calculate shear strength in retrofitted beams by UHPFRC jacketing. Thus, it would be necessary to achieve an analytical model to predict the shear strength of the composite beams. Therefore, the aim would be the implementation of a quite simple procedure able to calculate/estimate the shear strength, which could be incorporated in the design formulations of building codes.
The need for more experimental and numerical data for the retrofitting using UHPFRC is the main motivation for this work.
In particular, this research has the primary objective to study the shear strengthening of existing RC and prestressed concrete beams by means of a thin jacket made of UHPFRC.

1.2 Objectives and scope of the research

In this work, the use of Ultra-High Performance Fibre Reinforced Concrete (UHPFRC) for strengthening and repairing RC structures will be discussed. Attention will be focused on the positive effects that thin UHPFRC jacket has on the bearing capacity of RC members in shear.
Experimental and analytical works were undertaken to address the aim of this thesis, subdivided into the following stages:

1. analysis of the influence of the substrate concrete compressive strength on the bond strength and the evaluation of the possible effect of substrate surface roughness on the interface bond strength in composite elements;
2. investigation of the possibility to use thin jacket made of UHPFRC to shear strengthen a wide range of RC beams having different parameters;
3. investigation of the efficacy of UHPFRC jacketing in existing prestressed concrete beam on shear strengths, failure mechanisms, crack control, and ductility;
4. proposal of an analytical formulation for predicting the shear strength of beams strengthened with UHPFRC jacketing.

To accomplish these objectives, an experimental and numerical research program will be carried out.

The numerical analyses could represent an alternative method for studying the response of a wide range of elements; for this reason, some nonlinear finite element analyses were performed on square slab panels, RC beams having different parameters, and existing prestressed concrete beams.

1.3 Organization of the thesis

This thesis presents the work undertaken to study the shear strengthening of reinforced concrete (RC) elements using thin jacket made of Ultra-High Performance Fibre Reinforced Concrete (UHPFRC). The program addressed in this thesis and the research objectives are reviewed in Chapter 1.

Chapter 2 is an overview of fibre reinforced concrete (FRC). Mechanics of fibres, mechanical properties of FRC, fracture mechanism of FRC, and σ-w law by inverse analysis are discussed. The second part of Chapter 2 includes a discussion of strengthening of RC elements with UHPFRC. This Sections reports the test results from previous studies. The third part of Chapter 2 investigates a bond strength between old and new concrete. The rest of this chapter is dedicated to the strengthening of shear beams. The main formulations present in the literature to calculate the FRC contribution to shear strength are reported.

Chapter 3 focuses on the tests to obtain mechanical properties of the materials used in the experimental program.

Chapter 4 details the shear bond test. The objectives of this test are to study the influence of a substrate compressive strength and a substrate surface roughness on the interface bond strength between a substrate and overlay concrete. Choice of studied parameters, specimens design, construction, and testing of specimens are also described in this chapter. Chapter 4 also presents the experimental program on square slab panels. The test results are reported and analysed in this chapter. The analyses include the comparison between shear stress measured by the shear bond tests and bending tests. Moreover, an in-situ load testing on a lightweight ribbed one-way reinforced concrete slab strengthened by means of UHPFRC overlay is presented.

Chapter 5 presents a nonlinear finite element modelling carried out on square slab panels and existing prestressed concrete beams. Additionally, a parametric study is conducted on RC beams reinforced with a UHPFRC jacketing by changing geometry, concrete compressive strength, longitudinal reinforcement ratio, and thickness of the UHPFRC layer.

Mechanic-based model to predict the shear strength of concrete beams reinforced with a UHPFRC jacketing, is presented in Chapter 6. Also, its validation against finite element analyses is illustrated.

Finally, Chapter 7 summarises the work performed, provides conclusions, and discusses recommendations for future work.

1.4 References

***ALAEE, F. J., & KARIHALOO, B. L.**, 2003. "Retrofitting of reinforced concrete beams with CARDIFRC", Journal of Composites for Construction, 7(3), 174-186.*

***AL-OSTA, M. A., ISA, M. N., BALUCH, M. H., & RAHMAN, M. K.**, 2017. "Flexural behavior of reinforced concrete beams strengthened with ultra-high performance fiber reinforced concrete", Construction and Building Materials, 134, 279-296.*

***BESCHI, C., RIVA, P., METELLI, G., & MEDA, A.**, 2015. "HPFRC jacketing of non seismically detailed RC corner joints", Journal of Earthquake Engineering, 19(1), 25-47.*

***BRÜHWILER, E., & DENARIÉ, E.**, 2008. "Rehabilitation of concrete structures using ultra-high performance fibre reinforced concrete", (No. CONF), University of Kassel.*

***BRÜHWILER, E., BASTIEN-MASSE, M., MÜHLBERG, H., HOURIET, B., FLEURY, B., CUENNET, S., & MAURER, M.**, 2015. September. "Strengthening the Chillon viaducts deck slabs with reinforced UHPFRC", in IABSE Symposium Report (Vol. 105, No. 24, pp. 1-8). International Association for Bridge and Structural Engineering.*

***EN 1992-1-1: EUROCODE 2**. Design of concrete structures. Part 1–1: General rules and rules for buildings; 2005.*

***FÉDÉRATION INTERNATIONALE DU BÉTON (FIB)**. 2013. Model Code 2010 for concrete structures (MC2010), International Federation for Structural Concrete, Lausanne, Switzerland, 2013, 289 p.*

***FERRARA, L., FRATESI, R., SIGNORINI, S., & SONZOGNI, F.** ,2005. Durability of steel-fibre reinforced concrete precast elements: Experiments and proposal of design recommendations. In proceedings of the 6th international RILEM symposium on fibre-reinforced concretes BEFIB 2004, Varenna, september 2004 (pp. 567-576).*

***FIB BULLETIN N. 14**, 2001. "Externally bonded FRP reinforcement for RC structures", Technical report, International Federation for Structural Concrete (fib), October 2001, 138 pp.*

***FIB BULLETIN N. 24**, 2003. "Seismic assessment of reinforced concrete buildings", State-of-art report, International Federation for Structural Concrete (fib) August 2003, 312 pp.*

***FIB BULLETIN N. 35**, 200) "Retrofitting of concrete structures by externally bonded FRPs, with emphasis on seismic applications", Technical report, International Federation for Structural Concrete (fib), April 2006, 220 pp.*

***FIB REPORT**, 1991 "Repair and strengthening of concrete strengthening of concrete structures. Guide to good practice", Thomas Telford Ltd., 37 pp.*

***LAMPROPOULOS, A. P., PASCHALIS, S. A., TSIOULOU, O. T., & DRITSOS, S. E.**, 2016. "Strengthening of reinforced concrete beams using ultra high performance fibre reinforced concrete (UHPFRC)", Engineering Structures, 106, 370-384.*

***LEE, S. C., CHO, J. Y., & VECCHIO, F. J.**, 2012. "Simplified Diverse Embedment Model for Steel Fiber Reinforced Concrete in Tension", ACI Material Journal.*

***MA, R.**, 2016. "Development of Contact Elements for Finite Element Analysis of Composite Structures", Report doctoral dissertation, University of Toronto.*

***MARTINOLA, G., MEDA, A., PLIZZARI, G. A., & RINALDI, Z.**, 2007, June. "An application of high performance fiber reinforced cementitious composites for R/C beams strengthening", in FraMCos-6. 6th Int. Conf. on Fracture Mechanics of concrete and concrete structures. Catania (Vol. 17, p. 22).*

***MARTINOLA, G., MEDA, A., PLIZZARI, G. A., & RINALDI, Z.**, 2010. "Strengthening and repair of RC beams with fiber reinforced concrete", Cement and concrete composites, 32(9), 731-739.*

***MASSICOTTE, B., DAGENAIS, M. A., & LAGIER, F.**, 2013, October. "Performance of UHPFRC jackets for the seismic strengthening of bridge piers", in Proceeding of the 2nd Int Symp on UHPFRC Designing and building with UHPFRC: from innovation to large-scale realizations. Marseille, France (pp. 1-11).*

***MEDA, A., MOSTOSI, S., RINALDI, Z., & RIVA, P.**, 2016. "Corroded RC columns repair and strengthening with high performance fiber reinforced concrete jacket", Materials and Structures, 49(5), 1967-1978.*

***NOSHIRAVANI, T., & BRÜHWILER, E.**, 2013. "Analytical model for predicting response and flexure-shear resistance of composite beams combining reinforced ultrahigh performance fiber-reinforced concrete and reinforced concrete", Journal of Structural Engineering, 140(6), 04014012.*

***NOSHIRAVANI, T., & BRÜHWILER, E.**, 2013. "Experimental investigation on reinforced ultra-high-performance fiber-reinforced concrete composite beams subjected to combined bending and shear", ACI Structural Journal, 110(ARTICLE), 251-261.*

***REGGIA, A., MORBI, A., & PLIZZARI, G. A.**, 2018. "Seismic Retrofitting of a Bridge Pier with Ultra High Performance Fibre Reinforced Concrete", in MATEC Web of Conferences (Vol. 199, p. 09015), EDP Sciences.*

***RUANO, G., ISLA, F., PEDRAZA, R. I., SFER, D., & LUCCIONI, B.**, 2014. "Shear retrofitting of reinforced concrete beams with steel fiber reinforced concrete", Construction and Building Materials, 54, 646-658.*

***SCHMIDT, M., & FEHLING, E., 2005**. "Ultra-high-performance concrete: research, development and application in Europe", ACI Special publication, 228, 51-78.*

***VECCHIO, F.J.**, 1990. "VecTor 2 Nonlinear Finite Element Analysis" program.*

***VECCHIO, F. J.**, 2000. "Disturbed stress field model for reinforced concrete: formulation", Journal of structural engineering, 126(9), 1070-1077.*

***VECCHIO, F. J., & COLLINS, M. P.**, 1986. "The modified compression-field theory for reinforced concrete elements subjected to shear", ACI J., 83(2), 219-231.*

2 LITERATURE SURVEY

2.1 Fibre Reinforced Concrete (FRC)

2.1.1 *Introduction*

Concrete is a brittle material, with low tensile strength and strain capacities. To help overcome these problems, there has been a constant increase over the past 40 years in the use of fibre reinforced concretes (FRC). The concept to use the fibres to reinforce concrete goes back to olden times. Fibres have been used to strengthen brittle materials that are characterized by low tensile strength and strain capacities. Ancient civilizations used straw and horsehair to reinforce sun-baked mud walls. In modern times, asbestos fibres have been used to reinforce Portland cement mortars [Bentur and Mindess, 2007]. In 1874 the idea of strengthening concrete with the help of the addition of steel splinters was patented [Maidl, 1995]. However, in the initial period after patenting, fibre reinforced concrete was not often used.

Steel fibres, as we know them today, were first patented in the United States by Romualdi and Batson Development Corporation in 1962 [Vondran, 1991]. The first research on fibre reinforced concrete were published in the early 1960s by Romualdi and Batson [1963] and Romualdi and Mandel [1964]. From the 1960s there has been an increased interest in fibre reinforced concrete. The primary use of steel fibres is to increase significantly the tensile strength of the concrete. Fibres carry out their action only after the cracking of the matrix of the concrete. The post-cracking behaviour of fibre reinforced concrete is less brittle than that of concrete without fibres and is characterized by a higher fracture energy.

Fibre reinforced concrete is not a substitute for conventional reinforcement. Fibres and steel bars have a different role to play in modern concrete technology, and there are many applications in which both fibres and continuous reinforcing bars should be used together. One of the differences between conventional reinforcement and fibre reinforcement is that a conventional reinforcement bar is oriented in the direction desired while fibres are randomly oriented. Direction fibre distributions influences the post crack resistance. Perpendicular fibres have no resistance after the tensile strength of the matrix is exceeded. Also, parallel fibres have about 30 percent more toughness than randomly distributed ones [Shah and Rangan, 1971]. Moreover, fibre reinforcement has many structural advances, particularly where cracking is independent of loading. Indeed, with fibres internal stresses are much more evenly distributed throughout the cross section of a structure [Grzybowski, 1989].

The applications of FRC are dictated by the types of fibres that have been used. Asbestos fibres have long been used in pipes and in corrugated or flat roofing sheets. Glass fibres are used primarily in precast panels (non-structural). Steel fibres have

been used in pavements, in shotcrete in dams, and in a variety of other structures. Increasingly, polypropylene fibres are being used as secondary reinforcement, to control plastic shrinkage cracking. Vegetable fibres have been used in low-cost building materials.
New production technologies have evolved as new fibres have been developed, and new applications found. Clearly, in order to produce useful FRC, the production techniques must be compatible with the fibres and matrix. This depends not only upon the fibre type, but also on the fibre geometry. Longer fibres of smaller diameter will be more efficient in hardened FRC but will make fresh FRC more difficult to handle [Bentur and Mindess, 2007].

2.1.2 *Mechanics of fibre reinforcement*

ACI Committee 544 [2009] provided the following definition of Steel Fibre Reinforced Concrete:
"Concrete made of hydraulic cements containing fine and coarse aggregate and discontinuous discrete steel fibres".
To improve further the behaviour of FRC, Ultra-High Performance Fibre Reinforced Concrete (UHPFRC) are been developed. The UHPFRC refers to a class of FRC characterized by a strain-hardening behaviour in tension, which occurs after first cracking, and high compressive strength as well [Schmidt and Fehling, 2005]. Due to the excellent mechanical properties and structural durability, the UHPFRC materials can represent an asset for the construction industry to face the challenges imposed by the needs of our continuously and fast evolving society [Ferrara, 2019].
Early steel fibres were usually straight, smooth, and round. Over the years, improvements have been made in the fibre profile to increase the pull-out resistance of the fibres. Most fibres nowadays typically utilise a mechanical end anchorage, such as hooked- or flattened-ends, or a crimped profile. These improvements have led to enhanced bond strength between the fibres and the concrete matrix. In addition to normal strength steel fibres (f_{uf} ≈ 1100 MPa), high strength steel fibres are also available, with ultimate tensile strength (f_{uf}) as high as 2300 MPa.

2.1.2.1 Aspect ratio

Fibre aspect ratio is a factor with influences the effectiveness of the fibre reinforcement. The fibre aspect ratio, defined as the ratio of the fibre length to fibre diameter, provides an indication of the stiffness of the fibre [Johnston, C.D., 2001].
A high fibre aspect ratio leads to better composite action. This is attributable to the higher surface area of fibres with a high aspect ratio than that of fibres with a low aspect ratio under the same fibre volume. The higher surface area may lead to an improved bond between the fibres and the concrete, and, thus, a better performance

of the composite. Research by Shah and Rangan [1971] has indicated that although the fibre aspect ratio did not significantly influence the tensile strength of the concrete, when fibres with a high aspect ratio have been used, substantial improvements in the residual post-cracking tensile strength and the toughness of the concrete have been observed. Table 2.1-1 shows the influence of fibre aspect ratio in the tensile strength of the fibre reinforced concrete.

Direction of fibres with respect to that of the applied load	Length of fibres [mm]	Aspect ratio (l_f/d_f)	Tensile strength [N]	Post cracking [N]	Relative toughness
Effect of fibre aspect ratio					
Random	25.4	100	3380	1425	1.5
Random	19.1	75	3515	1915	1.7
Random	12.7	50	3425	0	1.4
Random	6.4	25	3515	0	1.0

Note: Specimen length was 300 mm, test region length was 100 mm, cross-sectional area of test region was 50×25 mm.

Table 2.1-1: The influence of fibre aspect ratio on the uniaxial tensile behaviour of SFRC with 0.5% fibres by volume [Shah and Rangan, 1971].

2.1.2.2 Fibre orientation

Fibre orientation plays an important role in the mechanical performance of fibre-reinforced composites [Vandewalle *et al.*, 2008]. The increment of the mechanical properties of FRC is significantly affected by a variety of factors, such as the constituent materials of the fibres, geometry, and surface treatments. It is evident that fibre dosage influences performance due to the presence of more fibres acting at a certain surface. Moreover, as published research dealing with fibre pull-out has shown [Li *et al.*, 1990, Robins *et al.*, 2002], the action of such fibres varies with fibre inclination and the embedded length. Therefore, the distribution and orientation of the fibres modifies the structural response because it entails variations of the number of fibres involved, the fibre angle and embedded length. As indicated in Table 2.1-2, the most efficient condition is when all fibres are aligned parallel to the direction of the tensile stress. As the fibres become more oblique to the loading direction, their actual embedment length and the number of fibres crossing the cracks will decrease, and this leads to a reduction in the fibre reinforcement effectiveness [Shah and Rangan, 1971]. In such a sense, the reliable use of the fibres is directly associated with knowledge about fibre final positioning in the concrete pieces [Alberti *et al.*, 2016].
If one type of fibre is studied and its dosage is maintained at a steady rate, the main factors that influence fibre distribution and orientation are the concrete properties,

pouring and compaction procedure of the fresh concrete (vibration needles, vibration table, etc.), and the formwork and mould sizes.

Direction of fibres with respect to that of the applied load	Length of fibres [mm]	Aspect ratio (l_f/d_f)	Tensile strength [N]	Post cracking [N]	Relative toughness
Effect of fibre orientation					
Parallel	25.4	100	3960	1555	1.7
Random	25.4	100	3380	1425	1.3
Perpendicular	25.4	100	3360	0	1.0

Note: Specimen length was 300 mm, test region length was 100 mm, cross-sectional area of test region was 50×25 mm.

Table 2.1-2: The influence of fibre orientation on the uniaxial tensile behaviour of SFRC with 0.5% fibres by volume [Shah and Rangan, 1971].

2.1.3 *Characterization of fibre Reinforced Concrete*

Structural design of fibre reinforced concrete elements is based on the post-cracking residual strength provided by the fibre reinforcement. In point of fact, the main advantage of adding fibres to concrete is that they generate a post-cracking residual tensile strength in combination with a large tensile strain. As such, the material fibre reinforced concrete is characterized by substantial ductility and toughness.

It is nowadays believed that a proper characterization of fibres should be undertaken by considering the post-cracking behaviour itself, rather than considering the geometry and the amount of fibres provided in the matrix. In fact, the same amount of fibre in different concretes results in a quite different post-cracking behaviour of the composite [Bentur and Mindess, 2007]. The appropriate facture mechanics test should be performed in order to find out the actual post-cracking properties.

Naaman and Reinhardt [2003] have proposed a performance classification scheme to the UHPFRC which places cementitious composites into the following categories of behaviour (Figure 2.1-1):

- (Level 1) deflection softening or crack controlling with little enhancement in mechanical properties;
- (Level 2) deflection hardening;
- (Level 3) tensile strain hardening;
- (Level 4) high energy absorbing. Level 0 has been added to the performance classification to illustrate the behaviour of non-fibre reinforced concrete as a reference material.

The most important aspect of FRC is the behaviour in tension. There are various test methods to determine it. The uniaxial tension test would be the most suitable test for

determining tension behaviour; despite this, FRC post-cracking laws are generally determined through indirect methods.

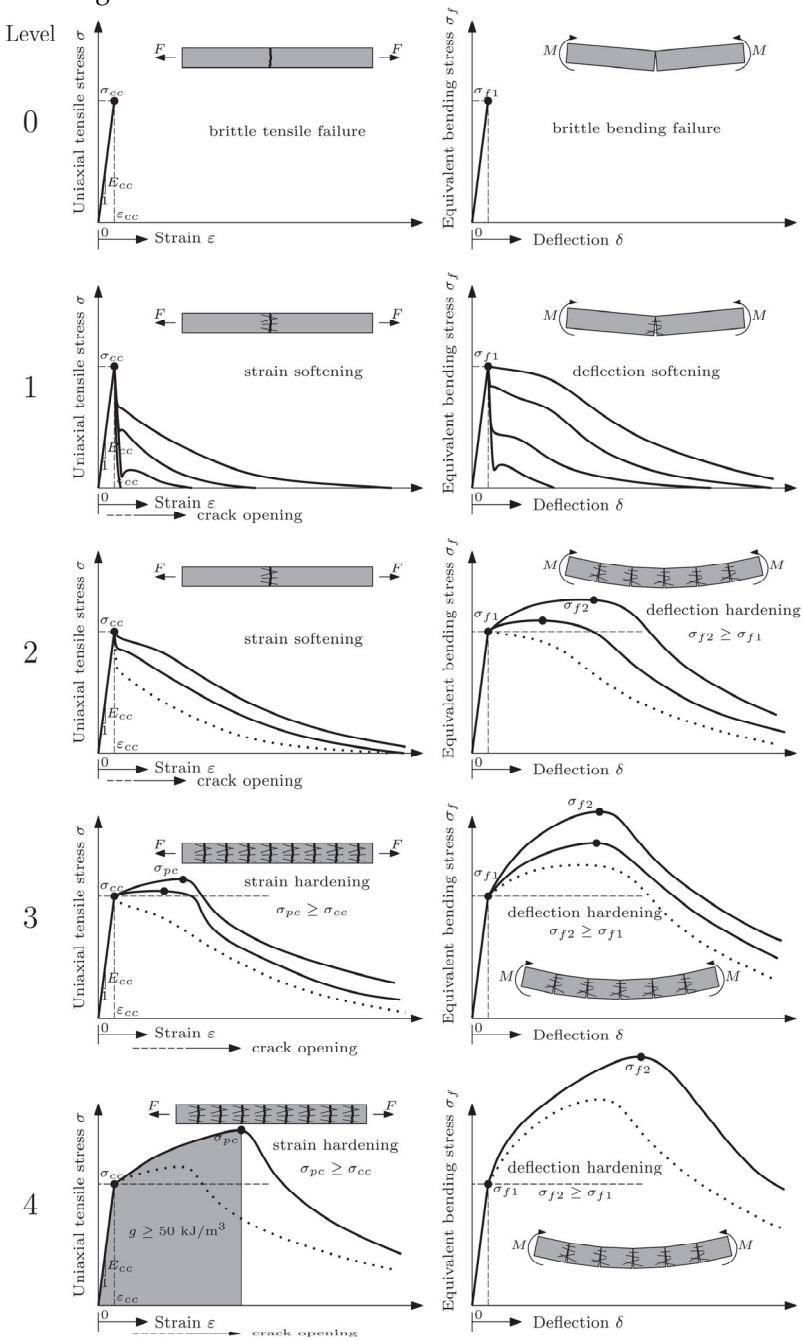

Figure 2.1-1: Performance levels of fibre reinforced concrete [Wille et al., 2014].

2.1.3.1 UNI EN 14651

European Standard EN 14651 [2007] specifies a method for measuring the flexural tensile strength of metallic fibre reinforced concrete using moulded test specimens. The method provides for the determination of the Limit of Proportionality (LOP) and of a set of residual flexural tensile strength values.
The European Standard is based on fracture mechanics Crack Mouth Opening Displacement (CMOD) controlled tests on notched beams loaded with a three point system. The tensile behaviour of fibre reinforced concrete is evaluated in terms of residual flexural tensile strength values determined from Load vs. Deformation curve obtained by applying a centre point load. Deformation is expressed in terms of CMOD or mid-span deflection (MPD). Crack Tip Opening Displacement (CTOD) measures the resistance of a material to the propagation of a crack.
The test specimens have a nominal size of 150 mm and a length L so that 550 ≤ L ≤ 700 mm. the notch h_{sp} have to be125 mm ± 1mm.
Figure 2.1-2 illustrates the specimen geometry, the loading condition, and the position where the LVTDs are to be placed.

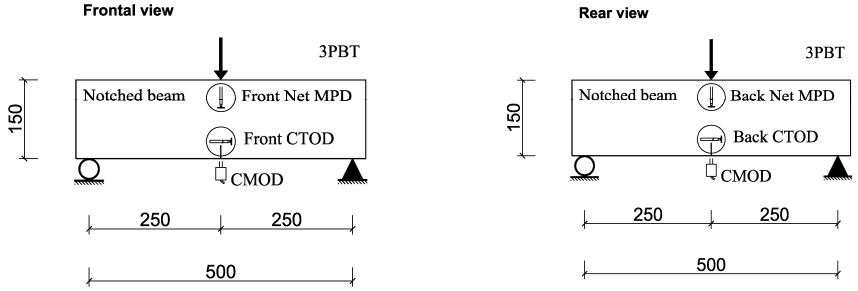

Figure 2.1-2: Three bending test set-up: a) front view; b) back view (dimension in mm).

The limit of proportionality (LOP) is given by the following expression:

$$f_{ct,L}^{f} = \frac{3F_L L}{2bh_{sp}^2} \qquad (2.1\text{-}1)$$

where:

$f_{ct,L}^{f}$	is the LOP [MPa]
F_L	is the load corresponding to the LOP [N]
L	is the span length [mm]
b	is the width of the specimen [mm]
h_{sp}	is the distance between the tip of the notch and the top of the specimen [mm]

The load value F_L shall be determined by drawing a line at distance of 0.05 mm and parallel to the load axis of the Load vs. CMOD curve and taking F_L the highest load value in the interval of 0.05 mm (Figure 2.1-3).

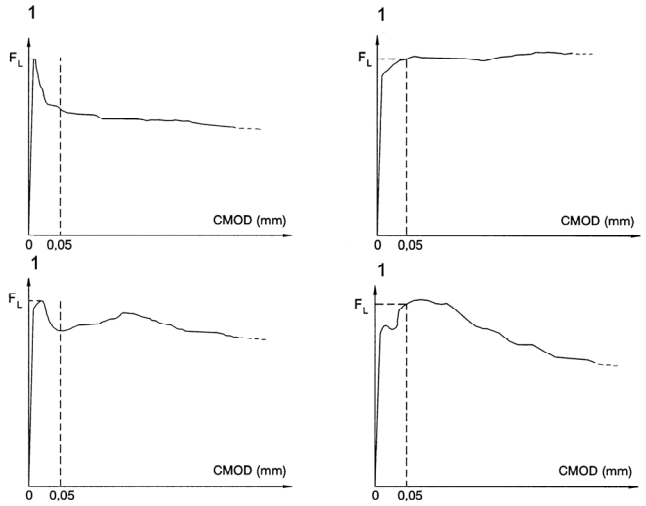

Figure 2.1-3: Load-CMOD diagrams and F_L [European Standard EN 14651, 2007].

Parameters, $f_{R,j}$ represent the residual flexural tensile strength. They are evaluated from diagram of applied force versus the deformation. The deformation is generally expressed in terms of CMOD. $f_{R,j}$ is given by using equation:

$$f_{R,j} = \frac{3F_j L}{2bh_{sp}^2} \qquad (2.1\text{-}2)$$

where:

$f_{R,j}$	is the residual flexural tensile strength corresponding with CMOD=$CMOD_j$ [MPa]
F_j	is the load corresponding with CMOD=$CMOD_j$[N]
L	is the span length [mm]
b	is the width of the specimen [mm]
h_{sp}	is the distance between the tip of the notch and the top of the specimen [mm]

Figure 2.1-4 shows the diagram of the applied force versus CMOD.

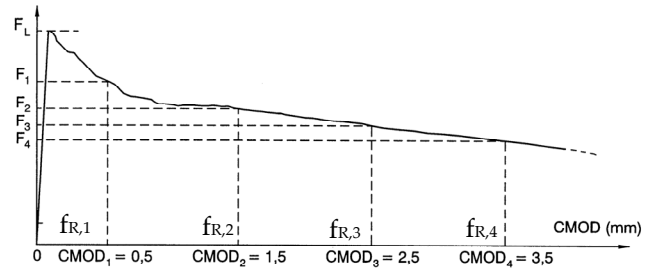

Figure 2.1-4: Load-CMOD curve and F_j(j=1,2,3,4)

2.1.3.2 Fib Model Code for Concrete Structures 2010

Classification is an important requirement for structural materials. A minimum mechanical performance of FRC must be guaranteed. For structural applications the material classification is based on the nominal properties of the composite material, referring to post-cracking tensile strength, determined from bending tests on notched prisms according to EN 14651 [2007]. *fib* Model Code for Concrete Structures 2010 (MC2010) introduces a special design rules to the classification for FRC.

To classify the post-cracking strength of FRC, it is necessary to consider the characteristic flexural residual strength values, which characterize the material behaviour at the serviceability ($f_{R,1k}$) and at the ultimate ($f_{R,3k}$) conditions. In particular two parameters are used to classified FRC material: the first one is a number denoting the $f_{R1k,}$ representing the strength interval, the second is a letter *a,b,c,d,* or *e*, that represents the $f_{R,3k}/f_{R,1k}$ ratio. The strength interval is defined by two subsequent numbers in the series: 1.0, 1.2, 2.0, 2.5, 3.0, 4.0, 5.0, 6.0, 7.0, 8.0, 10.0, 12.0, 14.0 MPa, while the letters *a,b,c,d, e* correspond to the residual strength ratios:

a if $0.5 \leq f_{R,3k}/ f_{R,1k} < 0.7$;
b if $0.7 \leq f_{R,3k}/ f_{R,1k} < 0.9$;
c if $0.9 \leq f_{R,3k}/ f_{R,1k} < 1.1$;
d if $1.1 \leq f_{R,3k}/ f_{R,1k} < 1.3$;
e if $1.3 \leq f_{R,3k}/ f_{R,1k}$.

The designer has to specify the residual strength class and the $f_{R,3k}/f_{R,1k}$ ratio as well as the material of the fibre. Fibre reinforcement can substitute, even partially, conventional reinforcement at ULS, if the following relationships are fulfilled:

$f_{R,1k}/ f_{L,k} > 0.4$;
$f_{R,3k}/ f_{R,1k} > 0.5$;

where f_{Lk} is the characteristic value of the nominal strength that corresponds to the highest stress value in the interval of 0.05 mm of CMOD, determined from a three-point bending test.

2.1.4 *Mechanical Properties of Steel Fibre Reinforced Concrete*

In fibre reinforced concrete composites, the major role played by the fibres occurs in the post-cracking zone, in which the fibres bridge across the cracked matrix. In fact, experimental results have shown the effectiveness of fibres in reducing the crack opening [Barros *et al.*, 2005; Buratti and Mazzotti, 2012]. In the cracking zone, the fibres may increase the strength of the composite over that of the matrix by providing a means of transferring stresses and loads across the crack. This implies an ascending stress-strain curve after first cracking, and this behaviour is referred to as strain hardening. Moreover, the fibres increase the toughness of the concrete by providing an energy absorption mechanism [Buratti and Mazzotti, 2012], related to the

debonding and pull-out processes of the fibres bridging the cracks [Bentur and Mindess, 2007]. The behaviour of fibre reinforced concrete before cracking is not remarkably modified by fibres. Therefore, fibres have a limited effect on the modulus of elasticity, creep, Poisson's ratio, compressive strength, and electrical conductivity [Vondran, 1991]. The advantage of using fibres is that they can prevent microcracks from propagating and thus protect the concrete members from aggressive environment and external attacks. Adding fibres to a plain concrete matrix has a little effect on its pre-cracking behaviour but does substantially enhance its post-cracking response. In accordance with Fanellana and Naaman [1985], this leads to a noticeable increase in the peak strain and a significant increase in ductility and toughness.

The mechanical properties of fibre reinforced concrete are influenced by several factors. The major properties are:

- type of fibres (the fibre material and its shape);
- length-diameter ratio (aspect ratio), l_f/d_f;
- amount of fibre in percentage by volume, V_f;
- spacing of the fibres, s_f;
- strength of the concrete matrix;
- size, shape and method of preparation of the specimen.

Zollo [1997] has observed that fibre content is one factor that significantly influences the concrete properties and the workability of freshly mixed concrete. The effect of fibre addition on concrete properties becomes more significant with an increase in fibre content.

Shah and Rangan [1971] in their research have indicated that by doubling the fibre content from 0.5% to 1.0% the concrete flexural toughness increased from five times to fifteen times that of the plain concrete. Also, the flexural tensile strength increased from 1.1 times to 1.7 times that of plain concrete. An increase, albeit smaller, has been also observed in the uniaxial tensile strength and toughness of the concrete (see Figure 2.1-5) [Shah and Rangan, 1971].

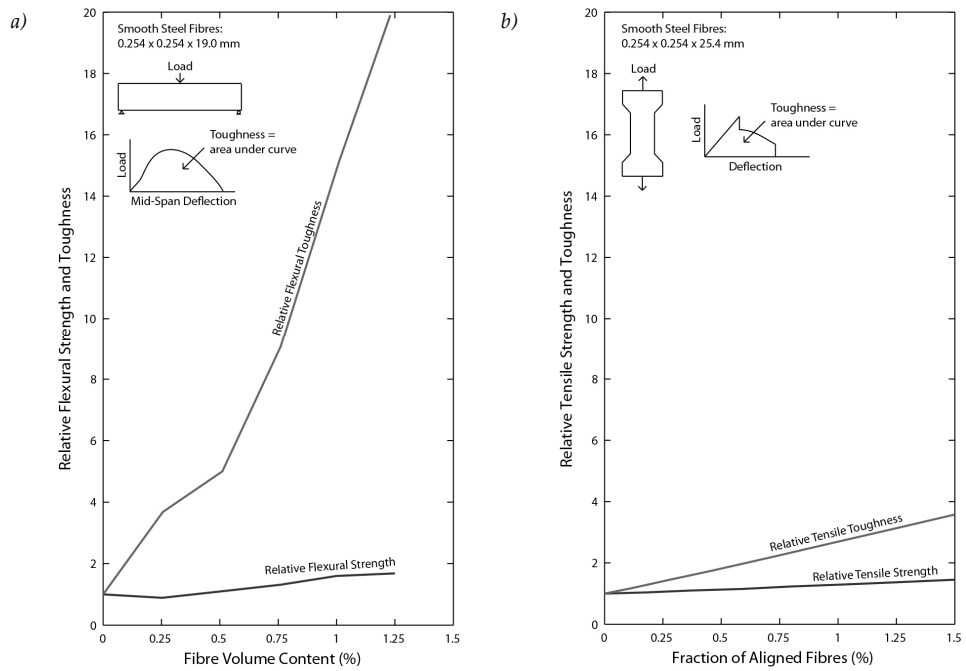

Figure 2.1-5: The influence of fibre volume content on the behaviour of SFRC: (a) flexural strength and toughness and (b) tensile strength and toughness [Shah and Rangan, 1971].

As fibres influence the performance of the FRC in all material resistance capacities, such as in compressive, flexural, direct tension and shear, it is important to evaluate the test specimen performance with regard to those parameters.

2.1.4.1 Compressive properties

The addition of steel fibres increases the strain corresponding to the peak stress but does not produce any significant changes in the compressive strength (peak stress). However, adding fibres to the concrete matrix produces a significant increase in ductility and toughness as a function of the increases in volume fraction, aspect ratios, and post-cracking characteristic of the fibres used.
Fanella and Naaman [1985] have investigated the effect of the increase in volume fraction on the stress-strain relationship of the fibre reinforced concrete through increasing the fibre volume from 0% (control) to 3% in three different mortar matrix. Moreover, for steel fibres three different aspect ratios (l_f/d_f) were used: 47, 83, and 100. Figure 2.1-6 and Figure 2.1-7 show the effect of the increase in volume fraction and aspect ratio on the compressive stress-strain curve.

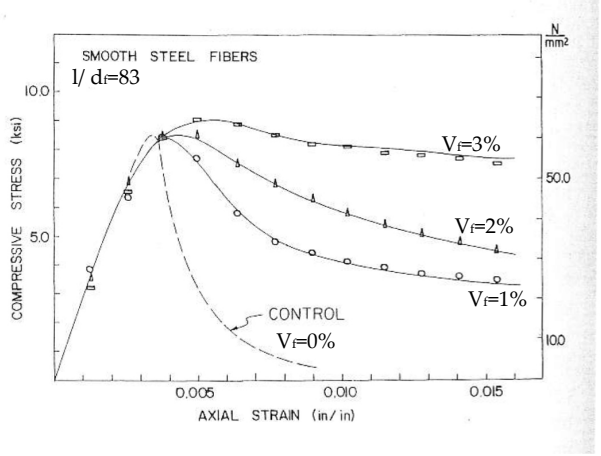

Figure 2.1-6: Influence of the volume fraction of fibres on the compressive stress-strain curve [Fanella and Naaman, 1985].

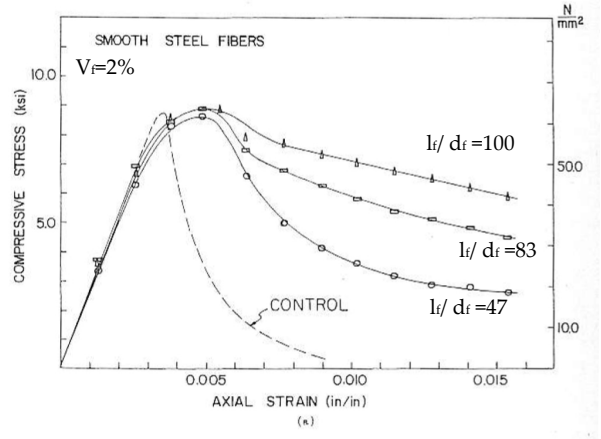

Figure 2.1-7: Influence of the aspect ratio of fibres on the compressive stress-strain curve [Fanella and Naaman, 1985].

In these curves, a substantial increase in the strain at the peak stress can be noted. The slope of the descending portion is less steep than that of control specimens without fibres. Additionally, Figure 2.1-6 and Figure 2.1-7 demonstrate that the toughness increases with the volume fraction and aspect ratio of fibres. Toughness is a measure of ability to absorb energy during deformation. It can be estimated from the area under the stress-strain diagram or load-deformation diagram.
Hsu and Hsu [1994] defined the toughness index as the ratio of the area under stress-strain curve of fibre concrete and the ratio of the area under stress-strain curve of plain concrete. Figure 2.1-8 shows the toughness index (TI) at different volume fraction of fibres.

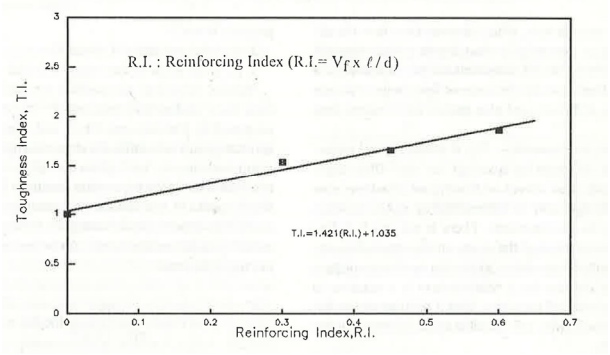

Figure 2.1-8: Variation of toughness index with reinforcing index of fibrous composite [Hsu and Hsu, 1994].

A toughness index expression derived by Figure 2.1-8 gives:

$$TI = 1.421\ (RI) + 1.035 \qquad (2.1\text{-}3)$$

where RI is the reinforcement index, which is defined as the ratio of the volume fraction of fibres and aspect ratio ($RI = {V_f}/{l_f/d_f}$).

Bencardino *et al.* [2008] in their research compared experimental results available in the literature [SorouShian and Lee, 1989; Dwarakanath and Nagaraj, 1992; Elzeldin and Balaguru, 1992; Wafa and Ashour, 1992; Barros and Figueiras, 1999; Mansur *et al.*, 1999; Nataraja *et al.*, 1999; Jo *et al.*, 2001; Campione and Mendola, 2004 ; Campione *et al.*, 2005; Bencardino *et al.*, 2007] that define the compression strength of fibre reinforced concrete. The experimental curves obtained from their investigation are similar to observed in other published test results. The addition of fibres does not significantly affect the compressive strength of concrete. In their study, it was observed that the increase in volume fraction of fibres improves the post-peak behaviour and produces a more extended softening branch. Löfgren [2005] observed that with fibres present in the matrix, the concrete become more ductile (see Figure 2.1-9), and the main effect of fibres appears to be that they offer resistance against the longitudinal crack growth.

The considerable increase in toughness and ductility of FRC implies that fibres perform an important confining action inside a loaded structural member. However, the effect of fibres is highly dependent on the type of fibre used, the size and properties of the fibres, the volume fraction added, and the properties of the matrix.

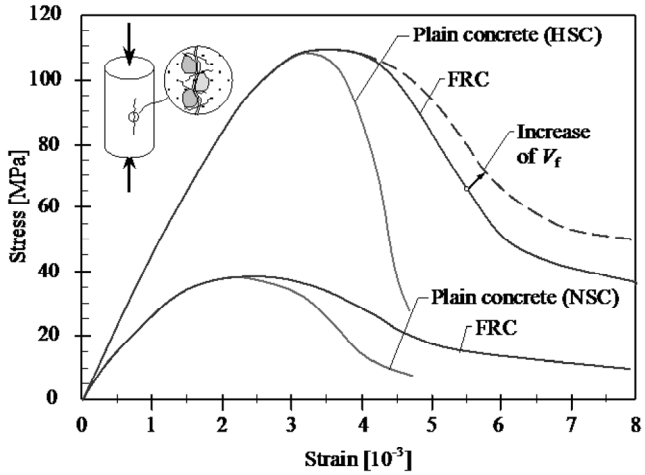

Figure 2.1-9: Schematic description of the behaviour of concrete and FRC in compression [Löfgren, 2005].

2.1.4.2 Tensile properties

It is well established that the strength of unreinforced concrete in tension reduces quickly to zero after cracking. In steel fibre reinforced concrete, the fibres are capable of bridging cracks and transmitting tensile force across them to enhance the post-cracking tensile behaviour. For fibre reinforced concrete, the most important aspect of its mechanical properties is probably the tensile behaviour. Nevertheless, no standard test exists to determine the stress-strain curve of FRC. Study by Löfgren [2005] classified the tensile behaviour of fibre reinforced concrete as either strain-softening or strain-hardening, according to one distinguishing characteristic of their stress-strain response in tension (Figure 2.1-10).
In the strain-softening case, a localised single crack occurs immediately after first cracking and, with increasing elongation, the stress after first cracking is smaller than that at first cracking. Figure 2.1-11 (a) illustrates the response in tension (stress versus elongation) of a strain-softening composite. Strain-hardening FRC composites are characterized by a stress that after first cracking increases with strain, and multiple cracking occurs up to the maximum post-cracking stress (Figure 2.1-11 (b)).

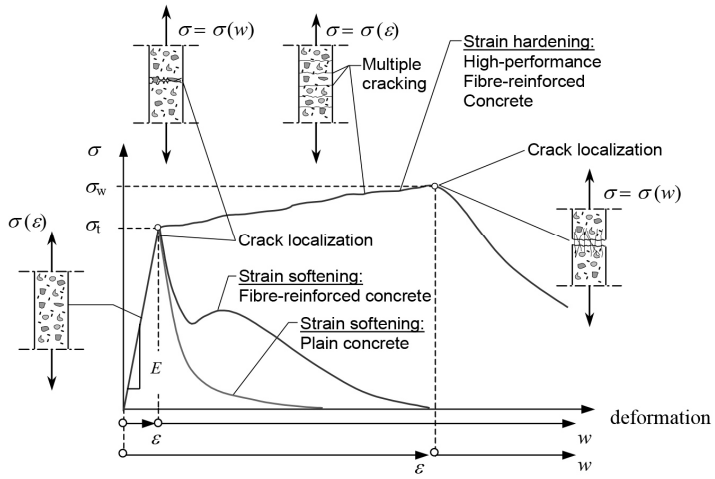

Figure 2.1-10: Classification of tensile behaviour of cement-based materials [Löfgren, 2005].

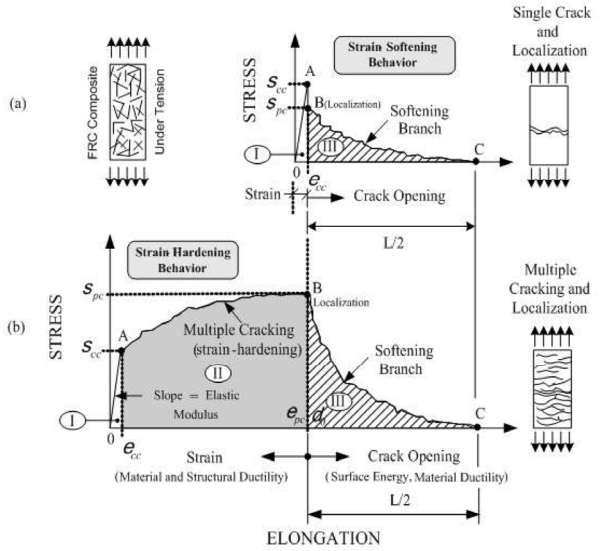

Figure 2.1-11: Typical stress-elongation curves in tension of fibre reinforced cement composites: (a) Strain-softening behaviour. (b) Strain-hardening behaviour [Naaman, 2007].

Naaman in "High performance fiber reinforced cement composites" [2008] has used the term High Performance to describe strain hardening FRC composites. In the third chapter he used the following definition:
"High Performance fiber reinforced cement composites are a class of FRC composites characterized by a strain-hardening behaviour in tension after first cracking, accompanied by multiple cracking up to relatively high strain levels."

The term "High Performance" defines the performance according to some characteristics, such as high strength or high durability. The strain hardening material, in contrast to a strain softening one, exhibits an increased load-bearing capacity after cracking. And, in addition, multiple cracking is achieved. Figure 2.1-12 shows the stress strain curve for a typical UHPFRC material tested in direct tension. Following the definition of Naaman and Reinhardt [2003], the material is strain hardening, because its tensile stress, σ_{pc} (composite tensile stress or post-cracking stress), is in excess of its cracking stress, σ_{cc} (cracking stress).
The idealized modelling approach distinguishes the tensile behaviour into three parts as follows:
Part I): *strain based elastic part*, in the strain hardening material the first cracking corresponding at a load higher than a conventional fibre reinforced concrete.
Part II): *strain based strain hardening part*, after the first cracking, in the high-performance fibre reinforced concrete, the tensile load continues to increase. This is in total contrast with what happens in strain softening materials, in which there is a significant reduction of the tensile strength after first cracking. The increase of the load after the first cracking is called strain hardening. The strain hardening phase is characterized by a diffuse multiple cracking.
Part III): *crack opening based softening part*, after the achievement of the tensile strength of the material, the load begins to decrease. The cracks continue to open, and the fibres are extracted, the matrix still presents some resistance to the opening of the cracks. This phase is called tensile softening. When the fibres are completely extracted, there is no resistance and tensile stress is equal to zero.
In a tensile strain hardening material, *Part II* is associated with multiple cracking, while *Part III* pertains to the softening curve associated with crack localization [Wille, 2014].
Figure 2.1-13 illustrates the different behaviour for a strain softening and strain hardening fibre reinforced concrete.

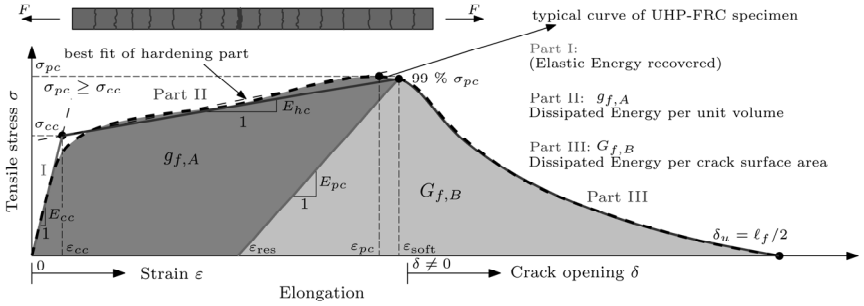

Figure 2.1-12: Strain hardening tensile behaviour of UHPFRC and idealized modelling approach [Wille at al., 2014].

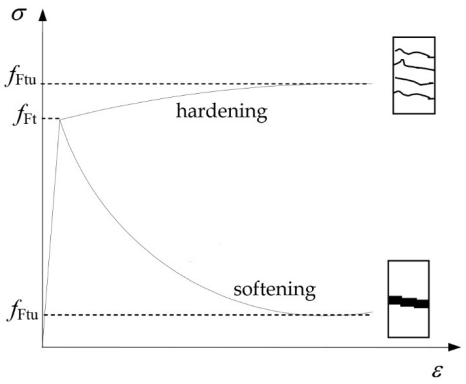

Figure 2.1-13: Tensile behaviour of fibre reinforced concrete, from CNR-DT 204/2006.

During the last decades, different methods have been proposed and used to characterise the tensile behaviour of fibre reinforced concrete. The main tests set up used are:

- uniaxial tension test;
- flexural test (three-point bending test);
- splitting tension test.

2.1.4.3 Shear properties

In reinforced concrete, the reinforcement crossing a shear plane influences the shear friction and the shear capacity due to dowel effects. Barragán [2002] observed a similar effect in FRC. For fibre reinforced concrete, at low and moderate fibre dosages the cracking strength is not affected but, as soon as the matrix cracks, the fibres are activated and start to be pulled out, resulting in a significant toughening behaviour. Fibres can reduce the amount of stirrups and congestion of reinforcement in high shear regions. Fibres do not only increase shear capacity but also provide substantial post-peak resistance and ductility.
In the past years, several studies have been carried out on the shear behaviour of FRC beams [Sharma, 1986; Mansur *et al.*, 1986; Narayanan and Darwish, 1987; Ashour *et al.*, 1992; Casanova and Rossi, 1997; Gustafsson and Noghabai, 1999; Khuntia *et al.*, 1999; Vandewalle, 2000; Meda *et al.*, 2005; Parra-Montesinos; 2006; Dinh *et al.*, 2010].
In the FRC beams without stirrup reinforcement, the fibres play a role similar to that of the stirrup reinforcement in the RC beams. Indeed, the fibres carry redistributed tensile stress and delay the propagation and opening of diagonal cracks. Additionally, they prevent premature concrete splitting along the tensile reinforcement. The steel fibres are effective in controlling crack width and fostering the formation of multiple diagonal cracks. This role is even more evident in beams made of strain-hardening, for example in UHPFRC.

2.1.5 *Fracture mechanism based material testing of FRC*

Work by Löfgren [2005] has proposed a fictitious crack model (Figure 2.1-14). The main parameters are the tensile strength, the modulus of elasticity, the fracture energy G_f and the stress–crack width relationship (σ-w).

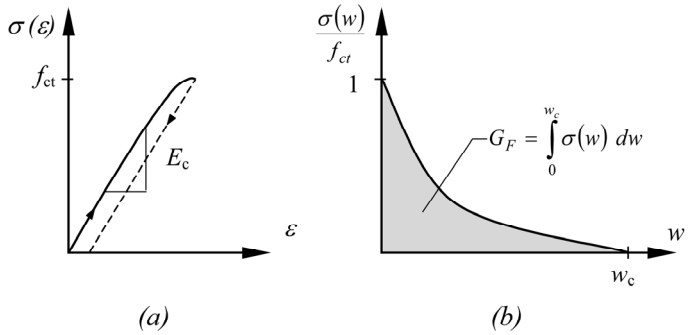

Figure 2.1-14: Description of the tensile behaviour in the fictitious crack model: a) a stress-strain curve and b) a stress crack-opening curve (where G_f is the fracture energy and wc is the critical crack opening) [Löfgren, 2005].

Study by Cunha has affirmed that the more appropriate way for determining the fracture energy, G_f, is by performing a uniaxial tension test in notched specimens, under closed-loop displacement control [2010]. Thus, the fracture energy can be computed from the following equation:

$$G_f = \int_{w=0}^{w_{lim}} \sigma(w) \cdot dw \qquad (2.1\text{-}4)$$

where w is the crack mouth opening (excluding deformation up to the peak load) and σ is the tensile stress, i.e. the load divided by the net cross section area of the specimen, whereas w_{lim} is the crack mouth opening for a null residual stress. Despite the uniaxial tension test being the most suitable test for determining fracture energy FRC post-cracking laws are generally determined through indirect methods [ASTM C496, 2004; EN 14651, 2007; Skocek and Stang, 2008; ASTM C1609, 2012].

According to research by De Montaignac *et al.* [2012], prior to cracking, the characteristic behaviour of FRC in tension is typically represented by its stress-strain response. The post-cracking tensile behaviour of reinforced concrete can be described by a stress–crack width relationship. The σ-w law is the most adequate to simulate the post-cracking behaviour of low fibre content FRC.

Study by Van Mier and Van Vliet [2002] have affirmed that the uniaxial tension test is the most fundamental test to determine the fracture properties of a material and the stress–crack width relationship. In spite of the uniaxial tension being the most suitable test for determining the fracture behaviour, the testing rigs to perform this kind of tests are not available in all laboratories. Therefore, a simpler test, such as the

three-point bending test of notched specimens and the splitting tensile test, has been used for that purpose. In the three-point bending test, the post-cracking behaviour is described by the stress versus crack opening displacement (σ-w) relationship (Figure 2.1-15).

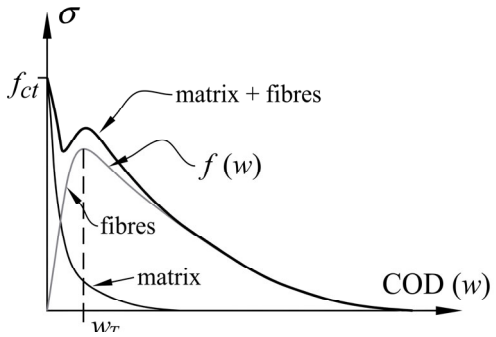

Figure 2.1-15: Stress versus crack COD for FRC [Amin et al., 2015].

The σ-w response can be obtained through a uniaxial tension test or possibly by an indirect method using three-point bending tests on prism beam specimens in conjunction with an inverse analysis. In indirect tensile tests, the σ–w response of FRC is assessed by an inverse analysis procedure that takes into account the experimental test results. This is summarized in Figure 2.1-16.

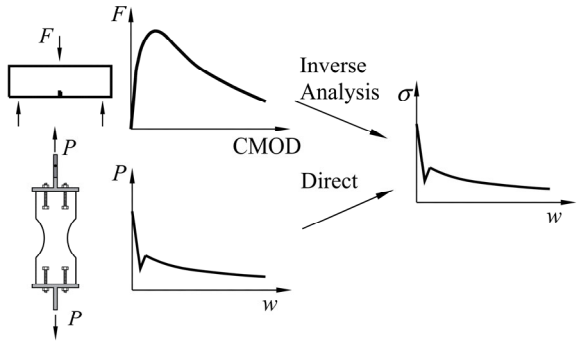

Figure 2.1-16: Approaches to determine the tensile properties of FRC [Amin et al., 2015].

Many researchers [Strack, 2008; Cunha *et al.*, 2012; Abrishambaf *et al.*, 2015] have demonstrated that the stress–crack width relationships obtained through indirect methods generally tend to overestimate the tensile strength obtained from the uniaxial tension tests.

2.1.6 *Determination of the σ-w law by inverse analysis*

The stress-crack width law of FRC is evaluated through an inverse analysis procedure, based on numerical analyses carried out by using a discrete crack approach. Inverse analysis can be used to determine a σ–w relationship from the three-point bending test and the splitting tension test.
The starting point of the inverse analysis is the assumption of a multi-linear post-cracking cohesive law, which is set inside the numerical model in order to start the calculation and to obtain the numerical flexural curve. The post-cracking constitutive laws have been obtained by comparing the numerical curve with the mean flexural experimental one, in order to achieve a maximum error of 10%. When the above reported accuracy criteria is achieved, the chosen uniaxial tensile law can be used as the actual post-cracking tensile behaviour of concrete. On the contrary, if the permissible maximum error is exceeded, the multi-linear tensile law needs to be manually refined until satisfying the accuracy criteria, according to the iterative inverse analysis procedure. The inverse analysis schematic procedure used to calculate the stress-crack width relationship from the three-point bending test is schematically is represented in Figure 2.1-17.

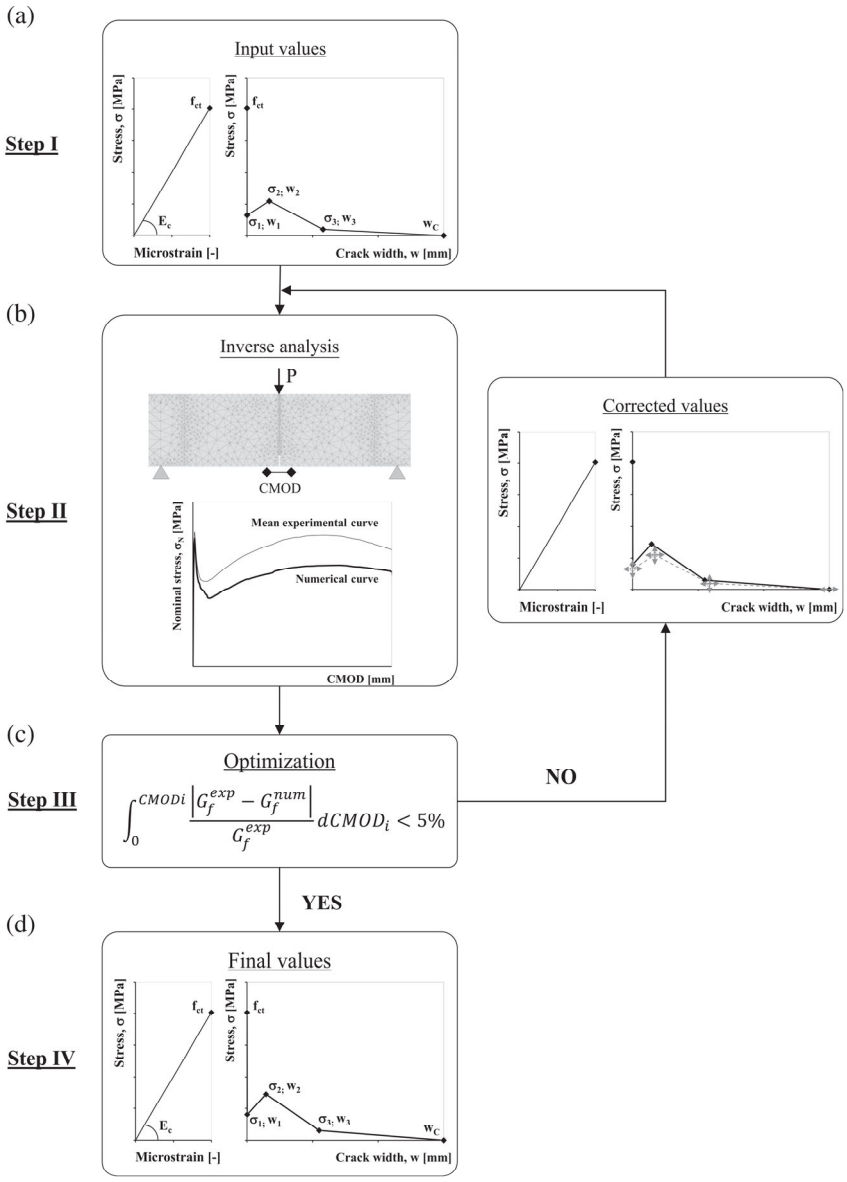

Figure 2.1-17: Inverse analysis procedure used to calculate the stress–crack width relationship from the three point bending tests: Input assumed values (a), comparison between flexural curves (numerical and experimental) and uniaxial constitutive law refinement (b), adopted accuracy criteria (c), and actual uniaxial tensile law (d) [Mudadu et al.,2019].

2.1.7 *Different fibre geometry*

There are many different types of available fibres that are used in fibre reinforced concrete. Fibres differ in their shape as well as in their materials. For FRC fibres made of steel, glass and plastic are predominantly used.
Since fibres bridge cracks and control the crack propagation in the first phase of cracking, it is important to select the right fibre in shape and material that can fulfil this task. Indeed, fibres of different geometry or material properties have a different effect on concrete behaviour.
Buratti *et al.* [2010] have investigated the behaviour of beams cast using fibre reinforced self-compacting concrete containing fibres made different materials (steel and synthetic). Their experimental campaign has demonstrated that the lowest long-term damage was obtained for the specimen containing a combination of steel fibres of different sizes and of synthetic fibres which usually employed to reduce shrinkage.
The geometry ranges from straight to irregular forms and all have their advantages as well as disadvantages. Reinforcing fibres can be found in different shapes. In general, the cross-section of an individual fibre can be circular, rectangular, triangular, polygonal, irregular or varying shape. They may be straight or bent, and come in various lengths [Shah *et al.*, 1988]. Many types of fibres have been investigated in the last years. Figure 2.1-18 presents some typical profiles of steel fibres commonly used in concrete technology.

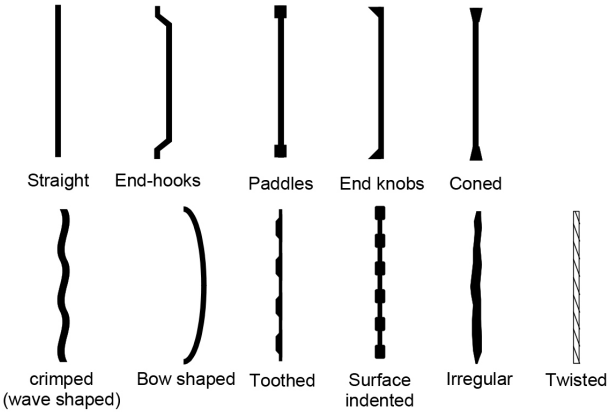

Figure 2.1-18: Examples of some typical fibre geometries [Löfgren, 2005].

Shah *et al.* [1978] have established that the different shape of fibre has effect on the tensile stress behaviour of FRC in direct tension. Figure 2.1-19 show the stress-strain curves. The descending portions of the plots prove that fibres with enhanced anchorage quality increase the tensile resistance of the fibre concrete beyond the first cracking load.

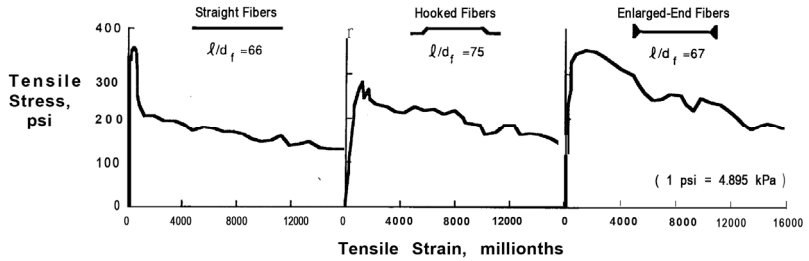

Figure 2.1-19: Stress-strain curves for steel fibre reinforced mortars in tension (1.73 percent fibres by volume) [Shah et al., 1978].

A combination of different typologies of fibres was investigated by Meda *et al.* [2004]. In Figure 2.1-20 depicts the experimental behaviour of specimens made of plain concrete and FRC with different typologies of fibres.

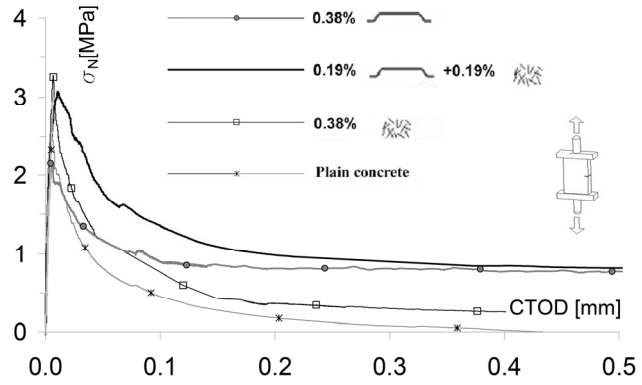

Figure 2.1-20: Nominal stess-CTOD curves for different FRC material under uni-axial tensile tests [Meda et al., 2004].

Hybrid combination of long and short steel fibres improves concrete toughness for both small and large crack opening displacements. In addition, other synergic effects from the combination of macro and micro fibres, such as the reduction of shrinkage cracking, can be attained for short-term and long-term behaviour of structures. Meda *et al.* [2004] have also developed non-linear analyses. They defined a tension softening relationships (stress-crack opening law σ-w) for the different materials investigated. Figure 2.1-21 illustrates the response of the material due to the combination of macro and micro fibres.

The strength of steel fibre reinforced concrete in direct tension is generally of the same order as that of unreinforced concrete, i.e., 300 to 600 psi (2 to 4 MPa) [ACI COMMITTEE 544, 1999].

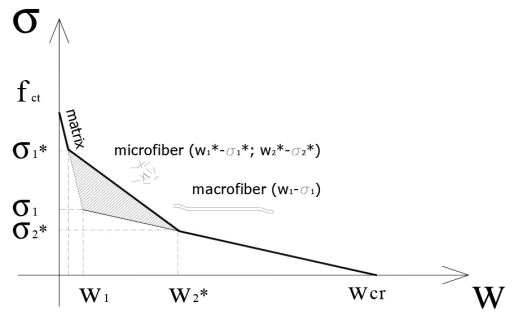

Figure 2.1-21: Softening law by bi-linear or tri-linear curve [Meda et al., 2004].

2.2 Strengthening RC elements with UHPFRC

2.2.1 *Introduction*

Over the last few years, efforts to improve the behaviour of cementitious materials by incorporating fibres have led to the emergence Ultra-High Performance Fibre Reinforced Concrete (UHPFRC). The UHPFRC are characterized by a strain-hardening behaviour in tension, and high compressive strength as well. Additionally, the UHPFRC possesses other excellent mechanical properties like high flexural and tensile strength, high fracture toughness, ductility, and high durability [Schmidt and Fehling, 2005].

The research carried out in the area of rehabilitation using UHPFRC as retrofitting material has two main motivations. First, it is aimed at solving the durability and aging problems, prolonging the service life of the structure [Ferrara, 2019]. Second, it aims to improve the strength and structural efficiency. These innovative building materials provide numerous properties. Among these are the main ones: an extremely low permeability that prevents the ingress of detrimental substances such as water and chlorides, a high strength including compressive strengths higher than 150 MPa, and tensile strengths higher than 10 MPa [Brühwiler and Denarié, 2013]. The tensile behaviour shows significant strain hardening and softening behaviour. The concept to use UHPFRC is an idea that combines efficiently the protection and resistance properties of UHPFRC. The structural performance in terms of durability and life-cycle costs of the rehabilitated concrete structure significantly improves. Additionally, the use of fibres in the retrofitting concrete layer helps control the shrinkage cracking.

UHPFRC is applied on existing reinforced concrete elements as thin watertight overlays, as reinforcement layers and often combined with reinforcement bars (R-UHPFRC). Actually, adding of steel reinforcing bars results in a significant improvement of the tensile behaviour of reinforcement layers of UHPFRC. The small diameter steel reinforcing bars (arranged with relatively small spacing) provide in-

plane continuity to the UHPFRC layer and assure a monolithic behaviour with the RC element in flexural members [Habel, 2004; Oesterlee, 2010]. The reinforcing bars enhance the tensile behaviour of UHPFRC. In fact, the rebars not only increase the resistance but also improve the deformation capacity and the strain-hardening behaviour of UHPFRC.

2.2.2 *Strengthening RC columns*

Various techniques are proposed for the seismic retrofitting of RC columns [fib Report, 1991; fib Bulletin n. 14, 2001; fib Bulletin n. 24, 2003; fib Bulletin n. 35, 2006;]. Regarding the strengthening of existing columns, the possibility of using RC jackets is usually considered, mainly when the elements are made of low strength concrete. The jacketing in reinforced concrete presents some inconvenience, due to the jacket thickness being governed by the steel cover (both external and internal). This often leads to a jacket thickness higher than 70–100 mm [fib Bulletin n. 24, 2003]. The increase of the section geometry leads to an increase of both mass and stiffness. Consequently, it requires special attention with respect to the overall seismic response of the retrofitted structure. This aspect is particularly important when small columns have been considered (e.g., 250-300 mm width).
In recent years, the techniques of retrofitting of existing structures, in particular the jacketing of reinforced concrete columns, are based on the use of thin jackets made with UHPFRC. This technique consists of encasing structural concrete elements in a thin layer of UHPFRC (30-40 mm). The existing concrete surface must to be previously sandblasting. No bonding agent is usually needed due to the high bond properties of the UHPFRC material. The main aim of the retrofit intervention is to increase the column durability in addition to restoring the original bearing capacity. Beschi *et al.* [2011] in their research have demonstrated the efficiency of the UHPFRC jacketing technique. The authors have shown that with the application of a UHPFRC jacket it is possible to increase the bearing capacity of a column, reaching also an adequate level of ductility.
Meda *et al.* [2016] investigated the possibility of repairing and strengthening corrosion damaged columns with UHPFRC jacketing. The authors performed a full-scale tests on RC columns under cyclic loads. The load–drift diagrams obtained of the specimens are compared in Figure 2.2-1. The results showed that by applying a high performance jacket it is possible to increase the bearing capacity of the column with corroded rebars. Moreover, the results have shown that the maximum strength reached is greater than the one of the undamaged element. The authors reported that this technique is suitable for strengthening existing RC structures characterized by low reinforcement ratio, low concrete strength, concrete damage and reinforcement corrosion. Additionally, the use of a high performance concrete layer can protect the internal column and increase its durability.

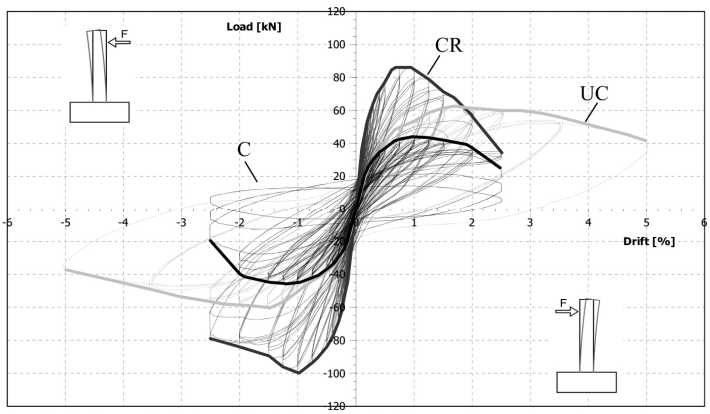

Figure 2.2-1: Load–drift relationship: comparison. UC (un-corroded), C (corroded) and CR (corroded and repaired) [Meda et al., 2006].

2.2.3 *Strengthening RC beams*

Previous works have studied the possibility of using concrete materials with tensile hardening behaviour, such as Ultra-High Performance Fibre Reinforced Concrete, for strengthening RC beams.
In order to validate the effectiveness of the proposed solution, Alaee and Karihaloo [2003] investigated a UHPFRC material to retrofit damaged concrete flexural elements using various strengthening configurations. Table 2.2-1 summarises the results of four-point bending tests. The results show an increase in the failure load of the retrofitted beams for all strengthening configurations.

	Retrofit Pattern	Thick. [mm]	Beam No	Failure load P_u [kN]	Increase in P_u [kN]	Failure mode
Control Beams	-	-	*#1*	40.47	-	Flexure
			#2	43.20	-	Flexure
			#3	42.42	-	Flexure
Retrofitted Beams		16	*#1*	48.90	16%	Flexure
			#2	52.38	25%	Flexure
		20	*#1*	56.75	35%	Flexure
			#2	59.44	41%	Flexure
		16	*#1*	52.42	25%	Flexure
			#2	50.79	21%	Flexure
		20	*#1*	50.29	20%	Flexure
			#2	49.47	18%	Flexure
		16	*#1*	74.04	76%	Flexure
			#2	78.55	87%	Flexure
		20	*#1*	74.77	78%	Flexure

Table 2.2-1: Test Results (Four-Point Bending) [Alaee and Karihaloo, 2003].

Martinola *et al.* [2007] examined full-scale experimental tests on beams. The beams were strengthened with a jacket in UHPFRC, as shown in Figure 2.2-2.
From the results obtained in their study the authors concluded that the application of a layer of UHPFRC remarkably increases the maximum load (2.15 time, as shown in Figure 2.2-3). Moreover, the strengthening layer provided a remarkable stiffness increase. As a consequence, the midspan displacement at service conditions was reduced by about a factor of 12.

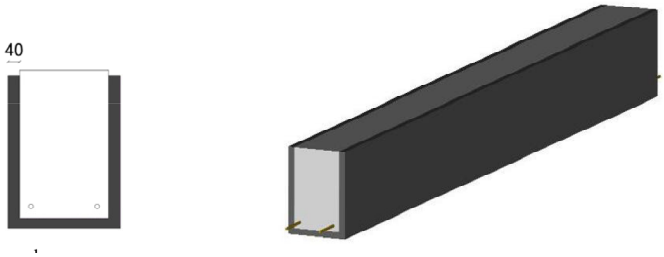

Figure 2.2-2: Strengthened with a jacket in UHPFRC [Martinola et al., 2007].

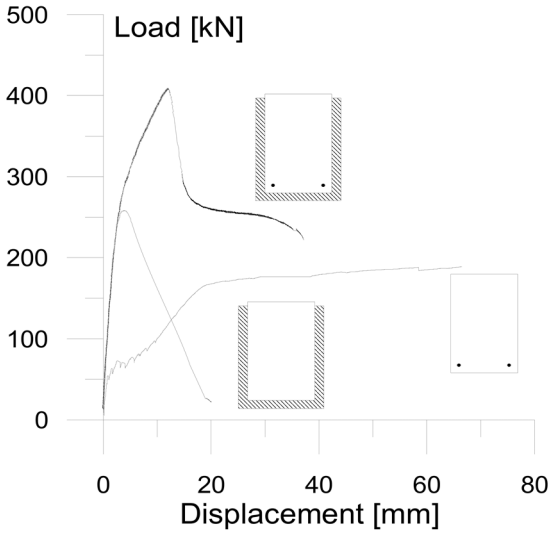

Figure 2.2-3: Comparison between the experimental results [Martinola et al., 2007].

Jacket reinforcement with UHPFRC is also used for the repair of damaged RC beams. Martinola *et al.* [2010] investigated this reinforced technique. Their experimental test demonstrated that the use of UHPFRC for the repair of a damaged RC beam allows an increase of its bearing capacity (1.90 times compared to RC beam).
Noshiravani and Brühwiler [2013] presented an experimental study on a series of composite beams combining a reinforced concrete element and a reinforced UHPFRC element. The experiment tests showed that R-UHPFRC members have a significantly higher stiffness and ultimate resistance than their RC elements alone.

The additional R-UHPFRC reinforcement may increase the ultimate resistance to up to 2.77 times that of the RC beam. The in-plane and the out-of-plane resistance of R-UHPFRC elements contributed to the member shear resistance. The specimens with the wide stirrup spacing should have failed in shear at a much lower resistance, in according to the models for RC beams. Instead, the presence of the R-UHPFRC element allowed most of specimens to reach the bending capacity. Hence, according the authors, the addition of a tensile R-UHPFRC reinforcement may be used as an effective shear strengthening method. The experimental study by Noshiravani and Brühwiler [2013] proved that R-UHPFRC element contributes to the resistance of UHPFRC -RC members by three different means. First, the bending resistance of the R-UHPFRC elements allows the element to carry a part of the shear stresses, which are introduced into the element by the prying action of RC segments formed by diagonal flexure-shear cracks. Second, the R-UHPFRC elements control the widening of a flexure-shear collapse crack in the RC element, thus improving the contribution of concrete to the shear resistance. Third, the crack induced debonding zone (ICD zone) between the elements modifies the stress fields in the member and lowers the intensity of the stresses that need to be carried across the flexure-shear collapse cracks. The authors observed that for UHPFRC-RC members with a flexure-shear failure, the deflection is between 80 and 90% of their matching RC specimen. This is especially important considering that the flexure-shear resistances of these UHPFRC-RC beams are 2.0 to 2.3 times that of the latter. The measured crack widths indicate that concrete carries only a minor part of the shear stresses. The increase in rotation capacity is due to the formation of the ICD zone.

Ruano *et al.* [2014] confirmed that use of fibre reinforced concrete jacketing looks like an efficient method for the shear strengthening of reinforced concrete beams with stirrups. Their experimental studies demonstrated that the repaired beams with high strength concrete and high strength fibre reinforced concrete increased the load bearing capacity. In most cases, the beams repaired with fibre reinforced concrete presented greater strength than the original beams. The authors concluded that fibre reinforced concrete jacketing seems to be an efficient shear repairing method for reinforced concrete beams with stirrups. The percentage of load bearing recovery is dependent on the severity of previous damage.

In another study, Lampropoulos *et al.* [2016] investigated different technique of retrofitting. The locations of a layer of UHPFRC that were considered are the following: on the compression side (CS), on tension side (TS) and in three-side jacketing (3SJ). The result shows that the strengthened beams exhibited superior performance (Figure 2.2-4 and Figure 2.2-5).

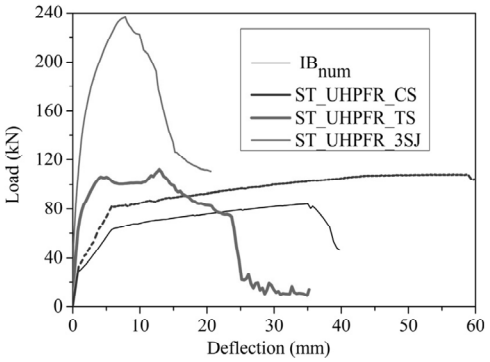

Figure 2.2-4: Numerical results for strengthened beams and for the Initial Beam (IB) [Lampropoulos et al., 2016].

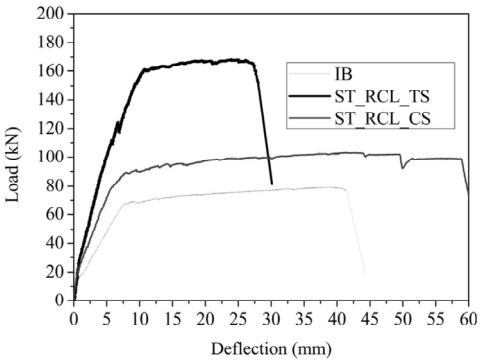

Figure 2.2-5: Load–deflection results for IB, ST_RCL_TS and ST_RCL_CS [Lampropoulos et al., 2016].

According to results, Lampropoulos *et al.* [2016] reported that strengthening RC beam specimens with UHPFRC showed an increased yielding and ultimate moment capacity for all strengthened specimens.

Al-Osta *et al.* [2017] carried out an experimental and analytical study on the flexural strengthening of RC beams using UHPFRC. The authors observed that the strengthening techniques increased the cracking load of the beam specimens. The UHPFRC jacketing decreased the number and spread of cracks along the span and reduced the crack width openings. In addition, the flexure-shear cracks, observed towards the supports in the case of RC-Control, were eliminated; thus, the shear strength of the beam section was enhanced, mainly with the UHPFRC jacket provided on the sides of the beam. Figure 2.2-6 shows that with increased use of UHPFRC as part of the tensile retrofit, a resulting loss of ductility was observed. In fact, the enhancement of strength resulted in a decrease of beam ductility, ending with an unsolicited softening mode of failure.

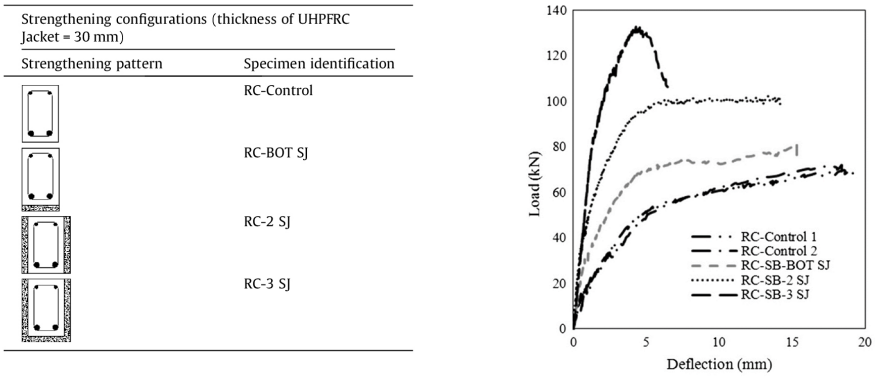

a) *b)*

Figure 2.2-6: a) Strengthening schemes of beams specimens; b) Load-deflection behaviour of beam specimens [Al-Osta et al., 2017].

The authors observed that decrease of the ductility is qualitatively similar to the behaviour of over-reinforced concrete beams. Increasing amounts of tension effective UHPFRC in the configurations adopted led to a sudden and softening type of post-peak failure mode in the case of the 3-sided jacketing.

The use of jackets made of UHPFRC for the strengthening of existing RC beams resulted in a significant increase in the structured resistance [Alaee and Karihaloo, 2003; Martinola *et al.*, 2007; Martinola *et al.*, 2010; Noshiravani and Brühwiler, 2013; Ruano *et al.*, 2014; Lampropoulos *et al.*, 2016; Al-Osta *et al.*, 2017]. As a drawback, however, reduced ductility has been observed.

Mostosi *et al.* [2011] proposed an enhancement of this technique, obtained by adding a high strength steel mesh in the jacket with the aim to increase the ductility. The solution is based on the use of a high performance jacket made of high strength steel mesh, having high tensile resistance, embedded in a thin layer of UHPFRC. In order to validate the effectiveness of the proposed strengthening technique, a four point flexural experimental test was carried out. The results of the experimental test (Figure 2.2-7) show that the use of a very thin UHPFRC jacket allows an increase in beam ultimate resistance. Additionally, and perhaps more importantly, the proposed technique allows one to largely increase the structure deformation capacity and ductility, which are the main objectives of every seismic strengthening design. The applied jacket increases the shear capacity and alters their brittle failure mode to a more ductile one.

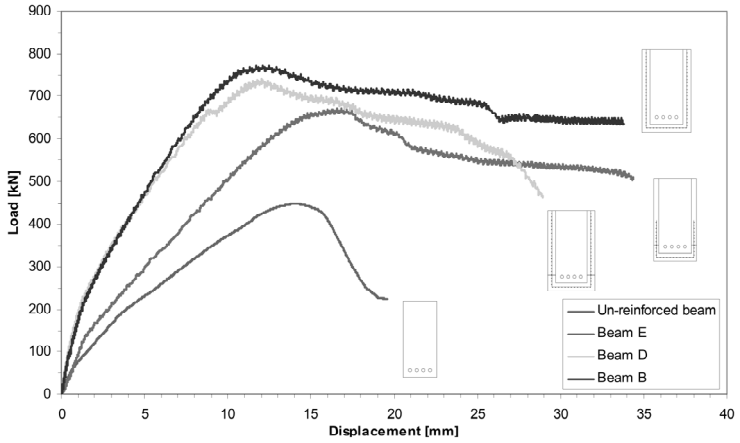

Figure 2.2-7: Load– Midspan displacement results: comparison of the result [Mostosi et al., 2011].

Another research [Chalioris and Pourzitidis, 2012] studied the application of small diameter steel bars and U-formed stirrups. In this study reinforced, a self-compacting concrete jacketing technique was used. The jackets encased the bottom width and both vertical sides of the beams including the small diameter steel bars and the U-formed stirrups. Test results indicated that the strength and the overall performance of the jacketed beams was ameliorated with respect to the initial specimens; thus this jacketing technique is a promising rehabilitation method (Figure 2.2-8).

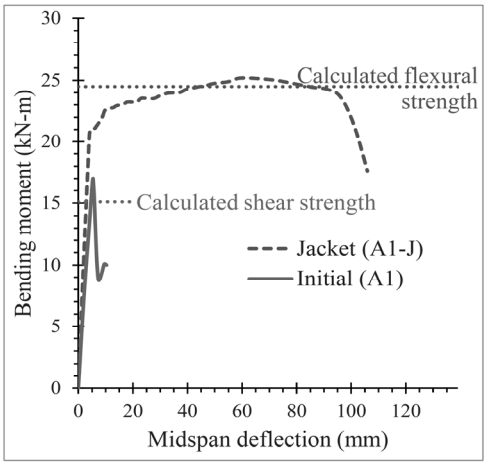

Figure 2.2-8: Experimental behavior of the initially tested and the jacketed beams and predicted values of ultimate flexural and shear capacities [Chalioris and Pourzitidis, 2012].

The mentioned experimental studies [Mostosi *et al.*, 2011; Chalioris and Pourzitidis, 2012] have shown that by adding a steel mesh in the jacketing the ductility is improved. The same technique was validated by Marini and Meda [2009]. Their solution is based on the use of a high performance jacket made of high strength steel mesh, embedded in a thin layer of high performance concrete. The study confirms the efficiency of the proposed solution in significantly increasing the structure resistance, deformation capacity and above all the ductility.

2.2.4 *Strengthening RC beam-column joints*

Reinforced concrete exterior beam-column joints with deficiency in resisting shear have been identified as the vulnerable and critical zone of RC frame structures when they are subjected to the large cyclic lateral loads (i.e., seismic loading). During large seismic activity, the beam-column joint region is subjected to very high shear stresses as compared to the adjoining structural members. These joint shear stresses and the axial stresses in a column lead to the development of principal tensile and compressive stresses in the joint core, which result in the formation of diagonal cracking and crushing of concrete in the joint region. In this way, joints behave like stress concentration points in RC frames. Therefore, beam-column joints should be designed to resist shear stresses in order to maintain the overall integrity and stability of the structures. Modern design codes enforce what is commonly referred to as "capacity design", whereby a strength hierarchy is maintained such that a ductile beam-sway mechanism develops [Park and Paulay, 1975]. Since older design codes did not enforce these capacity design requirements, many buildings possess weak storey's that are vulnerable to developing a nonductile column sway collapse mechanism. Therefore, the development of repair and strengthening techniques has become an important and urgent issue. UHPFRC can be used for repairing and strengthening of RC elements. The effectiveness of a UHPFRC jacket for the seismic retrofitting of existing RC corner beam-column joints was experimentally investigated in the last few years.

Beschi *et al.* [2015] confirmed that application of thin UHPFRC jackets appears a promising technique to strengthen poorly-detailed RC joints. The authors presented and discussed in detail, focusing on the effectiveness of the adopted retrofitting technique. The experimental results in un-retrofitted subassemblies showed significant shear damage of the joint panel region and the slip of the beam bars in the joint with the expulsion of a concrete wedge due to the thrust action of the hooks in compression. The application of UHPFRC thin jacketing has been able to shift the brittle joint shear failure to a more ductile beam flexural failure. The damage of the retrofitted subassembly has been limited to the joint-beam interface with diagonal crack width in the panel. The UHPFRC jacket has efficiently confined the joint avoiding the wedge concrete expulsion due to the thrust of the hooked-end

anchorages. Moreover, the proposed technique has significantly improved the displacement capacity of the beam-column joint sub-assembly. For the un-retrofitted test units, three failure mechanisms were clearly identified: beam failure with the vertical crack at the beam-joint interface, joint shear failure with the diagonal cracks in the panel zone, and the thrust of the hooked end beam bars in the column at the bottom of the joint (Figure 2.2-9 (a) and (b)). For the retrofitted test units, the damage localized mostly in the crack at the beam-joint interface (Figure 2.2-9 (c) and (Figure 2.2-9d)).
Figure 2.2-9 shows the un-retrofitted (Figure 2.2-9 (a) and (b)) and retrofitted test units at failure (Figure 2.2-9 (c) and (Figure 2.2-9d)). It is clear that for the retrofitted test units, the damage localized mostly in the crack at the beam-joint interface.

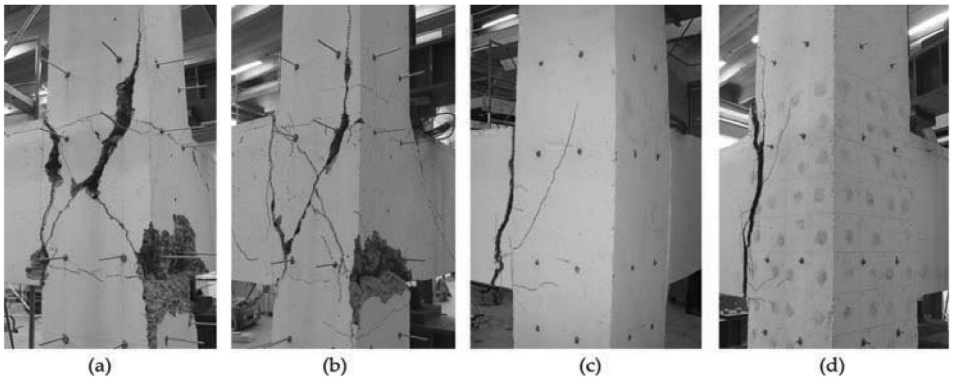

Figure 2.2-9: The test units at the end of the tests: (a) CJ1; (b) CJ2; (c) RCJ1; and (d) RCJ2 [Beschi et al., 2015].

Study by Khan *et al.* [2018] reported beam column joints strengthened by 30 mm thick UHPFRC jacket. The analysis of test results showed that the method of strengthening has been highly effective in terms of shear capacity, deformation capacity, stiffness characteristics and energy dissipation capacity. Figure 2.2-10 illustrates the damage evolution in the all beam column joints specimens. Khan *et al.* [2018] concluded that the UHPFRC jacket successfully confined the beam-column joint. Indeed, the jacket has provided a significant increase in strength, over the reference specimen. This is mainly due to the high level of confinement provided by the UHPFRC jacket at the joint region and the high mechanical properties of UHPFRC. Due to its ability to distribute the stresses, the UHPFRC layer developed fine cracks before the development of major cracks. The crack bridging ability is due to the presence of the steel fibres, excellent ductility, and strain hardening behaviour under tensile stresses.

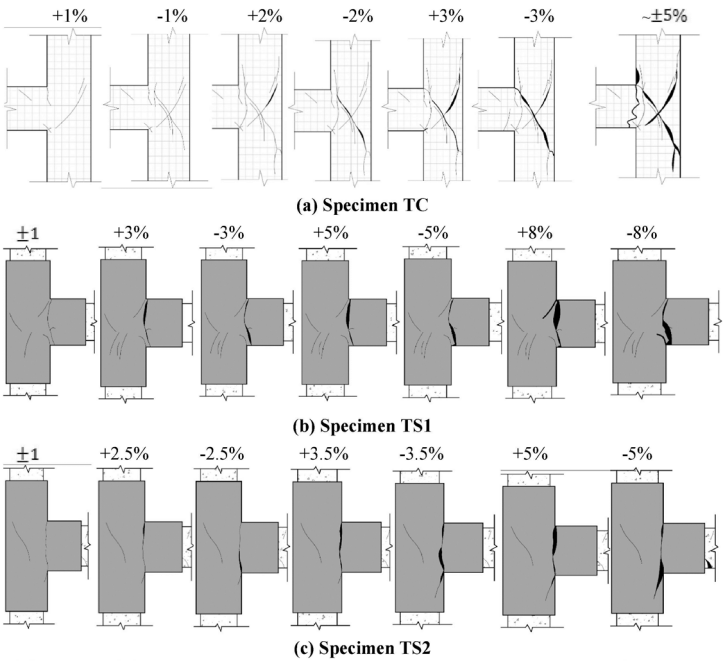

Figure 2.2-10: Damage evolution in beam column joints specimens: TC: un-retrofitted specimen, TS: retrofitted specimens [Khan et al., 2018].

Del Vecchio *et al.* [2018] investigated the experimental behaviour of old-style RC beam-column joints extracted from a real building damaged. Their study proposed an innovative application of FRC thin jacketing of the joint panel. Before the jacketing concrete cover was removed using a jackhammer. This procedure resulting in a high roughness of the concrete substrate, improving the bond with the FRC jacketing. The proposed strengthening solution significantly increased the performance of the tested subassembly. The jacketing resulted in a significant increase in terms of shear strength. Del Vecchio *et al.* believe that this solution could be a viable and resilient alternative to the classic RC jacketing or concrete cover replacement before the application of an externally bonded FRP system in the case of poor-quality concrete substrate.

2.2.5 *Strengthening of slabs*

Floor diaphragms may provide an effective solution for reducing the seismic vulnerability of masonry buildings. Unfortunately, diaphragms are usually not present in old RC buildings where floors have been made without shear reinforcement. The solution of the ordinary concrete slab can be easily applied to irregular shaped floors and is fairly economical. In this reinforced technique the in-plane shear resistance is provided by the steel mesh embedded in the slab [Giuriani and Frangipane, 1993]. The thickness of the slab depends on the height of the mesh and of the concrete cover and is usually equal to 50-60 mm. As major drawbacks, the solution of the concrete slab can significantly increase the self-weight and the seismic action; furthermore, the placement of the steel mesh requires labour time and is expensive. The use of high performance concrete, combined with a thin cold formed wire steel mesh, enables halving the thickness of the slab and it is acknowledged as a recent improvement of the concrete slab technique [Meda and Riva, 2001]. Nevertheless, the construction issues related to the placement of the steel mesh still remain. In order to remove the steel mesh some suitable solutions may be obtained by means of FRC or UHPFRC. The use of UHPFRC can significantly decrease the diaphragm thickness, with the major advantage of limiting the additional dead loads and seismic actions. The substitution of the traditional steel mesh with steel fibres allows a duction the slab thickness by overcoming the construction issues, which are typical of the traditional RC solution, and which are related to the mesh placement and to the required minimum cover. The diaphragm thickness can be minimized by increasing the fibre content [Marini *et al.*, 2008]. Some examples of application of UHPFRC thin layers for strengthening RC elements are already present in the literature. For instance, RC slabs have been successfully repaired by placing a thin UHPFRC layer at the upper surface of the bridge deck [Denarié, 2005; Makita and Brühwiler, 2012; Brühwiler *et al.*, 2015].

In the last years, experimental programs, supported by analytical and numerical studies, have investigated the feasibility and the effectiveness of FRC diaphragms [Marini *et al.*, 2008; Zanotti *et al.*, 2009; Marini *et al.*, 2010; Naghibdehi *et al.*, 2014]. These researches demonstrated the efficiency of UHPFRC thin layers for strengthening RC slabs.

Naghibdehi *et al.* [2014] studied nineteen slabs under flexural loadings. Their study examined rehabilitation of slabs with reinforced concrete, polypropylene fibre reinforced concrete and with steel fibre reinforced concrete. The authors investigated the fibrous material effects on the initial crack force, the maximum loading carrying capacity, the absorbed energy and the ductility. Among the results that emerged, the use of FRC layers leads to increases in load-carrying capacity, ductility and absorbed energy.

UHPFRC layers may be used to repair and strength RC slabs damaged by fire. Studies have evaluated the possibility of adopting UHPFRC jacketing technique for the repair of fire damaged elements [Haddad *et al.*, 2007; Haddad *et al.*, 2011].
Haddad *et al.* [2011] investigated the behaviour of slabs heat-damaged and repaired with UHPFRC layers. A slab's exposure to an accidental fire may result in cracking and loss in the bearing capacity. Repair of heat-damaged high strength slabs would be the only solution, mainly when damage is limited, and the cost of demolishing and rebuilding is more expensive than that of repair. The research showed that the repair techniques proposed may be considered as promising methods for restoring the flexural capacity of heat-damaged RC slabs. Actually, the slabs repaired with UHPFRC layers regained fully the first cracking load. Moreover, the stiffness was increased and corresponding mid-span deflections at ultimate load decreased.

2.2.6 *Strengthening of bridges*

Ultra-High Performances Fibre Reinforced Concretes are characterised by an extremely low permeability and outstanding mechanical properties. These characteristics make UHPFRC suitable for locally "harden" reinforced concrete structures subjected to aggressive environments and/or mechanical stresses, such as bridge decks, bridge piers or crash barrier walls on highway bridges.

2.2.6.1 Retrofitting of a bridge deck

Since 2004, UHPFRC has been utilized in Switzerland on existing RC structures: on bridge deck slabs as thin watertight overlays (in replacement of currently used water-proofing membranes) as well as on bridge and building slabs as reinforcement layers in UHPFRC. This layer provides structural resistance capacity for bridge elements and slabs in buildings without increasing the dead load of the structure.
Figure 2.2-11 illustrates schematically the concept of application of UHPFRC for the rehabilitation of bridge deck. An "everlasting winter coat" is applied on the bridge superstructure in zones of severe environmental and mechanical loads.

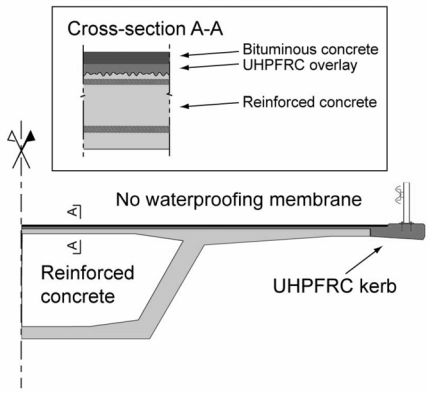

Figure 2.2-11: Concept of application of the local "hardening" of bridge superstructures with UHPFRC [Brüwhiler et al., 2004; Brüwhiler et al., 2005; Brüwhiler et al., 2005].

The first field application of the rehabilitation of a bridge deck, using UHPFRC, was carried out on a bridge with a span of 10 m over the river la Morge, in Chateauneuf/Conthey in the Swiss Alps in 2004 [Brühwiler and Denarié, 2008]. The intervention consisted of casting a layer of UHPFRC on top of the deck slab with the objective of improving the durability and restoring the structural safety. The bridge was severely damaged by chlorides that induced the corrosion. Considering its design, geometry and condition it was assumed that the date of construction of the bridge was from the period between 1940 and 1950. The upper deck surface of the bridge was rehabilitated with 3 cm of UHPFRC.

Numerous more applications following the same principle have been conducted in recent years. Brühwiler and Denarié [2013] presented another study on the rehabilitation and strengthening of bridges using UHPFRC. In their research the authors discussed an application in Switzerland on existing RC structures on bridge deck slabs as thin watertight overlays (in replacement of currently used waterproofing membranes) as well as on bridge and building slabs as reinforcement layers in UHPFRC.

In 2012, the Chillon viaduct (Figure 2.2-12), located on the shores of Lake Geneva near Montreux in Switzerland, was retrofitted using UHPFRC [Brühwiler *et al.*, 2015]. The slabs were strengthened by adding a layer of 40 mm of a UHPFRC reinforced with steel rebars. Figure 2.2-13 illustrates the typical composite cross section.

Figure 2.2-12: Chillon viaducts along Lake Geneva [Brühwiler et al., 2015].

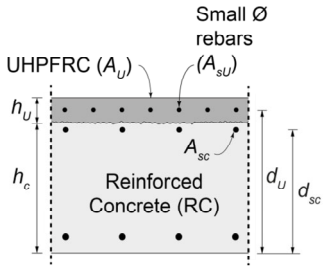

Figure 2.2-13: Typical composite cross section [Brühwiler et al., 2015].

Large experimental campaigns have been carried out on full-scale composite elements such as beams and slabs to characterize the properties of UHPFRC materials and the structural behaviour of R-UHPFRC–RC composite structural members. Based on the results, Brühwiler *et al.* [2015] developed analytical models to calculate the bending, shear or fatigue resistance of a composite element. Their models were used to design the UHPFRC strengthening of the Chillon viaducts.
Several experimental studies [Brühwiler and Denarié, 2003; Alaee and Karihaloo, 2003; Oesterlee, 2010] have shown that with good surface preparation, in pure bending, no debonding occurs between the concrete section and the UHPFRC layer. Thus, the composite section has a monolithic behaviour up to maximum resistance. The transversal bending resistance of the deck slab can thus calculate using plane-section analysis. Figure 2.2-14 shows plane-section analysis UHPFRC in tension due to negative bending moments.

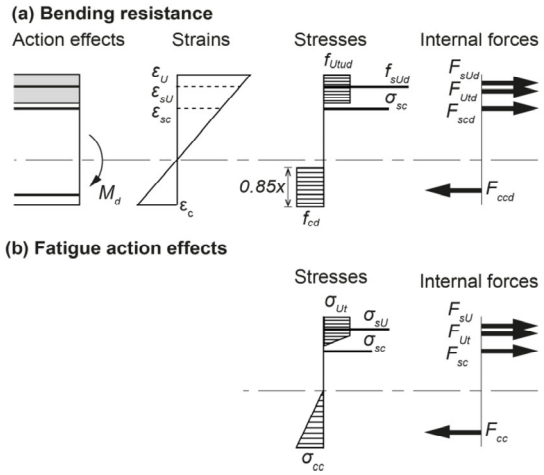

Figure 2.2-14: Plane section analysis: (a) bending resistance (adapted from Habel et al. [2006]; (b) fatigue action effects.

Tests on composite beams [Noshiravani and Brühwiler, 2013] have shown that the addition of a layer of UHPFRC delays the formation of the inclined shear crack in the concrete section. In fact, the layer of UHPFRC modifies the failure mode from brittle shear failure to a ductile flexural failure mode. The shear resistance v_{Rd} of the composite element is calculated as a combination of the concrete contribution v_{Rc}, shear steel reinforcement contribution v_{Rs} (if the concrete structures have a shear reinforcement) and the UHPFRC contribution v_{RU}:

$$v_{Rd} = v_{Rc} + v_{Rs} + v_{RU} \qquad (2.2\text{-}1)$$

The contribution from concrete thus depends on its compressive strength f_{cd} and on the angle of the inclined shear crack α_c. The widening of the inclined crack in the concrete section creates a prying action on the UHPFRC layer which resists by bending out of plane in double curvature. This is accompanied by a softening of the concrete in the concrete volume under the UHPFRC layer called Intermediate Crack induced Debonding zone (ICD). The contribution of UHPFRC to the shear resistance is thus a function of its bending resistance m_U in double curvature over the length of the ICD zone l_z:

$$v_{RU} = \frac{2m_U}{l_z} \qquad (2.2\text{-}2)$$

The length of the ICD zone l_z is estimated from the mouth of the inclined crack to the position of the concentrated load. It thus depends on the angle of the inclined shear crack α_c and the shear span a_0.

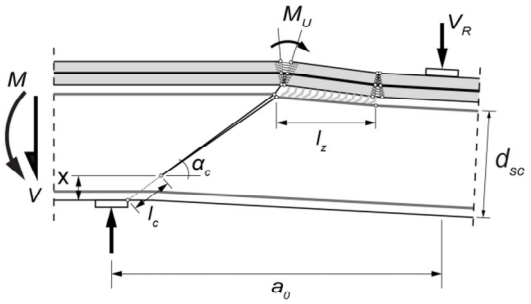

Figure 2.2-15: Shear failure mode for slab-like strips [Noshiravani and Brühwiler, 2013].

The design of the slab strengthening using R-UHPFRC has been validated by numerical analysis and an experimental campaign. The results obtained have shown that the deck slab's ultimate resistance in bending and shear is significantly increased.
As has been demonstrated by the application on the Chillon viaducts, strengthening with UHPFRC can be a technique suitable also for large scale structures.

2.2.6.2 Retrofitting of a bridge pier

A thin layer of UHPFRC, cast around an existing RC element, can both improve its structural performance and enhance its durability against environmental actions.
Massicotte *et al.* [2013] presented the strengthening technique of a bridge pier with the confinement provided by the UHPFRC cover. From their experimental program the authors concluded that UHPFRC can be used to strengthen deficiently detailed lap-splice regions. The lap splice failure, the concrete cover spalling, and the longitudinal bar buckling were eliminated following the retrofit. Although their main objective was to develop a new solution for strengthening the lap splice of highly rectangular columns, it might also applies to any column shape and might be an alternative to conventional jacketing techniques.
More recently, Reggia *et al.* [2018] defined a reinforcement strategy of a highway bridge pier reinforced with a 30 mm layer of UHPFRC. They proved experimental, by means of a laboratory specimen scaled 1:4, the possibility to enhance the seismic response a highway bridge pier. Figure 2.2-16 shows how the UHPFRC jacketing around the existing RC bridge pier improved the structural behaviour despite with a small thickness. The authors concluded that UHPFRC jacketing may be considered in further as a promising technique for seismic retrofitting of bridge piers.

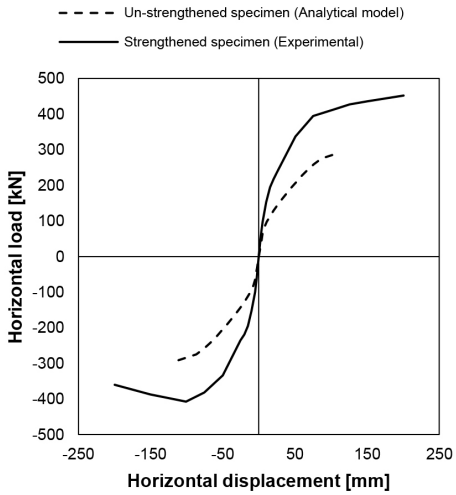

Figure 2.2-16: Comparison between the experimental response of the strengthened specimen and the un-strengthened specimen (analytical model prediction) [Reggia et al., 2018].

2.2.7 *Strengthening shear walls*

In existing buildings RC walls are often present, commonly located near the stair wall and the elevator cores, or along the structure perimeter. These elements are often reinforced to resist the vertical loads, without considering the seismic actions. In some cases, the elements may be reinforced against horizontal wind loads but may be ineffective against the design seismic actions recommended by modern standards. In order to transform the existing RC walls into seismic resistant shear walls, different retrofit techniques are traditionally proposed. The retrofit can be obtained by applying either traditional reinforced concrete jackets. This technique is not always easy to apply to existing structures. In fact, the strengthening of an existing RC wall by means of traditional RC jackets might require excessive thicknesses (80-100 mm), which could compromise the future usage of the structure. Recently, a new technique based on the use of thin jackets made with UHPFRC was utilized. By using UHPFRC the jacket thickness can be significantly reduced with respect to a traditional solution in ordinary reinforced concrete. Marini and Meda [2009] have enhanced this technique by adding a high strength steel mesh in the jacket with the aim of increasing the ductility. The proposed technique was validated by means of an experimental test on a 1:3 scaled shear wall. Moreover, a numerical study was also carried out to compare the performance of un-reinforced RC and strengthened shear walls. The remarkable stiffening and strengthening effect of the reinforcing jacket can be observed in Figure 2.2-17. The maximum base shear force was more than twice as large as the maximum resistance of the traditional RC wall. More importantly, observe that the ductility was also significantly increased.

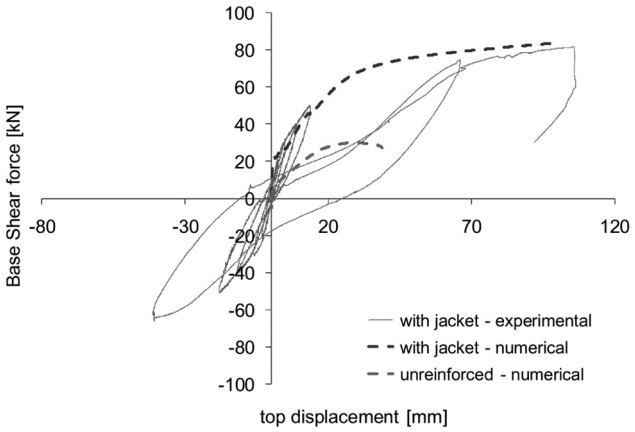

Figure 2.2-17: Applied horizontal load versus top displacement experimental curve for the strengthened shear wall and numerical response for the unreinforced RC wall [Marini and Meda, 2009].

2.3 Bond strength between old-new concrete

2.3.1 *Introduction*

Bonded concrete overlays are widely used for strengthening and repair of concrete members. The aim of a concrete repair is to restore the load-carrying capacity and the stiffness of a concrete member and to extend the service life of the structure. This can be achieved by providing a protective layer to a damaged substrate. The bond at the interface between differently aged concrete plays an important role in ensuring effective performance and durability of a concrete repair. In fact, the bond between substrate and overlay is often the main factor concerning the serviceability of a composite member consisting of concrete of different ages [Beushausen and Alexander, 2008]. Appropriate bond of a repair material to concrete is of vital importance in the application and performance of concrete repairs. Good adhesion is a key factor for providing monolithic action in bonded concrete overlays.

2.3.2 *Definition of bond strength*

The term "adhesion" describes the condition in the boundary layer between two connecting materials with a common interface [Bissonnette *et al.*, 2012]. Adhesion mechanisms can be divided basically into mechanical adhesion and specific adhesion, as presented in Figure 2.3-1.
All bond mechanisms depend on the true surface area, as opposed to the geometric surface area and the contact effective surface area (Figure 2.3-2).
It is important to note that the mechanical adhesion in tension differs significantly from that in shear. For example, a high interface roughness may improve shear bond strength, whereas tensile bond strength primarily depends on vertical anchorage in pores and voids (Figure 2.3-3).

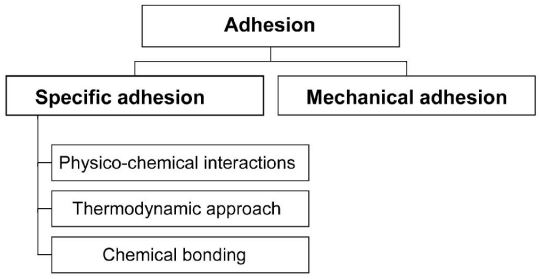

Figure 2.3-1 :Principles of the theory of adhesion [Silfwerbrand et al., 2011].

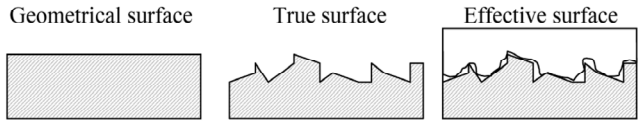

Figure 2.3-2: Geometrical, true, and effective surface areas between substrate and overlay [Silfwerbrand et al., 2011].

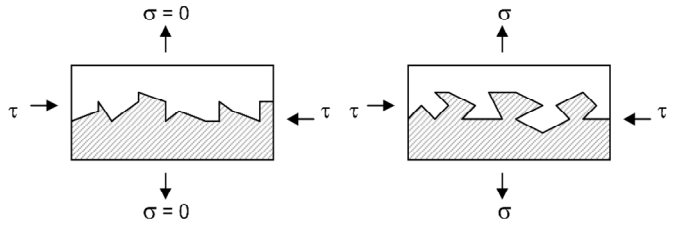

Figure 2.3-3: Mechanical tensile and shear bond between substrate and overlay [Silfwerbrand et al., 2011].

Bond strength is the stress required to separate substrate and overlay and provide information on the overall location of failure that is, "substrate", "interface" or "overlay" failure [Beushausen and Alexander, 2008]. Bond mechanisms between concrete of different ages must be based on information on the weakest link in the composite member. It appears important to examine the characteristic of the overlay interface zone, which may exist at the interface between substrate and overlay similarly to the interfacial transition zone (ITZ) between aggregate and cement paste.

2.3.3 *Factors influencing bond strength*

The strength and integrity of bond depend on not only the physical and chemical characteristics of the overlay and substrate, but also workmanship involved, the condition of the substrate, such as surface roughness and soundness, and the concrete properties.
Based on extensive experimental tests and case studies, Silfwerbrand and Paulsson [1998] identified the following five factors as most significant:

- substrate cleanliness;
- absence of micro-cracks on the substrate surface;
- absence of laitance on the substrate surface;
- compaction of the overlay;
- curing of the overlay.

The main factor affecting the bond between newly added and exiting concrete can be broadly classified into the following: concrete properties, removal of deteriorated concrete, condition on the surface, and presence of a bonding agent.

2.3.3.1 Repair material properties

The selection of the repair material influences the material properties of the overlay and, hence, also the bond.

2.3.3.1.1 Fresh repair material properties

The fresh repair material properties are relevant to both the early age bond strength development and bond durability. The workability of the freshly placed overlay influences its ability to fill open cavities and voids on the substrate concrete surface, and hence determines the effective contact area between the two composites. A relatively fluid overlay further enhances capillary suction in the substrate and, therefore, improves physical anchorage in substrate surfaces pores and cavities.
Lacombe *et al*. [1999] studied the performance in terms of filling ability and bonding characteristics of three different concrete mixes: ordinary vibrate concrete, self-levelling concrete and, dry-mixture shotcrete. It was observed that the interface between shotcrete and old concrete was visually almost perfect. The quality of the

bond appeared so good that it was impossible to see the difference in microstructure between shotcrete and old concrete. For these reasons, shotcrete appeared to be the best technique for overhead repairs. Moreover, the self-levelling concrete repair performed well in terms of filling ability and quality of interface. It has been found that self-levelling concrete also shows good results. Contrary, it appears that ordinary concrete does not possess filling capacity to perform good overhead repair; thus, this method was not proper to achieve quality overhead repair.

2.3.3.1.2 Hardened repair material properties

The mechanical strength of the repair material influences bond strength [Bissonnette *et al.*, 2012]. Of equal importance are the material properties that influence the development of stresses in the overlay and at the interface, such as shrinkage, elastic modulus, thermal coefficient, creep, permeability and additions like fibre reinforcement and admixtures.
Tensile strength is important as it affects crack development and, therefore, the formation of boundary conditions that may support the initiation of debonding. Dalette *et al.* [2000] found that an increase in early age concrete strength increased both tensile and shear bond strength significantly.
Fibre reinforced overlay influences bond durability. Granju [1996] investigated the use of fibre reinforced overlay to improve the durability of the bond between new concrete and old concrete. His research found that fibres enhance bond durability through the control of crack development.

2.3.3.1.3 Overlay strength

Pigeon and Saucier [1992] considered that the interface between old concrete and new concrete is similar to the bond between aggregates and cement paste. A wall effect exists between overlay and substrate. This effect results in a transition zone that creates a layer of weakness (Figure 2.3-4).
According to Van Mier *et al.* [1991], the bond mechanisms between aggregate and cement paste depend largely on the porosity of the aggregate.
Dalette *et al.* [2000] linked bond strength to the maturity of the overlay, which in turn relates to the material strength. The use of high strength concrete is beneficial to bond strength [Randl *et al.*, 2016]. Experimental studies by Júlio *et al.*, [2006] indicate that increasing the compressive strength of added concrete relative to the compressive strength of the substrate concrete improves the bond strength and changes the rupture mode from adhesive to monolithic.

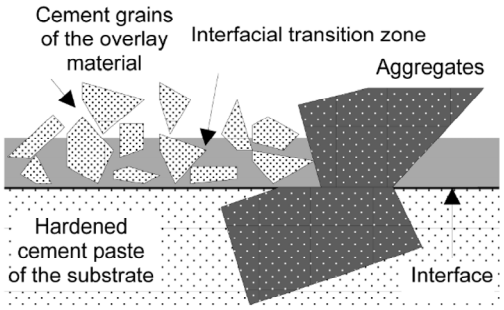

Figure 2.3-4: Transition zone between substrate and overlay, according to Pigeon and Saucier [1992]

2.3.3.2 Substrate mechanical strength

The substrate mechanical properties influence interface bond strength. Bonaldo *et al.* [2005] investigated the influence of the strength class of concrete substrate and concrete overlay on the adhesion performance between these materials. For the substrate three different strength classes were adopted, while the overlay was reinforced with steel fibres (SFRC). The results indicated that the strength of the substrate is closely related to the pull-off strength. Moreover, the shape, the maximum diameter and the strength of coarse aggregates plays an important role in the pull-off strength. In a substrate of low or medium strength, the crack surface developed at the interface between the coarse aggregate and the cement paste, while in the substrate of high concrete strength the coarse aggregate was also crossed by the failure surface.

2.3.3.3 Surface preparation

According to Vayburd and McDonald [1999] the process of concrete surface preparation for repair is the process by which sound, clean and suitably roughened surface is produced on concrete substrates. The surface preparation and the cleaning of the concrete substrate are considered the most crucial step in a concrete repair project. Surface preparation includes the removal of damaged and/or deteriorated parts of old concrete and the removal of loose particles and contaminants on the surface.

2.3.3.3.1 Removal of deteriorated concrete

The method of concrete removal is a key factor on both the surface of the remaining concrete and the properties of the uppermost layer of the remaining concrete. Some removal methods leave a rough and sound surface that promotes a good bond, while others may even introduce micro-cracks to a certain depth in the remaining concrete. Common surface preparation methods include mechanical roughening and blast methods using abrasives, high pressure water, or a mixture of them. Table 2.3-1 by Silfwerbrand *et al.*, [2011] summarises some of the most frequently used methods for removing concrete.

Removal method	**Principle behaviour**	**Concrete removal capability**	**Important advantages**	**Important disadvantages**
Sandblasting	Blasting with sand	No	No microcracking,	Not selective, leaves considerable sand
Scrabbling	Pneumatically driven bits impact the surface	Little (6)	No microcracking, no dust	Not selective
Shotblasting	Blasting with steel balls	Little (12)	No microcracking, no dust	Not selective
Grinding (planning)	Grinding with rotating lamella	Little (12)	Removes uneven parts	Dust development, not selective
Flame cleaning	Thermal lance	No	Effective against pollutions and painting, useful in industrial and nuclear facilities	The reinforcement may be damage, smoke and gas development, safety considerations limit use, not selective
Milling (scarifying)	Longitudinal tracks are introduced by rotating metal lamellas	Yes (75)	Suitable for large volume work, good bond if followed by water flushing	Microcracking is likely, reinforcement maybe damaged, dust development, not selective

Table 2.3-1 (Pt. 1 of 2)

Pneumatic (jack) hammers, (chipping), hand-held or boom-mounted	Compressed air operated chipping	Yes	Simple and flexible use, large ones are effective	Microcracking, damages reinforcement, poor working environment, slow production rate, not selective
Explosive Blasting	Controlled blasting using small, densely spaced blasting charges	Yes	Effective for large removal volumes	Difficult to limit to damaged concrete, safety and environmental regulations limit use, not selective
Water-jetting (hydro-demolition)	High pressure water jet from a unit with a movable nozzle	Yes	Effective (especially on horizontal surfaces), selective, does not damage reinforcement or concrete, improved working environment	Water handling, removal in frost degrees, costs for establishment

(Pt. 2 of 2)

Table 2.3-1: Methods of concrete removal [Silfwerbrand et al., 2011].

The surface of the remaining concrete needs to be free from microcracking. The amount of microcracking is governed by the selected methods of concrete removal. The use of heavy mechanical techniques such as milling and pneumatic jack hammer can introduce micro-cracking at the substrate surface which has a detrimental effect on bond strength. According to Silfwerbrand [2000; 2003] water-jetting is the most effective removal technique due to its efficiency, selectivity and result. It removes deteriorated concrete and leaves sound concrete and a rough surface without microcracks.

2.3.3.3.2 *Cleaning after concrete removal*

Surface cleanliness is the most important factor influencing bond. If the surface is contaminated at the time of overlay placement, the bond will be poor [Silfwerbrand and Paulsson, 1998]. The first cleaning has to be done after water-jetting to prevent loose concrete particles to bond surface. The second cleaning has to be carried out prior to overlay placement to make sure that surface is free from dust, sand or other particles originating from construction work or the environment. The best methods are hosing down with high-pressure water [Silfwerbrand and Paulsson, 1998].
The influence of surface moisture can have a significant on bond strength. A too dry surface may absorb water from the fresh concrete overlay with the risk that the repair material may not hydrate properly which may result in a weak interfacial repair layer and low bond strength. On the other hand, if the surface is too wet, an overlay zone with a high water-cement ratio will develop close to the interface, which will lead to a local reduction in overlay strength and bond strength. Free water at the surface may destroy the bond completely [Bissonnette *et al.*, 2012].

2.3.3.4 *Surface properties*

The roughness of the substrate surface depends to a large extend on the method of substrate surface preparation. Mechanical methods of concrete removal leave the substrate surface much rougher than blast methods. The surface roughness for concrete repairs is commonly measured in millimetres (mm). The most widespread test method for evaluating it is the sand area method [Kaufmann, 1971]. In this method, sand of known volume is spread over the concrete surface to form a circle until all sand has settled in the surface cavities (Figure 2.3-5).

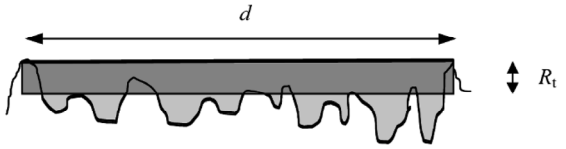

Figure 2.3-5: Determination of surface roughness using the sand area method [Kaufmann, 1971].

The roughness R_t can be calculated from the diameter d of the circle, using the following equation:

$$R_t[\text{mm}] = \frac{4 \cdot V\ [\text{mm}^3]}{\pi \cdot (d[\text{mm}])^2} \qquad (2.3\text{-}1)$$

Where the V is the known volume of the sand.
MC2010 [2013] classifies the surface roughness into different categories. Depending on the roughness R_t derived from the sand patch method, the applied roughening method the following categories can be defined:

Category:	**R_t [mm]**
Very smooth (e.g. cast against steel formwork)	not measurable
Smooth (e.g. untreated, slightly roughened)	<1.5 mm
Rough (e.g. sand blasted, high pressure water blasted etc.)	≥1.5 mm
Very rough (e.g. high-pressure water jetting, indented)	>3.0

Table 2.3-2: Classification of surface roughness.

Several researches have linked surface roughness to bond strength. The substrate roughness is often considered an important factor affecting bond strength between the old concrete and repair material. Some studies reported that bond test results have shown that surface roughness has only a minor influence on tensile bond. Silfwerbrand [1990] compared interface strength resulting from different surface treatments and different roughness. He concluded that there is a roughness threshold value beyond which further improvement in roughness does not seem to enhance bond strength. Tschegg *et al.* [2000] compared the roughness of 0.07 inch (1.75 mm) to 0.03 inch (0.65 mm) on water blasted surfaces and found better bond characteristics for the rougher interface. Beushausen [2005] argued that the tensile pull-off test methods are not very susceptible to the effects of surface roughness. He stated that it appears reasonable to assume that the interface roughness has an influence on shear bond strength, while it is of minor importance for tensile bond mechanisms.

2.3.3.5 Bonding agents

Bonding agents, e.g., Portland cement grout, latex modified Portland cement grout and poxy resins, are sometimes used to improve bond [ACI Committee 546, 1980]. However, bonding agents cannot compensate for bad substrate surface and preparation. They may act as a bond breaker when used inappropriately [Pigeon and Saucier, 1992; Schrader, 1992]. Silfwerbrand *et al.*, [2011] maintained that bonding agents should normally be avoided. They point out that the use of bonding agents leads to two interfaces and thus to the creation of two possible planes of weakness instead of one. Moreover, a grout often has a high water-cement ratio leading to a low strength and the risk of cohesive failure within the bonding agent itself. On the over hand, a bonding agent may improve the bond strength for certain materials, especially stiff repair mortars that cannot fill pores and cavities. Indeed, grouts may have an ability to assimilate loose particles on an insufficiently cleaned surface. This assimilation may increase the bond strength for this specific case. The efficiency of bonding agents further depends on the interface texture [Wells *et al*., 1999].

2.3.4 *Test methods*

Silfwerbrand *et al.* [2011] noted that the results and the interpretation of interface bond tests depend to a large extent on the test method used. Existing tests to determine the bond between concrete substrate and repair material can be divided into several categories [Momayes *et al.*, 2004]. The first category of tests measures the bond under tension stress. Pull-off, direct tension and splitting are the main tests under this category. The second one measures the bond under shear stresses and are called direct shear methods. Several tests fall under this category, including L-shape, mono-surface shear. In most cases, the bond surface for a direct shear test is actually subject to shear stress and small bending stress. The third one measures the bond strength under a state of stress that combines shear and compression. The slant shear test uses a square prism or cylindrical sample made of two identical halves bonded at 30° and tested under axial compression. During loading, the interface surface is under compression and shear stresses. Figure 2.3-6 gives a schematic overview of the most common test set-up to determine interface bond strength between concrete substrate and overlay.

In a direct tension test, the specimen is pulled apart by loads applied perpendicular to the bond interface. The most common test method is the pull-off test, with can be carried out in-situ (Figure 2.3-6A) and in the laboratory (Figure 2.3-6B). A very careful alignment of the specimen along the axis of loading is essential. Even a very small amount of misalignment may introduce eccentricities that will cause large scatter in the test results. Therefore, the main problem encountered with the pull-off test is the eccentricity in the load application and damage during coring [Delatte *et al.*, 2000].

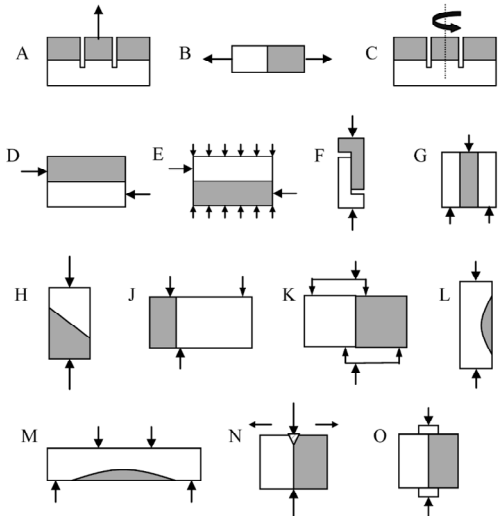

Figure 2.3-6: Various test methods to determine interface bond strength between concrete substrate and overlay [Silfwerbrand et al., 2011].

Vayburd and McDonald [1999] tested 257 partial-depth cores in 77 experimental repairs in order to examine the effect of material properties and environmental conditions on the bond between repair material and the concrete substrate. The main results of this study can be summarized in the following conclusions:

- the results obtained from the pull-off test have been variable;
- variations in exposure conditions did not appear to have a significant effect on the failure modes or bond strengths of the repair materials;
- the load must be perpendicular to the repair surface under test and increased gradually with a specified speed. In particular Vayburd and McDonald [1999] recommend 0.02 MPa/s. Silfwerbrand and Paulsson in their field test on Swedish concrete bridge decks [Silfwerbrand and Paulsson, 1998] had chosen 0.064 MPa/s.

Silfwerbrand [2003] developed an in-situ test for torsional bond strength, the test specimen is the same as the in-situ pull-off test. The difference is that a torsional moment is applied to the core instead of a tensile force (Figure 2.3-6C). This test method can be equated to interface shear strength [Silfwerbrand *et al.*, 2011]. Common shear bond tests apply a force parallel to the interface (Figure 2.3-6D). Many variations of the shear test have been used by researchers to study interface bond strength. Modified shear bond methods have been presented by Pigeon and Saucier [1992] (Figure 2.3-6E) and El-Rakib *et al.* [2003] (Figure 2.3-6F).

The push-out specimen method (Figure 2.3-6G) has been used by some researchers (Chen and Chung, 1995; Momayez *et al.*, 2004; Zanotti and Randl, 2019] to study interface bond strength. This test method has the disadvantage of having two interfaces, which does not represent site conditions, thus making the test very impractical [Silfwerbrand *et al.*, 2011]. The slant shear test (Figure 2.3-6H) measures bond strength under a combination of shear and compression. Some studies [Emberson and Mays, 1990; Austin *et al.*, 1999; Delatte *et al.*, 2000] indicated shortcomings of this test with respect to unrealistic loading conditions and the vast number of parameters which may affect the test results. The guillotine test (Figure 2.3-6J) can be used both on cores and prisms. Delatte *et al.* [2000], however, reported difficulties with the alignment of the loading head for use on cores.

The disadvantage of most common shear test methods is the occurrence of an interface bending moment due to force eccentricity. The Federation Internationale de la Précontrainte (FIP) [1978] developed a test method for interface shear strength in which the interface is theoretically subjected to pure shear forces (Figure 2.3-6K). Robins and Austin [1995] developed different patch tests which measure interface shear and tensile bond strength under structural loading (Figure 2.3-6L and Figure 2.3-6M). The uniaxial wedge splitting test device characterises bond by fracture mechanical properties of old-new concrete such as crack opening and specific fracture energy, and tensile interface strength in bending (Figure 2.3-6N) [Tschegg *et*

al., 2000]. Li *et al.* [1999] measured interface tensile strength with a prism splitting test device (Figure 2.3-6O).
Zanotti and Randl [2019] analysed and compared the effect of various test methods on interface bond strength between concrete substrate and repair materials. Their campaign comprised different set-ups and specimen geometries. Figure 2.3-7 illustrates the different test set-ups.
Table 2.3-3. gives the details of the different bond shear and tension test performed.

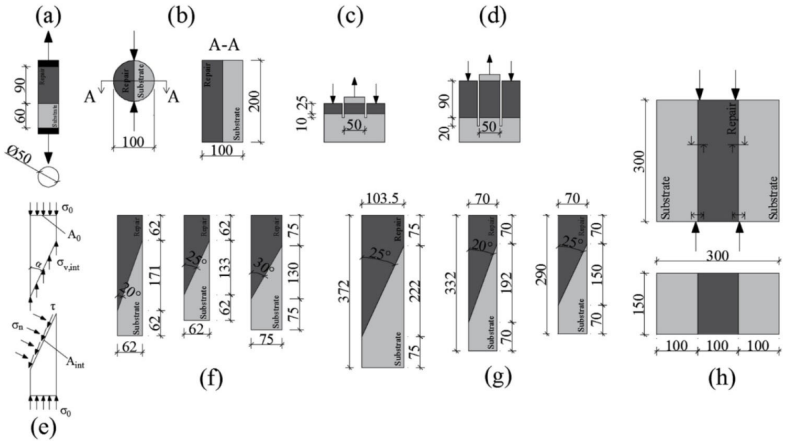

Figure 2.3-7: Bond test performed used in Zanotti and Randl [2019] (all dimensions in mm).

Debonding mechanism	**Test set-up**	**Interface inclination from the vertical [deg]**	**Dimensions [mm]**
Shear	Slant shear cylinders (Figure 2.3-7e-g)	30° 25° 20° 25° 25° 20°	280 x 75 257 x 62 295 x 62 372 x 103.5 290 x 70 332 x 70
Tension	Push-out (Figure 2.3-7h) Direct (Figure 2.3-7a) Splitting (Figure 2.3-7b) Pull-off (Figure 2.3-7c and d)	0° 180° 0° 180° 180°	300 x 150 x 300 150x 50 200 x 100 35 x 50 110 x 50

Table 2.3-3: Overview of bond test performed used in Zanotti and Randl [2019].

Their study was based on test programs in two different labs, and encompassed normal strength, high strength and fibre reinforced concretes. Four different repair material were investigated. Concrete substrates were cast first, covered with plastic sheets and cured in standard conditions in a moist/temperature-controlled atmosphere. After at least 14 days of curing, the substrates were sandblasted (estimated roughness amplitude of 1.2-1.5 mm) and cured again until they reached at least 28 days before the repair material was cast. Overlay materials cured for 28 days following the same curing procedure detailed for the substrate. Figure 2.3-8 shows the shear bond stresses at failure obtained from slant shear and push-out tests of the above study. Interfacial shear stresses at failure decreased for decreasing normal-shear stress ratios at the interface, because of a decrease in interfacial friction. The highest values were achieved with the standard slant shear test (largest slant, α=30°) and the lowest values were obtained with the push-out tests.
Figure 2.3-9 compares the tensile bond stresses with the various testing set-up discussed in this research. It can be observed that the pull-off and direct tension tests had a larger scatter due to higher resulting sensitivity to the local effect, the stress disturbance and the drilling-induced damage.
A variety of bond tests have been described in this research demonstrate that test geometry significantly affects failure modes, stress paths and resulting bond values.

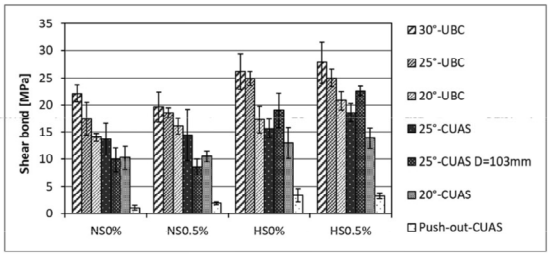

Figure 2.3-8: Bond stresses at failure for different repair materials, obtained from slant shear test with various slants (20°, 25°,30°) and push-out test (Figure 2.3-7e-h) [Zanotti and Randl 2019].

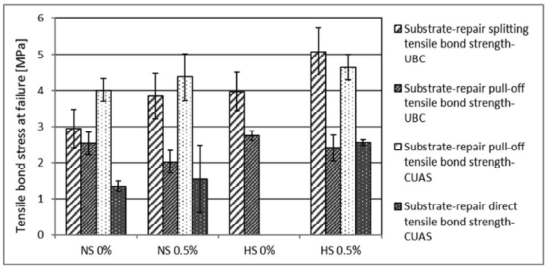

Figure 2.3-9: Tensile bond stresses at failure for different repair materials, obtained from various tensile bond test (Figure 2.3-7a-d) [Zanotti and Randl 2019].

2.3.4.1 Comparison between tensile bond strength

Even though it is questionable to relate interface shear and tension bond strengths, since the bond mechanisms have different characteristics, some researchers have obtained a correlation between the two. The main advantage offered by such a relation is that shear bond strength can then be readily expressed in terms of tensile bond strength. This is advantageous because interface bond failure is predominantly tensile in nature [Van Mier *et al.*, 1991].

Several studies [Emmons, 1993; Jùlio *et al.* 2004; Silfwerbrand, 2003] reported that bond strength values obtained by the slant shear test or by the direct shear methods are generally higher that direct tension results. Based on experimental tests, Jùlio *et al.* [2004] observed a linear correlation between the slant shear test results and the pull-off test results, with a correlation coefficient of 0.948. Silfwerbrand [2003] suggested a torsion test as an alternative to other shear bond tests, with the benefit that it can also be performed on-site. His studies indicated that, with cast in place repair concrete, the ratio between the average shear stress and the tensile stress varied between 1.9 and 3.1, and with shotcrete, this ratio varied between 2 and 7. Momayez *et al.* [2004; 2005] reported the results from 164 specimens using four different test methods: pull-off, splitting prisms, Bi-Surface shear (direct shear) and slant shear. The authors concluded that bond strength measured is greatly dependent on the test method used. Moreover, they found that the bond strength decreased with the test method in the following order: slant shear, bi-surface shear (pure shear), splitting and pull-off.

Zanotti and Randl [2019] concluded that the comparisons between tensile and shear bond strength can be challenging. The bond results not only are significantly affected by differences of test set-up in tension and shear, but also shear and tensile bond are differently correlated to interfacial factors (e.g. roughness and texture). This study indicated that the ratio between the shear bond and the tension bond has ranged between a minimum of 0.6 with the push-out test to a maximum of 2.8 with the slant shear test.

2.3.5 *Bonding mechanism at the interface of repair material and concrete substrate*

UHPFRC members can be designed without any mechanical device or stirrups connecting the two elements [Noshiravani and Brühwiler, 2013]. Nevertheless, surface preparation of the substrate concrete is considered essential to achieving a durable repair. Naaman *et al.* [1995] agree that one of the reason for failure of concrete repairs has been the lack of knowledge regarding bonding mechanisms and bond properties at the interface between the repair material and the concrete substrate. They centred their research on the bond between reinforcing/repairing layers and old

concrete. It is the most important issue when considering the durability. The performance of retrofitted structural elements significantly depends on the bond behaviour of freshly laid and old concrete. Tayeh *et al.* [2012] carried out the experimental investigation to evaluate the relationship between concrete substrate roughness parameters and the bonding performance of UHPFRC used as a repair material. They concluded that the substrate surface preparation method significantly influences the bonding strength between UHPFRC and the concrete substrate. The composite UHPFRC/substrate exhibited a behaviour closely as a monolithic structure when the surface was prepared by the sandblasting method. Research on the flexural resistance and load-bearing behaviour of UHPFRC-RC beams and slab strips [Brühwiler and Denarié, 2003; Alaee and Karihaloo, 2003; Oesterlee, 2010] showed monolithic behaviour of the two elements up to the maximum bending resistance. Thus, the effect of debonding on the behaviour of UHPFRC members is small enough to be neglected [Alaee and Karihaloo, 2003; Brühwiler and Denarié, 2008]. Nevertheless, the results of the tests presented by Noshiravani and Brühwiler [2013] showed that, in the presence of bending and high shear stresses, the near interface concrete cracking prior to the maximum bending resistance and the UHPFRC strain softening influences the bond between the reinforced concrete and its reinforced UHPFRC overlay. In fact, the response of UHPFRC -RC members is strongly influenced by the formation of the ICD zone that softens the connection between the UHPFRC and RC elements, thus increasing the deformation capacity. As the ICD progresses, the plane section theory no longer holds for the composite member. However, it still remains valid for each individual element with bonded reinforcement. The ICD zone is more pronounced in members that carry higher shear stresses; that is, members with higher ratios of ribbed longitudinal reinforcement in the UHPFRC element [Noshiravani and Brühwiler, 2013].

Aaleti *et al.* [2013] observed that the horizontal shear stresses can be effectively transferred if the existing concrete surface is sufficiently roughened prior to placement of the overlay. In fact, the surface roughness is critical for composite action and horizontal shear transfer; therefore, the degree of surface roughness required for horizontal shear transfer was studied. Their study concluded that a minimum surface roughness amplitude of 2 mm was required for a reinforced concrete member with a UHPC overlay to achieve good flexural performance.

Another study [Haber *et al.*, 2018] found that thixotropic UHPC overlays can develop adequate bond strength to substrate concrete if good overlay consolidation can be achieved with a percentage of interface voids below 10%. If this state can be achieved, the concrete surface roughness becomes less critical in developing adequate direct tension bond strength. However, if sufficient consolidation cannot be achieved, some degree of surface roughness would be necessary to develop adequate bond strength.

Debonding of UHPFRC-strengthened structures seldom occurs owing to the fact that the tensile strength and the stiffness of UHPFRC are similar to that of the concrete substrate [Avadhanam *et al.*, 2019]. The studies on the effect of normal and shear stresses at the interface of the beam and UHPFRC layer are essential to determine the scheme of strengthening. For this reason, the work by Avadhanam *et al.* [2019] focuses on debonding characteristics of UHPFRC strengthened structures. Their work concentrates mainly on the strengthening scheme where UHPFRC is provided in the form of strips at the tension zone of concrete (Figure 2.3-10).

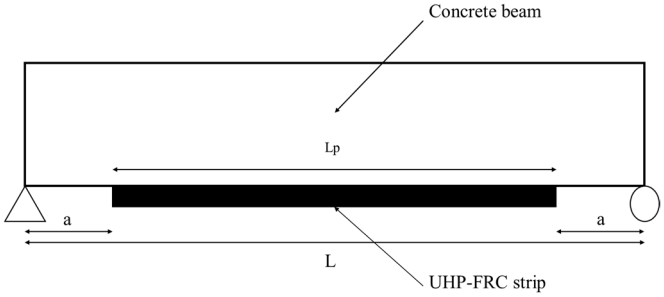

Figure 2.3-10: Simply supported beam strengthened with a UHPFRC strip [Avadhanam et al., 2019].

Figure 2.3-11 shows that no cases of debonding were observed during the experimental investigations on strengthened RC beams after failure.
The authors found that the UHPFRC develop lower values of shear and normal stresses at the interface for a given length and thickness of the strip. The maximum stresses occur at the free edge of the strip making it a vulnerable location for debonding. But the values of stresses developed in UHPFRC are well within their permissible limits, and hence it can be concluded, that the chances of debonding are limited.
The bond strength between newly laid UHPFRC and old concrete and confinement provided by UHPFRC are significant factors for improving the performance of initially stressed RC beams. The performance can be further improved by applying the surface preparation technique to increase the bond strength. The bond strength enables the UHPFRC to sustain the stresses for the longer duration [Garg *et al.*, 2019].

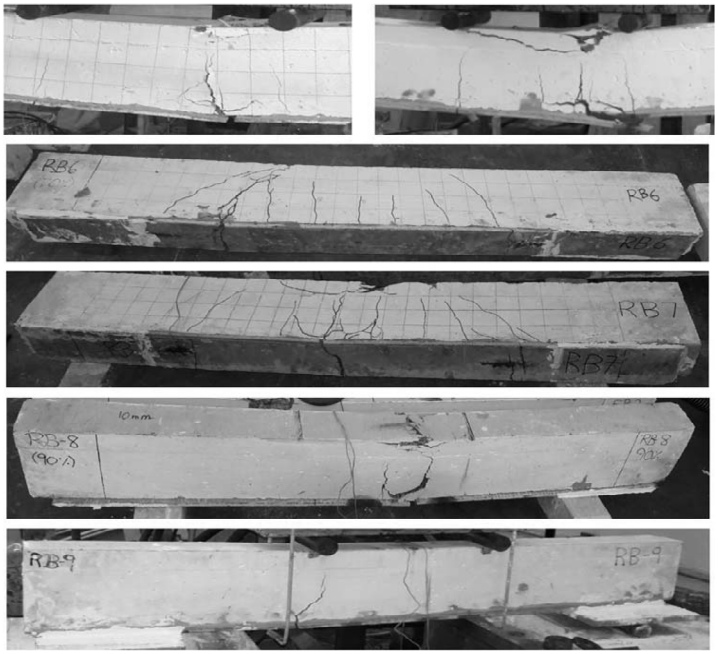

Figure 2.3-11: Typical bonding of UHPFRC on NSC beams after failure [Avadhanam et al., 2019].

2.4 Shear resistance

2.4.1 *Shear in concrete elements without transverse reinforcement*

Usually, shear failure in concrete elements is nonductile, indeed it is a brittle and unstable mechanism [Park and Paulay, 1975]. In any concrete elements, the shear forces have to be considered. All flexural elements are subjected to shear stresses; these stresses can produce diagonal cracks which may cause a premature brittle failure of the element

In RC elements, the shear and flexure forces combine to create a biaxial state of stress. When the principal stresses exceed the tensile strength of the concrete cracks develop. In the region where the bending moment is large, the tensile stresses are greatest at the extreme tensile fibre of the element and are responsible for the initiation of flexural cracks perpendicular to the axis of the member. In the region where shear force is dominant over the bending moment, significant principal tensile stresses may be generated at approximately 45° to the axis of the element, these can result in inclined cracks. With rare exceptions, these inclined cracks are extensions of flexural cracks. Only in rather special situations, as in webs of flanged beams, diagonal tension cracks are developed in the proximity of the neutral axis. Either a reinforced

concrete flexural member collapses immediately after the formation of diagonal cracks, or an entirely new shear carrying mechanism develops which is capable of sustaining further load in a cracked beam.
To predict the shear failure the conditions of the shear stress in the web are to be knows. Therefore, it has to be considered how the cracked concrete element transmits shear, combined with the axial load and the bending moment.
The shear transfer in a reinforced concrete element is described by five mechanisms [ACI committee 445, 1999]: (1) shear stresses in uncracked concrete, (2) interface shear transfer (called as "crack friction" or "aggregate interlock"), (3) dowel action of the longitudinal reinforcement, (4) residual tensile stresses transmitted directly across cracks, and (5) arch action. It is difficult to say which mechanism will contribute to the shear resistance, because a cracked concrete beam is influenced by many parameters. The mechanisms can be subdivided into two groups of acting, where (1), (2), (3) and (4) are summarized in "beam action in the shear span", and the other one (5) is called "arch action".
Determination of a shear failure mechanism remains a challenging task. In experimental studies, researchers often describe different shear failure mechanisms based on crack patterns. Primary beam failure modes, defined by ASCE-ACI Committee 426 [1974], are exposed in Figure 2.4-1.

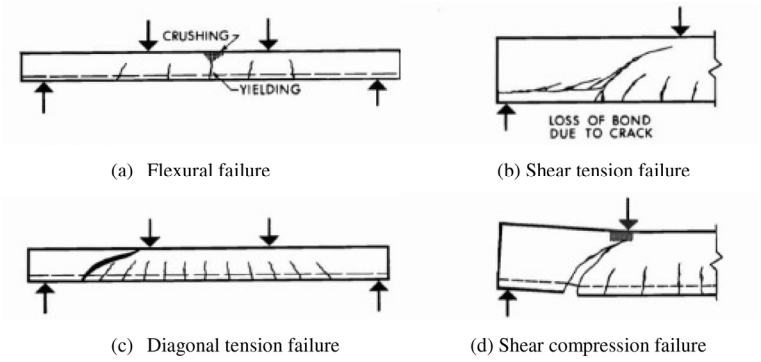

Figure 2.4-1: Beam failure modes [ACI-ASCE Committee 426, 1973].

2.4.2 *Shear in concrete elements with transverse reinforcement*

As shown experimentally by Richart [1927] and Moretto [1945], in RC beams, the stirrups reinforcement is only effective after the formation of diagonal cracks. After the formation of diagonal cracks, the stirrups reinforcement redistributes the shear stresses through tension. This tension is transferred back to the concrete, that may lead to the formation of additional diagonal cracks. The stirrup reinforcement has also the role to slows down the propagation of diagonal cracks. This phenomenon helps the compression region sustain shear force. It is also effective in preventing a

premature splitting failure along the tensile reinforcement. In addition, stirrup reinforcement controls crack opening, and hence, helps aggregate interlock resist shear. After the development of diagonal cracks, there is an interaction among the four main contributors to shear resistance: tensile reinforcement through dowel action, concrete compression region, aggregate interlock, and stirrup reinforcement.

2.4.3 *Shear strengthening of RC beams*

Fibre reinforced concrete jacketing also appears to be an efficient method for shear strengthening of reinforced concrete beams with stirrups. In an experimental work Ruando *et al.* [2014] tested beams without shear reinforcement, which were retrofitted with plain concrete and fibre reinforced concrete. They demonstrated that all the beams exhibited greater stiffness and shear strength than the unreinforced beam. Thus, the use of fibres improves the shear resistance in flexural members. Nevertheless, the failure of these beams was sudden and located in the larger side of the beams. Hence, the authors have concluded that UHPFRC retrofitting is not able to replace the stirrups.

Garg *et al.* [2019], in their experimental study, evaluated the efficiency of UHPFRC as a retrofitting material in shear-deficient RC beams. Their beams were initially stressed to 60% of their ultimate load carrying capacity. Afterward, two different techniques of retrofitting were applied to retrofit the shear-deficient beams. The methods utilized were: U-wrap, and external side face jacketing. Before retrofitting with UHPFRC, epoxy as a bonding agent between old concrete and UHPFRC was used. In the case of U-type retrofitting (UT), the damaged concrete cover was removed. UHPFRC was applied until the section attained the original dimension. In the external side face jacketing technique (EJ), the side faces were externally strengthened with a layer of UHPFRC over the existing cross section. The efficiency of both techniques was evaluated in terms of load-deflection behaviour, yield load, ultimate load, stiffness and energy absorption. It was observed that the U-type retrofitting technique improved the performance of the shear-deficient RC beams. In the Figure 2.4-2 it can be noted that the ductility increased when the beams were retrofitted by the U-type retrofitting technique. The premature failure due to the debonding of UHPFRC side face layer with old concrete led to a decrease in the ductility.

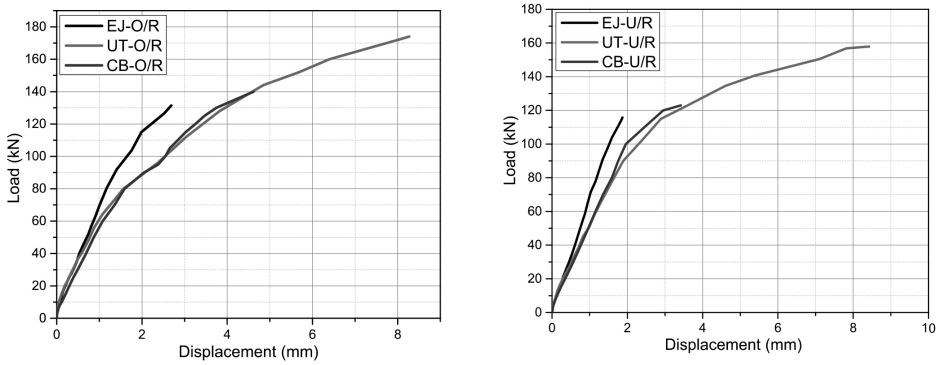

EJ: Under/Over reinforced section beams-strengthened side faces externally with 25 mm thick layer of UHPFRC; UT: Under/Over reinforced section beams retrofitted by replacing side faces and bottom cover in shear span using UHPFRC; CB: Under/Over reinforced section control beam.

Figure 2.4-2: Load versus deflection curve for retrofitted and control over-reinforced (O/R) section beam (left) and under-reinforced (U/R) section beam (right) [Garg et al., 2019].

2.4.4 *Shear in FRC beams*

From the literature survey analysed, it has been observed that few studies have been carried out on the shear behaviour of beams retrofitted using UHPFRC jacketing. On the other hand, several studies have been carried out on the shear behaviour of FRC beams [Sharma, 1986; Mansur *et al.*, 1986; Narayanan and Darwish, 1987; Ashour *et al.*, 1992; Casanova and Rossi, 1997; Gustafsson and Noghabai, 1999; Khuntia *et al.*, 1999; Vandewalle, 2000; Meda *et al.*, 2005; Parra-Montesinos; 2006; Dinh *et al.*, 2010].
The shear failure of FRC beams is complex. For such members, most of the predictive methods rely on a regression analysis. The factors considered to affect shear strength are decided based on a rational evaluation of the shear failure mechanism. The primary controlling factors are the shear span-to-effective depth ratio, the longitudinal reinforcement ratio, and other factors that affect the tensile strength of fibre reinforced concrete. These are the fibre aspect ratio, the fibre geometry, the fibre content, the fibre tensile strength and the concrete matrix properties.
The main formulations present in the literature to calculate the FRC contribution to shear strength are report in the following.

2.4.4.1 Sharma [1986]

Sharma proposed an empirical expression to predict the ultimate shear strength based on the shear span-to-effective depth ratio (a/d) and on the splitting tensile strength (f_{ct}).

$$v_u = (kf_{ct})\left(\frac{d}{a}\right)^{1/4} \quad (2.4\text{-}1)$$

The contribution of the fibres is not correlated in the previous equation (2.4-1). The product kf_{ct} is based on a previous work [Wright, 1995]. The direct tensile stress is in the order of 2/3 of the splitting tensile strength. Thus, kf_{ct} could be the direct tensile strength assuming that k is equal to 2/3. In the absence of f_{ct}, Sharma used the following expression in according to European Concrete Committee [Comité euro-international du Béton, 1993]:

$$f_{ct} = 0.95\sqrt{f_c'} \quad (2.4\text{-}2)$$

where f_{ct} is in psi.

2.4.4.2 Narayanan and Darwish [1987]

The shear contribution of FRC is calculated through the following equation:

$$v_u = eA'f_{ct} + eB'\rho\frac{d}{a} + v_b \quad (2.4\text{-}3)$$

The equation considers the splitting tensile strength (f_{ct}), dowel action (in function of the longitudinal reinforcement ratio, ρ), the shear span-to-effective depth ratio (a/d) and the fibre pull-out forces along the inclined crack (v_b).

The coefficient e considers the arch/beam action effect; it approximately equals 1.0 for slender beams (a/d > 2.8) and 2.8 d/a for shorter beams (a/d < 2.8). Narayanan and Darwish proposed calculating f_{ct} from the cube compressive strength (f_{cuf}) and the fibre factor (F).

$$f_{ct} = \frac{f_{cuf}}{20 - F} + 0.7 + \sqrt{F} \quad (2.4\text{-}4)$$

where

$$F = V_f\frac{L_f}{D_f}\beta \quad (2.4\text{-}5)$$

The term β is the bond factor. It depends on the fibre shape and it is 0.5, 0.75 and 1 for round, crimped, and indented fibres, respectively. A' and B' were determined based on a regression analysis of tests, leading led to A'=0.24 and B'=80 MPa. The v_b term is based on the bond stress of all fibres crossing a 45-degree diagonal.

$$v_b = 0.14\tau V_f\frac{L_f}{D_f} \quad (2.4\text{-}6)$$

where τ is the average fibre matrix interfacial bond stress. It is assumed to exist along ¼ of the fibre length.

2.4.4.3 Ashour, Hasanain, and Wafa [1992]

The authors modified one of the ACI Committee 318 [2008] equations on shear. They applied factors determined from a regression analysis to the parameters $\sqrt{f'_c}$ and $\rho\frac{d}{a}$. The equation assumes its final form as:

$$v_u = 0.7\frac{d}{a}\sqrt{f'_c} + 7\frac{d}{a}F + 17.2\rho\frac{d}{a} \qquad (2.4\text{-}7)$$

2.4.4.4 Khuntia, Stojadinovic and Goel [1999]

These researchers proposed an expression that takes into account the fibre factors, which is defined in equation (2.4-5). The contribution of the compression region, the aggregate interlock, and the dowel action are grouped into a single term, in according to ACI Committee 318 [2008]:

$$v_c = 0.167\sqrt{f'_c} \qquad (2.4\text{-}8)$$

The shear contribution of the fibres is defined in the equation below:

$$v_{fr} = 0.41 \cdot 0.68\sqrt{f'_c} \cdot F \cdot 0.9 = 0.25F\sqrt{f'_c} \qquad (2.4\text{-}9)$$

The contribution of fibres is based on the post-cracking tensile strength, which is absented equivalent to $0.14\tau F$. The bond stress is assumed equal to $0.68\sqrt{f'_c}$ and the vertical projection of the diagonal crack equal to $0.9d$.
Thus, adding the two contributions, the total shear strength becomes:

$$v_u = (0.167\alpha + 0.25F)\sqrt{f'_c} \qquad (2.4\text{-}10)$$

The term v_c is multiplied by the arch action factor α, equal to $2.5d/a$.

2.4.4.5 Minelli [2005]

The model proposed by Minelli aimed at including the performance parameter of FRC in the EC2 [2003] formulation for shear. The equations of EC2 for members without shear reinforcement is:

$$V_c = \left[\frac{0.18}{\gamma_c} \cdot k \cdot (100 \cdot \rho_1 \cdot f_{ck})^{1/3} + 0.15\sigma_{CP}\right] \cdot b_w \cdot d \qquad (2.4\text{-}11)$$

To consider the fibre contributions, the equation reported above assumes its final form:

$$V_u = \left\{ \frac{0.18}{\gamma_c} \cdot k \cdot \left[100 \cdot \rho_1 \cdot (1 + 2.5 \cdot \frac{f_{eq(0.6-3)}}{0.30 \cdot (f_{ck})^{2/3}}) \cdot f_{ck} \right]^{1/3} + 0.15\sigma_{CP} \right\} \cdot b_w \cdot d \quad (2.4\text{-}12)$$

where $f_{eq(0.6-3)}$is the post-cracking strength related to the ULS, it is defined in the Italian Standard UNI 11039 [2003]. In European Standard EN 14651 [2007], it is defined as $f_{R,3}$.

2.4.4.6 Dinh, Parra-Montesinos and Wight [2010]

Dinh *et al.*, according to their proposed model, calculated the shear strength of a FRC beam as the sum of the two contributions: shear force across the compression region (V_{cc}) and the shear force due to the fibre tension (V_f).

$$V_{cc} = (0.11f'_c) \cdot (\beta_1 c) \cdot b = 0.11\beta_1 f'_c bc \quad (2.4\text{-}13)$$

In this research the authors proposed a uniform shear stress of $0.11f'_c$. This shear stress is assumed then to act over a reduced depth of $\beta_1 c$, where c is the depth of the compression zone and is calculated based on equilibrium of the normal forces at the section considered, as follows:

$$c = \frac{A_s f_y}{0.85\beta_1 f'_c b} \quad (2.4\text{-}14)$$

To calculate the compression zone, a uniform stress block with a stress intensity of $0.85f'_c$, acting over a depth $\beta_1 c$ in assumed. The factor β_1 was proposed by Mattock *et al.* [1961] and it was improved for the case of high strength concrete by Kaar *et al.* [1978]. β_1 is equal to:

$$\beta_1 = \begin{cases} 0.85 \text{ if } f'_c \leq 4000\ psi\ (28\ MPa) \\ 1.05 - 0.05f'_c/1000 \text{ if } 4000\ psi < f'_c \leq 8000\ psi\ (55\ MPa) \\ 0.65 \text{ if } f'_c > 8000\ psi\ (55\ MPa) \end{cases} \quad (2.4\text{-}15)$$

The tensile force transferred across the critical crack through fibre tension depends on the crack width. For that, the contribution of fibre tension to the beam shear strength assumes the following shape:

$$V_f = T_f \cos\alpha = \left[\sigma_{fu} b \left(\frac{d-c}{\sin\alpha} \right) \right] \cdot \cos\alpha = \sigma_{fu} b(d-c)\cot\alpha \quad (2.4\text{-}16)$$

This proposed model relies on a crack of varying width, thus the uniform tensile stress $\sigma_{fu}$is obtained from material bending tests following ASTM 1609 or a similar method. The average angle α is with respect to the critical inclined cracks; it can be assumed of 45 degrees.

The shear stress has thus the below form:

$$v_u = \frac{V_c + V_f}{bd} = 0.11\beta_1 f'_c \frac{c}{d} + \sigma_{fu}(1 - \frac{c}{d})\cot\alpha \quad (2.4\text{-}17)$$

2.5 *Modified Compression Field Theory (MCFT)*

2.5.1 *Introduction*

The Modified Compression Field Theory (MCFT) was formulated as a model for predicting the behaviour of reinforced concrete subjected to shear and normal stresses [Vecchio and Collins, 1986], as shown in Figure 2.5-1.

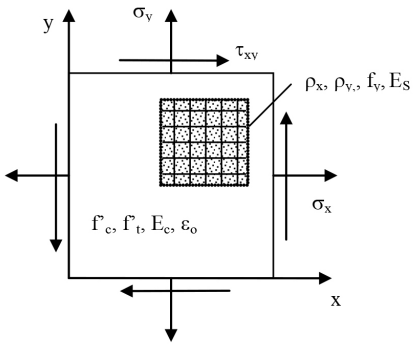

Figure 2.5-1: Reinforced concrete membrane element subject to in-plane stresses [Wong and Vecchio, 2002].

The MCFT determines the average and local strains and stresses of the concrete and reinforcement, and the widths and orientation of cracks throughout the load-deformation response of the element. Based on this information, the failure mode of the element can also be determined.

The MCFT models cracked concrete as an orthotropic material using a smeared rotating crack approach. Cracked concrete is treated as a solid continuum with cracks distributed over the membrane element, as opposed to a solid interrupted by discrete physical discontinuities. The smeared cracks freely reorient, remaining coaxial with the changing direction of the principal concrete compressive stress field.

As well as being computationally convenient, the smeared rotating crack approach is consistent with the distributed and meandering crack patterns observed in many reinforced concrete structures.

The theory is comprised of three sets of relationships: compatibility relationships for concrete and reinforcement average strains; equilibrium relationships involving average stresses in the concrete and reinforcement; and constitutive relationships for cracked concrete and reinforcement. The constitutive relationships for cracked concrete result from tests of reinforced concrete panels using a purpose-built Panel Element Tester at the University of Toronto. As such, the formulation of the MCFT incorporates realistic constitutive models for concrete based on experimentally observed phenomena. While cracks are smeared and the relationships are formulated

in terms of average stresses and strains, a critical aspect of the MCFT is the consideration of local strain and stress conditions at cracks.

2.5.2 *Assumptions*

- Reinforcement is uniformly distributed within the element.
- Shear and normal stresses are uniformly applied on the element.
- Uniformly distributed and rotating cracks.
- Unique stress state for each strain state, without consideration of strain history.
- Strains and stresses are average over a distance including several cracks.
- Orientations of principal strain, $\theta\varepsilon$, and orientations of principal stress, $\theta\sigma$, are the same.
- Perfect bond between the concrete and the reinforcement
- Independent constitutive relationships for concrete and reinforcement
- Negligible shear stresses in reinforcement.

2.5.3 *Compatibility relationships*

Figure 2.5-2 depicts the compatibility relationships pertain to the average strains in the concrete and reinforcement components.

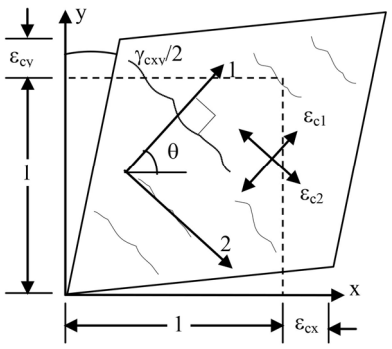

Figure 2.5-2: Average concrete strains due to average stress-strain response of concrete [Wong and Vecchio, 2002].

Having assumed the perfect bond condition between the concrete and the reinforcement, it follows that average strains experienced by the concrete are equally experienced by the reinforcement.
Therefore, for non-prestressed reinforcement, the average strains in the concrete, ε_c, and the reinforcement, ε_s, will be the same. Although the MCFT can address any number of reinforcement components and orientations, consider the orthogonally reinforced membrane element of figure. The strains of reinforcement parallel to the

x and y-directions are denoted by ε_{sx} and ε_{sy}, respectively. The compatibility relationships are expressed by the following equations:

$$\varepsilon_x = \varepsilon_{cx} = \varepsilon_{sx} \quad (2.5\text{-}1)$$

$$\varepsilon_y = \varepsilon_{cy} = \varepsilon_{sy} \quad (2.5\text{-}2)$$

With a value for the shear strain, γ_{xy}, relationships from Mohr's circle of strain determine the average principal concrete tensile strain, ε_{c1}, and the average principal concrete compressive strain, ε_{c2}, as follows:

$$\varepsilon_{c1}, \varepsilon_{c2} = \frac{1}{2}\left(\varepsilon_x + \varepsilon_y\right) \pm \frac{1}{2}\left[\left(\varepsilon_x - \varepsilon_y\right)^2 + {\gamma_{xy}}^2\right]^{1/2} \quad (2.5\text{-}3)$$

Relationships from Mohr's circle also determine the orientations of the average principal tensile strain axis, θ_ε, and stress axis, θ_σ, with respect to the x-axis:

$$\theta = \theta_\varepsilon = \theta_\sigma = \frac{1}{2} tan^{-1}\left(\frac{\gamma_{xy}}{\varepsilon_x - \varepsilon_y}\right) \quad (2.5\text{-}4)$$

2.5.4 *Equilibrium relationships*

The forces applied to the reinforced concrete element are resisted by stresses in the concrete and stresses in the reinforcement.
Consider the free body diagram of the member element, in Figure 2.5-3.

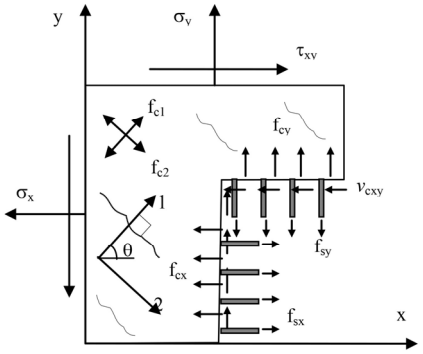

Figure 2.5-3: Free body diagram of reinforced concrete element showing average stresses [Wong and Vecchio, 2002].

Equilibrium of forces in the x and y-directions necessitates that the resultants of the applied normal stresses, σ_x and σ_y, be balanced by the resultants of the average concrete stresses, f_{cx} and f_{cy}, and the reinforcement stresses f_{sx} and f_{sy}. Equilibrium of moments requires that the applied shear stresses, τ_{xy}, are entirely resisted by average shear stresses in the concrete, v_{cxy}, (assuming the reinforcement does not exhibit dowel action). These equilibrium relationships for average stresses may be summarized as follows:

$$\sigma_x = f_{cx} + \rho_{sx} f_{sx} \quad (2.5\text{-}5)$$

$$\sigma_y = f_{cy} + \rho_{sy} f_{sy} \quad (2.5\text{-}6)$$

$$\tau_{xy} = \nu_{cxy} \quad (2.5\text{-}7)$$

where ρ_{sx} and ρ_{sy} are the reinforcement ratios in the x and y directions, respectively. As cracked concrete is orthotropic with respect to the principal stress directions, Mohr's circle of stress can be used to relate the average concrete stresses, f_{cx} and f_{cy}, to the average principal concrete tensile stress, f_{c1}:

$$f_{cx} = f_{c1} - \nu_{cxy} \cdot \cot(90 - \theta_\sigma) \quad (2.5\text{-}8)$$

$$f_{cy} = f_{c1} - \nu_{cxy} \cdot \tan(90 - \theta_\sigma) \quad (2.5\text{-}9)$$

2.5.5 *Constitutive relationships*

Constitutive relationships are required to link average stresses to average strains for both the reinforcement and the concrete. As described by Vecchio and Collins [1986], thirty reinforced concrete elements measuring 890x890x70 mm were subject to in-plane stress conditions by Panel Element Tester at the University of Toronto. The test results were analysed to develop constitutive models for cracked concrete in compression and tension.

With regards to concrete in compression, the constitutive relationships relate the principal compressive stress, f_{c2}, to the principal compressive strain, ε_{c2}. Panel test results indicate that the compressive strength and stiffness decrease as coexisting principal tensile strains, ε_{c1}, increase. This behaviour is known as "compression softening effect", it is incorporated by softening the stress-strain response of concrete in uniaxial compression. The proposed relationship is as follows:

$$f_{c2} = \frac{f_c'[2(\varepsilon_{c2}/\varepsilon_0) - (\varepsilon_{c2}/\varepsilon_0)^2]}{0.8 - 0.34(\varepsilon_{c1}/\varepsilon_0)} \quad (2.5\text{-}10)$$

The term in the numerator is the Hognestad parabolic relationship for concrete in uniaxial compression, often used for normal strength concretes. The value ε_0 is the concrete cylinder strain (a negative value) corresponding to the peak compressive stress, f'_c, as determined from uniaxial compression tests of concrete cylinders. The term in the denominator reflects the softening effect of principal tensile strains.

With regards to concrete in tension, the constitutive relationship relates the principal tensile stress, f_{c1}, to the principal tensile strain, ε_{c1}. It is first necessary to determine the uniaxial cracking strength, f'_t, and corresponding cracking strain, ε_{cr}. In the absence of information, they may be estimated as follow:

$$f_t' = 0.33\sqrt{f_c'} \quad (2.5\text{-}11)$$

$$\varepsilon_{cr} = \frac{f_t'}{E_c} \quad (2.5\text{-}12)$$

where E_c is the initial tangent stiffness of the concrete, estimated as:

$$E_c = 5000\sqrt{f_c'} \quad (2.5\text{-}13)$$

Before cracking, the concrete behaves linear-elastically in tension as follow:

$$f_{c1} = E_c \cdot \varepsilon_{c1} \quad for\ 0 < \varepsilon_{c1} < \varepsilon_{cr} \tag{2.5-14}$$

After the cracking, tensile stresses may be continued to exist in the concrete between cracks in reinforced concrete due to bond interactions between the concrete and reinforcement. The concrete tensile stress decays from the tensile strength as the principal concrete tensile strain increases. This phenomenon is known as "tension stiffening". The MCFT proposed relationship is as follows:

$$f_{c1} = \frac{f_t'}{1 + \sqrt{200\varepsilon_{c1}}} \tag{2.5-15}$$

As for the reinforcement in compression and tension, the MCFT uses a bilinear relationship between the average stress, f_s, and average strain ε_s. An initial ascending linear-elastic branch is followed by a yield plateau, as described by the following equations:

$$f_{sx} = E_s \cdot \varepsilon_{sx} \leq f_{sxyield} \tag{2.5-16}$$

$$f_{sy} = E_s \cdot \varepsilon_{sy} \leq f_{syyield} \tag{2.5-17}$$

Where E_s is the elastic modulus of the reinforcement, and $f_{sxyield}$ and $f_{syyield}$ are the yield stress of the reinforcement in the x and y-directions, respectively.

2.5.6 *Consideration of local crack conditions*

Given a compatible average strain condition, the preceding relationships can determine the average stresses in the concrete and reinforcement and the applied shear and normal stresses that they equilibrate.

However, the stress and strain formulations described above do not give information regarding local variations. At a crack, the tensile stresses in the reinforcement will be higher than average, while midway between cracks they will be lower than average. On the overhand, the concrete tensile stress will be zero at a crack and higher than average midway between cracks. To address these variations, the MCFT limits the local stresses at the crack and the average concrete tensile stress. Stresses field in reinforced concrete vary from the average condition between cracks to the local condition at the crack. Consider Figure 2.5-4 a, which illustrates the average stresses at a section between cracks perpendicular to the principal tensile stress direction, and Figure 2.5-4 b, which shows the local stresses at the free surface of the crack.

At a free surface of a crack, the average concrete tensile stresses diminish to virtually zero. To transmit the average tensile stress across the crack, the reinforcement stress and strain must increase locally at the crack. Static equivalency of the average and local stresses in the direction normal to the crack surface results in the following equation:

$$f_{c1} = \rho_x(f_{scrx} - f_{sx})cos^2\theta_{nx} + \rho_y(f_{scry} - f_{sy})cos^2\theta_{ny} \tag{2.5-18}$$

where f_{scrx} and f_{scry} are the local reinforcement stresses at a crack, and θ_{nx} and θ_{ny} are the angles between the normal to the crack reinforcement. Considering the above

equation, it is apparent that the average tensile concrete stress is limited by the yielding of the reinforcement at the crack. If the reinforcement yield strength is substituted for the local reinforcement stresses, the terms in parentheses define the reserve capacity of the reinforcement, which limits the post-cracking concrete tensile stress as follows:

$$f_{c1} = \rho_x(f_{sxyield} - f_{sx})cos^2\theta_{nx} + \rho_y(f_{syyield} - f_{sy})cos^2\theta_{ny} \qquad (2.5\text{-}19)$$

As a principal plane, shear stresses are absent from the section in Fig. However, as the reinforcement generally crosses the crack at a skew angle, local shear stresses, v_{ci}, are present on the crack surface. Static equivalency of average and local stresses in the direction tangential to the crack determines the local stresses as follows:

$$v_{ci} = \rho_x(f_{scrx} - f_{sx})\cos\theta_{nx} \cdot \sin\theta_{nx} + \rho_y(f_{scry} - f_{sy})\cos\theta_{ny} \cdot \sin\theta_{ny} \qquad (2.5\text{-}20)$$

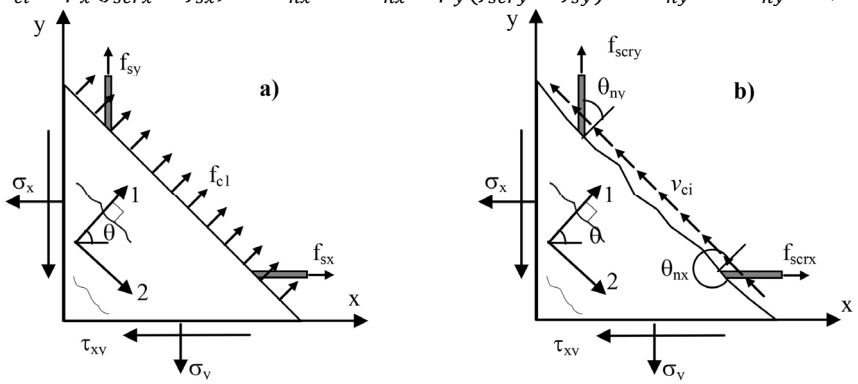

a) average stresses between crack *b) local stresses at crack free surface*

Figure 2.5-4: Comparison of average and local stresses at a crack [Wong and Vecchio, 2002].

Independently of the above equation, local shear stresses can only become so large before sliding shear failure occurs. The shear stress is limited by aggregate interlock mechanisms, which decrease in efficacy as the crack width, w, increases and the maximum aggregate size, a, decrease. Based on the analysis of aggregate interlock by Walraven [1981], the MCFT limits the shear stress on the crack as follows:

$$v_{ci} = \frac{\sqrt{f_c'}}{0.31 + 24\,w/(a + 26)} \quad (in\ mm, MPa) \qquad (2.5\text{-}21)$$

The average crack width, w, is the product of the principle concrete tensile strain and the average crack spacing perpendicular to the crack, s_θ:

$$w = \varepsilon_{c1} s_\theta \qquad (2.5\text{-}22)$$

$$s_\theta = \frac{1}{\frac{\cos\theta}{s_{mx}} + \frac{\sin\theta}{s_{my}}} \qquad (2.5\text{-}23)$$

The average crack spacing in the x-direction, s_{mx}, and y-direction, s_{my}, may be estimated from the bond properties and layout of the reinforcement. Refer to Collins and Mitchell [1997].

If either the maximum permitted average concrete tensile stress or local shear stress at a crack is exceed, then the strain state of the element is modified to result in a lower average concrete tensile stress.
A summary of the MCFT is schematized in Figure 2.5-5 and Figure 2.5-6.

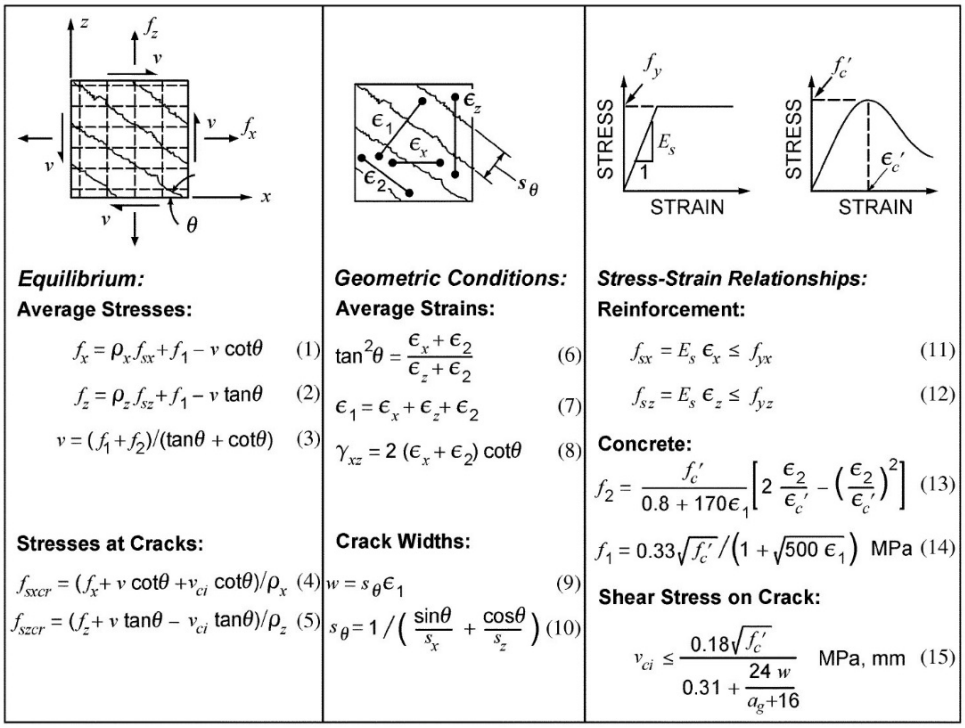

Figure 2.5-5: Summary of MCFT [Bentz et al., 2006].

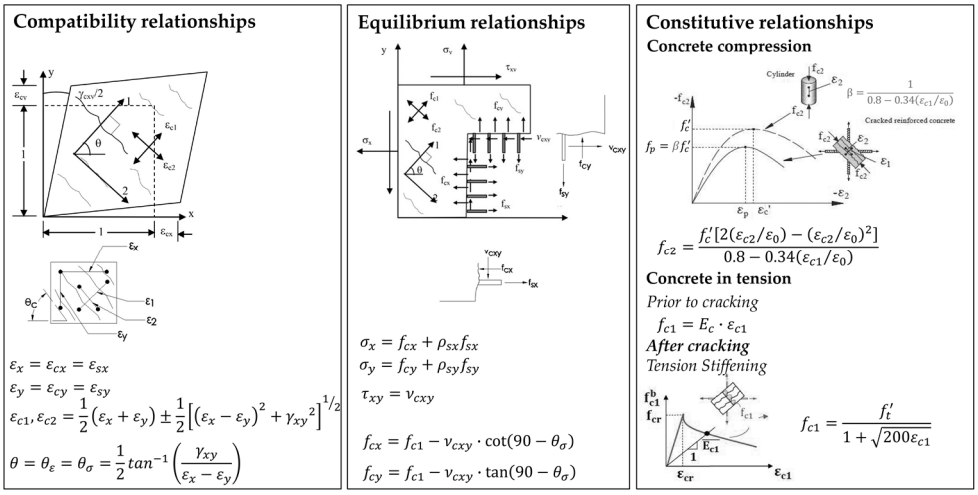

Figure 2.5-6: Aspects of MCFT.

2.6 *Finite Element Analysis*

2.6.1 *Introduction*

Use of external layers or jackets of reinforced Ultra-High Performance Fibre Reinforced Concrete (UHPFRC), in connection to existing elements, is an emerging technique for strengthening reinforced concrete (RC) structures. The layer of UHPFRC significantly increases the maximum resistance and deformation capacity of RC elements [Noshiravani and Brühwiler, 2013], thus creating a composite element, that is referred to as RU-RC elements.
The current *fib* Model Code for Concrete Structures 2010 (MC2010) allows FRC as a new structural material, facilitating its usage in innovative structural applications. FRC is considered primarily a material with a non-negligible residual strength after cracking [Facconi and Minelli, 2017].
In recent years, there have been important advances in the finite element analysis (FEA) of UHPFRC elements [Marini and Spacone, 2006].

2.6.2 *Review of finite element analysis of strengthening RC beams*

In recent years, various studies [Martinola *et al.*, 2010; Mostosi, 2012; Lampropoulos, 2016; Al-Osta *et al.*, 2017; Bahraq *et al.*, 2019] have reported on the use of FEA for studying the behaviour of strengthened beams.
Martinola *et al.* [2010] used a jacket made of UHPFRC for strengthening RC beams. They proposed a numerical analysis in order to understand the reinforcement behaviour. For the finite element analysis, DIANA 9.3 [DIANA FEA, 2009] software was used, and a 3D model was adopted. Concrete and steel properties were determined by preliminary studies on RC beam without UHPFRC jacket. In this model, a perfect bond between steel and concrete was assumed. The tensile properties of UHPFRC, characterized by hardening behaviour, were experimentally determined from uniaxial tensile tests on dog-bone specimens. Before cracking, a stress-strain relationship was adopted and, after cracking, a stress-crack opening law was used [Martinola *et al.*, 2010]. Back analysis was carried out to calibrate a constitutive stress-crack width law representing the tensile behaviour of the UHPFRC material. Figure 2.6-1 illustrates the modelling law of the UHPFRC material.

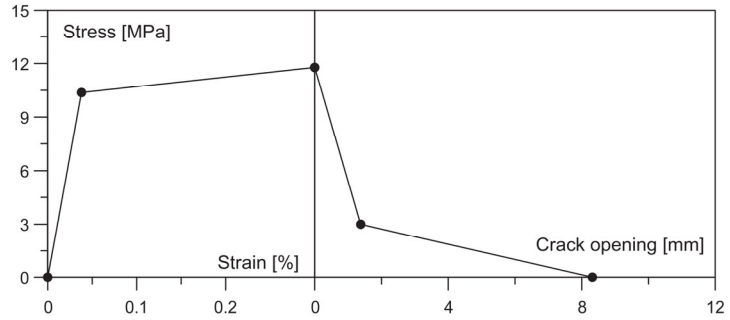

Figure 2.6-1: Tensile behaviour of the UHPFRC material [Martinola et al., 2010].

A FE model was employed to simulate the flexural tests. Perfect bond at the interface between concrete and UHPFRC was considered. The efficacy of the numerical model was confirmed by analysis of the crack pattern at collapse.
A study by Mostosi [2012] proposed a jacket made of UHPFRC for strengthening RC beams. She used a FE analysis to validate the reinforcement technique. The beams were modelled with 3D model. For the numerical analysis, DIANA 9.3 [DIANA FEA, 2009] was utilized. The analysis was conducted in displacement control with an increment of 1 mm. Figure 2.6-2 shows the mesh for the strengthening beam that was used for the FE analysis.

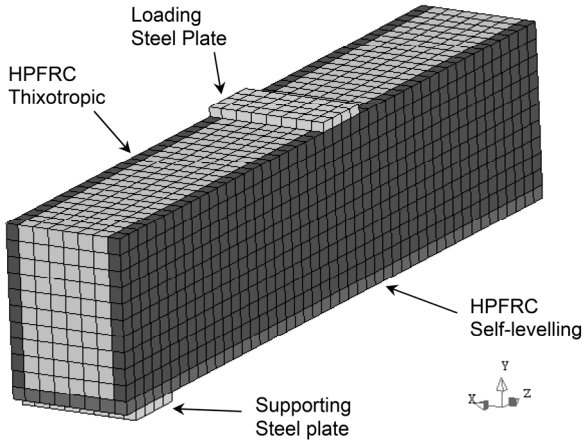

Figure 2.6-2: Mesh for the strengthening beam [Mostosi, 2012].

To model the concrete, the total strain crack model was used. This model describes the tensile and compressive behaviour of the concrete with one stress-strain relationship. The tensile behaviour has two phases: an elastic portion and a softening (or descending) portion. The compressive behaviour was modelled with a parabolic model. Steel reinforcements was definite using the results of the tensile test. The UHPFRC was modelled by a total strain rotating crack model. The compressive and

tensile strengths of the material were obtained from uniaxial compression tests on cubes and from direct tensile test on dog-bone specimens. UHPFRC has a hardening behaviour in tensile. The tensile behaviour of UHPFRC was modelled using a multilinear tension softening curve. The stress-strain curve was estimated by a line of four constituent branches. The first part was linear elastic, the second one was a hardening behaviour and the third and fourth parts were a softening branch. [Mostosi, 2012]. Figure 2.6-3 and Figure 2.6-4 report the tensile curves for the two UHPFRC materials that have been used in the model.

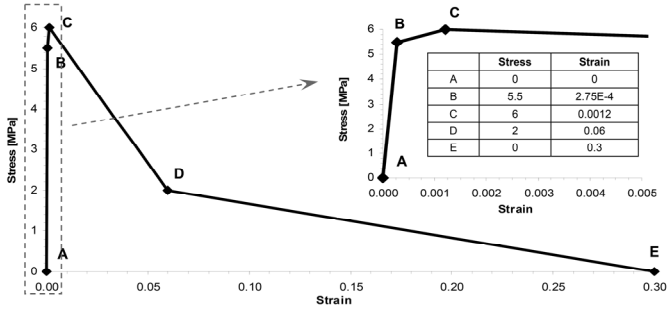

Figure 2.6-3: Stress-strain relationship for self-levelling UHPFRC material [Mostosi, 2012].

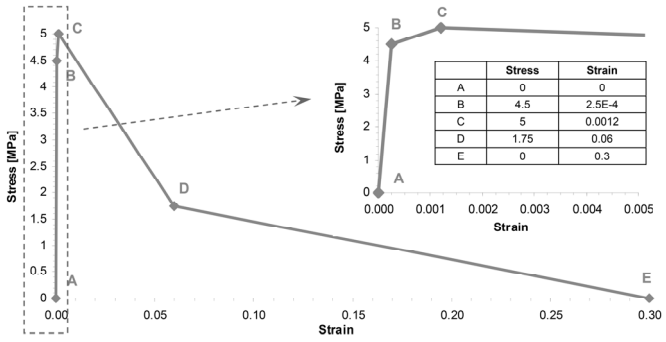

Figure 2.6-4: Stress-strain relationship for thixotropic UHPFRC material [Mostosi, 2012].

The crack pattern of experimental test was compared with the numerical analysis. They are very similar, confirming the accuracy of the model.

The numerical model by Lampropoulos [2016] was based on a previous experimental program. The numerical analysis was performed with FEM program ATENA [Červenka *et al.*, 2013]. In this numerical modelling, the concrete of the initial beam was simulated with non-linear behaviour and softening branches in both tension and compression. For the numerical model of UHPFRC, the material properties adopted in the model were based on the experimental results of compressive and tensile tests. The behaviour of UHPFRC was modelled with an elastic behaviour up to initiation of the microcracking. After the formation of the macrocrack at ultimate resistance,

there is the strain softening phase which was modelled by a bi-linear model. Thus, into the phase of strain hardening with multiple microcracking, the behaviour was linear. This model is in accord with the model proposed by Habel *et al.* [2006] and adopted by Noshiravani and Brühwiler [2014]. The interface between the initial beam and the UHPFRC was modelled using special two-dimensional elements with a coefficient of friction and cohesion such as to represent a well-roughened interface. The stress-strain model proposed by Lampropoulos predicts an accurate response of UHPFRC.

Al-Osta *et al.* [2017] investigated the effectiveness and efficiency of different techniques for strengthening of RC beams using UHPFRC. To better understand the flexural response of the strengthened beams, FE analysis was developed. The finite element analysis was performed with ABAQUS 6.13 [2013], and a 3D finite element model was used. They adopted a concrete damage plasticity theory [Lubliner *et al.*, 1989; Lee and Fenves, 1998; Rodríguez Soler *et al.*, 2013] to model the nonlinear behaviour of both normal concrete and UHPFRC. Their compressive behaviour was obtained from uniaxial compression test on cylindrical specimens. The behaviour in tension of UHPFRC was determined by a direct uniaxial test on dog-bone specimens. Steel reinforcement properties was achieved by experimental test and it was simulated by an elastic-perfectly plastic relationship. Linear brick elements (solid continuum) were used to model both the normal concrete and UHPFRC. Truss elements were used to model the steel reinforcing bars and stirrups. Figure 2.6-5 shows the mesh of the beam specimen.

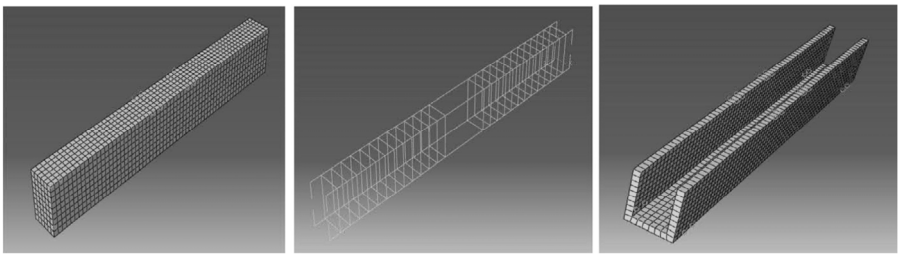

(a) concrete element *(b) steel reinforcement* *(c) UHPFRC element*

Figure 2.6-5: Mesh of strengthening beam specimen [Al-Osta et al., 2017].

Al-Osta *et al.* [2017] found that their model predicts the load-deflection response and the crack patterns in close agreement with the experimental results.

In addition to the experimental investigation, Bahraq *et al.* [2019] studied the shear behaviour of the strengthened beams using finite element analysis. ABAQUS [2013] FEA software was utilized for the numerical modelling and 3D finite element model was used. The materials properties of normal concrete, UHPFRC and steel reinforcement were modelled using the results obtained through the experimental tests. During previous experimental tests, there was no debonding observed, thus

the bond between normal concrete and UHPFRC was considered as perfect bond. Failure load, crack pattern, failure mode and load-deflection curves obtained through the FE modelling were compared with experimental data. This comparison indicated that the FE analysis is accurate, because failure modes and crack pattern are good agreement with that obtained through the experimental program.

2.6.3 *VecTor2 Program*

VecTor2 is a nonlinear finite element program for the analysis of two-dimensional reinforced concrete membrane structures. The program was developed at University of Toronto [Vecchio, 1990]. The theoretical foundations of VecTor2 are the Modified Compression Field Theory (MCFT) [Vecchio and Collins, 1986] and the Disturbed Stress Field Model (DSFM) [Vecchio, 2000]. VecTor2 models cracked concrete as an orthotropic material with smeared and rotating cracks. Flow chart in Figure 2.6-6 summarizes the VecTor2 algorithm for nonlinear finite element analysis.
VecTor2 has a user friendly pre-processor FormWorks [Wong and Vecchio, 2002], and post-processor Augustus [©Bentz, 1996-2007]. For detailed summary of the program functionality and material library refer to the FormWorks manual by Wong and Vecchio [2002]. To the accuracy of the VecTor2 results, the concrete constitutive and behavioural models are fundamental. At each load step, the structure stiffness is defined from the stresses and strains determined from the constitutive models. Additionally, the inclusion or omission of a model determines the appropriateness of the results of the analysis [Wong and Vecchio, 2002].

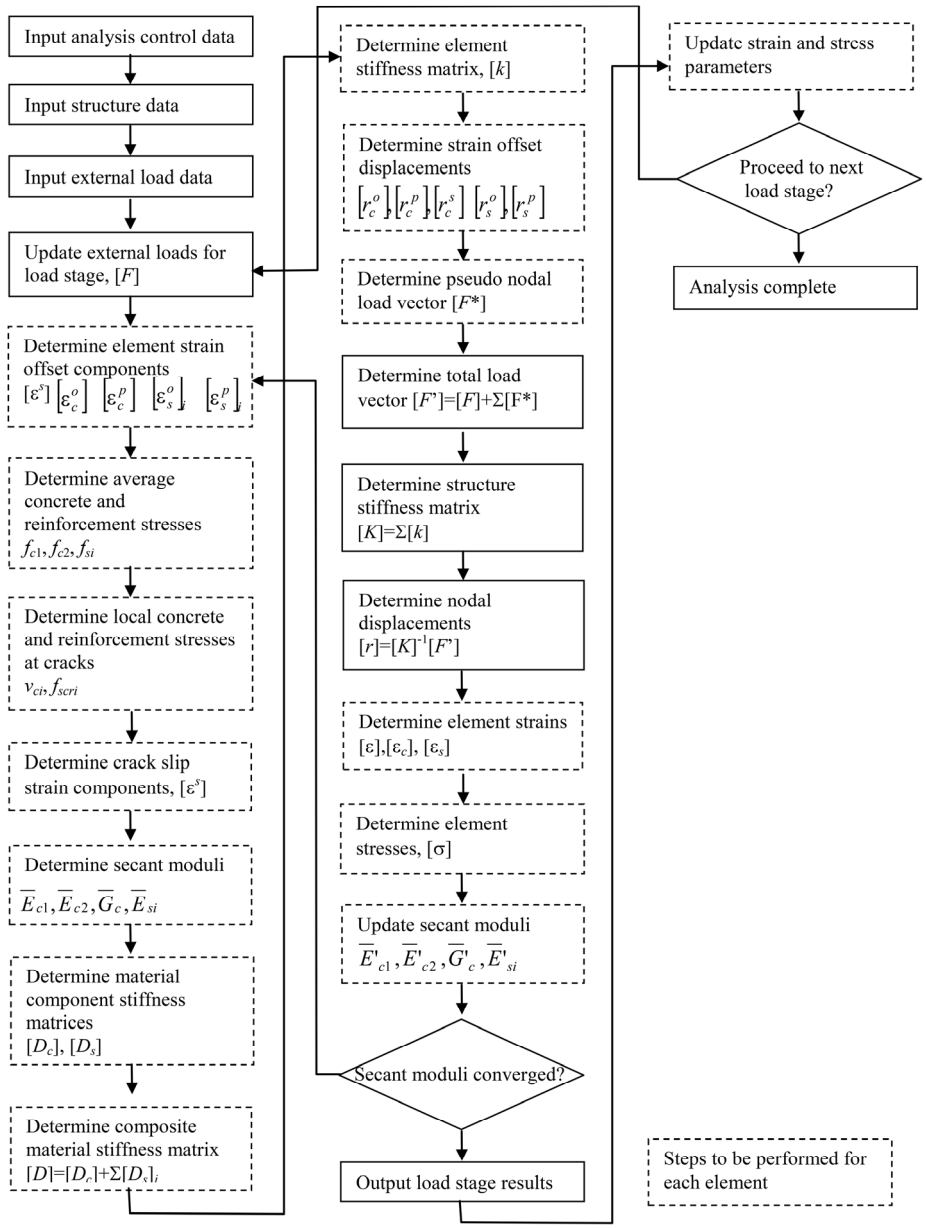

Figure 2.6-6: VecTor2 nonlinear finite element analysis algorithm [Wong and Vecchio, 2002].

2.6.3.1 Fibre reinforced concrete in VecTor2

In VecTor2, models for the FRC are available. These models are:

- Simplified Diverse Embedment Model (SDEM)-Monotonic [Lee *et al.*, 2012];
- Simplified Diverse Embedment Model (SDEM)-Cyclic;
- Diverse Embedment Model (DEM) [Lee *et al.*, 2011];
- Variable Engagement Model (VEM) [Voo and Foster, 2003];
- *fib* Model Code 2010 [2010].

The contribution of steel fibre reinforcement to concrete is considered in the calculation of tensile strength. The detailed information on models are given in the "VecTor2 & FormWorks User's Manual" by Wong and Vecchio [2002].

2.6.3.1.1 SDEM-Monotonic [Lee et al., 2012]

For monotonic loading conditions, in the Simplified Diverse Embedment Model (SDEM), the tensile stress in the fibres is expressed by the frictional bond behaviour in straight fibres and the additional mechanical anchorage in hooked-end fibres.

2.6.3.1.2 SDEM-Cyclic

For the cyclic behaviour of FRC, in the SDEM-Cyclic model, the unloading and reloading stiffness for the tensile stress attained by the fibres is calculated. For the envelope tensile stress-crack width response of fibre reinforced concrete, the stress attained by the fibres are calculated as in the SDEM-Monotonic model.

2.6.3.1.3 Diverse Embedment Model (DEM) [Lee et al., 2011]

The Diverse Embedment Model (DEM) considers the pull-out behaviour of individual fibres, the random distribution of fibres, and the effects of finite member dimensions. From the analysis for the pull-out behaviour of a fibre embedded on both sides, the fibre tensile stress at crack can be calculated. In this model, both mechanical anchorage effect of an end-hooked fibre and frictional bond behaviour of a straight fibre are represented. Additionally, the fibre orientation factor is calculated.

2.6.3.1.4 Variable Engagement Model (VEM) [Voo and Foster, 2003]

In the Variable Engagement Model (VEM) the crack opening displacement is calculated and the force in a single steel fibre is expressed. For mechanically anchored fibres, once the adhesive between the concrete and fibre is broken, slip must occur before anchorage is engaged.

2.6.3.1.5 Fib Model Code 2010 [2010]

The *fib* Model Code formulation for FRC in tension is based on the bending test results. Bending tests on prism beam with a notch is carried out aiming at determining the *load-deflection* relation. The results are used for deriving the *stress-crack width* relations by inverse analysis. In Section 2.1.6, the procedure is descripted.

2.6.3.2 Bond in VecTor2

The bond at the interface between substrate and overlay plays an important role in ensuring effective performance and durability of a concrete rehabilitation [Beushausen and Alexander, 2008]. In bonded concrete overlays, good adhesion is a key factor for providing monolithic action.
The bond behaviour between substrate and overlay can be modelled using bond-slip elements. In the finite element analysis program VecTor2 there are two types of bond-slip elements: link elements and contact elements. The precision of the bond-slip elements depends upon the variation in slip between successive nodes. The discrepancy between the theoretical strain energy and strain energy of bond elements to model given slip variations is a measure to evaluate the accuracy of the bond-slip elements [Wong and Vecchio, 2002]. Gan [2000] and Wong [2001] found that both bond-slip elements types give similar and good precision when the mesh is sufficiently fine [Wong and Vecchio, 2002]. Link elements [Ngo and Scordelis, 1967] are two-nodded nondimensional elements. They are only used to modelling concrete-rebar bond behaviour. Contact elements are a four-nodded elements. They have a linear dimension, thus they can better capture linear slip variations.
In the FE analysis of reinforced concrete, contact elements are a relatively new type of bond element [Gan, 2000]. These elements can be used to model bond behaviour across composite surfaces [Ma, 2016]. In the composite material, a new type of bond model is required to model the interaction between substrate and overlay [Ma, 2016]. In order for the components to work together, the interface between the substrate and overlay must facilitate large transfers of forces. Thus, the interface bond model is important to determine the failure mode of the structure.
Models for bond behaviour between concrete and UHPFRC interfaces are not established. Therefore, experimental bond stress-slip relationship must be included in the FE analysis of composite structures. Experimental stress-slip relationships are attained through the tests discussed in Section 2.3.4.

2.6.3.2.1 Contact elements

Contact elements are defined by four different node numbers in the sequence *j, k, m, n*. Figure 2.6-7 exemplifies the contact element in VecTor2 program.

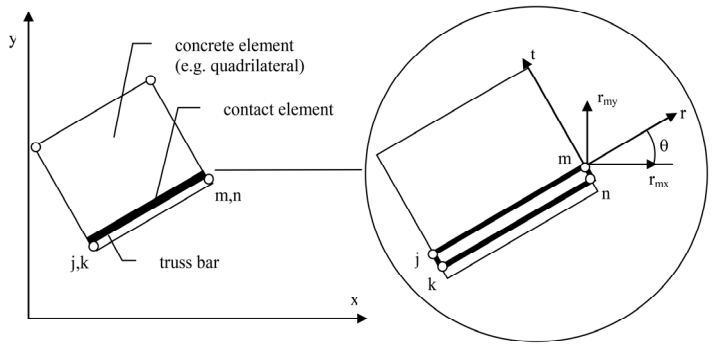

Figure 2.6-7: Contact element [Wong and Vecchio, 2002].

Nodes *j* and *k*, and node *m* and *n*, are defined at the same coordinate. Nodes *j* and *m* are attached to one element, while nodes *k* and *n* are attached to the adjacent element that is bonded to the first element. The contact element can assume any orientation in the *x, y* plane, but they cannot assume slips in the out-of-plane direction. The displacements are linearly interpolated along the element from the values at the two node pairs. Thus, the deformations within both adjacent elements and to model linear slip variations are ensured.

The bond stress, τ, is related to the tangential displacement, $\Delta_t$by the stiffness, k_t. The radial stress, σ, is related to the radial displacement, Δ_r, by the stiffness, k_r, as follows:

$$\begin{bmatrix}\tau\\ \sigma\end{bmatrix} = \begin{bmatrix}k_t & 0\\ 0 & k_r\end{bmatrix}\begin{bmatrix}\Delta_t\\ \Delta_r\end{bmatrix}$$

The stiffness, k_t, is obtained from the bond-slip curve, and it relates to the bond stress to the bond slip.

Contact elements have eight degrees of freedom. The contact elemental stiffness matrix $[k]$assumes the following form:

$$[k] = [T]^T[k]'[T]$$

where:

$$[k]' = \frac{A}{6}\left[\begin{array}{cccc:cccc} 2k_t & 0 & -2k_t & 0 & k_t & 0 & -k_t & 0 \\ 0 & 2k_t & 0 & -2k_t & 0 & k_t & 0 & -k_t \\ -2k_t & 0 & 2k_t & 0 & -k_t & 0 & k_t & \\ 0 & -2k_t & 0 & 2k_t & 0 & -k_t & 0 & k_t \\ \hdashline k_t & 0 & -k_t & 0 & 2k_t & 0 & -2k_t & 0 \\ 0 & k_t & 0 & -k_t & 0 & 2k_t & 0 & -2k_t \\ -k_t & 0 & k_t & & -2k_t & 0 & 2k_t & 0 \\ 0 & -k_t & 0 & k_t & 0 & -2k_t & 0 & 2k_t \end{array}\right]$$

$$[T] = \left[\begin{array}{cccc:cccc} \cos\theta & \sin\theta & 0 & 0 & 0 & 0 & 0 & 0 \\ \sin\theta & \cos\theta & 0 & 0 & 0 & 0 & 0 & 0 \\ 0 & 0 & \cos\theta & \sin\theta & 0 & 0 & 0 & 0 \\ 0 & 0 & -\sin\theta & \cos\theta & 0 & 0 & 0 & 0 \\ \hdashline 0 & 0 & 0 & 0 & \cos\theta & \sin\theta & 0 & 0 \\ 0 & 0 & 0 & 0 & -\sin\theta & \cos\theta & 0 & 0 \\ 0 & 0 & 0 & 0 & 0 & 0 & \cos\theta & \sin\theta \\ 0 & 0 & 0 & 0 & 0 & 0 & -\sin\theta & \cos\theta \end{array}\right]$$

A is the bonded surface area tributary to the contact element.

Ma [2016] proposed a modification factor for the tangent stiffness of the contact element. In particularly, he assumed the tangential stiffness k_t as the stiffness obtained from bond stress-slip relationships k_{t0} multiplied by a modification factor μ_2:

$$\mathrm{k}_t = \mu_2 k_{t0}$$

where μ_2 is a function of the perpendicular stress σ acting across the contact element [Ma, 2016].

In this study, the relationship between the perpendicular stress and the change in the tangential stiffness of the bond element was estimated piecewise linear. A more appropriate model could be more asymptotic or curved, or partially curved and partially linear.

2.7 Summary

The addition of fibres to the concrete matrix has been shown to significantly improve the behaviour of otherwise brittle concrete. Enhancements in the behaviour of the concrete were particularly seen in:

- increased tensile and flexural strength of the concrete [Shah and Rangan, 1971; Dwarakanath and Nagaraj, 1992];
- increased post-cracking ductility of the concrete [Fanella and Naaman, 1985; Löfgren, 2005];
- increased energy absorption capacity of the concrete [Bentur and Mindess, 2007];
- reduced crack width and crack spacing [Fanella and Naaman, 1985].

The effectiveness of steel fibres in improving the behaviour of concrete depends on a number of factors: the fibre volume content, the fibre length, the fibre aspect ratio, the fibre tensile strength, the strength of the concrete matrix, and the orientation of the fibre.

The Ultra-High Performance Fibre Reinforced Concrete (UHPFRC) materials are characterized by high compressive strength, strain-hardening behaviour in tension, high fracture toughness, ductility and high durability. These characteristics make

UHPFRC suitable for the seismic retrofitting and the strengthening of RC elements. UHPFRC is applied on existing reinforced concrete elements as thin watertight overlays, as reinforcement layers and often combined with reinforcement bars.

The use of jackets or overlays made of UHPFRC has been recently proposed for the strengthening of existing RC columns [Beschi *et al.*, 2011; Meda *et al.*, 2016], beams [Alaee and Karihaloo, 2003; Martinola *et al.*, 2007; Martinola *et al.*, 2010; Noshiravani and Brühwiler, 2013; Ruano *et al.*, 2014; Lampropoulos *et al.*, 2016; Al-Osta *et al.*, 2017], bridge decks [Brühwiler and Denarié, 2008; Brühwiler *et al.*, 2015] and piers [Massicotte *et al.*, 2013; Reggia *et al.*, 2018].

Using high performance materials, the jacket thickness or the overlay can be significantly reduced with respect to a traditional solution in ordinary reinforced concrete. This technique allows the use of a 30-40 mm thickness. Thus, it does not lead to the increase of the section geometry, and consequently an increase of both mass and stiffness.

Several experiment studies have shown that UHPFRC composite elements have a significantly higher stiffness and ultimate resistance than corresponding RC elements alone. The additional R-UHPFRC reinforcement may increase the ultimate resistance. Another important contribution due to the UHPFRC retrofit is that the layer of UHPFRC modifies the failure mode from brittle shear failure to a ductile flexural failure mode. In fact, several tests on composite RC element have shown that the addition of a layer of UHPFRC delays the formation of the inclined shear crack in the concrete section. Many research studies confirm that the use of fibre reinforced concrete jacketing has the potential to be an efficient method for shear strengthening of reinforced concrete.

Some authors have observed that in UHPFRC composite elements the ductility decreases [Martinola *et al.*, 2007; Lampropoulos *et al.*, 2016; Al-Osta *et al.*, 2017]. To solve this problem some works [Park and Paulay, 1975; Mostosi *et al.*, 2011; Chalioris and Pourzitidis, 2012] have proposed adding a high strength steel mesh in the jacket. The solution is based on the use of a high performance jacket made of high strength steel mesh, having a higher tensile resistance, embedded in a thin layer of UHPFRC. The results have shown that the proposed technique allows for a large increase in the structure deformation capacity and ductility.

UHPFRC members can be designed without any mechanical device or stirrups connecting the two elements. Nevertheless, the surface preparation of the substrate concrete plays an important role in achieving a durable repair. In fact, the substrate surface preparation method considerably influences the bonding strength between the concrete substrate and UHPFRC. A number of experimental studies have shown that with good surface preparation no debonding occurs between the concrete section and the UHPFRC layer [Alaee and Karihaloo, 2003; Habel, 2004; Brühwiler

and Denarié, 2008; Oesterlee, 2010]. Thus, with good surface preparation, the monolithic behaviour can be assumed.
In conclusion, diverse works have demonstrated the efficiency of the UHPFRC retrofit technique on columns, beams, beam columns joints, slabs, bridges and walls. As mentioned above, the application of a layer of UHPFRC modifies the failure mode from brittle shear failure to a ductile flexural failure mode. In fact, the addition of a layer of UHPFRC delays the formation of the inclined shear crack in the concrete section.
The calculation of the transverse bending resistance of the compound section can be easily calculated using the analysis of the flat section, while, the calculation of the shear capacity in UHPFRC retrofit elements is complex. Numerous experimental tests have evaluated the efficiency of the UHPFRC as a retrofitting material in the shear-deficient RC beams. However, there are few analytical formulations available to calculate the strength shear increase.
Noshiravani and Brühwiler [2013] proposed a formulation to calculate the shear contributions in FRC. The shear resistance v_{Rd} of the composite element is calculated as a combination of the concrete contribution v_{Rc}, shear steel reinforcement contribution v_{Rs} and the UHPFRC contribution v_{RU}. The contribution of UHPFRC is calculated in reference to the rehabilitation and the strengthening of the Chillon viaduct. Formulation proposed can be applied only in the strengthening with top layer.
There are a several studies on the shear behaviour of FRC elements, but few refer to composite elements in UHPFRC-RC. Therefore, the existing models for FRC members should be perfected to determine the shear resistance of RU-RC members.

2.8 References

***AALETI, S., SRITHARAN, S., & ABU-HAWASH, A.**, 2013. "Innovative UHPC-normal concrete composite bridge deck. In Proceedings of the RILEM-fib-AFGC International Symposium on Ultra-High Performance Reinforced Concrete", Eds: F. Toutlemonde, J. Resplendino, Rilem Publications SARL, Bagneux, France (pp. 217-226).*

***ABAQUS 6.13**, 2013. "User Manual, Online Documentation Simulia", Dassault Systems.*

***ABRISHAMBAF, A., BARROS, J. A., & CUNHA, V. M.**, 2015. "Tensile stress–crack width law for steel fibre reinforced self-compacting concrete obtained from indirect (splitting) tensile tests", Cement and Concrete Composites, 57, 153-165.*

***ASCE-ACI Committee 426**.,1974. The shear strength of reinforced concrete members—slabs. J. Struct. Div., ASCE, 100(8), 1543-1591.*

***ACI COMMITTEE 445**, 1999 (Reapproved 2009). "recent approaches to shear design of structural concrete, (ACI 445R-99)", American concrete institute*

***ACI COMMITTEE 544**, 1988 (Reapproved 1999). "Design considerations for steel fibre reinforced concrete (ACI-544.4R-88)", American concrete institute.*

***ACI COMMITTEE 546**, 1980. "Guide for Repair of Concrete Bridge Superstructures (ACI 546.1 R-80)", American Concrete Institute, Detroit, 20 pp.*

***ACI COMMITTEE, & INTERNATIONAL ORGANIZATION FOR STANDARDIZATION**, 2008. "Building code requirements for structural concrete (ACI 318-08) and commentary", American Concrete Institute.*

***ALAEE, F. J., & KARIHALOO, B. L.**, 2003. "Retrofitting of reinforced concrete beams with CARDIFRC", Journal of Composites for Construction, 7(3), 174-186.*

***ALBERTI, M. G., ENFEDAQUE, A., GÁLVEZ, J. C., & AGRAWAL, V.**, 2016. "Fibre distribution and orientation of macro-synthetic polyolefin fibre reinforced concrete elements", Construction and Building Materials, 122, 505-517.*

***AL-OSTA, M. A., ISA, M. N., BALUCH, M. H., & RAHMAN, M. K.**, 2017. "Flexural behavior of reinforced concrete beams strengthened with ultra-high performance fiber reinforced concrete", Construction and Building Materials, 134, 279-296.*

***AMIN, A., FOSTER, S. J., & MUTTONI, A.**, 2015. "Derivation of the σ-w relationship for SFRC from prism bending tests", Structural Concrete, 16(1), 93-105.*

***ASHOUR, S. A., HASANAIN, G. S., & WAFA, F. F.**, 1992. "Shear behavior of high-strength fiber reinforced concrete beams", Structural Journal, 89(2), 176-184.*

***ASTM C1609**, 2012. "Standard test method for flexural performance of fiberreinforced concrete (using beam with third-point loading)", American Standard.*

***ASTM C496**, 2004. "Standard test method for splitting tensile strength of cylindrical concrete specimens", Annual Book of ASTM Standards: American Society of Testing Materials.*

***AUSTIN, S., ROBINS, P., & PAN, Y.**, 1999. "Shear bond testing of concrete repairs", Cement and concrete research, 29(7), 1067-1076.*

***AVADHANAM, R. M., MURALIDHARAN, A., & PRAKASAM, G.**, 2019. "Analytical Studies on Debonding Behaviour of RC Beams Strengthened with UHPFRC Overlay", Journal of The Institution of Engineers (India): Series A, 100(2), 241-252.*

***BAHRAQ, A. A., AL-OSTA, M. A., AHMAD, S., AL-ZAHRANI, M. M., AL-DULAIJAN, S. O., & RAHMAN, M. K.**, 2019. "Experimental and Numerical Investigation of Shear Behavior of RC Beams Strengthened by Ultra-High Performance Concrete", International Journal of Concrete Structures and Materials, 13(1), 6.*

***BARRAGÁN, B. E.**, 2002. "Failure and toughness of steel fiber reinforced concrete under tension and shear", Universitat Politècnica de Catalunya, 71-91.*

BARROS, J. A., CUNHA, V. M., RIBEIRO, A. F., & ANTUNES, J. A. B. *,2005. Post-cracking behaviour of steel fibre reinforced concrete. Materials and Structures, 38(1), 47-56.*

BARROS, J. A., & FIGUEIRAS, J. A.*, 1999. "Flexural behavior of SFRC: testing and modelling", Journal of materials in civil engineering, 11(4), 331-339.*

BENCARDINO, F., RIZZUTI, L., & SPADEA, G.*, 2007. "Experimental tests v/s theoretical modeling for FRC in compression", in Proceedings of 6th International Conference on Fracture Mechanics of Concrete and Concrete Structures-FraMCoS (Vol. 6, pp. 1473-1480).*

BENCARDINO, F., RIZZUTI, L., SPADEA, G., & SWAMY, R. N.*, 2008. "Stress-strain behavior of steel fiber-reinforced concrete in compression", Journal of Materials in Civil Engineering, 20(3), 255-263.*

BENTUR, A., & MINDESS, S.*, 2007. "Fibre Reinforced Cementitious Composites", Civil Engineering, 625.*

BENTZ, E.*, 1996-2007. "Augustus-Finite Element Analysis of Reinforced Concrete Post-Processor for VecTor2 and TRIX", http://www.civ.utoronto.ca/vector, Last Accessed Sep. 17, 2007.*

BENTZ, E. C., VECCHIO, F. J., & COLLINS, M. P. *[2006]. Simplified modified compression field theory for calculating shear strength of reinforced concrete elements. ACI Materials Journal, 103(4), 614.*

BESCHI, C., MEDA, A., & RIVA, P.*, 2011. "Column and joint retrofitting with high performance fiber reinforced concrete jacketing", Journal of Earthquake Engineering, 15(7), 989-1014.*

BESCHI, C., RIVA, P., METELLI, G., & MEDA, A.*, 2015. "HPFRC jacketing of non seismically detailed RC corner joints", Journal of Earthquake Engineering, 19(1), 25-47.*

BEUSHAUSEN, H. D.*, 2005. "Long-term performance of bonded concrete overlays subjected to differential shrinkage" (Doctoral dissertation, University of Cape Town).*

BEUSHAUSEN, H., & ALEXANDER, M. G.*, 2008. "Bond strength development between concretes of different ages", Magazine of concrete research, 60(1), 65-74.*

BISSONNETTE, B., VAYSBURD, A. M., & VON FAY, K. F.*, 2012. "Best practices for preparing concrete surfaces prior to repairs and overlays" (No. MERL 12-17).*

BONALDO, E., BARROS, J. A., & LOURENÇO, P. B.*, 2005. "Bond characterization between concrete substrate and repairing SFRC using pull-off testing", International journal of adhesion and adhesives, 25(6), 463-474.*

BRÜHWILER, E., & DENARIÉ, E.*, 2008. "Rehabilitation of concrete structures using ultra-high performance fibre reinforced concrete", (No. CONF), University of Kassel.*

***BRÜHWILER, E., & DENARIÉ, E.**, 2013. "Rehabilitation and strengthening of concrete structures using ultra-high performance fibre reinforced concrete", Structural Engineering International, 23(4), 450-457.*

***BRÜHWILER, E., BASTIEN-MASSE, M., MÜHLBERG, H., HOURIET, B., FLEURY, B., CUENNET, S., & MAURER, M.**, 2015. September. "Strengthening the Chillon viaducts deck slabs with reinforced UHPFRC", in IABSE Symposium Report (Vol. 105, No. 24, pp. 1-8). International Association for Bridge and Structural Engineering.*

***BRÜHWILER, E., DENARIÉ, E., & HABEL, K.**, 2005. May. "Ultra-high performance fibre reinforced concrete for advanced rehabilitation of bridges", in Proc. fib-Symposium" Keep Concrete attractive", Budapest (Vol. 2, pp. 951-956).*

***BRÜHWILER, E., DENARIÉ, E., & PUTALLAZ, J. C.**, 2005. "Instandsetzung einer Betonbrücke mit ultrahochleistungsfähigem Faserfeinkornbeton (UHLFB)–Effizienzsteigerung bei der Bauausführung und Verbesserung der Leistungsfähigkeit der Brücke. Beton-und Stahlbetonbau", 100(9), 822-827.*

***BRÜHWILER, E., HABEL, K., & DENARIÉ, E.**, 2004. "Advanced reinforced concrete for the improvement of bridges", in Second international Conference on Bridge Maintenance, Safety and Management (IABMAS'04) (No. CONF).*

***BURATTI, N., MAZZOTTI, C., & SAVOIA, M.** ,2010. Long-term behaviour of fiber-reinforced self-compacting concrete beams. In Design, production and placement of self-consolidating concrete (pp. 439-450). Springer, Dordrecht.*

***BURATTI, N., & MAZZOTTI, C.**, 2012. Effects of different types and dosages of fibres on the long–term behaviour of fibre–reinforced self–compacting concrete. In Proceedings of 8th RILEM Inertnational Symposium on Fibre Reinforced Concrete, RILEM PRO88 (pp. 715-725).*

***CAMPIONE, G., & LA MENDOLA, L.**, 2004. "Behavior in compression of lightweight fiber reinforced concrete confined with transverse steel reinforcement", Cement and Concrete Composites, 26(6), 645-656.*

***CAMPIONE, G., CUCCHIARA, C., LA MENDOLA, L., & PAPIA, M.**, 2005. "Steel–concrete bond in lightweight fiber reinforced concrete under monotonic and cyclic actions. Engineering Structures", 27(6), 881-890.*

***CASANOVA, P., & ROSSI, P.**, 1997. "Can steel fibers replace transverse reinforcements in reinforced concrete beams?", Materials Journal, 94(5), 341-354.*

***ČERVENKA, V., JENDELE, L., & ČERVENKA, J.**, 2013. "ATENA Program Documentation", Part 1. Theory. 2016.*

***CHALIORIS, C. E., & POURZITIDIS, C. N.**, 2012. "Self-Compacting Concrete Jacketing–Tests and Analysis", AASRI Procedia, 3, 624-629.*

CHEN, P. W., FU, X., & CHUNG, D. D. L., *1995. "Improving the bonding between old and new concrete by adding carbon fibers to the new concrete", Cement and concrete research, 25(3), 491-496.*

CNR-DT 204/2006, *2006. "Istruzioni per la progettazione, l'esecuzione ed il controllo di strutture di calcestruzzo fibrorinforzato", 17.*

COLLINS, M.P., AND MITCHELL, D., *1997. "Prestressed Concrete Structures", Response Publications, Canada, 766 pp.*

COMITE EURO-INTERNATIONAL DU BETON, *1993. "CEB-FIP model code 1990: Design code (No. 213-214)", Telford.*

CUNHA, V. M., *2010. "Steel fibre reinforced self-compacting concrete (from micromechanics to composite behavior)" (Doctoral dissertation).*

CUNHA, V. M., BARROS, J. A., & SENA-CRUZ, J., *2012. "Numerical simulation of three-point bending tests: two distinct approaches", in befib2012-8th RILEM International Symposium on Fibre Reinforced Concrete: Challenges and Opportunities (pp. 1-12). Universidade do Minho.*

DE MONTAIGNAC, R., MASSICOTTE, B., CHARRON, J. P., & NOUR, A., *2012. "Design of SFRC structural elements: post-cracking tensile strength measurement", Materials and Structures, 45(4), 609-622.*

DEL VECCHIO, C., DI LUDOVICO, M., BALSAMO, A., & PROTA, A., *2018. "Seismic retrofit of real beam-column joints using fiber-reinforced cement composites", J. Struct. Eng, 144(5), 04018026.*

DELATTE, N. J., WILLIAMSON, M. S., & FOWLER, D. W., *2000. "Bond strength development with maturity of high-early-strength bonded concrete overlays", Materials Journal, 97(2), 201-207.*

DENARIÉ, E., *2005. "SAMARIS D22-Full scale application of UHPFRC for the rehabilitation of bridges–from the lab to the field (No. REP_WORK)", SAMARIS.*

DIANA FEA, *2009. "DIANA (Displacement Analyzer), Version 9.3. User manual", Delft, Netherlands.*

DINH, H. H., PARRA-MONTESINOS, G. J., & WIGHT, J. K., *2010. "Shear strength model for steel fiber reinforced concrete beams without stirrup reinforcement", Journal of Structural Engineering, 137(10), 1039-1051.*

DWARAKANATH, H. V., & NAGARAJ, T. S., *1992. "Comparative study of predictions of flexural strength of steel fiber concrete", Structural Journal, 88(6), 714-720.*

***EL-RAKIB, T. M., FARAHAT, A. M., EL-DEGWY, W. M., & SHAHEEN, H. H.**, 2003. "Shear transfer parameters at the interface between old and new concrete", Proceedings ICPCM.*

***EMBERSON, N. K., & MAYS, G. C.**, 1990. "Significance of property mismatch in the patch repair of structural concrete Part 1: Properties of repair systems", Magazine of Concrete Research, 42(152), 147-160.*

***EMMONS, R. H.**, 1993. "Concrete repair and maintenance illustrated", United State of America: Robert Means Co.*

***EUROCODE 2**, 2003. "Design of Concrete Structures", prEN 1992 Ver. December 2003.*

***EZELDIN, A. S., & BALAGURU, P. N.**, 1992. "Normal-and high-strength fiber-reinforced concrete under compression", Journal of materials in civil engineering, 4(4), 415-429.*

***FACCONI, L., & MINELLI, F.**, 2017. "Verification of structural elements made of FRC only: A critical discussion and proposal of a novel analytical method", Engineering Structures, 131, 530-541.*

***FANELLA, D. A., & NAAMAN, A. E.**, 1985. "Stress-strain properties of fiber reinforced mortar in compression", Journal of the American Concrete Institute, 82(4), 475-483.*

***FÉDÉRATION INTERNATIONALE DU BÉTON (fib)**, 2013. "Fib Model Code for concrete structures 2010", Fib Bulletin No. 65 and 66, fib (CEBFIP), Lausanne, Switzerland.*

***FENWICK, R. C., & PAULEY, T.** ,1968."Mechanism of shear resistance of concrete beams". Journal of the Structural Division, 94(10), 2325-2350.*

***FERRARA, L.** ,2019. High performance fibre reinforced cementitious composites: Six memos for the XXI century societal and economical challenges of civil engineering. Case Studies in Construction Materials, 10, e00219.*

***FIB BULLETIN N. 14**, 2001. "Externally bonded FRP reinforcement for RC structures", Technical report, International Federation for Structural Concrete (fib), October 2001, 138 pp.*

***FIB BULLETIN N. 24**, 2003. "Seismic assessment of reinforced concrete buildings", State-of-art report, International Federation for Structural Concrete (fib) August 2003, 312 pp.*

***FIB BULLETIN N. 35**, 200) "Retrofitting of concrete structures by externally bonded FRPs, with emphasis on seismic applications", Technical report, International Federation for Structural Concrete (fib), April 2006, 220 pp.*

***FIB REPORT**, 1991 "Repair and strengthening of concrete strengthening of concrete structures. Guide to good practice", Thomas Telford Ltd., 37 pp.*

***FIP FEDERATION INTERNATIONALE DE LA PRÉCONTRAINTE**, 1978, "Shear at the Interface of Precast and In-Situ Concrete", Technical Report.*

***GAN, Y.**, 2000. "Bond stress and slip modeling in nonlinear finite element analysis of reinforced concrete structures", University of Toronto.*

***GARG, V., BANSAL, P. P., & SHARMA, R.**, 2019. "Retrofitting of Shear-Deficient RC Beams Using UHPFRC. Iranian Journal of Science and Technology, Transactions of Civil Engineering, 1-10.*

***GIURIANI, E., & FRANGIPANE, A.**, 1993, June. "Wood-to-concrete composite section for stiffening of ancient wooden beam floors", In Proc., 1st Italian Workshop on Composite Structures (pp. 307-317).*

***GRANJU, J. L.**, 1996. "Thin bonded overlays: about the role of fiber reinforcement on the limitation of their debonding", Advanced Cement Based Materials, 4(1), 21-27.*

***GRZYBOWSKI, M.**, 1989, June. "Determination of crack-arresting properties of fiber-reinforced cementitious composites", Royal Institute of Technology, Stockholm, Sweden, Chapter 12.*

***GUSTAFSSON, J., & NOGHABAI, K.**, 1999. "Steel fibers as shear reinforcement in high strength concrete beams", Nordic Concrete Research-Publications-, 22, 35-52.*

***HABEL, K.**, 2004. "Structural behaviour of elements combining ultra-high performance fibre reinforced concretes (UHPFRC) and reinforced concrete (No. THESIS)", EPFL.*

***HABEL, K., DENARIÉ, E., & BRÜHWILER, E.**, 2006. "Structural response of elements combining ultrahigh-performance fiber-reinforced concretes and reinforced concrete", Journal of structural engineering, 132(11), 1793-1800.*

***HABER, Z. B., MUNOZ, J. F., DE LA VARGA, I., & GRAYBEAL, B. A.**, 2018. "Bond characterization of UHPC overlays for concrete bridge decks: Laboratory and field testing", Construction and Building Materials, 190, 1056-1068.*

***HADDAD, R. H., AL-MEKHLAFY, N., & ASHTEYAT, A. M.**, 2011. "Repair of heat-damaged reinforced concrete slabs using fibrous composite materials", Construction and Building Materials, 25(3), 1213-1221.*

***HADDAD, R. H., SHANNAG, M. J., & HAMAD, R. J.**, 2007. "Repair of heat-damaged reinforced concrete T-beams using FRC jackets", Magazine of Concrete Research, 59(3), 223-231.*

***HSU, L. S., & HSU, C. T.**, 1994. "Stress-strain behavior of steel-fiber high-strength concrete under compression", Structural Journal, 91(4), 448-457.*

***JO, B. W., SHON, Y. H., & KIM, Y. J.**, 2001. "The evalution of elastic modulus for steel fiber reinforced concrete", Russian Journal of Nondestructive Testing, 37(2), 152-161.*

***JOHNSTON, C.D.**, 2001. "Fibre-Reinforced Cements and Concretes", Gordon and Breach Science Publishers, Ottawa, Canada, 372 p.*

***JULIO, E. N., BRANCO, F. A., & SILVA, V. D.**, 2004. "Concrete-to-concrete bond strength. Influence of the roughness of the substrate surface", Construction and Building materials, 18(9), 675-681.*

***JÚLIO, E. N., BRANCO, F. A., SILVA, V. D., & LOURENÇO, J. F.**, 2006. "Influence of added concrete compressive strength on adhesion to an existing concrete substrate", Building and Environment, 41(12), 1934-1939.*

***KAAR, P. H., HANSON, N. W., & CAPELL, H. T.**, 1978. "Stress-strain characteristics of high-strength concrete", Special Publication, 55, 161-186.*

***KAUFMANN, N.**, 1971. "Das Sandflächenverfahren. Straßenbau-Technik", 24(3), 131-135.*

***KHAN, M. I., AL-OSTA, M. A., AHMAD, S., & RAHMAN, M. K.**, 2018. "Seismic behavior of beam-column joints strengthened with ultra-high performance fiber reinforced concrete", Composite Structures, 200, 103-119.*

***KHUNTIA, M., STOJADINOVIC, B., & GOEL, S. C.**, 1999. "Shear strength of normal and high-strength fiber reinforced concrete beams without stirrups", Structural Journal, 96(2), 282-289.*

***LACOMBE, P., BEAUPRÉ, D., & POULIOT, N.**, 1999. "Rheology and bonding characteristics of self-leveling concrete as a repair material", Materials and structures, 32(8), 593-600.*

***LAMPROPOULOS, A. P., PASCHALIS, S. A., TSIOULOU, O. T., & DRITSOS, S. E.**, 2016. "Strengthening of reinforced concrete beams using ultra high performance fibre reinforced concrete (UHPFRC)", Engineering Structures, 106, 370-384.*

***LEE, S. C., CHO, J. Y., & VECCHIO, F. J.**, 2011. "Diverse embedment model for steel fiber-reinforced concrete in tension: model development", ACI materials Journal, 108(5), 516.*

***LEE, S. C., CHO, J. Y., & VECCHIO, F. J.**, 2011. "Diverse embedment model for steel fiber-reinforced concrete in tension: Model verification", ACI Materials Journal, 108(5), 526.*

***LEE, S. C., CHO, J. Y., & VECCHIO, F. J.**, 2011. "Model for post-yield tension stiffening and rebar rupture in concrete members", Engineering Structures, 33(5), 1723-1733.*

***LEE, J., & FENVES, G. L.**, 1998. "Plastic-damage model for cyclic loading of concrete structures", Journal of engineering mechanics, 124(8), 892-900.*

***LEE, S. C., CHO, J. Y., & VECCHIO, F. J.**, 2012. "Simplified Diverse Embedment Model for Steel Fiber Reinforced Concrete in Tension", ACI Material Journal.*

***LEE, S. C., CHO, J. Y., & VECCHIO, F. J.**, 2013. "Tension-Stiffening Model for Steel Fiber-Reinforced Concrete Containing Conventional Reinforcement", ACI Structural Journal, 110(4).*

***LEE, S. C., OH, J. H., & CHO, J. Y.**, 2012. "Compressive Behavior of Normal and High Strength Concrete with End-Hooked Steel Fibers".*

***LI, S. E., GEISSERT, D. G., FRANTZ, G. C., & STEPHENS, J. E.**, 1999. "Freeze-thaw bond durability of rapid-setting concrete repair materials", Materials Journal, 96(2), 242-249.*

***LI, V. C., WANG, Y., & BACKER, S.**, 1990. "Effect of inclining angle, bundling and surface treatment on synthetic fibre pull-out from a cement matrix", Composites, 21(2), 132-140.*

***LÖFGREN, I.**, 2005. "Fibre-reinforced Concrete for Industrial Construction-a fracture mechanics approach to material testing and structural analysis", Chalmers University of Technology.*

***LUBLINER, J., OLIVER, J., OLLER, S., & OÑATE, E.**, 1989. "A plastic-damage model for concrete" International Journal of solids and structures, 25(3), 299-326.*

***MA, R.**, 2016. "Development of Contact Elements for Finite Element Analysis of Composite Structures", Report doctoral dissertation, University of Toronto.*

***MAIDL, B.R.**, 1995. "Steel Fibre Reinforced Concrete", Ernst & Sohn, Berlin, Germany.*

***MAKITA, T., & BRÜHWILER, E.**, 2012. "Fatigue behaviour of bridge deck slab elements strengthened with reinforced UHPFRC", Proceedings Bridge Maintenance, Safety, Management, Resilience and Sustainability, 1(CONF), 1974-1980.*

***MANSUR, M. A., CHIN, M. S., & WEE, T. H.**, 1999. "Stress-strain relationship of high-strength fiber concrete in compression", Journal of materials in civil engineering, 11(1), 21-29.*

***MANSUR, M. A., ONG, K. C. G., & PARAMASIVAM, P.**, 1986. "Shear strength of fibrous concrete beams without stirrups", Journal of structural engineering, 112(9), 2066-2079.*

***MARINI, A., & MEDA, A.**, 2009. "Retrofitting of R/C shear walls by means of high performance jackets", Engineering Structures, 31(12), 3059-3064.*

*1. **MARINI, A., PLIZZARI, G., & ZANOTTI, C.**, 2010. "Seismic Enhancement of Existing Buildings by Means of Fiber Reinforced Concrete Diaphragms", in Improving the Seismic Performance of Existing Buildings and Other Structures (pp. 1384-1395).*

***MARINI, A., & SPACONE, E.**, 2006. "Analysis of reinforced concrete elements including shear effects", ACI Structural Journal, 103(5), 645.*

MARINI, A., ZANOTTI, C., & PLIZZARI, G.*, 2008, September. "Seismic strengthening of existing structures by means of fibre reinforced concrete floor diaphragms", in BEFIB 2008: 7th RILEM International Symposium on Fibre Reinforced Concrete (pp. 977-987). RILEM Publications SARL.*

MARTINOLA, G., MEDA, A., PLIZZARI, G. A., & RINALDI, Z.*, 2007, June. "An application of high performance fiber reinforced cementitious composites for R/C beams strengthening", in FraMCos-6. 6th Int. Conf. on Fracture Mechanics of concrete and concrete structures. Catania (Vol. 17, p. 22).*

MARTINOLA, G., MEDA, A., PLIZZARI, G. A., & RINALDI, Z.*, 2010. "Strengthening and repair of RC beams with fiber reinforced concrete", Cement and concrete composites, 32(9), 731-739.*

MASSICOTTE, B., DAGENAIS, M. A., & LAGIER, F.*, 2013, October. "Performance of UHPFRC jackets for the seismic strengthening of bridge piers", in Proceeding of the 2nd Int Symp on UHPFRC Designing and building with UHPFRC: from innovation to large-scale realizations. Marseille, France (pp. 1-11).*

MATTOCK, A. H., KRIZ, L. B., & HOGNESTAD, E.*, 1961, February. "Rectangular concrete stress distribution in ultimate strength design", In Journal Proceedings (Vol. 57, No. 2, pp. 875-928).*

MEDA, A., & RIVA, P.*, 2001. "Strengthening of wooden floors with high performance concrete slabs", Internationale Zeitschrift für Bauinstandsetzen und Baudenkmalpflege, 7(6), 621-639.*

MEDA, A., MINELLI, F., PLIZZARI, G. A., & RIVA, P.*, 2005. "Shear behaviour of steel fibre reinforced concrete beams", Materials and structures, 38(3), 343-351.*

MEDA, A., MOSTOSI, S., RINALDI, Z., & RIVA, P.*, 2016. "Corroded RC columns repair and strengthening with high performance fiber reinforced concrete jacket", Materials and Structures, 49(5), 1967-1978.*

MEDA, A., PLIZZARI, G. A., & SORELLI, L.*, 2004. "Uni-axial and bending test for the determination of fracture properties of fiber reinforced concrete", in Proceedings of the Fifth International Conference on Fracture Mechanics of Concrete and Concrete Structures. Vail, USA (Vol. 2, pp. 1163-1170).*

MINELLI, F.*, 2005. "Plain and fiber reinforced concrete beams under shear loading: Structural behavior and design applications", Phd, University of Brescia.*

MOMAYEZ, A., EHSANI, M. R., RAMEZANIANPOUR., A. A., & RAJAIE, H.*, 2005. "Comparison of methods for evaluating bond strength between concrete substrate and repair materials", Cement and concrete research, 35(4), 748-757.*

***MOMAYEZ, A., RAMEZANIANPOUR, A. A., RAJAIE, H., & EHSANI, M. R.**, 2004. "Bi-surface shear test for evaluating bond between existing and new concrete", Materials Journal, 101(2), 99-106.*

***MORETTO, O.**,1945. "An Investigation of the Strength of Welded Stirrups in Reinforced Concrete Beam." ACI Journal Proceedings, 42(11), 141-162.*

***MOSTOSI, S.**, 2012. "Strengthening of rc beams with high performance concrete", Doctoral dissertation, University of Brescia.*

***MOSTOSI, S., RIVA, P., MARINGONI, S., & MEDA, A.**, 2011. "Shear strengthening of RC beams with high performance jacket", in fib Symposium 2011 in Prague: Concrete engineering for excellence and efficiency.*

***MUDADU, A., TIBERTI, G., PLIZZARI, G. A., & MORBI, A.**, 2019. "Post-cracking behavior of polypropylene fiber reinforced concrete under bending and uniaxial tensile tests", Structural Concrete.*

***NAAMAN, A. E.**, 2007, December. "High performance fiber reinforced cement composites: classification and applications", in CBM-CI international workshop, Karachi, Pakistan (pp. 389-401).*

***NAAMAN, A. E.**, 2008. "High performance fiber reinforced cement composites", Naaman AE. High-performance construction materials: science and applications, Singapore: World Scientific Publishing, 91-153.*

***NAAMAN, A. E., & REINHARDT, H. W.**, 2003, June. "Setting the stage: Toward performance based classification of FRC composites", in High Performance Fiber Reinforced Cement Composites (HPFRCC4), Proceeding of the Fourth International RILEM Workshop, AE Naaman & HW Reinhardt (ed.) (pp. 1-4).*

***NAAMAN, A. E., PARAMASIVAM, P., BALAZS, G. L., EIBL, J., ERDELYI, L., HASSOUN, N. M., & LOHRMAN, G.**, 1995. "Reinforced and prestressed concrete using HPFRCC matrices", in Proceedings of the 2nd International RILEM/ACI Workshop (pp. 291-347).*

***NAGHIBDEHI, M. G., SHARBATDAR, M. K., & MASTALI, M.**, 2014. "Repairing reinforced concrete slabs using composite layers", Materials & Design, 58, 136-144.*

***NARAYANAN, R., & DARWISH, I. Y. S.**, 1987. "Use of steel fibers as shear reinforcement", Structural Journal, 84(3), 216-227.*

***NATARAJA, M. C., DHANG, N., & GUPTA, A. P.**, 1999. "Stress–strain curves for steel-fiber reinforced concrete under compression", Cement and concrete composites, 21(5-6), 383-390.*

***NOSHIRAVANI, T., & BRÜHWILER, E.**, 2013. "Analytical model for predicting response and flexure-shear resistance of composite beams combining reinforced ultrahigh performance fiber-reinforced concrete and reinforced concrete", Journal of Structural Engineering, 140(6), 04014012.*

***NOSHIRAVANI, T., & BRÜHWILER, E.**, 2013. "Experimental investigation on reinforced ultra-high-performance fiber-reinforced concrete composite beams subjected to combined bending and shear", ACI Structural Journal, 110(ARTICLE), 251-261.*

***NTC**, 2018. "Aggiornamento delle Norme tecniche per le costruzioni (No. 8)". decreto 17-1-2018, Gazzetta Ufficiale 42, 20-02-2018, Ordinary Suppl.*

***OESTERLEE, C.**, 2010. "Structural response of reinforced UHPFRC and RC composite members", Doctoral dissertation, Verlag nicht ermittelbar.*

***PARK, R. AND PAULAY, T.**, 1975. "Reinforced Concrete Structures", John Wiley & Sons, Ltd, New York.*

***PARRA-MONTESINOS, G. J.**, 2006. "Shear strength of beams with deformed steel fibers", Concrete International, 28(11), 57-66.*

***PIGEON, M. & SAUCIER, F.**, 1992. "Durability of repaired concrete structures" in Proceedings, International Symposium on Advances in Concrete Technology, Athens, 11–12 May, pp. 741–773.*

***PIGEON, M. & SAUCIER, F.**, 1992. "Durability of repaired concrete structures", in Proceedings, International Symposium on Advances in Concrete Technology, Athens, 11–12 May, pp. 741–773.*

***REINECK, K. H.** 1992. "Ultimate Shear Force of Structural Concrete Members without Transverse Reinforcement Derived from a Mechanical Model-Closure", ACI Structural Journal, 89(4), 479-481.*

***RICHART, F. E.**,1927. "An Investigation of Web Stresses in Reinforced Concrete Members." Bulletin 166, Univeristy of Illinois Engineering Experiment Station, Urbana, IL.*

***RANDL, N., STEINER, M., & PEYERL, M.**, 2016. "Sustainable strengthening of RC members with high performance concrete overlays", Maintenance, Monitoring, Safety, Risk and Resilience of Bridges and Bridge Networks, 370.*

***REGGIA, A., MORBI, A., & PLIZZARI, G. A.**, 2018. "Seismic Retrofitting of a Bridge Pier with Ultra High Performance Fibre Reinforced Concrete", in MATEC Web of Conferences (Vol. 199, p. 09015), EDP Sciences.*

***ROBINS, P. J., & AUSTIN, S. A.**, 1995. "A unified failure envelope from the evaluation of concrete repair bond tests", Magazine of Concrete Research, 47(170).*

***ROBINS, P., AUSTIN, S., & JONES, P.**, 2002. "Pull-out behaviour of hooked steel fibres", Materials and structures, 35(7), 434-442.*

***RODRÍGUEZ SOLER, J., MARTINEZ CUTILLAS, F. J., & MARTI RODRIGUEZ, J.**, 2013. "Concrete constitutive model, calibration and applications", presented at the 2013 SIMULIA Community Conference.*

***ROMUALDI, J. P., & BATSON, G. B.**, 1963. "Mechanics of crack arrest in concrete", in R. Detwiler, K. Folliard, J. Olek, J. S. Popovics, & L. Snell (Eds.), Selected Landmark Papers in Concrete Materials Research-SP249 (pp. 239–264). American Concrete Institute.*

***ROMUALDI, J. P., & MANDEL, J. A.**, 1964, June. "Tensile strength of concrete affected by uniformly distributed and closely spaced short lengths of wire reinforcement", in Journal Proceedings (Vol. 61, No. 6, pp. 657-672). American Concrete Institute.*

***RUANO, G., ISLA, F., PEDRAZA, R. I., SFER, D., & LUCCIONI, B.**, 2014. "Shear retrofitting of reinforced concrete beams with steel fiber reinforced concrete", Construction and Building Materials, 54, 646-658.*

***SCHMIDT, M., & FEHLING, E.**, 2005. "Ultra-high-performance concrete: research, development and application in Europe", ACI Special publication, 228, 51-78.*

***SCHRADER, E. K.**, 1992. "Mistakes, Misconceptions, and Controversial Issues Concerning Concrete and Concrete Repairs", Part 1,2, and 3, Concrete International.*

***SHAH, S. P., & RANGAN, B. V.**, 1971. "Fiber Reinforced Concrete Properties", ACI Journal, 68(2), 126–137.*

***SHAH, S. P., STROEVEN, P., DALHUISEN, D., & VAN STEKELENBURG, P.**, 1978, September. "Complete stress-strain curves for steel fibre reinforced concrete in uniaxial tension and compression", in Proceedings (pp. 399-408).*

***SHAH, SURENDRA P., ET AL.**, 1988. "Design considerations for steel fiber reinforced concrete", ACI Structural Journal, 85(5), 563-579.*

***SHARMA, A. K.**, 1986, July. "Shear strength of steel fiber reinforced concrete beams", in Journal Proceedings (Vol. 83, No. 4, pp. 624-628).*

***SILFWERBRAND, J.**, 1990. "Improving concrete bond in repaired bridge decks", Concrete international, 12(9).*

***SILFWERBRAND, J.**, 2000. "Evaluation of tests on water-jet equipment", in Bhr Group Conference Series Publication (Vol. 41, pp. 113-120). Bury St. Edmunds; Professional Engineering Publishing; 1998.*

***SILFWERBRAND, J.**, 2003. "Shear bond strength in repaired concrete structures", Materials and Structures, 36(6), 419-424.*

***SILFWERBRAND, J., & PAULSSON, J.**, 1998. "Better bonding of bridge deck overlays", Concrete International, 20(10), 56-61.*

***SILFWERBRAND, J., BEUSHAUSEN, H., & COURARD, L.**, 2011. "Bond", in Bonded Cement-Based Material Overlays for the Repair, the Lining or the Strengthening of Slabs or Pavements (pp. 51-79). Springer, Dordrecht.*

***SKOČEK, J., & STANG, H.**, 2008. "Inverse analysis of the wedge-splitting test", Engineering Fracture Mechanics, 75(10), 3173-3188.*

***SOROUSHIAN, P., & LEE, C. D.**, 1989. "Constitutive modeling of steel fiber reinforced concrete under direct tension and compression. Fibre reinforced cements and concretes: recent developments", Proceedings of an international conference held at the university of wales, college of cardiff, school of engineering, united kingdom, september 18-20, 1989. Publication of: Elsevier Applied Science Publishers Limited.*

***STRACK, M.**, 2008. "Modelling of crack opening in steel fibre reinforced concrete under tension and bending", in BEFIB 2008: 7th RILEM International Symposium on Fibre Reinforced Concrete (pp. 323-332). RILEM Publications SARL.*

***TAYEH, B. A., BAKAR, B. A., JOHARI, M. M., & VOO, Y. L.**, 2012. "Mechanical and permeability properties of the interface between normal concrete substrate and ultra high performance fiber concrete overlay", Construction and building materials, 36, 538-548.*

***TAYLOR, H. P.** ,1974. "The fundamental behavior of reinforced concrete beams in bending and shear". Special Publication, 42, 43-78.*

***TSCHEGG, E. K., INGRUBER, M., SURBERG, C. H., & MUNGER, F.**, 2000. "Factors influencing fracture behavior of old-new concrete bonds", Materials Journal, 97(4), 447-453.*

***UNI 11039**, 2003, "Steel Fiber Reinforced Concrete –Part I: Definitions, Classification Specification and Conformity – Part II: Test Method for Measuring First Crack Strength and Ductility Indeces", Italian Board for Standardization.*

***UNI EN 14651**, 2007. "Precast concrete products – test method for metallic fibre concrete – Measuring the flexural tensile strength", European Standard.*

***VAN MIER, J. G. M., & VAN VLIET, M. R. A.**, 2002. "Uniaxial tension test for the determination of fracture parameters of concrete: state of the art", Engineering Fracture Mechanics, 69(2), 235-247.*

***VAN MIER, J. G., NOORU-MOHAMED, M. B., & TIMMERS, G.**, 1991. "An experimental study of shear fracture and aggregate interlock in cement based composites", HERON, 36 (4), 1991.*

***VANDEWALLE, L.**, 2000. "Recommendations of RILEM TC 162-TDF: Test and design methods for steel fibre reinforced concrete", Materials and Structures/Materiaux et Constructions, 33(225), 3-5.*

***VANDEWALLE, L., HEIRMAN, G., & VAN RICKSTAL, F.**, 2008. "Fibre orientation in self-compacting fibre reinforced concrete", in Proc. of the 7th Int. RILEM Symp. on Fibre Reinforced Concrete: Design and Applications (BEFIB2008) (pp. 719-728). RILEM Publications SARL; Bagneux.*

***VAYBURD, A. M., & MCDONALD, J. E.**, 1999. "An evaluation of equipment and procedures for tensile bond testing of concrete repairs (No. WES/TR/REMR-CS-61)", Army Engineer Waterways Experiment Station Vicksburg Ms.*

***VECCHIO, F.J.**, 1990. "VecTor 2 Nonlinear Finite Element Analysis" program.*

***VECCHIO, F. J.**, 2000. "Disturbed stress field model for reinforced concrete: formulation", Journal of structural engineering, 126(9), 1070-1077.*

***VECCHIO, F. J., & COLLINS, M. P.**, 1986. "The modified compression-field theory for reinforced concrete elements subjected to shear", ACI J., 83(2), 219-231.*

***VONDRAN, G. L.**, 1991. "Applications of steel fiber reinforced concrete", Concrete international, 13(11), 44-49.*

***VOO, J. Y. L., & FOSTER, S. J.**, 2003. "Variable Engagement Model for Fibre Reinforced Concrete in Tension," Uniciv Report No. R-420, School of Civil and Environmental Engineering, The University of New South Wales, Sydney, Australia.*

***WAFA, F. F., & ASHOUR, S. A.**, 1992. "Mechanical properties of high-strength fiber reinforced concrete", Materials Journal, 89(5), 449-455.*

***WALRAVEN, J.C.**, 1981. "Fundamental Analysis of Aggregate Interlock", ASCE Journal of the Structural Division, Vol. 107, No. 11, pp. 2245-2270.*

***WELLS, J. A., STARK, R. D., & POLYZOIS, D.**, 1999. "Getting better bond in concrete overlays. Concrete international, 21(3), 49-52.*

***WILLE, K., EL-TAWIL, S., & NAAMAN, A. E.**, 2014. "Properties of strain hardening ultra high performance fiber reinforced concrete (UHPFRC) under direct tensile loading", Cement and Concrete Composites, 48, 53-66.*

***WRIGHT, P. J. F.**, 1955. "Comments on an indirect tensile test on concrete cylinders", Magazine of Concrete Research, 7(20), 87-96.*

***WONG, R. S. Y.**, 2001. "Towards modelling of reinforced concrete members with externally-bonded fibre reinforced polymer, FRP, composites", Doctoral dissertation, National Library of Canada= Bibliothèque nationale du Canada.*

***WONG, P.S., & VECCHIO, F.J.**, 2002. "VecTor2 and FormWorks User's Manual", Technical Report, Department of Civil Engineering, University of Toronto.*

***ZANOTTI, C., & RANDL, N.**, 2019. "Are concrete-concrete bond tests comparable?", Cement and Concrete Composites, 99, 80-88.*

***ZANOTTI, C., MARINI, A., & PLIZZARI, G. A.**, 2009. "Nonlinear FE analysis of fiber reinforced concrete floor diaphragms undergoing horizontal seismic actions", in Protection of Historical Buildings: Proceedings of the International Conference on Protection of Historical Buildings, PROHITECH 09, Rome, Italy, 21-24 june 2009: PROHITECH 09 (pp. 1089-1094).*

***ZOLLO, R. F.**, 1997. "Fiber-reinforced concrete: an overview after 30 years of development", Cement and Concrete Composites, 19(2), 107-122.*

3 CHARACTERIZATION OF UHPFRC

In this chapter, a description is given of the materials used and of the experimental tests performed to characterize the materials, in terms of mechanical properties.
Experimental program was carried out at the Laboratory "Pietro Pisa" of the University of Brescia.

3.1 UHPFRC composition

Five commercial Ultra-High-Performance Fibre Reinforced Concrete (UHPFRC) products were selected for investigation: Planitop HPC Floor, Planitop HPC Floor 46, Planitop HPC Floor T, Planitop HPC Floor 46T, and Planitop HPC, henceforth PHF, PHF46, PHFT, PHF46T and PH.

3.1.1 *Planitop HPC Floor*

PHF by MAPEI S.p.A. is a fibre reinforced cementitious mortar. It is a shrinkage-compensated concrete mortar made up of high-strength cements, selected aggregates, special additives, and steel fibres, for repair of concrete on both vertical and horizontal surfaces. The mix design composition of the material is not stated on the datasheet. The maximum size of aggregate is 1 mm The steel fibres, DRAMIX®-RC-80/30 BD (Figure 3.1-1), are hooked with a length l_f = 30 mm, an aspect ratio l_f/d_f = 79, and volume content V_f=0.96%. Their tensile strength is high (f_y ≈ 3070 MPa) so that the fibres are pulled out of the UHPFRC matrix and do not break.

3.1.2 *Planitop HPC Floor 46*

PHF46 by MAPEI S.p.A. is ultra-high-performance free-flowing cementitious mortar reinforced with steel fibres. It is a shrinkage-compensated concrete mortar made up of high-strength cements, selected aggregates, special additives, and steel fibres, for repair of concrete on both vertical and horizontal surfaces. The mix design composition of the material is not stated on the datasheet. The maximum size of aggregate is 6 mm. The steel fibres, DRAMIX®-RC-80/30 BD (Figure 3.1-1),), are hooked with a length l_f = 30 mm, an aspect ratio l_f/d_f = 79, and volume content V_f=0.96%. Their tensile strength is high (f_y ≈ 3070 MPa) so that the fibres are pulled out of the UHPFRC matrix and do not break.

3.1.3 *Planitop HPC Floor T*

PHFT by MAPEI S.p.A. is high performance semi-fluid cementitious mortar reinforced with steel fibres. It is a shrinkage-compensated concrete mortar made up of high-strength cements, selected aggregates, special additives, and steel fibres, for repair strengthening the underside of floors. In particularly suitable for warped wooden floors. The mix design composition of the material is not stated on the datasheet. The maximum size of aggregate is 1 mm. The steel fibres, DRAMIX®-RC-80/30 BD (Figure 3.1-1),), are hooked with a length l_f = 30 mm, an aspect ratio l_f/d_f = 79, and volume content V_f=0.96%. Their tensile strength is high (f_y ≈ 3070 MPa) so that the fibres are pulled out of the UHPFRC matrix and do not break.

3.1.4 *Planitop HPC Floor 46 T*

PHF46T by MAPEI S.p.A. is high performance semi-fluid cementitious mortar reinforced with steel fibres. It is a shrinkage-compensated concrete mortar made up of high-strength cements, selected aggregates, special additives and steel fibres for repair strengthening horizontal structures. In particularly suitable for warped wooden floors. The mix design composition of the material is not stated on the datasheet. The maximum size of aggregate is 6 mm. The steel fibres, DRAMIX®-RC-80/30 BD (Figure 3.1-1),), are hooked with a length l_f = 30 mm, an aspect ratio l_f/d_f = 79, and volume content V_f=0.96%. Their tensile strength is high (f_{uf} ≈ 3070 MPa) so that the fibres are pulled out of the UHPFRC matrix and do not break.

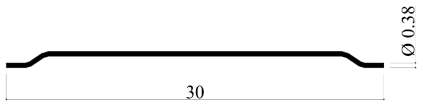

Figure 3.1-1: Geometry of fibres RC-80/30-BP.

3.1.5 *Planitop HPC*

PH by MAPEI S.p.A. is a two components cementitious mortar reinforced with steel fibres. It is a shrinkage-compensated concrete mortar made up of high-strength cements, selected aggregates, special additives, and steel fibres, for repair of concrete on both vertical and horizontal surfaces. The mix design composition of the material is not stated on the datasheet. The maximum size of aggregate is 1 mm. The steel fibres, DRAMIX®- OL-13/.20 (Figure 3.1-2), are short (l_f = 13 mm) and straight with an aspect ratio l_f/d_f =65 and volume content V_f=1.69%. Their tensile strength is high (f_{uf} ≈ 2600 MPa) so that the fibres are pulled out of the UHPFRC matrix and do not break.

Figure 3.1-2: Geometry of fibres OL-13/.20.

3.2 Compression properties

The compressive strength was evaluated on concrete cubes measuring 150 mm, following the guidelines given in UNI EN 12390-3 [2009]. Six specimens were tested for each material and their mean value was taken as the strength of the material. All the specimens were stored in water at the temperature of 23.0 ± 2.0°C prior to testing. Each material was tested at 28 days.

3.2.1 *Experimental results*

Table 3.2-1 lists the cube compressive strength $f_{c,cube}$ and the cylindrical compressive strength f_{cm}, the latter calculated as 83% of $f_{c,cube}$. The mean tensile strength (f_{ctm}) and the mean secant elastic modulus (E_{cm}) of the concretes were both calculated according Eurocode 2 [1992] as $f_{ctm} = 2{,}12 \cdot ln(1+(f_{cm}/10))$ and $E_{cm}=22 \cdot (f_{cm}/10)^{0.3}$

Concrete Designation	Batch	$f_{c,cube}$ [MPa]	$f_{cm} = 0.83\ f_{c,cube}$ [MPa]
PHF	#1	118.2	98.1
	#2	118.5	98.3
	#3	118.9	98.7
	#4	119.5	99.2
	#5	178.8	97.8
	#6	116.6	96.8
PHF46	#1	115.1	95.5
	#2	110.4	91.6
	#3	115.5	92.6
	#4	109.5	90.9
	#5	110.2	91.5
	#6	106.6	88.4
PHFT	#1	108.0	89.6
	#2	103.2	85.7
	#3	101.7	84.4
	#4	99.9	82.9
	#5	106.4	88.3
	#6	100.0	83.0
PHF46T	#1	105.6	87.6
	#2	106.5	88.4
	#3	107.8	89.5
	#4	105.6	87.6
	#5	105.4	87.5
	#6	104.4	86.7
PH	#1	120.2	99.8
	#2	122.8	102.0
	#3	118.3	98.2
	#4	122.8	101.9
	#5	119.4	99.1
	#6	112.4	99.3

Table 3.2-1: Compressive strength.

Table 3.2-2 gives the mean values (R_{cm} and f_{cm}) for all cubes tested. The minimum and maximum values are reported (in square brackets), together with the coefficient of variation, CV, (in round brackets), in order to provide information about the experimental scatter.

Concrete Designation	R_{cm} [MPa]	$f_{cm} = 0.83\ R_{cm}$ [MPa]	f_{ck} [MPa]	f_{ctm} [MPa]	E_{cm} [GPa]
PHF	**118.2** [119.5-116.6] (0.01)	**98.1**	**90.1**	**5.1**	**43.6**
PHF46	**110.5** [115.1-106.6] (0.03)	**91.8**	**83.7**	**4.9**	**42.8**
PHFT	**103.2** [99.9-108.0] (0.03)	**85.6**	**77.6**	**4.8**	**41.9**
PHF46T	**105.9** [104.4-107.8] (0.03)	**87.9**	**79.9**	**4.8**	**42.2**
PH	**119.2** [122.8-112.4] (0.03)	**99.0**	**91.0**	**5.1**	**43.8**

Table 3.2-2: Main results from compressive strength.

3.3 Tensile properties

The tensile stress–strain response of UHPFRC is a fundamental constitutive property. Reliable knowledge of this response is necessary for appropriate application of the tensile-carrying capacity of such advanced cement-based materials.
There are various test methods to determine it. The uniaxial tension test would be the most suitable test for determining tension behaviour; despite this, FRC post-cracking laws are generally determined through indirect methods.

3.3.1 *Set-up description*

According to the European Standard EN 14651 [2007], notched beams were tested under the three-point bending test for evaluation of the tensile behaviour of fibre reinforced concrete. The purpose of this test is to determine the residual flexural tensile strength through the diagram of the applied force versus the deformation expressed in terms of Crack Mouth Opening Displacement (CMOD). The test was achieved on notched prismatic specimens with dimensions 150x150x600 mm. Figure 3.3-1describes the geometry of the specimen.

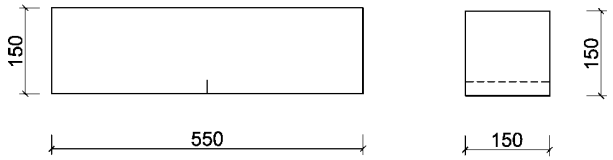

a) *b)*

Figure 3.3-1: Geometry of specimens: a): longitudinal view; b) section view.

A resistive clip gauge and four Linear Variable Differential Transformers (LVDTs) were used for experimental measurements: a clip gauge was fixed across the notch mouth and the LVTDs were glued on the two opposite faces of the beam, as shown in Figure 3.3-2. The clip gauge monitored the CMOD, which is the control parameter for the test, while the LVDTs recorded the Crack Tip Opening Displacement (CTOD) and the vertical displacement in mid-span (MPD) at front and back the specimens.
Regarding the test set-up, an INSTRON 1274 testing machine was used for these tests. Load was applied continuously and monotonically. The specimens were tested under CMOD control until a 5 mm, while from 5 mm to 8 mm under load control. Table 3.3-1 provides the rates at which the specimens were tested.

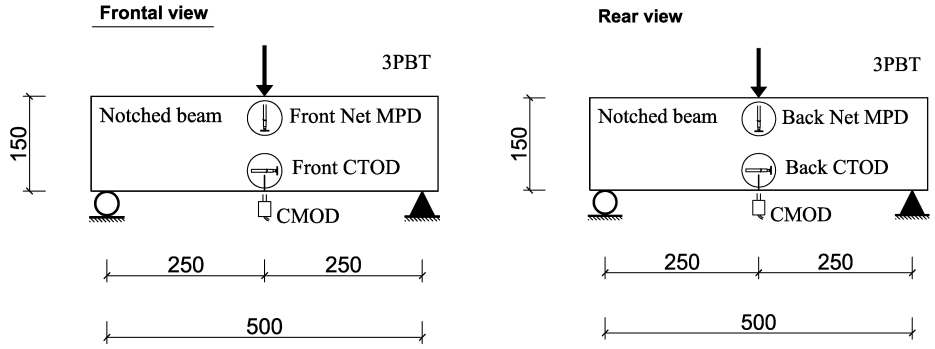

Figure 3.3-2: Three-point bending test set-up: a) front view; b) back view.

CMOD [mm]	Rate [mm/min]
Clip gauge	
0-0.01	0.05
0.01-2	0.2
2-5	0.3
Stroke control	
5-8	1

Table 3.3-1: Rate the load was applied.

3.3.2 *Experimental results*

Figure 3.3-3, Figure 3.3-4, Figure 3.3-5, Figure 3.3-6, and Figure 3.3-7 report the *Nominal stress versus CMOD* curves for the 12 beam samples PHF, PHF46, PHFT, PHF46T, and PH, respectively. The nominal stress is determined by assuming a linear stress distribution in the resistant part of the notched section.

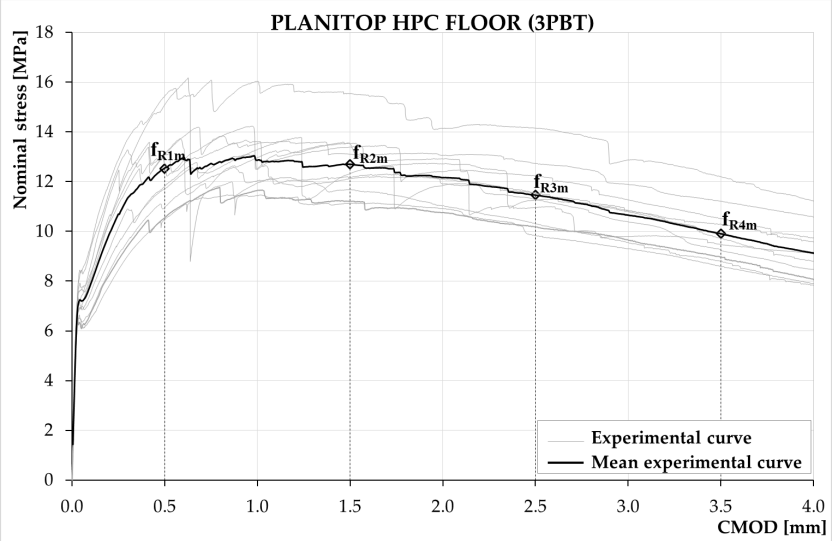

Figure 3.3-3: Nominal stress vs. CMOD curves for PHF.

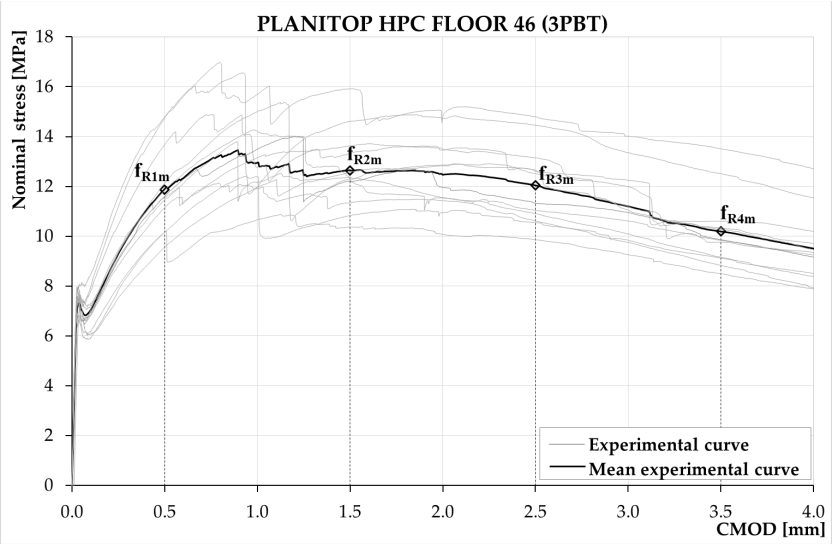

Figure 3.3-4: Nominal stress vs. CMOD curves for PHF46.

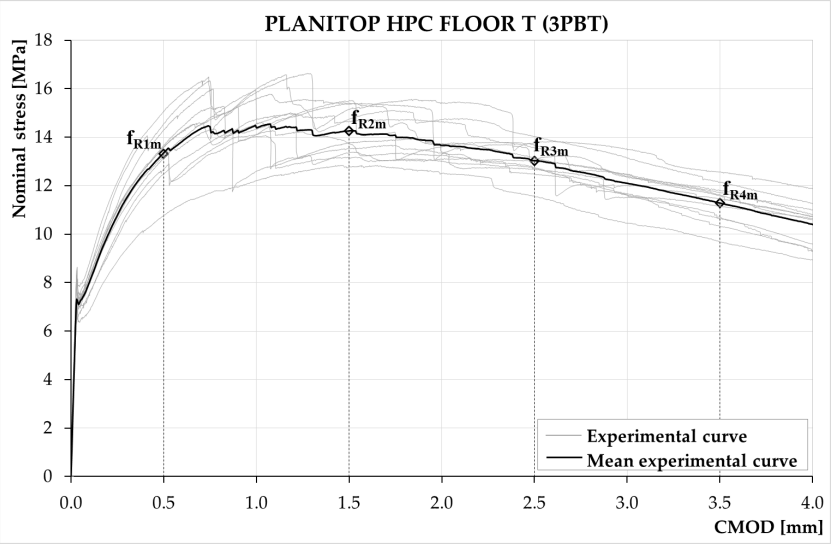

Figure 3.3-5: Nominal stress vs. CMOD curves for PHFT.

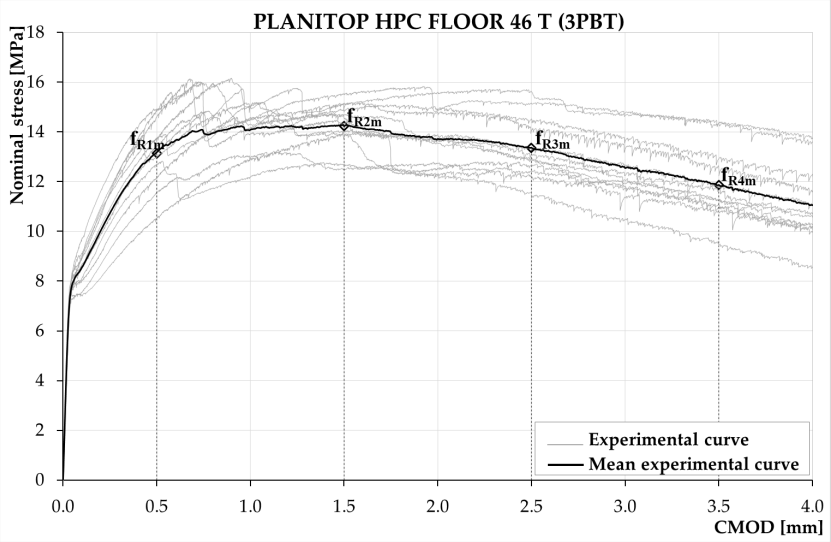

Figure 3.3-6: Nominal stress vs. CMOD curves for PHF46T.

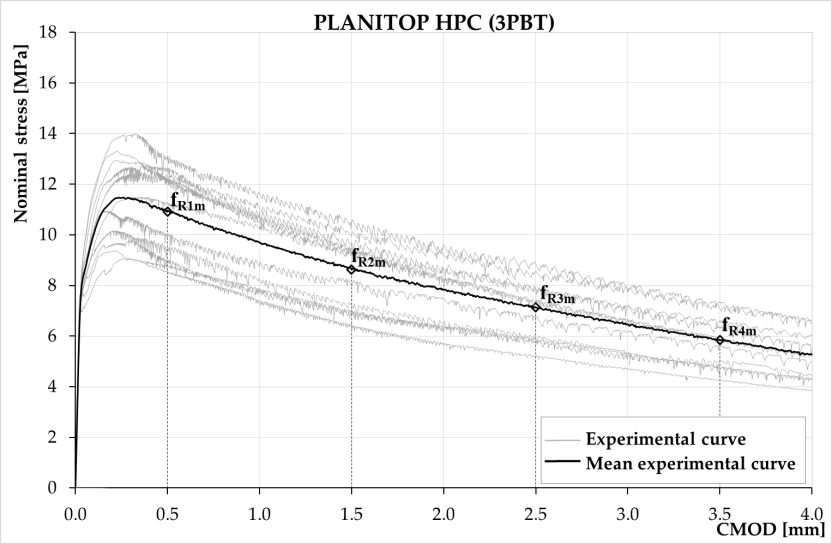

Figure 3.3-7: Nominal stress vs. CMOD curves for PH.

According to EN14651 [2019], Table 3.3-2 summarizes the mean values: limit of proportionality f_L and residual flexure strengths f_{R1}, f_{R2}, f_{R3}, f_{R4}, corresponding to different CMOD values (crack mouth opening displacement) of 0.5, 1.5, 2.5 and 3.5 mm for the 12 specimens. The minimum and maximum values of residual strengths are provided (in square brackets), together with the CV (in round brackets), in order to provide information about the experimental scatter.

Concrete Designation	f_{Lm} **[MPa]**	f_{R1m} **[MPa]**	f_{R2m} **[MPa]**	f_{R3m} **[MPa]**	f_{R4m} **[MPa]**	***FRC class*[1]**
PHF	**7.33** [6.51-8.45] (0.10)	**12.54** [10.49-15.44] (0.13)	**12.70** [11.12-15.53] (0.10)	**11.46** [9.83-14.15] (0.11)	**9.91** [8.59-12.20] (0.11)	**8c**
PHF46	**7.52** [6.81-8.07] (0.06)	**11.90** [9.56-14.78] (0.14)	**12.65** [10.37-15.92] (0.12)	**12.04** [9.86-14.80] (0.13)	**10.19** [8.50-13.51] (0.14)	**8c**
PHFT	**7.78** [6.80-8.64] (0.08)	**13.36** [10.77-15.08] (0.08)	**14.27** [12.77-15.51] (0.07)	**13.03** [11.56-14.04] (0.05)	**11.29** [9.69-12.57] (0.07)	**10c**
PHF46T	**7.93** [7.30-8.41] (0.04)	**13.18** [10.54-14.93] (0.10)	**14.23** [12.47-15.51] (0.07)	**13.35** [11.34-15.62] (0.09)	**11.87** [9.43-14.37] (0.12)	**10c**
PH	**8.61** [7.15-9.67] (0.09)	**10.96** [8.53-13.11] (0.15)	**8.64** [6.33-10.47] (0.17)	**7.14** [5.19-8.94] (0.17)	**5.85** [4.24-7.35] (0.18)	**8a**

[1]*FRC classification according fib Model Code 2010 [2013]*

Table 3.3-2: Limit of proportionality f_L and residual flexure strengths f_{R1}, f_{R2}, f_{R3}, f_{R4}.

The fracture energies at different values of deflection ($G_{f,2.0}$, $G_{f,4.0}$, $G_{f,6.0}$, $G_{f,8.0}$) were calculated (Table 3.3-3). The latter represents the area under the multi-linear curve up to the corresponding values of deflection of 2.0, 4.0, 6.0 and 8.0 mm, respectively.

Concrete Designation	$G_{f,2.0}$ **[N/mm]**	$G_{f,4.0}$ **[N/mm]**	$G_{f,6.0}$ **[N/mm]**	$G_{f,8.0}$ **[N/mm]**
PHF	**3.91** [3.38-4.74] (0.09)	**6.76** [5.88-8.16] (0.09)	**8.70** [7.47-10.53] (0.10)	**10.05** [8.62-12.07] (0.10)
PHF46	**3.78** [1.89-4.82] (0.20)	**6.60** [3.35-8.71] (0.21)	**8.54** [4.4-11.47] (0.21)	**9.89** [5.20-13.41] (0.22)
PHFT	**4.07** [3.09-4.70] (0.13)	**5.22** [4.51-5.86] (0.08)	**7.02** [6.10-7.65] (0.08)	**11.80** [7.07-14.58] (0.18)
PHF46T	**4.22** [3.68-4.74] (0.09)	**7.79** [4.85-9.29] (0.15)	**10.30** [6.61-12.37] (0.15)	**12.39** [10.31-14.36] (0.09)
PH	**2.73** [2.15-3.22] (0.14)	**4.30** [3.34-5.12] (0.14)	**5.17** [3.99-6.17] (0.15)	**5.65** [4.36-6.83] (0.15)

Table 3.3-3: Mean values of the fracture energies.

3.4 References

CHILWESA, M., MINELLI, F., REGGIA, A., & PLIZZARI, G. *2017. Evaluating the shear bond strength between old and new concrete through a new test method. Magazine of Concrete Research, 69(9), 425-435.*

FÉDÉRATION INTERNATIONALE DU BÉTON (FIB)*. 2013. Model Code 2010 for concrete structures (MC2010), International Federation for Structural Concrete, Lausanne, Switzerland.*

SILFWERBRAND, J., BEUSHAUSEN, H., & COURARD, L.*, 2011. "Bond", in Bonded Cement-Based Material Overlays for the Repair, the Lining or the Strengthening of Slabs or Pavements (pp. 51-79). Springer, Dordrecht.*

UNI EN 12390-3*, 2003. "Testing hardened concrete—Compressive strength of test specimens", European Standard.*

EN 1992-1-1: *Eurocode 2. 2005. Design of concrete structures. Part 1–1: General rules and rules for buildings.*

UNI EN 14651*, 2007. "Precast concrete products – test method for metallic fibre concrete – Measuring the flexural tensile strength", European Standard.*

4 BOND BETWEEN OVERLAY AND SUBSTRATE CONCRETE

4.1 Introduction

Bonded concrete overlays are generally used for repair and strengthening of concrete structures. The purpose of a concrete repair is to extend the service life of the structure restoring the load-carrying capacity and the stiffness of a concrete member. This can be accomplished by providing a protective layer to a damaged substrate. The interface between new concrete (overlay) and old concrete (substrate) is a key factor in the success of repair and rehabilitation works. Good adhesion is more importance for providing monolithic action in bonded concrete overlays. It is important that the interface between differently aged concrete has to withstand significant and durable bond. Appropriate bond of a repair material to concrete plays an important role in the application and performance of concrete repairs. The overlay has to contribute to both the stiffness and load carrying capacity of the element.
In this chapter, two experimental programs are presented. The first one was related to the shear bond test on prismatic specimens. The main purposes of this test are to study the influence of the substrate strength and of the substrate surface roughness on the interface bond strength between a substrate and overlay concrete. The second experimental program involved the design and testing of square slab panels subjected to a monotonically-increases load. This experimental program aims to study the influence of the substrate surface roughness on the interface bond strength between a substrate and overlay concrete in square slab elements. The shear stress obtained from the two different tests were presented and discussed.
Additionally, an in-situ load testing on a lightweight ribbed one-way reinforced concrete slab strengthened by means of UHPFRC overlay was presented. The in-situ load testing was conducted on two-story residential building in Piacenza (Italy) built in 1970s. The primary objective of this test was to assess the strengthening technique.

4.2 Shear bond test

The objectives of this test are to study the influence of the substrate strength and of the substrate surface roughness on the interface bond strength between a substrate and overlay concrete.
The following shear bond tests are based on the research of Chilwesa *et al.* [2017].
The experimental program consisted of two series of specimens: series PHF and series PHF46. Both series were characterized by three different substrates and three different roughnesses. There were four specimens for each one. This made a total of 72 specimens tested in the program. Specimens were constructed at Mapei S.p.A. – Cafiero (Milan). The tests were conducted at the Laboratory "Pietro Pisa" of the University of Brescia.

4.2.1 *Material and specimen geometry*

In this test, three types of concrete with different strength classes were chosen for the substrate and two types of Ultra-High-Performance Fibre Reinforced Concrete (UHPFRC) were selected for the overlay. Moreover, different roughness indexes were studied.

4.2.1.1 Substrate concrete

The three materials chosen for investigations are representative of a wide spectrum of material used for the construction of RC structures. They were: C12/15, C16/20, and C20/25.

4.2.1.2 Overlay

The UHPFRC for the specimen was provided by Mapei S.p.A. The materials PHF and PHF46 were chosen for investigation. The selected materials are representative of typical structural repair materials employed to reinforce slabs. The mechanical characterizations of PHF and PHF46 are presented in Chapter 3.

4.2.1.3 Specimen geometry

Figure 4.2-1 illustrates the geometry of the specimens for the interface bond test. The specimen consisted of two substrate prisms, each measuring 200 x 100 x 100 mm, on the sides of which overlay prisms were casted, measuring 300 x 100 x 100 mm, such that four contact surfaces between two materials were created. The substrate was reinforced with longitudinal rebar and stirrups, with a diameter of 6 mm. The contact surfaces area measured 100 x 100 mm^2. The contact surface on each substrate prism had to be prepared to ensure good roughness prior to casting of the overlays.

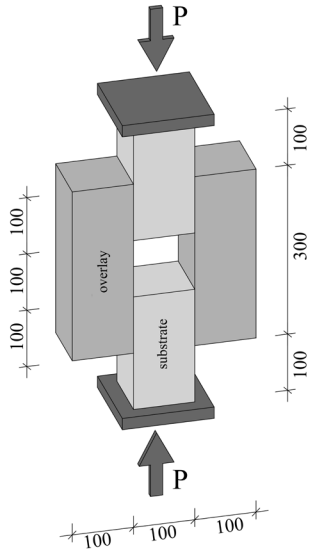

Figure 4.2-1: Geometry of specimen.

4.2.1.4 Substrate surface

One of the aims of the test was to study the influence of the substrate surface roughness on the interface bond strength. Therefore, three different roughness indexes were investigated:

- smooth surface;
- rough surface;
- very rough surface.

The smooth surface specimens were obtained by using a Bosch GSS 2300 Professional Orbital Sander. A needlegun scaler was used in the preparation of the rough and very rough surface specimens. The roughness of the samples was measured by a profilometer (Barton's comb). Table 4.3-2 reports the average roughness of the specimens and the classification of surface roughness according to *fib* Model Code for Concrete Structures 2010 (MC2010) [2013]. The standard deviation and coefficient of variation were not provided by the producer.

Figure 4.2-2 and Figure 4.2-3 show a schematic representation of the surface specimen and the comparison between the different substrate surface.

Roughness classification	**Average roughness R_t [mm]**
Smooth	<1.5
Rough	1.5-3.0
Very rough	>3.0

Table 4.2-1: Classification of surface roughness, Model Code 2010 [2013].

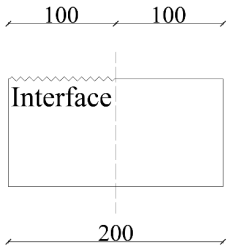

Figure 4.2-2: Schematic of the interface specimen.

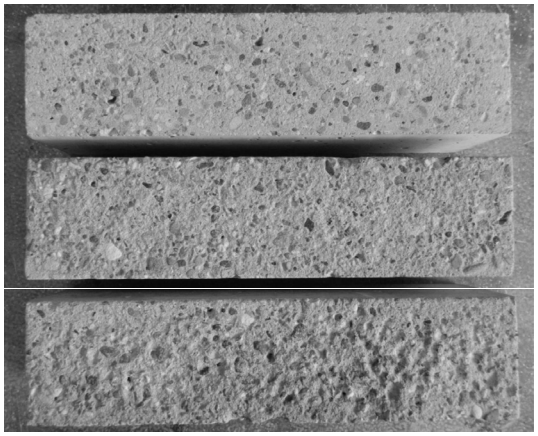

Figure 4.2-3: Comparison of the different substrate surfaces, a) smooth surface, b) rough surface and c) very rough surface.

4.2.1.5 Casting and curing specimens

The casting process began with the preparation of the substate prism, which incorporated 6 mm longitudinal rebars and stirrups, as mentioned above. The substrate prisms were casted at least 45 days prior to casting the overlay. The substrate prisms were subjected to the required treatment method to obtain the needed surface roughness parameter. Then the prisms were thoroughly cleaned with compressed air to remove dust and residual materials. Moreover, the substrate surface was moistened to obtain a condition of saturated surface dry (SSD). This procedure was done by wetting the surface until it was saturated, and letting it dry just enough to remove excess moisture. The SSD condition ensures that there is no free water at the surface and moisture loss by the overlay to the substrate.
The overlay was cast 45 days after the substrate prism. It was necessary to ensure that the interface area was free of air pockets which could compromise the bond. The specimens were stored in water at a temperature of 23.0 ± 2.0°C until the period of testing (28 days).

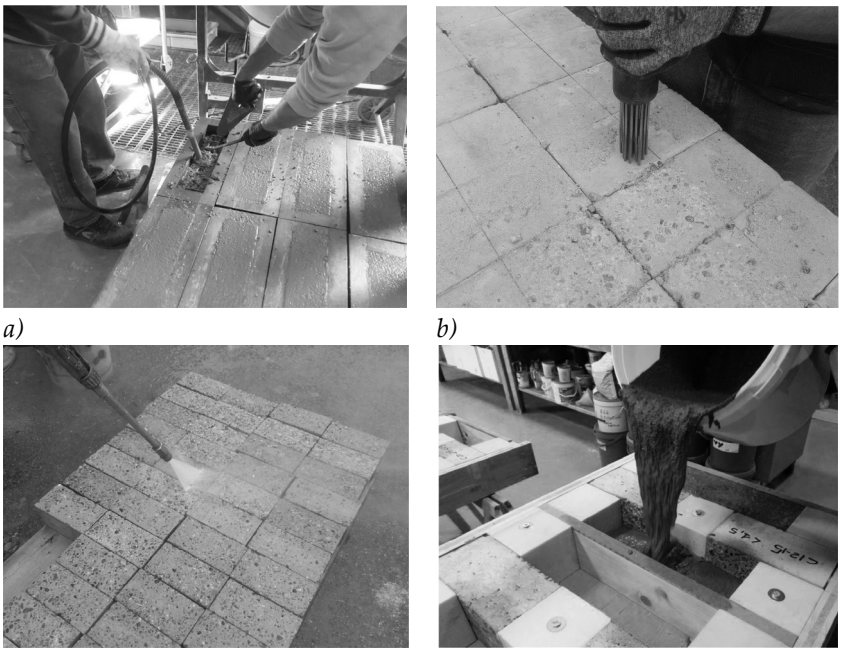

a) *b)*

c) *d)*

Figure 4.2-4: a) casted substrate prisms; b) substrate surface preparation; c) cleaned substrate prisms; d) casted overlay.

4.2.2 *Set-up description*

Figure 4.2-5 exemplifies the test set-up for the interface bond test. A state of compression was applied to the specimens using two steel plates at both ends. At specimen-to-steel plate interfaces, a thin layer of neoprene was used to prevent contact problems pertaining to any possible uneven surfaces and to equally distribute the total vertical load (P).

As shown in Figure 4.2-5 a resistive clip gauge and eight LVDTs were used for experimental measurements. The clip gauge was placed in the middle of the specimen to monitor the relative displacement between the substrate prisms. The LVDTs were placed at each contact surface (front and back side) to measure the relative displacement between substrate and overlay concrete i.e., the slip.

Figure 4.2-6 shows the specimen prior to the application of load. Tests were performed in displacement control mode. The INSTRON 1274 Universal Testing Machine was used for these tests. The load was monotonically increased at a constant speed. Three different speed were utilized: 0.02 mm/s (elastic range), 0.01 mm/s (intermediate range), and 0.005 mm/s (pre-peak until failure). This type of displacement control performed by the resistive clip gauge. Data was detected and stored by a data acquisition system at constant intervals of 0.5 s.

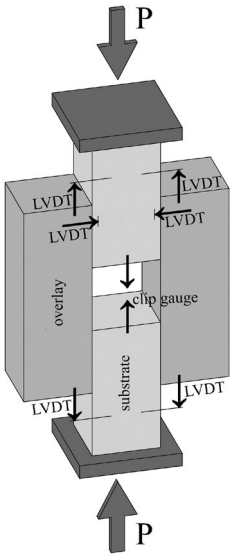

Figure 4.2-5: Set-up of test specimen

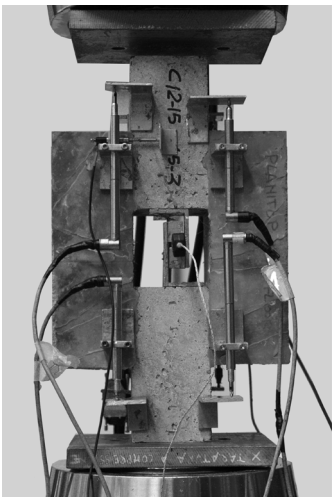

Figure 4.2-6: Specimen set-up in the INSTRON Testing Machine.

The average shear stress across an interface was calculated with the following equation:

$$\tau_a = \frac{P}{2A} \qquad (4.2\text{-}1)$$

where

τ_a is the average shear stress;

P is the maximum achieved load;

A is the interface contact area (10 000 mm^2).

4.2.3 *Experimental results*

The major objectives of the bond tests were the investigation of the influence of the substrate compressive strength on the bond strength and the evaluation of the possible effect of substrate surface roughness on interface bond strength.
The following paragraph gives the results of these tests. The results of the bond tests are presented in the form of *average shear stress vs. slip* (tangential displacement) curves. The *average shear stress vs. slip* graph represents the response of the interface to loading. The shear stress was calculated with Equation (4.2-1), thus it represents the average shear stress.
The experimental program consisted of 72 specimens: 36 specimens for series PHF and 36 for series PHF46, respectively. Both series were characterized by three different roughnesses (smooth, rough and very rough) and three different substrates (C12/15, C16/20 and C20/25). There were four specimens for each one.

4.2.3.1 Influence of substrate strength

Results on the possible influence of the substrate strength on the interface bond strength are given in this paragraph. Results are presented in form of *average shear stress vs. slip* curves for each surface preparation method i.e. smooth, rough and very rough specimens.
PHF
Figure 4.2-7 illustrates the mean curves for the smooth specimens (a), for the rough specimens (b), and for the very rough specimens (c).

a)

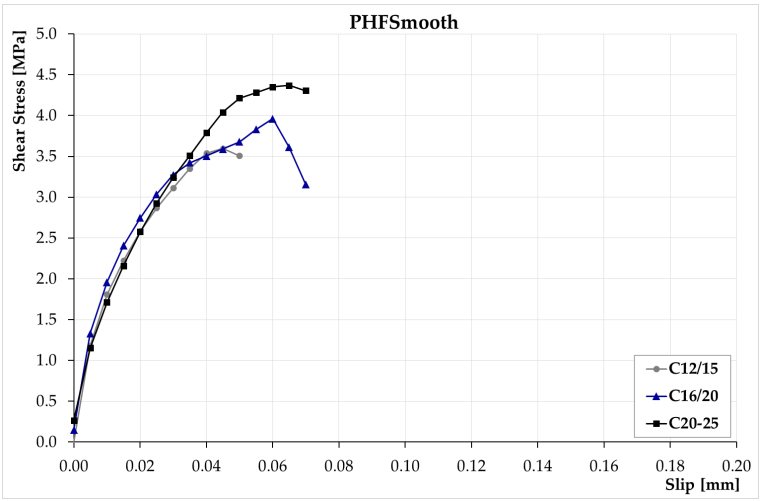

Figure 4.2-7 (Pt. 1 of 2)

b)

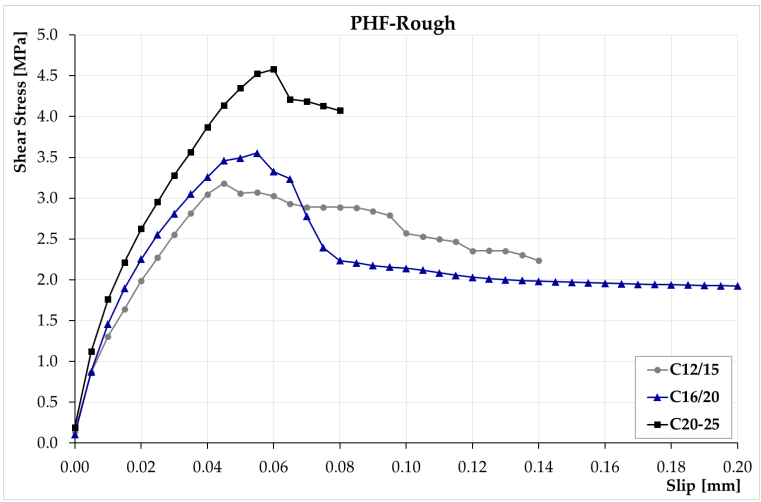

c)

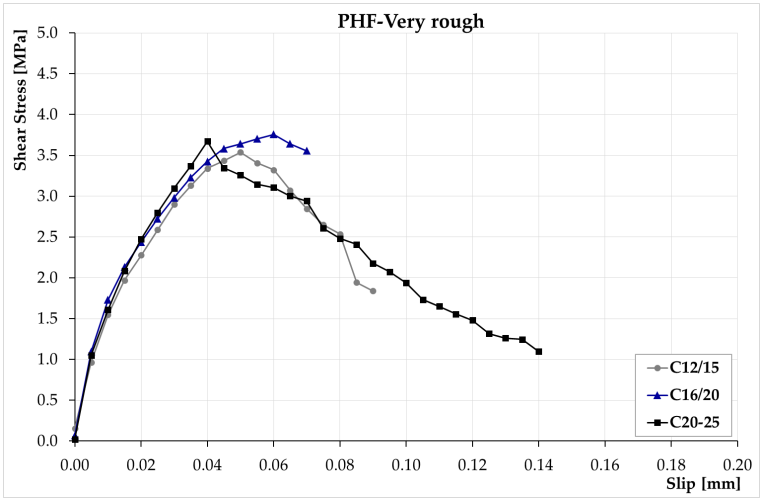

(Pt. 2 of 2)

Figure 4.2-7: Average shear stress vs. interface slip curve: a) smooth specimens; b) rough specimens; c) very rough specimens.

These results allow for some general comments. It may be observed that there is an increase in the bond strength with an increase in the substrate compressive strength. For smooth and rough specimens, the increase is higher than for very rough specimens. Moreover, curves a), b), and c) show that the slope in the pre-peak region is characterized by a very steep slope. After the peak stress, generally a significant softening behaviour is observed.

Table 4.2-2 gives the main shear stress results for each substrate strength. The minimum and maximum values are provided (in square brackets), together with the CV (in round brackets), to provide information about the experimental scatter.

PHF Specimen	C12/15	C16/20	C20/25
Mean shear stress τ_a [MPa]			
Smooth	3.8 [3.3-4.3] (0.12)	3.9 [3.8-4.1] (0.04)	4.5 [4.4-4.7] (0.03)
Rough	3.5 [2.7-4.1] (0.18)	3.7 [3.4-4.1] (0.08)	4.8 [4.4-5.0] (0.06)
Very rough	3.8 [3.9-4.5] (0.06)	3.9 [3.7-4.2] (0.06)	4.2 [3.9-4.5] (0.06)
Slip between substrate and overlay δ* [mm]			
Smooth	0.05 [0.04-0.06] (0.16)	0.05 [0.03-0.06] (0.35)	0.05 [0.03-0.06] (0.35)
Rough	0.05 [0.04-0.06] (0.19)	0.05 [0.05-0.06] (0.14)	0.07 [0.05-0.08] (0.14)
Very rough	0.06 [0.04-0.07] (0.23)	0.06 [0.04-0.08] (0.27)	0.06 [0.04-0.07] (0.17)

**slips reported are recorded at the maximum shear stress.*

Table 4.2-2: Main results from shear bond tests for each substrate strength.

In the smooth specimens, the percentage increase is 2.6% between C12/15 and C16/20, 18.4% between C12/15 and C20/25, and 15.4% between C16/20 and C20/25. For the rough specimens, the percentage increase is 5.7% between C12/15 and C16/20, 37.1% between C12/15 and C20/25, and 29.7% between C16/20 and C20/25. For the very rough specimens, the percentage increase is 2.6% between C12/15 and C16/20, 10.5% between C12/15 and C20/25, and 7.7% between C16/20 and C20/25.

PHF46

Figure 4.2-8 shows mean curves for (a) the smooth specimens, (b) the rough specimens, (c) and the very rough specimens.

a)

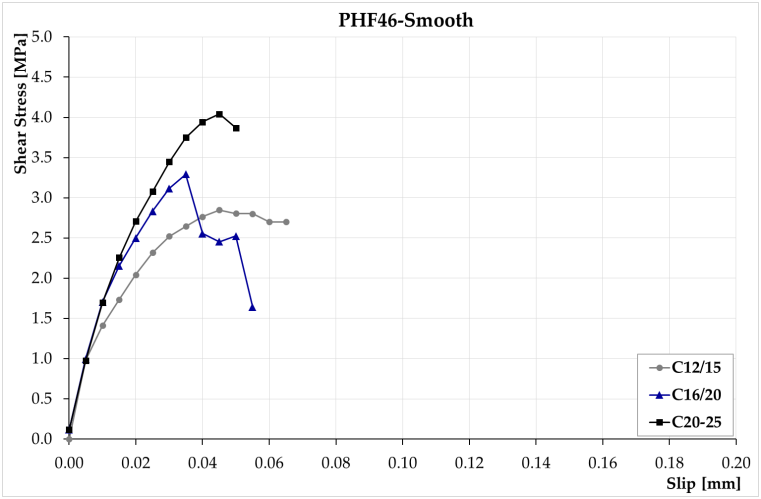

Figure 4.2-8 (Pt. 1 of 2)

b)

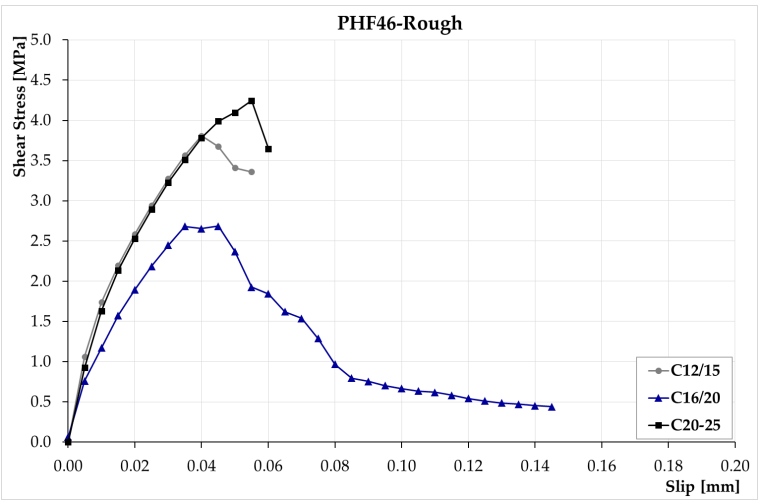

c)

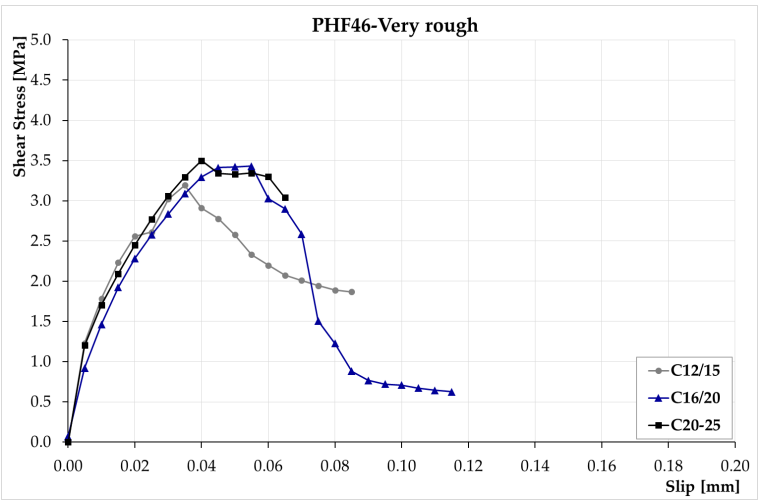

(Pt. 2 of 2)

Figure 4.2-8: Average shear stress vs. interface slip curve: a) smooth specimens; b) rough specimens; c) very rough specimens.

These results permit some general observations. It may be observed that there is an increase in the bond strength with an increase in the substrate compressive strength. The highest increase in shear stress is in the smooth specimens. Moreover, curves a), b), and c) show that the slope in the pre-peak region is characterized by a very steep slope. After the peak stress, generally a significant softening behaviour is observed. Table 4.2-3 reports the main shear stress results for each substrate strength. The minimum and maximum values are provided (in square brackets), together with the CV (in round brackets), in order to provide information about the experimental scatter.

PHF46 Specimen	C12/15	C16/20	C20/25
Mean shear stress τ_a [MPa]			
Smooth	3.0 [2.9-3.2] (0.05)	3.7 [3.4-3.9] (0.05)	4.3 [4.1-4.6] (0.06)
Rough	4.0 [2.6-3.6] (0.08)	3.0 [2.6-3.6] (0.14)	4.3 [3.9-4.9] (0.08)
Very rough	3.3 [2.9-3.9] (0.14)	3.9 [3.2-4.0] (0.06)	3.8 [3.3-4.2] (0.09)
Slip between substrate and overlay δ* [mm]			
Smooth	0.06 [0.04-0.09] (0.42)	0.04 [0.03-0.05] (0.24)	0.05 [0.04-0.06] (0.21)
Rough	0.05 [0.04-0.05] (0.10)	0.05 [0.04-0.05] (0.18)	0.05 [0.05-0.06] (0.10)
Very rough	0.05 [0.02-0.09] (0.63)	0.05 [0.04-0.06] (0.12)	0.05 [0.04-0.07] (0.29)

**slips reported are recorded at the maximum shear stress.*

Table 4.2-3: Main results from shear bond tests for each substrate strength.

It can be noted that for the C16/20 specimens with intermediate roughness, there is high dispersion in the results.

In the smooth specimens, the percentage increase is 23.3% between C12/15 and C16/20, 43.3% between C12/15 and C20/25, and 16.2% between C16/20 and C20/25. For the rough specimens, the percentage increase is -25.0% between C12/15 and C16/20, 7.5% between C12/15 and C20/25, and 43.3% between C16/20 and C20/25. For the very rough specimens, the percentage increase is 18.2% between C12/15 and C16/20, 15.2% between C12/15 and C20/25, and -2.6% between C16/20 and C20/25. In addition, for the HPF46 overlay, the increase for the very rough specimens is lower than for the smooth and rough specimens.

4.2.3.2 Influence of surface roughness

PHF-C12/15

In Figure 4.2-9 each curve represents the average of four identical specimens. The curves show that the slope in the pre-peak region is characterized by a very steep slope. After the peak stress, a low softening behaviour is observed. From Figure 4.2-9, it is seen that the smooth and the very rough specimens recorded the same shear bond strength, i.e. 3.8 MPa. The rough specimens have the lowest strength of 3.5 MPa. In addition, the rough specimens exhibit a higher energy absorption capacity, as evidenced by the more enlarged form of the softening branch of the curve.

Table 4.2-4 and Table 4.2-5 give the results of the bond tests for all the concrete C12/15 substrates tested. The minimum and maximum values are provided (in square brackets), together with the CV (in round brackets), in order to provide information about the experimental scatter.

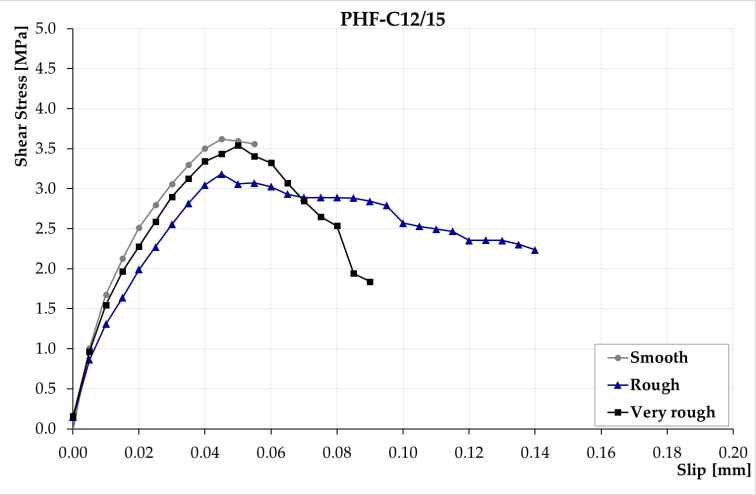

Figure 4.2-9: Average shear stress vs. interface slip curve.

	τ_a smooth [MPa]	τ_a rough [MPa]	τ_a very rough [MPa]
Mean Value	**3.8** [3.3-4.3] (0.12)	**3.5** [2.7-4.1] (0.18)	**3.8** [3.5-4.0] (0.05)

Table 4.2-4: Shear stress an interface.

	Slip smooth [mm]	Slip rough [mm]	Slip very rough [mm]
Mean Value	**0.05** [0.04-0.06] (0.16)	**0.05** [0.04-0.06] (0.19)	**0.06** [0.04-0.07] (0.23)

Note: the slips reported are recorded at the maximum shear stress.

Table 4.2-5: Slip between substrate and overlay.

Figure 4.2-10 shows the modes of failure in the three specimens with different roughness. In smooth and rough batch, the failure mode was characterized by debonding and substrate failure in regions close to the interface (Figure 4.2-11-a). The failure mode was uniform for almost all specimens (75%). In very rough specimens, the failure mode was characterized by substrate failure (100%) (Figure 4.2-11-b). In the specimens that have shown the substrate failure, no delamination occurred; therefore, the separation of the layers at the interface was not observed.

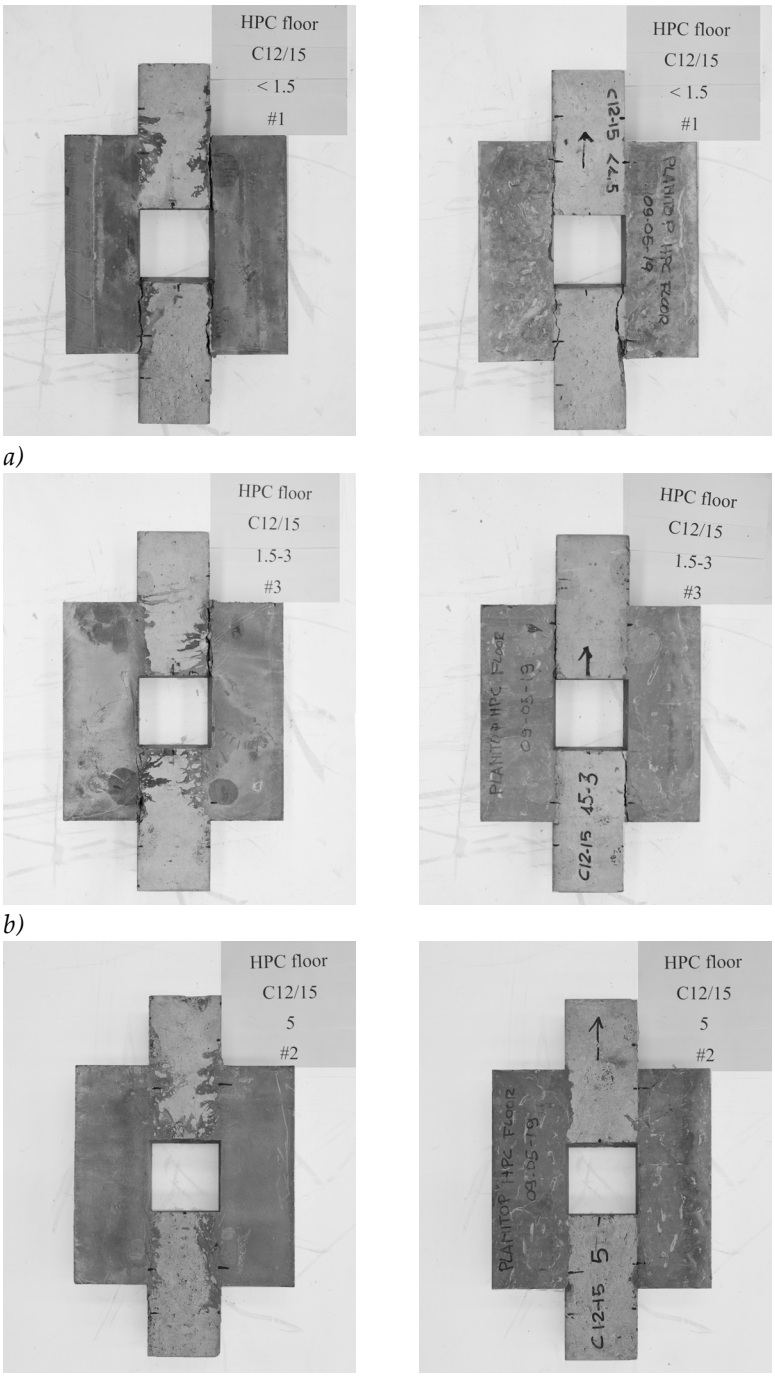

a)

b)

c)

Figure 4.2-10: The modes of failure in smooth bond specimens (a); in rough bond specimens (b) and in very rough bond specimens (c).

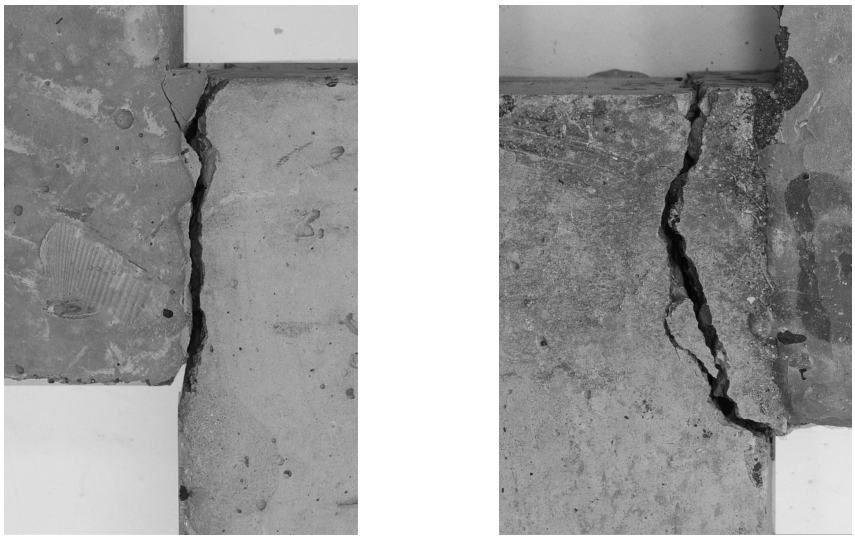

a) b)

Figure 4.2-11: Failure mode: a) material failure in regions close to the interface of the substrate concrete, b) substrate failure.

HPF-C16/20

In Figure 4.2-12 each curve represents the average of four identical specimens. The curves show that the slope in the pre-peak region is characterized by a very steep slope. After the peak stress, a low softening behaviour is observed. From the Figure 4.2-12, it is seen that smooth and very rough specimens recorded the same shear bond strength, i.e. 3.9 MPa. The rough specimens have the lowest strength of 3.7 MPa. In addition, the rough specimens exhibit a higher energy absorption capacity, as evidenced by the more enlarged form of the softening branch of the curve.

Table 4.2-6 and Table 4.2-7 give the results of the bond tests for all the concrete C16/20 substrates tested. The minimum and maximum values are provided (in square brackets), together with the CV (in round brackets), in order to provide information about the experimental scatter.

Figure 4.2-13 shows the modes of failure in the three specimens with different roughness.

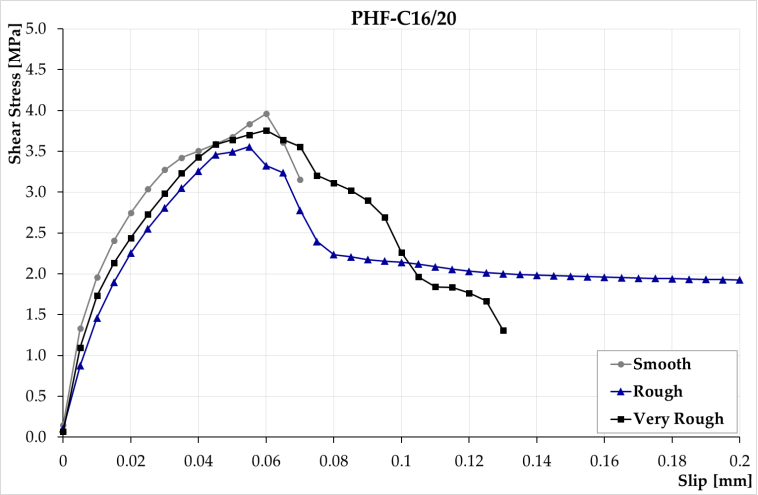

Figure 4.2-12: Average shear stress vs. interface slip curve.

	τ_a smooth [MPa]	**τ_a rough [MPa]**	**τ_a very rough [MPa]**
Mean Value	**3.9** [3.8-4.1] (0.04)	**3.7** [3.4-4.1] (0.08)	**3.9** [3.7-4.2] (0.06)

Table 4.2-6: Shear stress an interface.

	Slip smooth [mm]	**Slip rough [mm]**	**Slip very rough [mm]**
Mean Value	**0.05** [0.03-0.06] (0.35)	**0.05** [0.05-0.06] (0.14)	**0.06** [0.04-0.08] (0.27)

Note: the slips reported are recorded at the maximum shear stress.

Table 4.2-7: Slip between substrate and overlay.

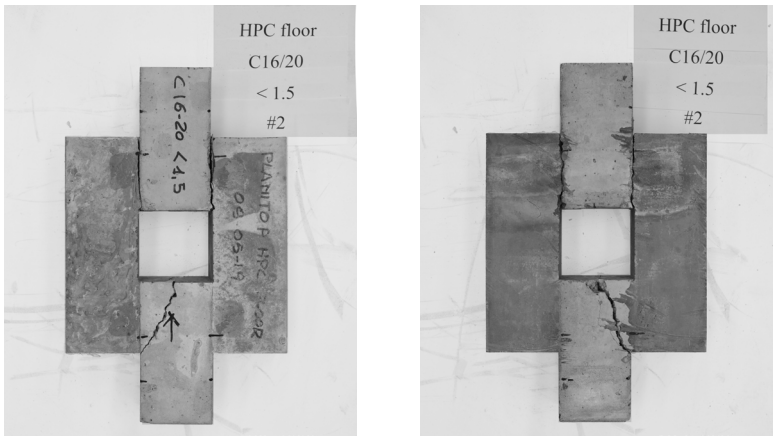

a)

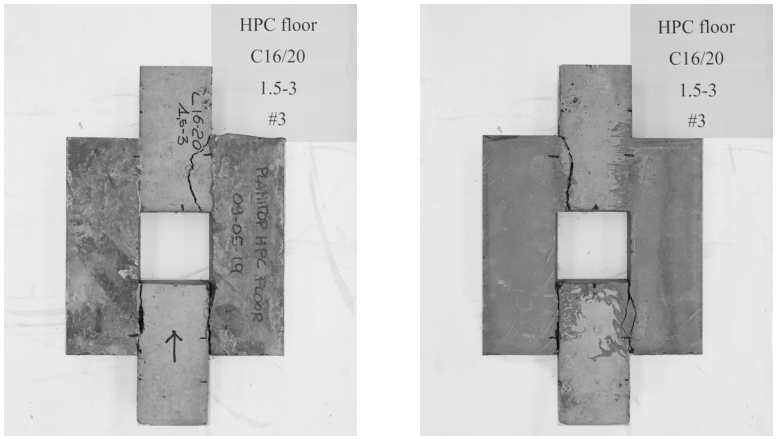

b)

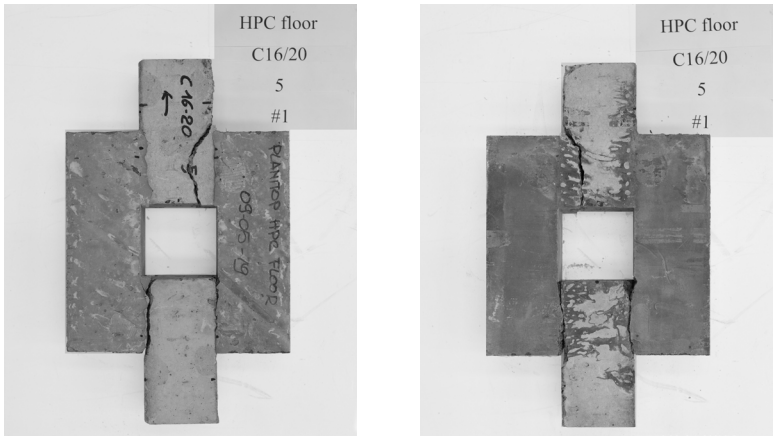

c)

Figure 4.2-13: The modes of failure in smooth bond specimens (a); in rough bond specimens (b) and in very rough bond specimens (c).

In smooth and rough batch, the failure mode was characterized by debonding and substrate failure in regions close to the interface. The failure mode was uniform for almost all specimens (75% and 100%, respectively). In very rough specimens, the failure mode was characterized by substrate failure (50%) and substrate failure in regions close to the interface (50%).

HPF-C20/25

In Figure 4.2-14 each curve represents the average of four identical specimens. The curves show that the slope in the pre-peak region is characterized by a very steep slope. After the peak stress, a low softening behaviour is observed. From the Figure 4.2-14, it is seen that smooth and rough specimens recorded the similar shear bond strength, i.e. 4.5 MPa (smooth specimens) and 4.8 MPa (rough specimens). The very rough specimens have the lowest strength of 4.2 MPa. In addition, the very rough specimens exhibit a higher energy absorption capacity, as evidenced by the more enlarged form of the softening branch of the curve.

Table 4.2-8 and Table 4.2-9 give the results of the bond tests for all the concrete C20/25 substrates tested. The minimum and maximum values are provided (in square brackets), together with the CV (in round brackets), in order to provide information about the experimental scatter.

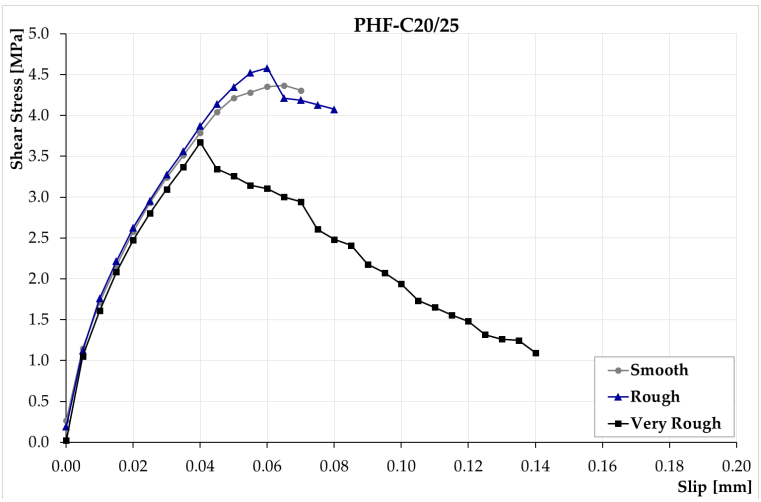

Figure 4.2-14: Average shear stress vs. interface slip curve.

	τ_a smooth [MPa]	**τ_a rough [MPa]**	**τ_a very rough [MPa]**
Mean Value	**4.5** [4.4-4.7] (0.03)	**4.8** [4.4-5.0] (0.06)	**4.2** [3.9-4.5] (0.06)

Table 4.2-8: Shear stress an interface.

	Slip smooth [mm]	**Slip rough [mm]**	**Slip very rough [mm]**
Mean Value	**0.05** [0.05-0.07] (0.13)	**0.07** [0.05-0.08] (0.14)	**0.06** [0.04-0.07] (0.17)

Note: the slips reported are recorded at the maximum shear stress.
Table 4.2-9: Slip between substrate and overlay.

Figure 4.2-15 shows the modes of failure in the three specimens with different roughness. In smooth and rough batch, the failure mode was characterized by debonding and substrate failure in regions close to the interface (100%). In very rough specimens, the failure mode was characterized by substrate failure (50%) and substrate failure in regions close to the interface (50%).

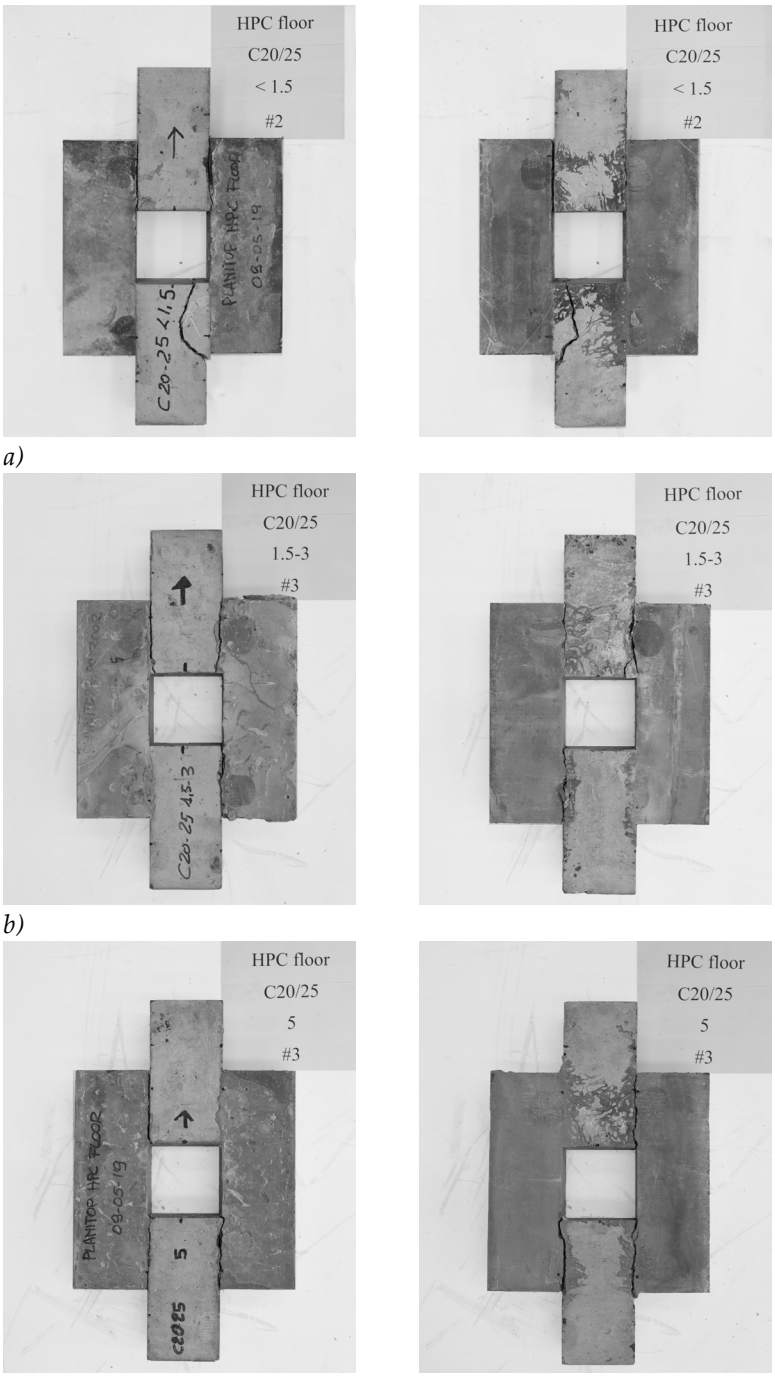

Figure 4.2-15: The modes of failure in smooth bond specimens (a); in rough bond specimens (b) and in very rough bond specimens (c).

PHF

From the results reported above, it may be noted that, the graphs were similar in terms of the pre-peak slope and the post-peak softening behaviour despite the different roughness. Moreover, it can be observed that the increase substrate surface roughness did not involve the increase in the area under the stress–displacement graph in the post-peak region. The increase in area signifies the ability of the element to absorb more energy and offer more ductile behaviour. Thus, it can be affirmed that there was not a definite increase in ductility as a result of surface preparation.

PHF46-C12/15

In Figure 4.2-16 each curve represents the average of four identical specimens. The curves show that the slope in the pre-peak region is characterized by a very steep slope. After the peak stress, a low softening behaviour is observed. From the Figure 4.2-16, it is seen that smooth and very rough specimens show a similar shear bond strength, i.e. 3.0 MPa (smooth specimens) and 3.3 MPa (very rough specimens). The rough specimens have the highest strength of 4.0 MPa. In addition, all three specimens exhibit a higher energy absorption capacity, as evidenced by the more enlarged form of the softening branch of the curve.

Table 4.2-10 and Table 4.2-11 give the results of the bond tests for all the concrete C12/15 substrate tested. The minimum and maximum values are provided (in square brackets), together with the CV (in round brackets), in order to provide information about the experimental scatter.

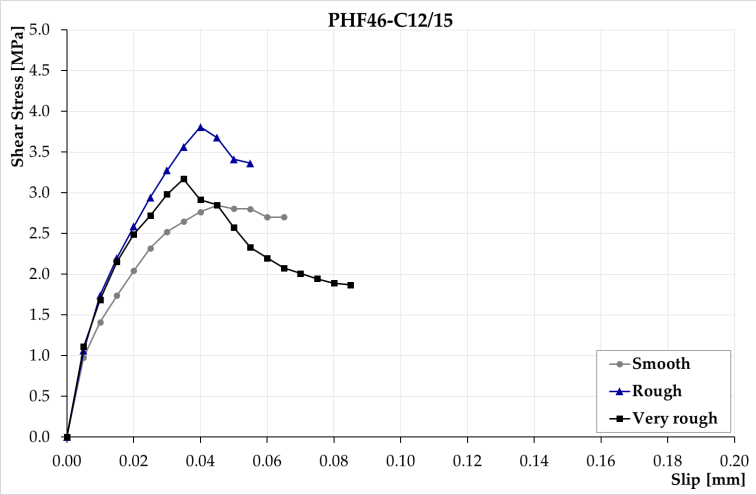

Figure 4.2-16: Average shear stress vs. interface slip curve.

	τ_a smooth [MPa]	**τ_a rough [MPa]**	**τ_a very rough [MPa]**
Mean Value	**3.0** [2.9-3.2] (0.05)	**4.0** [3.5-4.3] (0.08)	**3.3** [3.5-4.3] (0.14)

Table 4.2-10: Shear stress an interface.

	Slip smooth [mm]	**Slip rough [mm]**	**Slip very rough [mm]**
Mean Value	**0.06** [0.04-0.09] (0.42)	**0.05** [0.04-0.05] (0.10)	**0.05** [0.02-0.09] (0.63)

Note: the slips reported are recorded at the maximum shear stress.

Table 4.2-11: Slip between substrate and overlay.

Figure 4.2-17 shows the modes of failure in the three specimens with different roughness. In smooth and rough batch, the failure mode was characterized by debonding and substrate failure in regions close to the interface. The failure mode was uniform for almost all specimens (100% and 75%, respectively). In very rough specimens, the failure mode was characterized by substrate failure (75%) and substrate failure in regions close to the interface (25%).

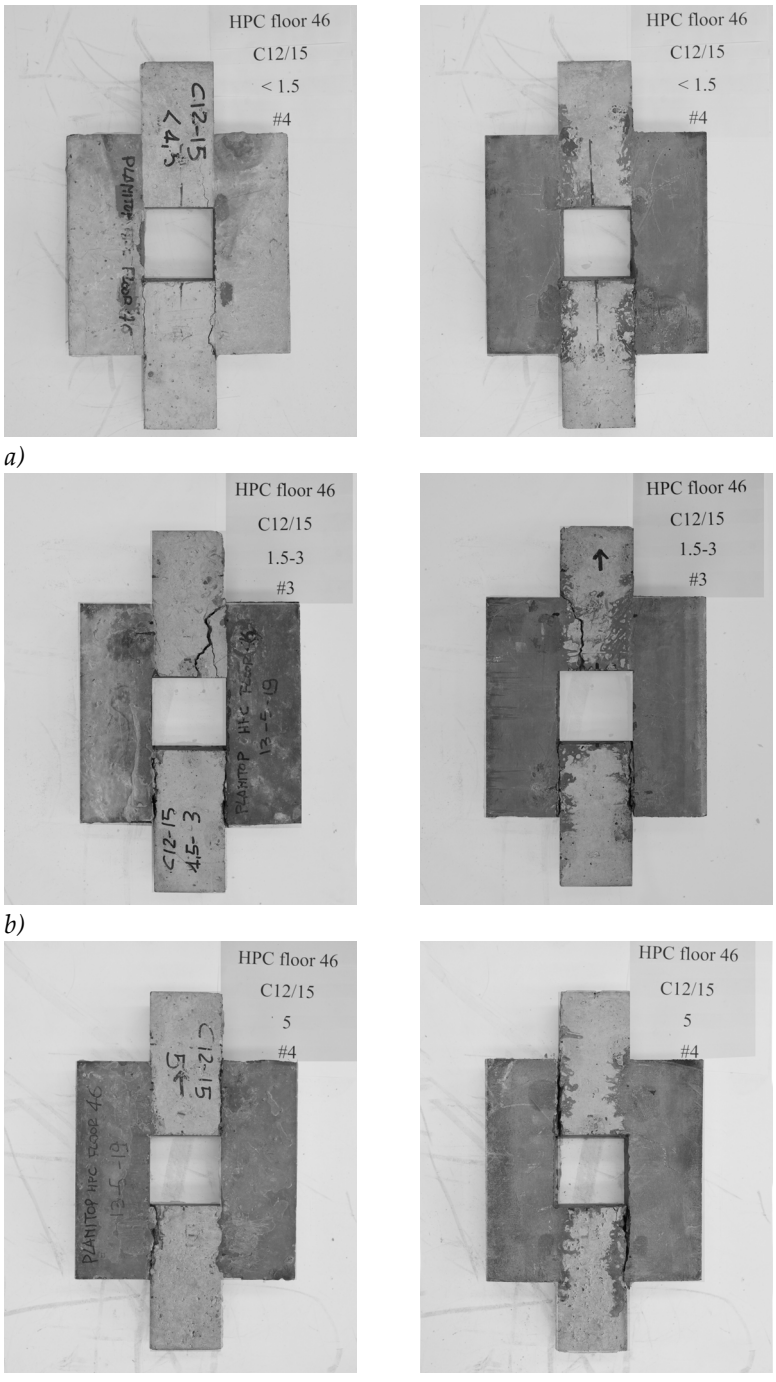

Figure 4.2-17: The modes of failure in smooth bond specimens (a); in rough bond specimens (b) and in very rough bond specimens (c).

HPF46-C16/20

In Figure 4.2-18 each curve represents the average of four identical specimens. The curves show that the slope in the pre-peak region is characterized by a very steep slope. After the peak stress, a low softening behaviour is observed. From the Figure 4.2-18, it is seen that smooth and very rough specimens show a similar shear bond strength, i.e. 3.7 MPa (smooth specimens) and 3.6 MPa (very rough specimens). The rough specimens have the lowest strength of 3.0 MPa. In addition, all three specimens exhibit a higher energy absorption capacity, as evidenced by the more enlarged form of the softening branch of the curve.

Table 4.2-12 and Table 4.2-13 give the results of the bond tests for all the concrete C16/20 substrates tested. The minimum and maximum values are provided in square brackets, and the CV in round brackets.

Figure 4.2-19 shows the modes of failure in the three specimens with different roughness. The failure mode was uniform for all the specimens, characterized by debonding and substrate failure in regions close to the interface.

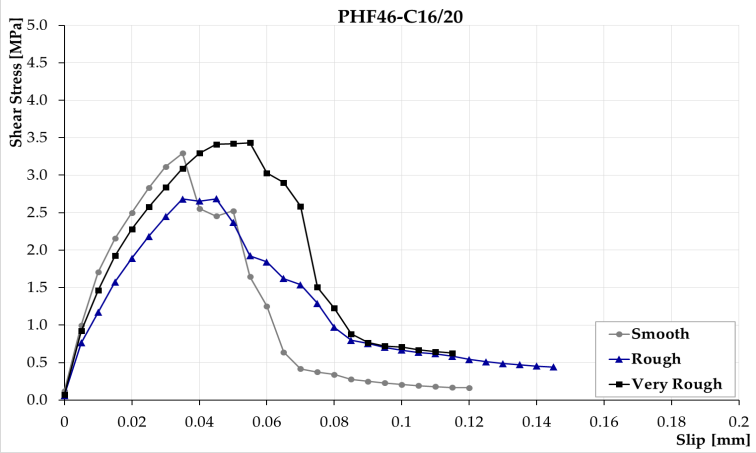

Figure 4.2-18: Average shear stress vs. interface slip curve.

	τ_a **smooth [MPa]**	τ_a **rough [MPa]**	τ_a **very rough [MPa]**
Mean Value	**3.7** [3.4-3.9] (0.05)	**3.0** [2.6-3.6] (0.14)	**3.6** [3.2-4.0] (0.11)

Table 4.2-12: Shear stress an interface.

	Slip smooth [mm]	**Slip rough [mm]**	**Slip very rough [mm]**
Mean Value	**0.04** [0.03-0.05] (0.24)	**0.05** [0.04-0.05] (0.18)	**0.05** [0.04-0.06] (0.12)

Note: the slips reported are recorded at the maximum shear stress.

Table 4.2-13: Slip between substrate and overlay.

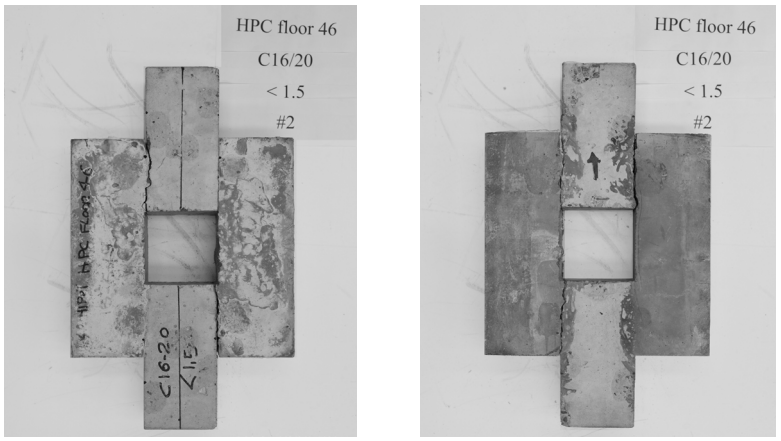

a)

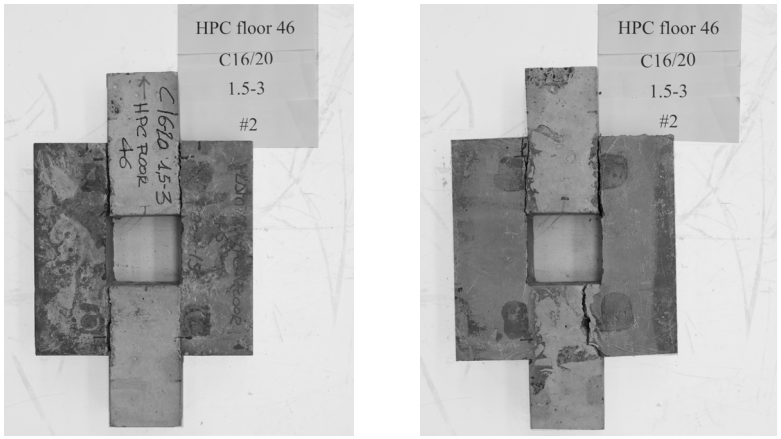

b)

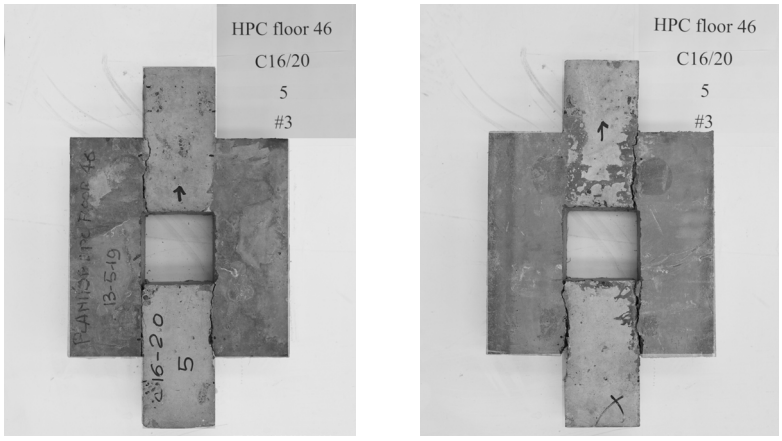

c)

Figure 4.2-19: The modes of failure in smooth bond specimens (a); in rough bond specimens (b) and in very rough bond specimens (c).

HPF46-C20/25

In Figure 4.2-20 each curve represents the average of four identical specimens. The curves show that the slope in the pre-peak region is characterized by a very steep slope. After the peak stress, a low softening behaviour is observed.

From the Figure 4.2-20, it is seen that smooth and rough specimens show the same shear bond strength, i.e. 4.3 MPa. The very rough specimens have the lowest strength of 3.8 MPa. In addition, the rough and the very rough specimens exhibit a higher energy absorption capacity, as evidenced by the more enlarged form of the softening branch of the curve.

Table 4.2-14 and Table 4.2-15 give the results of the bond tests for all the concrete C16/20 substrates tested. The minimum and maximum values are provided (in square brackets), together with the CV (in round brackets), in order to provide information about the experimental scatter.

Figure 4.2-21 shows the modes of failure in the three specimens with different roughness.

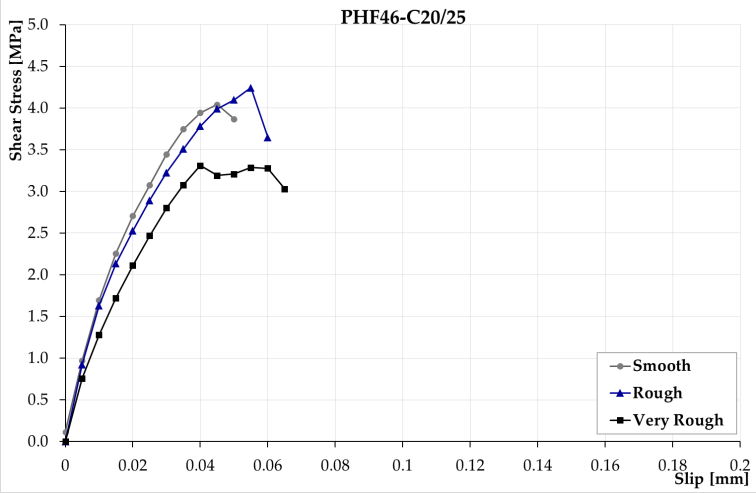

Figure 4.2-20: Average shear stress vs. interface slip curve.

	τ_a smooth [MPa]	**τ_a rough [MPa]**	**τ_a very rough [MPa]**
Mean Value	**4.3** [4.1-4.6] (0.06)	**4.3** [3.9-4.7] (0.08)	**3.8** [3.3-4.2] (0.09)

Table 4.2-14: Shear stress an interface.

	Slip smooth [mm]	**Slip rough [mm]**	**Slip very rough [mm]**
Mean Value	**0.05** [0.04-0.06] (0.21)	**0.05** [0.05-0.06] (0.10)	**0.05** [0.04-0.07] (0.29)

Note: the slips reported are recorded at the maximum shear stress.

Table 4.2-15: Slip between substrate and overlay.

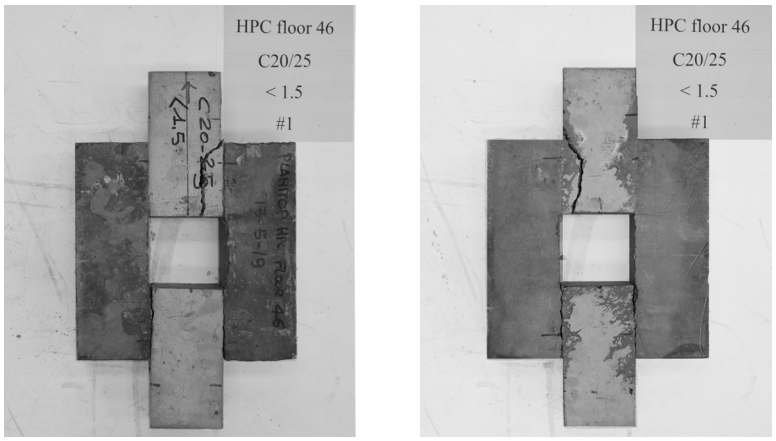

a)

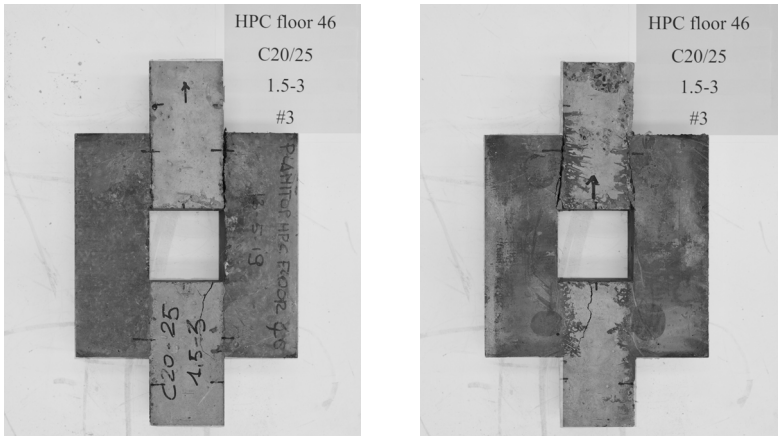

b)

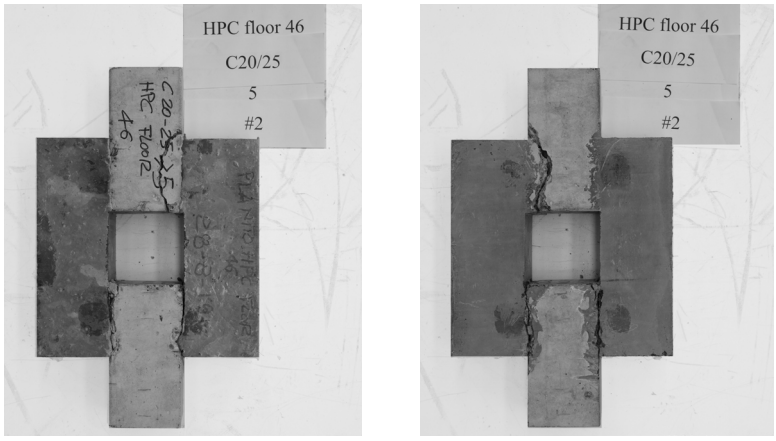

c)

Figure 4.2-21: The modes of failure in smooth bond specimens (a); in rough bond specimens (b) and in very rough bond specimens (c).

In smooth and rough batch, the failure mode was characterized by debonding and substrate failure in regions close to the interface. The failure mode was uniform for almost all specimens (75% and 100%, respectively). In very rough specimens, the failure mode was characterized by substrate failure in regions close to the interface (75%) and substrate failure (25%).

PHF46

As noted above for the PHF specimens, despite the different roughness, it can be seen that the graphs were similar in terms of the pre-peak slope and the post-peak softening behaviour. Moreover, it can be observed that the increase substrate surface roughness did not involve the increase in the area under the stress–displacement graph in the post-peak region. This increase signifies the ability of the element to absorb more energy and offer a more ductile behaviour. Thus, it can be affirmed that there was not a definite increase in ductility as a result of surface preparation.

It is necessary to note that despite the different surface preparation methods, the failure always appears localized partly or, in some cases, completely in the substrate. It is important to underscore that the bond strength equals this failure stress if the failure develops completely at the interface. In all other cases, the failure stress is only a lower bound of the bond strength [Silfwerbrand *et al*., 2011]. Therefore, in both series PHF and PHF46, when delamination does not occur, the bond strengths obtained represent a lower bound.

4.2.4 *Concluding remarks*

Figure 4.2-22 and Figure 4.2-23 summarise the results of bond tests for all the concrete substrates tested. It can be observed that there is an increase in shear stress with an increase in substrate compressive strength. This trend is quite consistent for series PHF, while it should be further validated by means of comparison specimens, for series PHF46.

The effect of substrate compressive strength is much more important for smooth and rough specimens, where the biggest increases in shear stress are observed.

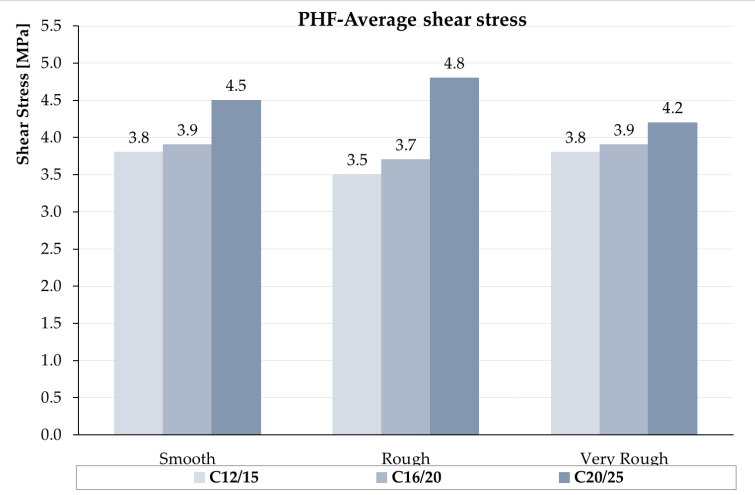

Figure 4.2-22: Summary of shear bond strength for PHF specimens.

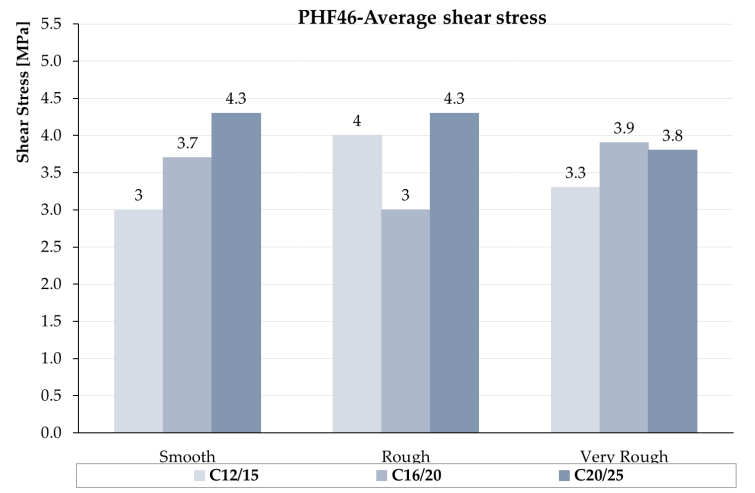

Figure 4.2-23: Summary of shear bond strength for PHF46 specimens.

The results of 72 specimens subjected to bond test have been presented in this paragrapher. Comparisons have been made between a sample with different substrate compressive strengths and different substrate surface roughnesses. Based on the experiments and discussion reported herein, the following main conclusions can be drawn:

- The dominant failure mode was characterized by substrate failure and material failure in regions close to the interface regardless of the substrate strength, surface roughness or material repairs. Actual, the failure stress obtained from this test represents a lower bound of the bond strength.
- For the substrate strength classes investigated, the influence of the substrate compressive strength seems to be a significant parameter affecting the shear stress between concretes with different ages. In particular, the highest increase in bond strength is noted for substrate C20-25. The effect of substrate compressive strength is much more important for smooth and rough specimens, where the biggest increases in shear stress are observed.
- For the substrate considered, despite the different roughnesses in the specimens tested, the pre-peak and the post-peak softening behaviour are similar. Moreover, the failure always appears localized partly or, in some cases, completely in the substrate.
- With the increase in surface roughness, the increase in the area under the stress–displacement graph in the post-peak region was not observed. This implies that the rougher specimens were not more ductile. It can be said that the ductility did not increase with the increase of the substrate roughness.

It is important to underline that these conclusions purely refer to the substrate compressive strengths investigated. Additional tests that consider a higher substrate compressive strength (i.e., in the case of bridges) could potentially lead to a shear failure at the interface, and to a more refined bond experimental model for a wide range of composite elements.

4.3 *Strengthening of square slab panels*

The experimental program of this section aims to study the influence of the substrate surface roughness on the interface bond strength between a substrate and overlay concrete in square slab elements.
The experimental program involved the design and testing of square slab panels subjected to a monotonically-increases load. A total of 24 specimens were tested. The tests to obtain mechanical properties (cylinder test, three-point bending test) are presented in Chapter 3.
The square slab panels were constructed at Mapei S.p.A. – Cafiero (Milan). The tests were conducted at the Laboratory "Pietro Pisa" of the University of Brescia.

4.3.1 *Materials and specimen geometry*

The experimental program consisted of two series of square slab panels depending on the overlay reinforcement: series PHF and series PHF46. Both series were characterized by three different roughnesses (smooth, rough and very rough). There were three square slab panels of the smooth and very rough type, and six square slab panels for the rough type. This made a total of 24 specimens tested in the program.

4.3.1.1 Substrate concrete

C16/20 concrete was chosen as the substrate for this investigation. Table 4.3-1 gives the detailed composition of the substrate material. Technocem CEM II/B-LL 32,5R was the cement type used.

	Type	**Weight [kg/m³]**
Cement	Technocem CEM II/B-LL 32,5R	262
Superplasticizer	Dynamon SP1	2.3
Filler		34
Total water		180
w/c		0.68

Table 4.3-1: Concrete C16/20 composition.

The compressive strength was evaluated on concrete cubes measuring 150 mm, following the guidelines given in UNI EN 12390-3 [2009]. Six specimens were tested for each material and their mean value was taken as the strength of the material. All the specimens were stored in water at a temperature of 23.0 ± 2.0°C prior to testing. At 28 days, the average compressive strength was R_{cm}=25 MPa.

4.3.1.2 Overlay

Ultra-High-Performance Fibre Reinforced Concrete (UHPFRC) for the specimen was provided by Mapei S.p.A. The materials Planitop HPC Floor (PHF) and Planitop HPC Floor 46 (PHF46) were chosen for investigation. The selected materials are representative of typical structural strengthening materials employed to reinforce square slab panels. The mechanical characterizations of PHF and PHF46 are presented in Section 3.2 and 3.3.

4.3.1.3 Specimen geometry

Figure 4.3-1 illustrates the geometry of the square slab panel. The specimens consisted of an old layer reinforcement concrete (substrate) and a new layer of UHPFRC (overlay). The panels had dimension of 1050 x 1050 mm. The thickness of the substrate was 80 mm, and that of the overlay was 40 mm. The substrate was reinforced with a steel mesh, which was composed of 8 mm diameter bars assembled with a spacing of 100 mm. The steel tensile strength was f_y=450 MPa.
The contact surface area measured 1102500 mm². The contact surface of the substrate was prepared to ensure good roughness prior to casting of the overlays.
The main variable parameter of the test series was the substrate roughness.

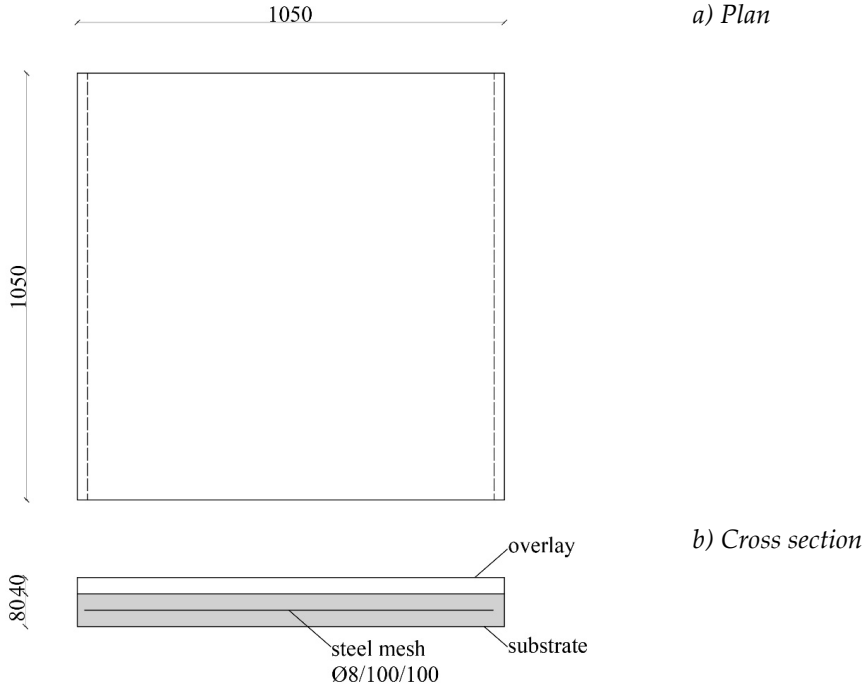

Figure 4.3-1: Geometry of specimen: a) plan; b) cross section.

4.3.1.4 Substrate surface

The purpose of the test was to study the influence of the substrate surface roughness on the interface bond strength. Therefore, three different roughness indexes were investigated:

- smooth surface;
- rough surface;
- very rough surface.

The smooth surface specimens were obtained by using a Bosch GSS 2300 Professional Orbital Sander. A trimmer scaler was used to prepare of the rough and very rough surface specimens. The roughness of the samples was measured by a profilometer (Barton's comb). Table 4.3-2 reports the average roughness of the specimens and the classification of surface roughness according to *fib* Model Code for Concrete Structures 2010 (MC2010) [2013].
Figure 4.3-2 shows the comparison between the different substrate surface.

Roughness classification	**Average roughness R_t [mm]**
Smooth	<1.5
Rough	1.5-3.0
Very rough	>3.0

Table 4.3-2: Classification of surface roughness, ModelCode 2010 [2013].

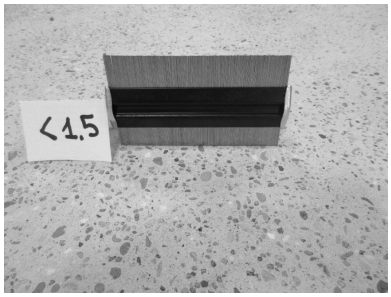

a)

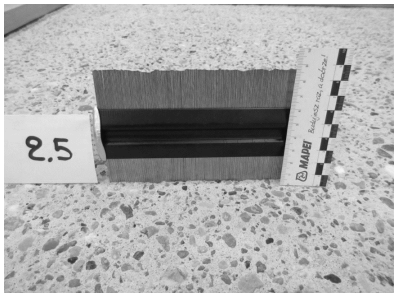

b)

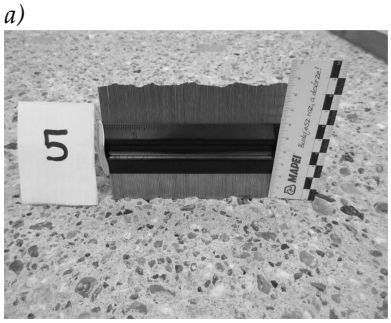

c)

Figure 4.3-2: Comparison of the different substrate surfaces, a) smooth surface, b) rough surface and c) very rough surface.

4.3.1.5 Casting and curing specimens

The casting process began with the preparation of the substate layer, which incorporated an 8 mm steel mesh, as mentioned above. The substrate layer was cast at least 56 days prior to casting the overlay. The substrate was subjected to the required treatment method to obtain the needed surface roughness parameter. Then the slabs were thoroughly cleaned with a professional water-jetting system (Putzmeister – Dynajet MG 500) to remove dust and residual materials. The working pressure applied was different for each roughness. Pressures of 200, 300, and 400 bars were used for the smooth, rough and very rough specimens, respectively. For the smooth, very rough and three rough specimens, the substrate surface was moistened to obtain a condition of saturated surface dry. This procedure was done by wetting the surface until it was saturated, and letting it dry just enough to remove excess moisture. For the three very rough specimens the substrate surface was dampened with Primer Mapei 3296, which is an acrylic primer in water dispersion (ratio of 1:1) with high penetration. The overlay was cast 56 days after the substrate layers. It was necessary to ensure that the interface area was free of air pockets which could compromise the bond. After casting the overlay, all specimens were moist cured and covered with plastic sheets.

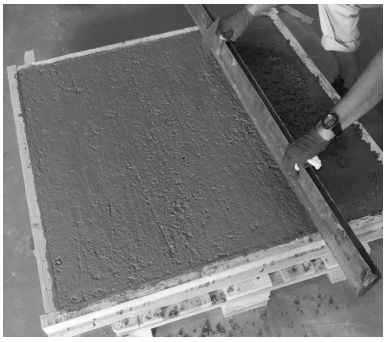

a)

b)

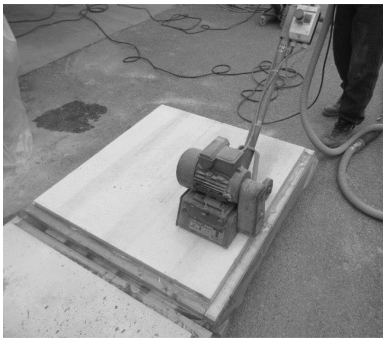

d)

e)

Figure 4.3-3 (Pt. 1 of 2)

f)

g)

h)

i)

(Pt. 2 of 2)

Figure 4.3-3: a) casting of substrate layer; b) smooth surface preparation; c) rough and very rough surface preparation d) cleaning of substrate layer with water-jetting system; e) moistening of surface layers; f) application of Primer Mapei 3296; g) cleaning substrate layers h) casting of overlay.

4.3.2 *Set-up description*

The tests were performed in displacement-control mode. Vertical load was applied by means of an electromechanical jack (Setec Sep 500) with a capacity of 500 kN. The square slab panels were positioned into a loading frame suitably connected to the strong floor. All specimens were placed on roller steel supports with a span of 1000 mm. The live-load was applied to four points having distance of L/4.
Figure 4.3-4 and Figure 4.3-5 show the steel loading frame.

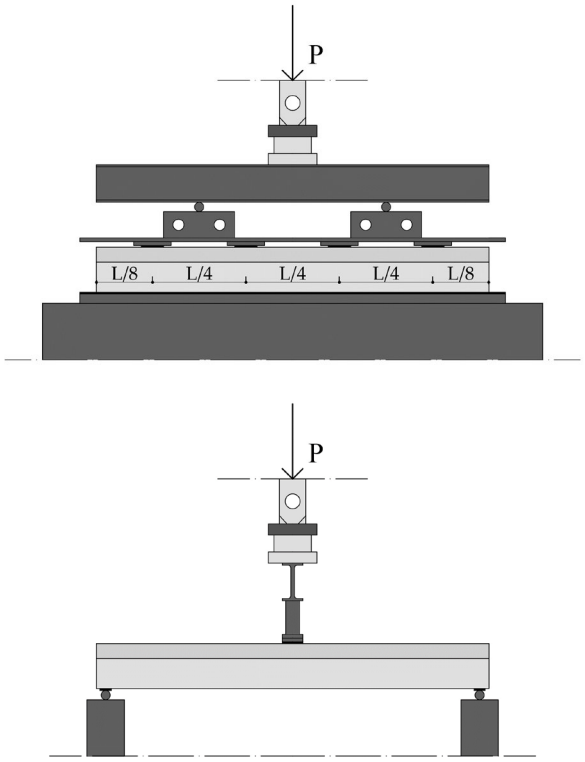

Figure 4.3-4: Schematic view of test set-up.

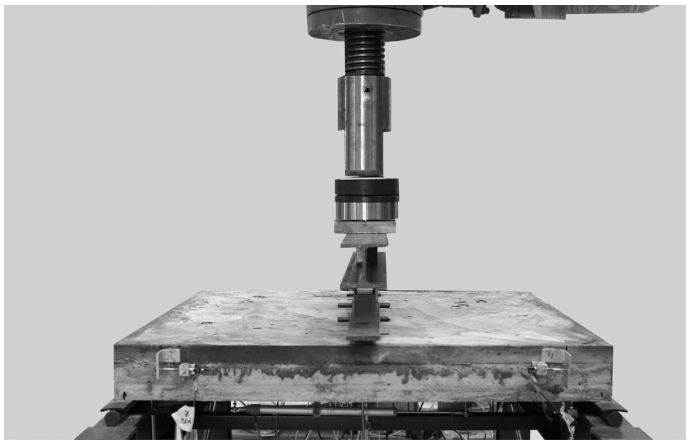

Front view

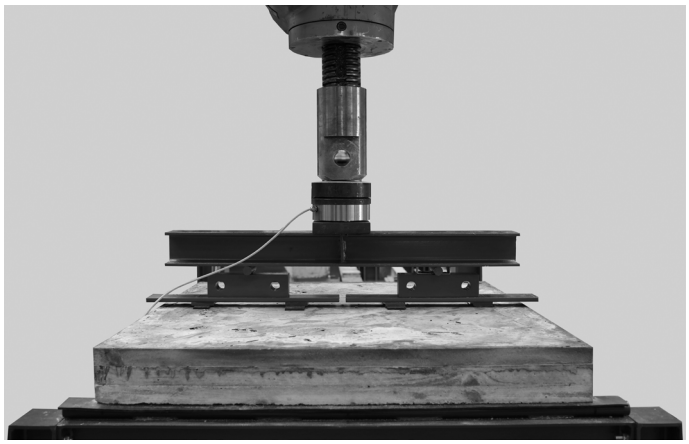

Lateral view

Figure 4.3-5: View of test set-up.

The Quantum data acquisition system was used to record all electronic test data from the outputs: load cell, LVTDs, and potentiometer transducers. The Linear Variable Differential Transformers (LVDTs) and potentiometers were utilized to monitor vertical deflections, slips between layers, and crack opening. Eleven LVDTs and three potentiometers were used in total and they were deployed as described in Table 4.3-3.

Range [mm]	Location on specimen
Vertical LVTD	
WA 100	Front mid-span deflection
WA 100	Centre mid-span deflection
WA 100	Back mid-span deflection
WA 20	Support deflection 1 front right
WA 20	Support deflection 2 front left
WA 20	Support deflection 3 back right
WA 20	Support deflection 4 back left
Horizontal LVTD	
WI 2.5	Interface substrate-overlay front right
WI 2.5	Interface substrate-overlay front left
WI 2.5	Interface substrate-overlay back right
WI 2.5	Interface substrate-overlay back left
Horizontal Potentiometer	
PC 500	Lower surface crack width front
PC 500	Lower surface crack width centre
PC 500	Lower surface crack width back

Table 4.3-3: Layout of instrumentation.

Three LVTDs were used to measure the deflection at mid-span (front, centre and back). The support displacements were monitored by four LVTDs. For measuring slips between the substrate and the overlay, four LVTDs were placed horizontally at the interface. Three horizontal potentiometers were installed at the lower surface to measure mid-span crack width.

4.3.3 *Experimental results*

The major objective of these tests was the investigation of the influence of the substrate surface roughness on the interface bond strength. The collected results are presented in the following paragraphs, in the form of *load vs. net mid-span deflection* curves. The mid-span deflection was calculated with the following equation:

$$d_{net} = \frac{d_{net,F} + d_{net,C} + d_{net,B}}{3} \qquad (4.3\text{-}1)$$

where:

d_{net} is the net mid-span deflection;

$d_{net,F} = d_F - \frac{\delta'_{F,L}+\delta'_{F,R}}{2}$ is the net front mid-span deflection;

$d_{net,C} = d_C - \frac{\delta'_{F,L}+\delta'_{F,R}+\delta'_{B,L}+\delta'_{B,R}}{4}$ is the net centre mid-span deflection;

$d_{net,B} = d_B - \frac{\delta'_{B,L}+\delta'_{B,R}}{2}$ is the net back mid-span deflection;

δ'_L are support displacements calculated at 60 mm from the left support (δ'_F front side and δ'_Bback side);

δ'_R are support displacements calculated at 60 mm from the right support (δ'_F front side and δ'_Bback side).

Additionally, *load vs. crack in mid-span* graphs are reported in this section. The crack in mid-span reported is the average between the values measure by the three horizontal potentiometers sited to the lower surface (right, centre and left).
Selective test photos, at the end of each tests, are presented.

4.3.3.1 Influence of surface roughness

The experimental program consisted of 24 square slab panels: 12 specimens for series PHF and 12 for series PHF46, respectively. Both series were characterized by three different roughnesses (smooth, rough, and very rough). There were three specimens for the smooth and very rough specimens and six for rough specimens (three for rough specimens and three for rough specimens dampened with Primer Mapei).
The mentioned abbreviations are used in the description of the tested elements:

- S1: square slab panels with smooth surface;
- S2 PM: square slab panels with rough surface and dampened with Primer Mapei;
- S2: square slab panels with rough surface;
- S3: square slab panels with very rough surface.

PHF

Figure 4.3-6 shows the *load vs. net mid-span deflection* curves for S1, S2 PM, S2, and S3. Figure 4.3-7 reports the mean experimental curve for PHF. Each curve represents the average of three identical square slab panels.

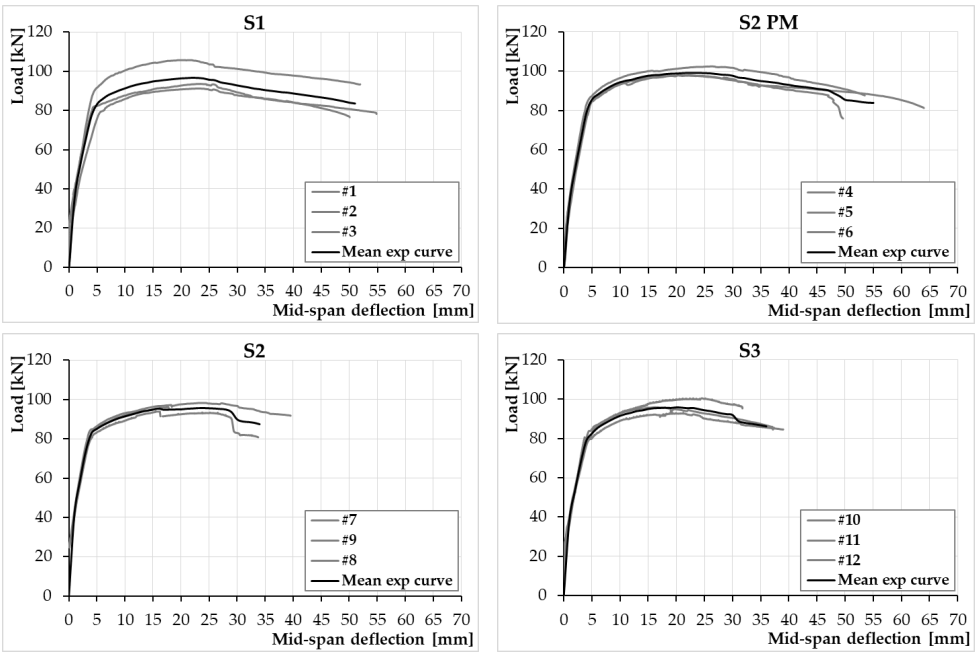

Figure 4.3-6: Load vs. net mid-span deflection S1, S2 PM, S2, and S3.

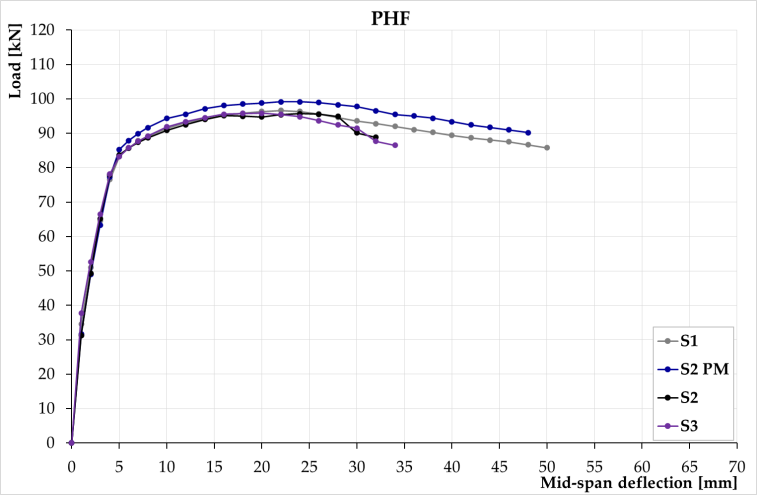

Figure 4.3-7: Average load vs. net mid-span deflection PHF.

Table 4.3-4 gives the peak load of the tests for all specimens tested. The minimum and maximum values of the peak load are reported (in square brackets), together with the coefficient of variation, CV, (in round brackets), in order to provide information about the experimental scatter.

	Load S1 [kN]	**Load S2 PM [kN]**	**Load S2 [kN]**	**Load S3 [kN]**
Mean Value	**96.9** [91.3-105.8] (0.08)	**99.5** [97.9-102.5] (0.03)	**97.2** [96.2-98.3] (0.01)	**96.4** [92.9-100.5] (0.04)

Table 4.3-4: Peak load.

Moreover, the shear stress (τ) across an interface at the peak load was calculated. τ can be evaluated from the following relation:

$$\tau = \frac{V}{b \cdot d} \qquad (4.3\text{-}2)$$

where:

$V = \frac{P}{2}$ is the maximum shear force for a statically determinate beam under a concentrated load;

b is the width, equal to 1050 mm;

d is the effective depth, equal to 90 mm.

Table 4.3-5 and Table 4.3-6 summarize the shear stress across the interface and the slips in micron between the substrate and overlay for all specimen tested. The minimum and maximum values are reported (in square brackets), together with the CV (in round brackets), to provide information about the experimental scatter.

Figure 4.3-8 shows the *load vs. crack in mid-span* graphs for S1, S2 PM, S2, and S3.

Figure 4.3-9 reports the mean experimental curve for PHF. Each curve represents the average of three identical square slab panels.

	τ **S1** **[MPa]**	τ **S2 PM** **[MPa]**	τ **S2** **[MPa]**	τ **S3** **[MPa]**
Mean Value	**0.51** [0.48-0.56] (0.08)	**0.53** [0.52-0.54] (0.02)	**0.51** [0.51-0.52] (0.01)	**0.51** [0.49-0.53] (0.04)

Table 4.3-5: Shear stress across interface.

	Slip S1 **[μm]**	**Slip S2 PM** **[μm]**	**Slip S2** **[μm]**	**Slip S3** **[μm]**
Mean Value	**3.3** [2.0-5.1] (0.48)	**3.2** [1.4-6.3] (0.86)	**2.2** [1.6-3.3] (0.42)	**0.7** [0.1-1.0] (0.74)

Table 4.3-6: Slips between substrate and overlay recorded at the peak load.

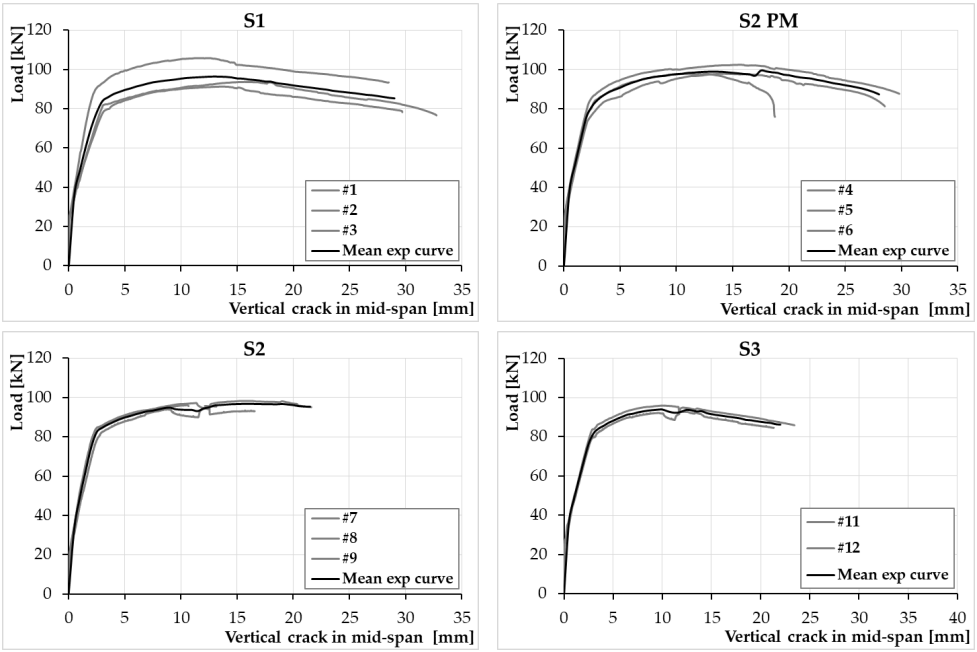

Figure 4.3-8: Load vs. crack in mid-span S1, S2 PM, S2, and S3.

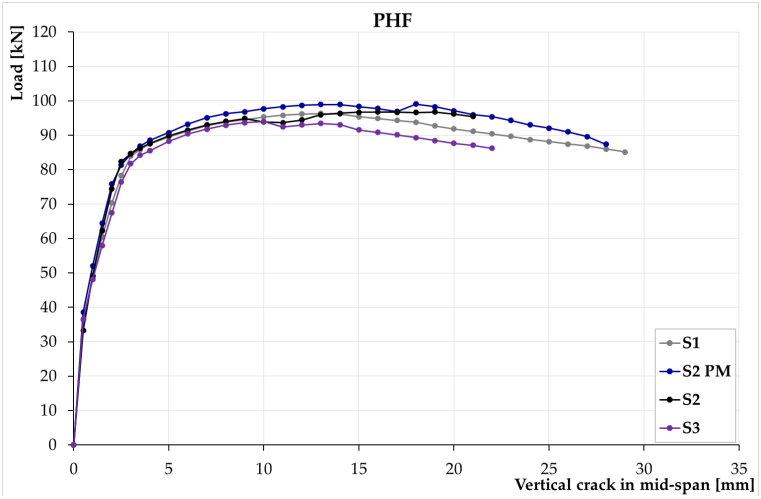

Figure 4.3-9: Average Load vs. crack in mid-span PHF.

It is seen that the specimens show similar peak loads. The maximum load is 102.5 kN in batch P2 PM. Despite the different roughness, in the square slab panels the pre-peak and the post-peak softening behaviour are similar. The influence of the substrate surface roughness can be observed in the slips between old and new concrete. Notwithstanding this, the slips between the substrate and the overlay are minimal; the maximum value is 6.3 μm in panel P2 PM. Therefore, no important slippage was observed between the layers, and in all cases the shear stresses were transferred between the layers through good bond. Consequently, good uniformity was achieved in the slabs' performances under bending. The use of Primer Mapei did not influence the slips between the layers.

Regarding the shear stress, the influence of the substrate surface roughness was not particularly significant. Indeed, the values were very similar. In all specimens, the damage mode was flexural, and at the end of test the steel rebars reached the ultimate tensile strength. It can be seen that there is a large crack at the mid-span of all slabs tested. The flexural crack was at most 33 mm wide at the end of the tests. In Specimen #9 (batch P2), two comparable cracks were observed.

Figure 4.3-10 groups the test photos depicting the bottom view of all the specimens at the conclusion of testing.

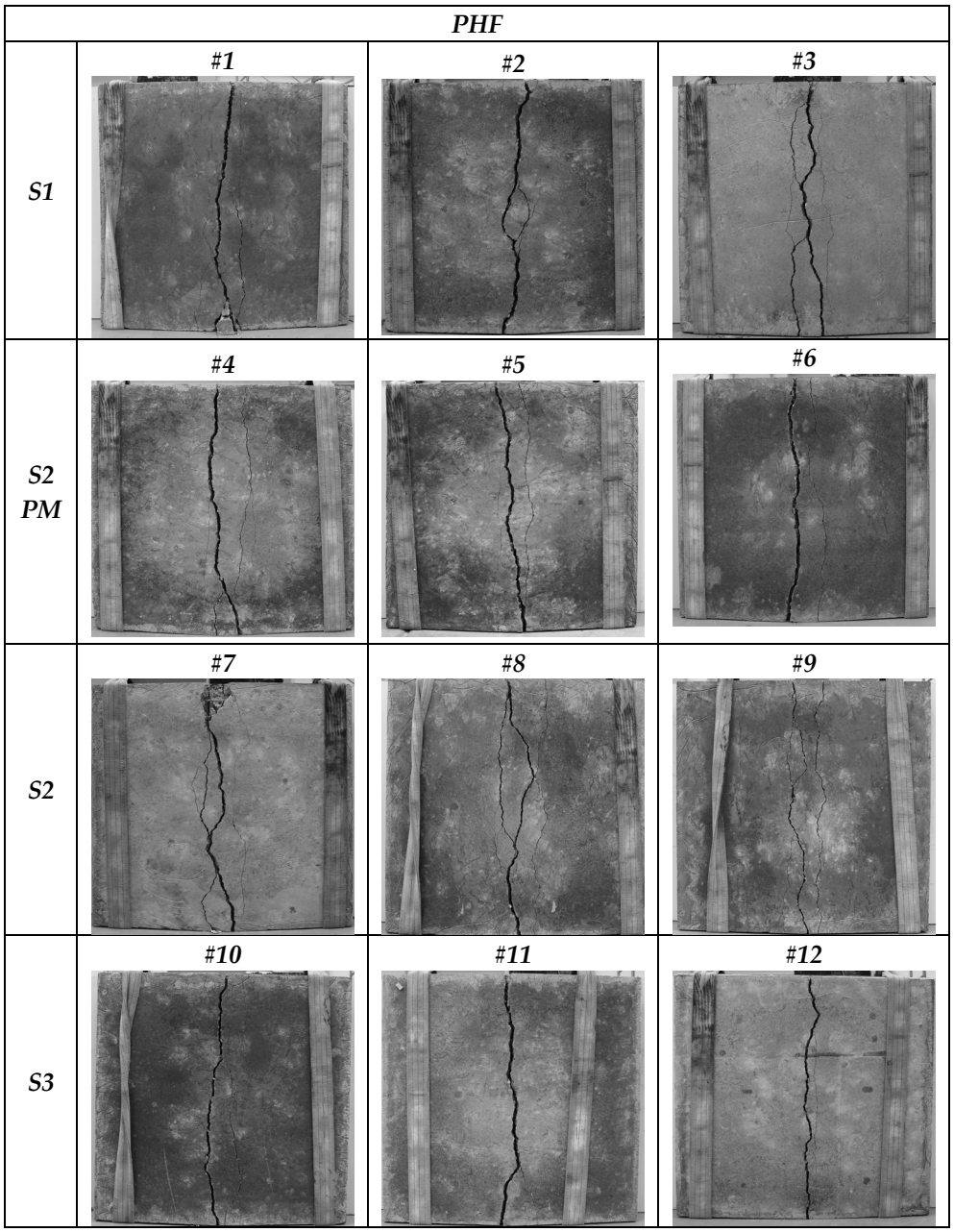

Figure 4.3-10: Bottom view of specimens.

PHF46

Figure 4.3-11 gives the *load vs. net mid-span deflection* curves for S1, S2 PM, S2, and S3. Figure 4.3-12 illustrates the mean experimental curve for PHF. Each curve represents the average of three identical square slab panels.

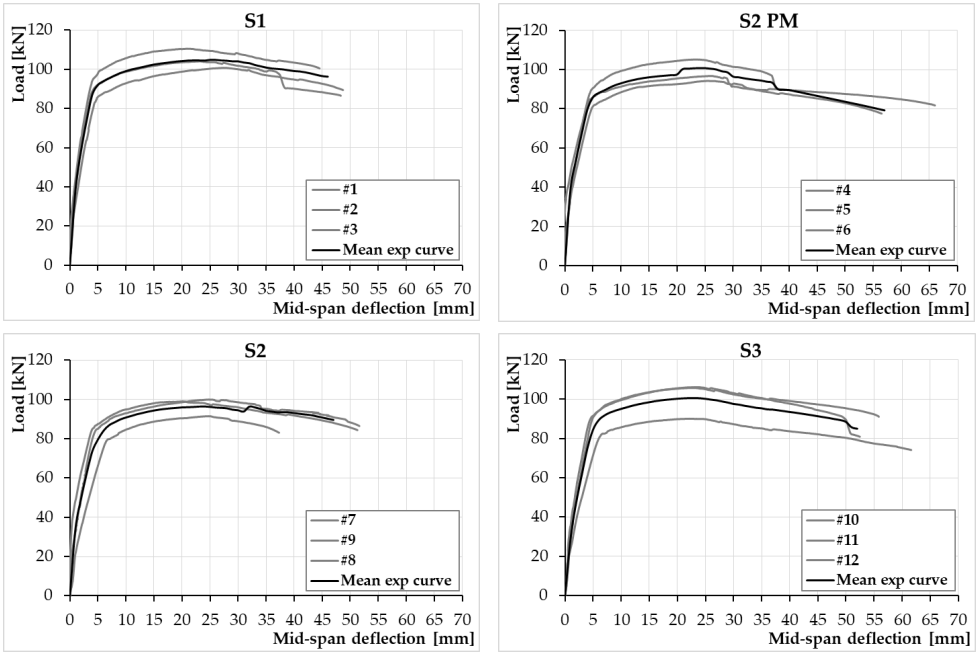

Figure 4.3-11: Load vs. net mid-span deflection S1, S2 PM, S2, and S3.

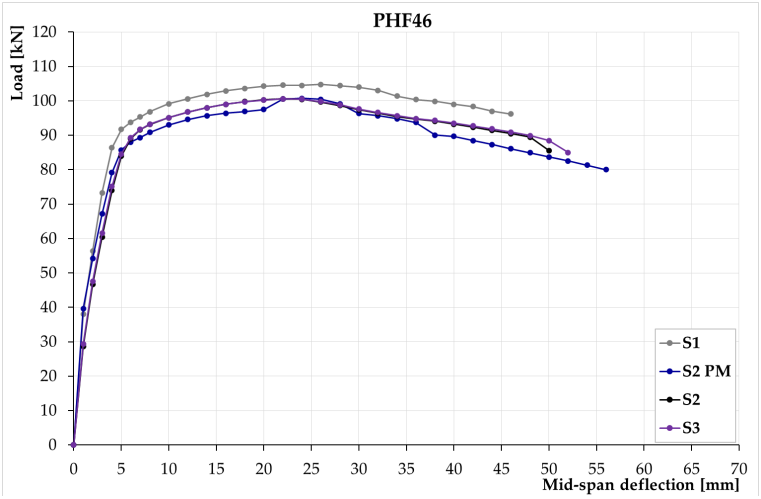

Figure 4.3-12: Average load vs. net mid-span deflection PHF46.

Table 4.3-7 gives the peak load for all specimens tested. The minimum and maximum values of the peak load are reported (in square brackets), together with the CV (in round brackets), in order to provide information about the experimental scatter.

	Load S1 [kN]	**Load S2 PM [kN]**	**Load S2 [kN]**	**Load S3 [kN]**
Mean Value	**105.2** [100.8-110.6] (0.05)	**98.7** [94.3-105.2] (0.06)	**96.9** [91.6-100.0] (0.05)	**100.7** [90.1-106.2] (0.04)

Table 4.3-7: Peak load.

Moreover, the shear stress (τ) across the interface at peak load was calculated. τ can be evaluated using the following relation:

$$\tau = \frac{V}{b \cdot d} \qquad (4.3\text{-}3)$$

where:

$V = \frac{P}{2}$ is the maximum shear force for a statically determinate beam under a concentrated load;

b is the width, equal to 1050 mm;

d is the effective depth, equal to 90 mm.

Table 4.3-8 and Table 4.3-9 report the shear stress across the interface and the slips in microns between the substrate and the overlay for all specimens tested. The minimum and maximum values are reported (in square brackets), together with the CV (in round brackets), to provide information about the experimental scatter.

	τ S1 [MPa]	**τ S2 PM [MPa]**	**τ S2 [MPa]**	**τ S3 [MPa]**
Mean Value	**0.56** [0.53-0.59] (0.05)	**0.52** [0.50-0.56] (0.06)	**0.51** [0.48-0.53] (0.05)	**0.53** [0.48-0.56] (0.09)

Table 4.3-8: Shear stress across interface.

	Slip S1 [μm]	**Slip S2 PM [μm]**	**Slip S2 [μm]**	**Slip S3 [μm]**
Mean Value	**1.5** [1.4-1.6] (0.07)	**1.9** [0.2-3.0] (0.79)	**2.1** [1.7-2.9] (0.31)	**1.4** [1.2-1.5] (0.12)

Table 4.3-9: Slips between substrate and overlay recorded at the peak load.

Refer to Figure 4.3-13 for *load vs. crack in mid-span* graphs for S1, S2 PM, S2 and S3.

Figure 4.3-14 reports the mean experimental curve for PHF46. Each curve represents the average of three identical square slab panels.

Figure 4.3-15 illustrates the bottom view of all specimens at the end of testing.

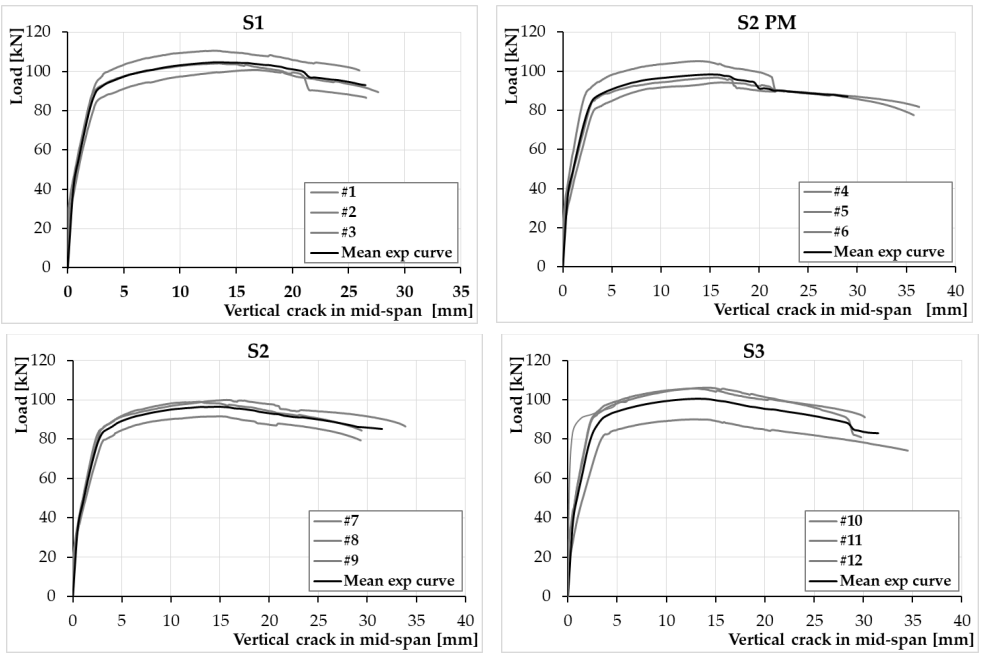

Figure 4.3-13: Load vs. crack in mid-span S1, S2 PM, S2, and S3.

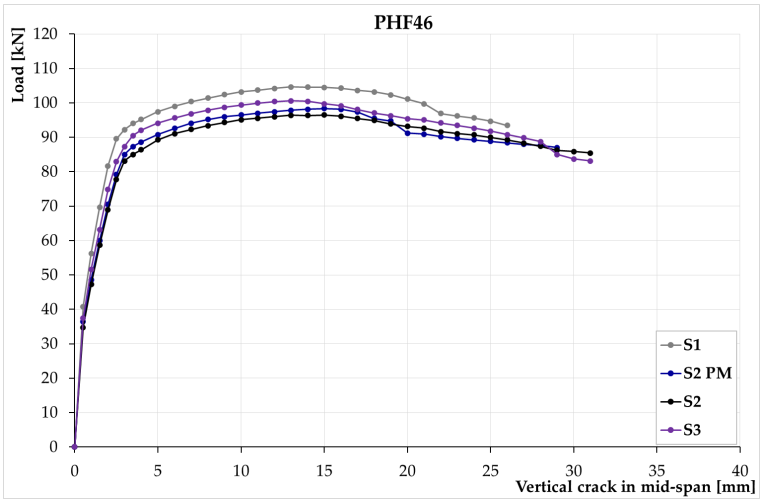

Figure 4.3-14: Average load vs. crack in mid-span HPF46.

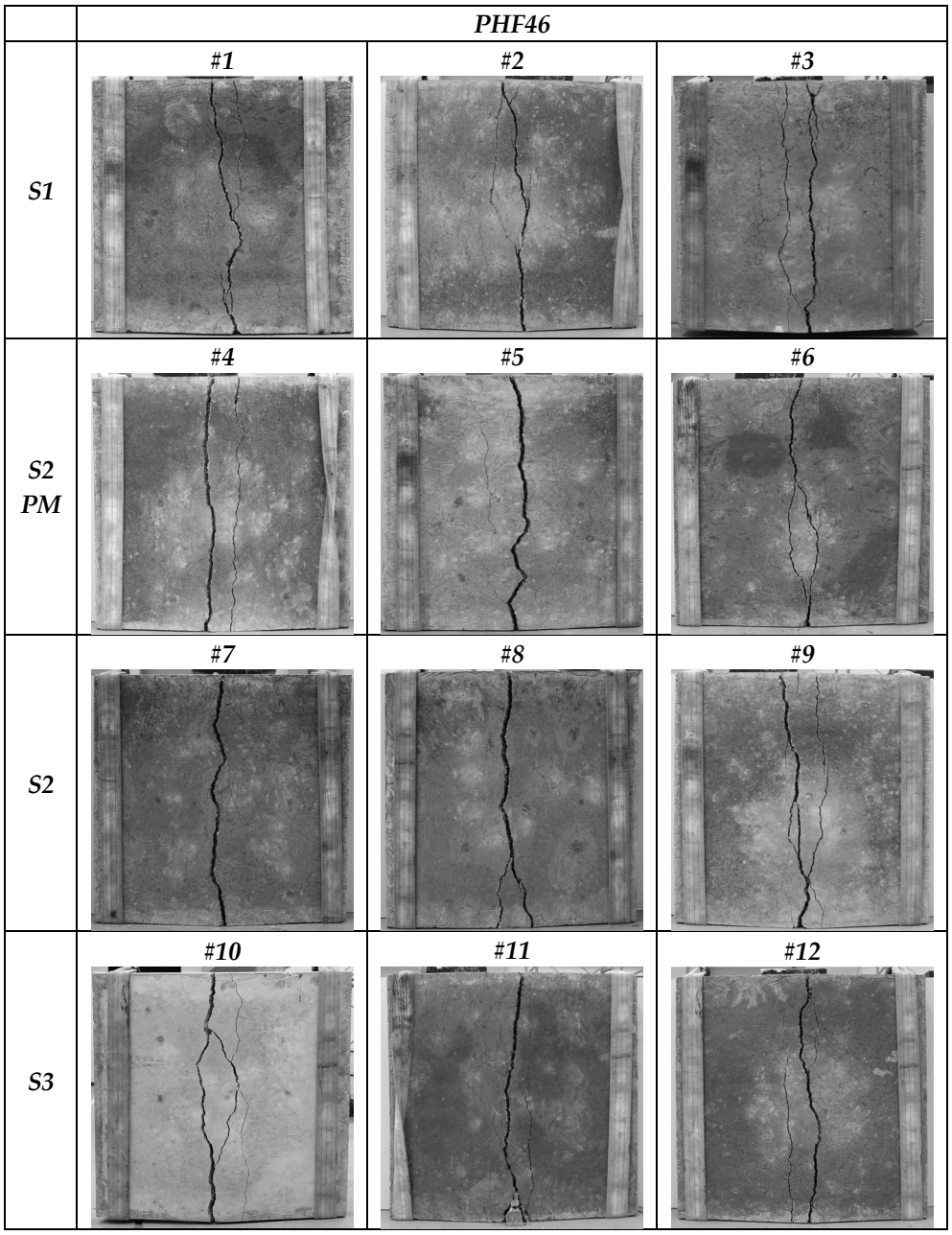

Figure 4.3-15: Bottom view of specimens.

It can be observed that the maximum peak load was 106.2 kN in the very rough specimens. Nevertheless, it can be affirmed that the specimens showed comparable peak loads. Indeed, in the specimens with different roughness, the pre-peak and the post-peak softening behaviours were similar. Moreover, the substrate surface roughness did not influence the slips between old and new concrete. In fact, the slip between layers was negligible in all specimens; the maximum value was 3.0 μm in the P2 PM specimens. Therefore, no significant slippage was observed between layers and the shear stresses were transferred between the layers through good bond. Consequently, good uniformity was achieved in the slabs' performances under bending. Concerning the shear stress, the influence of the substrate surface roughness was not particularly important. Indeed, the values were very similar. In all specimens tested, the failure mode was flexural. The steel mesh reached the ultimate tensile strength in all slabs at the end of the tests. At the most heavily damaged state, the largest crack was at the mid-span. The largest flexural crack observed was 36 mm wide in P2 PM at the end of tests.

4.3.4 *Concluding remarks*

From the test results obtained, it can be concluded that:

- The shear stresses from these tests are reasonable and representative of the shear stresses in actual structures.
- No significant slip between the layers was observed. Consequently, good uniformity was achieved in the slabs' performance under bending, and the shear stresses are transferred between the layers through good bond.
- Both series give very similar results in terms of failure load, failure mode, and load versus displacement response.
- The peak load is not influenced by the substrate surface roughness. Despite the different roughnesses in the specimens, the pre-peak and the post-peak softening behaviours are similar. Therefore, the influence of the substrate surface roughness is not particularly important to the interface bond strength.

4.4 Comparison of shear stress obtained from two different tests

This section provides a comparison between shear stress measured by the shear bond tests and bending tests, respectively.
As mentioned in Section 4.2, the shear bond test program consisted of two series of specimens: series PHF and series PHF46. Both series were characterized by three different substrates and three different roughnesses. There were four specimens for each one. This made a total of 72 specimens tested in the program.
The experimental results of the prism specimens, with substrate C16/20, and the square slab panels are presented in the paragraph below.
The minimum and maximum shear stresses of the PHF-C16/20 prism specimens were 2.7 MPa and 5.0 MPa, respectively. Whereas, for the PHF-C16/20 slabs, the minimum shear stress was 0.48 MPa and the maximum was 0.56 MPa. Regarding the material PHF46, the minimum and maximum shear stresses of the PHF46-C16/20 prism specimens were 2.6 MPa and 4.7 MPa, respectively. The minimum and maximum shear stresses of the PHF46-C16/20 slabs were 0.48 MPa and 0.59 MPa. Based on these observations, it is clear that the shear stresses in the slabs were lower than those in the prism specimens. Nevertheless, the shear stresses recorded during the bending tests on the slabs are reasonable and representative of the shear stresses in actual structures.
In other words, the two tests herein compared investigate different levels of shear slippage. While the first test is characterized by a typical slippage-critical set-up, the second aims simulate a typical state of stress in a strengthened floor, with values of slippage values much smaller than in the first case. The experimental results were examined to determine the shear stress at the interface corresponding to 2 μm of slip (the mean value recorded in the square slab panels) in both prism specimens and square slab panels. Table 4.4-1, Table 4.4-2, Table 4.4-3, and Table 4.4-4 report the shear stress at the interface between substrate and overlay corresponding to 2 μm of slip.
Figure 4.4-1 compares the shear stresses corresponding to 2 μm of slip obtained from the two different tests.

Prism specimen PHF	**Smooth [MPa]**	**Rough [MPa]**	**Very rough [MPa]**
#1	1.48*	0.35	0.63
#2	0.35	0.42	0.48
#3	0.75	0.62	0.34
#4	0.45	0.32	0.87
Mean Value	**0.51**	**0.43**	**0.58**
Standard deviation	**0.21**	**0.14**	**0.23**
CV	**0.41**	**0.32**	**0.39**

* *the shear stress value of the #1 specimen was excluded in mean value calculation.*

Table 4.4-1: Shear stresses at 2 μm of slip in prims specimens, series PHF.

Square slab panel PHF	**Smooth [MPa]**	**Rough [MPa]**	**Very rough [MPa]**
#1	0.49	0.49	0.45
#2	0.37	0.50	0.35
#3	0.41	0.40	0.52
Mean Value	**0.42**	**0.46**	**0.44**
Standard deviation	**0.06**	**0.06**	**0.09**
CV	**0.15**	**0.12**	**0.19**

Table 4.4-2: Shear stresses at 2 μm of slip in square slab panels, series PHF.

Prism specimen PHF46	**Smooth [MPa]**	**Rough [MPa]**	**Very rough [MPa]**
#1	0.73	0.33	0.81
#2	0.19	0.30	0.28
#3	0.47	0.78	0.40
#4	0.51	0.76	0.51
Mean Value	**0.47**	**0.54**	**0.50**
Standard deviation	**0.22**	**0.26**	**0.23**
CV	**0.47**	**0.48**	**0.45**

Table 4.4-3: Shear stresses at 2 μm of slip in prims specimens, series PHF46.

Square slab panel PHF46	**Smooth [MPa]**	**Rough [MPa]**	**Very rough [MPa]**
#1	0.53	0.47	0.39
#2	0.46	0.45	0.48
#3	0.47	0.52	0.43
Mean Value	**0.49**	**0.48**	**0.43**
Standard deviation	**0.04**	**0.04**	**0.05**
CV	**0.08**	**0.08**	**0.10**

Table 4.4-4: Shear stresses at 2 μm of slip in square slab panels, series PHF46.

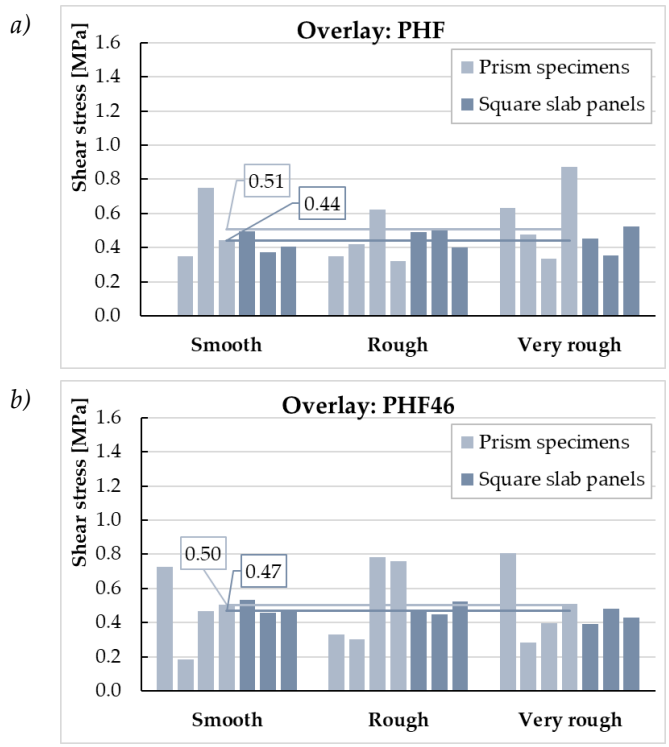

Figure 4.4-1: Shear stresses at 2 μm of slip in prims specimens and in square slab panels: a) series PHF, b) series PHF46.

From the comparison above, it can be observed that the shear stresses corresponding to 2 μm obtained from the two different tests are comparable. In the series PHF, the mean value in square slab panels is 13.7% lower than the mean value in prism specimens. While, in the series PHF46, the mean value in square slab panels is 6% lower than the mean value in prism specimens. It can be supposed that the shear stresses measured in the prism specimens represent the most critical situation, while the shear stresses measured in the square slab panels an elastic horizontal shear stress typical of actual structures.

4.5 In-situ load testing to evaluate UHPFRC overlay techniques

4.5.1 *Introduction*

Ultra-High Performance Fibre Reinforced Concrete (UHPFRC) overlay could be a possible strengthening technique for reducing the seismic vulnerability of masonry buildings. In the last years, experimental programs, supported by analytical and numerical studies, have investigated the feasibility and the effectiveness of fibre reinforced concrete diaphragms [Marini *et al.*, 2008; Zanotti *et al.*, 2009; Marini *et al.*, 2010; Naghibdehi *et al.*, 2014]. These researches demonstrated the efficiency of UHPFRC thin overlayer for strengthening RC slabs. The research showed that the repair techniques proposed can be considered as promising methods for restoring the flexural capacity of RC slabs. In the slabs repaired with UHPFRC overlayer, the stiffness was increased and the mid-span deflections at ultimate load decreased.

This section presents the results obtained from the in-situ load testing on a lightweight ribbed one-way reinforced concrete slab strengthened by means of UHPFRC overlay. In-situ load testing is a relevant procedure to evaluate the safety at serviceability limit states (SLS) of an existing concrete structure with respect to a particular load effect. The primary objective of in-situ load testing was to evaluate the strengthening technique, especially in terms of increase of stiffness and possible slip between substrate and overlay.

The considered structure was a residential building located in Piacenza (Italy). The structure, built in 1970s, is a two-story masonry building with a lightweight ribbed one-way reinforced concrete slab.

The test was conducted on the lightweight ribbed one-way reinforced concrete slab before and after the strengthening. Deflections and slip between the substrate and the overlay were measured at their critical locations during the loading and unloading cycles. The deflections measured on the strengthened floor during the load test were compared with the deflections measured on the reference lightweight ribbed one-way reinforced concrete slab.

The in-situ load testing was operated by University of Brescia.

4.5.2 *Case study*

4.5.2.1 Building geometries and material characterization

The building under investigation is a two-story residential building in Piacenza (Italy) built in 1970s.
A field investigation, based on visual inspection and the use of an electromagnetic rebar locator, showed that the reference slab was 160 mm thick and 4100 mm long. The longitudinal reinforcement consisted of three steel bars of 4 mm diameter located on the bottom of hollow bricks. The ultimate strength of steel bars was determined through the Rockwell hardness testing. The steel bars tested showed an average ultimate strength of f_u=555 N/mm^2. Prior to testing, the concrete properties were evaluated using the Turner-sclerometer in different locations. The average concrete cylinder strength measured was f'_c=16 N/mm^2. The mean secant elastic modulus (E_{cm}) of the concretes was calculated according the Eurocode 2 [2005] as $E_{cm}=22\cdot(f_{cm}/10)^{0.3}$. The value of mean secant elastic modulus found was E_{cm}=25.3 GPa.
Figure 4.5-1 schematizes the lightweight ribbed one-way reinforced concrete slab prior to the strengthening.

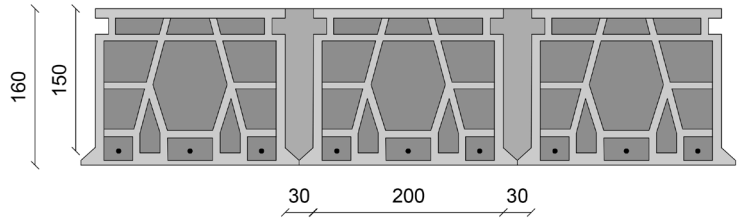

Figure 4.5-1: Lightweight ribbed one-way reinforced concrete slab representation.

4.5.3 *Structural analysis*

An elastic analysis was performed in order to determine the magnitude of the load to be applied to the slab. The objective was to find the service distributed load for which the slab was designed and then back calculate an equivalent point load. It was found that the distributed load for the slab was 2.13 kN/m, corresponding to a total concentrated load of 8.73 kN to be applied during the in-situ load test.

4.5.4 *Load test set up and instrumentations*

The load test was conducted using a concentrate load configuration. The load was applied in cement bags of 25 kg each in two points located at ¼ and ¾ of the span. The cement bags had a footprint of 0.65x0.85 m. Figure 4.5-2 illustrates the load configuration for the test.

Real-time measurement of structural response was achieved using seven comparator gauges all with an accuracy of 0.01 mm, used to measure deflection at chosen locations where maximum and critical displacements were expected. Three Metric Dial Indicators (MDI) were placed at midspan, where maximum deflections are expected; two MDI were placed under the loads and the two remaining were placed at supports.

Figure 4.5-3 shows the load test area and the on-site instrumentation.

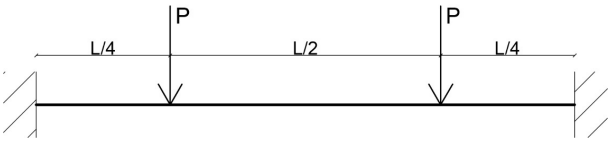

Figure 4.5-2: Test load configuration.

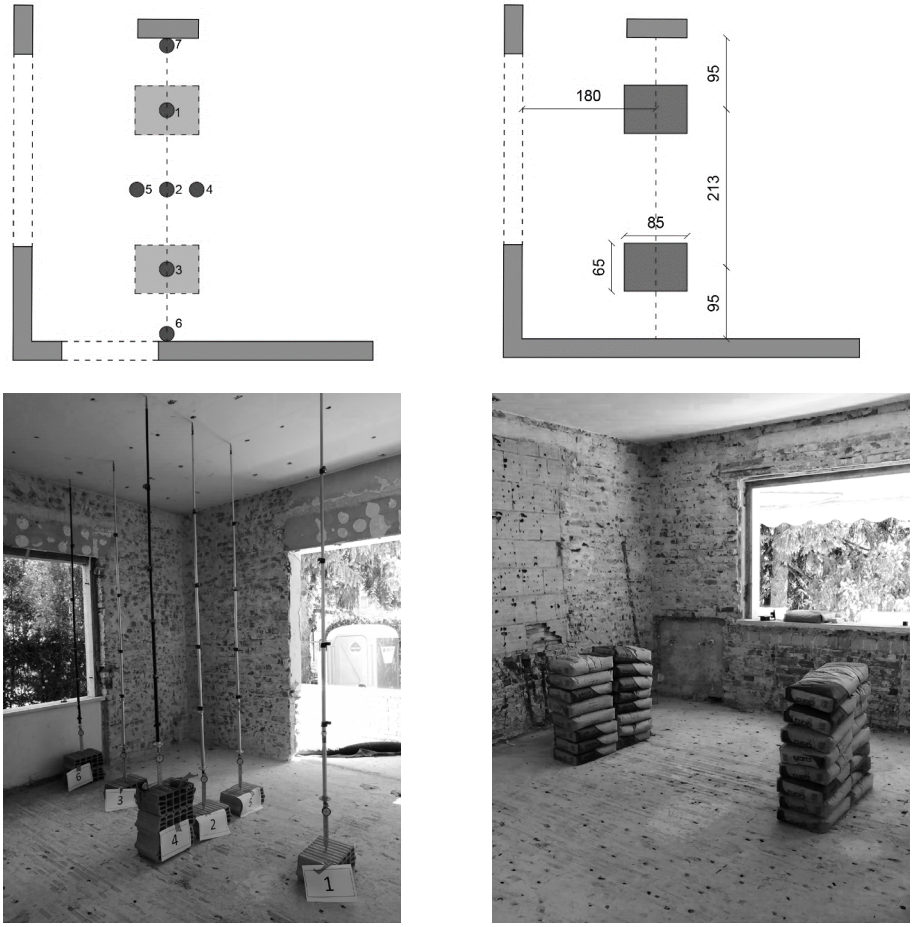

a) Level below the one to be tested *b) Level to be tested*

Figure 4.5-3: Load test area and on-site instrumentation.

4.5.5 *Load test results*

After recording initial readings from each instrument, the test load was applied in seven increments, and the deflections were recorded at the end of each load step. Once the maximum load was achieved, it was kept constant for fifteen minutes and measurements were repeated and recorded. The slab was then unloaded in four steps and the structure was inspected at each unload decrement. Fifteen minutes after complete unloading, the final response was recorded. In Figure 4.5-4, the maximum deflections obtained from test data are shown.

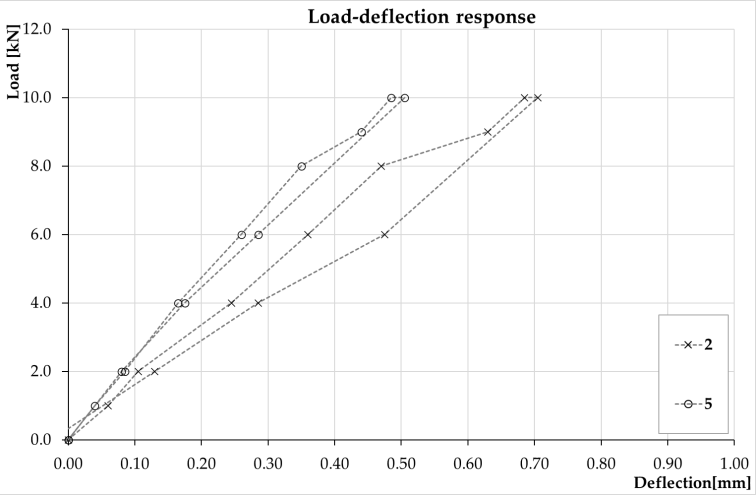

Load-central mid-span deflection response.

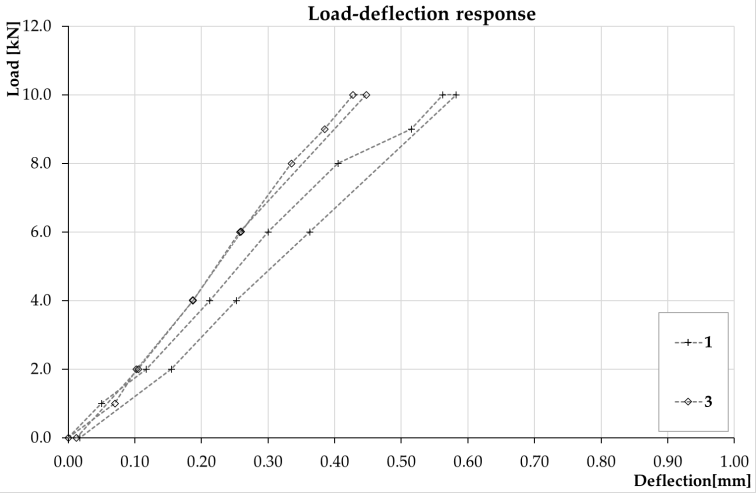

Load-deflection response at load points.

Figure 4.5-4: Load-deflection response.

The load in the graphs represents the total load applied by cement bags and distributed in two points. As indicated by the results above, the maximum load achieved (2P) was 10 kN (distributed in two point), and the maximum deflection, measured at the mid-span (point 2), was 0.71 mm. The MDI #4 did not record reliable results; for this reason the deflection is not reported.

4.5.6 *UHPFRC overlay strengthened*

The strengthening technique consisted in overlaying a thin UHPFRC slab. The material Planitop HPC Floor 46 (PHF46) was chosen to strengthen the lightweight ribbed one-way reinforced concrete slab. The thickness of overlay was 30 mm. The mechanical characterizations of PHF46 are presented in Chapter 3. The ratio of the concrete mean secant elastic modulus to the UHPFRC mean secant elastic modulus was 1.7. In the slabs repaired with UHPFRC overlay the stiffness was increased, and the moment of inertia of strengthened slab (J=8.66 10^3 cm^4) was 2.5 times compared to the moment of inertia of reference slab (J=3.49 10^3 cm^4).
Figure 4.5-5 schematizes the lightweight ribbed one-way reinforced concrete slab strengthened by means of UHPFRC overlayer.

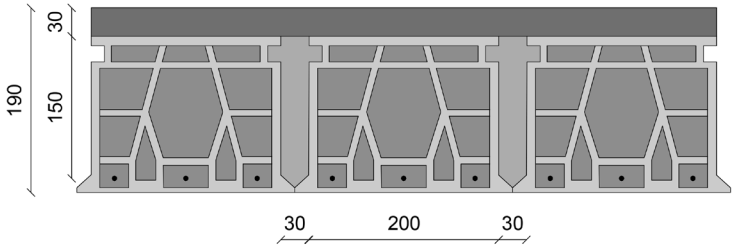

Figure 4.5-5: Lightweight ribbed one-way reinforced concrete slabs strengthened by means of UHPFRC overlay.

4.5.7 *Load test set up and instrumentations*

Subsequently to the strengthening by means of a UHPFRC overlay, a second load test was conducted. The second load test was performed at the same conditions as the previous one (see Figure 4.5-2).
The load test on the strengthened slab was conducted on a different slab compared to the reference one (as shown in Figure 4.5-6), even though identical in geometry and inertia properties, due to some difficulties in the constructions side.
Figure 4.5-7 shows the load test area and the on-site instrumentation.

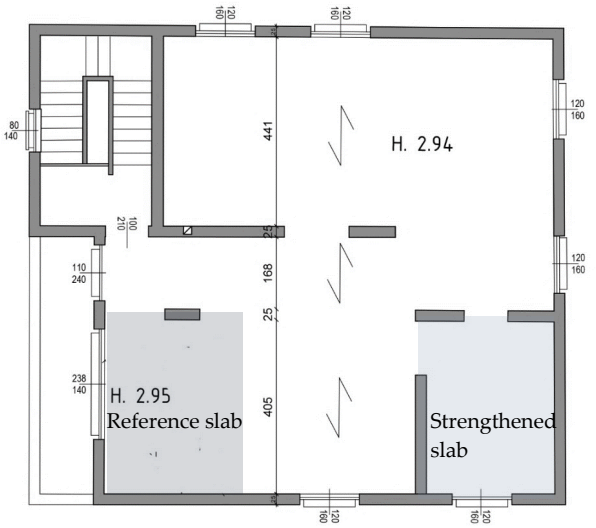

Figure 4.5-6: Plan view of first floor.

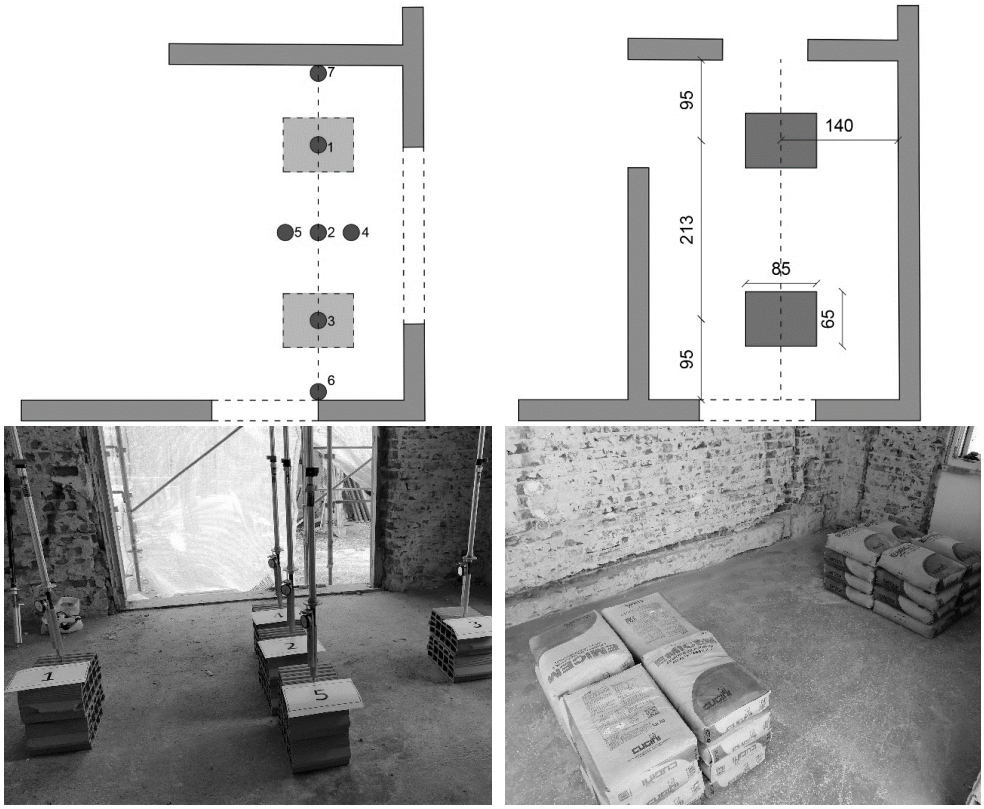

a) Level below the one to be tested *b) Level to be tested*

Figure 4.5-7: Load test area and on-site instrumentation.

Real-time measurement of structural response was achieved using seven comparator gauges all with an accuracy of 0.01 mm, used to measure deflection at chosen locations where maximum and critical displacements were expected. Three MDI were placed along the mid-span, where maximum deflections were expected, two MDI were placed under the loads, and the two remaining were placed close to the support. Moreover, two MDI with an accuracy of 0.001 mm were used to measure the slips between the substrate and the overlay.

4.5.8 *Load test results*

After recording initial readings from each instrument, the test load was applied in eight increments, and the deflections were recorded at the end of each load step. Once the maximum load was achieved, it was kept constant for fifteen minutes and measurements were recorded. The slab was then unloaded in six steps and the structure was inspected at each unloading decrement. Fifteen after complete unloading, the final response was recorded. The maximum deflections obtained from test data were shown in Figure 4.5-8. The load in the graphs represents the total load applied by cement bags and distributed in two points.

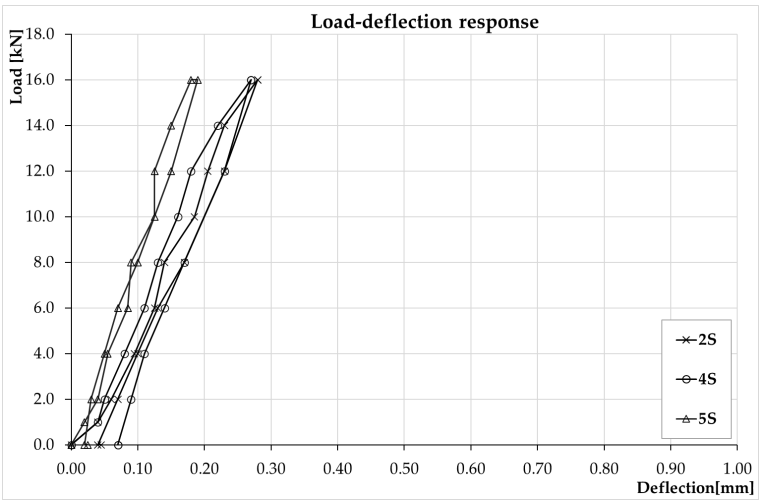

Load-central mid-span deflection response.

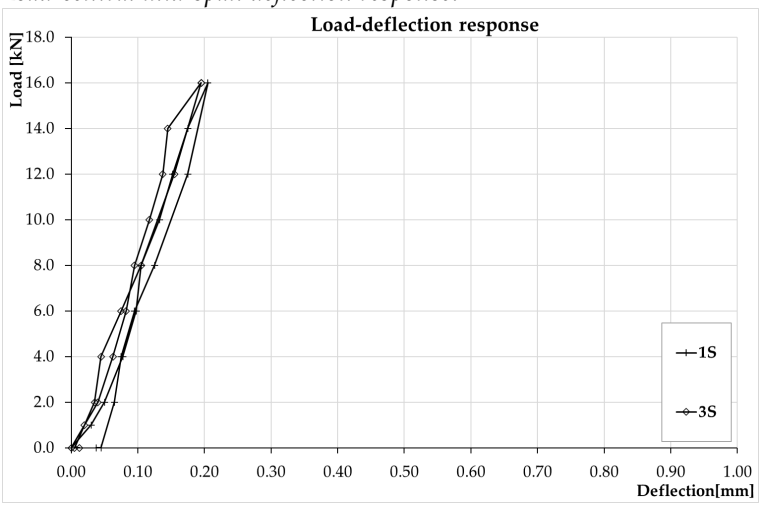

Load-deflection response at load points.
Figure 4.5-8: Load-deflection response.

As indicated by the results above, the maximum load (2P) achieved was 16 kN (distributed in two points), and the maximum deflection, measured at the mid-span (point 2), was 0.28 mm. Moreover, as shown in Figure 4.5-9, in the strengthened slab minor residual deformations were recorded: the measured maximum residual deflection was 0.07 mm at the point 4 at mid-span.
During the loading and unloading steps, the maximum slip recorded was 0.003 mm, clearly indicating that the slip between substrate and overlay is negligible.

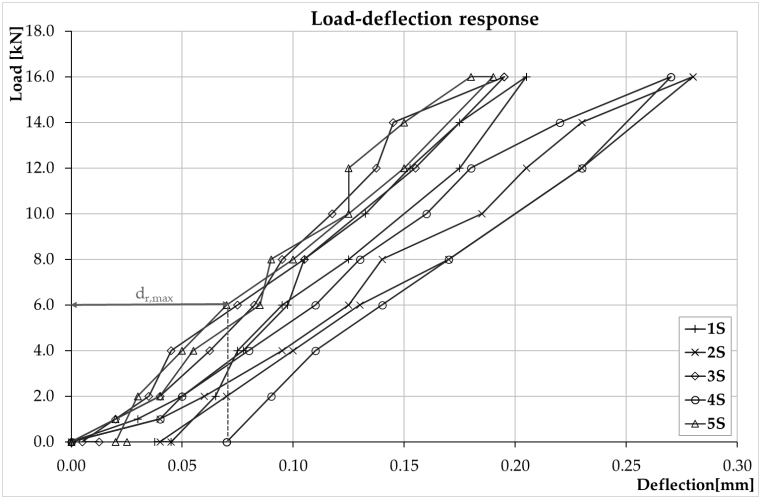

Figure 4.5-9: Measured maximum residual deflection in the load-deflection response.

4.5.9 *Shear stress*

The composite action between overlay and substrate depends on the shear stresses at their interface. The interface between the two different materials is a key factor in the success of repair and rehabilitation works. Good adhesion is importance for providing monolithic action in bonded concrete overlays. For this reason, the shear stress (τ) across an interface at the peak load was calculated in the strengthened slab. τ can be evaluated from the following relation:

$$\tau = \frac{V\,Q}{J_{tr} \cdot b} \qquad (4.5\text{-}1)$$

where:
V is the maximum shear force;
Q is the first moment of inertia at the interface;
b is the width;
J_{tr} is the moment of inertia from the transformed section.

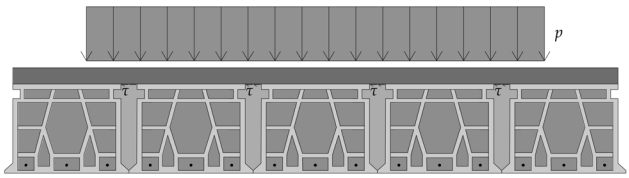

The load footprint interested four concrete joists; therefore, the shear stresses was evaluated considering a width equal to 120 mm (30 mm x 4 joists). The shear stress across the interface was 0.097 MPa. The shear stress was even lower than the shear stress recorded during the bending tests on the square slab panels.
Figure 4.5-10 shows the shear stress distribution in T section.

From the shear stress distribution, it can be noted that in the flange, the shear stress is distributed parabolically up to the neutral axis. While in the web, the shear stress is distributed uniformly.

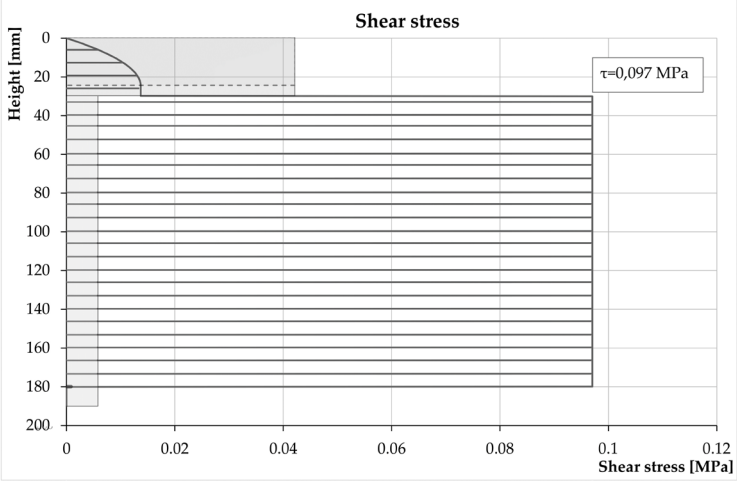

Figure 4.5-10: Shear stress distribution in T section.

4.5.10 *Concluding remarks*

Figure 4.5-11 shows a comparison between the load-deflection response before and after the UHPFRC strengthening. From the load-deflection response, it can be observed that there is an increase in stiffness and a decrease in mid-span deflection at ultimate load. In particular, the mean maximum deflection at midspan (mean values on MDI 2,4 and 5) turned out to be more than 3 times higher in the unstrengthened slab compared to that after intervention, similar to the ratio between the sectional inertia before and after the intervention (2.5).
From the test results reported herein, it can be concluded that:

- The deflections recorded in the strengthened slab were lower than those in reference slab.
- The slips between the substrate and the overlay recorded were negligible.
- The shear stress at the interface was not significant.
- The use of UHPFRC layers leads to a significant increase of stiffness of this lightweight ribbed slab.

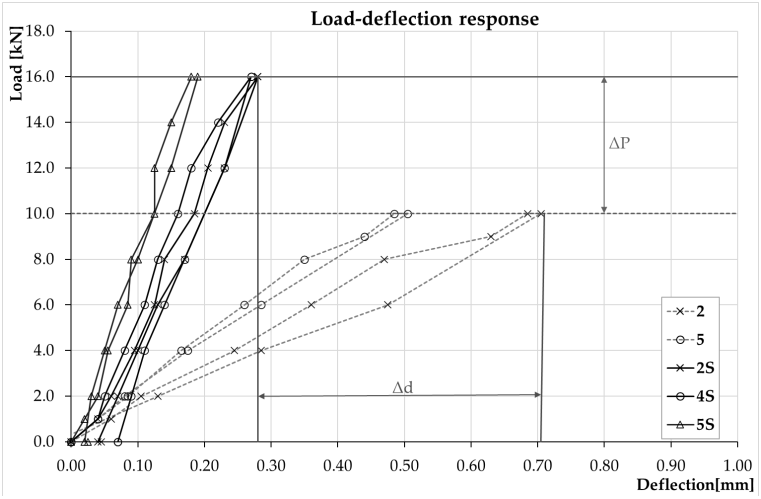

Load-central mid-span deflection response.

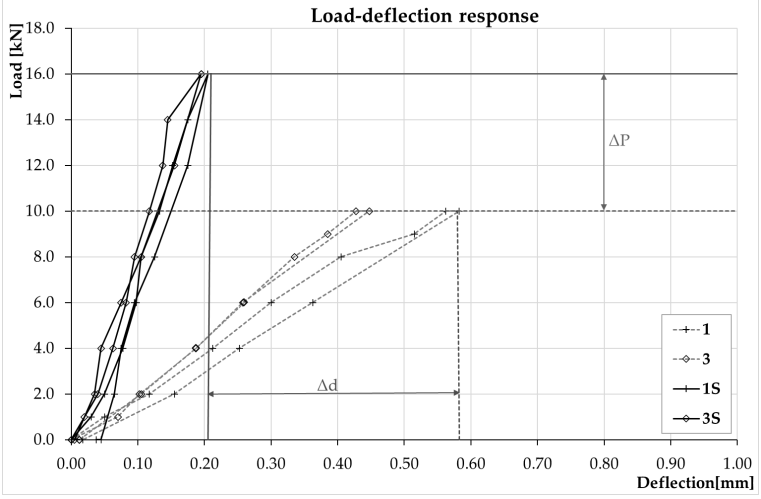

Load-deflection response at load points.

Figure 4.5-11: Comparison between the load-deflection response before and after the strengthening technique.

4.6 References

EN 1992-1-1: *Eurocode 2. 2005. Design of concrete structures. Part 1–1: General rules and rules for buildings.*

FÉDÉRATION INTERNATIONALE DU BÉTON (FIB)*. 2013. Model Code 2010 for concrete structures (MC2010), International Federation for Structural Concrete, Lausanne, Switzerland.*

MARINI, A., ZANOTTI, C., & PLIZZARI, G.*, 2008, September. "Seismic strengthening of existing structures by means of fibre reinforced concrete floor diaphragms", in BEFIB 2008: 7th RILEM International Symposium on Fibre Reinforced Concrete (pp. 977-987). RILEM Publications SARL.*

NAGHIBDEHI, M. G., SHARBATDAR, M. K., & MASTALI, M.*, 2014. "Repairing reinforced concrete slabs using composite layers", Materials & Design, 58, 136-144.*

UNI EN 12390-3*, 2003. "Testing hardened concrete—Compressive strength of test specimens", European Standard.*

UNI EN 14651*, 2007. "Precast concrete products – test method for metallic fibre concrete – Measuring the flexural tensile strength", European Standard.*

ZANOTTI, C., MARINI, A., & PLIZZARI, G. A.*, 2009. "Nonlinear FE analysis of fiber reinforced concrete floor diaphragms undergoing horizontal seismic actions", in Protection of Historical Buildings: Proceedings of the International Conference on Protection of Historical Buildings, PROHITECH 09, Rome, Italy, 21-24 june 2009: PROHITECH 09 (pp. 1089-1094).*

5 FINITE ELEMENT ANALYSES

The behaviour of Ultra-High Performance Fibre Reinforced Concrete (UHPFRC) composite elements is still today an area that needs further studies to establish design and analysis methods. Aiming at that, numerical analyses could represent an alternative way for studying the response of an ample range of structural elements, once the model is verified through limited experimental tests.
This chapter presents nonlinear finite element analyses that were carried out on:

- square slab panels strengthened with UHPFRC (experiments contained in Chapter 4);
- RC beams (parametric study);
- existing prestressed concrete beam.

Numerical analyses were performed adopting a 2D plane stress finite element (FE) model based on the Modified Compression Field Theory (MCFT) [Vecchio and Collins, 1986] and the Disturbed Stress Field Model (DSFM) [Vecchio, 2000]. The analyses were carried out with the 2017 version of VecTor2. The models were constructed with VecTor2's pre-processor software, FormWorks 4.2 [2017]. The results were processed and visualized using post-processor Augustus [Bentz, 2013].

5.1 Numerical analyses of square slab panels

5.1.1 *Introduction*

Finite element (FE) analyses were conducted to investigate the behaviour of the square slab panels strengthened with UHPFRC.
The square slab panels were tested at the University of Brescia and the collected results are presented in Chapter 4. The experimental and analysis results are compared and described in the following paragraphs.

5.1.2 *Numerical modelling of the square slab panels*

The square slab panels consisted of a layer of existing reinforced concrete (substrate) and a new layer of UHPFRC (overlay). The square slab panels were modelled as two series depending on the overlay reinforcement: series PHF and series PHF46. Moreover, the reference square slab panel in RC was also modelled. The panels had dimension of 1050 x 1050 mm. The thickness of the substrate was 80 mm, and that of the overlay was 40 mm. The substrate was reinforced with a steel mesh, which was composed of 8 mm diameter deformed bars assembled with a spacing of 100 mm. The elements were subjected to a monotonically-increasing load.

In VecTor2, the square slab panels were modelled using rectangular concrete elements, truss elements, and link elements. Due to the symmetry of the square slab panels and the loading scheme, only half of each slab was modelled.
The square slab panels were restrained in the x- and y-directions at the nodal supports. Moreover, the elements were restrained against movement in the x-direction at the mid-span cross-section (plane of symmetry). Refer to Figure 5.1-1 and Figure 5.1-2.
The square slab panels were loaded in bending, with the load applied as a monotonically increasing displacement at the mid-span of the element. The analysis was conducted in displacement-control with an increment step size of 0.1 mm. The load was transferred to the top surface of the element by a steel plate (same material and dimensions as used for the supports). Figure 5.1-2 and Figure 5.1-1 illustrate the finite element model.

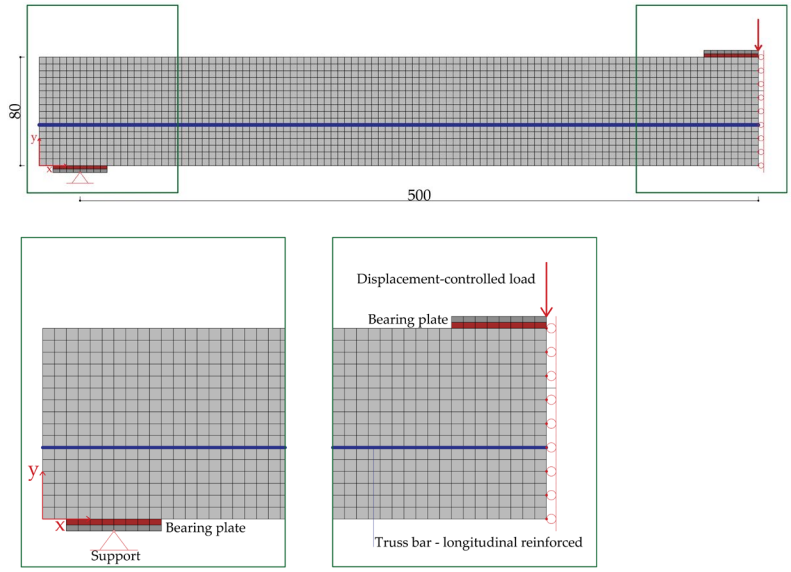

Figure 5.1-1: Finite element modelling of the reference square slab panel.

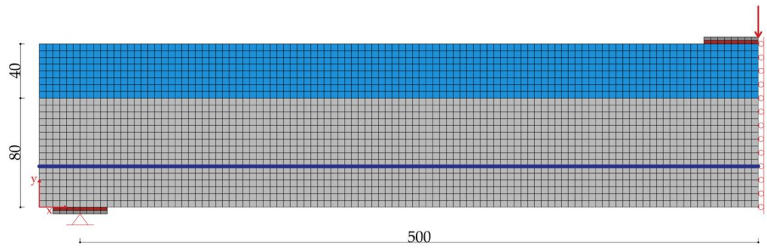

Figure 5.1-2: Finite element modelling of the strengthened square slab panel.

With UHPFRC materials in VecTor2, fibres are input as a smeared reinforcement. The reference type was discrete steel fibre in the reinforcement component of the reinforced concrete. The inputs required for the fibre reinforcement definition are the fibre type, the fibre volume fraction (V_f), the length and the diameter of the fibres (L_f and D_f), the ultimate tensile strength of the fibres (F_u), and the average interfacial bond strength between the fibre and the concrete matrix (T_u). Moreover, the residual flexural strength (f_1* and f_3*) are required for MC 2010 option only. If the average interfacial bond strength input is set equal to zero, the VecTor2 default value will be used. For hooked-end fibres, Voo and Foster [2003] suggested that it should be evaluated as $\tau_u=2.5\ f_{ct}$, with f_{ct} being the tensile strength of the plain concrete in MPa. The UHPFRC properties specified were the tensile strength, f_t', the initial tangent modulus, E_c, and the density, as measured from the experiment data (Section 3.2, Section 3.3, and Section 5.2). The concrete property specified was the concrete compression strength, calculated as 83% of R_{cm}. Table 5.1-1 shows the default VecTor2 relationship and values for the concrete properties.

Concrete Properties			
Thickness (mm)	required input	**C_c (/°C)**	10×10^{-6} †
f_c' (MPa)	required input	**Max. agg. size (mm)**	10
f_t' (MPa)	$0.33\sqrt{f'_c}$ †	**Density (kg/m³)**	2400 †
E_c (MPa)	$3320\sqrt{f'_c}+6900$ †	**K*c* (mm²/s)**	1.2 †
ε_o (mm/m)	$1.8 + 0.0075\ f'_c$ †	**S*x* (mm)**	input
μ	0.15 †	**S_y (mm)**	input

Note: The program limits to 5000 mm the spacing of cracks parallel to the Y axis, S_x and parallel to the X axis, S_y. The crack spacing is calculated based on the CSA A23. 3-14 [2014].
†Default properties assumed by VecTor2 unless otherwise specified.
Table 5.1-1: Material properties.

Table 5.1-2 lists the concrete and fibre properties.

	f_c [MPa]	**E_c [MPa]**	**Density [kg/m³]**	**Fibre type**	**V_f [%]**	**L_f [mm]**	**D_f [mm]**	**F_u [MPa]**	***f_1*[1] [MPa]**	***f_3*[1] [MPa]**
C16/20	20	21750	2400	-	0	-	-	-	0.1	0
PHF	98	43600	1400	Hooked	0.96	30	0.38	3070	4.72	2.83
PHF46	92	42800	1400	Hooked	0.96	30	0.38	3070	4.74	2.99

[1]Residual flexural strengths, f_1 and f_3*, were calculated through the method showed in Appendix B.*
Table 5.1-2: Concrete and fibre properties used in VecTor2.

Longitudinal reinforcement in the x-direction was modelled using discrete truss elements. Additionally, reinforcement in the z-direction (i.e., out-of-plane direction in the 2D model) was modelled as smeared reinforcement embedded within the concrete element.
Table 5.1-3 gives the properties of the ductile steel reinforcement.

	x-direction	z-direction
Cross section area [mm²]	500	-
Reinforcement ratio [%]	-	0.55
Reinforcement diameter [mm]	8	8
Yield strength [MPa]	480	480
Ultimate strength [MPa]	600	600
Elastic modulus [MPa]	210000	210000

Table 5.1-3: Reinforcement properties used in VecTor2.

The interface between the substrate concrete and overlay was modelled in two ways: (1) assuming perfect bond conditions, and (2) using bond elements.
In VecTor2, there are two types of bond elements available: link elements and contact elements. The latter can be used to model bond behaviour across composite surfaces [Ma, 2016]. The interface or bonded plates/fabrics reference type was chosen.
Figure 5.1-3 illustrates the interface element between the two materials: RC concrete and UHPFRC.

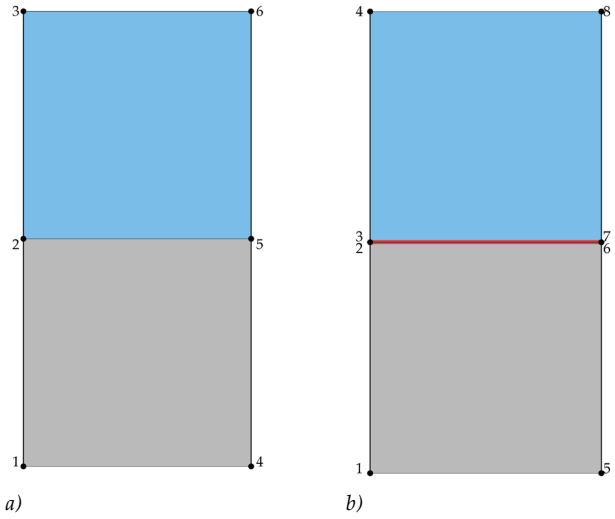

Figure 5.1-3: Bond conditions assumed in VecTor2: a) perfect bond conditions, b) interface bond elements.

The stress-slip relationship was obtained by a shear bond test. The shear stresses and slips measured by the bond tests were presented in Section 4.2. As observed in Section 4.4, the shear stresses in the slabs were lower than those in the prism specimens. In fact, the shear stresses measured in the square slab panels represent only the initial plastic part the first growth of the shear stresses recorded in the prism specimens. Thus, the stress-slip relationship used in VecTor2 corresponds to the shear stresses and slips measured by the bond tests in the range 0-0.01 mm.

It was observed that in this range the correlation between shear stress and slip was not dependent on the roughness indexes. Therefore, one bond type was used for both series. The bonded surface area was 1050000 mm²/m.
The abbreviations denoted below are used in the description of the finite analysis elements:

- S0: reference square slab panel in RC;
- S-PB: square slab panels with perfect bond conditions;
- S-IE: square slab panels with interface elements.

Figure 5.1-4 and Figure 5.1-5 show the stress-slip relationship measured by the bond tests in the range 0-0.01 mm.

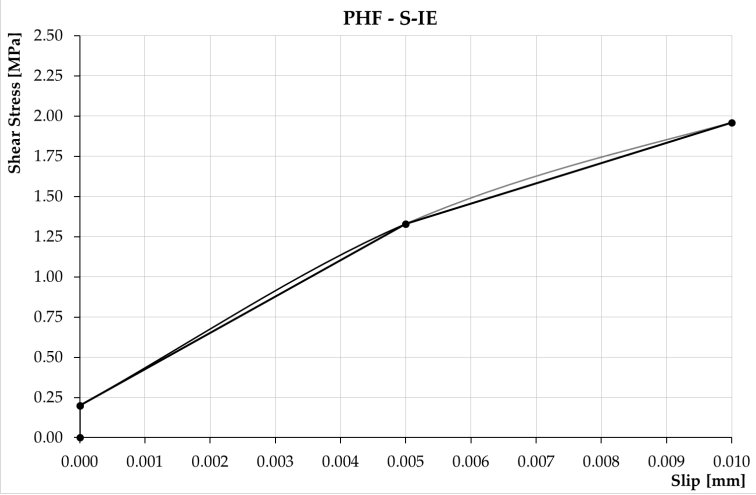

Figure 5.1-4: Shear stress vs. interface slip curve for PHF series.

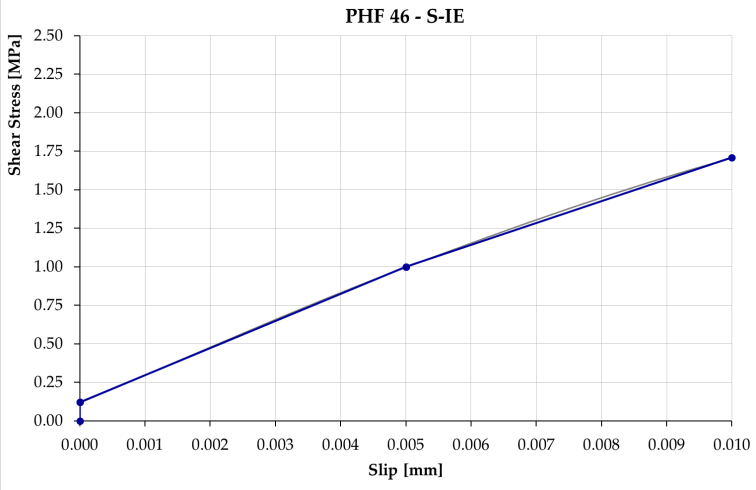

Figure 5.1-5: Shear stress vs. interface slip curve for PHF46 series.

Table 5.1-4 reports the bond stress-slip curve reference points for series PHF and series PHF46, respectively.

	U_1 [MPa]	U_2 [MPa]	U_3 [MPa]	s_1 [mm]	s_2 [mm]	s_3 [mm]
PHF	0.20	1.33	1.96	0.00	0.005	0.01
PHF46	0.12	1.00	1.71	0.00	0.005	0.01

Table 5.1-4: Bond stress-slip curve reference points.

The constitutive models used in the finite element analysis were the default models in VecTor2. In VecTor2, the default model for FRC in tension is the Simplified Diverse Embedment Model (SDEM) [Lee et al., 2012]. For monotonic loading conditions, in the SDEM, the tensile stress in the fibres is expressed by the frictional bond behaviour in straight fibres and the additional mechanical anchorage in hooked-end fibres. The Variable Engagement Model (VEM) [Voo and Foster 2003] was used. In the Variable Engagement Model, the crack opening displacement is calculated and the force in a single steel fibre is expressed. For mechanically anchored fibres, once the adhesive between the concrete and fibre is broken, slip must occur before anchorage is engaged. In addition, the *fib* Model Code 2010 [2013] was used to compare the responses obtained by two different FRC tension models. The *fib* Model Code formulation for FRC in tension is based on the bending test results.
The identification of the tensile behaviour of UHPFRC materials used was carried out according to the European Standard EN 14651 [2007] (refer to Section 2.1). The European Standard is based on fracture mechanics Crack Mouth Opening Displacement (CMOD) controlled tests on notched beams (150x150x600 mm) loaded with a three-point system. The tensile behaviour of fibre reinforced concrete is evaluated in terms of residual flexural tensile strength values determined from *load vs. deformation* curve obtained by applying a centre point load. The three-point bending test (3PBT) for evaluation of the tensile behaviour of fibre reinforced concrete was carry out at the Laboratory "Pietro Pisa" of the University of Brescia. The experimental results were collected in Section 3.3.
In order to find a *stress-crack* opening constitutive relationship after cracking, numerical analyses were performed using the finite element program DIANA 10.1 [2016], which is based on a discrete crack approach.
Figure 5.1-6 illustrates the numerical response of the 3PBT obtained by calibrating suitable σ-w law. It can be noted that the numerical response is in close agreement with the experimental results.

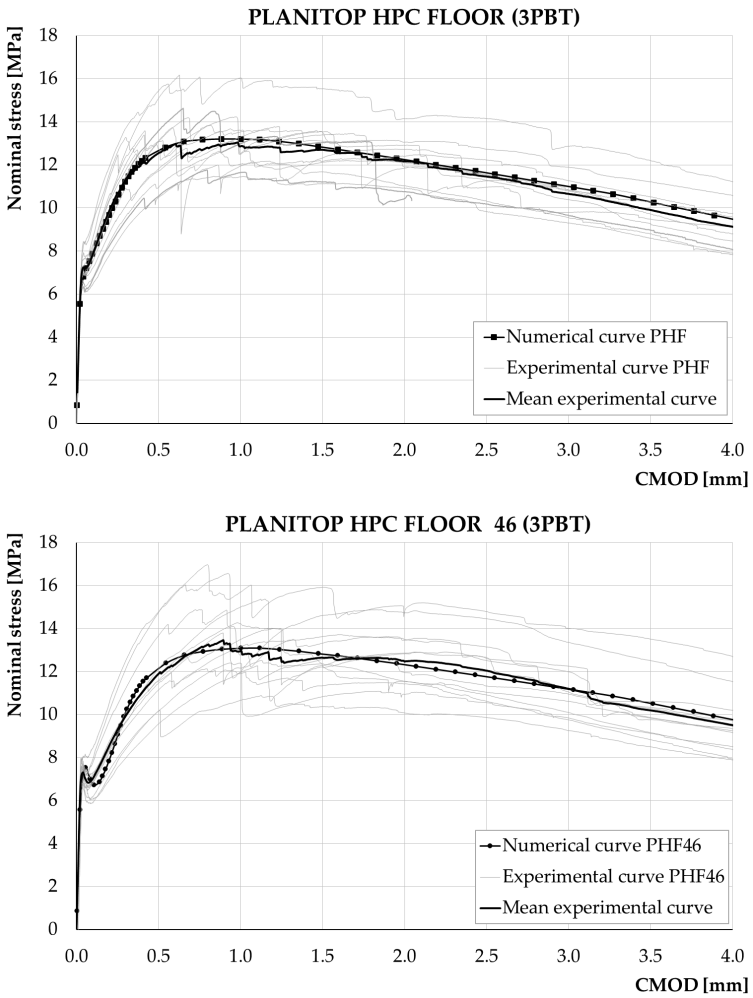

Figure 5.1-6: Experimental and numerical 3PBT on PHF beams and on PHF46 beams.

The *stress-crack width* relationship, reported in Figure 5.1-7, was incorporated in the code of VecTor2 and used to performed the FRC materials as showed in Appendix B. Table 5.1-5 lists the *σ-w* incorporated into the crack-based custom tension softening model.

PHF		**PHF46**	
Crack width [mm]	**Stress [MPa]**	**Crack width [mm]**	**Stress [MPa]**
0	5	0	5
0.02	3	0.05	1.8
0.2	5	0.2	5
5.5	0	5.8	0

Table 5.1-5: Stress-crack width relationships for PHF and PHF46

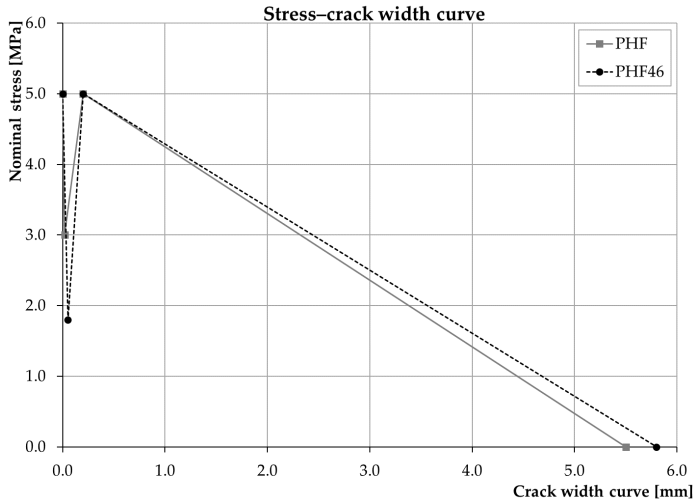

Figure 5.1-7: Constitutive stress-crack width tension softening laws adopted for FRC.

For the *fib* Model Code 2010 option, VecTor2 input request the residual flexural strength f_1* and f_3* also for plain concrete. Therefore, a second reinforcement component was added to RC substrate. The fibre volume fraction inputted was equal to 0.001%, and the residual flexural strength f_1* and f_3* represented the response of plain concrete. Table 5.1-6 lists the concrete and reinforcement constitutive models used in VecTor2.

Concrete Models			
Compression Pre-Peak	Hoshikuma et al. (parabola) †	**Dilation**	Variable – isotropic †
Compression Post-Peak	Modified Park-Kent †	**Cracking Criterion**	Mohr – Coulomb (stress) †
Compression Softening	Vecchio 1992-A †	**Crack Stress Calculation**	Basic (DSFM/MCFT) †
Tension Stiffening	Modified Bentz 2003 †	**Crack Width Check**	Agg/2.5 max crack width †
Tension Softening	Nonlinear (Hordijk) †	**Crack-Slip Calculation**	Walraven †
FRC Tension	VEM (Voo and Foster 2003)/ *fib* Model Code 2010	**Creep and Relaxation**	Not considered †
Confined Strength	Kupfer / Richart †	**Hysteretic Response**	Nonlinear w/ Plastic offsets †
Reinforcement Models			
Hysteretic Response	Bauschinger Effect (Seckin) †	**Buckling**	Akkaya 2012 †
Dowel Effect	Tassios (Crack Slip) †	**Concrete Bond**	Eligehausen †

†*Default models assumed by VecTor2 unless specified otherwise.*

Table 5.1-6: Concrete and reinforcement constitutive model used in VecTor2.

5.1.3 *Comparison of numerical and experimental results*

The finite element analysis results for square slab panels are reported and described in this section. Moreover, the experimental and analysis responses are compared.
The finite element analyses of the fibre reinforced concrete square slab panels were conducted using two methods to incorporate the fibres in the analyses: (1) VEM - Voo and Foster 2003 FRC tension model and (2) *fib* Model Code 2010 FRC tension model.

5.1.3.1 PHF (VEM - Voo and Foster 2003 FRC tension model)

Figure 5.1-8 shows the *load vs. net mid-span deflection* curves for square slab panels S-PB and S-IE obtained from VecTor2, and from the experimental program. The FE analyses were conducted using VEM - Voo and Foster 2003 FRC tension model. Figure 5.1-9 reports the finite element analyses results of the square slab panel for PHF series compared to reference square slab panel in RC.
Table 5.1-7 summarizes and compares the experimental and FE analysis results.

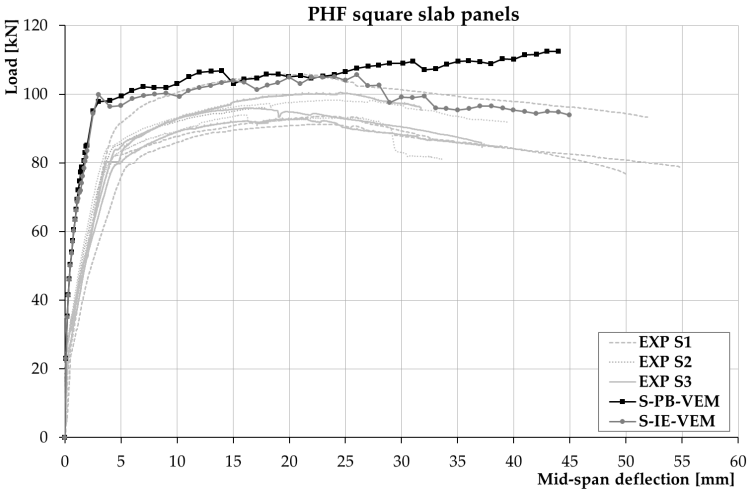

Figure 5.1-8: Comparison between FE analysis (VEM - Voo and Foster 2003) and experimental data for PHF series.

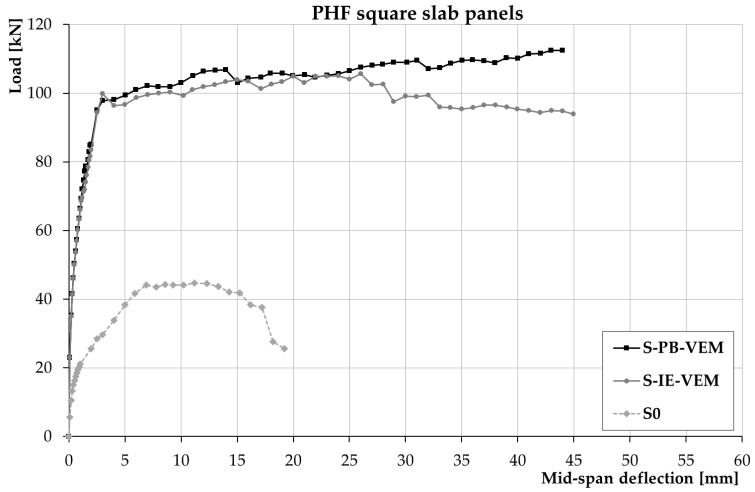

Figure 5.1-9: FE analysis results of the square slab panel for PHF series.

PANEL ID	Peak load [kN]	Displ. at peak load [mm]	Displ. at failure load [mm]	Shear stress at peak load[1] [MPa]
S0	45.0	11.6	19.2	0.38
EXP S1	96.9 [91.3-105.8] (0.08)	22.6 [20.7-23.1] (0.08)	52.4 [50.1-54.8] (0.05)	0.51
EXP S2	97.2 [95.0-98.3] (0.01)	20.3 [16.7-24.3] (0.22)	30.4 [17.8-39.5] (0.37)	0.51
EXP S3	96.4 [93.1-100.5] (0.04)	20.2 [16.1-21.2] (0.19)	36.0 [31.8-39.0] (0.10)	0.51
S-PB	112.5	44.0	44.0	0.60
S-IE	105.6	26.0	45.0	0.58
S-PB/ EXP S1	1.16	1.95	0.84	1.18
S-PB/ EXP S2	1.16	2.16	1.45	1.18
S-PB/ EXP S3	1.17	2.18	1.22	1.18
S-IE/ EXP S1	1.09	1.15	0.86	1.14
S-IE/ EXP S2	1.09	1.28	1.48	1.14
S-IE/ EXP S3	1.10	1.29	1.25	1.14

[min-max] minimum and maximum values are reported in square brackets
(CV%) Coefficient of Variation reported in round brackets
[1]Experimental shear stress was calculated with the following equation: $\tau_a = P/2bd$
Table 5.1-7: Summary of the FE analysis results of the square slab panel for PHF series.

Based on Figure 5.1-9 and on Table 5.1-7, it is evident that the application of a UHPFRC layer remarkably increased the maximum load (2.5 times for S-PB and 2.35 times for S-IE). The stiffness of the composite square slab panels was significantly increased compared to the original RC elements. Moreover, the additional UHPFRC

overlay increased the mid-span deflection: the maximum displacement was doubled for the strengthened square slab panels. The reference square slab panel in RC failed due to the crushing of concrete. As indicated by the results above, the perfect bond condition and the interface contact element produced a slightly different response.

With perfect bond conditions (S-PB) the calculated maximum load of 112.5 kN was 17% higher than the test values. The ratios of the predicted peak load to the peak load obtained from the experiments were 1.16 for S-PB/ EXP S1 and S-PB/ EXP S2, and 1.17 for S-PB/ EXP S3. The mid-span deflection corresponding to the peak load was twice as large as the experimental values. The ratios of the S-PB-predicted displacement to the displacement at the peak load obtained from the tests were 1.95 for square slab panel S1, 2.16 for S2, and 2.18 for S3. Nevertheless, the deformation capacity of the FE square slab panel was in close agreement with the experimental results, especially for the S1 specimens (16% lower than the test values). Instead, the deformation capacity in square slab panels S2 and S3 was 45% and 22% higher than average experimental values. The average ratio of the predicted shear strength to the shear strength obtained from the experiments was 1.18. It is noteworthy to state that the ratio between the predicted and the experimental values of the peak force and the shear stress are different from each other; indeed, the numerical calculation of the shear stress (VecTor2) is more refined with respect to the analytical prediction (τ_a= P/2bd).

For the S-IE model, the peak loads obtained from the VecTor2 analyses were within 10% of the average experimental values. The ratios of the predicted peak load to the peak load obtained from the experiments were 1.09 for S-IE/ EXP S1 and S-IE/ EXP S2, and 1.10 for S-IE/ EXP S3. The corresponding mid-span deflection was 29% larger than experimental result. The ratios of the S-IE-predicted displacement to the displacement at the failure load obtained from the tests were 0.86 for square slab panel S1, 1.48 for S2, and 1.25 for S3. The average ratio of the predicted shear strength to the shear strength obtained from the experiments was 1.14.

For both sets of analyses, VecTor2 predicted the same failure, i.e. crushing of concrete with yielding of the longitudinal reinforcement, in accordance to with observed in the experiment tests. Indeed, the concrete principal compressive stress and the x-direction reinforcement stress obtained from VecTor2 analyses were above their maximum strength values as in the experimental tests. This confirmed that both the concrete crushing and longitudinal reinforcement yielding occurred. However, the FE analyses indicated that the peak load and the shear stress were higher than the experimental results. The VecTor2 analyses showed that the initial post-cracked stiffness was significantly higher than the corresponding experimental response. Therefore, the VecTor2 model was not able to accurately predict the pre-peak behaviour of the square slab panels tested. This could be caused by the assumption that the square slab panels were not subjected to shrinkage in the overlay. In fact, in differently aged concrete, the differential shrinkage creates tensile stresses that may

be induced in the concrete. These stresses could cause cracking, which affects the post-cracked stiffness. Nevertheless, as observed from Figure 5.1-8, S-IE produced a reasonable predicted response with the peak load of 102.6 kN – 10% higher than test values. On the other hand, the perfect bond conditions over-estimated the maximum load by 17%, with a corresponding mid-span deflection 2.1% larger than the experimental values.

5.1.3.2 PHF (fib Model Code 2010 FRC tension model)

Figure 5.1-10 illustrates the finite element analysis results for square slab panels S-PB and S-IE obtained from VecTor2, and from the experimental results. The FE analyses were conducted using the *fib* Model Code 2010 FRC option to model the FRC tension behaviour.

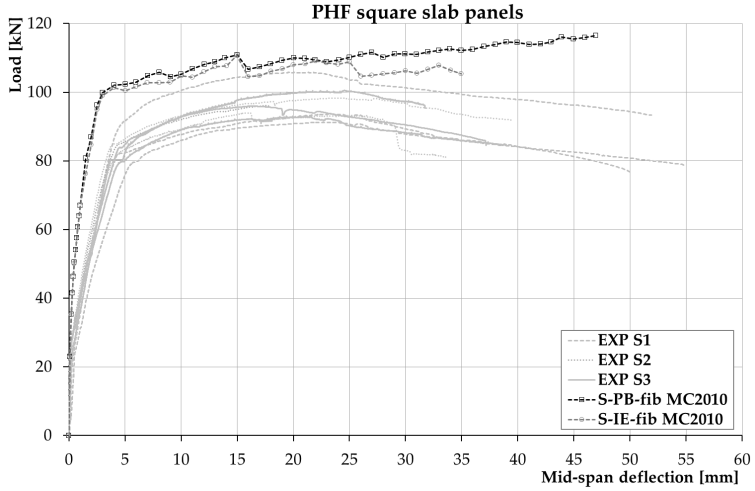

Figure 5.1-10: Comparison between FE analysis (fib MC 2010) and experimental data for PHF series.

As indicated by the results above, the VecTor2 analysis with the *fib* Model Code 2010 FRC tension model predicted a good behaviour of the square slab panels, especially for the interface contact element conditions (S-IE). In fact, the results above show that the perfect bond condition and the interface contact element produced a different response. With perfect bond conditions, the maximum load obtained from the VecTor2 analyses was 116.5 kN. It was 20% higher than the average experimental values. The ratios of the predicted peak load to the peak load obtained from the experiments were 1.20 for S-PB/ EXP S1 and S-PB/ EXP S2, and 1.21 for S-PB/ EXP S3. The mid-span deflection at the peak load was not in agreement with the experimental results. The ratios of the S-PB-predicted displacement to the displacement at the peak load obtained from the tests were 2.08 for square slab panel S1, 2.31 for S2, and 2.32

for S3. Nevertheless, for the square slab panel S1 the deformation capacity was predicted correctly (10%). While, for the square slab panels S2 and S3 the deformation capacity was over-estimated (55% and 30% respectively). The average ratio of the predicted shear strength to the shear strength obtained from the experiments was 1.18. In the S-IE analyses, the calculated maximum load of 110.8 kN was 21% higher than the average experimental values. The ratios of the predicted peak load to the peak load obtained from the experiments were 1.20 for S-PB/ EXP S1 and S-PB/ EXP S2, and 1.21 for S-PB/ EXP S3. The mid-span deflection corresponding at the peak load was in close agreement with the experimental values. Moreover, the deformation capacity of the FE square slab panel was generally within 15% of the experimental data. The prediction was particularly good for square slab panel S3 (0.97 S-IE/EXP S3). For square slab panels S1, the predicted deformation was 34% lower than that obtained from the tests. For the S3, the predicted mid-span deflection at failure was 15% greater than that obtained from the experiment tests. The average ratio of the predicted shear strength to the shear strength obtained from the experiments was 1.18. As observed for FE analysis results of the square slab panels obtained using VEM FRC tension model, the initial post-cracked stiffness was higher than the corresponding experimental one. Also in this case, this could be caused by the assumption that the UHPFRC overlay were not subjected to concrete shrinkage. Table 5.1-8 lists and compares the experimental and FE analysis results.

PANEL ID	Peak load [kN]	Displ. at peak load[mm]	Displ. at failure load[mm]	Shear stress at peak load[1] [MPa]
S0	45.0	11.6	19.2	0.38
EXP S1	96.9 [91.3-105.8] (0.08)	22.6 [20.7-23.1] (0.08)	52.4 [50.1-54.8] (0.05)	0.51
EXP S2	97.2 [95.0-98.3] (0.01)	20.3 [16.7-24.3] (0.22)	30.4 [17.8-39.5] (0.37)	0.51
EXP S3	96.4 [93.1-100.5] (0.04)	20.2 [16.1-21.2] (0.19)	36.0 [31.8-39.0] (0.10)	0.51
S-PB	116.5	47.0	47	0.61
S-IE	110.8	15.0	34.9	0.61
S-PB/ EXP S1	1.20	2.08	0.90	1.20
S-PB/ EXP S2	1.20	2.31	1.55	1.20
S-PB/ EXP S3	1.21	2.32	1.30	1.20
S-IE/ EXP S1	1.14	0.66	0.66	1.20
S-IE/ EXP S2	1.14	0.74	1.15	1.20
S-IE/ EXP S3	1.15	0.74	0.97	1.20

[min-max] minimum and maximum values are reported in square brackets
(CV%) Coefficient of Variation reported in round brackets
[1]Experimental shear stress was calculated with the following equation: $\tau_u = P/2bd$
Table 5.1-8: Summary of the FE analysis results of the square slab panel for PHF series.

Figure 5.1-11 compares the FE analysis results of the square slab panel obtained by VecTor2 using the two methods: VEM - Voo and Foster 2003 FRC tension model and *fib* Model Code 2010 FRC tension model.

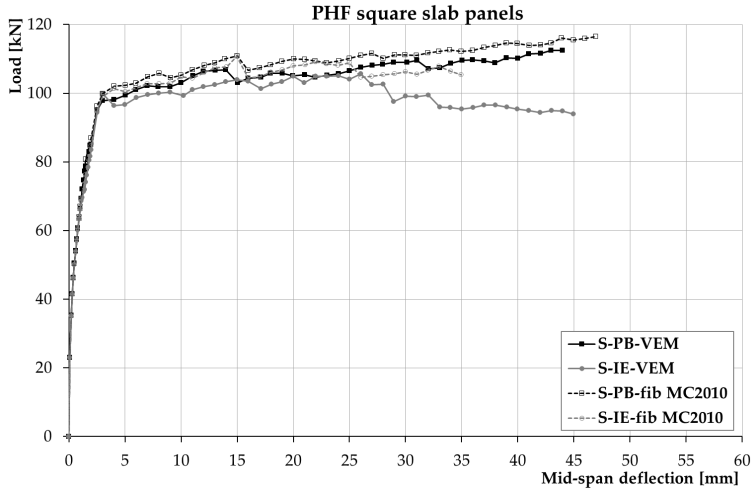

Figure 5.1-11: FE analysis results of the square slab panel for PHF series.

Large discrepancies were not encountered between the responses obtained from VecTor2 using the VEM - Voo and Foster 2003 FRC tension model, and the response obtained using the *fib* Model Code 2010 FRC tension model. The use of *fib* Model Code 2010 to model the FRC tension gave a higher response than that obtained from the VEM - Voo and Foster 2003 FRC model.

With perfect bond conditions, the peak load was higher than both the experimental responses (21%) and FE response obtained using the VEM - Voo and Foster 2003 (3%). Also for S-IE, the peak load was greater than both the experimental responses (15%) and FE response obtained using the VEM - Voo and Foster 2003 (5%). The FE analysis conducted using VEM – Voo and Foster (2003) in square slab panels S2 and S3 over-estimated the deformation capacity. The predicted mid-span deflection at failure was generally 15-25% stronger than those obtained from the experiments. For square slab panel S1, the deformation capacity was under-estimated, both in S-PB and S-IE (6% and 4% respectively). To the contrary, the deformation capacity obtained using *fib* Model Code 2010 was more in agreement with the tests compared to the responses obtained using the VEM - Voo and Foster 2003 option. The prediction was particularly good for S-IE model. From a comparison between the responses obtained using *fib* Model Code 2010 and VEM - Voo and Foster 2003 to model FRC tension, it can be noted that the pre-peak behaviour is the same for the two methods. Moreover, the perfect bond conditions over-estimated the response in both methods. The curve obtained from S-IE using VEM - Voo and Foster 2003 to model FRC tension was the response that was in better agreement with the experimental results.

5.1.3.3 PHF46 (VEM - Voo and Foster 2003 FRC tension model)

Figure 5.1-12 shows the *load vs. net mid-span deflection* responses for square slab panels S-PB and S-IE obtained from VecTor2 and from the experimental program. The FE analyses were conducted using VEM - Voo and Foster 2003 to model the FRC tension behaviour.
Figure 5.1-13 reports the FE analysis results of the square slab panel for PHF46 series compared to the reference square slab panel in RC.
Table 5.1-9 summarizes and compares the experimental and FE analysis results.

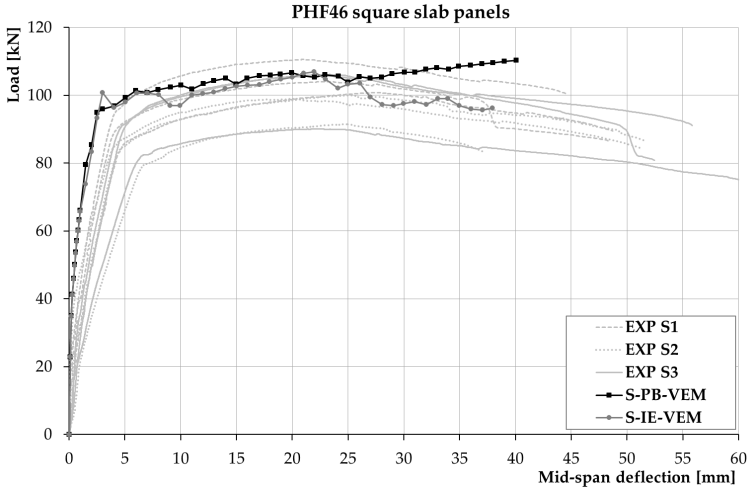

Figure 5.1-12: Comparison between FE analysis (VEM - Voo and Foster 2003) and experimental data for PHF46 series.

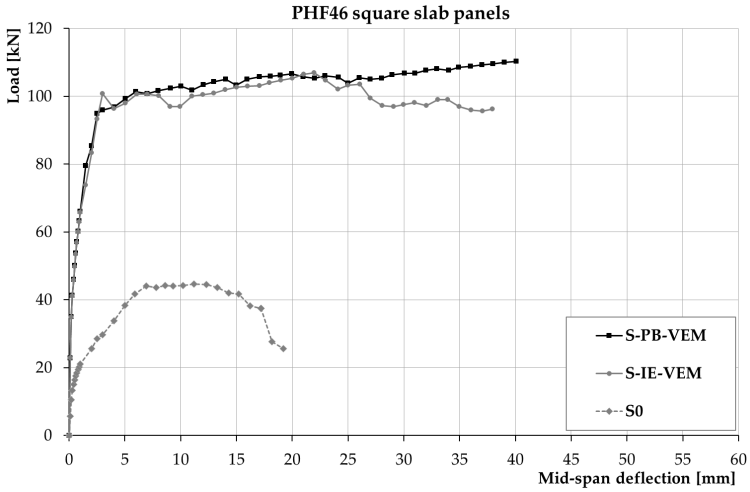

Figure 5.1-13: FE analysis results of the square slab panel for PHF46 series.

PANEL ID	Peak load [kN]	Displ. at peak load[mm]	Displ. at failure load[mm]	Shear stress at peak load[1] [MPa]
S0	44.1	9.3	19.2	0.38
EXP S1	105.2 [100.8-110.6] (0.05)	23.7 [20.9-27.3] (0.14)	47.2 [44.5-48.7] (0.05)	0.56
EXP S2	96.9 [91.5-100.0] (0.05)	23.1 [20.3-24.8] (0.12)	44.3 [30.0-51.6] (0.28)	0.51
EXP S3	100.7 [90.1-106.2] (0.04)	22.4 [22.1-23.3] (0.03)	56.6 [52.5-61.6] (0.08)	0.53
S-PB	110.3	40.1	40.1	0.60
S-IE	106.9	22.0	38.0	0.58
S-PB/ EXP S1	1.05	1.69	0.85	1.07
S-PB/ EXP S2	1.14	1.74	0.91	1.18
S-PB/ EXP S3	1.09	1.79	0.71	1.13
S-IE/ EXP S1	1.02	0.93	0.80	1.04
S-IE/ EXP S2	1.10	0.95	0.86	1.14
S-IE/ EXP S3	1.06	0.98	0.67	1.13

[min-max] minimum and maximum values are reported in square brackets
(CV%) Coefficient of Variation reported in round brackets
[1]Experimental shear stress was calculated with the following equation: $\tau_u = P/2bd$
Table 5.1-9: Summary of the FE analysis results of the square slab panel for PHF46 series.

As showed in Figure 5.1-13 and on Table 5.1-9, the composite square slab panels had a significantly higher stiffness and ultimate resistance than reference square slab panel in RC. Furthermore, Figure 5.1-13 indicates that the additional UHPFRC overlay increased the peak load. Based on results reported, the maximum load was doubled for the strengthened square slab panels. The reference square slab panel in RC failed due to the crushing of concrete.

As indicated by the results above, the perfect bond condition and the interface contact element presented the same pre-peak behaviour. Nevertheless, the post-peak response was different.

With perfect bond conditions (S-PB) the peak loads obtained from the VecTor2 analyses were generally 5%-15% higher than those obtained from the experiments. The predictions were particularly in accordance with the experimental square slab panel S1 (1.05 S-PB/ EXP S1) and S3 (1.09 S-PB/ EXP S3). For the remaining square slab panel S2, the average ratio of the predicted peak load to the peak load obtained from the experiments was 1.14. The mid-span deflection corresponding at the peak load was larger than those obtained from experimental tests (1.69 S-PB/ EXP S1, 1.74 S-PB/ EXP S2, and 1.79 S-PB/ EXP S3). The average ratios of the predicted shear strength to the shear strength obtained from the experiments were 1.07 for S-PB/ EXP S1, 1.18 for S-PB/ EXP S2, and 1.13 for S-PB/ EXP S3. Therefore, The FE analyses exhibited shear strengths that were slightly higher than the experimental results.

For S-IE, the peak load obtained from VecTor2 analyses was within 10% of the average experimental values. The prediction was particularly good for the experimental square slab panel S1 (1.02 S-PB/ EXP S1). For the remaining square slab panels (S2 and S3), the average ratios of the predicted peak load to the peak load obtained from the experiments were 1.10 and 1.06, respectively. The ratios of the S-IE-predicted displacement to the displacement at the failure load obtained from the tests were 0.80 for square slab panel S1, 0.86 for square slab panel S2, and 0.67 for square slab panel S3. The average ratios of the predicted shear strength to the shear strength obtained from the experiments were 1.04, 1.14, and 1.13, for S1, S2, and S3, respectively.

For both bond conditions (S-PB and S-IE), the VecTor2 analyses indicated that the initial pre-cracked stiffness was higher than the corresponding experimental response. As mentioned above, the different pre-cracked stiffness between experimental and FEA curves could be caused by the assumption that the square slab panels were not subjected to concrete shrinkage.

VecTor2 predicted the same failure, i.e. crushing of concrete with yielding of the longitudinal reinforcement, in accordance to with observed in the experiments. The analyses conducted using VecTor2 indicated that the concrete principal compressive stress and the x-direction reinforcement stress were higher than their maximum strength values.

From Figure 5.1-12, it can be observed that the S-IE model produced a reasonable predicted response with the peak load of 106.9 kN – within 10% of the average experimental values. The perfect bond conditions over-estimated the maximum load by 14% (5% for S1 and 9% for S3). In both sets of analyses, the deformation capacity was under-estimated (2%-7% for S-PB, and 14%-33% for S-IE).

5.1.3.4 PHF46 (fib Model Code 2010 FRC tension model)

Figure 5.1-14 illustrates the finite element analysis results for square slab panels S-PB and S-IE obtained from VecTor2, and from the experimental results. The FE analyses were conducted using *fib* Model Code 2010 FRC to model the FRC tension behaviour.

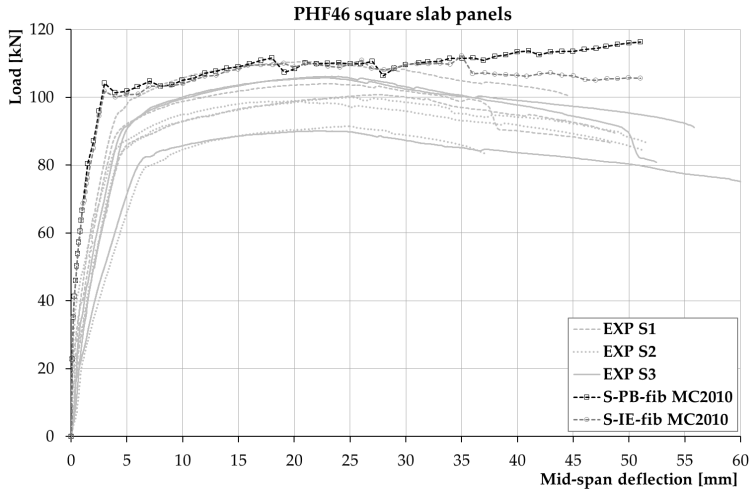

Figure 5.1-14: Comparison between FE analysis (fib MC 2010) and experimental data for PHF46 series.

As indicated by Figure 5.1-14, the VecTor2 analysis conducted using the *fib* Model Code 2010 FRC tension model predicted a reasonable response of the square slab panels. The perfect bond condition and the interface contact element produced roughly the same response.

With perfect bond conditions (S-PB), the calculated maximum load obtained from the VecTor2 analysis was 116.3 kN. The FEA result was 10-20% higher than the average experimental values. The ratios of the predicted peak load to the peak load obtained from the experiments were 1.10 for S-PB/ EXP S1, 1.20 for S-PB/ EXP S2, and 1.15 for S-PB/ EXP S3. The mid-span deflection corresponding at the peak load was not in agreement with the experimental values. The ratios of the S-PB-predicted displacement to the displacement at the peak load obtained from the tests were 2.15 for square slab panel S1, 2.21 for square slab panel S2, and 2.27 for square slab panel S3. However, the deformation capacity of the FE square slab panel was predicted correctly, especially for the S1 specimens (8% higher than the test values). For the square slab panels S2 the deformation capacity was 15% higher than average experimental values. For S3, it was 10% lower than that obtained from the tests. The average ratios of the predicted shear strength to the shear strength obtained from the experiments were 1.09, 1.20, and 1.15, for S1, S2, and S3, respectively.

For S-IE, the calculated maximum load was 112.3 kN. It was 16% higher than the average experimental values. The ratios of the predicted peak load to the peak load obtained from the experiments were 1.07 for S-PB/ EXP S1, 1.16 for S-PB/ EXP S2, and 1.11 for S-PB/ EXP S3. The mid-span deflection corresponding at the peak load was not in close agreement with the experimental values. It was larger than those obtained from experimental tests (1.47 S-PB/ EXP S1, 1.51 S-PB/ EXP S2, and 1.56 S-PB/ EXP S3). The deformation capacity of the FE square slab panel was generally within 15% of the experimental data. The prediction was particularly good for square slab panel S1 (it was 8% higher than experimental values) and S3 (it was 9% lower than experimental values). For square slab panel S2, the predicted deformation was 15% larger than that obtained from the tests. The average ratios of the predicted shear strength to the shear strength obtained from the experiments were 1.07 for S1, 1.18 for S2, and 1.13 S3.

As observed for FE analysis results of the square slab panels obtained using VEM FRC tension model, the initial post-cracked stiffness was higher than the corresponding experimental response. Also in this case, the concrete shrinkage was not assumed. This could explain the different pre-cracked stiffness between experimental and FEA curves.

Table 5.1-10 lists and compares the experimental and FE analysis results.

PANEL ID	**Peak load [kN]**	**Displ. at peak load [mm]**	**Displ. at failure load [mm]**	**Shear stress at peak load[1] [MPa]**
S0	44.1	9.3	19.2	0.38
EXP S1	105.2 [100.8-110.6] (0.05)	23.7 [20.9-27.3] (0.14)	47.2 [44.5-48.7] (0.05)	0.56
EXP S2	96.9 [91.5-100.0] (0.05)	23.1 [20.3-24.8] (0.12)	44.3 [30.0-51.6] (0.28)	0.51
EXP S3	100.7 [90.1-106.2] (0.04)	22.4 [22.1-23.3] (0.03)	56.6 [52.5-61.6] (0.08)	0.53
S-PB	116.3	51.0	51.0	0.61
S-IE	112.3	35.0	51.1	0.60
S-PB/ EXP S1	1.10	2.15	1.08	1.09
S-PB/ EXP S2	1.20	2.21	1.15	1.20
S-PB/ EXP S3	1.15	2.27	0.90	1.15
S-IE/ EXP S1	1.07	1.47	1.08	1.07
S-IE/ EXP S2	1.16	1.51	1.15	1.18
S-IE/ EXP S3	1.11	1.56	0.90	1.13

[min-max] minimum and maximum values are reported in square brackets

(CV%) Coefficient of Variation reported in round brackets

[1]Experimental shear stress was calculated with the following equation: $\tau_u = P/2bd$

Table 5.1-10: Summary of the FE analysis results of the square slab panel for PHF46 series.

Figure 5.1-15 compares the FE analysis results of the square slab panel obtained by VecTor2 using the two methods: SDEM - monotonic FRC tension model and *fib* Model Code 2010 FRC tension model.
Figure 5.1-15 shows that large differences were not encountered between the responses obtained from VecTor2 using the VEM - Voo and Foster 2003 FRC tension model, and the response obtained using the *fib* Model Code 2010 FRC tension model. The use of *fib* Model Code 2010 to model the FRC tension gave a higher response than that obtained from the VEM - Voo and Foster 2003 FRC model.

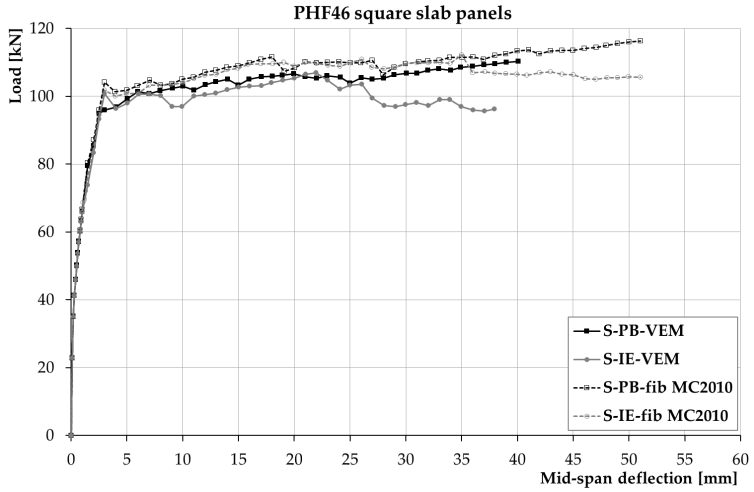

Figure 5.1-15: FE analysis results of the square slab panel for PHF46 series.

With perfect bond conditions, the peak load was higher than both the experimental responses (20%) and FE response obtained using the VEM - Voo and Foster 2003 (6%). Also in S-IE, the peak load was greater than both the experimental responses (16%) and FE response obtained using the VEM - Voo and Foster 2003 (5%). The FE analysis conducted using VEM – Voo and Foster (2003) under-estimated the deformation capacity. The predicted mid-span deflection at failure load was generally 5-30% lower than those obtained from the experiments. The deformation capacity obtained using *fib* Model Code 2010 was more in agreement with the tests compared to the response obtained using the VEM - Voo and Foster 2003. The predicted mid-span deflection at failure load was generally within 15% of the experimental data. From a comparison between the responses obtained using *fib* Model Code 2010 and VEM - Voo and Foster 2003 to model FRC tension, it can be observed that the pre-peak behaviour is the same for the two methods. The mid-span deflection at failure was under-estimated by the VEM – Voo and Foster 2003 model, but it was over-estimated by the *fib* Model Code 2010 model, except for square slab panel S3 (S / EXP S3 0.9).
The curves obtained from S-IE using VEM - Voo and Foster 2003 to model FRC tension and using *fib* Model Code 2010 showed roughly the same response.

5.1.4 *Influence of shrinkage*

The finite element analyses conducted above, were based on the assumption that the square slab panels were not subjected to concrete shrinkage. In some cases, shrinkage strain occurs in a concrete member. This could be a case where the composite slabs were subjected to differential shrinkage. In fact, due to the differently aged concrete, substrate and overlay have a differential concrete shrinkage. This condition creates tensile stresses that will be induced in the overlay. These stresses can cause cracking, which affects the appearance of the element and may impair its durability.
To examine the effect of the concrete shrinkage on the response of strengthening square slab panels, additional analyses were conducted assuming two different shrinkage deformation: uniform and linear. The additional analyses were conducted using three different values of shrinkage deformation: 600, 800, and 1000 micro-strain.
Figure 5.1-16 schematizes the two different shrinkage deformation: uniform distribution (a), and linear distribution (b).

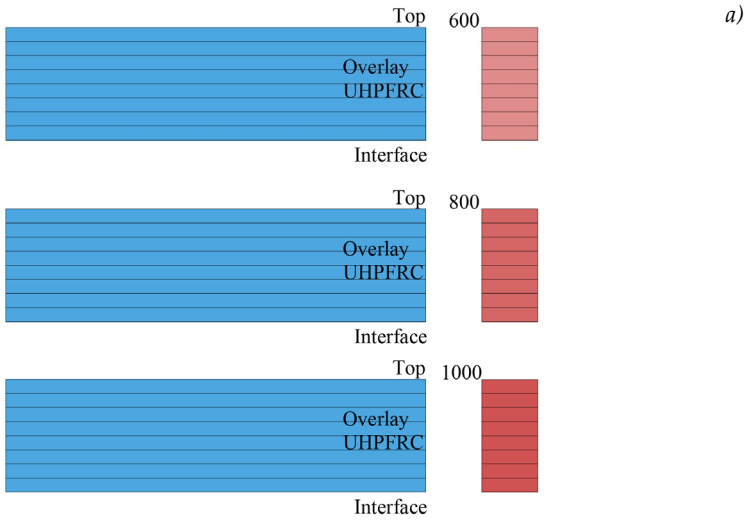

Figure 5.1-16 (Pt. 1 of 2)

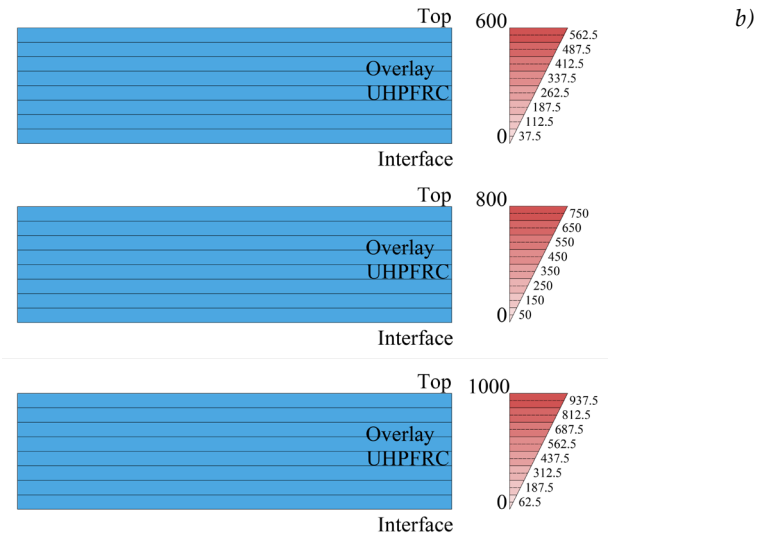

(Pt. 2 of 2)
Figure 5.1-16: a) uniform distribution; b) linear distribution.

In a square slab panels, only the overlay was subjected to shrinkage. This because generally the overlay is subjected to shrinkage and thermal effects, while the existing concrete deformations are negligible.
In VecTor2 the shrinkage strains can be input using the *'Concrete Pre-strains'* loading type. The shrinkage strain was applied as uniform type, with negative value in millistrain.
The FEA of the strengthening square slab panels were conducted using VEM - Voo and Foster 2003 FRC tension model. The effect of the concrete shrinkage was considered both on the model S-PB (perfect bond conditions) and S-IE (bond elements).

5.1.4.1 PHF (VEM - Voo and Foster 2003 FRC tension model)

5.1.4.1.1 Uniform shrinkage deformation

Figure 5.1-17 illustrates the results of the FE analyses for perfect bond conditions (S-PB) analyses assuming uniform shrinkage. The curves show the comparison between the experimental results (EXP), the response obtained from the square slab panel that was not subjected to the concrete shrinkage (S-PB-VEM), and the responses obtained from the square slab panels that were subjected to the shrinkage deformation (S-PB-0.8U, S-PB-0.8U, and S-PB-1U). Moreover, Figure 5.1-18 shows the first part of *load vs. net mid-span deflection* curves with perfect bond conditions, explaining both the uncracked and cracked stages.

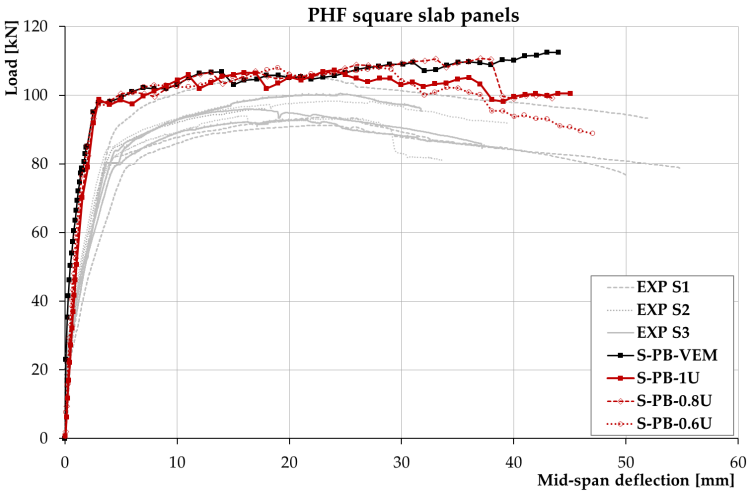

Figure 5.1-17: Influence of shrinkage on S-PB square slab panels (VEM - Voo and Foster 2003).

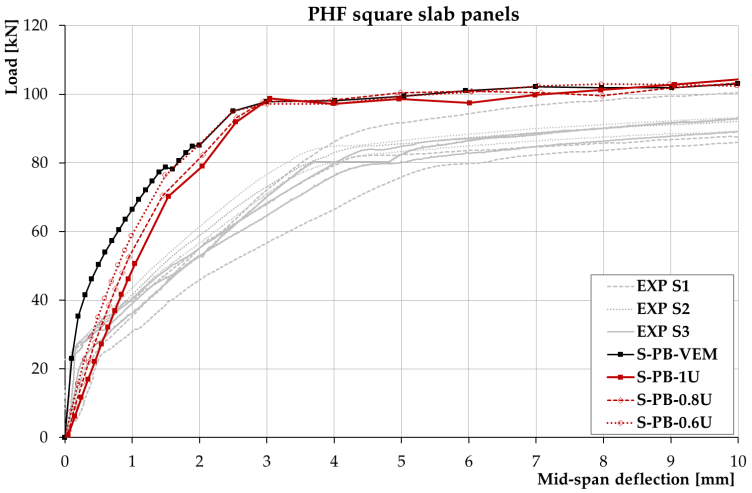

Figure 5.1-18: Influence of shrinkage on S-PB square slab panels (VEM - Voo and Foster 2003), first part of curve.

With perfect bond condition (refer to Figure 5.1-17), the ultimate capacities of the strengthening square slab panels did not change when the square slab panels were subjected to uniform concrete shrinkage. As expected, a decrease in stiffness was observed with increasing the shrinkage deformation values. Moreover, the square slab panels shown different early load cracking.

The S-PB-0.6U curve was in close agreement with experimental response. Nevertheless, the square slab panels subjected to uniform shrinkage deformation were not able to accurately predict the pre-peak behaviour of the specimens tested.

The overlay deformations caused direct stresses and interface shear stresses in both overlay and substrate. The FE analysis results remarked that the restrained shrinkage caused an increase of the horizontal stress and horizontal strain. These stresses caused cracking both in the overlay and substrate. Figure 5.1-19 shows the crack pattern at the three different values of shrinkage in square slab panel.
Figure 5.1-20 presents the responses of the FE analyses for the S-IE analyses assuming uniform shrinkage deformation (S-IE-0.6U, S-IE-0.8U, and S-IE-1U).

a)

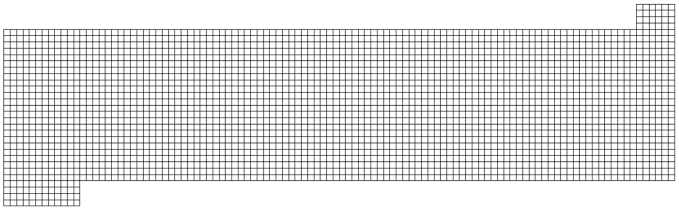

Step 0: w_{cr}=0 mm

b)

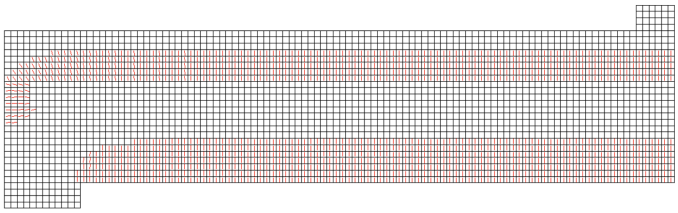

Step 0: $w_{cr,max}$=0.1 mm

c)

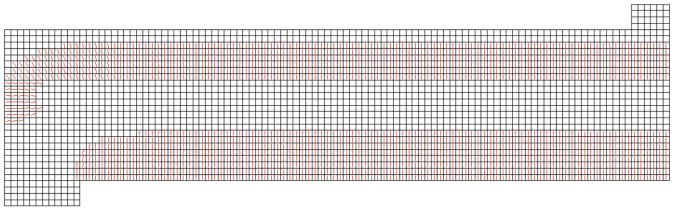

Step 0: $w_{cr,max}$=0.1 mm

d)

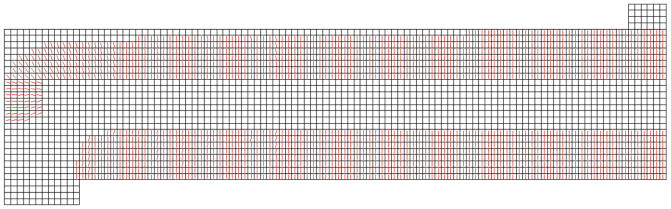

Step 0: $w_{cr,max}$=0.1 mm

Figure 5.1-19: Crack pattern at three different values of shrinkage deformation: a) null; b) S-PB-0.6U; c) S-PB-0.8U; d) S-PB-1U.

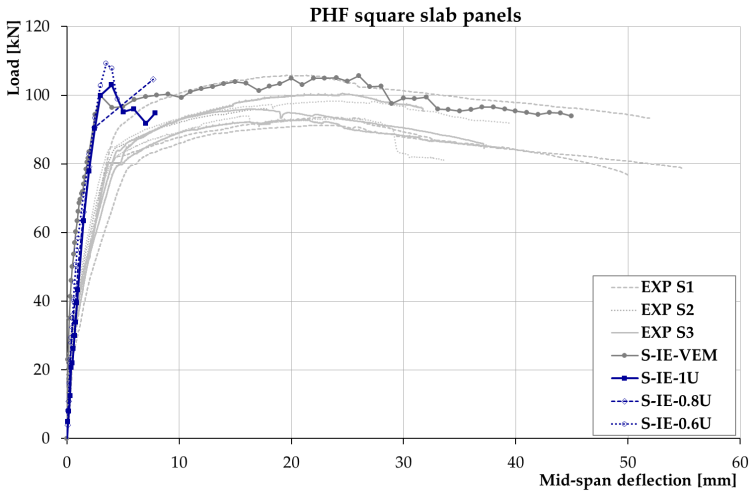

Figure 5.1-20: Influence of shrinkage on S-IE square slab panels (VEM - Voo and Foster 2003)

Contrarily to perfect bond conditions, in the S-IE analyses, the response was modified when the uniform concrete shrinkage was considered. In the square slab panels subjected to the uniform shrinkage deformation, slips between the overlay and substrate were observed. Moreover, the convergence of the analyses could not be achieved, and the analyses were sometimes terminated.
Based on the FE analysis results, it can be concluded that with perfect bond condition the shrinkage effects had a negative influence on composite slabs reducing their flexural stiffness. Nevertheless, the ultimate capacities of the square slab panels were roughly the same. On the contrary, in the S-IE analysis, the concrete shrinkage modified the response. In fact, when the shrinkage deformation was applied, the slips between exiting concrete and UHPFRC overlay were noticed, contrary to what observed in the experimental tests, where the slips at the interface were negligible (the maximum value is 6.3 μm). However, in the case of the square slab panels subjected to uniform shrinkage deformation, both VecTor2 models (S-PB and S-IE) were not able to accurately predict the pre-peak behaviour of the specimens tested.

5.1.4.1.2 Linear shrinkage deformation

Figure 5.1-21 reports the results of the FE analyses for perfect bond conditions (S-PB) assuming linear shrinkage deformation. The curves compare the experimental results (EXP), the response obtained from the square slab panel that was not subjected to the concrete shrinkage (S-PB VEM), and the responses obtained from the square slab panels that were subjected to the linear shrinkage deformation (S-PB-0.6L, S-PB-0.8L, and S-PB-1L). Moreover, the Figure 5.1-22 shows the first part of *load vs. net mid-span deflection* curves with perfect bond conditions.

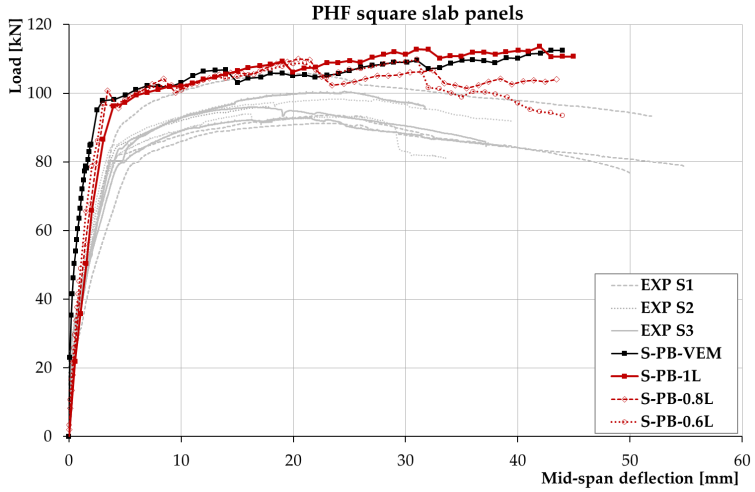

Figure 5.1-21: Influence of shrinkage on S-PB square slab panels (VEM - Voo and Foster 2003).

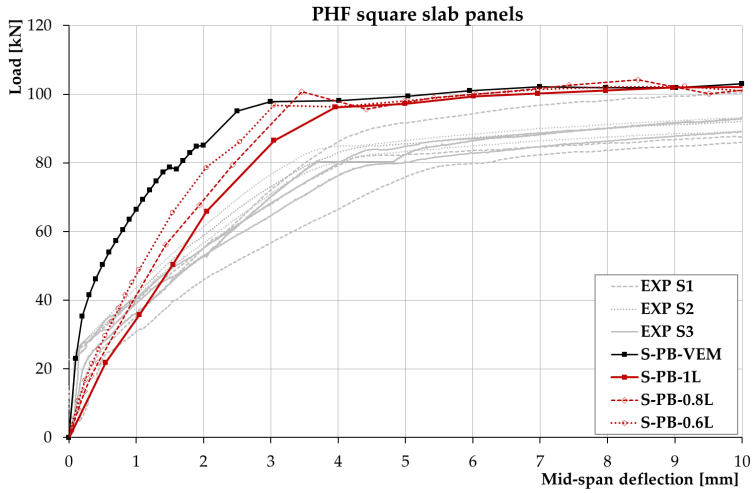

Figure 5.1-22: Influence of shrinkage on S-PB square slab panels (VEM - Voo and Foster 2003), first part of curve.

With perfect bond condition (refer to Figure 5.1-21), the ultimate capacities of the strengthening square slab panels did not change when the square slab panels were subjected to linear shrinkage deformation. As expected, a decrease in stiffness was observed with increasing the shrinkage deformation values. Differently to uniform shrinkage distribution, Figure 5.1-22 shows that when the linear shrinkage deformation was considered, Vector2 model was able to better predict the pre-peak behaviour of the square slab panels tested even though with still some overestimation. From the results above, it can be observed that consider the linear

shrinkage deformation is more appropriate than the uniform shrinkage distribution. The prediction was particularly good for model S-PB-0.6L. Figure 5.1-23 compares the response obtained from the experimental tests (EXP), and the response obtained from the square slab panel that was subjected to the linear shrinkage deformation of 600 micro-strain.

Figure 5.1-24 shows the crack pattern at the three different values of shrinkage in square slab panel.

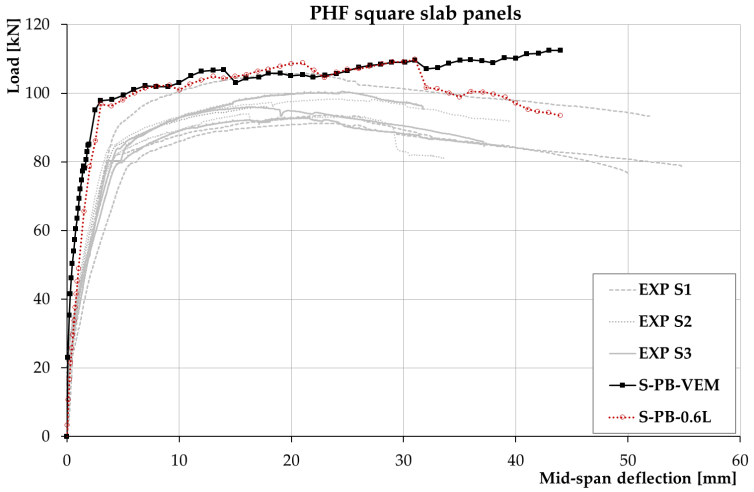

Figure 5.1-23: Comparison between S-PB-0.6L square slab panel (VEM - Voo and Foster 2003) and experimental curves.

a)

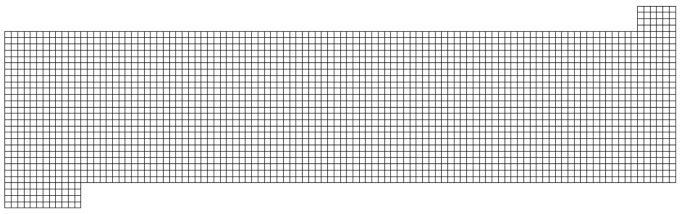

Step 0: w_{cr}=0 mm

b)

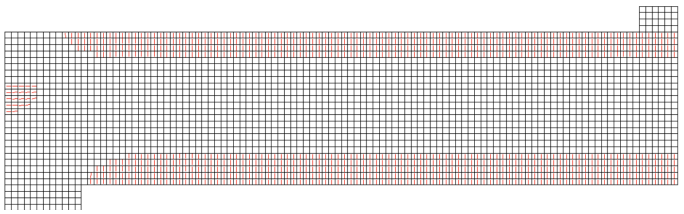

Step 0: $w_{cr,max}$=0.1 mm

Figure 5.1-24 (Pt. 1 of 2)

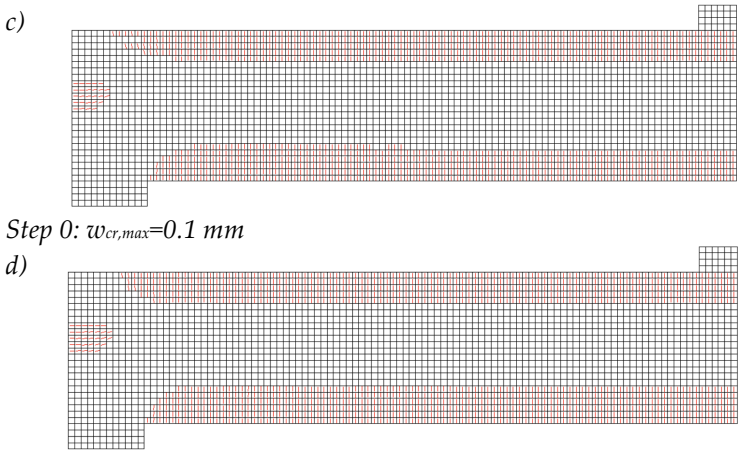

(Pt. 2 of 2)

Figure 5.1-24: Crack pattern at three different values of shrinkage deformation: a) null; b) 1 S-PB-0.6U; c) S-PB-0.8U; d) S-PB-1U.

Figure 5.1-25 presents the responses of the FE analyses for the S-IE analyses assuming linear shrinkage deformation (S-IE-0.6L, S-IE-0.8L, and S-IE-1L).

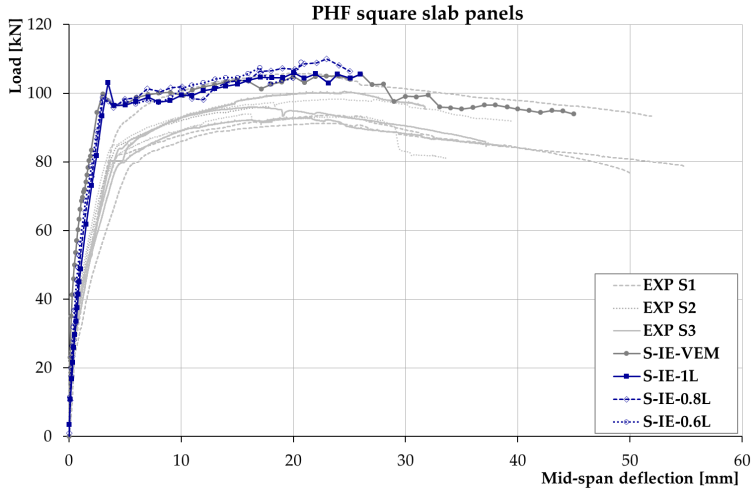

Figure 5.1-25: Influence of shrinkage on S-IE square slab panels (VEM - Voo and Foster 2003)

As observed in uniform shrinkage distributions, in the S-IE-L analyses, the response was modified respect to perfect bond conditions. In the square slab panels subjected to the linear shrinkage deformation, the slips between the overlay and substrate were observed. Differently to uniform shrinkage distributions, the slips were observed at

20 mm of mid-span deflection. Moreover, also in these cases, the convergence of the analyses could not be achieved, and the analyses were terminated.
Based on the FE analysis results, it can be observed that with perfect bond condition the linear shrinkage effects had an influence on composite slabs reducing their flexural stiffness. Moreover, when the linear shrinkage deformation was considered, Vector2 model was able to predict the behaviour of the square slab panels tested, especially for the model S-IE-0.6L. It can be concluded that considering the linear shrinkage deformation is more appropriate than the uniform shrinkage deformation. On the contrary, in the S-IE analysis, the concrete shrinkage modified the response. In fact, when the shrinkage deformation was applied, the slips between exsiting concrete and UHPFRC overlay were noticed, contrary to what observed in the experiment tests, where the slips at the interface were negligible (the maximum value is 6.3 μm).

5.1.4.2 PHF46 (VEM - Voo and Foster 2003 FRC tension model)

5.1.4.2.1 Uniform shrinkage deformation

Figure 5.1-26 shows the results of the FE analyses (S-PB-VEM: no shrinkage, S-PB-0.6U, S-PB-0.8U, S-PB-1U: uniform shrinkage) and the experimental tests. Figure 5.1-27 reports the first part of *load vs. net mid-span deflection* curves in perfect bond conditions.

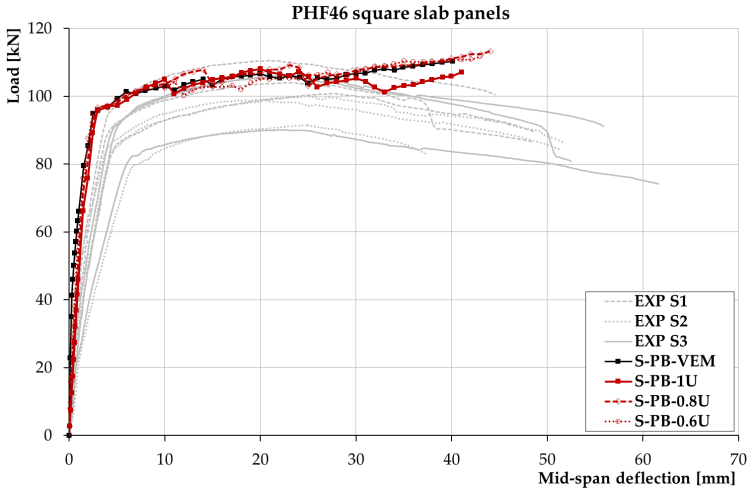

Figure 5.1-26: Influence of shrinkage on S-PB square slab panels (VEM - Voo and Foster 2003).

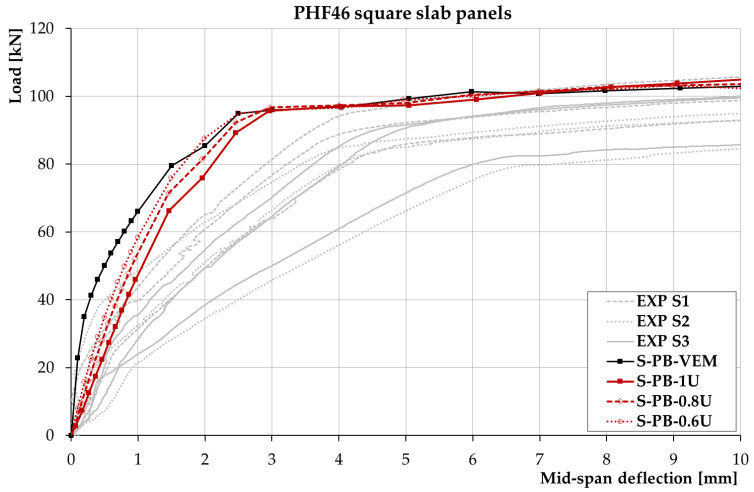

Figure 5.1-27: Influence of shrinkage on S-PB square slab panels (VEM - Voo and Foster 2003), first part of curve.

The responses obtained are the same that were observed in the PHF series
Figure 5.1-28 presents the responses of the FE analyses for the S-IE analyses assuming uniform shrinkage deformation (S-IE-0.6U, S-IE-0.8U, and S-IE-1U).
Differently from S-PB, in the S-IE analyses (Figure 5.1-28), the responses of the square slab panels were different respect to response of the square slab panels not subjected to concrete shrinkage as observed in the PHF series

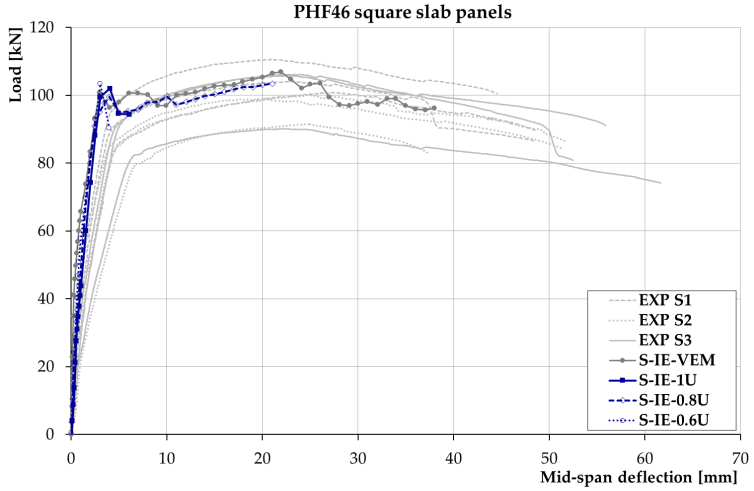

Figure 5.1-28: Influence of shrinkage on S-IE square slab panels (VEM - Voo and Foster 2003).

Based on the FE analysis results, it can be concluded that both VecTor2 models (S-PB and S-IE) were not able to accurately predict the pre-peak behaviour of the specimens tested.

5.1.4.2.2 Linear shrinkage deformation

Figure 5.1-29 explains the results of the FE analyses for perfect bond conditions (S-PB-VEM) analyses assuming linear shrinkage. The curves compare the experimental results (EXP), the response obtained from the square slab panel that was not subjected to the concrete shrinkage (S-PB-VEM), and the responses obtained from the square slab panels that were subjected to the linear shrinkage deformation (S-PB-0.6L, S-PB-0.8L, and S-PB-1L). Moreover, the Figure 5.1-30 shows the first part of *load vs. net mid-span deflection* curves with perfect bond conditions.

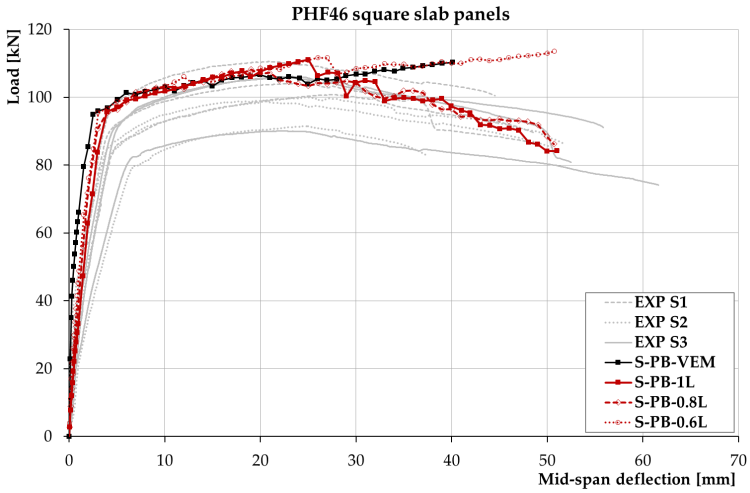

Figure 5.1-29: Influence of shrinkage on S-PB square slab panels (VEM - Voo and Foster 2003).

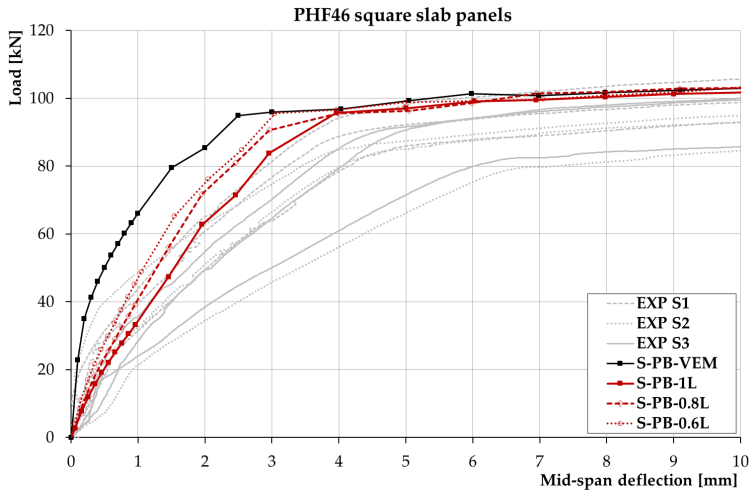

Figure 5.1-30: Influence of shrinkage on S-PB square slab panels (VEM - Voo and Foster 2003), first part of curve.

With perfect bond condition (refer to Figure 5.1-29), the ultimate capacities of the strengthening square slab panels changed when the square slab panels were subjected to linear shrinkage deformation. Contrarily to the S-PB-VEM, the ultimate capacities of the S-PB-0.6L, S-PB-0.8L, and S-PB-1L were in close agreement with the experimental results. Furthermore, Figure 5.1-30 demonstrates that when the linear shrinkage deformation was considered, Vector2 model was able to predict the pre-peak behaviour of the square slab panels tested. From these results, it can be concluded that consider the linear shrinkage deformation is more appropriate than the uniform shrinkage deformation. It can be established that the assumption of the linear shrinkage distributions is appropriate. In particular, the S-PB-0.8L and S-PB-1L analyses produced a valid predicted response. Figure 5.1-31 compares the response obtained from the experimental tests (EXP), and the responses obtained from the square slab panels that were subjected to the linear shrinkage deformation of 800 and 1000 micro-strain.

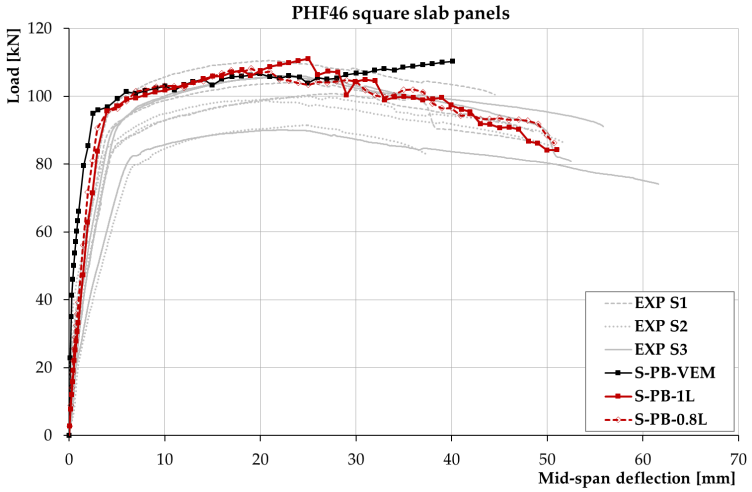

Figure 5.1-31: Comparison between S-PB-0.6L square slab panel (VEM - Voo and Foster 2003) and experimental curves.

Figure 5.1-32 presents the responses of the FE analyses for the S-IE analyses assuming linear shrinkage deformation (S-IE-0.6L, S-IE-0.8L, and S-IE-1L).
As observed in uniform shrinkage distributions, in the S-IE-L analyses, the response was different respect to perfect bond conditions. In the square slab panels subjected to the linear shrinkage deformation, the slips between the overlay and substrate were observed, contrary to what observed in the experiment tests, where the slips at the interface were negligible (the maximum value is 6.3 μm). Moreover, the convergence of the analyses could not be achieved, and the analyses were terminated.

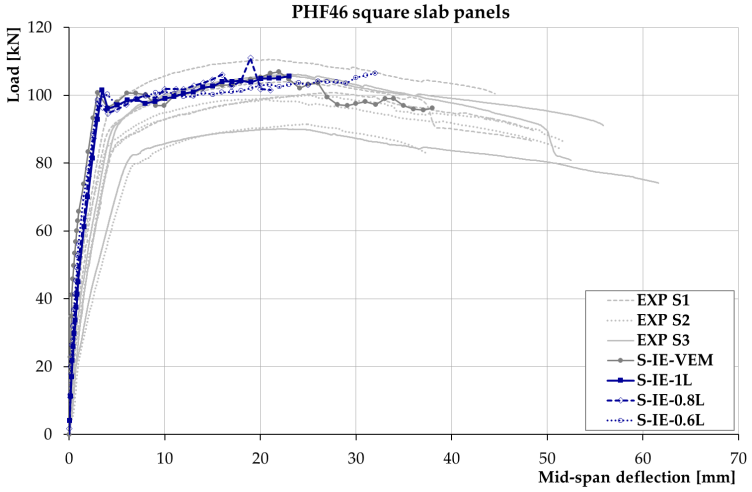

Figure 5.1-32: Influence of shrinkage on S-IE square slab panels (VEM - Voo and Foster 2003)

5.1.5 *Concluding remarks*

Based on the comparison between the experimental and FE analysis results reported in this chapter, the following main conclusions can be drawn:

- In the finite element analyses conducted using VEM - Voo and Foster 2003 FRC tension model, the perfect bond condition and the interface contact element produced different responses.
- S-IE-VEM analyses produced a reasonable predicted response. In PHF series, the peak load of 102.6 kN was 10% higher than test values. In PHF46 series, the peak load was 106.9 kN - within 10% of the average experimental values. On the other hand, the perfect bond condition over-estimated the maximum load. In PHF series, the maximum load (112.5 kN) was 17% higher than experimental results. In PHF46 series, the peak load was 110.3 kN; the perfect bond conditions over-estimated the maximum load by 14%. The deformation capacities of the PHF square slab panels (both S-PB and S-IE), were in close agreement with the experimental result. In PHF46, the deformation capacities both for S-PB and S-IE were under-estimated (9%-29% for S-PB, and 14%-33% for S-IE). For both bond conditions (S-PB and S-IE), the initial pre-cracked stiffness was higher than the corresponding experimental response. Additionally, the square slab panels failed due to the crushing of concrete and the yielding of the longitudinal reinforcement, as observed in the experimental tests.
- In the FE analyses conducted using *fib* Model Code 2010 to model the FRC tension behaviour, the perfect bond condition and the interface contact element produced different responses.
- In the PHF S-IE-fibMC2010 analyses, the peak load of 110.8 kN was 15% higher than test values. In PHF46 series, the peak load was 112.3 kN - within 16% of the average experimental values. The perfect bond condition over-estimated the maximum load. In PHF series, the maximum load was 116.5 kN, it was 21% higher than experimental results. In PHF46 series, the peak load was 116.3 kN; the perfect bond conditions over-estimated the maximum load by 20%. The deformation capacities of the PHF square slab panels (both S-PB and S-IE), were not in close agreement with the experimental result. In PHF46, the deformation capacities for S-PB and for S-IE were under-estimated (10%-15% both for S-PB and S-IE). For both bond conditions (S-PB and S-IE), the initial pre-cracked stiffness was higher than the corresponding experimental response. Additionally, the square slab panels failed due to the crushing of concrete and the yielding of the longitudinal reinforcement, as what was observed in the experimental tests.
- Large discrepancies were not encountered between the responses obtained from VecTor2 using the VEM - Voo and Foster 2003 FRC tension model, and

the response obtained using the *fib* Model Code 2010 FRC tension model. The use of *fib* Model Code 2010 to model the FRC tension gave a higher response than that obtained from the VEM - Voo and Foster 2003 FRC model. The pre-peak behaviour is the same for the two methods. The perfect bond conditions over-estimated the maximum load in both methods.

- The uniform shrinkage deformation caused a decrease of stiffness. Moreover, an increase of the horizontal strain was observed. These stresses cause cracking both in the overlay and substrate concrete.
- With perfect bond condition, the ultimate capacities of the strengthening square slab panels did not change when the square slab panel subjected to uniform concrete shrinkage. The curves obtained were in close agreement with experimental response. Nevertheless, the square slab panels subjected to uniform shrinkage deformation were not able to accurately predict the pre-peak behaviour of the specimens tested. In the S-IE analyses, the response was modified when the concrete shrinkage was considered. In fact, the shrinkage deformation produced the slips between the UHPFRC overlay and concrete substrate.
- With perfect bond condition, the linear shrinkage deformation is more appropriate than the uniform shrinkage distribution. In fact, the analyses conducted considering the linear shrinkage showed that the models were able to predict the behaviour of the square slab panels tested. The predictions were particularly good for PH46 series. Therefore, it can be concluded that the assumption of the linear shrinkage distributions is appropriate. Contrarily, in the S-IE analyses, the response was modified when the concrete shrinkage was considered. In fact, the shrinkage deformation produced the slips between the UHPFRC overlay and concrete substrate.

5.2 *Numerical analyses of RC beams: parametric study*

5.2.1 *Introduction*

With the purpose of studying the response of a wide range of elements, numerical analyses on beams having different parameters were performed.
The numerical research program conducted in this work provides the analyses of reinforced concrete beams strengthened with a UHPFRC jacket. The following section provides a discussion of the effect of the UHPFRC jacket on the valley of diagonal shear failure, investigated for:

- three sizes of beams: small (S), medium (M), and large (L);
- five shear span-to-effective depth ratios (a/d): 2.5, 3.0, 3.5, 4.0, and 4.5;
- three concrete cylinder compressive strengths (f_c): 25, 50, and 70 MPa;
- four different longitudinal reinforcement ratios (ρ): 0.9%, 1.6%, 2.1%, and 2.4%;
- three typologies of retrofitting, having different thicknesses of UHPFRC jacketing (s_l): 30, 40, and 50 mm (the thickness was increased when the retrofitted beam still showed a shear failure). In case the failure mode did not change, and the jacketing was not an efficient shear repairing method, a high strength steel mesh (SM) was added in the jacket.

For all series, a reference beam and a beam reinforced with the UHPFRC jacket were modelled. Each beam was given a proper code in order to identify all the features: B-f_c (compressive strength) - size (S, M or L) - fibres (NN: none, NF: fibres) - thickness of UHPFRC (30, 40, 50) - reinforcement ratio (0.9, 1.6, 2.1, 2.4).
The analyses were conducted to investigate the efficacy of the UHPFRC jacket on shear strength, failure mechanism, crack control, and ductility.
Typical shear-mid-span deflection curves and representative crack patterns of these studies are presented and discussed in this section.
Moreover, a number of 3D plots of the valley of shear diagonal failure ($M_u/M_{u,fl}$ versus a/d ratio), as a function of the reinforcement ratio, are discussed in the following. The ultimate moment M_u is the moment at which the collapse of the structure occurred (whether under shear or flexure) numerically. For RC beams, the ultimate flexural moment was calculated by assuming the yielding of rebars and a classical stress-block approach. For UHPFRC-RC beams, the $M_{u,fl}$ was calculated assuming the yielding of rebars, a classical stress–block approach for plain concrete and UHPFRC in compression, and a tensile stress-block having a constant tension for UHPFRC.

5.2.2 *Numerical modelling of the beams*

In VecTor2, all beams were modelled using rectangular concrete elements. Due to the symmetry of the beams and the loading scheme, only half of each reference beams and only one-quarter of each strengthened beams were modelled. In size S, the mesh size used was 20 x 20 mm, in size M and L, it was 40 x 40 mm. The beams were restrained in the x- and y-directions at the nodal supports. Moreover, the elements were restrained against movement in the x-direction at the mid-span cross section (plane of symmetry), as shown in Figure 5.2-1.
The beams were loaded under a four-point bending configuration, with the load applied as a monotonically increasing displacement. The analysis was conducted in displacement-control with an increment step size of 0.1 mm. The load was transferred to the top surface of the element by a steel plate (same material and dimensions as used for the supports). Figure 5.2-1 and Figure 5.2-2 illustrate the finite element models, and Table 5.2-1 gives the geometric details of beams.
In VecTor2, the fibres were input as smeared reinforcement. The reference type was discrete steel fibre in the reinforcement component of the reinforced concrete. The inputs required for the fibre reinforcement definition were the fibre type, the fibre volume fraction (V_f), the length and the diameter of the fibres (L_f and D_f), the ultimate tensile strength of the fibres (F_u), and the average interfacial bond strength between the fibre and the concrete matrix (T_u). If the average interfacial bond strength input is set equal to zero, the VecTor2 default value will be used. For hooked-end fibres, Voo and Foster [2003] suggested that it should be evaluated as $\tau_u = 2.5\, f_{ct}$, with f_{ct} being the tensile strength of the plain concrete in MPa.

Series S

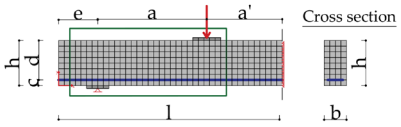

Series M

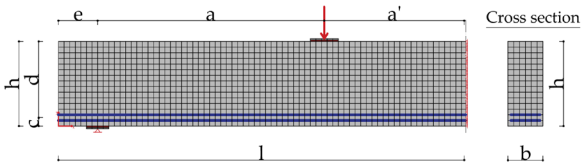

Series L

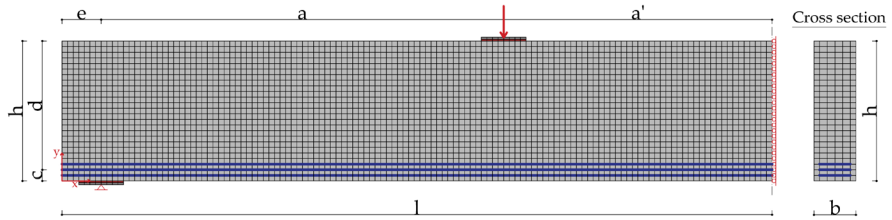

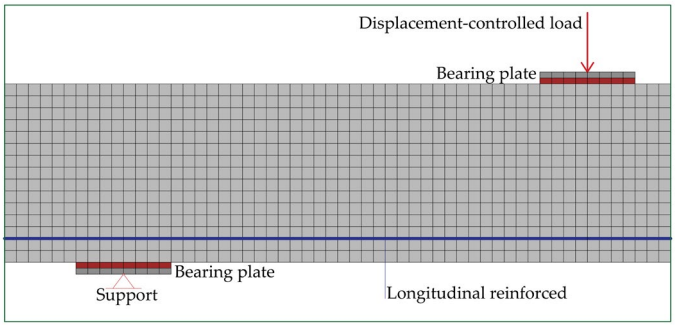

Figure 5.2-1: Finite element modelling of the reference beam.

Series S

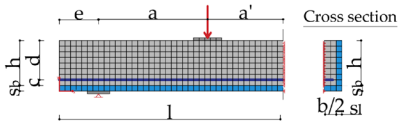

Series M

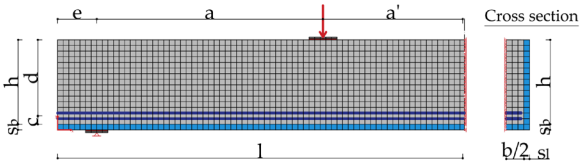

Series L

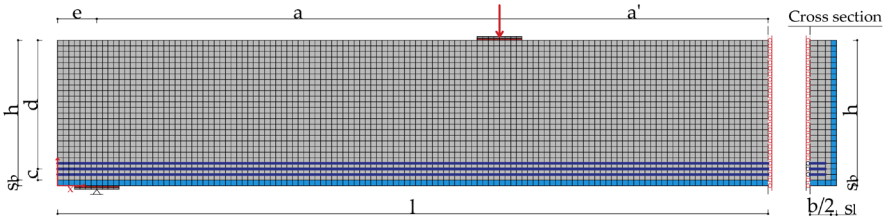

Figure 5.2-2: Finite element modelling of the strengthened beam.

Dimension	**Series S**	**Series M**	**Serie L**
b	150 mm	250 mm	300 mm
h	300 mm	600 mm	1000 mm
d	260 mm	540 mm	920 mm
a	640 mm 780 mm 900 mm 1040 mm 1160 mm	1320 mm 1600 mm 1880 mm 2160 mm 2440 mm	2300 mm 2760 mm 3220 mm 3680 mm 4140 mm
a′	520 mm	1000 mm	2040 mm
e	280 mm	280 mm	280 mm
c	40 mm	40 mm	40 mm
s_l	30 mm 40 mm 50 mm	30 mm 40 mm 50 mm	30 mm 40 mm 50 mm
s_b	40 mm	40 mm	40 mm
l_{eff}=2(e+a+a′)	2880 mm 3160 mm 3400 mm 3680 mm 3920 mm	5200 mm 5760 mm 6320 mm 6680 mm 7440 mm	9240 mm 10160 mm 11080 mm 22520 mm 12920 mm

Table 5.2-1: Geometric details of reference beams.

The UHPFRC properties specified were the tensile strength (f_t'), the initial tangent modulus (E_c), and the density, as measured from the experiment data, which were presented in Section 3.2, Section 3.3, and Section 5.1.2.
The only concrete property specified was the concrete compression strength. Table 5.2-2 shows the default VecTor2 relationship and values for the concrete properties.

Concrete Properties			
Thickness (mm)	required input	**C_c (/°C)**	10×10^{-6} †
f_c' (MPa)	required input	**Max. agg. size (mm)**	10
f_t' (MPa)	$0.33\sqrt{f'_c}$ †	**Density (kg/m³)**	2400 †
E_c (MPa)	$3320\sqrt{f'_c}+6900$ †	**K*c* (mm²/s)**	1.2 †
ε_o (mm/m)	$1.8 + 0.0075\, f'_c$ †	**S*x* (mm)**	input
μ	0.15 †	**S_y (mm)**	input

Note: The program limits to 5000 mm the spacing of cracks parallel to the Y axis, S_x and parallel to the X axis, S_y. The crack spacing is calculated based on the CSA A23. 3-14 [2014].
†Default properties assumed by VecTor2 unless specified otherwise.
Table 5.2-2: Material properties.

Between the concrete substrate and the UHPFRC jacket, perfect bond condition was assumed. Figure 5.2-3 illustrates the interface element between the two materials: RC concrete and UHPFRC.

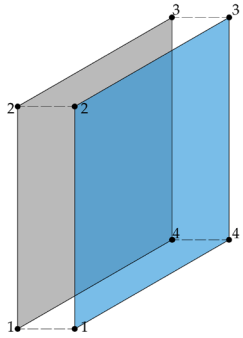

Figure 5.2-3: Perfect bond conditions assumed in VecTor2.

Longitudinal reinforcement in the x-direction was modelled using discrete truss elements. The reinforcement properties specified in the analysis were the yield strength, the ultimate strength, and the modulus of elasticity. Table 5.2-3 gives the properties of the ductile steel reinforcement for each beam.
When present, the steel mesh embedded in the layer of UHPFRC was modelled as smeared reinforcement. The steel mesh, having high tensile resistance (f_y=1100 MPa, f_u=1700), was made of 5 mm diameter bent wires, assembled with a spacing of 50 mm. The inputs were reinforcement direction, reinforcement ratio (calculated based on the spacing), reinforcement diameter, yield strength, ultimate strength, and elastic modulus.

Dimension	Series S				Series M				Series L			
ρ [%]	***0.9***	***1.6***	***2.1***	***2.4***	***0.9***	***1.6***	***2.1***	***2.4***	***0.9***	***1.6***	***2.1***	***2.4***
Cross section area [mm²]	339	603	804	942	1206	2211	2826	3140	2412	4396	5652	6594
Reinforcement diameter [mm]	12	16	16	20	16	16	20	20	16	20	20	20
Yield strength [MPa]	510	510	510	510	510	510	510	510	510	510	510	510
Ultimate strength [MPa]	600	600	600	600	600	600	600	600	600	600	600	600

Table 5.2-3: Reinforcement properties used in VecTor2.

The constitutive models used in the finite element analysis were the default models in VecTor2, with the exception of the pre-peak compression model in the beam with f_c=70 MPa, which used the Popovics-High Strength model. In VecTor2, the default model for FRC in tension is the Simplified Diverse Embedment Model (SDEM) [Lee et al., 2012]. For monotonic loading conditions, in the SDEM, the tensile stress in the fibres is expressed by the frictional bond behaviour in straight fibres and the additional mechanical anchorage in hooked-end fibres.
Table 5.2-4 lists the concrete and reinforcement constitutive models used in VecTor2.

Concrete Models			
Compression Pre-Peak	Hoshikuma et al. (parabola) † / Popovics-HSC	**Dilation**	Variable – isotropic †
Compression Post-Peak	Modified Park-Kent †	**Cracking Criterion**	Mohr – Coulomb (stress) †
Compression Softening	Vecchio 1992-A †	**Crack Stress Calculation**	Basic (DSFM/MCFT) †
Tension Stiffening	Modified Bentz 2003 †	**Crack Width Check** [1]	1 mm max crack width / Agg/2.5 max crack width †
Tension Softening	Nonlinear (Hordijk) †	**Crack-Slip Calculation**	Walraven †
FRC Tension	SDEM-Monotonic†	**Creep and Relaxation**	Not considered †
Confined Strength	Kupfer / Richart †	**Hysteretic Response**	Nonlinear w/ Plastic offsets †
Reinforcement Models			
Hysteretic Response	Bauschinger Effect (Seckin) †	**Buckling**	Akkaya 2012 †
Dowel Effect	Tassios (Crack Slip) †	**Concrete Bond**	Eligehausen †

[1]*The crack width check serves to reduce average compressive stresses when crack widths exceed a specified limit. For RC beams the maximum crack width of 1 mm was selected. For strengthened beams default model was assumed.*
†*Default models assumed by VecTor2 unless specified otherwise.*
Table 5.2-4: Concrete and reinforcement constitutive model used in VecTor2.

5.2.3 *Finite element analysis results*

The finite element analyses of the RC beams strengthened with a UHPFRC jacket are reported in this section.
The shear strength, the ultimate shear stress ($v_u = \frac{P}{bd}$), the normalized ultimate shear stress ($\frac{v_u}{\sqrt{f_c}}$), and the failure mechanism are presented. Moreover, a number of 3D plots of the valley of shear diagonal failure ($M_u/M_{u,fl}$ versus a/d ratio), as a function of the reinforcement ratio (ρ) are discussed in the following. Linear interpolation of the results was chosen among the numerical values obtained.
The numerical research program discussed in this section are presented in detail in Appendix D. In the following, only typical analysis responses (shear-mid-span deflection curves and representative crack patterns) of these studies are showed and discussed.

5.2.3.1 B25S

The behaviour of the B25S beams was nearly identical to each other, therefore typical responses are discussed in the following.
Figure 5.2-4 shows the typical *shear vs. mid-span deflection* curves for B25S specimens having different reinforcement ratio: *a)* 0.9%, *b)* 1.6%, *c)* 2.1%, *d)* 2.4%.

a)

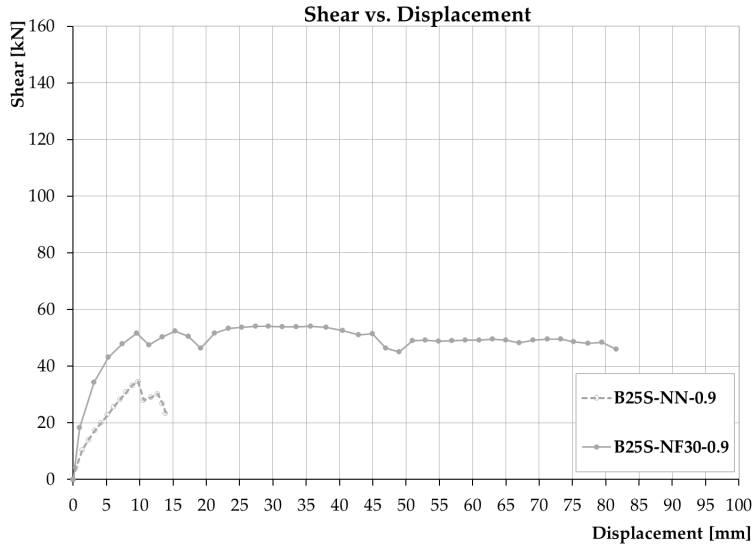

Figure 5.2-4 (Pt. 1 of 3)

b)

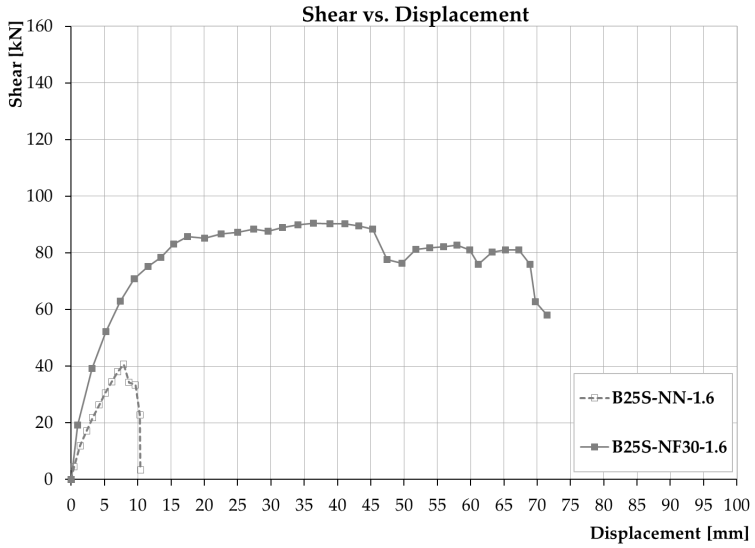

c)

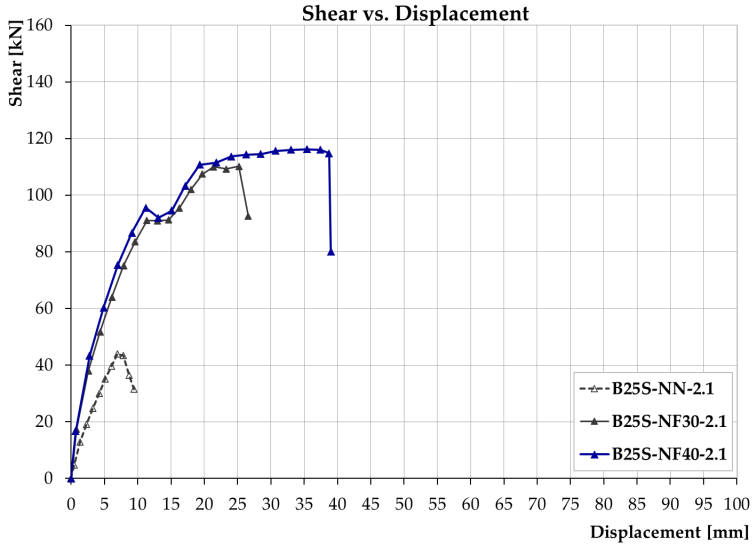

Figure 5.2-4 (Pt. 2 of 3)

d)

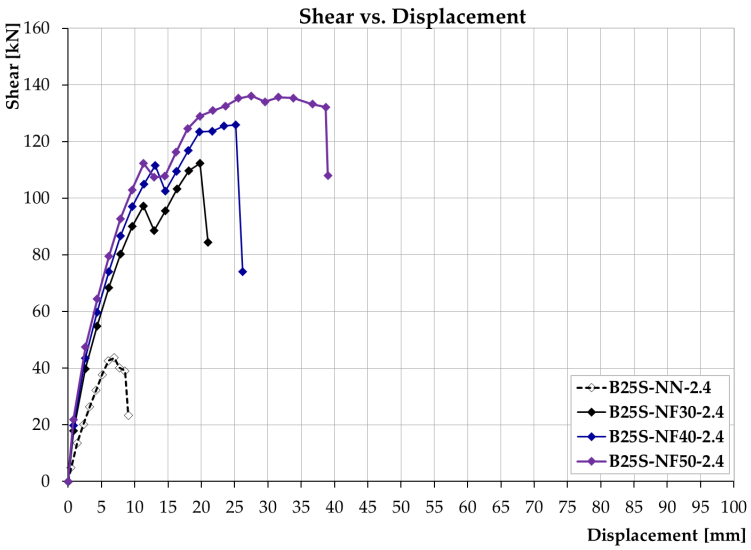

(Pt. 3 of 3)

Figure 5.2-4: Typical shear vs. mid-span deflection curves for B25S specimens.

Considering a compressive strength of 25 MPa, all reference beams analysed presented a shear failure mechanism. The beams had a brittle behaviour: they failed quickly after reaching the peak load. The numerical analyses showed that the reference beams failed due to the opening of a diagonal crack that connected the loading point and the support. Flexural cracks first developed from the bottom surface of the beam in the region below the loading point, where the maximum moment occurred. As the applied load increased, the flexural cracks spread out toward the support. When the load was sufficient to impose a diagonal tension greater than the concrete tensile strength, the inclined crack occurred, immediately followed by failure of the beam. Figure 5.2-5 shows the critical inclined crack at an angle of approx. 30 degrees from the horizontal. At the lower end of the critical inclined crack, cracking propagated along the top layer of the tension reinforcing rebar (Figure 5.2-5-b), which could be attributed to bond failure between the concrete and the reinforcement bars.

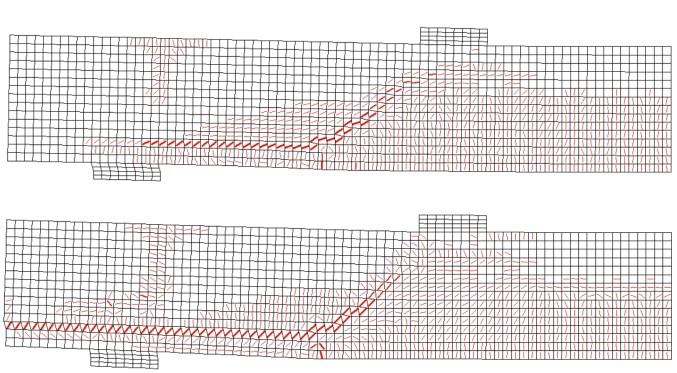

Figure 5.2-5:Schematic crack patterns at different load stages in reference beam.

In the strengthened beams, with increasing the longitudinal reinforcement ratio, the behaviour tended to become brittle, and the shear failure was still presented. The strengthened beams exhibited a crack pattern more distributed than the reference beams. At first, the beam exhibited several flexural cracks in the bottom surface of the beam, and as the load increased, the flexural cracks developed toward the support. Despite the several flexural cracks, the beams failed suddenly due to the inclined crack. Figure 5.2-6 represents the typical crack patterns in strengthened beams that presented the shear failure. It can be observed that the beams showed several flexural cracks, diagonal cracks, and some concrete crushing at the top of the critical inclined cracks. Moreover, an extensive crack due to splitting along the longitudinal bars can be observed.

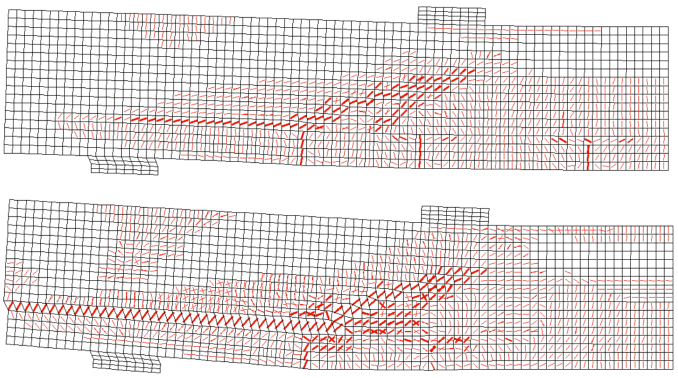

Figure 5.2-6: Schematic crack patterns at different load stages in strengthened beam that presented shear failure.

Increasing the UHPFRC thickness (up to 50 mm) brought all beams strengthened with the UHPFRC jacket to a flexure failure. The response in Figure 5.2-4 shows a yielding plateau in the shear-deflection curve, and the peak load is reached at approximately midway of the plateau. The plateau was due to the yielding of the longitudinal reinforcement. The response of the beams having ρ =2.1% and ρ =2.4%

shows a short yielding plateau with respect to the response of the beams having a lower reinforcement ratio. Prior to yielding, the beams exhibited several inclined cracks that spread over the shear span. In fact, despite the ductile response, the beams presented limited shear effects (diagonal cracks). Nonetheless, the UHPFRC layer was able to provide sufficient shear capacity and consequently change the collapse from shear to bending.

Figure 5.2-7 illustrates the typical crack patterns in the strengthened beam where the flexural failure was present. Different from the reference beams, the strengthened beams exhibited a widely distributed crack patterns prior to a complete failure.

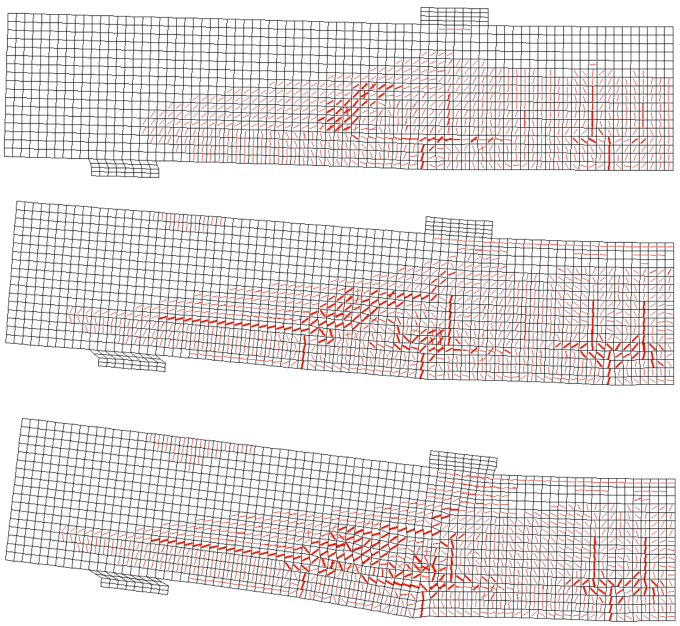

Figure 5.2-7: Schematic crack patterns at different load stages in strengthened beam.

Figure 5.2-8 shows a summary of results of the shear capacities of the reference (NN) and retrofitted (NF) beams for five shear span-to-effective depth ratios (a/d = 2.5, 3.0, 3.5, 4.0, and 4.5).

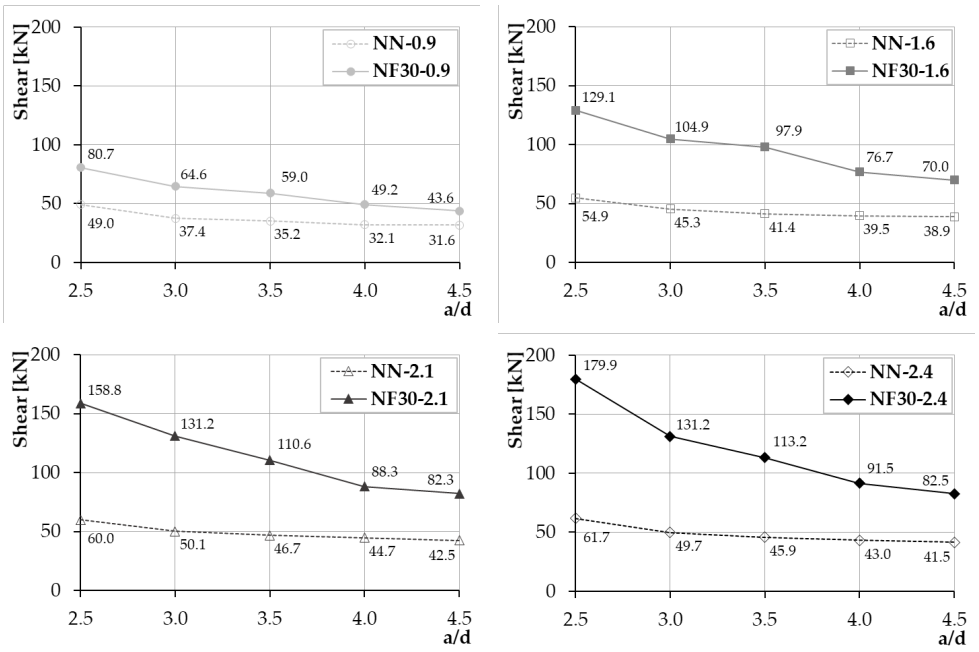

Figure 5.2-8: Summary results of shear capacities of the reference beams (NN) and retrofitted beams (NF).

The 3D plots of the valley of shear diagonal failure ($M_u/M_{u,fl}$ versus a/d ratio), as a function of the reinforcement ratio, are illustrated in Figure 5.2-9.

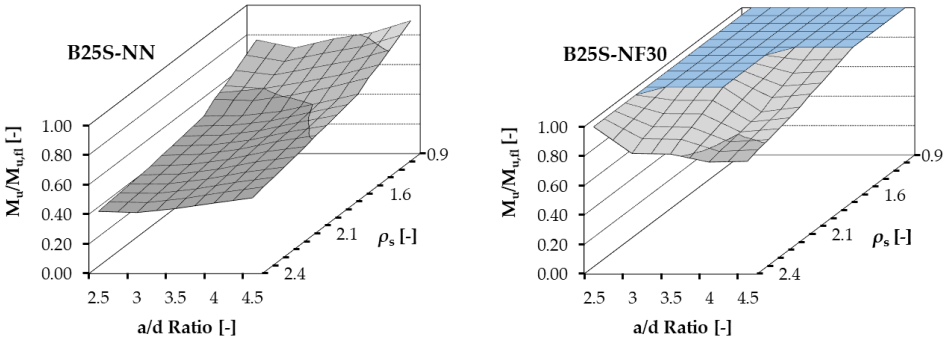

Figure 5.2-9: Influence of the longitudinal reinforcement ratio on the valley of shear failure.

Table 5.2-5 summarizes the value of $M_u/M_{u,fl}$ obtained from the set of the numerical analyses performed on models of B25S series.

a/d	ρ =0.9%		ρ =1.6%		ρ =2.1%		ρ =2.4%	
	NN	NF30	NN	NF30	NN	NF30	NN	NF30
2.5	0.77	1.00	0.52	1.00	0.46	1.00	0.42	1.00
3.0	0.71	1.00	0.52	1.00	0.46	1.00	0.41	0.82
3.5	0.77	1.00	0.55	1.00	0.50	1.00	0.44	0.81
4.0	0.81	1.00	0.61	1.00	0.55	0.83	0.48	0.76
4.5	0.89	1.00	0.67	1.00	0.59	0.86	0.51	0.77
$M_{u,fl}$ **[kN]**	41	58	67	89	84	111	94	125

Table 5.2-5: Values of $M_u/M_{u,fl}$ obtained from the numerical analyses of models of B25S series.

As mentioned above, the reference beams showed a regime of shear failure for all ranges of *a*/*d* and longitudinal reinforcement ratios. In the strengthened beams, with increasing the longitudinal reinforcement ratio, the valley of diagonal shear failure tended to become deeper. The NF-beams having ρ =2.1% and ρ =2.4% showed a limited regime of shear failure, while for the longitudinal reinforcement ratio 0.9% and 1.6% the valley of shear diagonal failure disappeared completely. However, reinforcement ratios higher than 1.6% are generally not used in practical applications. From the graphs above reported, it is clear that the UHPFRC jacketing improves the shear resistance reducing the brittleness of elements by forcing a flexure failure rather than an early shear failure. When the retrofitted beam still showed a shear failure, the thickness was increased up to 50 mm.
The values of peak load, shear strength, ultimate shear stress, and normalized ultimate shear stress are reported in Table 5.2-6 for each member.

Beam type	P_{max} **[kN]**	**V [kN]**	v_u **[MPa]**	$\frac{v_u}{\sqrt{f_c}}$	**Failure mode**	**Reinf. yielded**
a/d=2.5						
B25S-NN-0.9	98.0	49.0	1.26	0.25	S	No
B25S-NF30-0.9	161.4	80.7	2.07	0.41	F	Yes
B25S-NN-1.6	109.7	54.9	1.41	0.28	S	No
B25S-NF30-1.6	258.2	129.1	3.31	0.66	F	Yes
B25S-NN-2.1	120.1	60.0	1.54	0.31	S	No
B25S-NF30-2.1	317.6	158.8	4.07	0.81	F	Yes
B25S-NN-2.4	123.3	61.7	1.58	0.32	S	No
B25S-NF30-2.4	359.9	179.9	4.61	0.92	F	Yes

Table 5.2-6 (Pt. 1 of 3)

a/d=3.0						
B25S-NN-0.9	74.8	37.4	0.96	0.19	S	No
B25S-NF30-0.9	129.3	64.6	1.66	0.33	F	Yes
B25S-NN-1.6	90.6	45.3	1.16	0.23	S	No
B25S-NF30-1.6	209.8	104.9	2.69	0.54	F	Yes
B25S-NN-2.1	100.3	50.1	1.29	0.26	S	No
B25S-NF30-2.1	262.3	131.2	3.36	0.67	F	Yes
B25S-NN-2.4	99.4	49.7	1.27	0.25	S	No
B25S-NF30-2.4	262.5	131.3	3.37	0.67	S	No
B25S-NF40-2.4	300.9	150.5	3.86	0.77	F	Yes
a/d=3.5						
B25S-NN-0.9	70.4	35.2	0.90	0.18	S	No
B25S-NF30-0.9	118.0	59.00	1.51	0.30	F	Yes
B25S-NN-1.6	82.9	41.4	1.06	0.21	S	No
B25S-NF30-1.6	195.7	97.9	2.51	0.50	F	Yes
B25S-NN-2.1	93.4	46.7	1.20	0.24	S	No
B25S-NF30-2.1	221.2	110.6	2.84	0.57	S	Yes
B25S-NF40-2.1	234.4	117.2	3.00	0.60	F	Yes
B25S-NN-2.4	91.7	45.9	1.18	0.24	S	No
B25S-NF30-2.4	226.5	113.2	2.90	0.58	S	No
B25S-NF40-2.4	253.7	126.8	3.25	0.65	S	Yes
B25S-NF50-2.4	273.8	136.9	3.51	0.70	F	Yes
a/d=4.0						
B25S-NN-0.9	64.2	32.1	0.82	0.16	S	No
B25S-NF30-0.9	98.4	49.2	1.26	0.25	F	Yes
B25S-NN-1.6	79.0	39.5	1.01	0.20	S	No
B25S-NF30-1.6	153.3	76.7	1.97	0.39	F	Yes
B25S-NN-2.1	89.4	44.7	1.15	0.23	S	No
B25S-NF30-2.1	176.6	88.3	2.26	0.45	S	No
B25S-NF40-2.1	199.4	99.7	2.56	0.51	F	Yes
B25S-NF50-2.1	211.3	105.6	2.71	0.54	F	Yes
B25S-NN-2.4	86.1	43.1	1.10	0.22	S	No
B25S-NF30-2.4	182.9	91.5	2.35	0.47	S	No
B25S-NF40-2.4	218.6	109.3	2.80	0.56	S	No
B25S-NF50-2.4	236.1	118.0	3.03	0.61	F	Yes

Table 5.2-6 (Pt. 2 of 3)

a/d=4.5						
B25S-NN-0.9	63.2	31.6	0.81	0.16	S	No
B25S-NF30-0.9	87.3	43.6	1.12	0.22	F	Yes
B25S-NN-1.6	77.8	38.9	1.00	0.20	S	No
B25S-NF30-1.6	140.0	70.0	1.79	0.36	F	Yes
B25S-NN-2.1	85.0	42.5	1.09	0.22	S	No
B25S-NF30-2.1	164.7	82.3	2.11	0.42	S	No
B25S-NF40-2.1	180.7	90.4	2.32	0.46	F	Yes
B25S-NN-2.4	82.9	41.5	1.06	0.21	S	No
B25S-NF30-2.4	165.1	82.5	2.12	0.42	S	No
B25S-NF40-2.4	185.8	92.9	2.38	0.48	S	No
B25S-NF50-2.4	205.5	102.7	2.63	0.53	F	Yes

Notes: - Notation for failure modes: S: Shear; and F: Flexural.
(Pt. 3 of 3)
Table 5.2-6: Summary of finite element analysis results.

In some cases the UHPFRC layer equal to 30 mm was not enough, and the retrofitted beam still showed a shear failure. In particular, this was true for beams having a/d=3 (in case of ρ=2.4%), and for beams having a/d=3.5, 4, and 4.5 (in case of ρ=2.1% and ρ 2.4%). Increasing the UHPFRC thickness, all beams strengthened with the UHPFRC jacket exhibited a flexure failure, with limited shear effects. FE analyses demonstrated the effect that the UHPFRC jackets have on the failure mode, as well as on the post-cracking behaviour, and on the formation and evolution of cracks.
To investigate the suitability of the hypothesis of perfect bond conditions, the shear stresses were plotted. The shear stresses were analysed at the peak load, and at the distance d from the support.
Figure 5.2-10 represents the numerical shear stress at the interface between the substrate and the UHPFRC layer in the beams having a/d=3. In the B25S beams having different shear spans, the shear stresses were nearly the same. For this reason, only typical curves were plotted.

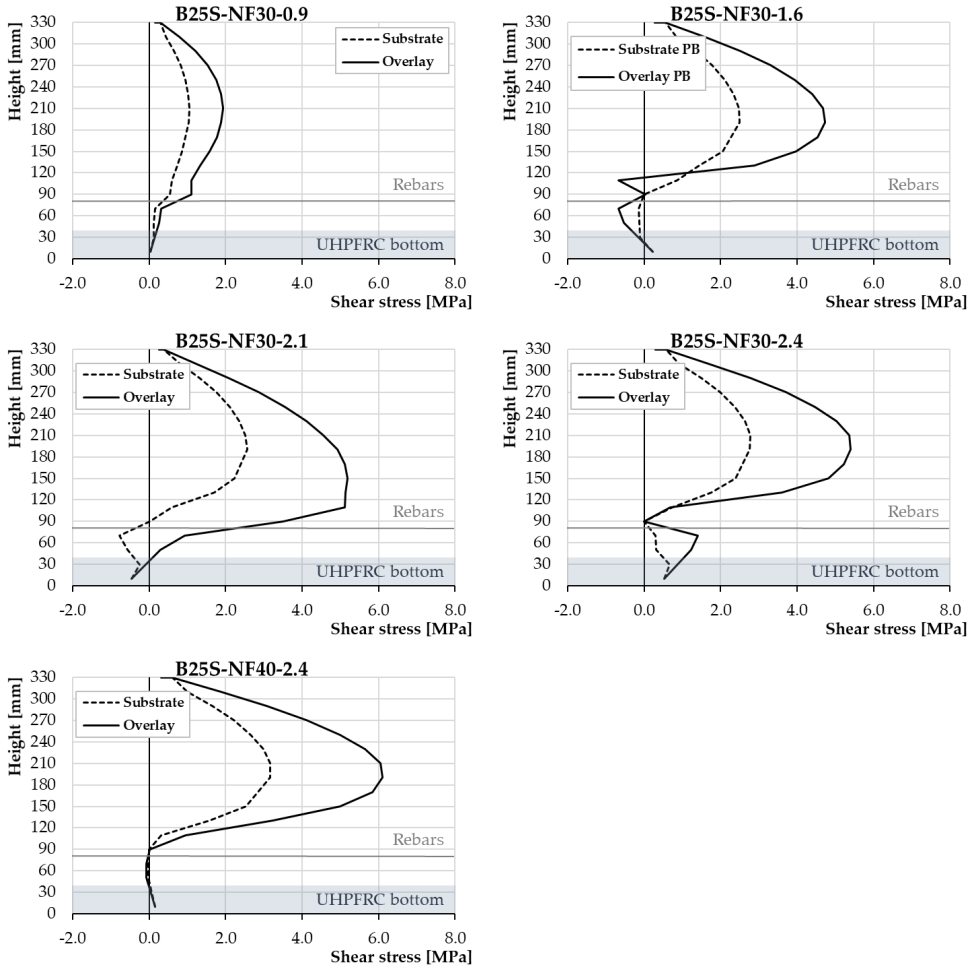

Note: In the graphs, the thickness of UHPFRC layer and the level of rebars are reported.
Figure 5.2-10: Shear stress at the interface between substrate and UHPFRC layer.

It is reasonable to consider that, after the formation of cracks, due to the attainment of the tensile strength of concrete, a retribution of the stresses arises, resulting in a decay of the intensity of shear stresses in the cracked region and an increase in the uncracked portion of the section with respect to the parabolic distribution in a uncracked region.
In the overlay, the shear stresses were greater than the shear stresses observed in the substrate concrete. Moreover, it can be noted that the shear stresses increase with increasing longitudinal reinforcement ratio.
In the UHPFRC, the shear stresses exceeded the maximum shear stresses measured during the bond test (presented in Section 4.2). It is necessary to remember that the shear stresses obtained from the bond test represent a lower bound of the bond

strength at the interface. In fact, the failure always appears localized partly or, in some cases, completely in the substrate.
Referring to the bond test results, for substrate concrete C20/25 and overlay HPF46, the maximum shear stress recorded at the interface was 4.3 MPa.
Considering that in some cases the shear stresses were greater than 4.3 MPa, a modelling of the strengthened beams that did not assume the perfect bond was undertaken. The interface between the substrate concrete and overlay was modelled using bond elements. In VecTor2, the link elements were used to model bond behaviour across composite surfaces. The interface or bonded plates/fabrics reference type was chosen. The stress-slip relationship was obtained by a shear bond test presented in Section 4.2. Despite the concrete compressive strength in the beams being different with respect to specimens used for the shear bond test, it was decided to use the bond test experimental results. This is reasonable as, in the shear bond test, it was observed that there was an increase in shear stress with an increase in substrate compressive strength. Therefore, using the bond experimental values corresponding to substate C20/25 (see Chapter 4), the stress-slip relationship should be underestimated. Moreover, the shear stresses do not represent the failure shear bond but a lower bound. Considering these observations, further investigations on substrate characterized by compressive strength higher should be necessary.
Figure 5.2-11 schematics the interface element between the two materials: RC concrete and UHPFRC.
Figure 5.2-12 gives the comparison between the responses obtained considering the perfect bond (PB) conditions and using bond elements (IE).

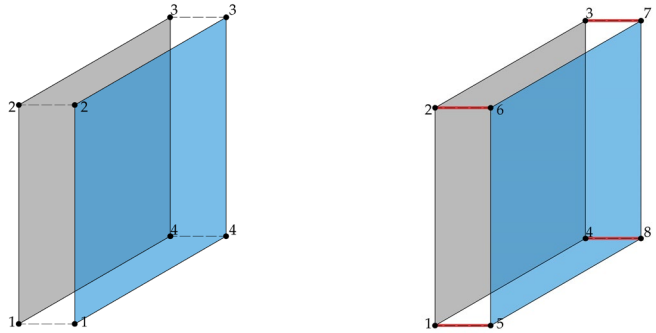

a) *b)*

Figure 5.2-11: Bond conditions assumed in VecTor2: a) perfect bond conditions, b) interface bond elements.

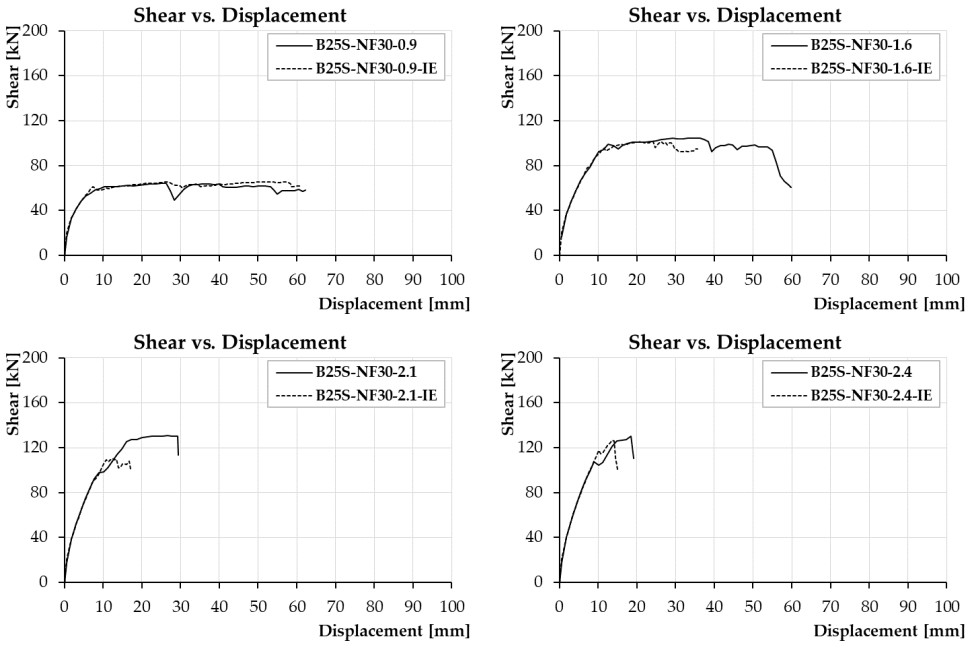

Figure 5.2-12: Comparison between shear vs. mid-span deflection curves obtained from model-PB and model-IE.

Based on the comparison between PB-model and IE-model, it can be noted that in the beam having ρ=0.9% the two models present the same response. This is reasonable due to the shear stresses being lower than the ultimate shear stresses measured in the shear test. Differently, in the beam having ρ higher than 0.9%, the behaviour changed. In the B25-NF30-1.6 and B25S-NF-30-2.4 models, the peak load remained unchanged, while the ductility decreased. This can be caused by the high shear stresses at the interface between the substrate and overlay. The IE-responses changed with respect to PB-responses when the maximum shear stress achieved 5.01 MPa and 5.39 MPa, respectably for B25-NF30-1.6 and B25S-NF-30-2.4. In the B25-NF30-2.1 model, the maximum shear stress was 5.19 MPa: in this case, both peak load and ductility decreased.

5.2.3.2 B50S

The response of the B50S beams, having an equal reinforcement ratio, was nearly the same to each other, so a typical behaviour is described below in a single paragraph. Figure 5.2-13 represents the typical *shear vs. mid-span deflection* curves for small beams (*a)* ρ=0.9%, *b)* ρ=1.6%, *c)* ρ=2.1%, *d)* ρ=2.4%).

a)

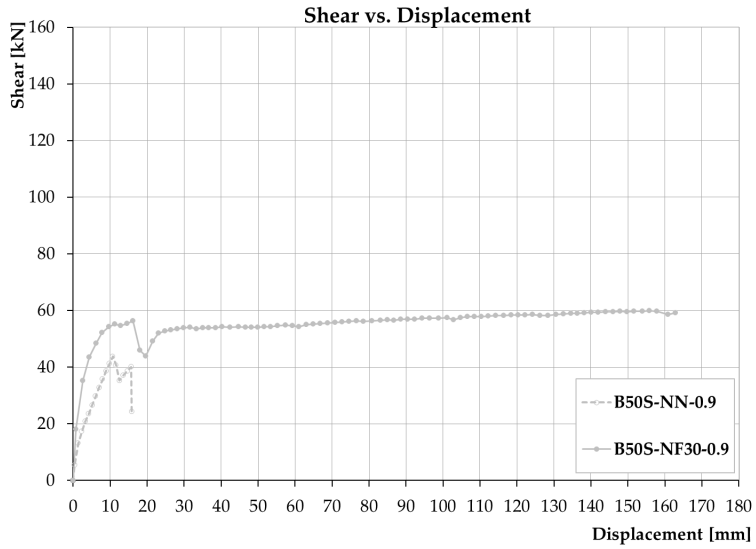

b)

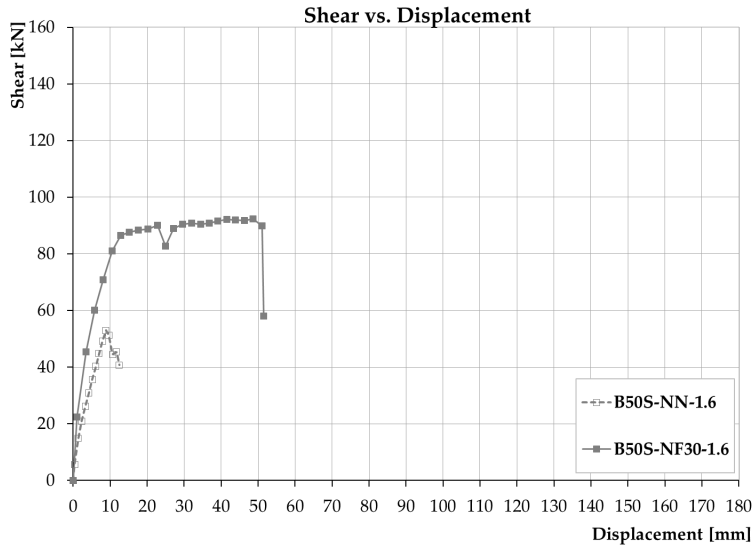

Figure 5.2-13 (Pt. 1 of 2)

c)

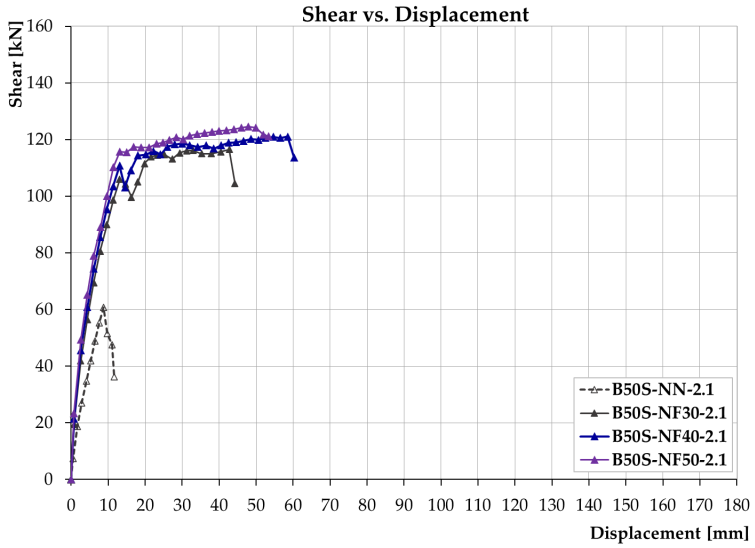

d)

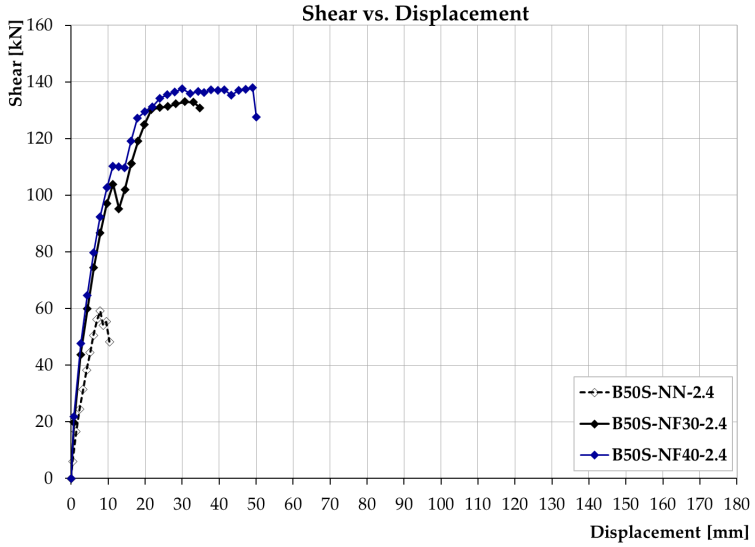

(Pt. 2 of 2)

Figure 5.2-13: Typical shear vs. mid-span deflection curves for B50S specimens.

As also observed in B25S beams, all reference B50S beams presented a shear failure mechanism. The beams had a brittle response, and the failure reached quickly after the peak load. The crack pattern of B50S-NN beams was similar to that in B25S-NN beams. Flexural cracks first developed from the bottom surface of the beam, where the maximum moment occurred. Later, increasing the load, the flexural cracks spread out toward the support. When the load was sufficient to impose a diagonal tension greater than the concrete tensile strength, an inclined crack appeared in the span

between load points and support. This crack caused the sudden failure of the beam. Figure 5.2-14 shows the diagonal crack and the crack which propagated along the top layer of the longitudinal bars in tension.
In the strengthened beams with a longitudinal reinforcement ratio higher than 2.4%, the beams still showed a shear failure. In these cases, the thickness of the UHPFRC was increased up to 50 mm, and the beams showed a ductile behaviour. The yielding of the longitudinal reinforcement led to a yielding plateau on the shear versus deflection curve. The peak was reached at approximately midway of the plateau.

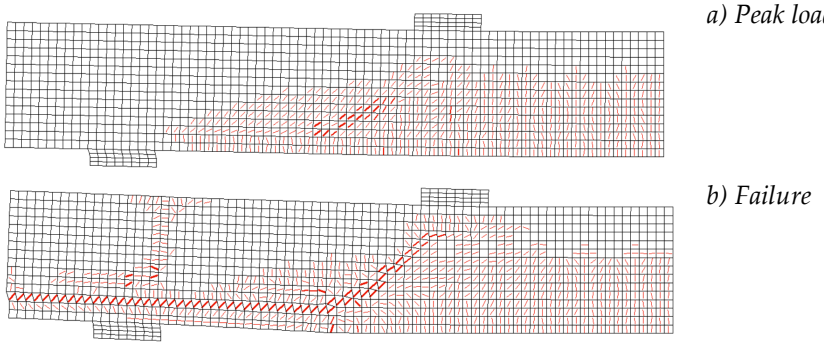

Figure 5.2-14:Schematic crack patterns at different load stages in reference beam.

Figure 5.2-15 reports the typical crack patterns in the strengthened beam where the flexural failure was presented. Compared with the B25S beams, the B50 beams showed a larger number of flexural cracks. In spite of the ductile response, the beams presented some inclined cracks in the shear span and below the loading point, but the fibres were able to provide sufficient shear capacity and therefore alter the collapse from shear to bending.
It should be said that in the NF beams with a reinforcement ratio of 0.9%, the shear effect was limited. Figure 5.2-7 illustrates the typical crack patterns in the strengthened beam where the flexural failure was presented. Different from reference beams, the strengthened beams exhibited a widely distributed crack pattern prior to a complete failure.

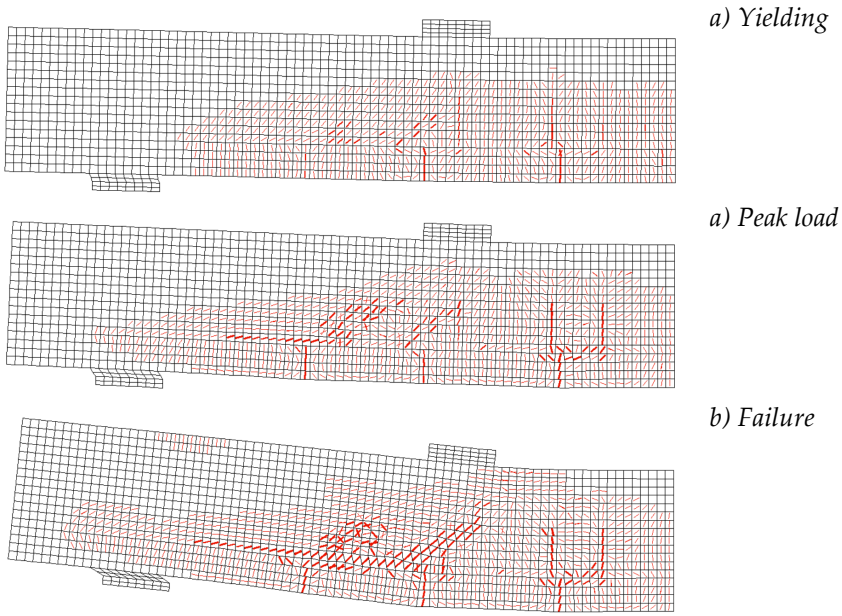

Figure 5.2-15: Schematic crack patterns at different load stages in strengthened beam.

Shear capacities results of the reference (NN) and retrofitted (NF) beams for five shear span-to-effective depth ratios are presented in Figure 5.2-16.
Figure 5.2-17 illustrates the plot of Kani's valley for each model, as a function of the longitudinal reinforcement ratio.

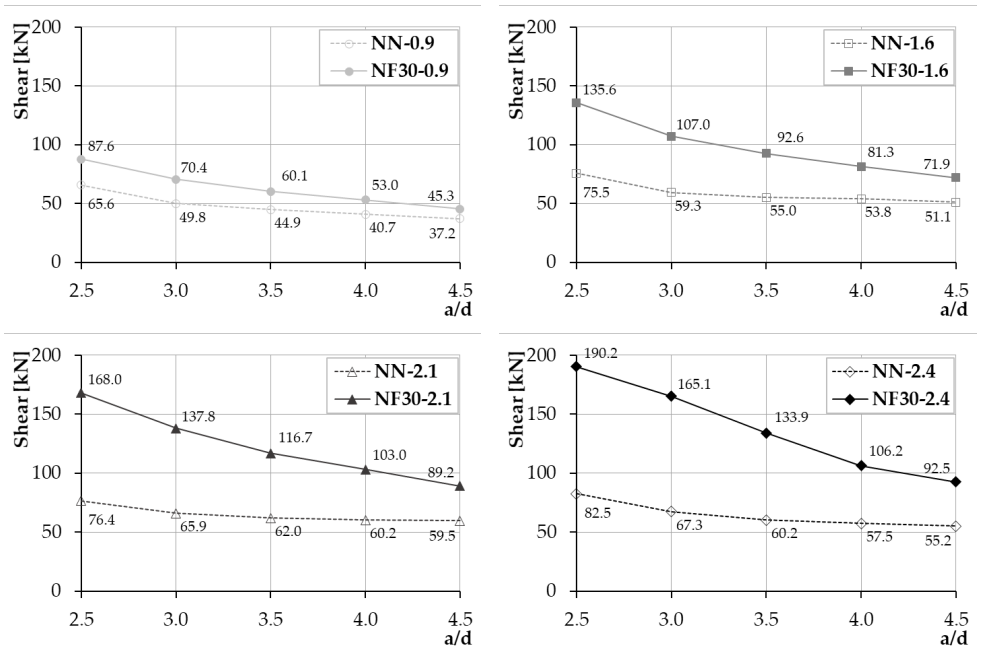

Figure 5.2-16: Summary results of shear capacities of the reference beams (NN) and retrofitted beams (NF).

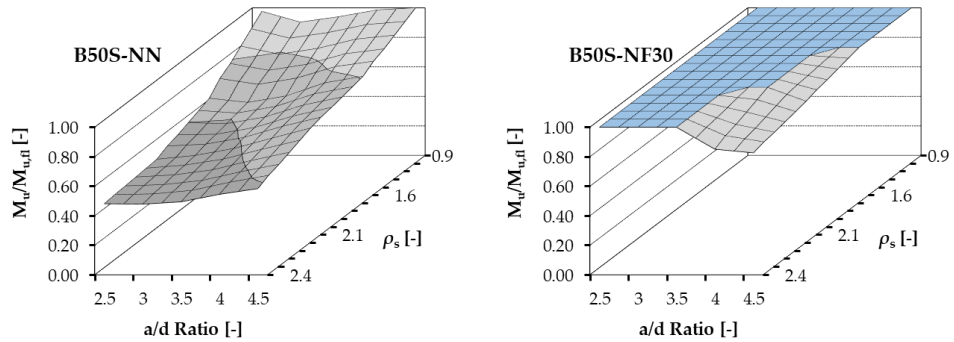

Figure 5.2-17: Influence of the longitudinal reinforcement ratio on the valley of shear failure.

Table 5.2-7 lists the value of $M_u/M_{u,fl}$ obtained from the set of the numerical analyses performed on models of the B50S series.

a/d	ρ=0.9%		ρ=1.6%		ρ=2.1%		ρ =2.4%	
	NN	NF30	NN	NF30	NN	NF30	NN	NF30
2.5	0.98	1.00	0.66	1.00	0.51	1.00	0.48	1.00
3.0	0.90	1.00	0.63	1.00	0.54	1.00	0.48	1.00
3.5	0.94	1.00	0.67	1.00	0.59	1.00	0.49	1.00
4.0	0.99	1.00	0.76	1.00	0.66	1.00	0.55	0.85
4.5	1.00	1.00	0.80	1.00	0.72	0.91	0.58	0.83
$M_{u,fl}$ [kN]	43	59	74	91	95	114	110	130

Table 5.2-7: Values of $M_u/M_{u,fl}$ obtained from the numerical analyses of models of B50S series.

As observed in the B25 series, the reference beams exhibited a regime of shear failure for all ranges of *a*/*d* and longitudinal reinforcement ratios.
In the strengthened beams, the valley of diagonal shear failure deepened with increasing longitudinal reinforcement ratio. In the NF models with the highest reinforcement ratio, the shear failure occurred, while for model NF-0.9 and NF-1.6, the shear failure did not appear for any value of *a*/*d*.
From the graphs above reported, it can be observed that the UHPFRC jacketing improved the shear resistance reducing the brittleness of elements by forcing a flexural failure rather than an early shear failure.
For values of *a*/*d*=3.5, 4, and 4.5, the retrofitted beam in the case of ρ=2.1% and ρ=2.4% still showed a shear failure. In these cases, the thickness was increased (up to 50 mm).
Table 5.2-8 provides the values of peak load, shear strength, ultimate shear stress, and normalized ultimate shear stress for each beam.

Beam type	P_{max} [kN]	V [kN]	v_u [MPa]	$\frac{v_u}{\sqrt{f_c}}$	Failure mode	Reinf. yielded
a/d=2.5						
B50S-NN-0.9	131.1	65.6	1.68	0.24	S	No
B50S-NF30-0.9	175.2	87.6	2.25	0.32	F	Yes
B50S-NN-1.6	151.0	75.5	1.94	0.27	S	No
B50S-NF30-1.6	271.3	135.6	3.48	0.49	F	Yes
B50S-NN-2.1	152.9	76.4	1.96	0.28	S	No
B50S-NF30-2.1	336.1	168.0	4.31	0.61	F	Yes
B50S-NN-2.4	164.9	82.5	2.11	0.30	S	No
B50S-NF30-2.4	380.4	190.2	4.88	0.69	F	Yes
a/d=3.0						
B50S-NN-0.9	99.5	49.8	1.28	0.18	S	No
B50S-NF30-0.9	140.9	70.4	1.81	0.26	F	Yes
B50S-NN-1.6	118.5	59.3	1.52	0.21	S	No
B50S-NF30-1.6	213.9	107.0	2.74	0.39	F	Yes
B50S-NN-2.1	131.7	65.9	1.69	0.24	S	No
B50S-NF30-2.1	275.7	137.8	3.53	0.50	F	Yes
B50S-NN-2.4	134.5	67.3	1.72	0.24	S	No
B50S-NF30-2.4	330.3	165.1	4.23	0.60	F	Yes

Table 5.2-8 (Pt. 1 of 2)

a/d=3.5						
B50S-NN-0.9	89.8	44.9	1.15	0.16	S	No
B50S-NF30-0.9	120.2	60.1	1.54	0.22	F	Yes
B50S-NN-1.6	109.9	55.0	1.41	0.20	S	No
B50S-NF30-1.6	185.1	92.6	2.37	0.34	F	Yes
B50S-NN-2.1	124.1	62.0	1.59	0.23	S	No
B50S-NF30-2.1	233.4	116.7	2.99	0.42	S	Yes
B50S-NF40-2.1	242.9	121.5	3.11	0.44	S	Yes
B50S-NF50-2.1	249.6	124.8	3.20	0.45	F	Yes
B50S-NN-2.4	120.4	60.2	1.54	0.22	S	No
B50S-NF30-2.4	267.8	133.9	3.43	0.49	S	Yes
B50S-NF40-2.4	276.4	138.2	3.54	0.50	F	Yes
a/d=4.0						
B50S-NN-0.9	81.5	40.7	1.04	0.15	S	No
B50S-NF30-0.9	106.0	53.0	1.36	0.19	F	Yes
B50S-NN-1.6	107.6	53.8	1.38	0.20	S	No
B50S-NF30-1.6	162.5	81.3	2.08	0.29	F	Yes
B50S-NN-2.1	120.3	60.2	1.54	0.22	S	No
B50S-NF30-2.1	206.0	103.0	2.64	0.37	F	Yes
B50S-NN-2.4	114.9	57.5	1.47	0.21	S	No
B50S-NF30-2.4	212.4	106.2	2.72	0.39	S	No
B50S-NF40-2.5	239.0	119.5	3.06	0.43	F	Yes
a/d=4.5						
B50S-NN-0.9	74.3	37.2	0.95	0.13	S	No
B50S-NF30-0.9	90.5	45.3	1.16	0.16	F	Yes
B50S-NN-1.6	102.1	51.1	1.31	0.19	S	No
B50S-NF30-1.6	143.8	71.9	1.84	0.26	F	Yes
B50S-NN-2.1	119.0	59.5	1.53	0.22	S	No
B50S-NF30-2.1	178.4	89.2	2.29	0.32	F	Yes
B50S-NN-2.4	110.4	55.2	1.42	0.20	S	No
B50S-NF30-2.4	184.9	92.5	2.37	0.34	S	No
B50S-NF40-2.4	202.0	101.0	2.59	0.37	S	No
B50S-NF50-2.4	213.0	106.5	2.73	0.39	F/S	Yes

Notes: - Notation for failure modes: S: Shear; and F: Flexural.
(Pt. 2 of 2)
Table 5.2-8: Summary of finite element analysis results.

Increasing the thickness, all beams strengthened with the UHPFRC jacket exhibited a flexure failure (with limited shear effects). FE analyses demonstrated that the UHPFRC jackets have on the failure mode, as well as on the post-cracking behaviour and on the formation and evolution of cracks.

For the B25S and B50S series beam, the shear stresses were plotted. The shear stresses were analysed at the peak load, and at the distance d from the support.

Figure 5.2-23 represents the numerical shear stresses at the interface between the substrate and the UHPFRC layer in the beams having a/d=3. In the B50S beams having different shear spans, the shear stresses were nearly the same. For that series, only the typical curves were reported.

The shear stresses have the same distribution observed in B25S beams. In the overlay, the shear stresses were greater than the shear stresses observed in the substrate concrete. Moreover, it can be noted that the shear stresses increase with increasing longitudinal reinforcement ratio.

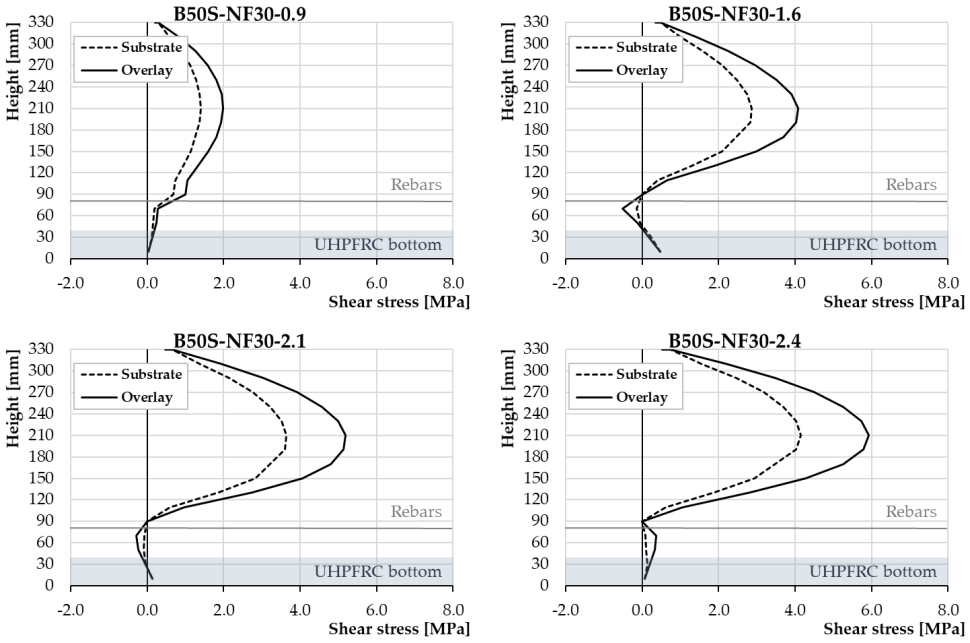

Note: in the graphs, the thickness of UHPFRC layer and the level of rebars are reported.
Figure 5.2-18: Shear stress at the interface between substrate and UHPFRC layer.

As observed in B25S beams, in some cases, in the UHPFRC, the shear stresses exceeded the maximum shear stresses measured during the bond test (presented in Section 4.2). However, assuming a longitudinal reinforcement ratio of 0.9 and 1.6, the shear stresses were lower than the ultimate shear stresses measured in the bond test. The shear stresses observed in B50S were lower than the shear stresses recorded in the B25S beams. Therefore, increasing the concrete compressive strength, the shear stresses decrease.

As with previous beams, analyses were performed of strengthened beams that did not assume the perfect bond condition.

Figure 5.2-19 provides the comparison between the responses obtained considering perfect bond (PB) conditions and using bond elements (IE).

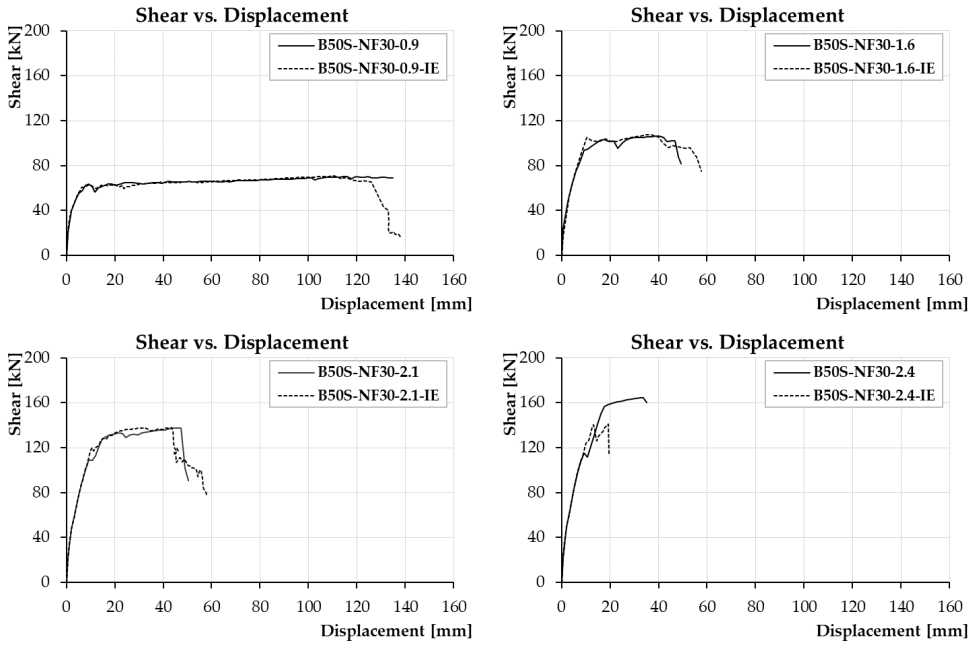

Figure 5.2-19: Comparison between shear vs. mid-span deflection curves obtained from model-PB and model-IE.

Based on the comparison between the PB-model and the IE-model, it can be observed that in the beam having ρ=0.9%, ρ=1.6%, and ρ=2.1% the models have nearly identical responses, despite that in some cases the shear stresses were higher than the ultimate shear stresses measured in the shear test. Considering the results above presented and the results obtained for B25S beams, it can be further conformed that the influence of the substrate compressive strength could be a parameter that affects the shear bond stress. To confirm this, further shear bond tests should be conducted on substrates with higher compressive strength.

5.2.3.3 B70S

Compared with the previous beams, the B70S beams had nearly identical responses. Therefore, only the summary results are reported; further details of the curves are illustrated in Appendix D.

In Figure 5.2-20 summary results of the shear capacities of reference and retrofitted beams for five shear span-to-effective depth ratios are illustrated.

Figure 5.2-21 shows the 3D plots of the valley of shear diagonal failure as a function of the reinforcement ratio.

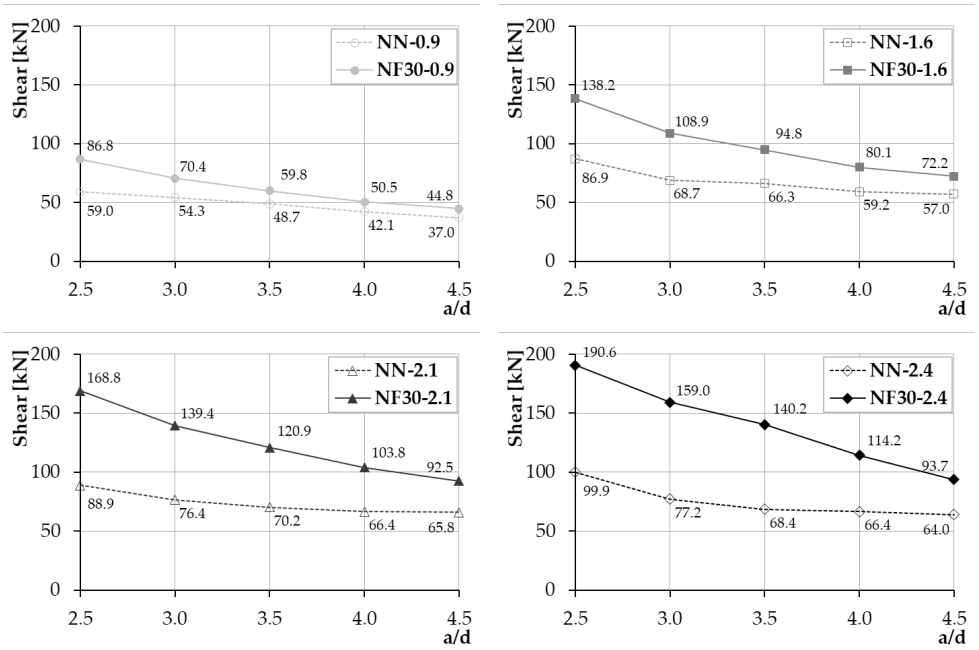

Figure 5.2-20: Summary results of shear capacities of the reference beams (NN) and retrofitted beams (NF).

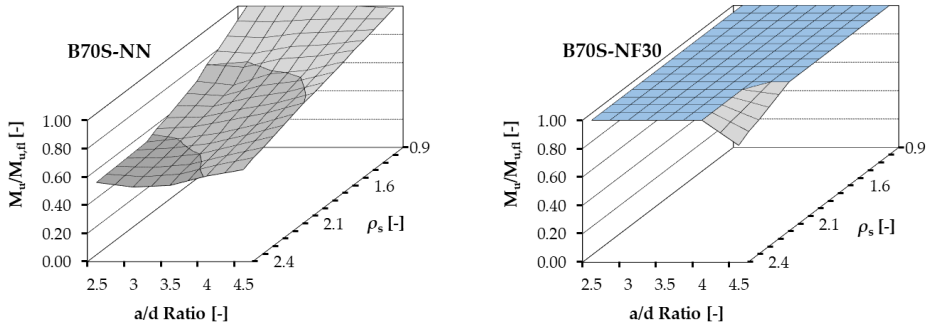

Figure 5.2-21: Influence of the longitudinal reinforcement ratio on the valley of shear failure.

Table 5.2-9 summarizes the value of $M_u/M_{u,fl}$ obtained from the set of the numerical analyses performed on models of the B70S series.

a/d	ρ=0.9%		ρ=1.6%		ρ=2.1%		ρ=2.4%	
	NN	NF	NN	NF	NN	NF	NN	NF
2.5	1.00	1.00	0.74	1.00	0.58	1.00	0.56	1.00
3.0	1.00	1.00	0.71	1.00	0.60	1.00	0.53	1.00
3.5	1.00	1.00	0.79	1.00	0.64	1.00	0.54	1.00
4.0	1.00	1.00	0.81	1.00	0.70	1.00	0.61	1.00
4.5	0.98	1.00	0.88	1.00	0.77	1.00	0.65	0.82
$M_{u,fl}$ **[kN]**	44	60	76	92	99	116	114	132

Table 5.2-9: Values of $M_u/M_{u,fl}$ obtained from the numerical analyses of models of B70S series.

The reference beams showed a regime of shear failure for all ranges of a/d and longitudinal reinforcement ratios, as observed in the previous series.
In the strengthened beams (except in case of a/d=4 and 4.5 with ρ=2.4%) the valley of shear diagonal failure disappeared completely.
From the graphs above, it can be observed that the UHPFRC jacketing improved the shear resistance reducing the brittleness of elements by forcing a flexural failure rather than an early shear failure.
For the value of a/d=4 and 4.5, the retrofitted beam in case of ρ= 2.4% still showed a shear failure. In B70S-NF40-2.4 beam with a/d=4, the reinforcement yielded but the beam exhibited a shear failure. In this case, the thickness was increased (up to 50 mm).
For each specimen, the values of peak load, shear strength, ultimate shear stress, and normalized ultimate shear stress are reported in Table 5.2-10.

Beam type	**P_{max} [kN]**	**V [kN]**	**v_u [MPa]**	**$\frac{v_u}{\sqrt{f_c}}$**	**Failure mode**	**Reinf. yielded**
a/d=2.5						
B70S-NN-0.9	118.0	59.0	1.51	0.18	S	Yes
B70S-NF30-0.9	173.6	86.8	2.23	0.27	F	Yes
B70S-NN-1.6	173.9	86.9	2.23	0.27	S	No
B70S-NF30-1.6	276.4	138.2	3.54	0.42	F	Yes
B70S-NN-2.1	177.8	88.9	2.28	0.27	S	No
B70S-NF30-2.1	337.6	168.8	4.33	0.52	F	Yes
B70S-NN-2.4	199.8	99.9	2.56	0.31	S	No
B70S-NF30-2.4	381.3	190.6	4.89	0.58	F	Yes

Table 5.2-10 (Pt. 1 of 2)

a/d=3.0						
B70S-NN-0.9	108.6	54.3	1.39	0.17	S	Yes
B70S-NF30-0.9	140.9	70.4	1.81	0.22	F	Yes
B70S-NN-1.6	137.4	68.7	1.76	0.21	S	No
B70S-NF30-1.6	217.8	108.9	2.79	0.33	F	Yes
B70S-NN-2.1	152.8	76.4	1.96	0.23	S	No
B70S-NF30-2.1	278.9	139.4	3.58	0.43	F	Yes
B70S-NN-2.4	154.3	77.2	1.98	0.24	S	No
B70S-NF30-2.4	318.1	159.0	4.08	0.49	F	Yes
a/d=3.5						
B70S-NN-0.9	97.4	48.7	1.25	0.15	S	Yes
B70S-NF30-0.9	119.6	59.8	1.53	0.18	F	Yes
B70S-NN-1.6	132.5	66.3	1.70	0.20	S	No
B70S-NF30-1.6	189.5	94.8	2.43	0.29	F	Yes
B70S-NN-2.1	140.4	70.2	1.80	0.22	S	No
B70S-NF30-2.1	241.7	120.9	3.10	0.37	F	Yes
B70S-NN-2.4	136.8	68.4	1.75	0.21	S	No
B70S-NF30-2.4	280.3	140.2	3.59	0.43	F	Yes
a/d=4.0						
B70S-NN-0.9	84.1	42.1	1.08	0.13	S	Yes
B70S-NF30-0.9	101.0	50.5	1.29	0.15	F	Yes
B70S-NN-1.6	118.3	59.2	1.52	0.18	S	No
B70S-NF30-1.6	160.1	80.1	2.05	0.25	F/S	Yes
B70S-NN-2.1	132.8	66.4	1.70	0.20	S	No
B70S-NF30-2.1	207.7	103.8	2.66	0.32	F/S	Yes
B70S-NN-2.4	132.8	66.4	1.70	0.20	S	No
B70S-NF30-2.4	228.3	114.2	2.93	0.35	S	Yes
B70S-NF40-2.4	239.7	119.9	3.07	0.37	F	Yes
a/d=4.5						
B70S-NN-0.9	74.0	37.0	0.95	0.11	S	No
B70S-NF30-0.9	89.6	44.8	1.15	0.14	F	Yes
B70S-NN-1.6	113.9	57.0	1.46	0.17	S	No
B70S-NF30-1.6	144.5	72.2	1.85	0.22	F	Yes
B70S-NN-2.1	131.6	65.8	1.69	0.20	S	No
B70S-NF30-2.1	185.0	92.5	2.37	0.28	F	Yes
B70S-NN-2.4	128.0	64.0	1.64	0.20	S	No
B70S-NF30-2.4	187.4	93.7	2.40	0.29	S	No
B70S-NF40-2.4	213.1	106.6	2.73	0.33	F	Yes

Notes: - Notation for failure modes: S: Shear; and F: Flexural.

(Pt. 2 of 2)

Table 5.2-10: Summary of finite element analysis results.

Increasing the thickness, the beams strengthened with the UHPFRC jacket exhibited a flexure failure. FE analyses demonstrated the effect that the UHPFRC jackets have on the failure mode, as well as on the post-cracking behaviour, and on the formation and evolution of cracks.
Also, in the B70S beams the shear stresses were considered; therefore, the B70S beams were modelled using bond elements at the interface.
Figure 5.2-27 shows the comparison between the response obtained considering the perfect bond (PB) conditions and using bond elements (IE).

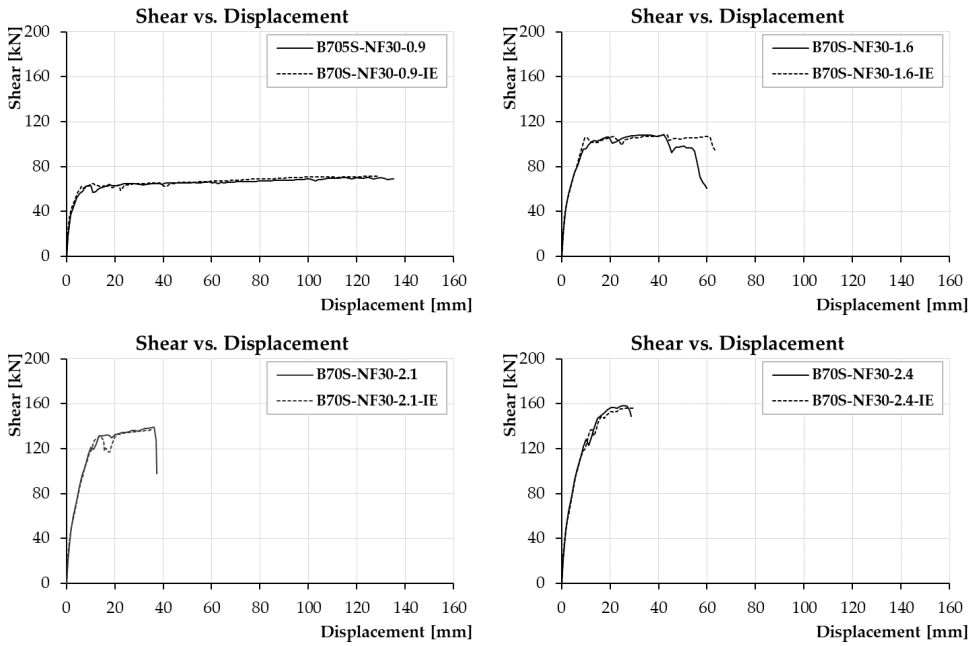

Figure 5.2-22: Comparison between shear vs. mid-span deflection curves obtained from model-PB and model-IE.

Based on the comparison between PB-model and IE-models, it can be observed that, all models have nearly identical responses each other, despite in some cases where the shear stresses were higher than the ultimate shear stresses measured in the shear test. This is reasonable and could confirm that the influence of the substrate compressive strength is important affecting the interface bond between substrate and overlay.

5.2.3.4 B25M

The responses of the B25M beams were nearly identical to each other; consequently, in the following, typical responses are presented and discussed.
The typical *shear vs. mid-span deflection* curves for the B25M specimens are shown in Figure 5.2-23. Each graph represents the behaviour of beams having different reinforcement ratios: *a)* 0.9%, *b)* 1.6%, *c)* 2.1%, and *d)* 2.4%.

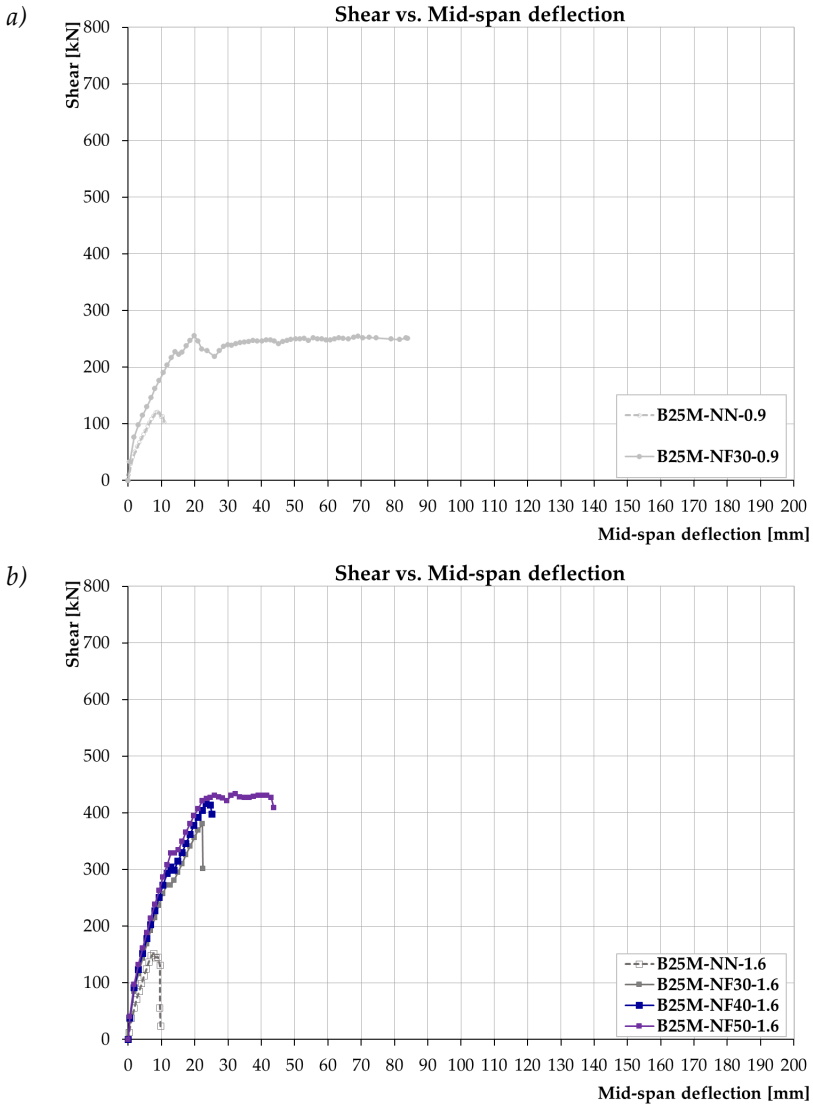

Figure 5.2-23 (Pt. 1 of 2)

c)

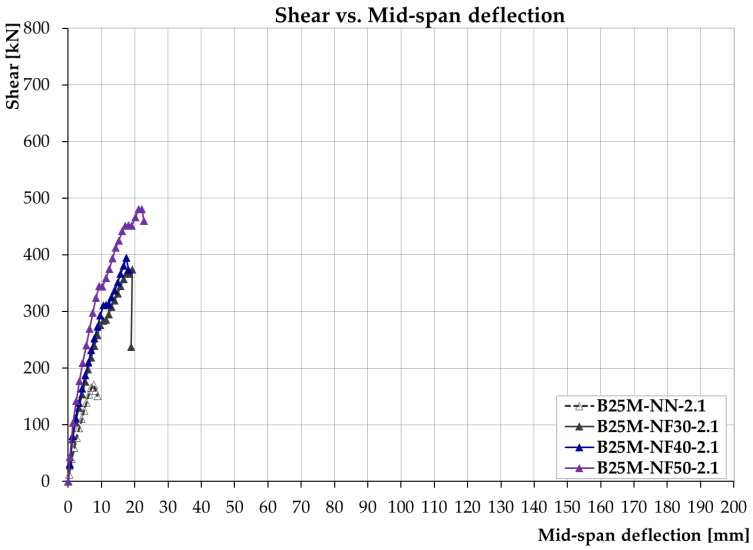

d)

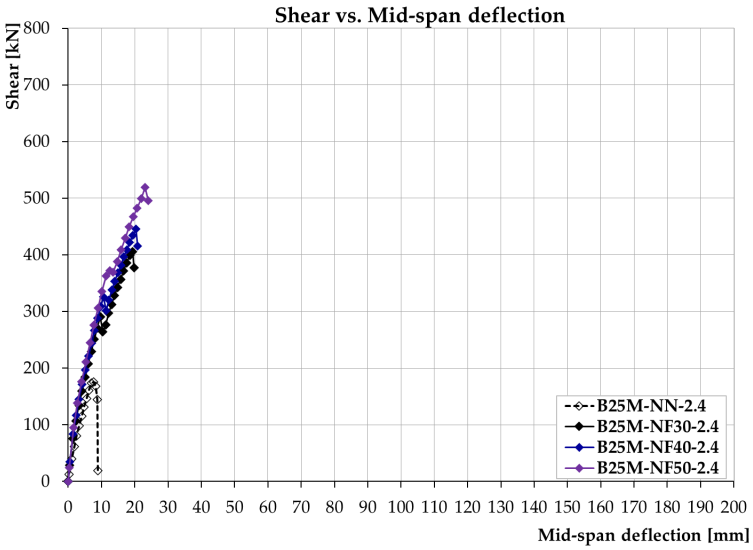

(Pt. 2 of 2)

Figure 5.2-23: Typical shear vs. mid-span deflection curves for B25M specimens.

The FE analyses showed that the reference beams were characterized by shear failure. The beams, independently of the reinforcement ratio, reached the peak load and they failed suddenly showing a brittle response. The crack patterns, illustrated in Figure 5.2-24, show that the reference beams failed owing to the wide diagonal crack that opened in the shear span. At first, flexural cracks developed in the bottom surface of the beams, where the bending moment was maximum. Increasing the load, the flexural cracks extended toward the support. When the concreate tensile strength

was exceeded, the shear-critical crack occurred, immediately followed by failure of the beam.

In the strengthened beams, with the longitudinal reinforcement ratio greater than 0.9%, the behaviour was brittle, and the shear failure was still present. Nonetheless, compared with the reference beams, the strengthened beams exhibited a crack pattern more distributed. Several flexural cracks developed on the bottom surface of the beams; increasing the applied load, the flexural cracks extended in the direction of the support. Despite the cracks being distributed, when the inclined crack occurred, a sudden failure was observed. Figure 5.2-25 represents the typical crack patterns in the strengthened beams that exhibited shear failure. It can be observed that the beams showed several flexural cracks, diagonal crack, and some concrete crushing at the top of the critical inclined cracks. Moreover, the critical diagonal crack progressed at the lower end along the reinforcing rebar causing splitting.

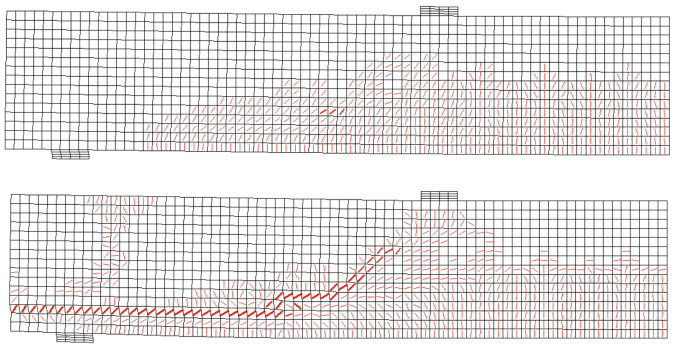

Figure 5.2-24:Schematic crack patterns at different load stages in reference beam.

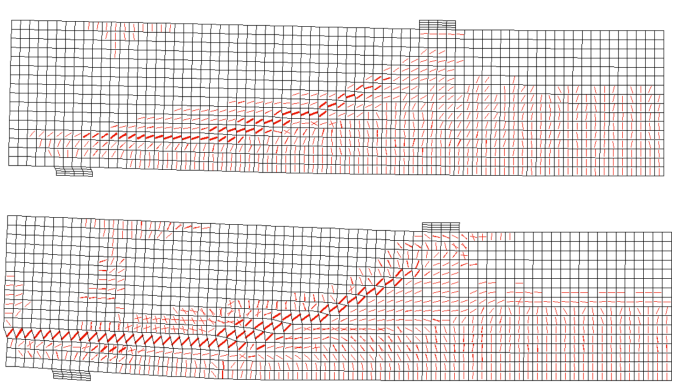

Figure 5.2-25: Schematic crack patterns at different load stages in strengthened beam that presented shear failure.

Increasing the thickness (up to 50 mm), only the strengthened beams having a reinforcement ratio of 0.9% presented a flexure failure. They exhibited a yielding plateau on the shear-deflection curve and the peak was reached at approximately midway along the plateau. Prior to yielding, the beams showed several inclined cracks that diffused in the shear span. In fact, despite the ductile response, the beams exhibited limited shear effects (diagonal cracks). Figure 5.1-26 illustrates the typical crack patterns in B25M-NF-0.9 where flexural failure was observed. Different from the reference beams, the strengthened beams exhibited a widely distributed crack pattern prior to a complete failure.

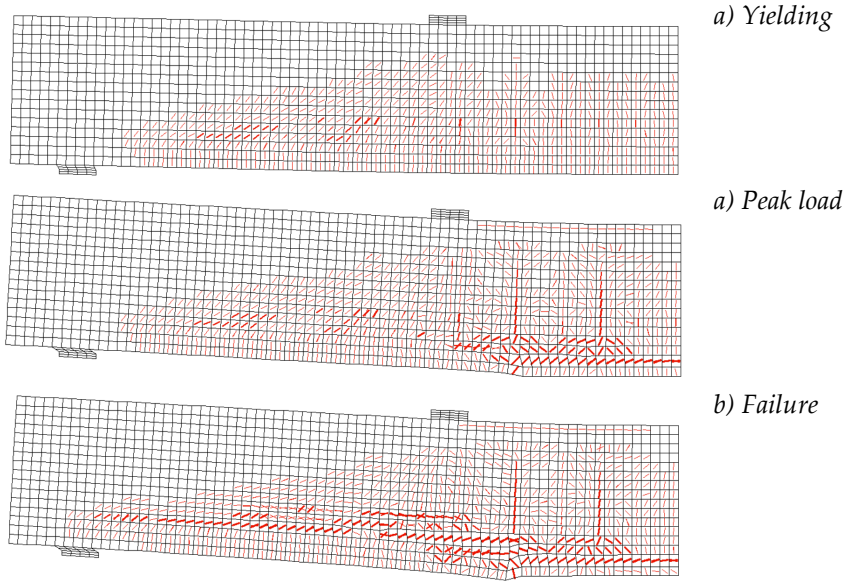

Figure 5.2-26: Schematic crack patterns at different load stages in strengthened beam.

When ductile response was not achieved, a steel mesh was embedded in the layer of UHPFRC. All beams reinforced with the UHPFRC jacket and steel mesh showed the same response; typical curves and representative crack patterns are reported in the following. From Figure 5.2-27, it can be noted that the responses of the beams with steel mesh were ductile. The shear-deflection curves show a clear yielding plateau due to the yielding of the reinforcement bars. After the peak load was achieved, the UHPFRC compressive strength was exceeded, and the beam strength dropped. Despite this, the failure did not occur. Nevertheless, when the load dropped more by 15% compared to the peak load, the following response was considered not structurally significant and, therefore, it was neglected.

a)

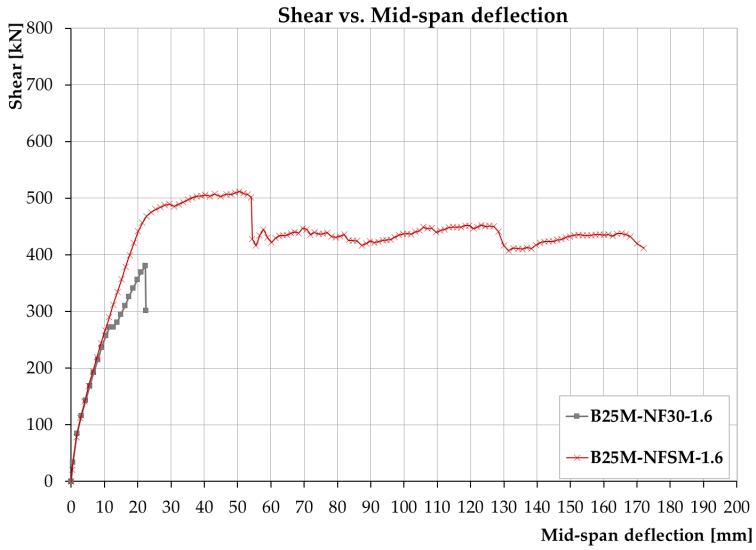

b)

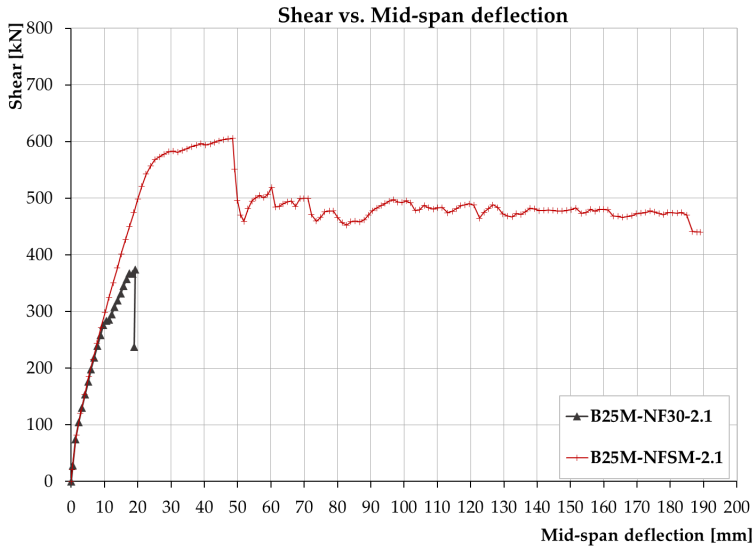

Figure 5.2-27 (Pt. 1 of 2)

c)

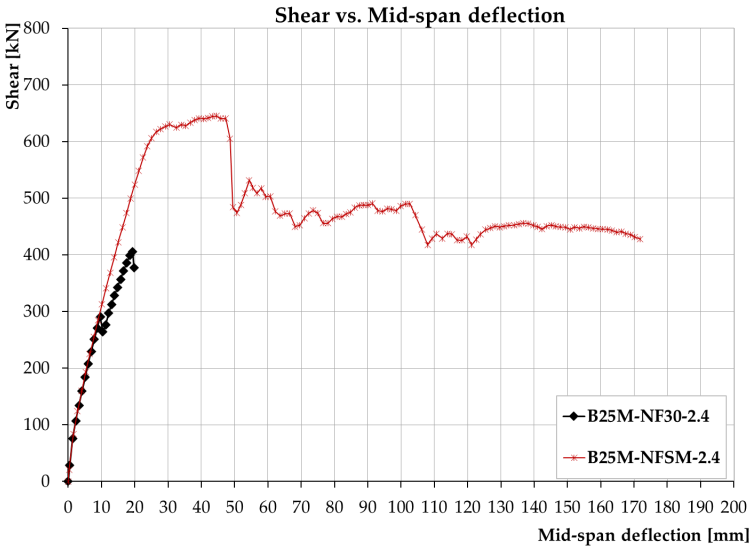

(Pt. 2 of 2)

Figure 5.2-27: Typical shear vs. mid-span deflection curves for B25M specimens.

The beams were characterized by a wide distributed crack pattern, as shown in Figure 5.2-28. At first, flexural cracks developed in the mid-span, where the bending moment was maximum. Increasing the load, the flexural cracks extended. The fibres and the steel mesh were able to control the cracks. It can be concluded that the steel mesh embedded in the layer of UHPFRC is an efficient technique for shear repair in cases where the UHPFRC layer is not sufficient.

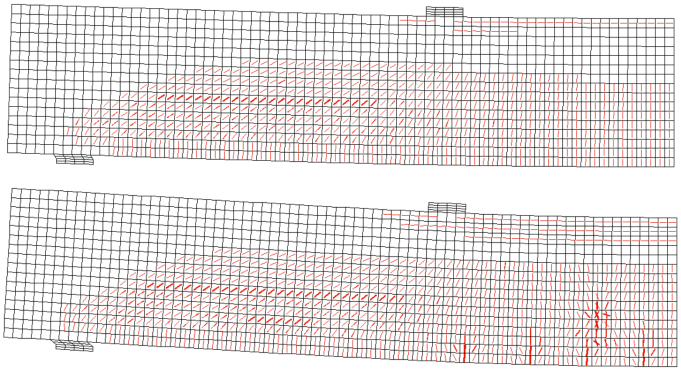

a) Yielding

a) Peak load

Figure 5.2-28 (Pt. 1 of 2)

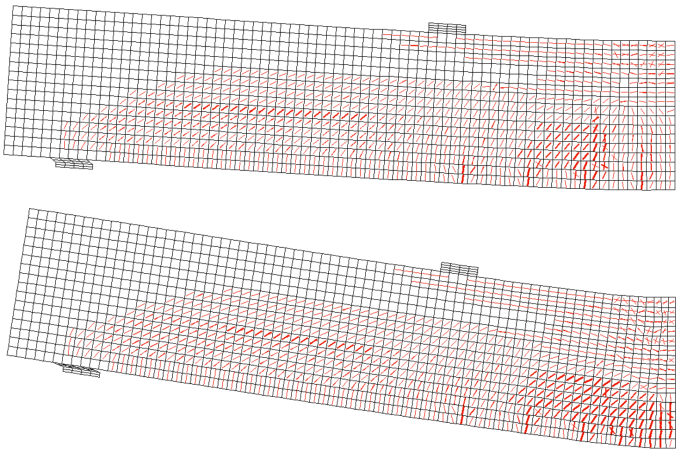

b) UHPFRC compressive strength exceeded

c) Failure

(Pt. 2 of 2)

Figure 5.2-28: Schematic crack patterns at different load stages in strengthened beam.

Shown in Figure 5.2-29 are summaries of the results for the shear capacities of the reference and retrofitted beams for five shear span-to-effective depth ratios (a/d = 2.5, 3.0, 3.5, 4.0, and 4.5).

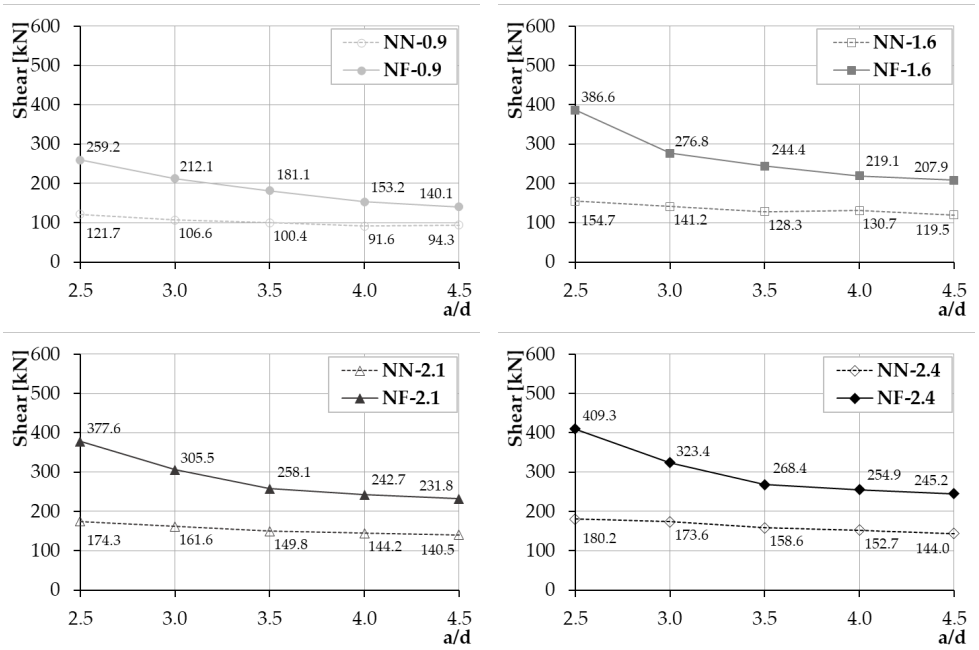

Figure 5.2-29: Summary results of shear capacity of the reference beams (NN) and retrofitted beams (NF).

The 3D plots of the valley of shear diagonal failure ($M_u/M_{u,fl}$ versus a/d ratio), as a function of the reinforcement ratio, are illustrated in Figure 5.2-30.

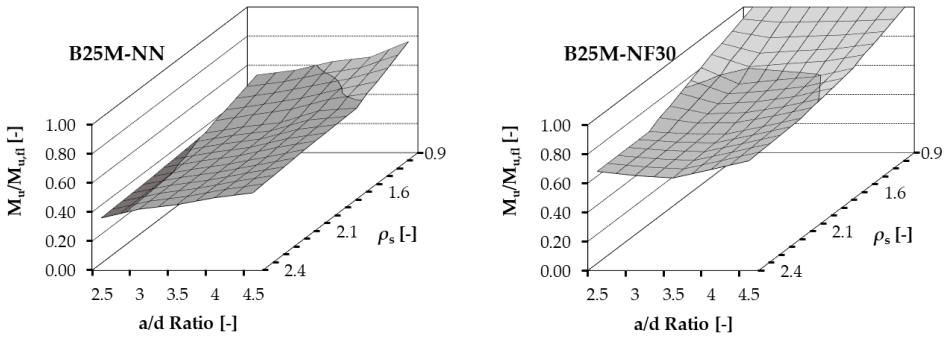

Figure 5.2-30: Influence of the longitudinal reinforcement ratio on the valley of shear failure.

Table 5.2-11 lists the value of $M_u/M_{u,fl}$ obtained from numerical analyses performed on models of B25M series.

a/d	ρ=0.9%		ρ=1.6%		ρ=2.1%		ρ=2.4%	
	NN	NF30	NN	NF30	NN	NF30	NN	NF30
2.5	0.53	1.00	0.40	0.85	0.38	0.68	0.36	0.68
3.0	0.57	1.00	0.45	0.74	0.42	0.67	0.42	0.65
3.5	0.63	1.00	0.48	0.77	0.46	0.66	0.45	0.64
4.0	0.66	1.00	0.56	0.79	0.51	0.72	0.50	0.69
4.5	0.76	1.00	0.57	0.85	0.56	0.78	0.53	0.75
$M_{u,fl}$ [kN]	302	365	507	598	612	730	660	794

Table 5.2-11: Values of $M_u/M_{u,fl}$ obtained from the numerical analyses of models of B25M series.

The RC beams showed a regime of shear failure for all ranges of a/d and longitudinal reinforcement ratios. Despite the retrofit intervention, the strengthened beams exhibited a shear failure, except for the NF beam having ρ=0.9%.
The effect of the UHPFRC jacketing improved the peak load but did not reduce the brittleness of elements, and the retrofitted beam still showed a shear failure. Therefore, the thickness was increased up to 50 mm.
The values of peak load, shear strength, ultimate shear stress, and normalized ultimate shear stress for each beam are reported in Table 5.2-12.

Beam type	P_{max} [kN]	V [kN]	v_u [MPa]	$\frac{v_u}{\sqrt{f_c}}$	Failure mode	Reinf. yielded
a/d=2.5						
B25M-NN-0.9	243.5	121.7	0.90	0.18	S	No
B25M-NF30-0.9	518.5	259.2	1.92	0.38	F	Yes
B25M-NN-1.6	309.3	154.7	1.15	0.23	S	No
B25M-NF30-1.6	771.8	385.9	2.86	0.57	S	No
B25M-NF40-1.6	839.1	419.6	3.11	0.62	S	Yes
B25M-NF50-1.6	870.2	435.1	3.22	0.64	F	Yes
B25M-NN-2.1	348.5	174.3	1.29	0.26	S	No
B25M-NF30-2.1	755.3	377.6	2.80	0.56	S	No
B25M-NF40-2.1	812.9	406.4	3.01	0.60	S	No
B25M-NF50-2.1	993.9	497.0	3.68	0.74	S	No
B25M-NN-2.4	360.3	180.2	1.33	0.27	S	No
B25M-NF30-2.4	818.6	409.3	3.03	0.61	S	No
B25M-NF40-2.4	915.9	458.0	3.39	0.68	S	No
B25M-NF50-2.4	1046.0	523.01	3.87	0.77	S	No
a/d=3.0						
B25M-NN-0.9	213.3	106.6	0.79	0.16	S	No
B25M-NF30-0.9	424.3	212.1	1.57	0.31	F	Yes
B25M-NN-1.6	282.4	141.2	1.05	0.21	S	No
B25M-NF30-1.6	553.7	276.8	2.05	0.41	S	No
B25M-NF40-1.6	655.6	327.8	2.43	0.49	S	No
B25M-NF50-1.6	682.9	341.5	2.53	0.51	S	Yes
B25M-NN-2.1	323.2	161.6	1.20	0.24	S	No
B25M-NF30-2.1	611.0	305.5	2.26	0.45	S	No
B25M-NF40-2.1	697.7	348.9	2.58	0.52	S	No
B25M-NF50-2.1	777.6	388.8	2.88	0.58	S	No
B25M-NN-2.4	347.2	173.6	1.29	0.26	S	No
B25M-NF30-2.4	646.7	323.4	2.40	0.48	S	No
B25M-NF40-2.4	724.8	362.4	2.68	0.54	S	No
B25M-NF50-2.4	782.1	391.0	2.90	0.58	S	No
a/d=3.5						
B25M-NN-0.9	200.8	100.4	0.74	0.15	S	No
B25M-NF30-0.9	362.3	181.1	1.34	0.27	F	Yes
B25M-NN-1.6	256.7	128.3	0.95	0.19	S	No
B25M-NF30-1.6	488.9	244.4	1.81	0.36	S	No
B25M-NF40-1.6	540.3	270.2	2.00	0.40	S	No
B25M-NF50-1.6	595.5	297.8	2.21	0.44	S	Yes
B25M-NN-2.1	299.5	149.8	1.11	0.22	S	No
B25M-NF30-2.1	516.2	258.1	1.91	0.38	S	No
B25M-NF40-2.1	578.4	289.2	2.14	0.43	S	No
B25M-NF50-2.1	642.3	321.2	2.38	0.48	S	No
B25M-NN-2.4	317.3	158.6	1.18	0.24	S	No
B25M-NF30-2.4	536.8	268.4	1.99	0.40	S	No
B25M-NF40-2.4	600.6	300.3	2.22	0.44	S	No
B25M-NF50-2.4	663.8	331.9	2.46	0.49	S	No

Table 5.2-12 (Pt. 1 of 2)

a/d=4.0						
B25M-NN-0.9	188.0	94.0	0.70	0.14	S	No
B25M-NF30-0.9	314.3	157.1	1.16	0.23	F	Yes
B25M-NN-1.6	263.8	131.9	0.98	0.20	S	No
B25M-NF30-1.6	449.9	225.0	1.67	0.33	S	No
B25M-NF40-1.6	485.9	242.9	1.80	0.36	S	No
B25M-NF50-1.6	540.2	270.1	2.00	0.40	S	Yes
B25M-NN-2.1	290.2	145.1	1.07	0.21	S	No
B25M-NF30-2.1	501.5	250.8	1.86	0.37	S	No
B25M-NF40-2.1	551.8	275.9	2.04	0.41	S	No
B25M-NF50-2.1	604.7	302.4	2.24	0.45	S	No
B25M-NN-2.4	314.0	157.0	1.16	0.23	S	No
B25M-NF30-2.4	520.4	260.2	1.93	0.39	S	No
B25M-NF40-2.4	578.8	289.4	2.14	0.43	S	No
B25M-NF50-2.4	632.1	316.0	2.34	0.47	S	No
a/d=4.5						
B25M-NN-0.9	188.5	94.3	0.70	0.14	S	No
B25M-NF30-0.9	280.3	140.1	1.04	0.21	F	Yes
B25M-NN-1.6	239.0	119.5	0.89	0.18	S	No
B25M-NF30-1.6	415.8	207.9	1.54	0.31	S	No
B25M-NF40-1.6	458.3	229.2	1.70	0.34	S	No
B25M-NF50-1.6	479.7	239.9	1.78	0.36	F	Yes
B25M-NN-2.1	280.9	140.5	1.04	0.21	S	No
B25M-NF30-2.1	463.7	231.8	1.72	0.34	S	No
B25M-NF40-2.1	524.0	262.0	1.94	0.39	S	No
B25M-NF50-2.1	568.1	284.1	2.10	0.42	S	Yes
B25M-NN-2.4	288.0	144.0	1.07	0.21	S	No
B25M-NF30-2.4	490.3	245.2	1.82	0.36	S	No
B25M-NF40-2.4	535.2	267.6	1.98	0.40	S	No
B25M-NF50-2.4	590.9	295.5	2.19	0.44	S	No

Notes: - Notation for failure modes: S: Shear; and F: Flexural.
(Pt. 2 of 2)
Table 5.2-12: Summary of finite element analysis results.

From the results above, it can be observed that, except for NF-0.9, the UHPFRC layer equal to 30 mm was not enough, and the retrofitted beams still showed a shear failure. Increasing the thickness (up to 50 mm), almost all the strengthened beams still exhibited a diagonal shear failure. FE analyses demonstrated that, with low concrete compressive strength (25MPa), reinforcement ratios higher than 0.9%, the jacketing seems to not be an efficient shear repairing method. In order to change the brittle failure mode to a more ductile one, a high strength steel mesh (SM) was added in the jacket. Using the steel mesh embedded in the layer of UHPFRC (with thickness of 30 mm), all beams strengthened with the UHPFRC jacket exhibited a flexure failure without shear effects.

5.2.3.5 B50M

Compared with previously discussed beams of the same sizes, the B50M beams had nearly identical responses. Therefore, only summary results are reported below; additional details of the curves are provided in Appendix D.
The shear capacities results of the reference (NN) and retrofitted (NF) beams for five shear span-to-effective depth ratios are presented in Figure 5.2-31.

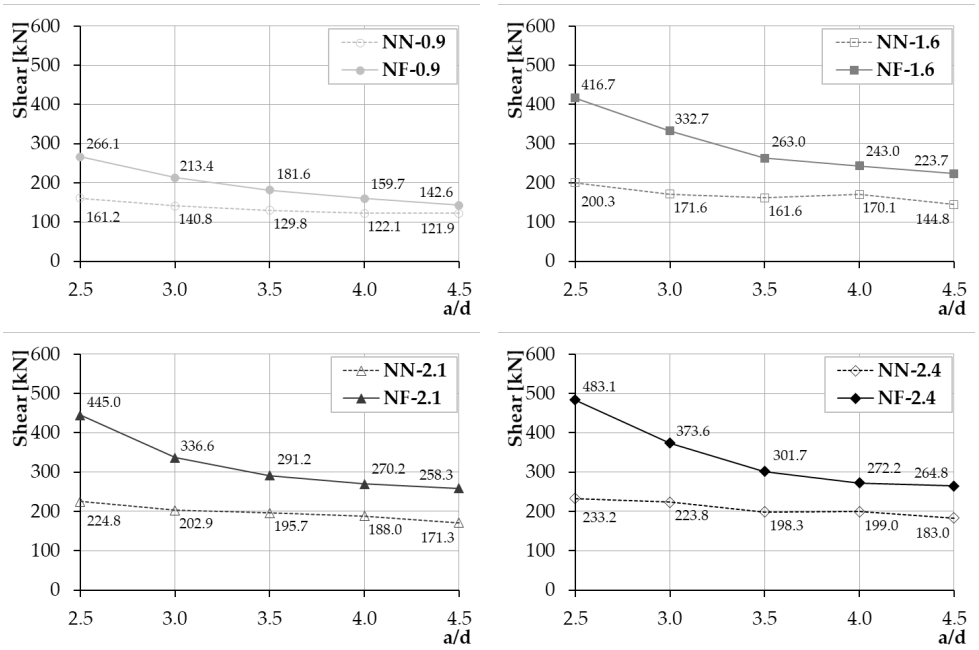

Figure 5.2-31: Summary results of shear capacities of the reference beams (NN) and retrofitted beams (NF).

Figure 5.2-32 illustrates the plot of Kani's valley for each model, as a function of the longitudinal reinforcement ratio.
Table 5.2-13 gives the value of $M_u/M_{u,fl}$ obtained from the set of the numerical analyses performed on models of B50M series.
As observed in the B25M series, the reference beams exhibited a regime of shear failure for all ranges of *a*/*d* and longitudinal reinforcement ratios.
In the strengthened beams with reinforcement ratios higher than 1.6% (included), a shear failure occurred, while for model NF-0.9 the shear failure did not appear for any value of *a*/*d*. It can be observed that the UHPFRC jacketing did not reduce the brittleness of elements still showing a shear failure. In these cases, the thickness was increased (up to 50 mm).

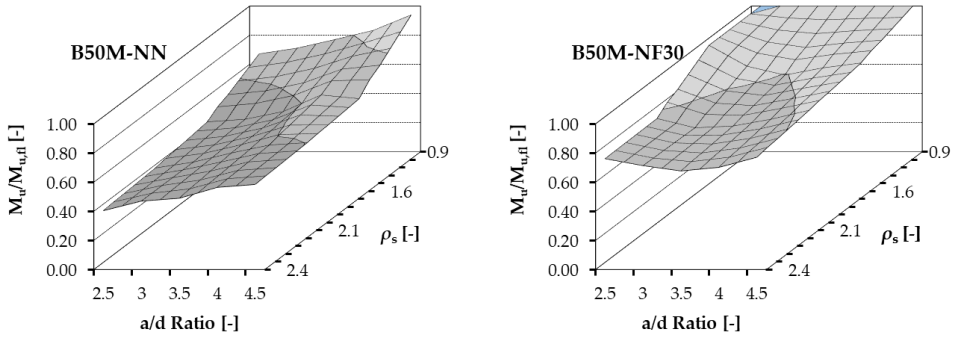

Figure 5.2-32: Influence of the longitudinal reinforcement ratio on the valley of shear failure.

a/d	ρ=0.9%		ρ=1.6%		ρ=2.1%		ρ=2.4%	
	NN	NF30	NN	NF30	NN	NF30	NN	NF30
2.5	0.67	1.00	0.47	1.00	0.43	0.77	0.40	0.76
3.0	0.71	1.00	0.49	0.86	0.47	0.70	0.47	0.71
3.5	0.77	1.00	0.54	0.80	0.53	0.71	0.49	0.68
4.0	0.83	1.00	0.66	0.84	0.58	0.76	0.56	0.70
4.5	0.94	1.00	0.63	0.88	0.60	0.82	0.58	0.77
$M_{u,fl}$ [kN]	317	374	558	622	695	766	762	838

Table 5.2-13: Values of $M_u/M_{u,fl}$ obtained from the numerical analyses of models of B50M series.

Table 5.2-14 provides the values of peak load, shear strength, ultimate shear stress, and normalized ultimate shear stress.

Beam type	P_{max} [kN]	V [kN]	v_u [MPa]	$\frac{v_u}{\sqrt{f_c}}$	Failure mode	Reinf. yielded
a/d=2.5						
B50M-NN-0.9	322.5	161.2	1.19	0.17	S	No
B50M-NF30-0.9	532.1	266.1	1.97	0.28	F	Yes
B50M-NN-1.6	400.6	200.3	1.48	0.21	S	No
B50M-NF30-1.6	833.4	416.7	3.09	0.44	S	Yes
B50M-NF40-1.6	887.2	443.6	3.29	0.46	S	Yes
B50M-NF50-1.6	902.1	451.1	3.34	0.47	F	Yes
B50M-NN-2.1	449.5	224.8	1.66	0.24	S	No
B50M-NF30-2.1	890.0	445.0	3.30	0.47	S	No
B50M-NF40-2.1	947.5	473.7	3.51	0.50	S	Yes
B50M-NF50-2.1	1058.2	529.1	3.92	0.55	S	Yes
B50M-NN-2.4	466.5	233.2	1.73	0.24	S	No
B50M-NF30-2.4	966.2	483.1	3.58	0.51	S	No
B50M-NF40-2.4	978.4	489.2	3.62	0.51	S	No
B50M-NF50-2.4	1101.1	550.5	4.08	0.58	S	No

Table 5.2-14 (Pt. 1 of 3)

a/d=3.0						
B50M-NN-0.9	281.6	140.8	1.04	0.15	S	No
B50M-NF30-0.9	426.7	213.4	1.58	0.22	F	Yes
B50M-NN-1.6	343.1	171.6	1.27	0.18	S	No
B50M-NF30-1.6	665.3	332.7	2.46	0.35	S	No
B50M-NF40-1.6	717.5	358.8	2.66	0.38	S	No
B50M-NF50-1.6	757.4	378.7	2.81	0.40	F	Yes
B50M-NN-2.1	405.8	202.9	1.50	0.21	S	No
B50M-NF30-2.1	673.2	336.6	2.49	0.35	S	No
B50M-NF40-2.1	766.9	383.4	2.84	0.40	S	No
B50M-NF50-2.1	820.4	410.2	3.04	0.43	S	No
B50M-NN-2.4	447.6	223.8	1.66	0.23	S	No
B50M-NF30-2.4	747.2	373.6	2.77	0.39	S	No
B50M-NF40-2.4	785.6	392.8	2.91	0.41	S	No
B50M-NF50-2.4	921.2	460.6	3.41	0.48	S	No
a/d=3.5						
B50M-NN-0.9	259.6	129.8	0.96	0.14	S	No
B50M-NF30-0.9	363.2	181.6	1.35	0.19	F	Yes
B50M-NN-1.6	323.3	161.6	1.20	0.17	S	No
B50M-NF30-1.6	525.9	263.0	1.95	0.28	S	No
B50M-NF40-1.6	580.1	290.0	2.15	0.30	S	Yes
B50M-NF50-1.6	613.1	306.5	2.27	0.32	S	Yes
B50M-NN-2.1	391.4	195.7	1.45	0.21	S	No
B50M-NF30-2.1	582.5	291.2	2.16	0.31	S	No
B50M-NF30-2.1	633.7	316.9	2.35	0.33	S	No
B50M-NF30-2.1	690.4	345.2	2.56	0.36	S	No
B50M-NN-2.4	396.7	198.3	1.47	0.21	S	No
B50M-NF30-2.4	603.4	301.7	2.23	0.32	S	No
B50M-NF40-2.4	660.6	330.3	2.45	0.35	S	No
B50M-NF50-2.4	718.9	359.4	2.66	0.38	S	No
a/d=4.0						
B50M-NN-0.9	245.0	122.5	0.91	0.13	S	No
B50M-NF30-0.9	320.2	160.1	1.19	0.17	F	Yes
B50M-NN-1.6	345.8	172.9	1.28	0.18	S	No
B50M-NF30-1.6	488.3	244.2	1.81	0.26	S	Yes
B50M-NF40-1.6	519.8	259.9	1.93	0.27	S	Yes
B50M-NF50-1.6	534.4	267.2	1.98	0.28	S	Yes
B50M-NN-2.1	379.8	189.9	1.41	0.20	S+F	No
B50M-NF30-2.1	547.7	273.9	2.03	0.29	S	No
B50M-NF30-2.1	566.2	283.1	2.10	0.30	S	No
B50M-NF30-2.1	620.1	310.0	2.30	0.32	S	No
B50M-NN-2.4	403.5	201.8	1.49	0.21	S+F	No
B50M-NF30-2.4	558.5	279.3	2.07	0.29	S	No
B50M-NF40-2.4	608.5	304.3	2.25	0.32	S	No
B50M-NF50-2.4	640.2	320.1	2.37	0.34	S	No

Table 5.2-14 (Pt. 2 of 3)

a/d=4.5						
B50M-NN-0.9	243.8	121.9	0.90	0.13	S	No
B50M-NF30-0.9	285.3	142.6	1.06	0.15	F	Yes
B50M-NN-1.6	289.6	144.8	1.07	0.15	S	No
B50M-NF30-1.6	447.4	223.7	1.66	0.23	S	No
B50M-NF40-1.6	489.1	244.5	1.81	0.26	F	Yes
B50M-NN-2.1	342.5	171.3	1.27	0.18	S	No
B50M-NF30-2.1	516.5	258.3	1.91	0.27	S	No
B50M-NF40-2.1	553.9	276.9	2.05	0.29	S	No
B50M-NF50-2.1	565.3	282.7	2.09	0.30	S	No
B50M-NN-2.4	366.0	183.0	1.36	0.19	S	No
B50M-NF30-2.4	529.7	264.8	1.96	0.28	S	No
B50M-NF40-2.4	569.4	284.7	2.11	0.30	S	No
B50M-NF50-2.4	644.6	322.3	2.39	0.34	S	No

Notes: - Notation for failure modes: S: Shear; and F: Flexural.
(Pt. 3 of 3)
Table 5.2-14: Summary of finite element analysis results.

The majority of cases, the UHPFRC layer equal to 30 mm was not enough, and the retrofitted beams still showed a shear failure. In increasing the thickness (up to 50 mm), almost all the strengthened beams still exhibited a diagonal shear failure. FE analyses demonstrated that, with reinforcement ratios higher than 1.6%, the jacketing is not an efficient shear repairing technique. With the aim of avoiding the brittle failure mode, a high strength steel mesh (SM) was added in the jacket (with thickness of 30 mm). As reported for the B25M beams, by using a steel mesh embedded in the layer of UHPFRC, all beams strengthened with the UHPFRC jacket exhibited a flexure failure without shear effects.

5.2.3.6 B70M

In the following, only summary results are reported for the B70M beams since they had nearly identical responses with respect to previous beams. Details of the curves are provided in Appendix D.

In Figure 5.2-33 summary results of the shear capacities of the reference and retrofitted beams for five shear span-to-effective depth ratios (a/d = 2.5, 3.0, 3.5, 4.0, and 4.5) are illustrated.

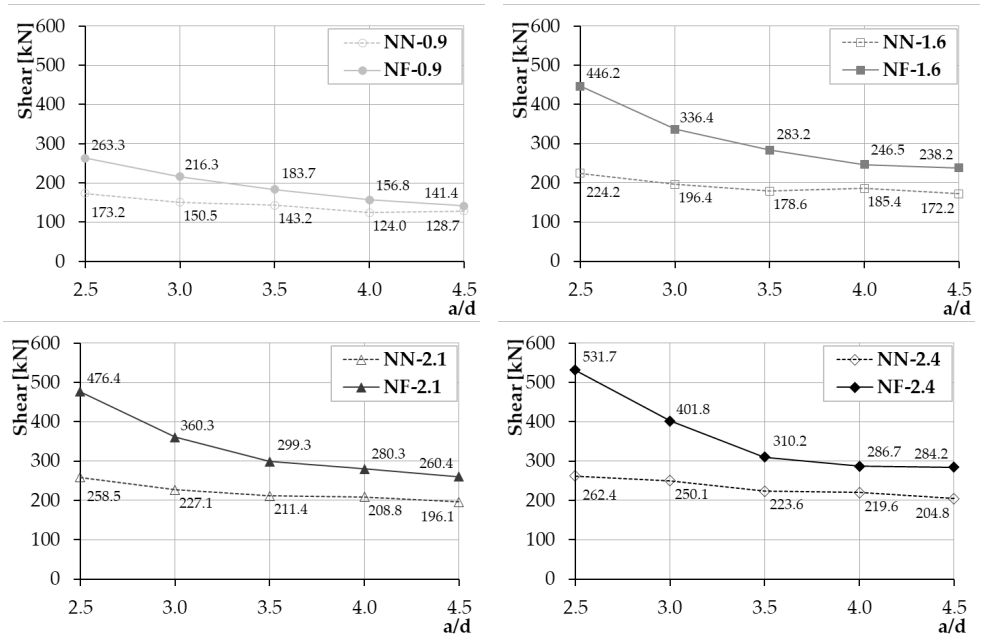

Figure 5.2-33: Summary results of shear capacities of the reference beams (NN) and retrofitted beams (NF).

Figure 5.2-34 shows the 3D plots of the valley of shear diagonal failure as a function of the reinforcement ratio.

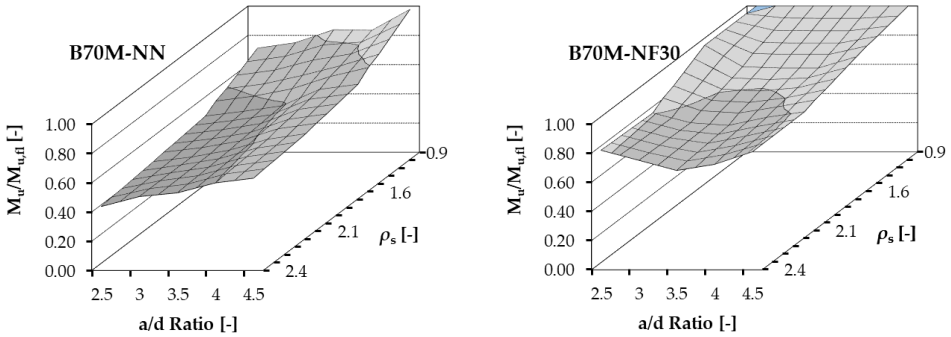

Figure 5.2-34: Influence of the longitudinal reinforcement ratio on the valley of shear failure.

Table 5.2-15 summarizes the value of $M_u/M_{u,fl}$ obtained from the set of the numerical analyses performed on models of B70M series.
The RC beams showed a regime of shear failure for all ranges of *a*/*d* and longitudinal reinforcement ratios, as observed in previous series.
In the strengthened beams, only in the case of ρ=0.9% the valley of shear diagonal failure disappeared completely, while for beams with the reinforcement ratio higher than 1.6% (included), the shear failure occurred. It can be observed that the UHPFRC jacketing did not reduce the brittleness of elements still showing a shear failure. In these cases, the thickness was increased (up to 50 mm). However, the UHPFRC layer was not enough, and the retrofitted beams still showed a shear failure.

a/d	**ρ=0.9%**		**ρ=1.6%**		**ρ=2.1%**		**ρ=2.4%**	
	NN	**NF30**	**NN**	**NF30**	**NN**	**NF30**	**NN**	**NF30**
2.5	0.71	1.00	0.52	1.00	0.47	0.80	0.44	0.82
3.0	0.75	1.00	0.55	0.85	0.51	0.74	0.51	0.75
3.5	0.84	1.00	0.59	0.84	0.55	0.72	0.53	0.68
4.0	0.83	1.00	0.70	0.84	0.63	0.77	0.60	0.72
4.5	0.98	1.00	0.73	0.92	0.67	0.81	0.63	0.81
$M_{u,fl}$ [kN]	321	377	573	631	719	781	791	856

Table 5.2-15: Values of $M_u/M_{u,fl}$ obtained from the numerical analyses of models of B70M series.

The values of peak load, shear strength, ultimate shear stress, and normalized ultimate shear stress are reported in Table 5.2-16.

Beam type	P_{max} [kN]	V [kN]	v_u [MPa]	$\frac{v_u}{\sqrt{f_c}}$	Failure mode	Reinf. yielded
a/d=2.5						
B70M-NN-0.9	346.5	173.2	1.28	0.15	S	No
B70M-NF30-0.9	526.6	263.3	1.95	0.23	F	Yes
B70M-NN-1.6	448.4	224.2	1.66	0.20	S	No
B70M-NF30-1.6	892.5	446.2	3.31	0.40	F	Yes
B70M-NF40-1.6	911.8	455.9	3.38	0.40	F	Yes
B70M-NN-2.1	516.9	258.5	1.91	0.23	S	No
B70M-NF30-2.1	952.8	476.4	3.53	0.42	S	No
B70M-NF40-2.1	1044.3	522.1	3.87	0.46	S	No
B70M-NF50-2.1	1135.1	567.6	4.20	0.50	S	Yes
B70M-NN-2.4	524.7	262.4	1.94	0.23	S	No
B70M-NF30-2.4	1063.4	531.7	3.94	0.47	S	No
B70M-NF40-2.4	1074.2	537.1	3.98	0.48	S	No
B70M-NF50-2.4	1160.9	580.4	4.30	0.51	S	No
a/d=3.0						
B70M-NN-0.9	301.1	150.5	1.12	0.13	S	No
B70M-NF30-0.9	432.6	216.3	1.60	0.19	S	Yes
B70M-NF40-0.9	442.4	221.2	1.64	0.20	F	Yes
B70M-NN-1.6	392.9	196.4	1.46	0.17	S	No
B70M-NF30-1.6	672.8	336.4	2.49	0.30	S	No
B70M-NF40-1.6	729.9	364.9	2.70	0.32	S	No
B70M-NF50-1.6	760.5	380.2	2.82	0.34	F	Yes
B70M-NN-2.1	454.2	227.1	1.68	0.20	S	No
B70M-NF30-2.1	720.5	360.3	2.67	0.32	S	No
B70M-NF40-2.1	806.9	403.5	2.99	0.36	S	No
B70M-NF50-2.1	885.4	442.7	3.28	0.39	S	No
B70M-NN-2.4	500.3	250.1	1.85	0.22	S	No
B70M-NF30-2.4	803.6	401.8	2.98	0.36	S	No
B70M-NF40-2.4	845.6	422.8	3.13	0.37	S	No
B70M-NF50-2.4	918.4	459.2	3.40	0.41	S	No
a/d=3.5						
B70M-NN-0.9	286.5	143.2	1.06	0.13	S	No
B70M-NF30-0.9	367.3	183.7	1.36	0.16	F	Yes
B70M-NN-1.6	357.1	178.6	1.32	0.16	S	No
B70M-NF30-1.6	566.4	283.2	2.10	0.25	S	No
B70M-NF40-1.6	593.1	296.5	2.20	0.26	S	Yes
B70M-NF50-1.6	646.8	323.4	2.40	0.29	F	Yes
B70M-NN-2.1	422.9	211.4	1.57	0.19	S	No
B70M-NF30-2.1	598.5	299.3	2.22	0.26	S	No
B70M-NF40-2.1	650.6	325.3	2.41	0.29	S	No
B70M-NF50-2.1	720.5	360.3	2.67	0.32	S	No
B70M-NN-2.4	447.2	223.6	1.66	0.20	S	No
B70M-NF30-2.4	620.4	310.2	2.30	0.27	S	No
B70M-NF40-2.4	691.3	345.6	2.56	0.31	S	No
B70M-NF40-2.4	742.0	371.0	2.75	0.33	S	No

Table 5.2-16 (Pt. 1 of 2)

a/d=4.0						
B70M-NN-0.9	249.5	124.8	0.92	0.11	S	No
B70M-NF30-0.9	321.0	160.5	1.19	0.14	F	Yes
B70M-NN-1.6	376.5	188.2	1.39	0.17	S	No
B70M-NF30-1.6	504.3	252.1	1.87	0.22	S	No
B70M-NF40-1.6	538.3	269.2	1.99	0.24	S	Yes
B70M-NF50-1.6	532.6	266.3	1.97	0.24	S	Yes
B70M-NN-2.1	424.7	212.4	1.57	0.19	S+F	No
B70M-NF30-2.1	564.5	282.2	2.09	0.25	S	No
B70M-NF40-2.1	606.3	303.1	2.25	0.27	S	No
B70M-NF50-2.1	604.8	302.4	2.24	0.27	S	No
B70M-NN-2.4	440.9	220.5	1.63	0.20	S+F	No
B70M-NF30-2.4	592.5	296.2	2.19	0.26	S	No
B70M-NF40-2.4	646.7	323.3	2.40	0.29	S	No
B70M-NF40-2.4	664.4	332.2	2.46	0.29	S	No
a/d=4.5						
B70M-NN-0.9	257.3	128.7	0.95	0.11	S	No
B70M-NF30-0.9	282.8	141.4	1.05	0.13	F	Yes
B70M-NN-1.6	344.4	172.2	1.28	0.15	S	No
B70M-NF30-1.6	476.4	238.2	1.76	0.21	F	No
B70M-NN-2.1	392.1	196.1	1.45	0.17	S	No
B70M-NF30-2.1	520.9	260.4	1.93	0.23	S	No
B70M-NF40-2.1	561.3	280.6	2.08	0.25	S	No
B70M-NF50-2.1	597.2	298.6	2.21	0.26	S	No
B70M-NN-2.4	409.6	204.8	1.52	0.18	S	No
B70M-NF30-2.4	568.3	284.2	2.10	0.25	S	No
B70M-NF40-2.4	604.8	302.4	2.24	0.27	S	No
B70M-NF50-2.4	608.1	304.0	2.25	0.27	S	No

Notes: - Notation for failure modes: S: Shear; and F: Flexural.
(Pt. 2 of 2)
Table 5.2-16: Summary of finite element analysis results.

To avoid the brittle failure mode, a high strength steel mesh was added in the jacket. Using the steel mesh embedded in the layer of UHPFRC, all retrofitted beams showed a flexure failure without shear effects. The behaviours obtained for B70M strengthened with the UHPFRC and steel mesh were nearly the same as obtained for B25M and B50M.

5.2.3.7 B25L

Figure 5.2-35 shows summary results of the shear capacities of reference and retrofitted beams for five shear span-to-effective depth ratios (a/d = 2.5, 3.0, 3.5, 4.0, and 4.5).

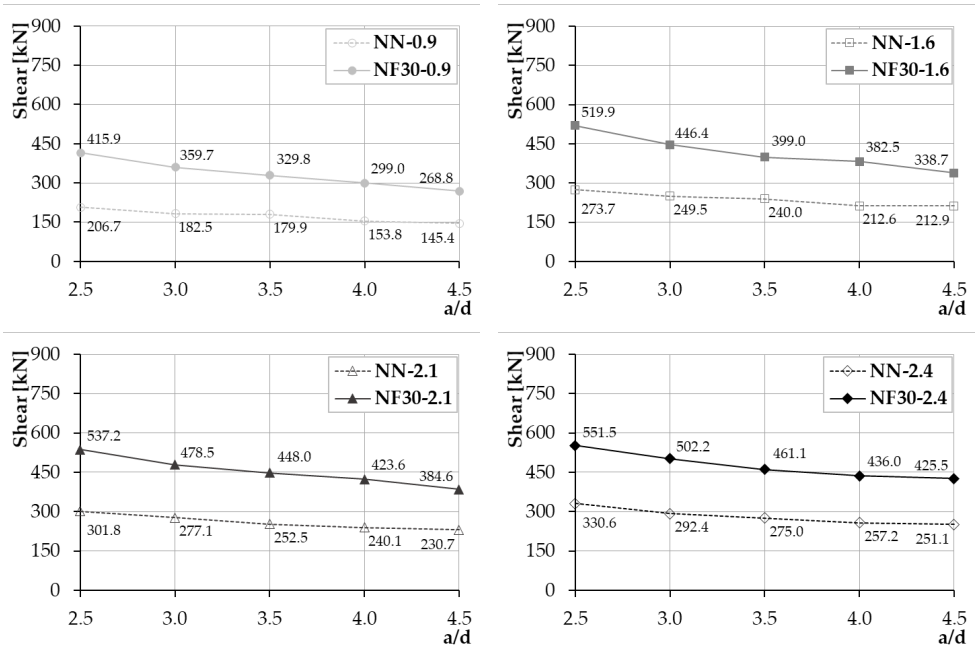

Figure 5.2-35: Summary results of shear capacities of the reference beams (NN) and retrofitted beams (NF).

The 3D plots of the valley of shear diagonal failure ($M_u/M_{u,fl}$ versus a/d ratio), as a function of the reinforcement ratio, are illustrated in Figure 5.2-36.

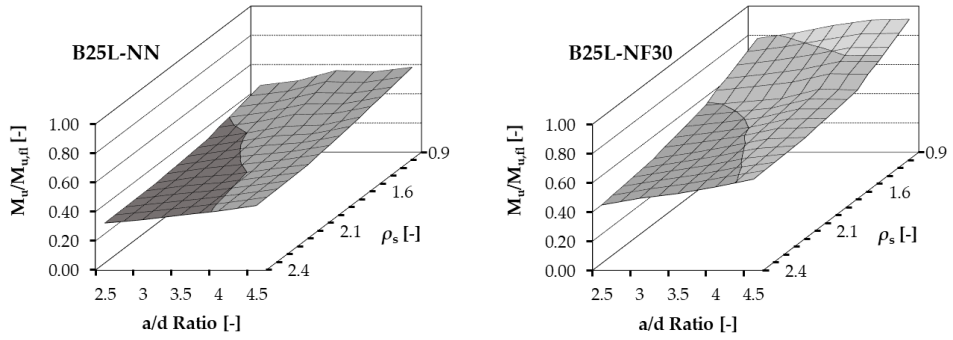

Figure 5.2-36: Influence of the longitudinal reinforcement ratio on the valley of shear failure.

Table 5.2-17 lists the value of $M_u/M_{u,fl}$ obtained from the set of the numerical analyses performed on models of B25L series.

a/d	ρ=0.9%		ρ=1.6%		ρ=2.1%		ρ=2.4%	
	NN	NF	NN	NF	NN	NF	NN	NF
2.5	0.46	0.78	0.36	0.59	0.33	0.49	0.32	0.45
3.0	0.49	0.82	0.40	0.61	0.37	0.53	0.35	0.49
3.5	0.56	0.87	0.45	0.64	0.39	0.58	0.38	0.53
4.0	0.55	0.90	0.45	0.70	0.42	0.63	0.41	0.57
4.5	0.58	0.91	0.51	0.69	0.45	0.64	0.44	0.62
$M_{u,fl}$ **[kN]**	1031	1217	1724	2008	2093	2475	2334	2808

Table 5.2-17: Values of $M_u/M_{u,fl}$ obtained from the numerical analyses of models of B25L series.

The reference beams showed a regime of shear failure for all ranges of *a/d* and longitudinal reinforcement ratios.
Series L (affected by size effect) showed higher shear values with respect to series S, hence the thickness needed will be higher. Despite the UHPFRC retrofitting (with thickness of 50 mm), all strengthened beams (except for NF-0.9) exhibited a shear failure.
Table 5.2-18 reports the values of peak load, shear strength, ultimate shear stress, and normalized ultimate shear stress.

Beam type	P_{max} [kN]	V [kN]	v_u [MPa]	$\frac{v_u}{\sqrt{f_c}}$	Failure mode	Reinf. yielded
a/d=2.5						
B25L-NN-0.9	413.3	206.7	0.75	0.15	S	No
B25L-NF30-0.9	831.8	415.9	1.51	0.30	S	Yes
B25L-NF40-0.9	984.7	492.3	1.78	0.36	F	Yes
B25L-NN-1.6	547.3	273.7	0.99	0.20	S	No
B25L-NF30-1.6	1039.7	519.9	1.88	0.38	S	No
B25L-NF40-1.6	1131.3	565.6	2.05	0.41	S	No
B25L-NF50-1.6	1200.1	600.0	2.17	0.43	S	No
B25L-NN-2.1	603.6	301.8	1.09	0.22	S	No
B25L-NF30-2.1	1074.4	537.2	1.95	0.39	S	No
B25L-NF40-2.1	1223.3	611.7	2.22	0.44	S	No
B25L-NF50-2.1	1324.4	662.2	2.40	0.48	S	No
B25L-NN-2.4	661.2	330.6	1.20	0.24	S	No
B25L-NF30-2.4	1103.0	551.5	2.00	0.40	S	No
B25L-NF40-2.4	1267.6	633.8	2.30	0.46	S	No
B25L-NF50-2.4	1403.3	701.6	2.54	0.51	S	No

Table 5.2-18 (Pt 1 of 3)

a/d=3.0						
B25L-NN-0.9	364.9	182.5	0.66	0.13	S	No
B25L-NF30-0.9	719.4	359.7	1.30	0.26	S	No
B25L-NF40-0.9	782.6	391.3	1.42	0.28	F	Yes
B25L-NN-1.6	499.0	249.5	0.90	0.18	S	No
B25L-NF30-1.6	892.8	446.4	1.62	0.32	S	No
B25L-NF40-1.6	880.2	440.1	1.59	0.32	S	No
B25L-NF50-1.6	962.4	481.2	1.74	0.35	S	No
B25L-NN-2.1	554.2	277.1	1.00	0.20	S	No
B25L-NF30-2.1	957.0	478.5	1.73	0.35	S	No
B25L-NF40-2.1	1042.5	521.2	1.89	0.38	S	No
B25L-NF50-2.1	1082.5	541.3	1.96	0.39	S	No
B25L-NN-2.4	584.8	292.4	1.06	0.21	S	No
B25L-NF30-2.4	1004.3	502.2	1.82	0.36	S	No
B25L-NF40-2.4	1099.4	549.7	1.99	0.40	S	No
B25L-NF50-2.4	1094.2	547.1	1.98	0.40	S	No
a/d=3.5						
B25L-NN-0.9	359.716	179.858	0.651659	0.130332	S	No
B25L-NF30-0.9	659.568	329.784	1.19487	0.238974	S	No
B25L-NF40-0.9	705.756	352.878	1.278543	0.255709	F	Yes
B25L-NN-1.6	480.076	240.038	0.869703	0.173941	S	No
B25L-NF30-1.6	798.096	399.048	1.445826	0.289165	S	No
B25L-NF40-1.6	869.46	434.73	1.575109	0.315022	S	No
B25L-NF50-1.6	869.932	434.966	1.575964	0.315193	S	No
B25L-NN-2.1	505.056	252.528	0.914957	0.182991	S	No
B25L-NF30-2.1	895.92	447.96	1.623043	0.324609	S	No
B25L-NF40-2.1	946.32	473.16	1.714348	0.34287	S	No
B25L-NF50-2.1	1024.736	512.368	1.856406	0.371281	S	No
B25L-NN-2.4	550.058	275.029	0.996482	0.199296	S	No
B25L-NF30-2.4	922.156	461.078	1.670572	0.334114	S	No
B25L-NF40-2.4	969.252	484.626	1.755891	0.351178	S	No
B25L-NF50-2.4	1075.9	537.95	1.949094	0.389819	S	No

Table 5.2-18 (Pt 2 of 3)

a/d=4.0						
B25L-NN-0.9	307.6	153.8	0.56	0.11	S	No
B25L-NF30-0.9	598.0	299.0	1.08	0.22	S	No
B25L-NF40-0.9	602.2	301.1	1.09	0.22	F	Yes
B25L-NN-1.6	425.1	212.6	0.77	0.15	S	No
B25L-NF30-1.6	765.0	382.5	1.39	0.28	S	No
B25L-NF40-1.6	813.8	406.9	1.47	0.29	S	No
B25L-NF50-1.6	847.5	423.8	1.54	0.31	S	No
B25L-NN-2.1	480.3	240.1	0.87	0.17	S	No
B25L-NF30-2.1	847.3	423.6	1.53	0.31	S	No
B25L-NF40-2.1	887.8	443.9	1.61	0.32	S	No
B25L-NF50-2.1	873.0	436.5	1.58	0.32	S	No
B25L-NN-2.4	514.3	257.2	0.93	0.19	S	No
B25L-NF30-2.4	872.1	436.0	1.58	0.32	S	No
B25L-NF40-2.4	942.3	471.2	1.71	0.34	S	No
B25L-NF50-2.4	1012.9	506.5	1.84	0.37	S	No
a/d=4.5						
B25L-NN-0.9	290.842	145.421	0.526888	0.105378	S	No
B25L-NF30-0.9	537.5	268.8	0.97	0.19	F	Yes
B25L-NN-1.6	425.9	212.9	0.77	0.15	S	No
B25L-NF30-1.6	677.3	338.7	1.23	0.25	S	No
B25L-NF40-1.6	747.6	373.8	1.35	0.27	S	No
B25L-NF50-1.6	722.2	361.1	1.31	0.26	S	No
B25L-NN-2.1	461.4	230.7	0.84	0.17	S	No
B25L-NF30-2.1	769.3	384.6	1.39	0.28	S	No
B25L-NF40-2.1	841.1	420.5	1.52	0.30	S	No
B25L-NF50-2.1	874.4	437.2	1.58	0.32	S	No
B25L-NN-2.4	502.2	251.1	0.91	0.18	S	No
B25L-NF30-2.4	850.9	425.5	1.54	0.31	S	No
B25L-NF40-2.4	901.4	450.7	1.63	0.33	S	No
B25L-NF50-2.4	975.2	487.6	1.77	0.35	S	No

Notes: - Notation for failure modes: S: Shear; and F: Flexural.
(Pt 3 of 3)
Table 5.2-18: Summary of finite element analysis results.

FE analyses demonstrated that, for beams with reinforcement ratios higher than 0.9%, jacketing seems to not be an efficient shear repairing method. In order to change the brittle failure mode to a more ductile one, a strength steel mesh (SM) was added to jackets having a thickness of 40 mm.

From Figure 5.2-37, it can be noted that the responses of the beams with steel mesh were ductile. The shear-deflection curves show a yielding plateau due to the yielding of the reinforcement bars. After the peak load was achieved, the UHPFRC compressive strength was exceeded, and the beam strength dropped.

a)

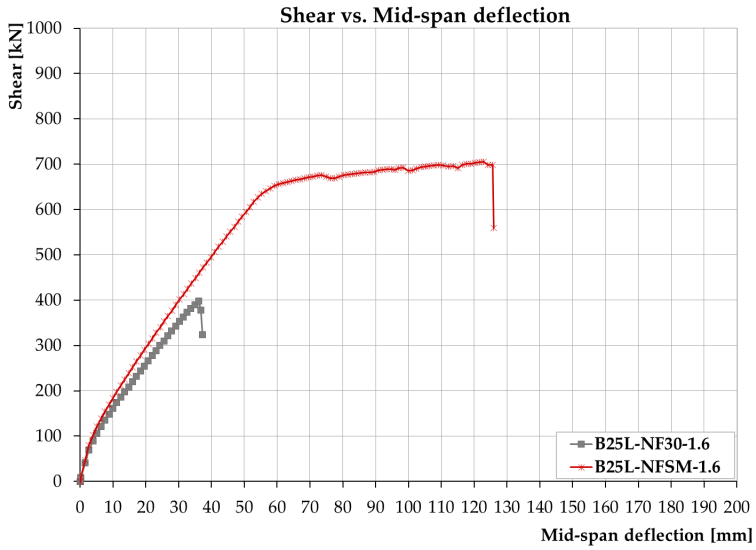

b)

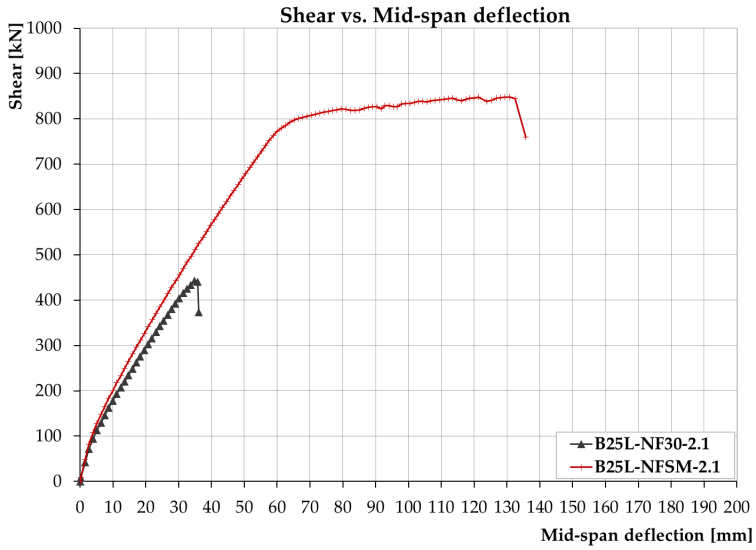

Figure 5.2-37 (Pt. 1 of 2)

c)

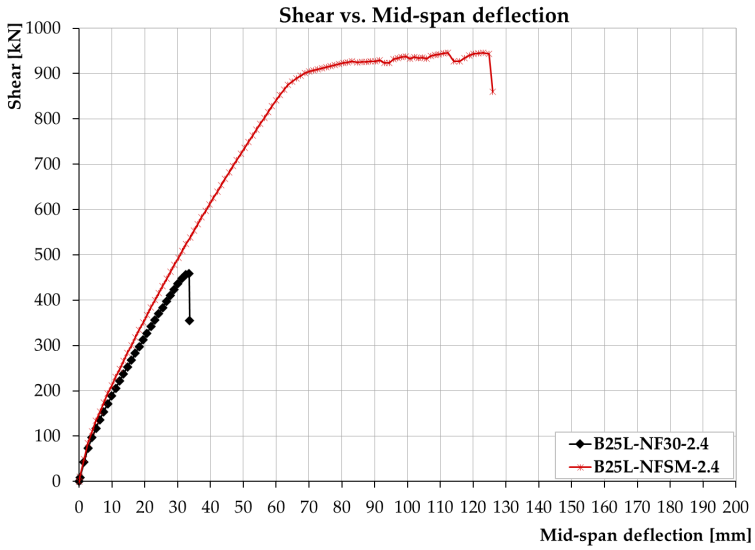

(Pt. 2 of 2)

Figure 5.2-37: Typical shear vs. mid-span deflection curves for B25L specimens.

It can be concluded that, by using a steel mesh embedded in the layer of UHPFRC, all beams exhibited a flexure failure without significant shear effects.

5.2.3.8 B50L

The shear capacities results of the reference (NN) and retrofitted (NF) beams for five shear span-to-effective depth ratios are presented in Figure 5.2-38.

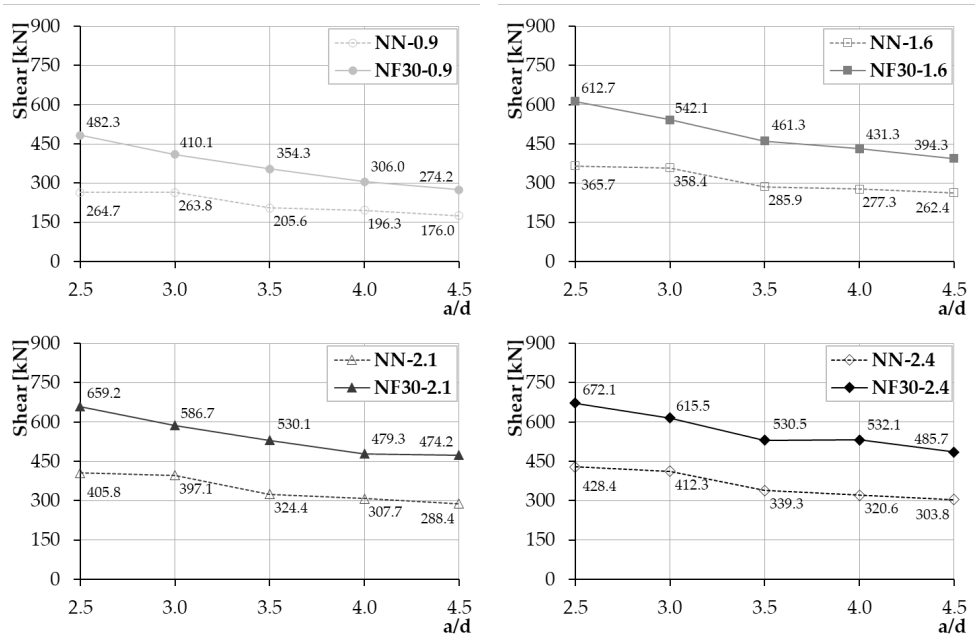

Figure 5.2-38: Summary results of shear capacities of the reference beams (NN) and retrofitted beams (NF).

Figure 5.2-39 illustrates the plot of Kani's valley for each model, as a function of the longitudinal reinforcement ratio.

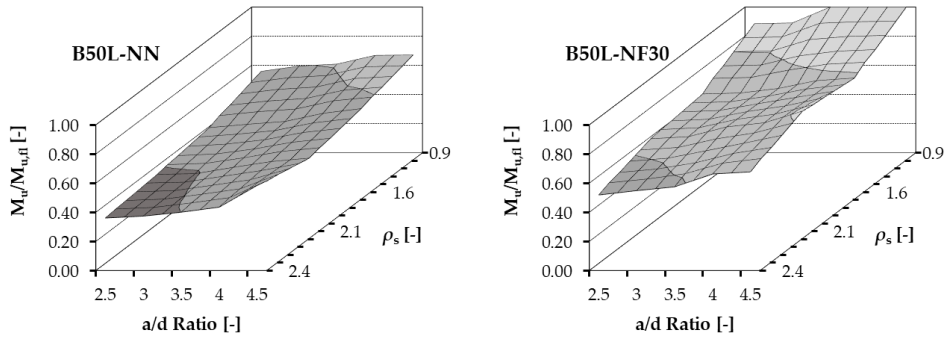

Figure 5.2-39: Influence of the longitudinal reinforcement ratio on the valley of shear failure.

Table 5.2-19 gives the value of $M_u/M_{u,fl}$ obtained from the set of the numerical analyses performed on models of B50L series.

a/d	ρ=0.9%		ρ=1.6%		ρ=2.1%		ρ=2.4%	
	NN	NF	NN	NF	NN	NF	NN	NF
2.5	0.56	0.89	0.44	0.67	0.39	0.63	0.36	0.52
3.0	0.59	0.89	0.46	0.68	0.39	0.65	0.37	0.55
3.5	0.61	1.00	0.48	0.71	0.44	0.72	0.40	0.57
4.0	0.67	1.00	0.54	0.76	0.48	0.74	0.44	0.66
4.5	0.67	1.00	0.57	0.78	0.50	0.82	0.58	0.68
$M_{u,fl}$ **[kN]**	1082	1242	1891	2078	2370	2586	2711	2955

Table 5.2-19: Values of $M_u/M_{u,fl}$ obtained from the numerical analyses of models of B50L series.

The reference beams exhibited a regime of shear failure for all ranges of *a*/*d* and longitudinal reinforcement ratios. Regarding strengthened beams, the shear failure did not appear only in the B50L-NF-0.9 beams for value of *a*/*d*= 3.5, 4.0, and 4.5. The UHPFRC jacketing did not reduce the brittleness of elements that still exhibited a shear failure.

Table 5.2-20 provides the values of peak load, shear strength, ultimate shear stress, and normalized ultimate shear stress.

Beam type	P_{max} [kN]	V [kN]	v_u [MPa]	$\frac{v_u}{\sqrt{f_c}}$	Failure mode	Reinf. yielded
a/d=2.5						
B50L-NN-0.9	529.4	264.7	0.96	0.14	S	No
B50L-NF30-0.9	964.7	482.3	1.75	0.25	S	Yes
B50L-NF40-0.9	1021.2	510.6	1.85	0.26	F	Yes
B50L-NN-1.6	731.4	365.7	1.33	0.19	S	No
B50L-NF30-1.6	1225.5	612.7	2.22	0.31	S	No
B50L-NF40-1.6	1312.5	656.3	2.38	0.34	S	No
B50L-NF50-1.6	1447.4	723.7	2.62	0.37	S	No
B50L-NN-2.1	811.7	405.8	1.47	0.21	S	No
B50L-NF30-2.1	1318.4	659.2	2.39	0.34	S	No
B50L-NF40-2.1	1384.8	692.4	2.51	0.35	S	No
B50L-NF50-2.1	1498.9	749.4	2.72	0.38	S	No
B50L-NN-2.4	856.8	428.4	1.55	0.22	S	No
B50L-NF30-2.4	1344.3	672.1	2.44	0.34	S	No
B50L-NF40-2.4	1470.6	735.3	2.66	0.38	S	No
B50L-NF50-2.4	1591.0	795.5	2.88	0.41	S	No

Table 5.2-20 (Pt. 1 of 3)

a/d=3.0						
B50L-NN-0.9	465.8	232.9	0.84	0.12	S	No
B50L-NF30-0.9	801.4	400.7	1.45	0.21	S	No
B50L-NF40-0.9	832.9	416.4	1.51	0.21	F	Yes
B50L-NN-1.6	635.9	317.9	1.15	0.16	S	No
B50L-NF30-1.6	1022.7	511.3	1.85	0.26	S	No
B50L-NF40-1.6	1075.7	537.9	1.95	0.28	S	No
B50L-NF50-1.6	1083.9	542.0	1.96	0.28	S	No
B50L-NN-2.1	677.3	338.6	1.23	0.17	S	No
B50L-NF30-2.1	1114.4	557.2	2.02	0.29	S	No
B50L-NF40-2.1	1178.3	589.2	2.13	0.30	S	No
B50L-NF50-2.1	1179.2	589.6	2.14	0.30	S	No
B50L-NN-2.4	734.0	367.0	1.33	0.19	S	No
B50L-NF30-2.4	1174.7	587.3	2.13	0.30	S	No
B50L-NF40-2.4	1223.9	612.0	2.22	0.31	S	No
B50L-NF50-2.4	1302.7	651.4	2.36	0.33	S	No
a/d=3.5						
B50L-NN-0.9	411.1	205.6	0.74	0.11	S	No
B50L-NF30-0.9	708.6	354.3	1.28	0.18	F	Yes
B50L-NN-1.6	571.7	285.9	1.04	0.15	S	No
B50L-NF30-1.6	922.7	461.3	1.67	0.24	S	No
B50L-NF40-1.6	968.6	484.3	1.75	0.25	S	No
B50L-NF50-1.6	1003.3	501.7	1.82	0.26	S	No
B50L-NN-2.1	648.9	324.4	1.18	0.17	S	No
B50L-NF30-2.1	1060.2	530.1	1.92	0.27	S	No
B50L-NF40-2.1	1106.4	553.2	2.00	0.28	S	No
B50L-NF50-2.1	1192.1	596.0	2.16	0.31	S	No
B50L-NN-2.4	678.7	339.3	1.23	0.17	S	No
B50L-NF30-2.4	1060.9	530.5	1.92	0.27	S	No
B50L-NF40-2.4	1162.6	581.3	2.11	0.30	S	No
B50L-NF50-2.4	1233.2	616.6	2.23	0.32	S	No
a/d=4.0						
B50L-NN-0.9	392.5	196.3	0.71	0.10	S	No
B50L-NF30-0.9	612.0	306.0	1.11	0.16	F	Yes
B50L-NN-1.6	624.4	312.2	1.13	0.16	F	Yes
B50L-NF30-1.6	554.6	277.3	1.00	0.14	S	No
B50L-NF40-1.6	862.7	431.3	1.56	0.22	S	No
B50L-NF50-1.6	893.1	446.5	1.62	0.23	S	No
B50L-NN-2.1	897.4	448.7	1.63	0.23	S	No
B50L-NF30-2.1	615.5	307.7	1.12	0.16	S	No
B50L-NF40-2.1	958.7	479.3	1.74	0.25	S	No
B50L-NF50-2.1	997.6	498.8	1.81	0.26	S	No
B50L-NN-2.4	1055.7	527.9	1.91	0.27	S	No
B50L-NF30-2.4	641.1	320.6	1.16	0.16	S	No
B50L-NF40-2.4	1064.2	532.1	1.93	0.27	S	No
B50L-NF50-2.4	1086.9	543.4	1.97	0.28	S	No

Table 5.2-20 (Pt. 2 of 3)

a/d=4.5						
B50L-NN-0.9	352.1	176.0	0.64	0.09	S	No
B50L-NF30-0.9	548.3	274.2	0.99	0.14	F	Yes
B50L-NN-1.6	524.8	262.4	0.95	0.13	S	No
B50L-NF30-1.6	788.6	394.3	1.43	0.20	S	No
B50L-NF40-1.6	857.3	428.6	1.55	0.22	S	No
B50L-NF50-1.6	837.3	418.7	1.52	0.21	S	No
B50L-NN-2.1	576.9	288.4	1.05	0.15	S	No
B50L-NF30-2.1	948.5	474.2	1.72	0.24	S	No
B50L-NF40-2.1	975.7	487.8	1.77	0.25	S	No
B50L-NF50-2.1	1036.5	518.3	1.88	0.27	S	No
B50L-NN-2.4	607.6	303.8	1.10	0.16	S	No
B50L-NF30-2.4	971.4	485.7	1.76	0.25	S	No
B50L-NF40-2.4	1037.9	519.0	1.88	0.27	S	No
B50L-NF50-2.4	1060.0	530.0	1.92	0.27	S	No

Notes: - Notation for failure modes: S: Shear; and F: Flexural.
(Pt. 3 of 3)
Table 5.2-20: Summary of finite element analysis results.

With the aim of avoiding the brittle failure mode, a strength steel mesh (SM) was added in the jacket. As observed in previous beams (B25L), when using the steel mesh embedded in the layer of UHPFRC, all beams strengthened with the UHPFRC jacket exhibited a flexure failure without significant shear effects.

5.2.3.9 B70L

Summary results of the shear capacities of reference and retrofitted beams for five shear span-to-effective depth ratios (a/d = 2.5, 3.0, 3.5, 4.0, and 4.5) are illustrated in Figure 5.2-40.

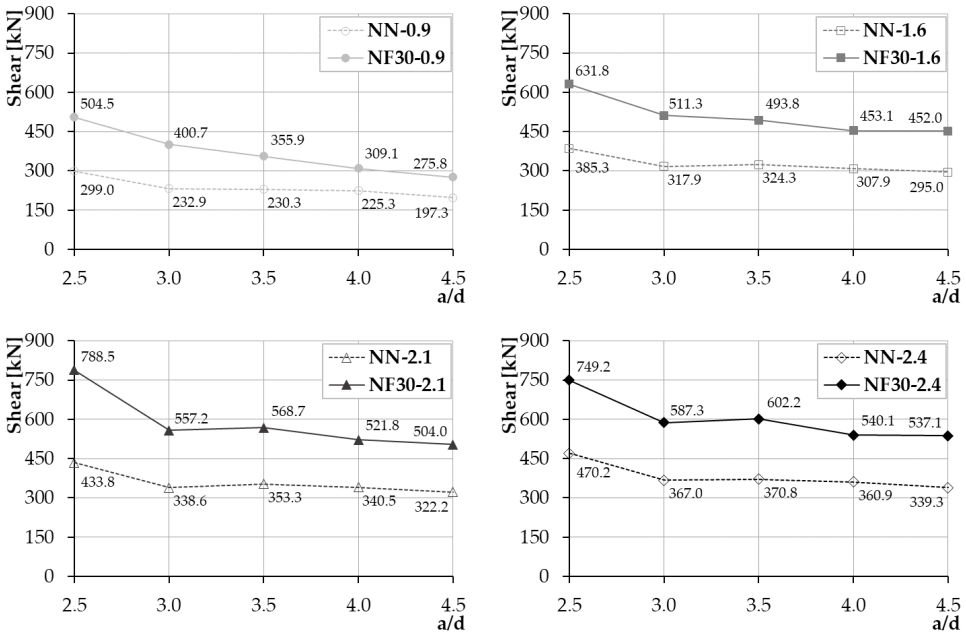

Figure 5.2-40: Summary results of shear capacities of the reference beams (NN) and retrofitted beams (NF).

Figure 5.2-41 shows the 3D plots of the valley of shear diagonal failure as a function of the reinforcement ratio.

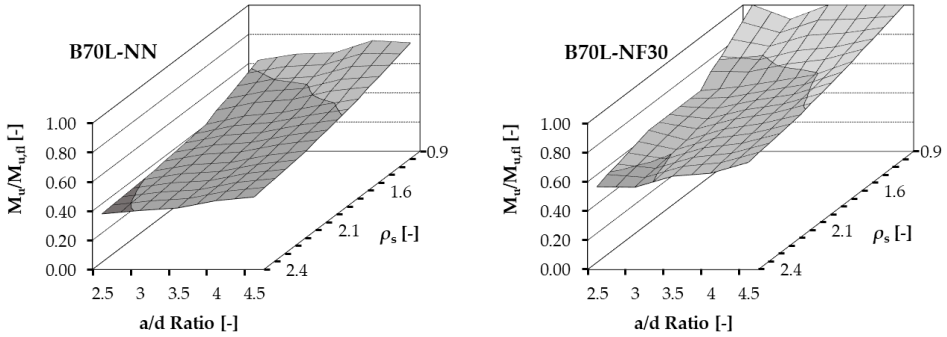

Figure 5.2-41: Influence of the longitudinal reinforcement ratio on the valley of shear failure.

Table 5.2-21 summarizes the value of $M_u/M_{u,fl}$ obtained from the set of the numerical analyses performed on models of the series B70L.

a/d	ρ=0.9%		ρ=1.6%		ρ=2.1%		ρ=2.4%	
	NN	NF	NN	NF	NN	NF	NN	NF
2.5	0.62	1.00	0.45	0.68	0.40	0.68	0.38	0.57
3.0	0.66	1.00	0.51	0.71	0.45	0.62	0.40	0.56
3.5	0.67	1.00	0.54	0.75	0.46	0.69	0.42	0.64
4.0	0.76	1.00	0.58	0.79	0.51	0.73	0.47	0.66
4.5	0.74	1.00	0.63	0.88	0.54	0.79	0.50	0.73
$M_{u,fl}$ **[kN]**	1096	1254	1939	2108	2450	2633	2819	3017

Table 5.2-21: Values of $M_u/M_{u,fl}$ obtained from the numerical analyses of models of B70L series.

The RC beams showed a regime of shear failure for all ranges of *a*/*d* and longitudinal reinforcement ratios, as observed in previous series.
The UHPFRC jacketing did not reduce the brittleness of elements, and they still showed a shear failure. To change the brittle failure, the thickness was increased (up to 50 mm).
The values of peak load, shear strength, ultimate shear stress, and normalized ultimate shear stress are reported in Table 5.2-22.

Beam type	P_{max} **[kN]**	**V [kN]**	v_u **[MPa]**	$\frac{v_u}{\sqrt{f_c}}$	**Failure mode**	**Reinf. yielded**
a/d=2.5						
B70L-NN-0.9	597.9	299.0	1.08	0.13	S	No
B70L-NF30-0.9	1009.0	504.5	1.83	0.22	F	Yes
B70L-NN-1.55	770.5	385.3	1.40	0.17	S	No
B70L-NF30-1.6	1263.6	631.8	2.29	0.27	S	No
B70L-NF40-1.6	1481.5	740.8	2.68	0.32	S	No
B70L-NF50-1.6	1515.2	757.6	2.74	0.33	S	No
B70L-NN-2.1	867.6	433.8	1.57	0.19	S	No
B70L-NF30-2.1	1606.5	803.3	2.91	0.35	S	No
B70L-NF40-2.1	1577.6	788.8	2.86	0.34	S	No
B70L-NF50-2.1	1564.3	782.1	2.83	0.34	S	No
B70L-NN-2.4	940.4	470.2	1.70	0.20	S	No
B70L-NF30-2.4	1498.4	749.2	2.71	0.32	S	No
B70L-NF40-2.4	1530.2	765.1	2.77	0.33	S	No
B70L-NF50-2.4	1653.5	826.8	3.00	0.36	S	No

Table 5.2-22 (Pt. 1 of 3)

a/d=3.0						
B70L-NN-0.9	527.5	263.8	0.96	0.11	S	No
B70L-NF30-0.9	820.1	410.1	1.49	0.18	S	No
B70L-NF40-0.9	838.4	419.2	1.52	0.18	F	Yes
B70L-NN-1.55	716.7	358.4	1.30	0.16	S	No
B70L-NF30-1.6	1084.2	542.1	1.96	0.23	S	No
B70L-NF40-1.6	1113.9	556.9	2.02	0.24	S	No
B70L-NF50-1.6	1135.0	567.5	2.06	0.25	S	No
B70L-NN-2.1	794.2	397.1	1.44	0.17	S	No
B70L-NF30-2.1	1173.5	586.7	2.13	0.25	S	No
B70L-NF40-2.1	1274.8	637.4	2.31	0.28	S	No
B70L-NF50-2.1	1324.9	662.4	2.40	0.29	S	No
B70L-NN-2.4	824.6	412.3	1.49	0.18	S	No
B70L-NF30-2.4	1231.0	615.5	2.23	0.27	S	No
B70L-NF40-2.4	1348.8	674.4	2.44	0.29	S	No
B70L-NF50-2.4	1387.4	693.7	2.51	0.30	S	No
a/d=3.5						
B70L-NN-0.9	460.6	230.3	0.83	0.10	S	No
B70L-NF30-0.9	711.8	355.9	1.29	0.15	F	Yes
B70L-NN-1.55	648.6	324.3	1.18	0.14	S	No
B70L-NF30-1.6	987.6	493.8	1.79	0.21	S	No
B70L-NF40-1.6	1039.4	519.7	1.88	0.23	S	No
B70L-NF50-1.6	1070.2	535.1	1.94	0.23	S	No
B70L-NN-2.1	706.6	353.3	1.28	0.15	S	No
B70L-NF30-2.1	1137.3	568.7	2.06	0.25	S	No
B70L-NF40-2.1	1190.5	595.3	2.16	0.26	S	No
B70L-NF50-2.1	1210.6	605.3	2.19	0.26	S	No
B70L-NN-2.4	741.6	370.8	1.34	0.16	S	No
B70L-NF30-2.4	1204.4	602.2	2.18	0.26	S	No
B70L-NF40-2.4	1257.6	628.8	2.28	0.27	S	No
B70L-NF50-2.4	1346.1	673.1	2.44	0.29	S	No
a/d=4.0						
B70L-NN-0.9	450.7	225.3	0.82	0.10	S	No
B70L-NF30-0.9	618.2	309.1	1.12	0.13	F	Yes
B70L-NN-1.55	615.8	307.9	1.12	0.13	S	No
B70L-NF30-1.6	906.2	453.1	1.64	0.20	S	No
B70L-NF40-1.6	938.9	469.4	1.70	0.20	S	No
B70L-NF50-1.6	976.7	488.4	1.77	0.21	S	No
B70L-NN-2.1	681.1	340.5	1.23	0.15	S	No
B70L-NF30-2.1	1043.7	521.8	1.89	0.23	S	No
B70L-NF40-2.1	1079.6	539.8	1.96	0.23	S	No
B70L-NF50-2.1	1119.0	559.5	2.03	0.24	S	No
B70L-NN-2.4	721.7	360.9	1.31	0.16	S	No
B70L-NF30-2.4	1080.1	540.1	1.96	0.23	S	No
B70L-NF40-2.4	1200.7	600.3	2.18	0.26	S	No
B70L-NF50-2.4	1220.9	610.5	2.21	0.26	S	No
B70L-NN-0.9	450.7	225.3	0.82	0.10	S	No

Table 5.2-22 (Pt. 2 of 3)

a/d=4.5						
B70L-NN-0.9	394.6	197.3	0.71	0.09	S	No
B70L-NF30-0.9	551.5	275.8	1.00	0.12	F	Yes
B70L-NN-1.55	589.9	295.0	1.07	0.13	S	No
B70L-NF30-1.6	903.9	452.0	1.64	0.20	S	No
B70L-NF40-1.6	870.4	435.2	1.58	0.19	S	No
B70L-NF50-1.6	935.2	467.6	1.69	0.20	S	No
B70L-NN-2.1	644.4	322.2	1.17	0.14	S	No
B70L-NF30-2.1	1007.9	504.0	1.83	0.22	S	No
B70L-NF40-2.1	1028.3	514.1	1.86	0.22	S	No
B70L-NF50-2.1	1064.8	532.4	1.93	0.23	S	No
B70L-NN-2.4	678.6	339.3	1.23	0.15	S	No
B70L-NF30-2.4	1074.1	537.1	1.946	0.233	S	No
B70L-NF40-2.4	1120.1	560.0	2.029	0.243	S	No
B70L-NF50-2.4	1160.8	580.4	2.103	0.251	S	No

Notes: - Notation for failure modes: S: Shear; and F: Flexural.
(Pt. 3 of 3)
Table 5.2-22: Summary of finite element analysis results.

As in the previous series, a high-strength steel mesh embedded in the layer of UHPFRC was necessary to have a flexure failure without shear effects.

5.2.4 *Concluding remarks*

The parametric study was conducted in order to determine the effect of a UHPFRC jacket, investigating the influence of geometric parameters, concrete compressive strength, longitudinal reinforcement ratio, and thickness of the UHPFRC layer.
The finite element analyses demonstrated the effect that the UHPFRC jackets have on the failure mode, as well as on the post-cracking behaviour, and on the formation and evolution of cracks.

Influence of beam sizes

The size S beams strengthened with the UHPFRC layer presented a flexure failure, with limited shear effects. Therefore, the jacket plays a role of shear reinforcement and may be considered as an effective shear strengthening method. Differently, in sizes M and L, the use of the UHPFRC layer seems to not be an efficient shear repairing method by itself. The use of steel mesh embedded in the layer of UHPFRC allowed one to largely increase the structure deformation capacity and ductility. It is worth noting that retrofitted beams by steel mesh embedded in the layer of UHPFRC exhibited a flexural failure. Therefore, this technique increased the shear capacity and modified the brittle failure mode to a more ductile one.

Influence of compressive concrete strength

When the perfect bond conditions were considered, the concrete compressive strength does not significantly influence the effect of the UHPFRC jacketing. On the other hand, in the IE-models, the concrete compressive strength is a significant

parameter affecting the interface bond between concretes with different ages. It is worth noting that the effect of substrate compressive strength is much more important for a high reinforcement ratio, where bihher shear stresses are achieved.

Influence of reinforcement ratio

In the strengthened beams, with increasing longitudinal reinforcement ratio, the valley of diagonal shear failure tends to become deeper. The NF-beams having a higher reinforcement ratio show a significant regime of shear failure, while for the lower longitudinal reinforcement ratio the valley of shear diagonal failure disappears completely. Moreover, it was observed that the shear stresses at the interface between substrate and overlay increase with increasing longitudinal reinforcement ratio.

Influence of UHPFRC layer

Figure 5.2-42 shows the type of reinforcement used to achieve flexural failure.

In the size S series, all retrofitted specimens exhibited a flexure failure.

In the size M series, 35% (for f_c=25 MPa), 40% (for f_c=50 MPa), and 45% (for f_c=70 MPa) of the beams strengthened with the UHPFRC jacket showed a flexural failure. Instead, using a steel mesh embedded in the layer of UHPFRC, all beams (100%) exhibited a flexural failure.

In size L, 25% (for f_c =25 MPa), 30% (for f_c =50 MPa), and 25% (for f_c =70 MPa) of the elements strengthened with the UHPFRC jacket showed a flexural failure. When a steel mesh embedded in the layer of UHPFRC was used, all beams exhibited a flexural failure.

It can be concluded that the retrofit intervention presented in this section is able to bring a structural member to its flexural capacity. The regime of the valley of diagonal shear failure in strengthened beams may abate or even disappear completely, depending on the thickness and on the presence of the steel mesh. The use of UHPFRC jacketing can be an efficient method for shear strengthening of RC beams, completed with a high-strength steel mesh especially when dealing with deep beams (affected by size effect) and high longitudinal reinforcement ratio.

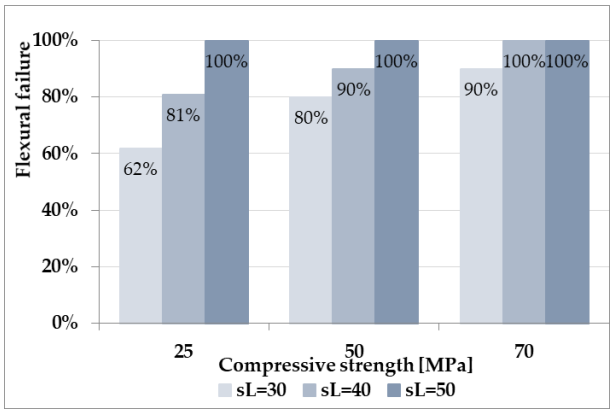

S sizes

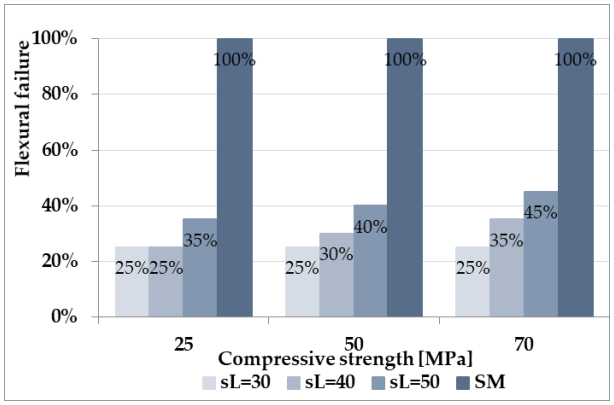

M seizes

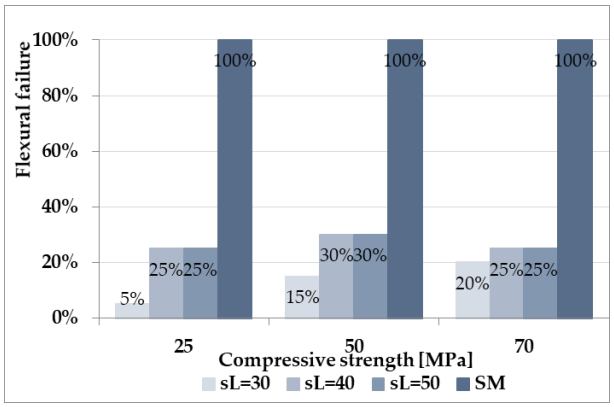

L sizes

Figure 5.2-42: Percentage of flexural failure in the strengthened beams having different types of reinforcement.

5.3 Case study: numerical analyses of existing damaged I-beams

5.3.1 *Introduction*

The behaviour of members in shear is an area of much concern. The shear failure is brittle; for this reason, it is necessary to prevent this type of failure and provide realistic assessment of the strength, stiffness, and ductility of structural elements under shear loading. With that aim, numerical analyses could represent an alternative way for studying the response of a wide range of beams.
This section presents predictive analyses for the suitable design of experimental tests, comprising loading scheme and instrumentations, of existing prestressed concrete beams. The main objective of these was to study the efficacy of Ultra-High-Performance Fibre Reinforced Concrete (UHPFRC) jacket on shear strengths, failure mechanisms, crack control, and ductility.
In this numerical study, two series were considered: I-Beam Series 1 and I-Beam Series 2. For the reference beam, the design state and the actual situation were modelled. Additionally, in the Series 2, the corrosion effect was considered. The corrosion process mainly results in a reduction of the steel cross section and a worsening of the reinforcing steel strength and ductility properties [Cairns *et al.*, 2005; Imperatore and Rinaldi, 2008; Rinaldi *et al.*,2010]. Two different corrosion morphologies can take place, uniform or localized ones, often associated to different degradation processes. For the purpose of this study, the corrosion was investigated in two simplified methods: (1) reducing the steel cross section and (2) worsening of the reinforcing steel strength and ductility properties. The steel cross section was reduced by 15% and 30%, while the steel strength and ductility properties were calculated according to the formulation proposed by Imperatore *et al.* [2017]. The degradation equations that consider the effect of uniform corrosion are presented in the following.

$$\sigma_{y,corr} = (1 - 0.0143453 \cdot M_{corr}) \cdot \sigma_{y,uncorr} \quad (5.3\text{-}1)$$

$$\sigma_{u,corr} = (1 - 0.0125301 \cdot M_{corr}) \cdot \sigma_{u,uncorr} \quad (5.3\text{-}2)$$

$$\varepsilon_{u,corr} = e^{-0.0204983 \cdot M_{corr}} \cdot \varepsilon_{u,uncorr} \quad (5.3\text{-}3)$$

where
$\sigma_{y,uncorr}$ and $\sigma_{u,uncorr}$ are the yielding and ultimate strengths of uncorroded rebars,
$\sigma_{y,corr}$ and $\sigma_{u,corr}$ are the yielding and ultimate strengths of corroded rebar,
$\varepsilon_{u,uncorr}$ and $\varepsilon_{u,corr}$ are the ultimate strains of uncorroded and corroded rebar,
M_{corr} is the percentage of mass lost.
These equations refer to the nominal section of the rebar (original section before corrosion).

In this study uniform corrosion on the stirrups was considered, and four scenarios of corrosion were evaluated:

i. steel cross section was reduced by 15%,
ii. steel cross section was reduced by 30%,
iii. strength and ductility properties calculated with M_{corr}=15%,
iv. strength and ductility properties calculated with M_{corr}=30%.

Furthermore, with the purpose of studying the efficiency of UHPFRC jacket, both series were reinforced with the UHPFRC jacket.

The following acronyms will be used to identify the different specimens:

- B1: I-Beam Series 1 (first set):
  - B1N-0: design prestressed concrete beam;
  - B1N-1: actual prestressed concrete beam;
  - B1F-1a: actual prestressed concrete beam reinforced with 50 mm of UHPFRC jacketing in the shear span;
  - B1F-1b: actual prestressed concrete beam reinforced with UHPFRC jacketing (50 mm) in the total length.
- B2: I-Beam Series 2 (second set):
  - B2N-0a: design prestressed concrete beam;
  - B2N-0b: corroded beam scenario i;
  - B2N-0c: corroded beam scenario ii;
  - B2N-0d: corroded beam scenario iii;
  - B2N-0e: corroded beam scenario iv;
  - B2N-1: actual prestressed concrete beam;
  - B2F-0a: actual prestressed concrete beam reinforced with UHPFRC jacketing;
  - B2F-0e: corroded prestressed concrete beam reinforced with UHPFRC jacketing.

The details and results of these studies are described in the following paragraphs.

5.3.2 *Numerical modelling of the beams*

The numerical research program conducted in this work provides the analysis of existing prestressed concrete beams. The existing specimens consisted of two sets of prestressed beams having different length.

The first set had a total length of 24.36 m. Figure 5.3-1 shows the cross section of the beam and the strand positions. The beam was characterized by thirty-four strands having a diameter of 3/8'' and one post-tension tendon consisting in twelve wires having a diameter of 7mm each. In addition, stirrups Ø10 were adopted, and their position is illustrated in Figure 5.3-2.

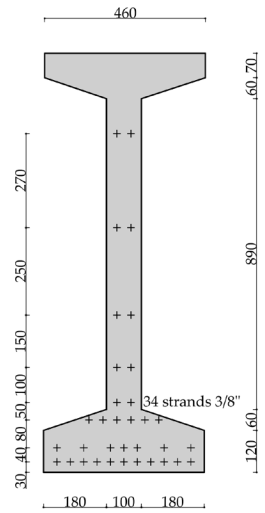

Figure 5.3-1: Cross section of the prestressed beam set 1.

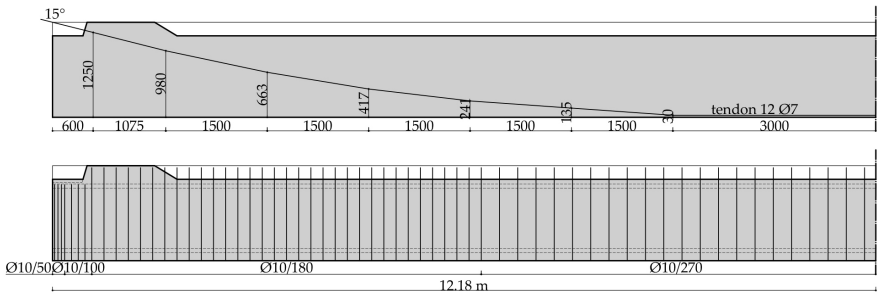

Figure 5.3-2: Geometry and reinforcement details of the prestressed beam set 1.

The second set was a prestressed beam having a total length of 10.27 m. The beam was characterized by twenty strands having a diameter of 3/8''. Figure 5.3-3 illustrates the cross section of the beam and the strand positions. In addition, stirrups Ø10 were adopted, and their position is illustrated in Figure 5.3-4.
Both sets were reinforced with a UHPFRC jacket and a steel mesh embedded in the layer of UHPFRC.

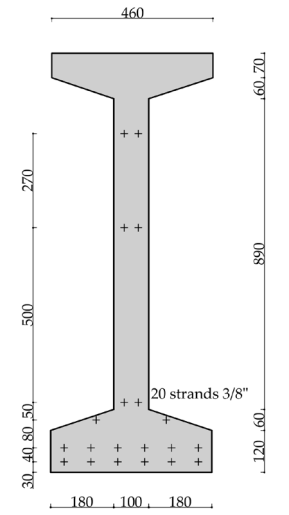

Figure 5.3-3: Cross section of the prestressed beam set 2.

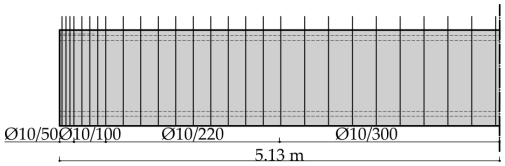

Figure 5.3-4: Geometry and reinforcement details of the prestressed beam set 2.

In the design beams, the material mechanical properties were based from the design report. The design compressive strength ($f_{c,cube}$) was 60 N/mm², the cylindrical compressive strength (f_{cm}) was calculated as 83% of $f_{c,cube}$. The tensile strength (f_{pt}) of prestressing strand was 1800 N/mm². The ductile steel reinforcement adopted was Aq 50, steel traditionally used in Italy in the 1960s. The yielding (f_{sy}) and tensile (f_{st}) strength were f_{sy}=370 N/mm² and f_{st}=545 N/mm², respectively. The values were based on experimental program conducted by Verderame *et al.* [2001].

In the actual beams, the material mechanical properties were based from field investigations. The compressive strength ($f_{c,cube}$ =42.1 N/mm²) was measured from cylinders with diameters and heights of 65 mm. The cylindrical compressive strength (f_{cm}) was calculated as 83% of $f_{c,cube}$. The tensile strength (f_{pt}) of prestressing strand, determined by tensile test, was 1490.45 N/mm². The yielding (f_{sy}) and tensile (f_{st}) strengths of the traditional steel reinforcement were f_{sy}=347 N/mm² and f_{st}=539.4 N/mm², respectively.

For the strengthening of the prestressed beams, Planitop HPC Floor 46 (PHF46) by MAPEI S.p.A. was used as the jacketing material. It is a high performance semi-fluid cementitious mortar reinforced with steel fibres. The steel fibres are DRAMIX®-RC-

80/30 BD. The mix design composition of the material is not stated on the datasheet. The mechanical properties of the UHPFRC were reported in Chapter 3.
In VecTor2, all beams were modelled using rectangular concrete elements and truss elements. In I-Beam Series 1N and 2N, the mesh was divided into five regions: four flange regions and one web region, according to the geometry of the I-beam. The beams could not be modelled as the actual members; in fact, VecTor2 cannot model a trapezoidal section. Therefore, the elements were modelled so that the areas and inertia were the same as those of the specimen sections. The elements in the flanges were divided into four regions having dimensions of 460 x 120 mm, 280 x 60 mm, 280 x 60 mm and 460 x 70 mm respectively; the elements in the web had a dimension of 100 x 890 mm.
In I-Beam Series 1F and 2F, the mesh was divided in six regions: four flange regions, one web region, and one UHPFRC jacketing region. The flange regions and web region had the same dimension of reference beams, and the UHPFRC region was a thickness of 50mm.
Figure 5.3-5 schematizes the FEA I-beam section respect to the existing specimen section; in Figure 5.3-6 the front views are reported.

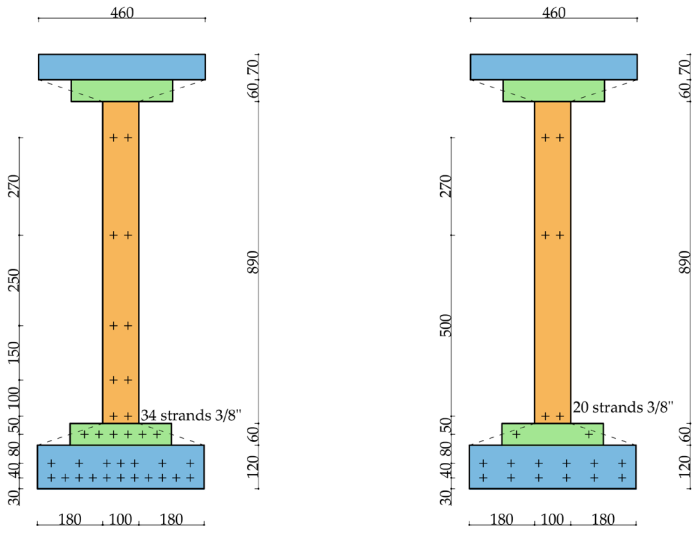

a) *b)*

Figure 5.3-5 (Pt. 1 of 2)

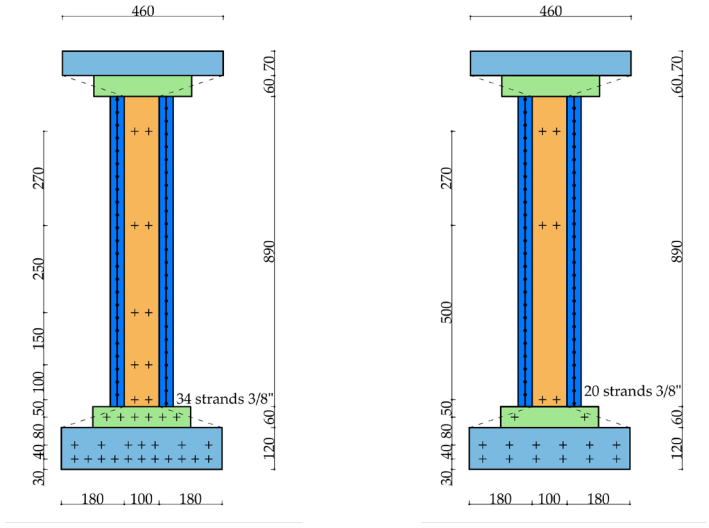

c) *d)*

(Pt. 2 of 2)

Figure 5.3-5: FE representation section of I-Beam Series 1N (a), I-Beam Series 2N (b), I-Beam Series 1F (c), and I-beam Series 2F (d).

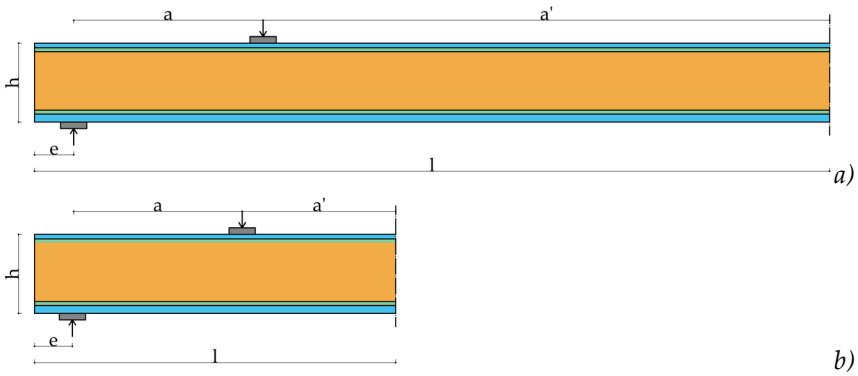

Figure 5.3-6 (Pt. 1 of 2)

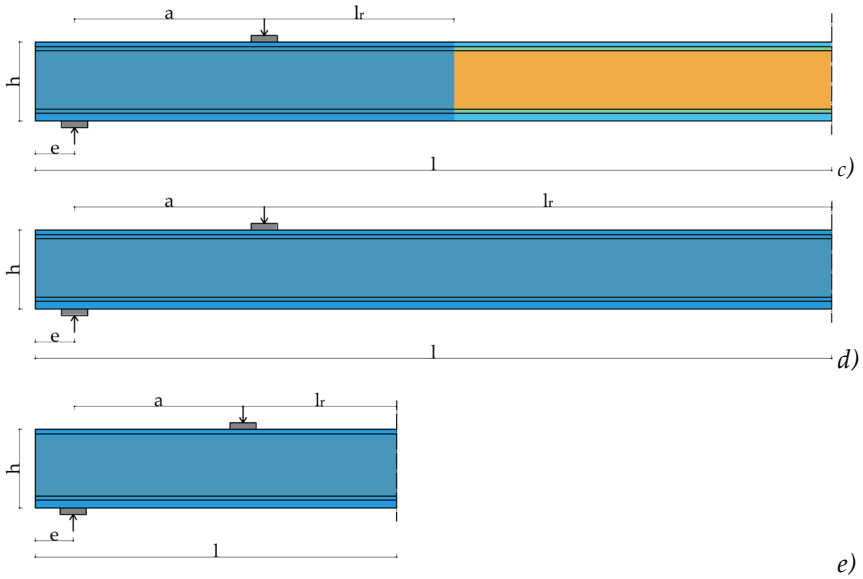

(Pt. 2 of 2)

Figure 5.3-6: Front view of I-Beam Series 1N (a), I-Beam Series 2N (b), I-Beam Series 1F-a (c), I-Beam Series 1F-b (d), and I-beam Series 2F (e).

In both series, the shear span-to-effective depth ratio, *a/d*, was selected to induce a shear failure mode. Nevertheless, *a/d* less than 2.5 was not chosen. In fact, for beams with an *a/d* ratio less than 2.5, a direct concrete strut from the loading point to the support is formed. On the other hand, if the beams are too slender, a flexural failure mode will be likely to happen. Due to these reasons, an *a/d* ratio of 3 (for the first set), and 2.7 (for the second set) was selected.
In Table 5.3-1 the geometric details of I-Beams are reported.

Dimension	**B1N**	**B1F-a**	**B1F-b**	**B2N**	**B2F**
b	0.28 m	0.28 m	0.28 m	0.28 m	0.28 m
B	0.46 m	0.46 m	0.46 m	0.46 m	0.46 m
t	0.1 m	0.1 m	0.1 m	0.1 m	0.1 m
h	1.2 m	1.2 m	1.2 m	1.2 m	1.2 m
a	2.9 m	2.9 m	2.9 m	2.6 m	2.6 m
a'	8.68 m	8.68 m	8.68 m	1.95 m	1.95 m
e	0.6 m	0.6 m	0.6 m	0.58 m	0.58 m
s_L	-	0.05 m	0.05 m	-	0.05 m
l_r	-	6.2 m	12.18 m	-	5.13 m
l	12.18 m	12.18 m	12.18 m	5.13 m	5.13 m

Table 5.3-1: Geometry details.

Due to the symmetry of the beams and the loading scheme, only half of each reference beams and only one-quarter of each strengthened beams were modelled. The beams were restrained in the x- and y-directions at the nodal supports. The elements were restrained against movement in the x-direction at mid-span cross-section (plane of symmetry).
Table 5.3-2 reports the main features of the meshes adopted for the different sets of beams considered.
The longitudinal and transverse reinforcement were modelled as truss elements. Moreover, the additional stirrups placed close to support were inputted as smeared reinforcement.

Specimens	**Concrete elements**	**Reinforcement elements**
I-Beam 1N-0 **I-Beam 1N-1**	2212 (mesh 90x90)	2013 truss elements
I-Beam 1F-1a **I-Beam 1F b**	2913 (mesh 90x90) 3554 (mesh 90x90)	2013 truss elements 2013 truss elements
I-Beam 2N-0 **I-Beam 2N-1**	3794 (mesh 50x50)	1836 truss elements
I-Beam 2F-1	5846 (mesh 50x50)	1836 truss elements

Table 5.3-2: Summary of numerical models.

The pretension loading was simulated by applying a prestrain to the tendons. In all beams, the prestrain was chosen equal to the design value, considering the losses in the amount of 28% of the total initial value. In order to account for the prestressing losses, a prestrain of 5.25 x 10^{-3} mm/mm (corresponding to a prestress of 972 MPa) was applied to all cables instead of the original 7.2 x 10^{-3} mm/mm (corresponding to a prestress of 1400 MPa). In the transfer zone, a linear development of prestrain was assumed in order to simulate the transfer phenomenon of the pretensioning from the beam end to a distance equal to 80 strand diameters (800 mm), beyond which the pretension action was assumed to be uniform and completely developed. In VecTor2, the linear development of prestrain was simplified considering four steps of increment.
In the post-tension tendon, the losses due to friction between the tendon and the duct were evaluated. The frictional loss was considered as consisting of two components: the curvature and the wobble frictional losses [Collins and Mitchell 1991].
In I-Beam 1N series, to consider the losses over the length of the post-tension tendon, the tendon was modelled using six materials each one with a different prestain value. An initial prestrain of 6.05 x 10^{-3} mm/mm (corresponding to a prestress of 1120 MPa) was applied.
Concrete and steel properties were reported in Table 5.3-3.

Beam type	Concrete			Reinforcement			
				Stirrups		Tendons	
	$f_{c,cube}$ [MPa]	f_c [MPa]	E_c [MPa]	f_{sy} [MPa]	f_u [MPa]	f_{sy} [MPa]	f_u [MPa]
I-Beam 1N-0	60	49.8	36000	370	545	1600	1800
I-Beam 1N-1	42.1	34.9	35490	347	539.4	1324	1490
I-Beam 1F-1	42.1	34.9	35490	347	539.4	1324	1490
I-Beam 2N-0	60	49.8	36000	370	545	1600	1800
I-Beam 2N-1	42.1	34.9	35490	347	539.4	1324	1490
I-Beam 2F-1	42.1	34.9	35490	347	539.4	1324	1490

Table 5.3-3: Summary of material properties.

To consider the corrosion effect, in Series 2 beams, the steel cross section and the steel strength and ductility properties were different with respect the reference beam. Table 5.3-4 lists the steel properties used in VecTor2.

	B2N-0a	B2N-0b	B2N-0c	B2N-0d	B2N-0e
A_s [mm²]	157	133	110	157	157
D_b [mm]	10	9.2	8.4	9.2	8.4
f_y [MPa]	370	370	370	290	211
f_u [MPa]	545	545	545	443	340
E_s [MPa]	200000	200000	200000	200000	200000
ε_{sh} [me]	10	10	10	10	10
ε_{su} [me]	260	260	260	191	141

Table 5.3-4: Steel properties.

In VecTor2, the fibres were input as smeared reinforcement. The reference type was discrete steel fibre in the reinforcement component of the reinforced concrete. The inputs required for the fibre reinforcement definition were the fibre type, the fibre volume fraction (V_f), the length and the diameter of the fibres (L_f and D_f), the ultimate tensile strength of the fibres (F_u), and the average interfacial bond strength between the fibre and the concrete matrix (T_u). If the average interfacial bond strength input is set equal to zero, the VecTor2 default value will be used. For hooked-end fibres, Voo and Foster [2003] suggested that it should be evaluated as $\tau_u=2.5\,f_{ct}$, with f_{ct} being the tensile strength of the plain concrete in MPa.
UHPFRC mechanical properties adopted in the numerical analyses were presented in Section 3.2, Section 3.3, and Section 5.2.
In the retrofitted models, between the concrete substrate and the UHPFRC jacket, perfect bond was assumed (as explained in Section 5.2.25.1.2).
The steel mesh embedded in the layer of UHPFRC was modelled as smeared reinforcement. The mesh, having high tensile strength (f_y=1100 MPa, f_u=1700), was made of 5 mm diameter bent wires, assembled with a spacing of 50 mm. The inputs were reinforcement direction, reinforcement ratio (calculated based on the spacing), reinforcement diameter, yield strength, ultimate strength, and elastic modulus.

The beams were loaded under a four-point bending configuration. In order to avoid unrealistic punching failure and numerical instability problems due to the load concentration, the load was transferred to the top surface of the element by a steel plate (same material and dimensions as used for the supports) perfectly connected to the concrete elements. For the I-Beam model, two load case analysis was defined: (1) dead load, and (2) point load. The point load was applied as a monotonically increasing displacement up to failure. The analysis was conducted in displacement-control with an increment step size of 0.5 mm.
The load was transferred to the top surface of the element by a bearing material and steel plate (same material and dimensions as used for the supports in Section 5.2.2)
The constitutive models used in the finite element analysis were the default models, with the exception of the compression pre-peak and compression post-peak, which used the Hoshikuma *et al.* [1997]. In VecTor2, the default model for FRC in tension is the Simplified Diverse Embedment Model (SDEM) [Lee et al., 2012]. For monotonic loading conditions, in the SDEM, the tensile stress in the fibres is expressed by the frictional bond behaviour in straight fibres and the additional mechanical anchorage in hooked-end fibres. Table 5.3-5 lists the concrete and reinforcement constitutive models used in VecTor2.

Concrete Models			
Compression Pre-Peak	Hoshikuma et al. (parabola)	**Dilation**	Variable – isotropic †
Compression Post-Peak	Hoshikuma et al. (parabola)	**Cracking Criterion**	Mohr – Coulomb (stress) †
Compression Softening	Vecchio 1992-A †	**Crack Stress Calculation**	Basic (DSFM/MCFT) †
Tension Stiffening	Modified Bentz 2003 †	**Crack Width Check**	Agg/2.5 max crack width †
Tension Softening	Nonlinear (Hordijk) †	**Crack-Slip Calculation**	Walraven †
FRC Tension	SDEM-Monotonic†	**Creep and Relaxation**	Not considered †
Confined Strength	Kupfer / Richart †	**Hysteretic Response**	Nonlinear w/ Plastic offsets †
Reinforcement Models			
Hysteretic Response	Bauschinger Effect (Seckin) †	**Buckling**	Akkaya 2012 †
Dowel Effect	Tassios (Crack Slip) †	**Concrete Bond**	Eligehausen †

†*Default models assumed by VecTor2 unless specified otherwise.*
Table 5.3-5: Concrete and reinforcement constitutive model used in VecTor2.

5.3.3 *Finite element analysis results*

The finite element analysis results for existing prestressed concrete beams are reported and described in this section.
The *shear vs. mid-span deflection* curves were plotted. A comparison between the design state and the actual situation was proposed. Additionally, for both series, the response of the reference beam was compared with the response of the strengthened beam.

5.3.3.1 I-Beam Series 1

The responses of the Series 1 I-beams are reported and discussed in the following.
Figure 5.3-7 shows the comparison between the *shear vs. mid-span deflection* curves of the design state (B1N-0) and the actual situation (B1N-1).

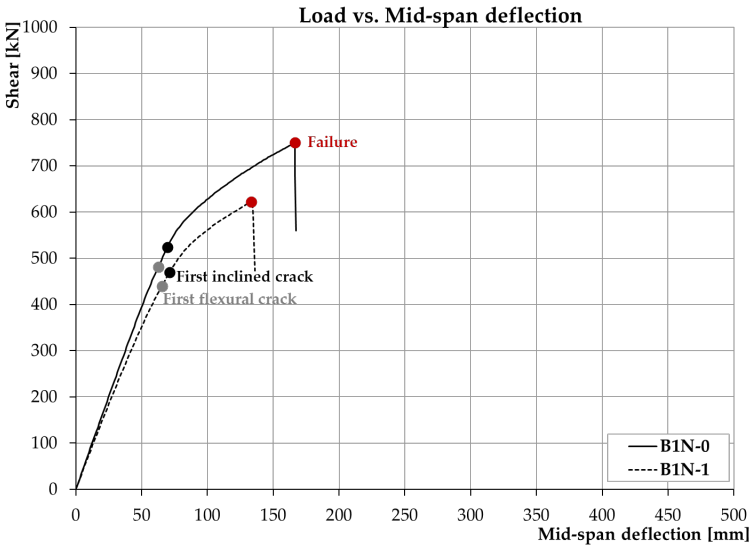

Figure 5.3-7: Shear vs. mid-span deflection curves (B1N-0: design prestressed concrete beam; B1N-1: actual prestressed concrete beam).

Both beams presented a brittle failure mechanism and the same crack patterns. Flexural cracks first developed from the bottom surface of the beam in the region below the loading point. As the applied load increased, an inclined crack occurred. B1N-0 beam developed the first flexural cracks and the first inclined cracks at the shear of 481 kN and 525 kN, respectively. The beam exhibited several inclined cracks prior to a complete failure. The maximum shear was 750 kN, 43% greater than the shear at which the first observed inclined cracks. Similarly, the shear in B1N-1 beam at first flexural cracking, first inclined crack, and failure was 440, 464, and, 624 kN, respectively.

In both cases, the stirrups yielded just before the failure, while yielding of the tendons did not occur.
Figure 5.3-8 illustrates the crack patterns of B1N-0 (a) and B1N-1 (b) beams after the failure.

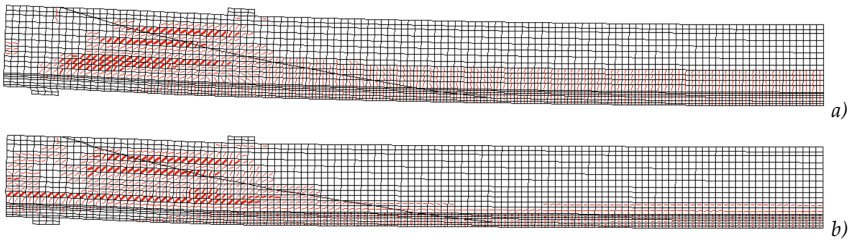

Figure 5.3-8: Schematic crack patterns after failure: a) B1N-0 (design prestressed concrete beam), b) B1N-1(actual prestressed concrete beam).

Figure 5.3-9 reports the comparison between the *shear vs. mid-span deflection* curves of the actual beam (B1N-1) and the strengthened beams (B1F-1a, B1F-1b).

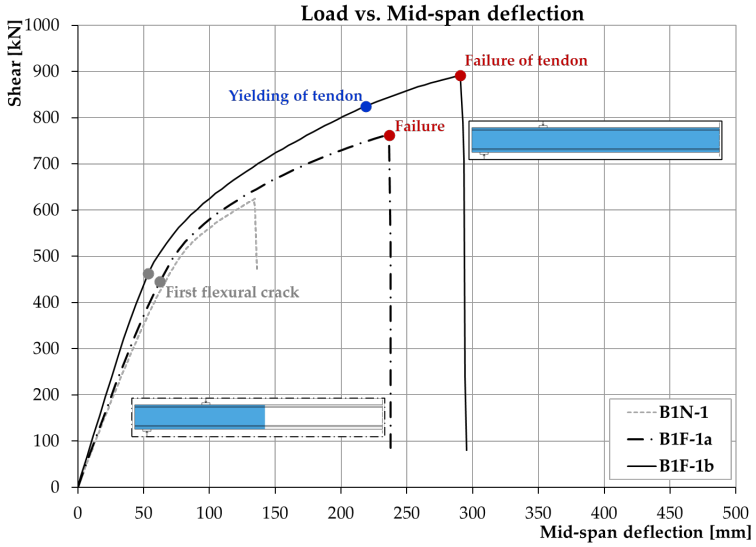

Figure 5.3-9: Shear vs. mid-span deflection curves (B1N-1: actual prestressed concrete beam; B1F-1a: actual prestressed concrete beam reinforced with 50 mm of UHPFRC jacketing in the shear span; B1F-1b: actual prestressed concrete beam reinforced with UHPFRC jacketing (50 mm) in the total length).

It is clear that the UHPFRC jacketing improved the resistance of the prestressed concrete beams. Compared with B1N-1 beam, which had a shear of 624 kN, B1F-1a and B1F-1b beams had a significantly higher shear of 762 kN and 850 kN, respectively. Concerning B1F-1a beam, the first flexural cracks appeared at a value of shear of 446 kN. After the first cracking point, vertical cracks developed in the

central portion of the specimen. Those cracks, with increasing load, propagated in width and in number even beyond the point load. After the peak load was achieved (shear of 762 kN), the beam failed due to crushing of concrete in the web region in the mid-span of the beam. In B1F-1a beam, yielding of stirrups and tendons did not occur.

B1F-1b beam developed the first flexural cracks at the value of shear of a 463 kN (3.7% greater than the first cracking point in the B1F-1a beam and quite the same cracking load of the B1N-1 beam). With increasing loading, the beam shown a more diffused cracking. However, no significant shear cracks were observed. For a load intensity of around 1650 kN (shear of 825 kN), the yielding of the tendons was observed. Before the collapse, considerable vertical cracks developed close to the load point. At the peak load, the tensile strength of the tendon achieved their ultimate tensile strength. Moreover, in the strengthened beam, the stirrups did not yield.

Figure 5.3-10 depicts the crack patterns for B1F-1a (a) and B1F-1b (b) beams after the failure.

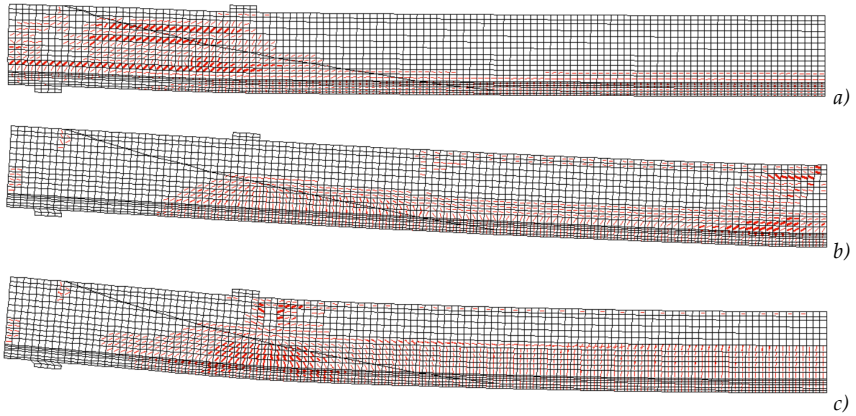

Figure 5.3-10: Schematic crack patterns after failure: a) B1N-1 (actual prestressed concrete beam), b) B1F-1a (actual prestressed concrete beam reinforced with 50 mm of UHPFRC jacketing in the shear span), c) B1F-1b (actual prestressed concrete beam reinforced with UHPFRC jacketing (50 mm) in the total length).

5.3.3.2 I-Beam Series 2

Below, the responses of the Series 2 I-beams are presented and discussed.
Figure 5.3-11 illustrates the *shear vs. mid-span deflection* curves for the design beam (B2N-0a) and the actual beam (B2N-1).

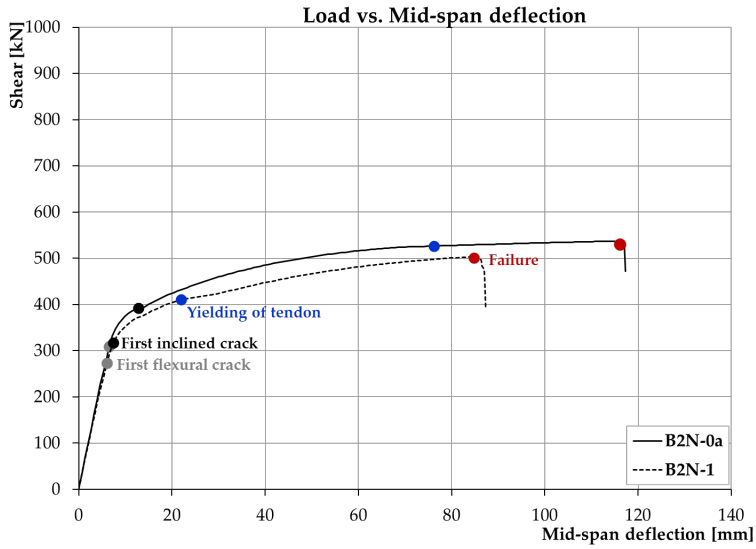

Figure 5.3-11: Shear vs. mid-span deflection curves (B2N-0a: design prestressed concrete beam; B2N-1: actual prestressed concrete beam)

In both beams, cracking appeared at the end of the elastic stage, with a shear value approximately equal to 310 kN (for B2N-0a) and 298 kN (for B2N-1). In the post-cracking response, some differences were observed in the behaviour of the two beams. B2N-0a beam developed the first inclined cracks at the applied load of around 734 kN (shear of 372 kN). Increasing the load, the flexural cracks widened and propagated in number in the central portion of the beam. Yielding of the tendons occurred around a shear value of 526 kN. At the maximum shear (537 kN), yielding of the stirrups was observed and immediately after the failure occurred.
In B2N-1 beam, the shear values at first flexural cracking, first inclined crack, and yielding of tendons were 298, 317, and,410 kN. As observed in B2N-0a beam, yielding of stirrups was immediately followed by the failure of the beam. In both cases the ultimate capacity was achieved.
The crack evolution was quite similar to that B2N-0a beam. In both cases, the beam shown a wide distributed flexural cracking in the central portion of the element. Nevertheless, it failed due to the crushing of concrete in the web region in the shear span.
Figure 5.3-12 illustrates the crack patterns of B2N-0a (a) and B2N-1 (b) beams after the failure.

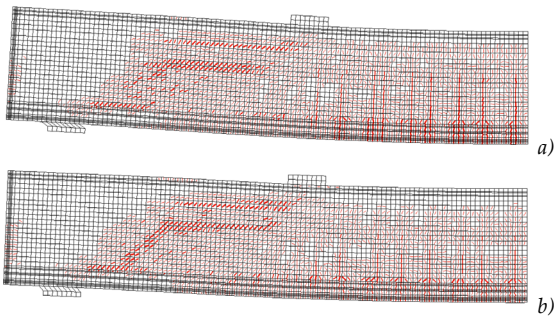

Figure 5.3-12: Schematic crack patterns after failure: a) B2N-0a, b) B2N-1.

As mentioned previously, in B2N-0 beam, the corrosion effect was considered. Figure 5.3-13 shows the comparison between the *shear vs. mid-span deflection* responses of the design beams and the four scenarios of corrosion.

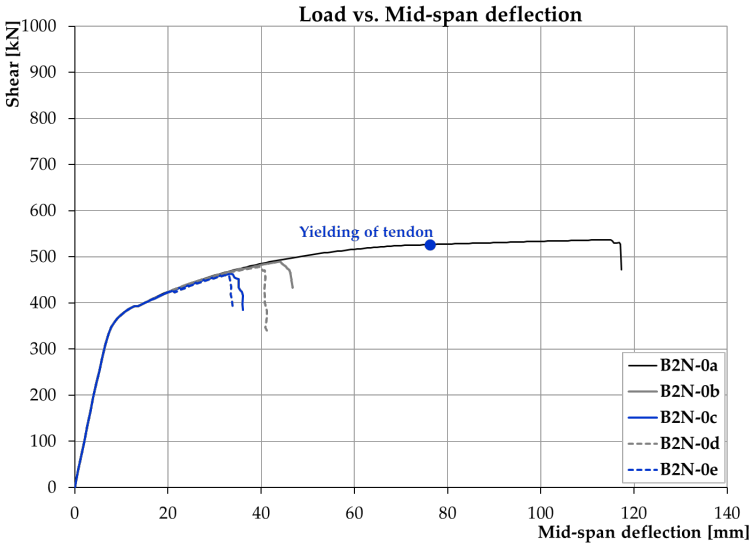

Figure 5.3-13: Shear vs. mid-span deflection curves (B2N-0a: design prestressed concrete beam; B2N-0b: corroded beam scenario i; B2N-0c: corroded beam scenario ii; B2N-0d: corroded beam scenario iii; B2N-0e: corroded beam scenario iv).

From the graphs above displayed, it can be observed that the stiffness of corroded beams did not change with respect to the uncorroded beam. On the other hand, as expected, the corrosion effect diminished the resistance of the prestressed concrete beams. Compared with the uncorroded B2N-0a beam, which had a shear of 537 kN, B1N-0b, 0c, 0d and 0e beams had a lower shear of 4909 463, 478, and 460 kN respectively. The corroded beams had a more brittle behaviour with respect to the uncorroded beam. The deflection was up to 71% lower than the deflection observed in the reference beam. Predictably, the B2N-0e beams (scenario iv) was the most

critical situation. The crack formations arose in a similar way in all corroded beams, as can see in Figure 5.3-14. The first inclined cracks developed at the shear value of approximately 180 kN. Increasing the load, the inclined cracks appeared in the shear span. At the peak load the yielding of the stirrups was observed, and the failure occurred.

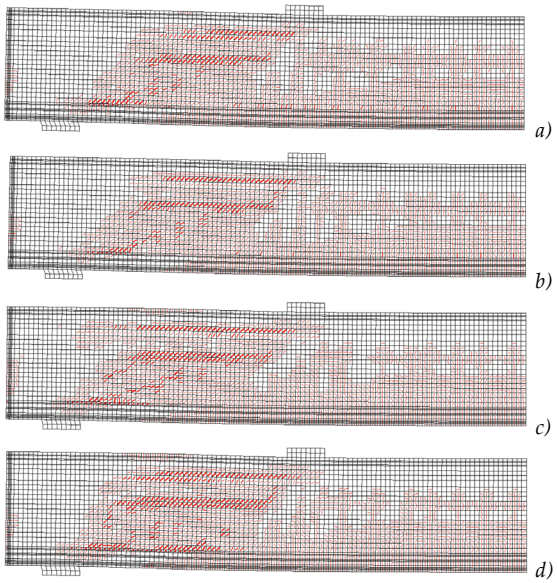

Figure 5.3-14: Schematic crack patterns after failure: a) B2N-0b, b) B2N-0c, c) B2N-0d, d) B2N-0e.

The UHPFRC retrofitting was performed on the B2N-0a (uncorroded beam) and on the B2N-0e (corroded beam). Figure 5.3-15 shows the *shear vs. mid-span deflection* responses of the reference uncorroded beam (B2N-0a), the reference corroded beam (B2N-0e), and the strengthened beams (B2F-0a and B2F-0e).

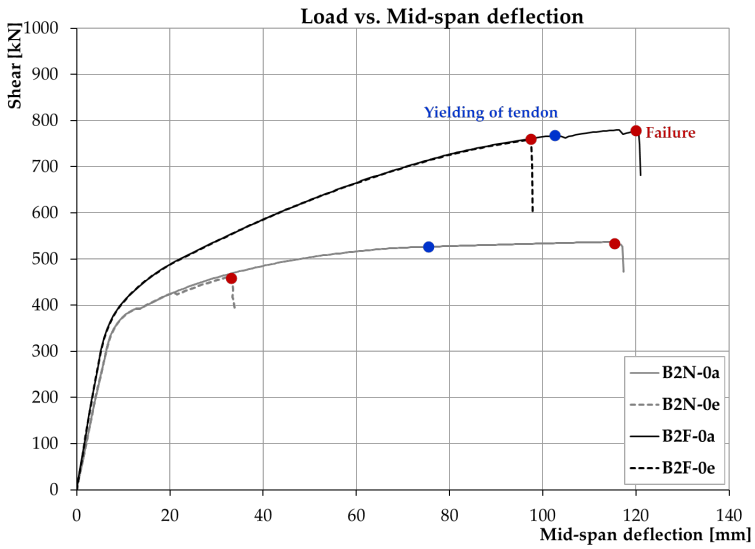

Figure 5.3-15: Shear vs. mid-span deflection curves (B2N-0a: design prestressed concrete beam; B2N-0e: corroded beam scenario iv; B2F-0a: actual prestressed concrete beam reinforced with UHPFRC jacketing; B2F-0e: corroded prestressed concrete beam reinforced with UHPFRC jacketing).

It can be observed that in both cases, the UHPFRC jacketing improved the resistance of the prestressed concrete beams. The B2F-0a and B2F-0e beams had a maximum shear higher of 31% and 41% than their reference beams, respectably 780 and 760 kN. As noted in the reference beams, also in the strengthened beam, the stiffness of corroded beam did not change with respect to the uncorroded beam.
Regarding B2F-0a beam, the first flexural cracks appeared at a shear value of 327 kN. After the cracking load, vertical cracks developed in the central portion of the beam. Those cracks, with increasing load, propagated in width and in number even beyond the point load. After the peak load was achieved (1560 kN), the beam failed due to the crushing of concrete in the web region in the mid-span of the beam.
It can be noted that, in the uncorroded beams, the UHPFRC jacketing did not improve the ductility. Contrarily, in the B2F-1e strengthened corroded beams, the ductility was remarkably increased (66%).
B2F-1e beam developed the first flexural cracks at the same shear of the Beam B2F-1a (327 kN). With increasing loading, the beam shown a diffused vertical crack in the middle of the beam and inclined cracks in the shear span. The latter caused the failure of the beam.
Figure 5.3-16 illustrates the crack patterns for B2N-0a beam (a), B2F-0a beam (b), B2N-0e beam (c) and B2F-0e beam (c) after failure.

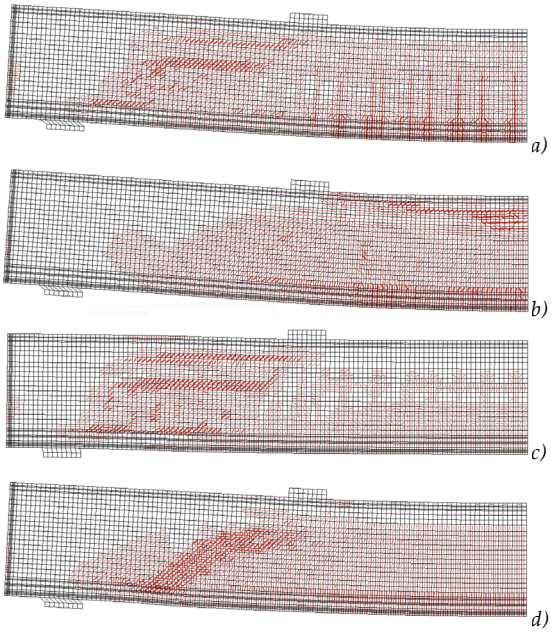

Figure 5.3-16: Schematic crack patterns after failure: a) B2N-0a, b) B2F-0a, c) B2N-0e, d) B2F-0e.

5.3.4 *Concluding remarks*

Nonlinear finite element analyses performed on existing prestressed concrete beams have been presented in this section.

The first series demonstrated the effect of Ultra-High-Performance Fibre Reinforced Concrete (UHPFRC) jacket in determining the failure mode as well as in influencing the post-cracking behaviour and the crack formation and evolution. The retrofit intervention using UHPFRC postponed the collapse and resulted in diffused cracking without significant shear cracks. Moreover, both strength and displacement level were improved.

The second series confirmed the efficiency of the UHPFRC retrofitting in the damaged prestressed concrete beams. In fact, though the corrosion was evaluated in a simplified method, the effect of the retrofit intervention was evident. The finite element analysis showed that the corroded strengthened beam had better post-cracking behaviour than its reference beam.

It can be concluded that the retrofit intervention presented in this section can improve the strength and the ductility in the prestressed concrete beams. Therefore, the use of UHPFRC jacketing (having a thickness of 50 mm each side and completed with a high-strength steel mesh) can be considered an efficient method for strengthening beams.

5.4 References

***BENTZ, E.**, 2013. "Augustus: Post Processor for VecTor2 (Version 5.8.3)," Copyright 1996-2013 E. Bentz.*

***CAIRNS, J., PLIZZARI, G. A., DU, Y., LAW, D. W., & FRANZONI, C.** ,2005. Mechanical properties of corrosion-damaged reinforcement. ACI Materials Journal, 102(4), 256.*

***CANADIAN STANDARDS ASSOCIATION**. 2014. Design of Concrete Structures (CSA A23. 3-14). CSA Group, Mississauga, ON, Canada.*

***COLLINS, M. P., & MITCHELL, D.** 1991. Prestressed concrete structures, Canada.*

***DIANA FEA**, 2016. "DIANA (Displacement Analyzer), Version 10.1. User manual", Delft, Netherlands.*

***EN 1992-1-1: EUROCODE 2**, 2005. Design of concrete structures. Part 1–1: General rules and rules for buildings.*

***FÉDÉRATION INTERNATIONALE DU BÉTON (FIB)**. 2013. Model Code 2010 for concrete structures (MC2010), International Federation for Structural Concrete, Lausanne, Switzerland, 2013.*

***HOSHIKUMA, J., KAWASHIMA, K., NAGAYA, K. AND TAYLOR, A.W.**, 1997. "Stress-Strain Model for Confined Reinforced Concrete in Bridge Piers", ASCE Journal of Structural Engineering, Vol. 123, No. 5, pp. 624-633.*

***IMPERATORE, S., & RINALDI, Z.** ,2008. Mechanical behaviour of corroded rebars and influence on the structural response of R/C elements. In Proceedings of the 2nd International conference on concrete repair, rehabilitation and retrofitting, Cape Town, South Africa (Vol. 2426).*

***IMPERATORE, S., RINALDI, Z., & DRAGO, C.**, 2017. Degradation relationships for the mechanical properties of corroded steel rebars. Construction and Building Materials, 148, 219-230.*

***MA, R.**, 2016. "Development of Contact Elements for Finite Element Analysis of Composite Structures", Report doctoral dissertation, University of Toronto.*

***LEE, S. C., CHO, J. Y., & VECCHIO, F. J.**, 2012. "Simplified Diverse Embedment Model for Steel Fiber Reinforced Concrete in Tension", ACI Material Journal.*

***RINALDI, Z., IMPERATORE, S., & VALENTE, C.** ,2010. Experimental evaluation of the flexural behavior of corroded P/C beams. Construction and Building Materials, 24(11), 2267-2278.*

***UNI EN 14651**, 2007. "Precast concrete products – test method for metallic fibre concrete – Measuring the flexural tensile strength", European Standard.*

***VECCHIO, F.J.**, 1990. "VecTor 2 Nonlinear Finite Element Analysis" program.*

***VECCHIO, F. J.**, 2000. "Disturbed stress field model for reinforced concrete: formulation", Journal of structural engineering, 126(9), 1070-1077.*

***VECCHIO, F. J., & COLLINS, M. P.**, 1986. "The modified compression-field theory for reinforced concrete elements subjected to shear", ACI J., 83(2), 219-231.*

***VERDERAME, G. M., STELLA, A., & COSENZA, E.** ,2001, September. Le proprietà meccaniche degli acciai impiegati nelle strutture in ca realizzate negli anni'60. In X Congresso Nazionale L'ingegneria Sismica in Italia, Potenza-Matera (pp. 9-13).*

***VOO, J. Y. L., & FOSTER, S. J.**, 2003. "Variable Engagement Model for Fibre Reinforced Concrete in Tension," Uniciv Report No. R-420, School of Civil and Environmental Engineering, The University of New South Wales, Sydney, Australia.*

6 DISCUSSION AND MODELING OF SHEAR

6.1 Introduction

Shear failure of reinforced concrete (RC) beams generally occurs due to tensile failure of concrete. Shear failure is brittle, for this reason, it is necessary to prevent this type of failure and improve the shear strength of the beams.
In recent years, several experimental researches [Alaee and Karihaloo, 2003; Martinola *et al.* 2007; Martinola *et al.* 2010; Mostosi *et al.* 2011; Chalioris and Pourzitidis, 2012; Noshiravani and Brühwiler 2013; Ruano *et al.* 2014; Lampropoulos *et al.* 2016; Al-Osta *et al.* 2017] have proposed a new technique based on the use of jackets made of Ultra Hight Performance Fibre Reinforced Concrete (UHPFRC) to increases the flexural and shear strength of existing RC beams. From these studies it appeared that the FRC jacketing is an efficient method for strengthening of RC beams. Nevertheless, analytical proposals available in the literature [Sharma, 1986; Narayanan and Darwish, 1987; Ashour, Hasanain, and Wafa, 1992; Khuntia, Stojadinovic and Goel, 1999; Minelli, 2005; Dinh, Parra-Montesinos and Wight, 2010] and in *fib* Model Code [2013] give predictions of shear capacity of the FRC members not considering the composite members (UHPFRC-RC). It would be necessary to achieve an analytical model to predict the shear capacity of the strengthened beams. Therefore, the main aim herein is the implementation of an analytical model able to calculate/estimate the shear strength, which could be incorporated in the design formulations of building codes.
This chapter describes three analytical formulations to predict the shear strength of composite beam without stirrup reinforcement, similar to those presented in the parametric study (Section 5.2).
These formulations are supported and compared by the numerical analyses of composite beams presented in Section 5.2.

6.2 Design aspect

In the following section, the actual draft of *fib* Model Code [2020] prescriptions, concerning the shear design of members in FRC, are described. The formulations presented regard the shear resistance of a member without shear reinforcement.

6.2.1 *Actual draft Model Code 2020*

In the actual draft of *fib* Model Code 2020, the shear verification of a web is based on the following inequality:

$$V_{Rd} \geq V_{Ed} \qquad (6.2\text{-}1)$$

where V_{Rd} is the design shear resistance and V_{Ed} is the design shear force.
The design shear force V_{Ed} should be determined for control sections at a location d from the face of supports, and in correspondence with the discontinuities of geometry or applied concentrated loads, as shown in Figure 6.2-1.

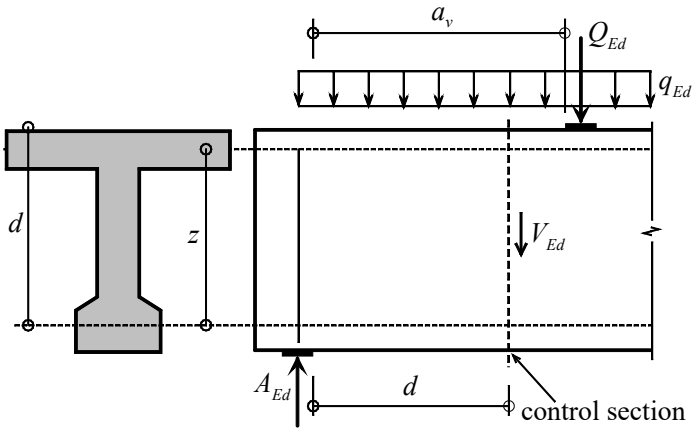

Figure 6.2-1: Definition of control section for sectional design.

Verification of members in shear requires the state of strain to be taken into considerations. The longitudinal strain, ε_x, is calculated at the mid-depth of the effective shear considered as follows:

$$\varepsilon_x = \frac{1}{2E_sA_s}\left(\frac{M_{Ed}}{z_v} + V_{Ed} + N_{Ed}\left(\frac{1}{2} \mp \frac{\Delta e}{z_v}\right)\right) \geq 0 \qquad (6.2\text{-}2)$$

In the use of Equation (6.2-2) the following conditions are applied:

- M_{Ed} and V_{Ed} shall be taken as positive quantities, and N_{Ed} as positive for tension and negative for compression;
- it is permissible to use a value of ε_x that is greater than half the yield strain of the longitudinal bars ($\varepsilon_{sy}/2$) but a more detailed cross sectional analysis shall be undertaken. Anyway, the strain ε_x shall not exceed 0.003;
- A_s comprises the main longitudinal reinforcing bars in the tensile chord; any distributed longitudinal reinforcement is neglected.

For FRC members without shear reinforcement, the design value for the shear resistance is give as follows:

$$V_{Rd} = V_{Rd,c} + V_{Rd,FRC} \qquad (6.2\text{-}3)$$

where:

$$V_{Rd,c} = k_v \frac{\sqrt{f_{ck}}}{\gamma_c} \cdot z_v \cdot b_w \qquad (6.2\text{-}4)$$

is the contribution of concrete;

$$V_{Rd,FRC} = \frac{f_{Ftuk}}{\gamma_F} \cdot cot(\theta) \cdot z_v \cdot b_w \qquad (6.2\text{-}5)$$

is the contribution of residual tensile strength related to fibres;
f_{ck} is the characteristic value of the compressive strength (in MPa). The value of $\sqrt{f_{ck}}$ cannot be taken as greater than 8 MPa;
f_{FTUk} is the characteristic value of the ultimate residual tensile strength for FRC for a crack width w=2.5 mm (in MPa).

6.2.1.1 Level I approximation

For members with no significant axial load, with $f_{ck} \leq 70$ MPa, with $d_g \geq 10$ mm, and not more than 1000 mm depth, the design shear resistance is determined follows the Equation (6.2-5), where:

$$k_v = \frac{0.4}{1 + 750 \cdot f_{yd}/E_s + \zeta} \cdot \frac{1300}{1000 + 1.25 \cdot z_v} \quad (z_v \; in \; mm) \tag{6.2-6}$$

$$\zeta = \left(20 - 7000 \frac{f_{yd}}{E_s}\right) \frac{f_{Ftuk}}{f_{ck}} \geq 0 \tag{6.2-7}$$

$$\theta = 29° + 3500 \frac{f_{yd}}{E_s} \tag{6.2-8}$$

6.2.1.2 Level II approximation

For the level II approximation, the design shear resistance is determined with Equation (6.2-5), where:

$$k_v = \frac{0.4}{(1 + 1500\varepsilon_x) + \zeta} \cdot \frac{1300}{1000 + k_{dg} \cdot z_v} \quad (z_v \; in \; mm) \tag{6.2-9}$$

$$k_{dg} = \frac{32}{16 + d_g} \tag{6.2-10}$$

$$\zeta = (20 - 14000\varepsilon_x) \frac{f_{Ftuk}}{f_{ck}} \geq 0 \tag{6.2-11}$$

$$\theta = 29° + 7000\varepsilon_x \tag{6.2-12}$$

6.2.1.3 Level III approximation

As for level II but with the stress provided by the fibre components, f_{Ftuk} determined by the inverse analysis procedure.

6.3 *Analytical model to predict the shear strength of composite beams*

The solution technique presented in this work is based on the idea to add the shear contribution of FRC jacketing to the shear contribution of the existing RC beam, as schematized in Figure 6.3-1.

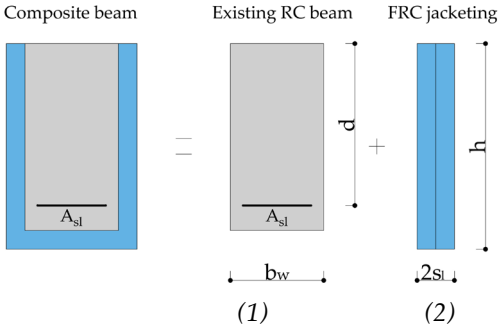

Figure 6.3-1: Schematic illustration of the contributes to calculate the shear capacity of composite beams: (1) existing RC beam and (2) FRC jacketing.

In this section, three approaches to evaluate the shear capacity of composite beams are presented.

In the first and second approach, the shear resistance of existing RC beams is calculated according to Eurocode 2 [2005] as:

$$V_{Rd,c,e} = \left[0.18 \cdot k \cdot (100 \cdot \rho_1 \cdot f_{cm})^{1/3}\right] \cdot b_w \cdot d \qquad (6.3\text{-}1)$$

where:

f_{cm} is the mean value of the compressive strength (in MPa) for existing concrete;

$$k = 1 + \sqrt{\frac{200}{d}} \leq 2.0 \;\; (d \; in \; mm); \qquad (6.3\text{-}2)$$

$$\rho_1 = \frac{A_{sl}}{b_w \cdot d} \leq 0.02; \qquad (6.3\text{-}3)$$

A_{sl} is the area of the longitudinal reinforcement (in mm²);

b_w is the smallest width of the cross section in the tensile area (in mm);

d is the effective depth (in mm).

In the third approach, the shear resistance of existing RC beams is calculated according to the actual draft of *fib* Model Code [2020] as:

$$V_{Rd,c,e} = k_{v,c} \sqrt{f_{cm}} \cdot z_v \cdot b_w \qquad (6.3\text{-}4)$$

where:

$$k_{v,c} = \frac{0.4}{(1 + 1500\varepsilon_x)} \cdot \frac{1300}{1000 + k_{dg,c} \cdot z_v}; \qquad (6.3\text{-}5)$$

$$k_{dg,c} = \frac{32}{16 + d_{g,c}}. \qquad (6.3\text{-}6)$$

FRC jacketing shear contribution is explained in the following paragraphs.

6.3.1 *Approach 1*

The shear contribution of the FRC jacketing is evaluated considering the fibres as distributed reinforcement in function of the FRC toughness. The toughness parameter is conventionally assumed as the residual post-cracking strength $f_{R,3}$, defined in EN 14651 [2007]. The FRC shear contribution can be written as:

$$V_{Rd,FRC} = f_{Ftum} \cdot 2s_l \cdot h \qquad (6.3\text{-}7)$$

where:

$f_{FTum} = f_{R,3}/3$ is the mean value of the ultimate residual tensile strength for FRC for a crack width $w=2.5\ mm$ (in MPa);

s_l is the thickness of the jacketing;

h is the total height of the composite beam.

The shear capacity of composite beams can be written as:

$$V_{Rd} = \left[0.18 \cdot k \cdot (100 \cdot \rho_1 \cdot f_{cm})^{1/3}\right] \cdot b_w \cdot d + f_{Ftum} \cdot 2s_l \cdot h \qquad (6.3\text{-}8)$$

In this approach, the FRC shear contribution is given by the residual strength of fibres, the compressive strength for FRC is not considered.

6.3.2 *Approach 2*

The shear contribution of the FRC jacketing is evaluated using the model proposed in the *fib* Model Code [2013] for the shear strength of FRC members without shear reinforcement. This formulation is derived starting from the work of Minelli [2005] presented in Section 2.4.3. The model includes the contribution of FRC toughness in the EC2 [2005] formulation. In this model, a perfect bond conditions between RC substrate and FRC overlay are assumed, therefore the longitudinal reinforcement ratio ρ is defined on the new composite section.

Considering the fibre contributions, the Equation (6.3-1) assumes its final form:

$$V_{Rd,FRC} = \left\{0.18 \cdot k \cdot \left[100 \cdot \rho_2 \cdot (1 + 7.5 \cdot \frac{f_{Ftum}}{f_{FRCcm}}) \cdot f_{FRCcm}\right]^{1/3}\right\} \cdot 2s_l \cdot h \qquad (6.3\text{-}9)$$

where:

$f_{FTum} = f_{R,3}/3$ is the mean value of the ultimate residual tensile strength for FRC for a crack width $w=2.5\ mm$ (in MPa);

f_{FRCcm} is the mean value of the compressive strength for FRC;

$$k = 1 + \sqrt{\frac{200}{h}} \leq 2.0 \ \ (h\ in\ mm); \qquad (6.3\text{-}10)$$

$$\rho_2 = \frac{A_{sl}}{(b_w + 2s_l) \cdot h} \qquad (6.3\text{-}11)$$

s_l is the thickness of the jacketing;

h is the total height of the composite beam.

The shear capacity of composite beams can be written as:

$$V_{Rd} = \left[0.18 \cdot k \cdot (100 \cdot \rho_1 \cdot f_{cm})^{1/3}\right] \cdot b_w \cdot d + \left\{0.18 \cdot k \cdot \left[100 \cdot \rho_2 \cdot (1 + 7.5 \cdot \frac{f_{Ftum}}{f_{FRCcm}}) \cdot f_{FRCcm}\right]^{1/3}\right\} \cdot 2s_l \cdot h \quad (6.3\text{-}12)$$

In the equation above, both the residual strength of fibres and compressive strength of FRC are considered.

6.3.3 *Approach 3*

The shear capacity of FRC jacketing, an adaptation from the actual draft of *fib* Model Code [2020] for FRC beam to FRC jacketing, can be written as:

$$V_{Rd,FRC} = k_{v,FRC} \sqrt{f_{FRCcm}} \cdot h \cdot 2s_l + f_{Ftum} \cdot cot(\theta) \cdot h \cdot 2s_l \quad (6.2\text{-}3)$$

where:

f_{FRCcm} is the mean value of the compressive strength (in MPa) for FRC;

f_{Ftum} is the mean value of the ultimate residual tensile strength for FRC for a crack width w=2.5 mm (in MPa);

s_l is the thickness of the jacketing;

h is the total height of the composite beam;

$$k_{v,FRC} = \frac{0.4}{(1 + 1500\varepsilon_x) + (20 - 1400\varepsilon_x)\frac{f_{Ftum}}{f_{FRCcm}}} \cdot \frac{1300}{1000 + k_{dg,FRC} \cdot h}; \quad (6.3\text{-}13)$$

$$k_{dg,FRC} = \frac{32}{16 + d_{g,FRC}}; \quad (6.3\text{-}14)$$

$$\theta = 29° + 7000\varepsilon_x. \quad (6.3\text{-}15)$$

The shear capacity of composite beams can be written as:

$$V_{Rd} = k_{v,c} \sqrt{f_{cm}} \cdot z_v \cdot b_w + k_{v,FRC} \sqrt{f_{FRCcm}} \cdot h \cdot 2s_l + f_{Ftum} \cdot cot(\theta) \cdot h \cdot 2s_l \quad (6.3\text{-}16)$$

In the solution technique, an iterative method is used to compute the shear resistance according to the following steps:

1. assume an initial value of longitudinal strain $\varepsilon_{x,0}$ equal to $\varepsilon_{sy}/2$;
2. using the values of ε_x to determine θ according to equation (6.3-15);
3. calculate the value of $k_{v,c}$ and $k_{v,FRC}$ using the equations (6.3-5) and (6.3-13). To calculate $k_{v,c}$ and $k_{v,FRC}$ the same θ was used;
4. determination of V_{Rd} following the equation (6.3-16);
5. calculate the bending moment as:
$$M_{Rd} = V_{Rd} \cdot (a - d) \quad (6.3\text{-}17)$$
6. where a is the shear span and d is the effective depth of existing RC beam. The bending moment was calculated for the control section at a location a-d from the face of support, where the shear stress is generally critical.

7. calculate F_L as follows:

$$F_L = \frac{M_{Rd}}{z} + V_{Rd} \cdot \cot\theta \qquad (6.3\text{-}18)$$

8. determine the strain of reinforcement as:

$$\varepsilon_s = \frac{F_L}{E_s\, A_s} \qquad (6.3\text{-}19)$$

9. Check yielding of the longitudinal reinforcement; if the reinforcement is yielding assume $\varepsilon_s = \varepsilon_{sy}$;
10. calculate ε_x^* as $\varepsilon_s/2$ and check against the value assumed in step 1;
11. repeat the process until convergence of ε_x;
12. calculate the value of θ according to equation (6.3-15);
13. calculate $k_{v,c}$ and $k_{v,FRC}$ following the equations (6.3-5) and (6.3-13);
14. determination of V_{Rd} using the equation (6.3-16).

The process to calculate the shear capacity in composite elements is schematized in Figure 6.3-2.

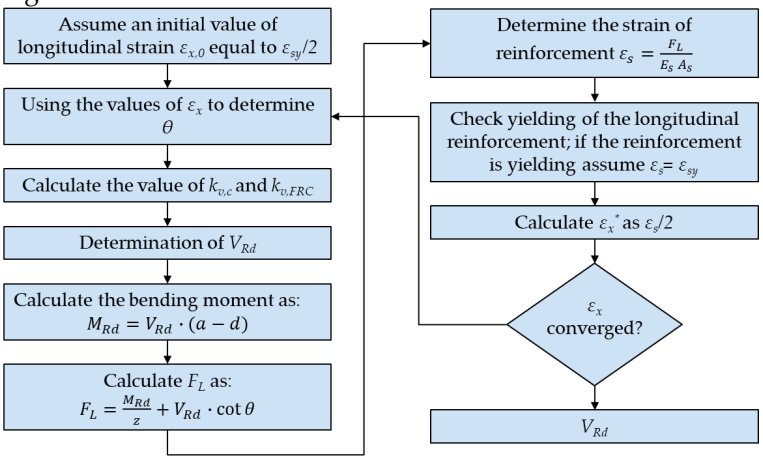

Figure 6.3-2:Iterative method to compute the shear resistance.

6.1 Prediction of shear strength of composite beams in numerical analyses

The shear capacity of strenthened beams analysed and described in Section 5.2 is calculated using the three approaches reported above.
This section compares the shear capacity obtained by FE analyses and the shear capacity calculated with the analytical approach. This discussion is limited to strengthened beams that exhibited a shear failure (i.e. brittle behaviour).
The following example illustrates the application of the three approaches to the calculation of the shear strength of Beam B50S-NF30-2.1.

Approach 1

1. The shear resistance of existing RC beams is:
   $V_{Rd,c,e} = \left[0.18 \cdot k \cdot (100 \cdot \rho_1 \cdot f_{cm})^{1/3}\right] \cdot b_w \cdot d =$
   $\left[0.18 \cdot 1.61 \cdot (100 \cdot 0.021 \cdot 50\ MPa)^{1/3}\right] \cdot 250\ mm \cdot 540\ mm = 184.2\ kN$
2. The shear contribution of the FRC jacketing is:
   $V_{Rd,FRC} = f_{Ftum} \cdot 2s_l \cdot h = 3.12\ MPa \cdot 2 \cdot 30\ mm \cdot 640\ mm = 119.8\ kN$
3. The shear capacity of composite beams is:
   $V_{Rd} = V_{Rd,c,e} + V_{Rd,FRC} = 184.2\ kN + 119.8\ kN = 304\ kN$

Approach 2

1. The shear resistance of existing RC beams is:
   $V_{Rd,c,e} = \left[0.18 \cdot k \cdot (100 \cdot \rho_1 \cdot f_{cm})^{1/3}\right] \cdot b_w \cdot d =$
   $\left[0.18 \cdot 1.61 \cdot (100 \cdot 0.021 \cdot 50\ MPa)^{1/3}\right] \cdot 250\ mm \cdot 540\ mm = 184.2\ kN$
2. The shear contribution of the FRC jacketing is:
   $V_{Rd,FRC} = \left\{0.18 \cdot k \cdot \left[100 \cdot \rho_2 \cdot \left(1 + 7.5 \cdot \frac{f_{Ftum}}{f_{FRCcm}}\right) \cdot f_{FRCcm}\right]^{1/3}\right\} \cdot 2s_l \cdot h =$
   $\left\{0.18 \cdot 1.58 \cdot \left[100 \cdot 0.015 \cdot \left(1 + 7.5 \cdot \frac{3.12\ MPa}{92\ MPa}\right) \cdot 92\ MPa\right]^{1/3}\right\} \cdot 2 \cdot 30\ mm$
   $\cdot 640\ mm = 61.0\ kN$
3. The shear capacity of composite beams is:
   $V_{Rd} = V_{Rd,c,e} + V_{Rd,FRC} = 184.2\ kN + 61.0\ kN = 245.2\ kN$

Approach 3

1. The shear resistance of existing RC beams is:
   $V_{Rd,c,e} = k_{v,c} \sqrt{f_{cm}} \cdot z_v \cdot b_w = 0.151 \sqrt{50\ MPa} \cdot 486\ mm \cdot 250\ mm = 129.9\ kN$
2. The shear contribution of the FRC jacketing is:
   $V_{Rd,FRC} = k_{v,FRC} \sqrt{f_{FRCcm}} \cdot h \cdot 2s_l + f_{Ftum} \cdot cot(\theta) \cdot h \cdot 2s_l = V_{Rd,FRC}$
   $= 0.1 \sqrt{92\ MPa} \cdot 640\ mm \cdot 2 \cdot 30\ mm + 3.12\ MPa \cdot cot(36) \cdot 640$
   $\cdot 2 \cdot 30\ mm = 201.9\ kN$
3. The shear capacity of composite beams is:
   $V_{Rd} = V_{Rd,c,e} + V_{Rd,FRC} = 129.9\ kN + 201.9\ kN = 331.8\ kN$

The ratio between the numerical shear strength (336.6 kN) and the analytical predicted shear strength is equal to 1.11, 1.37, and 1.01. The same steps are followed to calculate the shear strength for the other composite beams in the numerical program, and the strength predictions are reported in Appendix E.

Figure 6.1-1 shows a plot of the ratios between numerical and predicted shear strengths for the strengthened beams size M having *a/d* equal to 3 and 3.5.

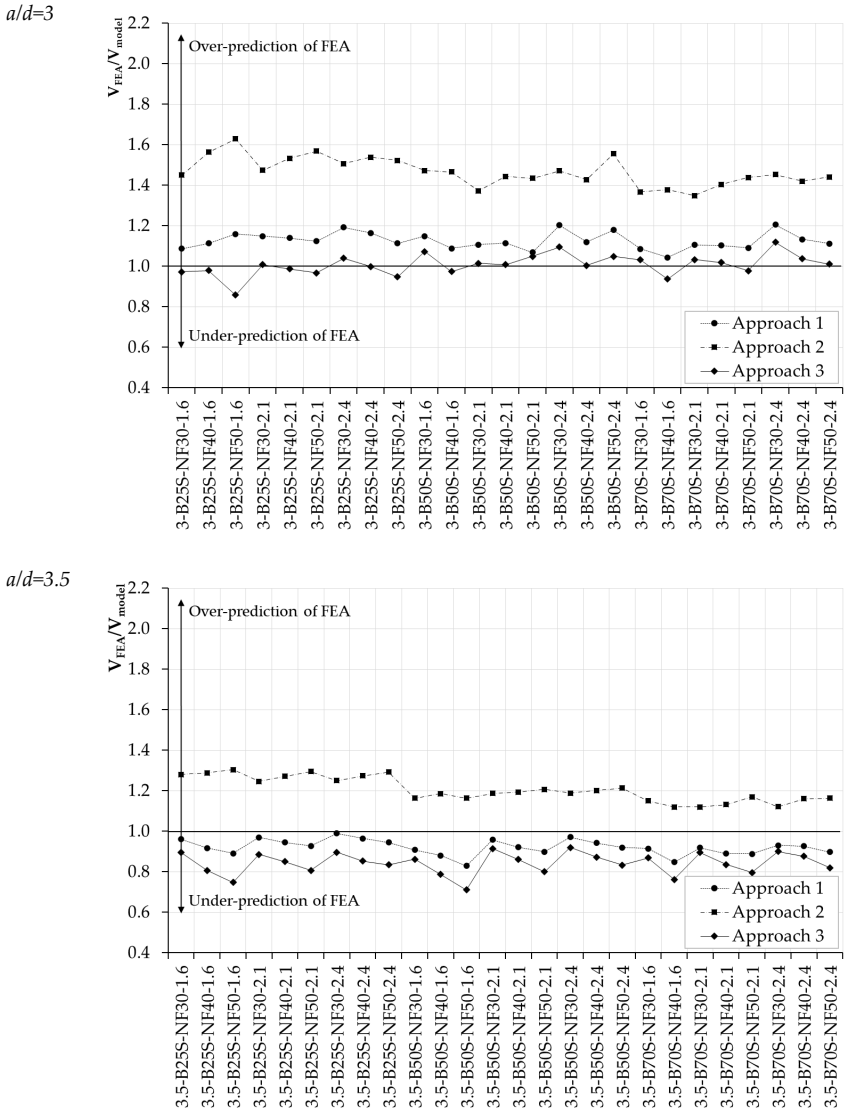

Figure 6.1-1: Predicted shear strengths of composite beams using the three approaches proposed.

Figure 6.1-2 illustrates the relationship between numerical beam shear strengths (V_{FEA}) and the shear strengths predicted using the three approaches proposed (V_1, V_2, and V_3). If a data point is above the continuous line, the FEA predicted shear strength is greater than the analitical shear strength; and vice versa. The dashed lines show the boundary of 20% offset from the measured shear strength. Moreover, mean value, standard deviation, and coefficient of variation of the 273 specimens are reported.

a)

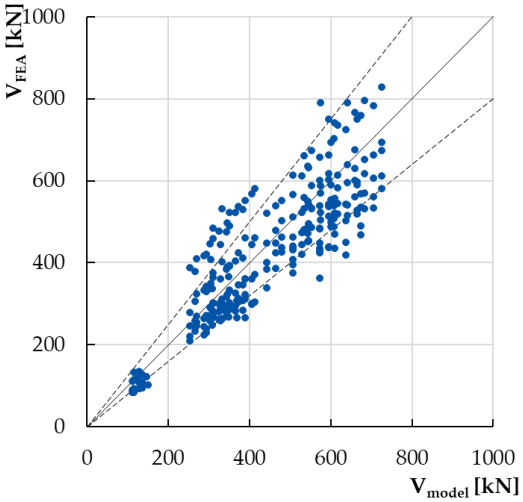

Mean: 0.96
Standard deviation: 0.20
c.v.: 0.20

b)

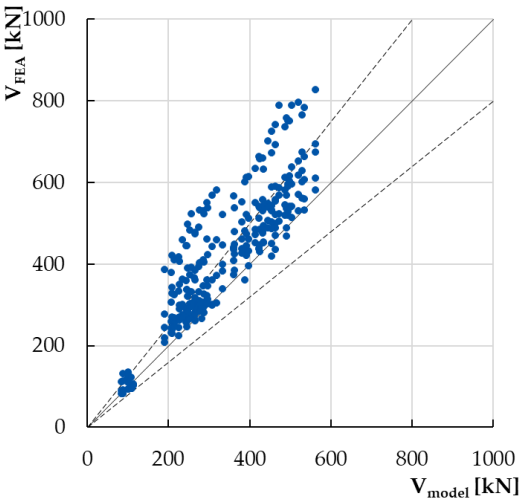

Mean: 1.26
Standard deviation: 0.25
c.v.: 0.20

Figure 6.1-2 (Pt. 2 of 2)

c)

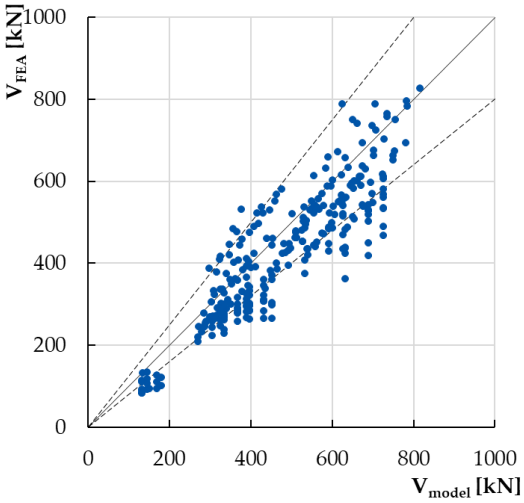

Mean: 0.89
Standard deviation: 0.16
c.v.: 0.18

(Pt. 2 of 2)

Figure 6.1-2: Shear strength prediction of composite beams using the three approaches proposed: a) Approach 1, b) Approach 2, c) Approach 3.

Focusing on approach 3, Figure 6.1-3 shows the relationship between numerical beam shear strengths (V_{FEA}) and the shear strengths predicted (V_3) for each size and each shear span.

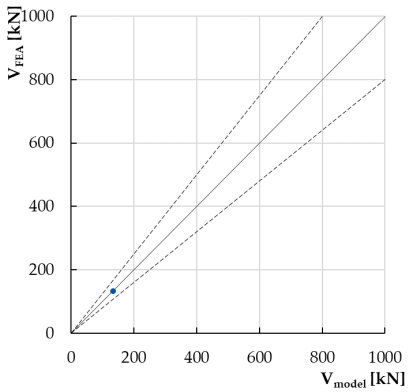

Beam S, a/d=3

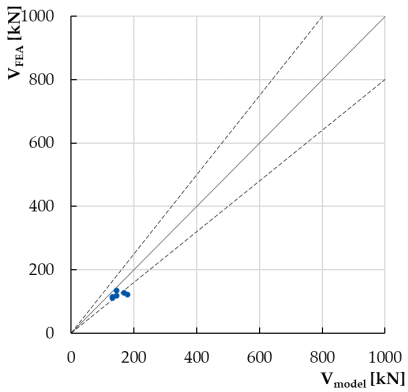

Beam S, a/d=3.5

Figure 6.1-3 (Pt. 1 of 3)

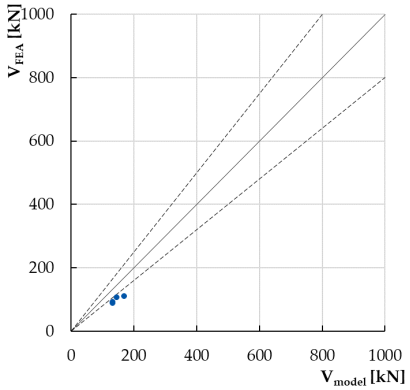

Beam S, a/d=4

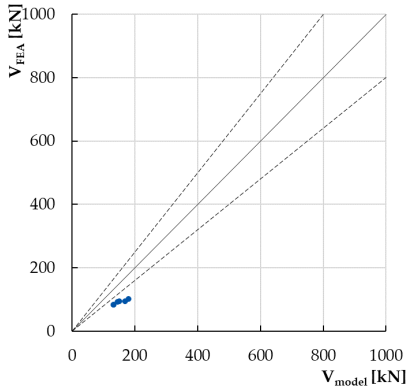

Beam S, a/d=4.5

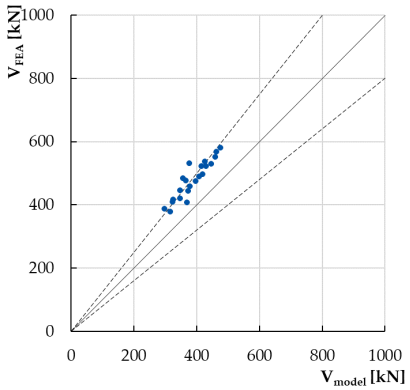

Beam M, a/d=2.5

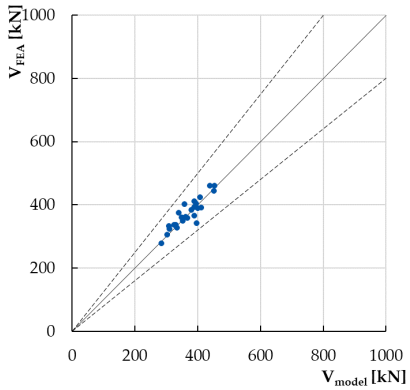

Beam M, a/d=3

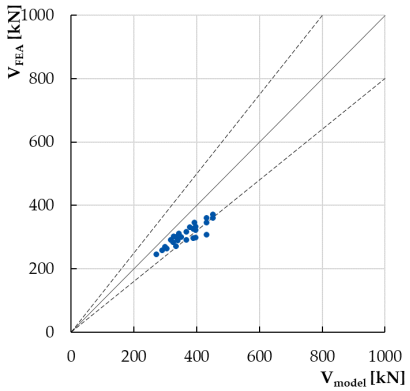

Beam M, a/d=3.5

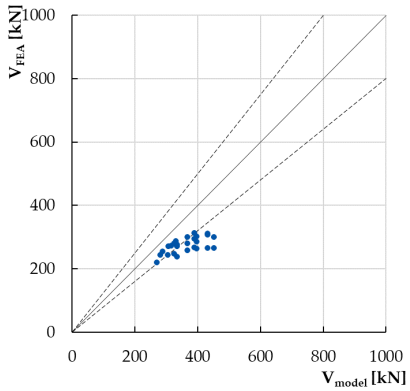

Beam M, a/d=4

Figure 6.1-3 (Pt. 1 of 3)

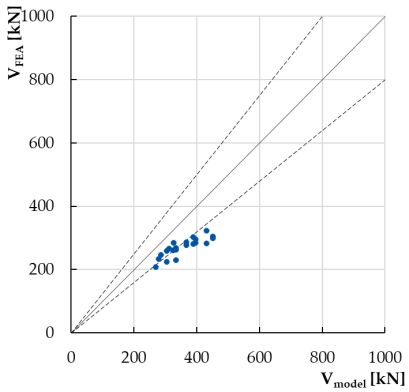

Beam M, a/d=4.5

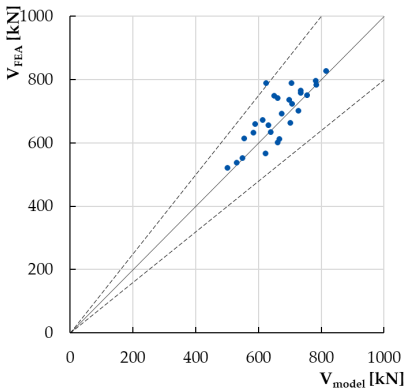

Beam L, a/d=2.5

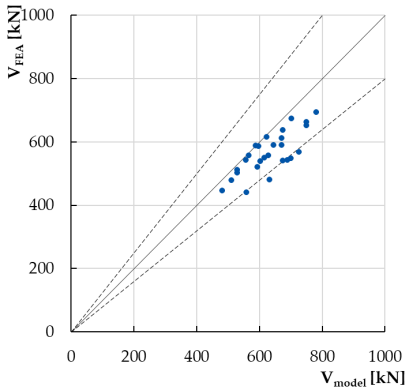

Beam L, a/d=3

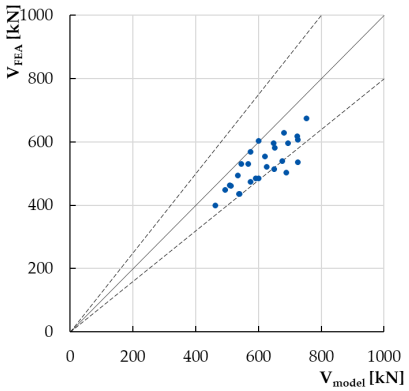

Beam L, a/d=3.5

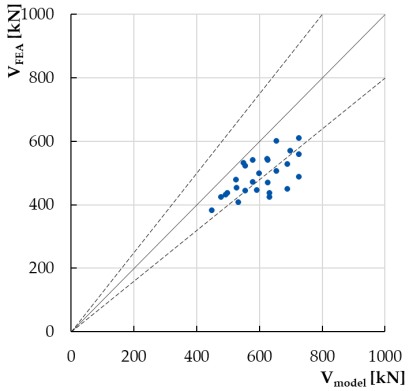

Beam L, a/d=4

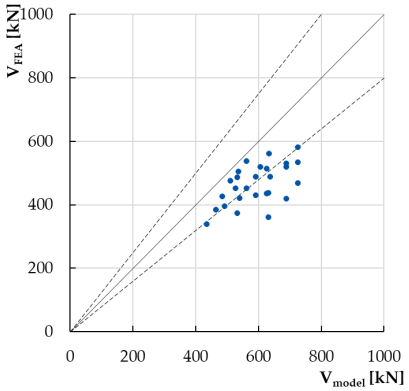

Beam L, a/d=4.5

(Pt. 3 of 3)

Figure 6.1-3: Shear strength prediction of composite beams using Approach 3.

6.2 Concluding remarks

Based on the results reported herein, it can be seen that the use of the second analytical approach led consistently to an under-prediction of shear strength compered to FEA. The shear predictions calculated with approach 1 and 3 are considered to give a more adequate prediction of the shear strength of composite beams.

In approach 3, it can be observed that by increasing the size and the shear span, the analytical shear strength over-estimates the numerical shear strength. It can be seen that most of the predicted shear strengths (about 70%) varied from 70 to 120% of the numerical shear strength. The better predictions are for Beams M-a/d=3 and Beams L-a/d=2.5.

It remains a pressing need to further corroborate these preliminary results with suitable experimental tests. At this stage model, three seems to be the most accurate as it is based on a strain and compatibility approach.

6.3 References

***ALAEE, F. J., & KARIHALOO, B. L.**, 2003. "Retrofitting of reinforced concrete beams with CARDIFRC", Journal of Composites for Construction, 7(3), 174-186.*

***AL-OSTA, M. A., ISA, M. N., BALUCH, M. H., & RAHMAN, M. K.**, 2017. "Flexural behavior of reinforced concrete beams strengthened with ultra-high performance fiber reinforced concrete", Construction and Building Materials, 134, 279-296.*

***ASHOUR, S. A., HASANAIN, G. S., & WAFA, F. F.**, 1992. "Shear behavior of high-strength fiber reinforced concrete beams", Structural Journal, 89(2), 176-184.*

***CHALIORIS, C. E., & POURZITIDIS, C. N.**, 2012. "Self-Compacting Concrete Jacketing–Tests and Analysis", AASRI Procedia, 3, 624-629.*

***DINH, H. H., PARRA-MONTESINOS, G. J., & WIGHT, J. K.**, 2010. "Shear strength model for steel fiber reinforced concrete beams without stirrup reinforcement", Journal of Structural Engineering, 137(10).*

***EN 1992-1-1:** Eurocode 2. 2005. Design of concrete structures. Part 1–1: General rules and rules for buildings.*

***UNI EN 14651**, 2007. "Precast concrete products – test method for metallic fibre concrete – Measuring the flexural tensile strength", European Standard.*

***FÉDÉRATION INTERNATIONALE DU BÉTON (FIB)**. 2013. Model Code 2010 for concrete structures (MC2010), International Federation for Structural Concrete, Lausanne, Switzerland.*

***FÉDÉRATION INTERNATIONALE DU BÉTON (FIB)**. 2020. Model Code 2020 — actual draft.*

***KHUNTIA, M., STOJADINOVIC, B., & GOEL, S. C.**, 1999. "Shear strength of normal and high-strength fiber reinforced concrete beams without stirrups", Structural Journal, 96(2), 282-289.*

***LAMPROPOULOS, A. P., PASCHALIS, S. A., TSIOULOU, O. T., & DRITSOS, S. E.**, 2016. "Strengthening of reinforced concrete beams using ultra high performance fibre reinforced concrete (UHPFRC)", Engineering Structures, 106, 370-384.*

***MARTINOLA, G., MEDA, A., PLIZZARI, G. A., & RINALDI, Z.**, 2007, June. "An application of high performance fiber reinforced cementitious composites for R/C beams strengthening", in FraMCos-6. 6th Int. Conf. on Fracture Mechanics of concrete and concrete structures. Catania (Vol. 17, p. 22).*

***MARTINOLA, G., MEDA, A., PLIZZARI, G. A., & RINALDI, Z**., 2010. "Strengthening and repair of RC beams with fiber reinforced concrete", Cement and concrete composites, 32(9), 731-739.*

***MINELLI, F.**, 2005. "Plain and fiber reinforced concrete beams under shear loading: Structural behavior and design applications", Phd, University of Brescia.*

***NARAYANAN, R., & DARWISH, I. Y. S.**, 1987. "Use of steel fibers as shear reinforcement", Structural Journal, 84(3), 216-227.*

***NOSHIRAVANI, T., & BRÜHWILER, E.**, 2013. "Analytical model for predicting response and flexure-shear resistance of composite beams combining reinforced ultrahigh performance fiber-reinforced concrete and reinforced concrete", Journal of Structural Engineering, 140(6), 04014012.*

***RUANO, G., ISLA, F., PEDRAZA, R. I., SFER, D., & LUCCIONI, B.**, 2014. "Shear retrofitting of reinforced concrete beams with steel fiber reinforced concrete", Construction and Building Materials, 54, 646-658.*

***SHARMA, A. K.**, 1986, July. "Shear strength of steel fiber reinforced concrete beams", in Journal Proceedings (Vol. 83, No. 4, pp. 624-628).*

7 CONCLUSIONS AND RECOMMENDATIONS FOR FUTURE WORK

The goal of this thesis was to better understand the positive influence that thin Ultra High Performance Fibre Reinforced Concrete (UHPFRC) jacket has on the structural behaviour of reinforced concrete (RC) members. Experimental and numerical works were undertaken to meet this goal.
The primary objective of this research was to study the shear strengthening of RC elements by means of a thin jacket made of UHPFRC.
At first, a material-level program was performed to quantify the mechanical properties of the UHPFRC.
Two experimental programs were conducted to analyse the influence of substrate concrete compressive strength, and the evaluation of the possible effect of surface roughness on the interface bond strength in composite elements. The first experimental program was related to the shear bond test on prismatic specimens. The second one involved the design and testing of square slab panels subjected to a monotonically-increases load. Additionally, an in-situ load testing on a lightweight ribbed one-way reinforced concrete slab strengthened by means of UHPFRC overlay was performed.
Regarding the shear strengthening of RC elements, finite element analyses were carried out performed on existing prestressed concrete beams and RC beams. For the latter, a parametric study was conducted to determine the effect of a UHPFRC jacket, investigating the influence of geometric parameters, concrete compressive strength, longitudinal reinforcement ratio, and thickness of the UHPFRC layer.
Additionally, the last aim was the implementation of a an analytical model able to calculate/estimate the shear strength, which could be implemented in the design formulations of building codes.

7.1 Conclusions

The conclusions derived from this research are summarized below according to the experimental investigations and the finite element analyses.
The following conclusions are made with respect to the results of the experimental program:

1. **The failure stress obtained from shear bond test is a lower bound of the bond strength**. No delamination occurred, and the dominant failure mode was characterized by substrate failure and material failure in regions close to the interface of the substrate concrete regardless of the substrate strength, surface roughness or material repairs.

2. **For the substrate strength classes investigated, the influence of the substrate compressive strength seems to be a significant parameter affecting the shear stress between concretes with different ages.** The effect of substrate compressive strength is much more important for smooth and rough specimens, where the biggest increases in shear stress are observed.
3. **For the substrate considered, the influence of the substrate surface roughness seems to be not particularly important in the bond strength.** Despite the different roughnesses in the specimens tested, the pre-peak and the post-peak softening behaviour are similar.
4. **No significant slip between the layers was observed in the square slab panels.** Consequently, good uniformity was achieved in the slabs' performance under bending, and the shear stresses were transferred between the layers through good bond.

With respect to the parametric study of this work, the following general conclusions are drawn:

1. **The beam sizes influenced the effectiveness of the retrofitting.** The size S beams strengthened with the UHPFRC layer presented a flexure failure, with limited shear effects. Therefore, the jacket plays a role of shear reinforcement and may be considered as an effective shear strengthening method. Differently, in sizes M and L, the use of the UHPFRC layer seems not to be an efficient shear repairing method. The use of steel mesh embedded in the layer of UHPFRC allowed one to largely increase the structure deformation capacity and ductility. It is worth noting that retrofitted beams by steel mesh embedded in the layer of UHPFRC exhibited a flexural failure. Therefore, this technique increased the shear capacity and modified the brittle failure mode to a more ductile one.
2. **The compressive concrete strength could change the bond conditions at the interface between substrate and overlay.** When the perfect bond conditions were considered, the concrete compressive strength does not significantly influence the effect of the UHPFRC jacketing. On the other hand, in the models that do not consider the perfect bond conditions, the concrete compressive strength is a parameter affecting the interface bond between concretes with different ages. It is worth noting that the effect of substrate compressive strength is much more important for a high reinforcement ratio, where the biggest shear stresses are achieved.
3. **The longitudinal reinforcement ratio is an important parameter that influenced the behaviour of the strengthened beams.** Indeed, in the strengthened beams, with increasing the longitudinal reinforcement ratio, the valley of diagonal shear failure tends to become deeper. The strengthened beams having a higher reinforcement ratio show a limited regime of shear failure, while for the lower longitudinal reinforcement ratio

the valley of shear diagonal failure disappears completely. Moreover, it was observed that the shear stresses at the interface between substrate and overlay increase with increasing longitudinal reinforcement ratio.

4. **The retrofit intervention presented in this research can bring a structural member to its flexural capacity.** The regime of the valley of diagonal shear failure in strengthened beams may significantly diminish or even disappear completely, depending on the thickness and on the presence of a steel mesh. The use of UHPFRC jacketing can be an efficient method for shear strengthening of RC beams.

7.2 Recommendations for future work

The objectives of this thesis were successfully met through the experimental and numerical programs undertaken.

Nevertheless, some limitations and deficiencies were identified. As such, the following recommendations are made for further improving computational capabilities for composite members:

1. The specimens investigated in the shear bond test were subjected to compression stress only. Additional specimens tested under cyclic sustained loading could be analysed in order to consider the potential influence of the fatigue on the bond strength.
2. In the shear bond tests, the range of substrate compressive strengths investigated are limited, therefore the experimental tests can be considered as a preliminary investigation. Additional tests that consider a higher substrate compressive strength (i.e., in the case of bridges) could potentially lead to a shear failure at the interface, and to a more refined bond experimental model for a wide range of composite elements.
3. An experimental campaign would be recommended for confirming the numerical results outlines in Chapter 5. Future work should provide the experimental behaviour on RC beams and on prestressed concrete beams.
4. A refinement in the numerical model adopted (VecTor2) should be studied to consider two different tension softening for concrete and for FRC in composite members. With a possible formulation related to the fracture energy of FRC, especially when dealing with member with little or no shear reinforcement, for which the tension softening of concrete plays a considerable role.
5. Lastly, with respect to the analytical formulation proposed for predicting the shear strength of the composite beams, further experimental studies are suggested to validate it.

APPENDIX A: MATERIAL TEST RESULTS

A.1. Cubic compression tests

A.1.1. *Test set PHF*

Cube	**Weight [g]**	**Length [mm]**	**Load [kN]**	$f_{c,cube}$ **28 days [MPa]**
#1	8106	150	2659	118
#2	8074	150	2665	118
#3	8083	150	2675	119
#4	8065	150	2689	120
#5	7950	150	2650	118
#6	8047	150	2623	117
Average				**118**
Std. dev.				**1.0**
C.V. (%)				**0.01**

A.1.2. *Test set PHF46*

Cube	**Weight [g]**	**Length [mm]**	**Load [kN]**	$f_{c,cube}$ **28 days [MPa]**
#1	8296	150	2589	115
#2	8261	150	2483	110
#3	8316	150	2509	112
#4	8258	150	2465	110
#5	8398	150	2479	110
#6	8282	150	2398	107
Average				**111**
Std. dev.				**2.8**
C.V. (%)				**0.03**

A.1.3. *Test set PHFT*

Cube	**Weight [g]**	**Length [mm]**	**Load [kN]**	$f_{c,cube}$ **28 days [MPa]**
#1	7953	150	2431	108
#2	7946	150	2321	103
#3	7898	150	2288	102
#4	8052	150	2247	100
#5	7925	150	2394	106
#6	7938	150	2250	100
Average				**103**
Std. dev.				**3.4**
C.V. (%)				**0.03**

A.1.4. *Test set PHF46T*

Cube	**Weight [g]**	**Length [mm]**	**Load [kN]**	$f_{c,cube}$ **28 days [MPa]**
#1	8043	150	2379	106
#2	8001	150	2396	106
#3	8122	150	2427	108
#4	7997	150	2375	106
#5	8076	150	2373	105
#6	7954	150	2350	104
Average				**106**
Std. dev.				**1.2**
C.V. (%)				**0.01**

A.1.5. *Test set PH*

Cube	**Weight [g]**	**Length [mm]**	**Load [kN]**	$f_{c,cube}$ **28 days [MPa]**
#1	8227	150	2705	120
#2	8280	150	2764	123
#3	8306	150	2661	118
#4	8305	150	2763	123
#5	83041	150	2687	119
#6	8305	150	2587	112
Average				**119**
Std. dev.				**3.8**
C.V. (%)				**0.03**

A.2. Three-point bending tests

A.2.1. *Test set PHF*

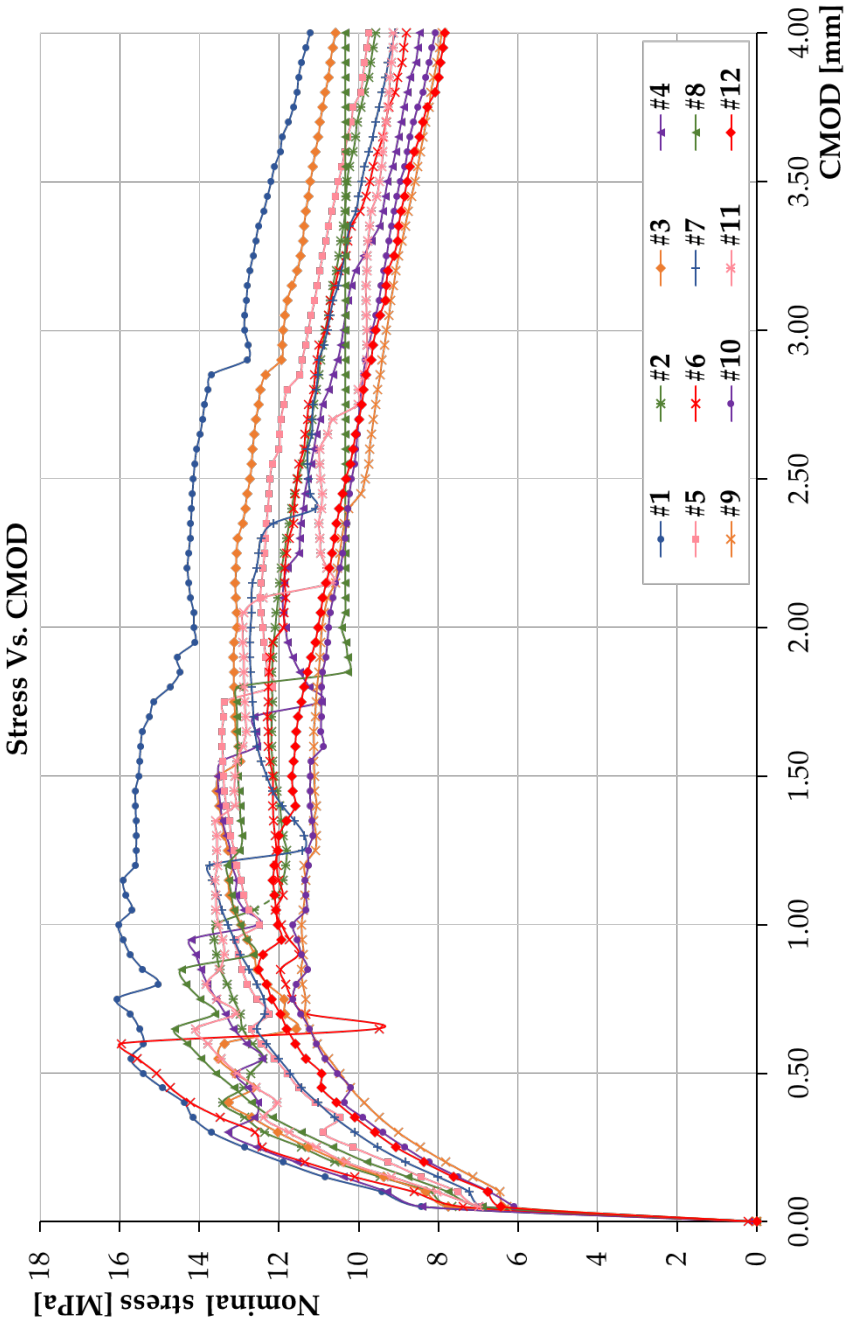

	f_L [MPa]	f_{R1} [MPa]	f_{R2} [MPa]	f_{R3} [MPa]	f_{R4} [MPa]
#1	8.4	15.4	15.5	14.2	12.2
#2	7.7	12.7	12.1	11.5	10.3
#3	7.9	13.1	13.5	12.7	11.2
#4	8.4	13.1	13.5	11.3	9.3
#5	7.2	11.8	13.4	12.2	10.5
#6	7.4	15.1	12.2	11.5	9.7
#7	6.9	11.7	12.3	11.3	9.9
#8	7.3	13.6	13.0	-	-
#9	6.6	10.5	11.1	9.8	8.6
#10	6.6	10.5	11.2	10.2	9.0
#11	7.0	13.1	13.1	11.0	9.5
#12	6.5	10.9	11.7	10.3	8.8
Average	**7.3**	**12.6**	**12.7**	**11.5**	**9.9**
Std. dev.	**0.7**	**1.6**	**1.2**	**3.5**	**3.0**
C.V. (%)	**0.09**	**0.13**	**0.10**	**0.31**	**0.31**

A.2.2. *Test set PHF46*

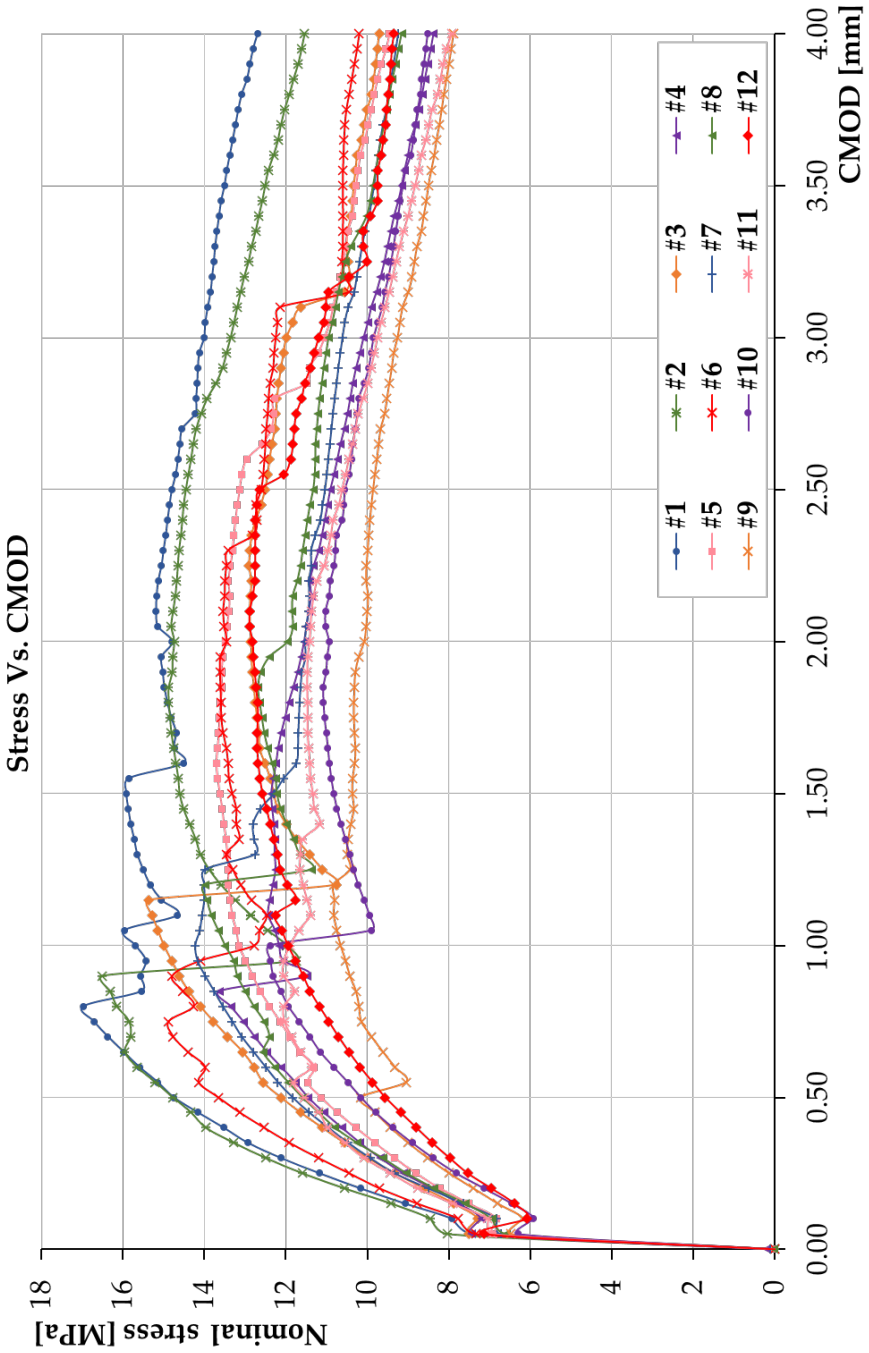

	f_L [MPa]	f_{R1} [MPa]	f_{R2} [MPa]	f_{R3} [MPa]	f_{R4} [MPa]
#1	7.8	14.8	15.9	14.8	13.5
#2	8.1	14.8	14.6	14.5	12.5
#3	7.7	12.1	12.3	12.5	10.3
#4	8.0	11.5	12.4	10.9	9.2
#5	8.0	11.1	13.6	13.1	10.3
#6	7.6	13.7	13.3	12.6	10.6
#7	6.8	11.8	12.3	11.0	9.8
#8	7.5	11.6	12.2	11.3	9.9
#9	6.9	10.2	10.4	9.9	8.5
#10	7.0	10.2	10.8	10.6	9.1
#11	7.6	11.6	11.3	10.6	8.8
#12	7.4	9.6	12.6	12.6	9.8
Average	**7.5**	**11.9**	**12.6**	**12.0**	**10.2**
Std. dev.	**0.4**	**1.7**	**1.6**	**1.6**	**1.5**
C.V. (%)	**0.06**	**0.14**	**0.12**	**0.13**	**0.14**

A.2.3. *Test set PHFT*

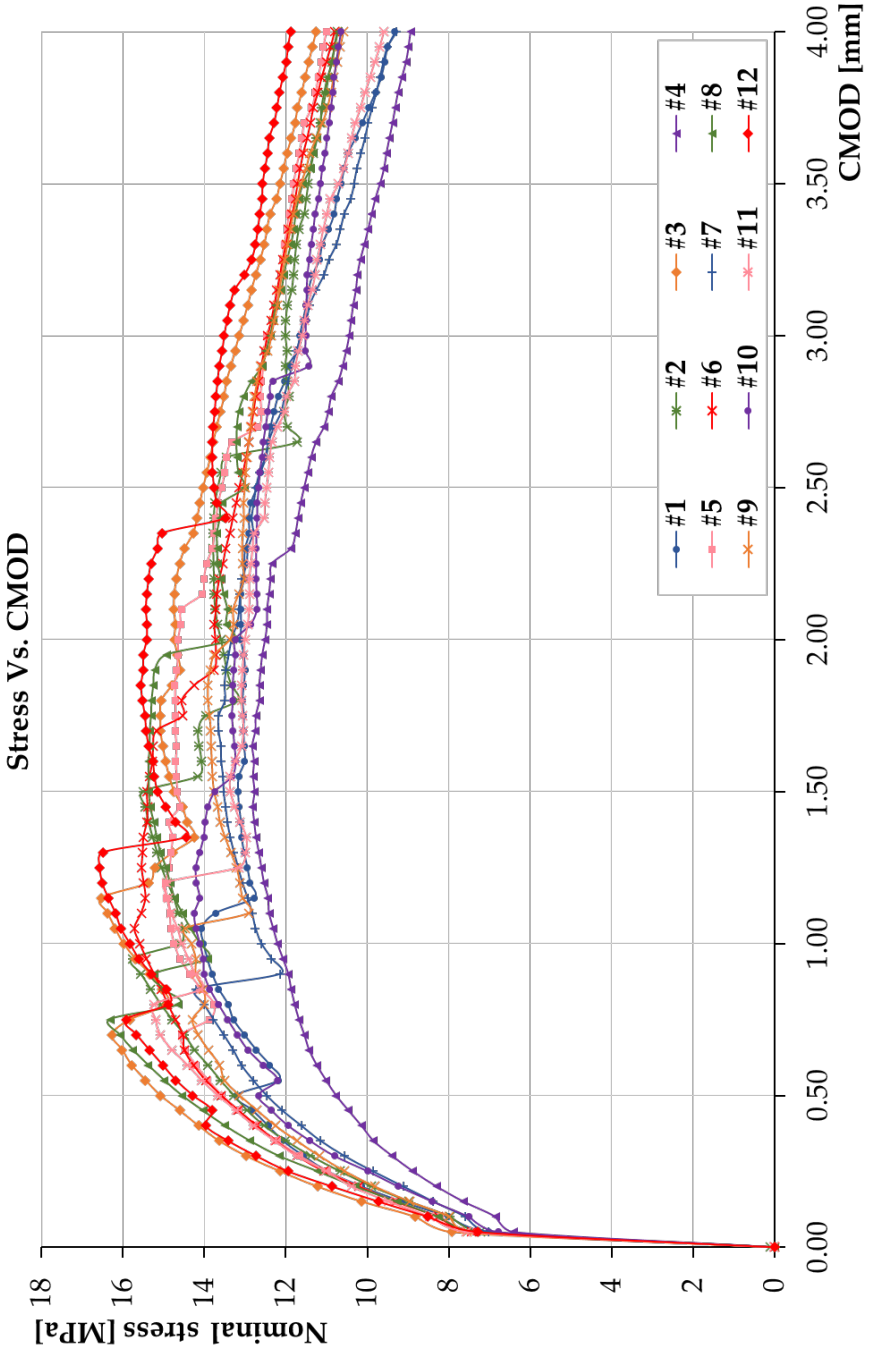

	f_L [MPa]	f_{R1} [MPa]	f_{R2} [MPa]	f_{R3} [MPa]	f_{R4} [MPa]
#1	8.5	13.2	13.2	12.7	10.6
#2	8.3	13.3	15.5	13.7	11.5
#3	8.2	15.1	14.7	14.0	12.1
#4	8.6	10.8	12.8	11.6	9.7
#5	8.6	13.6	14.7	13.6	11.8
#6	7.4	13.6	15.4	13.2	11.7
#7	7.0	12.5	13.5	12.7	10.3
#8	7.3	14.6	15.4	13.0	11.6
#9	7.6	13.1	13.8	13.0	11.6
#10	6.8	12.7	13.7	12.7	11.2
#11	7.6	13.7	13.4	12.5	10.7
#12	7.3	14.3	15.2	13.8	12.6
Average	**7.8**	**13.4**	**14.3**	**13.0**	**11.3**
Std. dev.	**0.6**	**1.1**	**1.0**	**0.7**	**0.8**
C.V. (%)	**0.08**	**0.08**	**0.07**	**0.05**	**0.07**

A.2.4. *Test set PHF46T*

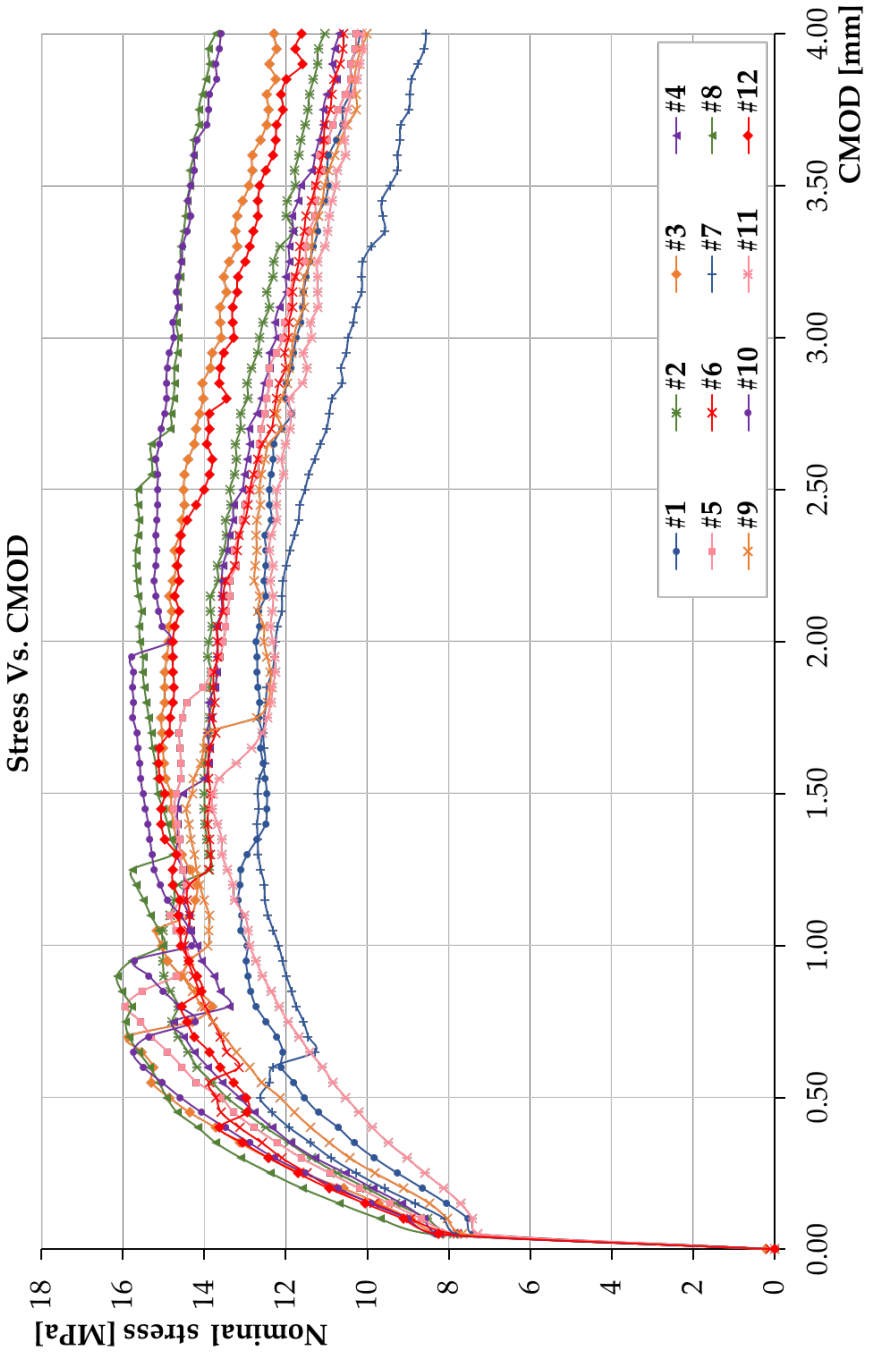

	f_L [MPa]	f_{R1} [MPa]	f_{R2} [MPa]	f_{R3} [MPa]	f_{R4} [MPa]
#1	7.5	11.6	12.5	12.4	11.0
#2	7.9	13.5	14.0	13.4	11.8
#3	8.2	14.9	14.8	14.5	12.9
#4	8.2	13.1	14.5	13.1	11.6
#5	7.8	13.6	14.7	12.9	11.3
#6	7.8	13.7	13.9	12.9	11.3
#7	7.8	12.6	12.7	11.3	9.4
#8	8.4	14.9	15.2	15.6	14.4
#9	7.7	12.2	14.3	12.7	11.1
#10	8.3	14.6	15.5	15.2	14.3
#11	7.3	10.5	13.8	12.2	10.8
#12	8.3	13.0	15.0	14.0	12.6
Average	**7.9**	**13.2**	**14.2**	**13.3**	**11.9**
Std. dev.	**0.3**	**1.3**	**0.9**	**1.3**	**1.5**
C.V. (%)	**0.04**	**0.10**	**0.07**	**0.09**	**0.12**

A.2.5. *Test set PH*

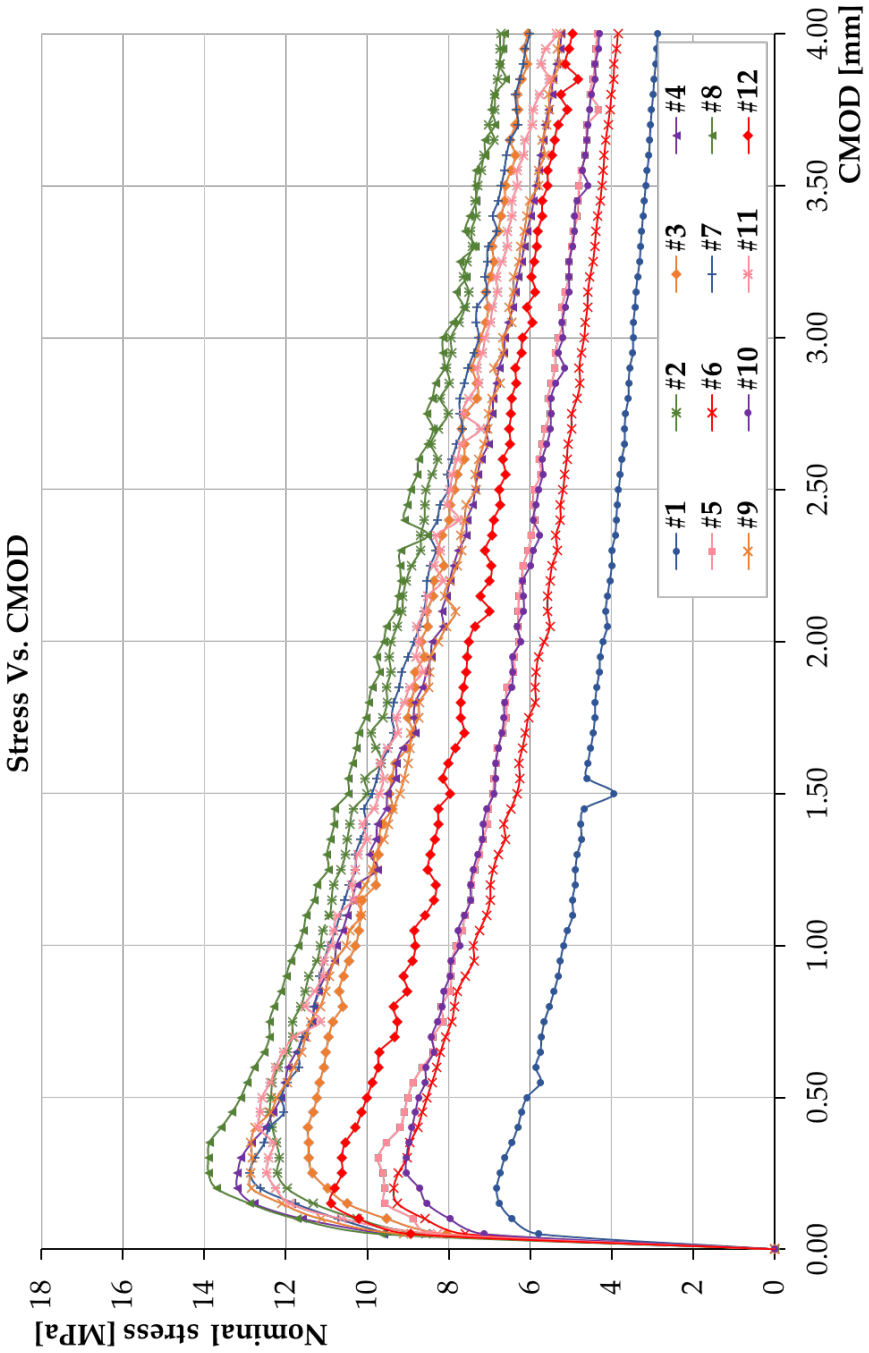

	f_L [MPa]	f_{R1} [MPa]	f_{R2} [MPa]	f_{R3} [MPa]	f_{R4} [MPa]
#1	8.6	12.4	10.0	8.6	7.3
#2	8.1	11.2	9.5	7.8	6.6
#3	9.6	12.1	9.5	7.4	5.9
#4	8.6	9.0	6.9	5.9	4.8
#5	7.7	8.5	6.3	5.2	4.2
#6	9.5	12.1	9.9	8.0	6.7
#7	9.7	13.1	10.5	8.9	7.4
#8	9.1	12.2	9.2	7.4	5.8
#9	7.2	8.7	6.9	5.8	4.7
#10	8.3	12.6	9.7	8.0	6.4
#11	8.9	10.0	8.0	6.8	5.6
#12	8.2	9.5	7.3	6.0	5.0
Average	**8.6**	**11.0**	**8.6**	**7.1**	**5.9**
Std. dev.	**0.8**	**1.7**	**1.5**	**1.2**	**1.0**
C.V. (%)	**0.09**	**0.15**	**0.17**	**0.17**	**0.18**

A.3. Shear bond tests

A.3.1. *Test set PHF-C12/15*

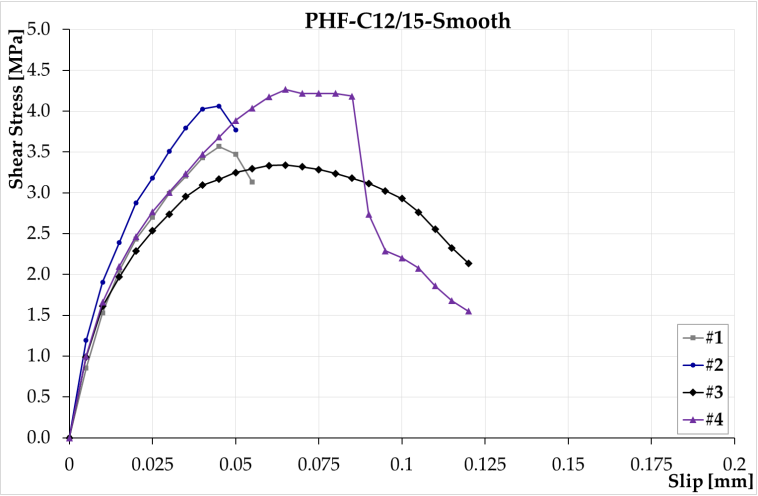

	τ [MPa]	**Slip [mm]**
#1	3.6	0.05
#2	4.1	0.04
#3	3.3	0.06
#4	4.3	0.04
Average	**3.8**	**0.05**
Std. dev.	**0.45**	**0.01**
C.V. (%)	**0.12**	**0.16**

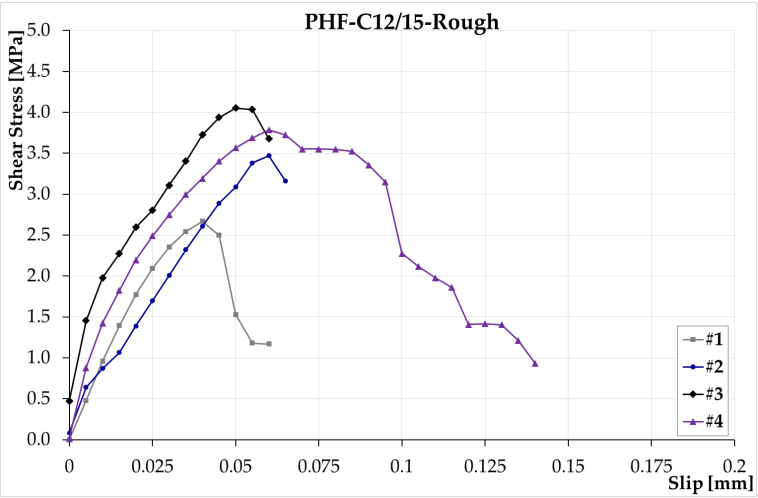

	τ [MPa]	Slip [mm]
#1	2.7	0.04
#2	3.5	0.06
#3	4.1	0.05
#4	3.8	0.06
Average	**3.5**	**0.05**
Std. dev.	**0.62**	**0.01**
C.V. (%)	**0.18**	**0.19**

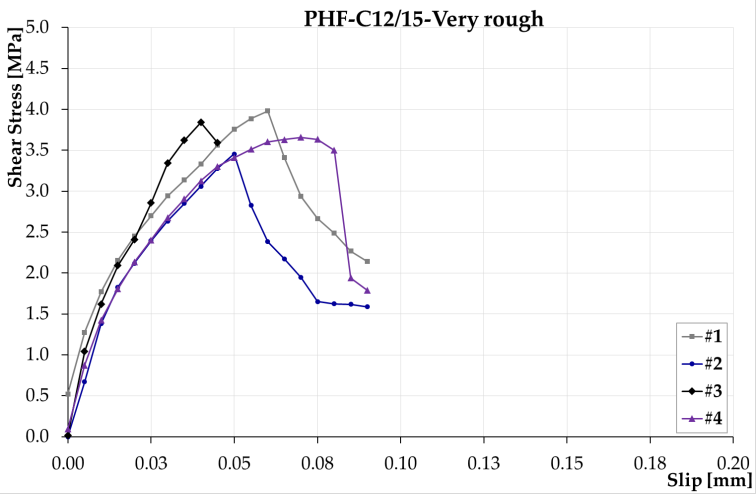

	τ [MPa]	Slip [mm]
#1	4.0	0.06
#2	3.5	0.05
#3	3.8	0.04
#4	3.7	0.07
Average	**3.8**	**0.06**
Std. dev.	**0.20**	**0.01**
C.V. (%)	**0.05**	**0.23**

A.3.2. *Test set PHF-C16/20*

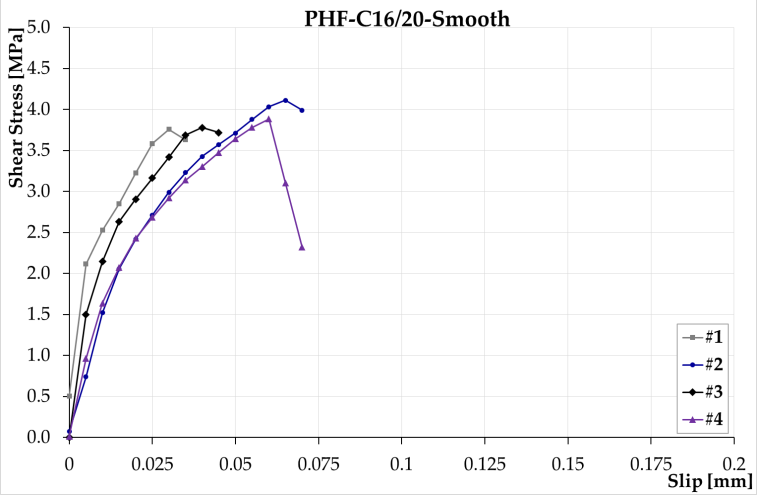

	τ [MPa]	Slip [mm]
#1	3.8	0.03
#2	4.1	0.06
#3	3.8	0.04
#4	3.9	0.06
Average	**3.9**	**0.05**
Std. dev.	**0.16**	**0.02**
C.V. (%)	**0.04**	**0.35**

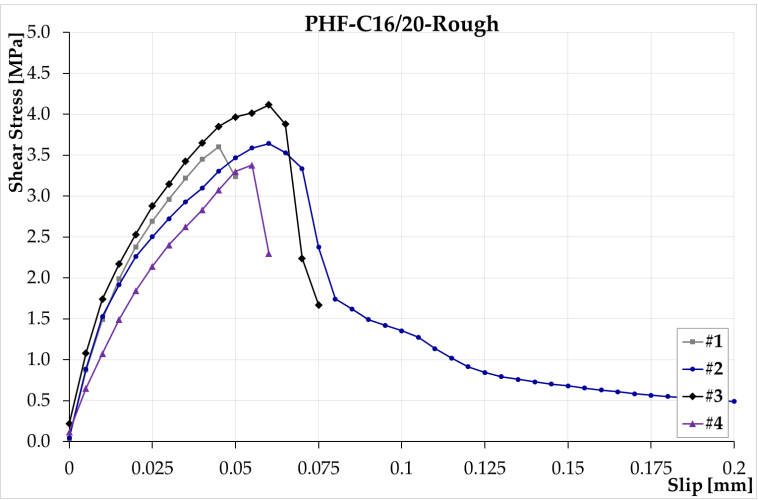

	τ [MPa]	Slip [mm]
#1	3.6	0.05
#2	3.7	0.06
#3	4.1	0.06
#4	3.4	0.05
Average	**3.7**	**0.05**
Std. dev.	**0.31**	**0.01**
C.V. (%)	**0.08**	**0.14**

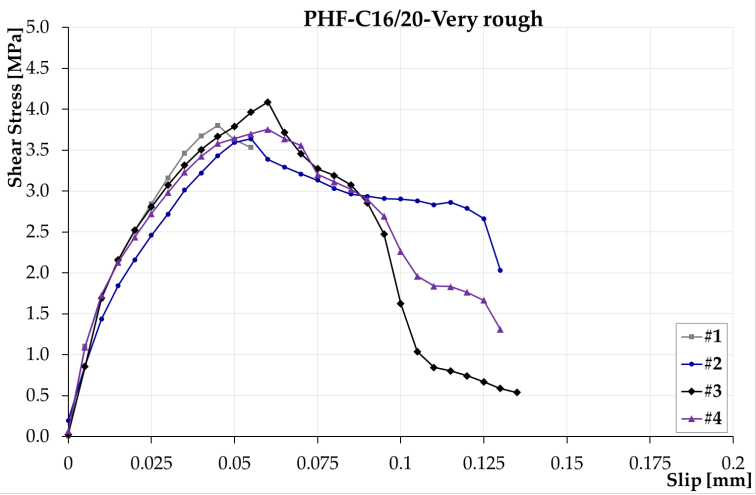

	τ [MPa]	Slip [mm]
#1	3.8	0.04
#2	3.7	0.05
#3	4.1	0.06
#4	4.2	0.08
Average	**3.9**	**0.06**
Std. dev.	**0.25**	**0.02**
C.V. (%)	**0.06**	**0.27**

A.3.3. *Test set PHF-C20/25*

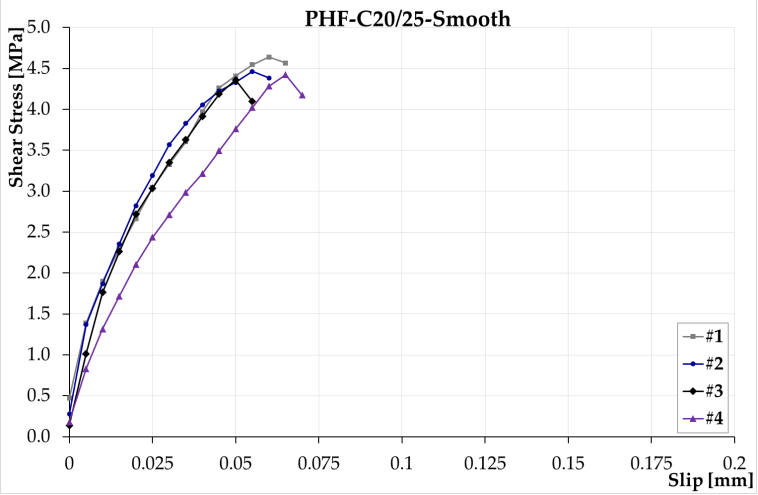

	τ [MPa]	Slip [mm]
#1	4.7	0.05
#2	4.5	0.05
#3	4.4	0.05
#4	4.4	0.07
Average	**4.5**	**0.07**
Std. dev.	**0.12**	**0.01**
C.V. (%)	**0.03**	**0.14**

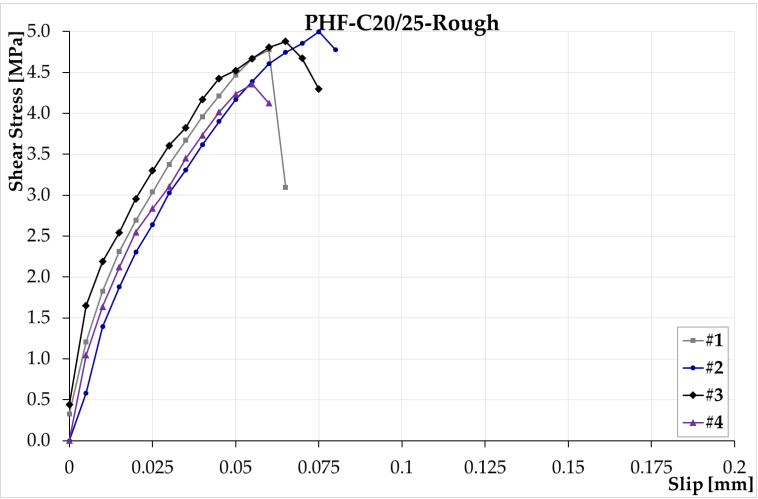

	τ [MPa]	**Slip [mm]**
#1	4.8	0.06
#2	5.0	0.08
#3	4.9	0.07
#4	4.4	0.05
Average	**4.8**	**0.07**
Std. dev.	**0.29**	**0.01**
C.V. (%)	**0.06**	**0.14**

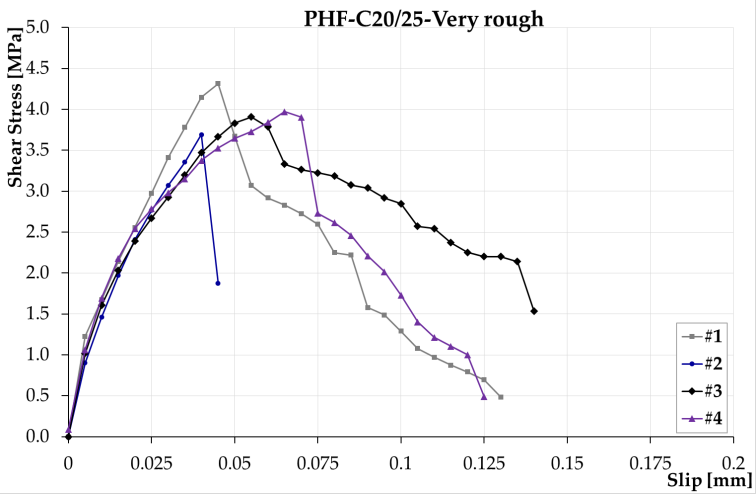

	τ [MPa]	**Slip [mm]**
#1	4.3	0.04
#2	4.5	0.06
#3	3.9	0.05
#4	4.0	0.07
Average	**4.2**	**0.06**
Std. dev.	**0.26**	**0.01**
C.V. (%)	**0.06**	**0.17**

A.3.4. *Test set PHF46-C12/15*

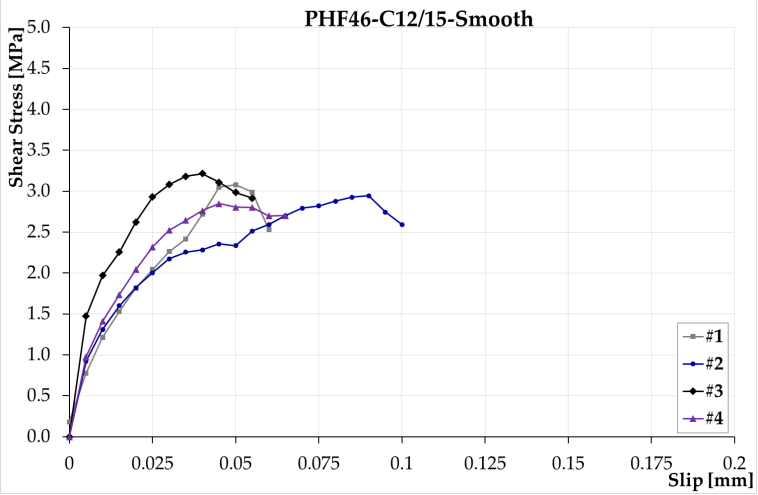

	τ [MPa]	Slip [mm]
#1	3.1	0.05
#2	3.0	0.09
#3	3.2	0.04
#4	2.9	0.05
Average	**3.0**	**0.06**
Std. dev.	**0.15**	**0.02**
C.V. (%)	**0.05**	**0.42**

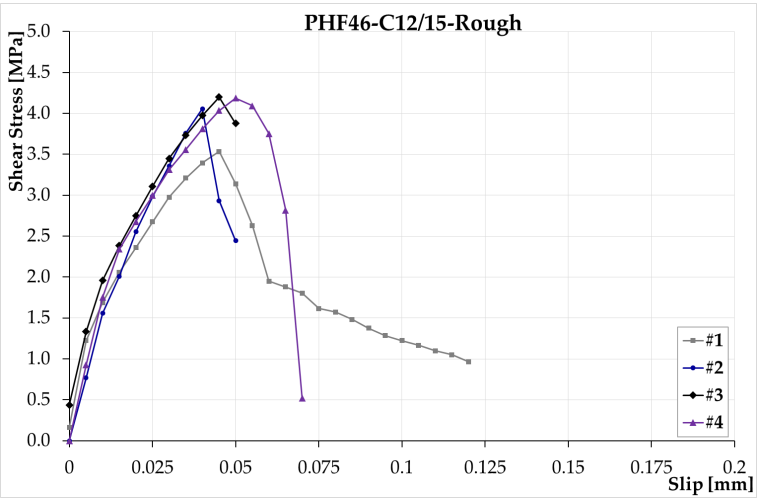

	τ [MPa]	Slip [mm]
#1	3.5	0.05
#2	4.1	0.04
#3	4.3	0.05
#4	4.2	0.05
Average	**4.0**	**0.05**
Std. dev.	**0.34**	**0.01**
C.V. (%)	**0.08**	**0.10**

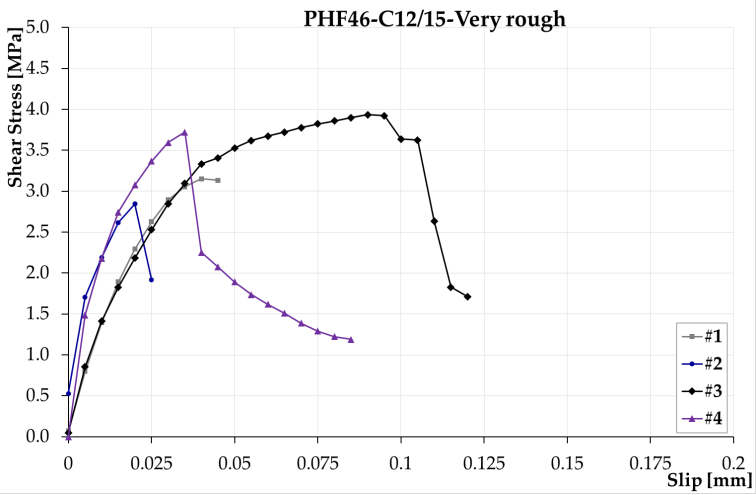

	τ [MPa]	Slip [mm]
#1	3.2	0.04
#2	2.9	0.02
#3	3.9	0.09
#4	3.7	0.04
Average	**3.3**	**0.05**
Std. dev.	**0.48**	**0.03**
C.V. (%)	**0.14**	**0.63**

A.3.5. *Test set PHF46-C16/20*

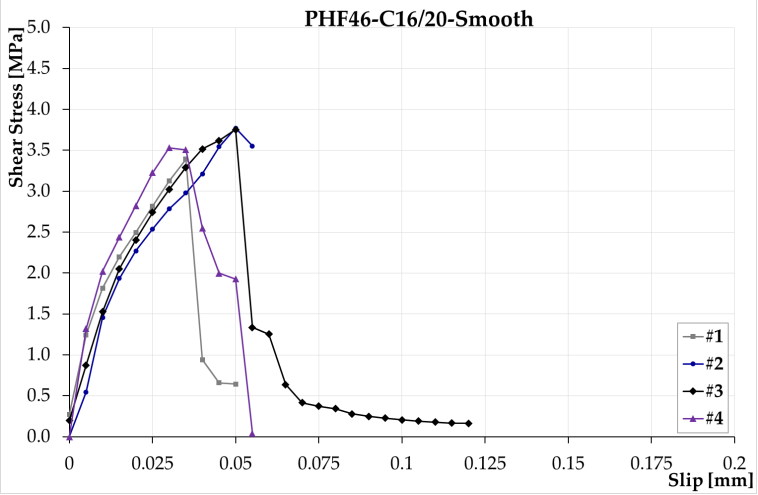

	τ [MPa]	Slip [mm]
#1	3.4	0.04
#2	3.9	0.05
#3	3.8	0.05
#4	3.7	0.03
Average	**3.7**	**0.04**
Std. dev.	**0.20**	**0.01**
C.V. (%)	**0.05**	**0.24**

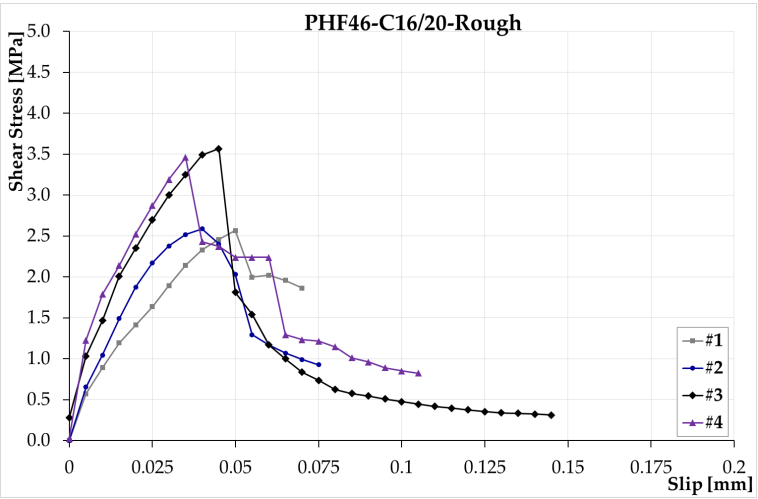

	τ [MPa]	Slip [mm]
#1	2.6	0.05
#2	2.6	0.04
#3	3.6	0.04
#4	3.5	0.04
Average	**3.0**	**0.04**
Std. dev.	**0.43**	**0.01**
C.V. (%)	**0.14**	**0.13**

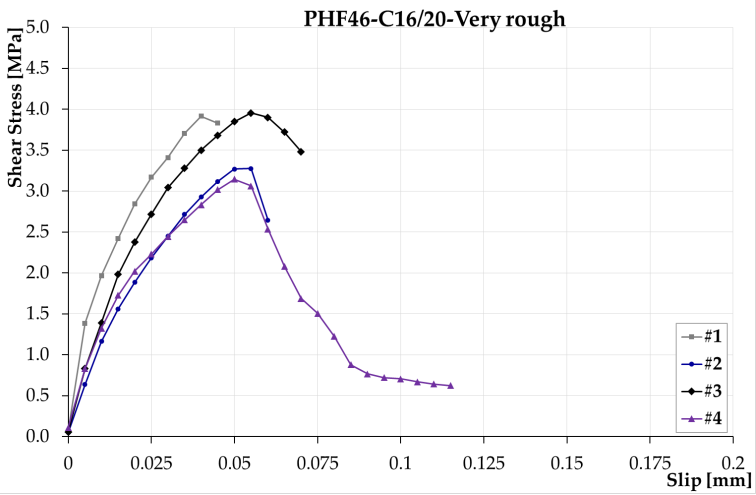

	τ [MPa]	Slip [mm]
#1	3.9	0.04
#2	3.3	0.05
#3	4.0	0.06
#4	3.2	0.05
Average	**3.6**	**0.05**
Std. dev.	**0.41**	**0.01**
C.V. (%)	**0.11**	**0.12**

A.3.6. *Test set PHF46-C20/25*

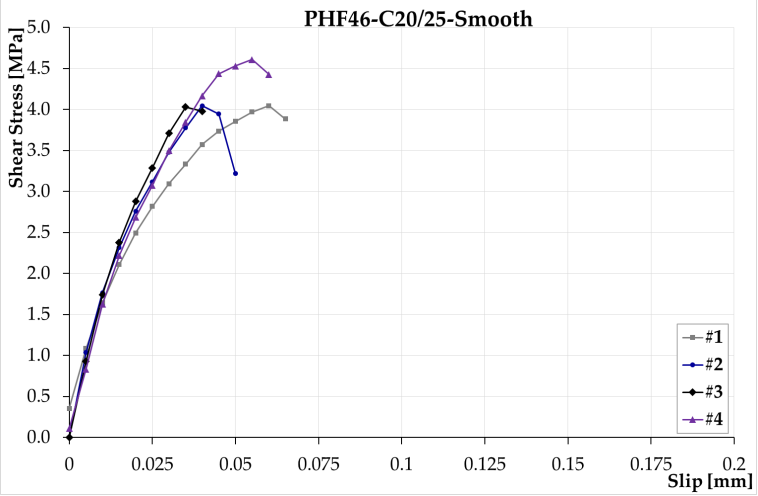

	τ [MPa]	**Slip [mm]**
#1	4.1	0.06
#2	4.1	0.04
#3	4.2	0.04
#4	4.6	0.05
Average	**4.3**	**0.05**
Std. dev.	**0.25**	**0.01**
C.V. (%)	**0.06**	**0.21**

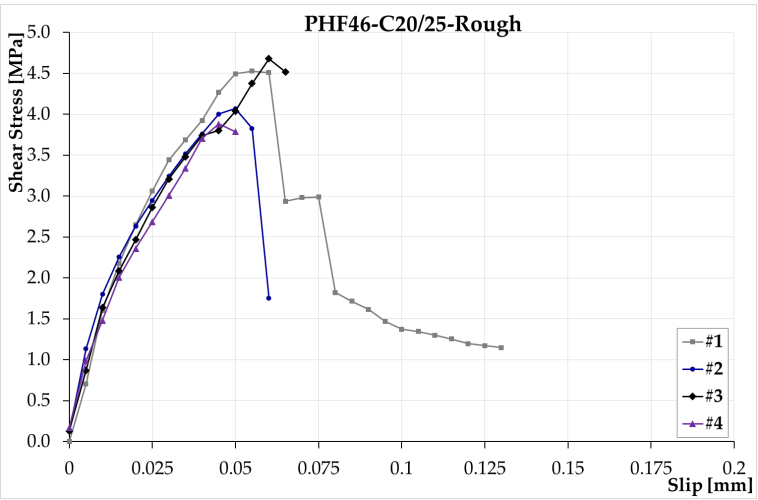

	τ [MPa]	Slip [mm]
#1	4.5	0.06
#2	4.1	0.05
#3	4.7	0.06
#4	3.9	0.05
Average	**4.3**	**0.05**
Std. dev.	**0.35**	**0.01**
C.V. (%)	**0.08**	**0.10**

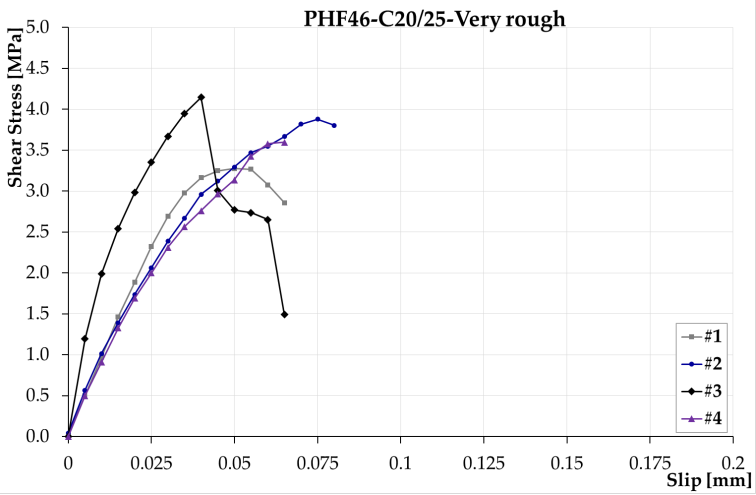

	τ [MPa]	Slip [mm]
#1	3.3	0.05
#2	3.9	0.07
#3	4.2	0.04
#4	3.8	0.04
Average	**3.8**	**0.05**
Std. dev.	**0.33**	**0.02**
C.V. (%)	**0.09**	**0.29**

APPENDIX B: DATA FOR THE FINITE ELEMENT MODELLING OF THE RC PANEL

B.1. Finite element model of the panels

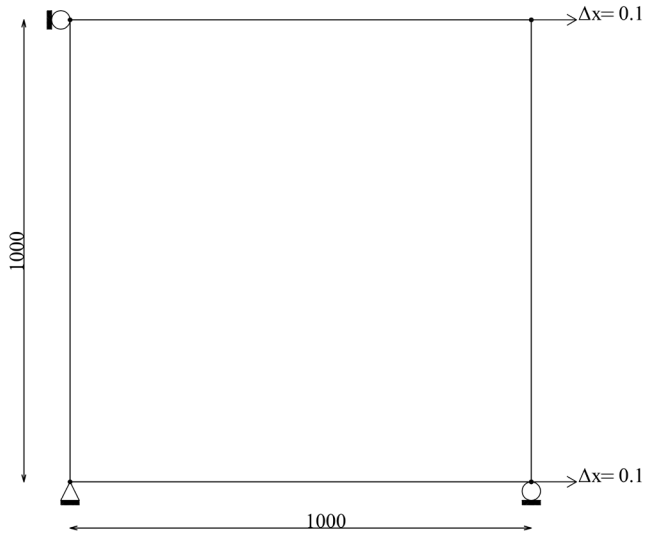

Figure 1: Finite element model of the FRC panels.

	f'_c [MPa]	E_c [MPa]	Fibre type	V_f [%]	L_f [mm]	D_f [mm]	F_u [MPa]
PHF	98	43600	Hooked	0.96	30	0.38	3070
PHF46	92	42800	Hooked	0.96	30	0.38	3070

Table 1: Concrete and fibre properties used in VecTor2.

Compression pre-peak	Hognestad (parabola)
Compression post-peak	Modified Park-Kent
Compression softening	Vecchio-1992A
Tension stiffening	Modified Bentz 2003
Tension softening	Custom Input (Crack Based)/ Nonlinear (Hordijk)
FRC tension	Not considers / FIB Model Code 2010
Confined strength	Kupfer / Richart
Dilation	Variable - isotropic
Cracking criterion	Mohr – Coulomb (stress)
Crack stress calculation	Basic (DSFM/MCFT)
Crack width check	Agg/2.5 max crack width
Crack slip calculation	Walraven
Creep and relaxation	Not considered

Table 2: Concrete constitutive model used in VecTor2.

Hysteretic response	Nonlinear w / plastic offsets
Dowel Action	Tassios model (Crack Slip)
Buckling	Akkaya 2012 model
Concrete Bond	Eligehausen model

Table 3: Reinforcement constitutive model used in VecTor2.

Strain History	Previous Loading Considered
Strain Rate Effect	Not considered
Structural Damping	Not considered
Geometry Nonlinearity	Considered
Analysis Mode	CEB-FIP 1978 - Deformed

Table 4: Analysis model used in VecTor2.

B.2. Residual flexural strengths

At first, the analyses were conducted using a crack-based custom tension softening model. The custom input was specified in the VecTor2 job file; four points representing the tensile stress-crack relationship of the UHPFRC have to be input in the VecTor2 auxiliary file (VT2.AUX). The four points input in the VecTor2 auxiliary file represents the tensile stress-crack opening displacement relationship of the UHPFRC. Note, that when the custom tension softening model is specified, the fibre reinforcement definition should not be given (i.e. zero fibre volume content have to be input) to avoid the double account of the influence of the fibres as the effect of the fibre addition has implicitly been expressed in the input custom tension softening curve.

Figure 1, Figure 2, and Figure 3 show the *stress-crack width* law of UHPFRC evaluated through an inverse analysis procedure performed using the FE program DIANA 10.1. The inverse analysis is used to determine a σ–w relationship from the three-point bending test and the splitting tension test.

Table 5 lists the values of the stress-crack width law that have to be input in the VecTor2 auxiliary file.

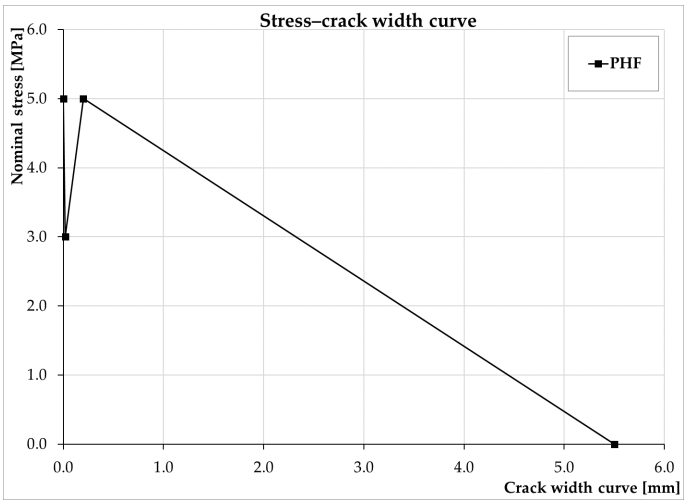

Figure 2: Tensile stress-crack width relationship for HPC Floor.

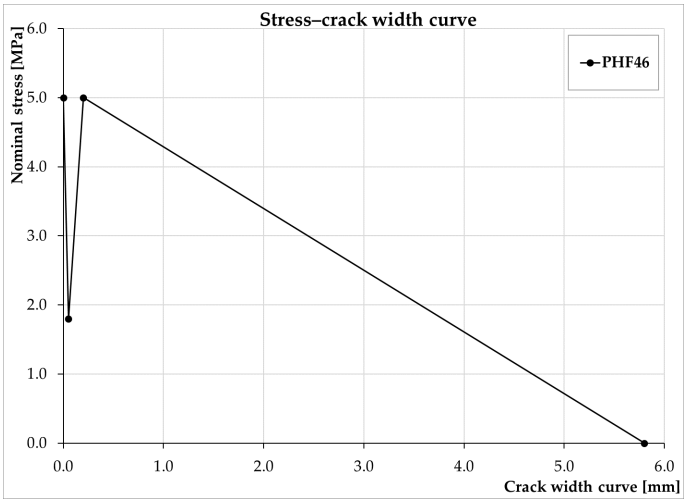

Figure 3: Tensile stress-crack width relationship for HPC Floor 46.

PHF		**PHF46**	
Crack width [mm]	**Stress [MPa]**	**Crack width [mm]**	**Stress [MPa]**
0	5.0	0	5.0
0.02	3.0	0.05	1.8
0.2	5.0	0.2	5.0
5.5	0	5.8	0

Table 5: Four points representing the tensile stress-crack relationship.

Subsequently, the analyses were conducted using fib Model Code 2010 FRC option to model the FRC tension behaviour. For the MC 2010 options, residual flexural strength (f_1* and f_3*) are required. The residual flexural strength corresponds respectively at 0.5 mm and 2.5 mm of crack width.
Table 6 illustrates the value of residual flexural strength obtained from the analyses conducted using a crack-based custom tension softening model.

	w_1 [mm]	f_1* [MPa]	w_3 [mm]	f_3* [MPa]
PHF	0.5	4.72	2.5	2.83
PHF46	0.5	4.74	2.5	2.99

Table 6: Residual flexural strengths, f_{R1} and f_{R3}.

Figure 4 and Figure 5 show the comparison between the stress-crack width relationships obtained though the two different analyses.

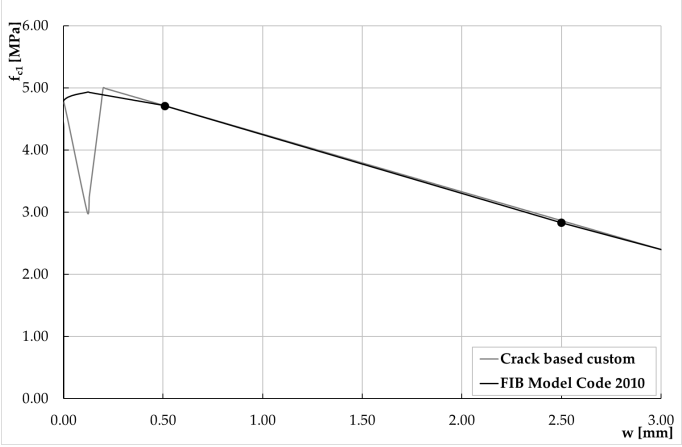

Figure 4: Stress-crack width relationships for PHF panel.

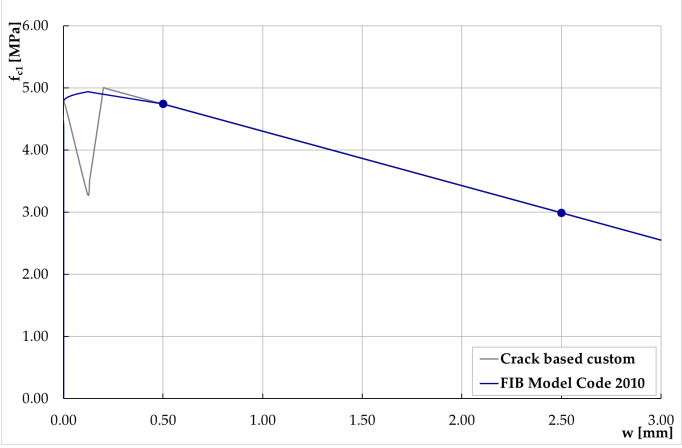

Figure 5: Stress-crack width relationships for PHF46 panel.

APPENDIX C: SQUARE SLAB PANEL TEST

In the following sections, the crack patterns observed during the testing of the square slab panel specimens are presented for both the top and bottom sides of each panel. For each set of measurements, a summary of peak load, P, shear stress, τ, slip (in microns) between the substrate and the overlay, s, and crack in mid-span, w, are presented.

C.1. Series PHF


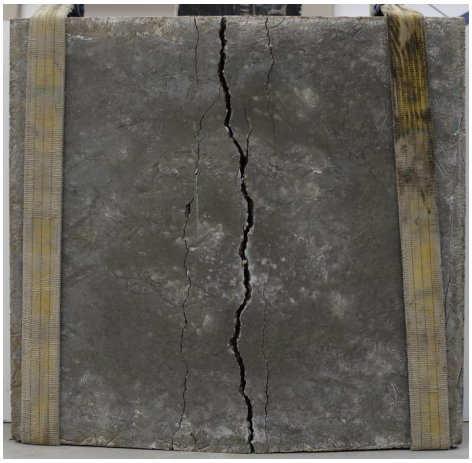

#1: P=105.8 kN, τ=0.56 MPa, s=2.0 μm, w=11.9 mm

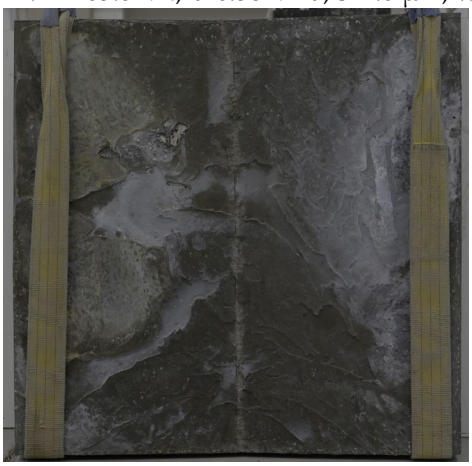


#2: P=91.3 kN, τ=0.48 MPa, s=5.1 μm, w=13.4 mm

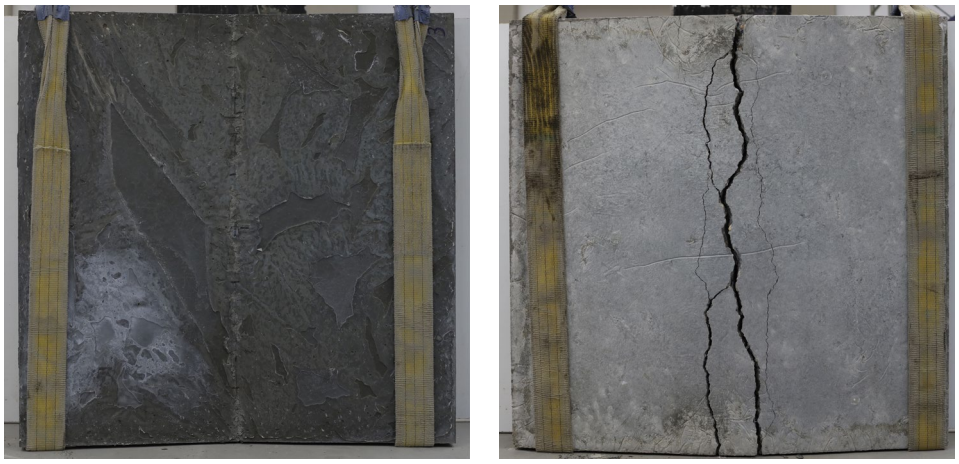

#3: P=93.6 kN, τ=0.49 MPa, s=2.9 μm, w=15.4 mm

#4: P=102.5 kN, τ=0.54 MPa, s=1.8 μm, w=13.1 mm

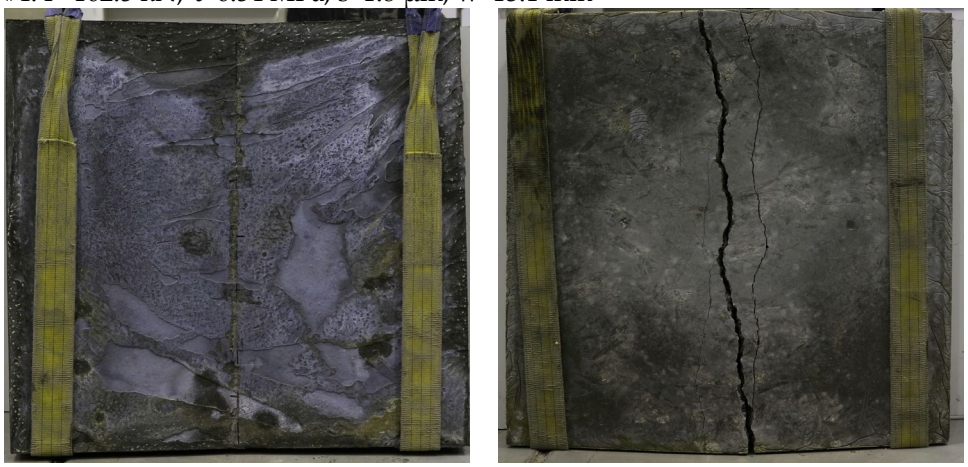

#5: P=98.0 kN, τ=0.52 MPa, s=6.3 μm, w=15.2 mm


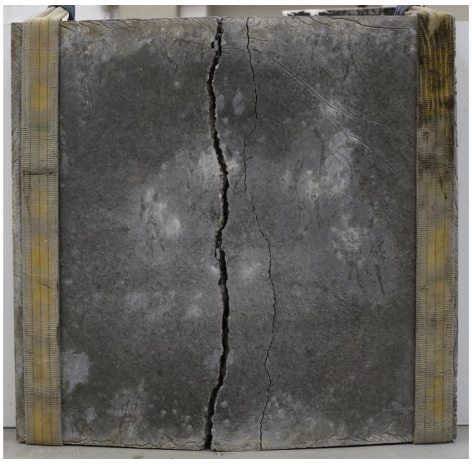

#6: P=97.2 kN, τ=0.52 MPa, s=1.4 μm, w=12.6 mm


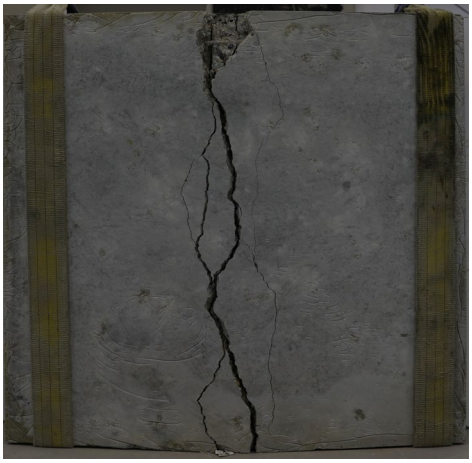

#7: P=96.2 kN, τ=0.51 MPa, s=1.6 μm, w=10.6 mm

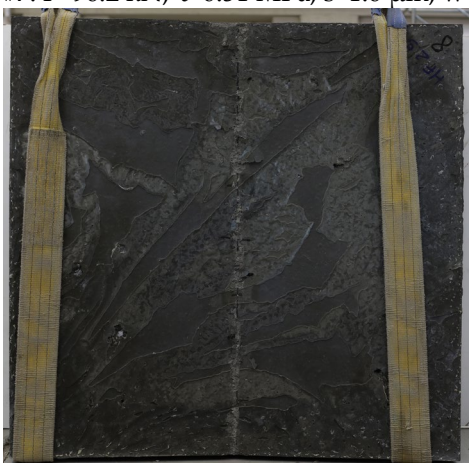
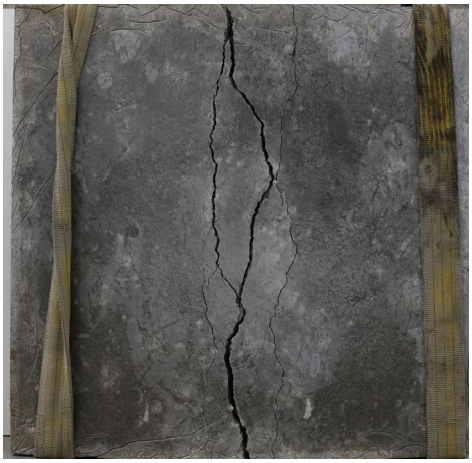

#8: P=98.3 kN, τ=0.52 MPa, s=1.8 μm, w=10.2 mm

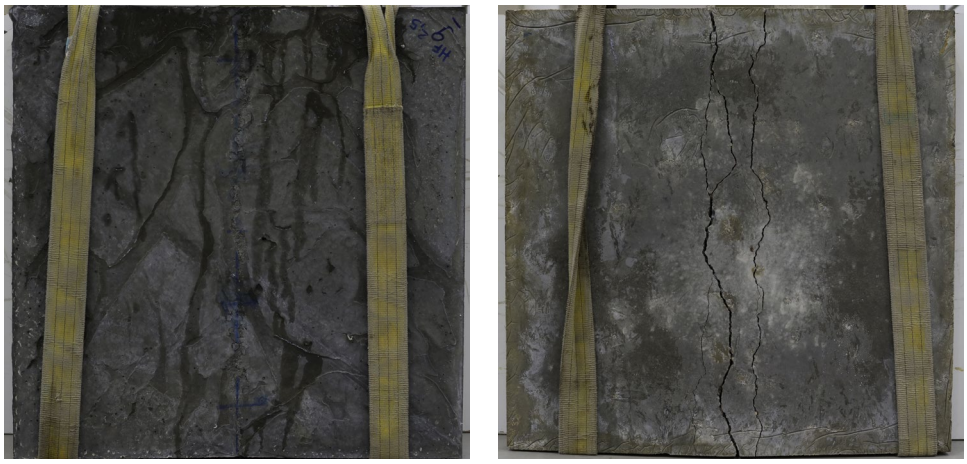

#9: P=96.2 kN, τ=0.51 MPa, s=3.3 μm, w=12.5 mm

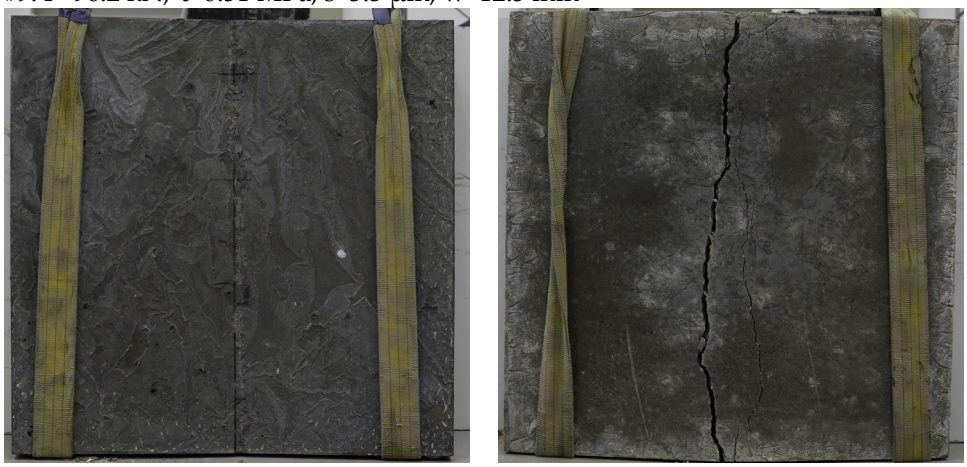

#10: P=100.5 kN, τ=0.53 MPa, s=0.1 μm, w=11.6 mm

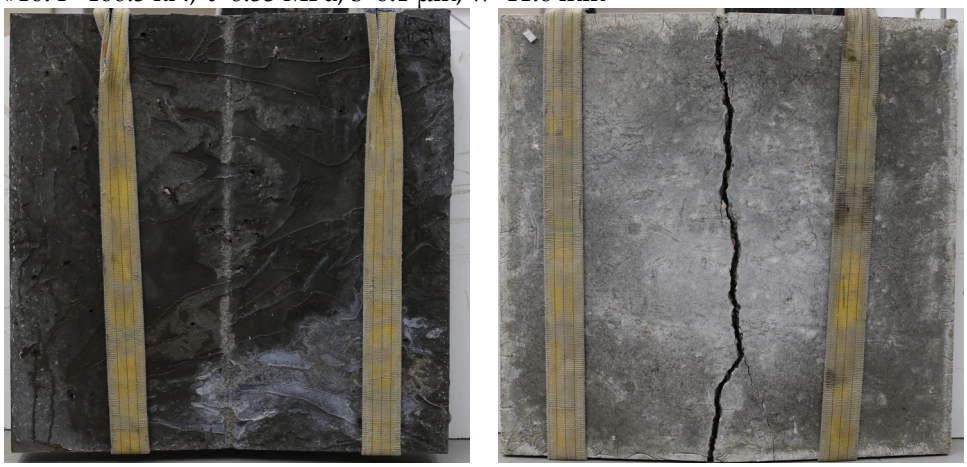

#11: P=95.9 kN, τ=0.51 MPa, s=1.0 μm, w=10.1 mm


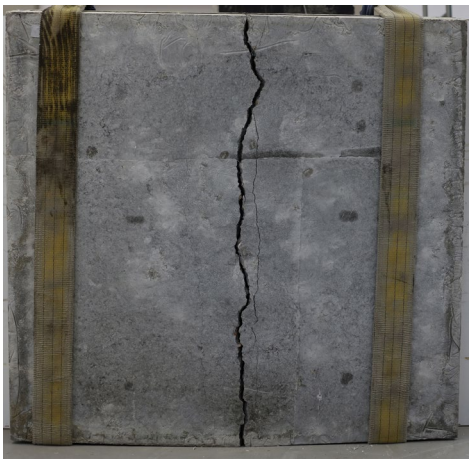

#12: P=92.9 kN, τ=0.49 MPa, s=0.9 μm, w=12.7 mm

C.2. Series PHF46


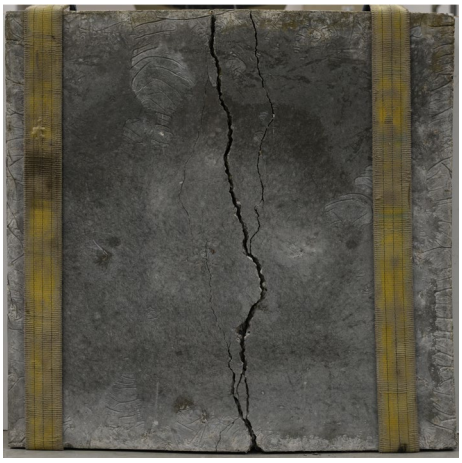

#1: P=110.6 kN, τ=0.59 MPa, s=1.4 μm, w=12.9mm


#2: P=104.1 kN, τ=0.55 MPa, s=1.3 μm, w=13.4 mm


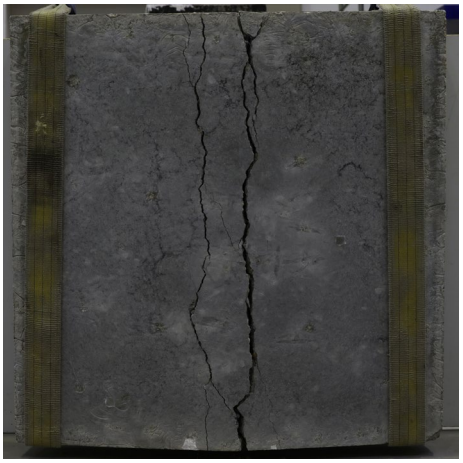

#3: P=100.8 kN, τ=0.53 MPa, s=1.6 μm, w=16.6mm


#4: P=96.8 kN, τ=0.51 MPa, s=3.0 μm, w=17.0 mm


#5: P=94.3 kN, τ=0.50 MPa, s=0.2 μm, w=15.1 mm

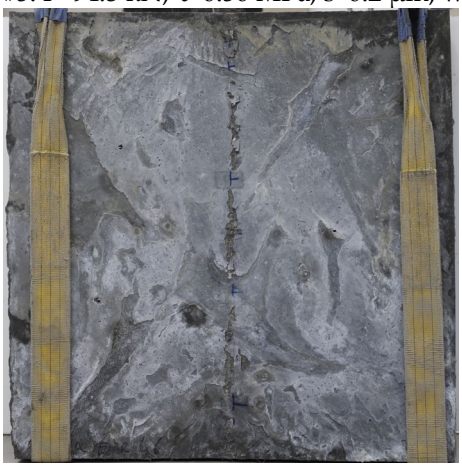


#6: P=105.2 kN, τ=0.56 MPa, s=2.4 μm, w=14.2 mm


#7: P=91.6 kN, τ=0.48 MPa, s=1.7 μm, w=13.3 mm


#8: P=99.0 kN, τ=0.52 MPa, s=1.8 μm, w=13.0 mm

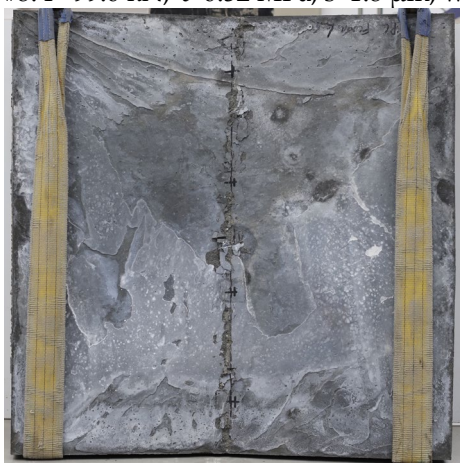


#9: P=100.0 kN, τ=0.53 MPa, s=2.9 μm, w=15.7 mm


#10: P=90.1 kN, τ=0.48 MPa, s=1.2 μm, w=12.8 mm

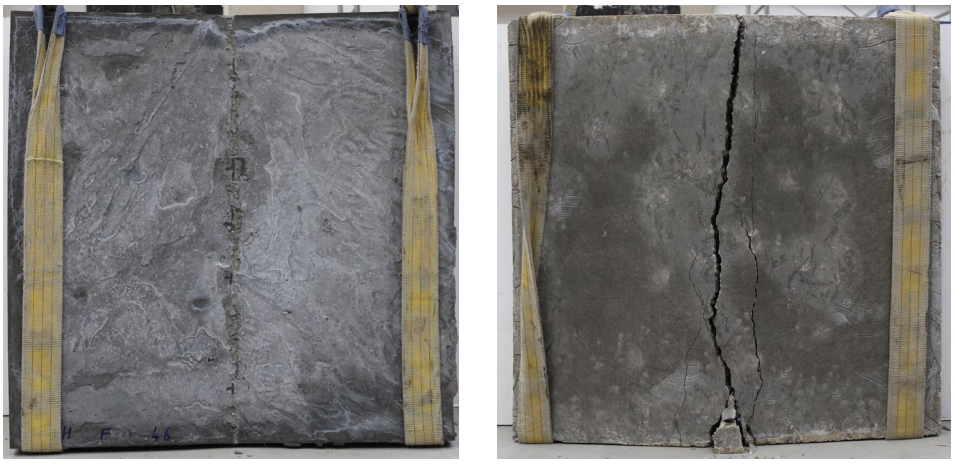

#11: P=105.8 kN, τ=0.56 MPa, s=1.5 μm, w=12.7 mm

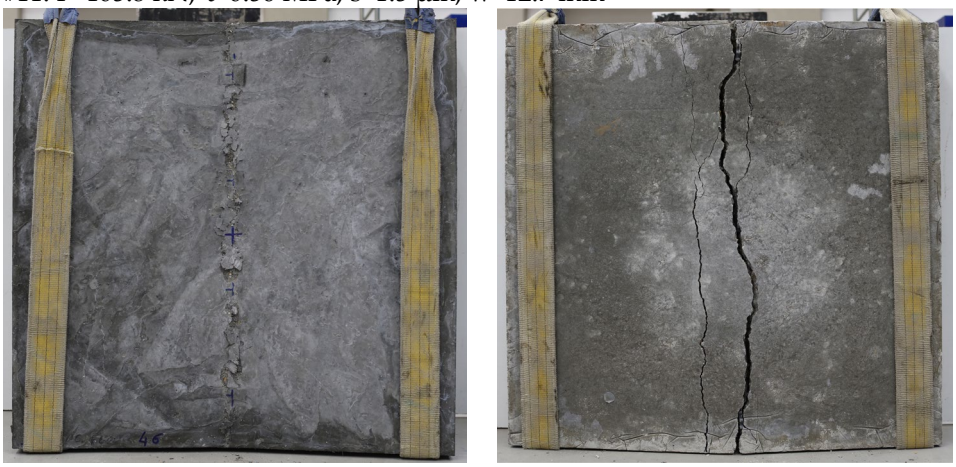

#12: P=106.2 kN, τ=0.56 MPa, s=1.5 μm, w=14.2 mm

APPENDIX D: NUMERICAL ANALYSES OF RC BEAMS: PARAMETRIC STUDY

The numerical research program discussed in Section 6.3 is presented in detail in the following. Each analysis responses are illustrated for:

- three size of beams: small (S), medium (M), and large (L);
- three concrete cylinder compressive strength (f_c): 25, 50, and 70 MPa;
- five shear span-to-effective depth ratio (a/d): 2.5, 3.0, 3.5, 4.0, and 4.5;
- four different longitudinal reinforcement ratio (ρ): 0.9%, 1.6%, 2.1%, and 2.4%;
- three typologies of retrofit, having different thickness of UHPFRC jacketing (s_j): 30, 40, and 50 mm.

Additionally, the peak load, P_{max}, the shear capacity, V_{FEA}, the maximum moment, M_{max}, the ratio between the maximum moment and the flexural moment, M_{max}/M_{fl}, and the ultimate vertical displacement at the mid-span, δ_u, are reported.

D.1. Size S

a/d=2.5
f_c= 25 MPa
ρ= 0.9%, 1.6%, 2.1%, 2.4%
s_f=30 mm

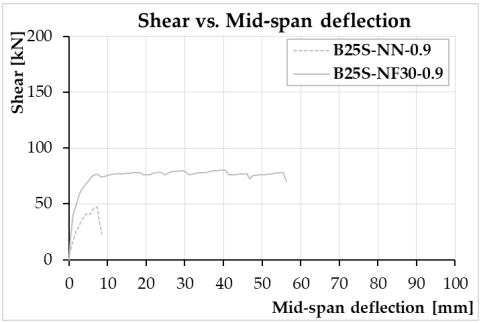

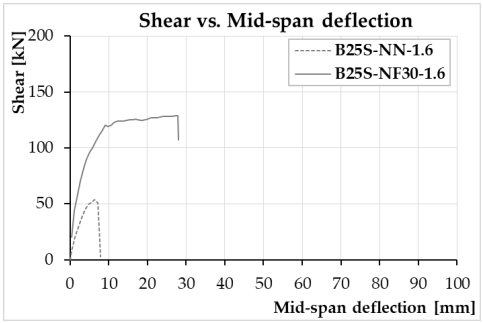

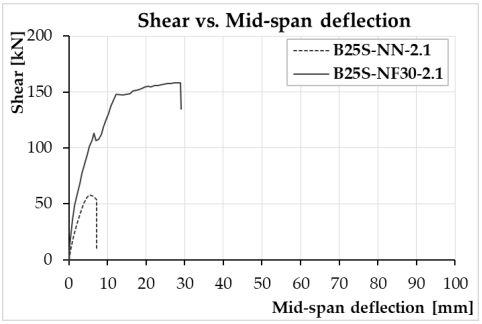

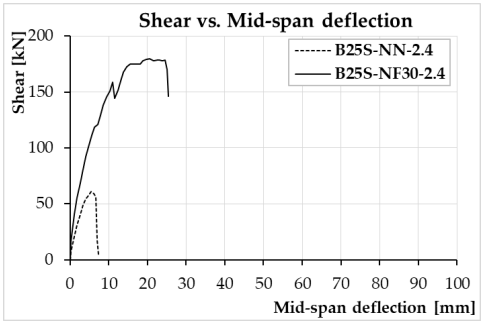

	P_{max} [kN]	V_{FEA} [kN]	M_{max} [kNm]	M_{max}/M_{fl} [-]	δ_u [mm]
B25S-NN-0.9	98.0	49.0	31.4	0.77	8.5
B25S-NF30-0.9	161.4	80.7	51.7	1.00	56.9
B25S-NN-1.6	109.7	54.9	35.1	0.52	7.9
B25S-NF30-1.6	258.2	129.1	82.6	1.00	28.7
B25S-NN-2.1	120.1	60.0	38.8	0.46	7.2
B25S-NF30-2.1	317.6	158.8	101.6	1.00	31.5
B25S-NN-2.4	123.3	61.7	39.5	0.42	7.4
B25S-NF30-2.4	359.9	179.9	115.2	1.00	25.5

a/d=2.5
f_c= 50 MPa
ρ= 0.9%, 1.6%, 2.1%, 2.4%
s_f=30 mm

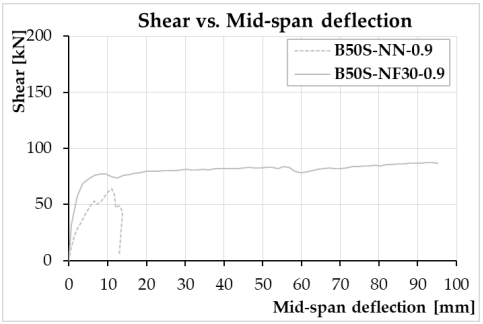

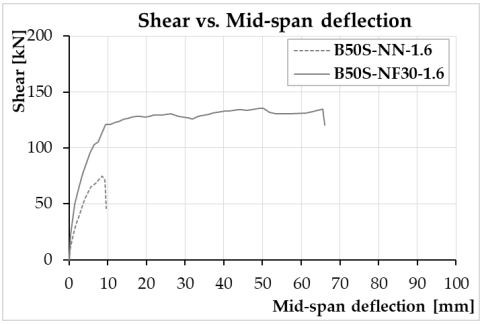

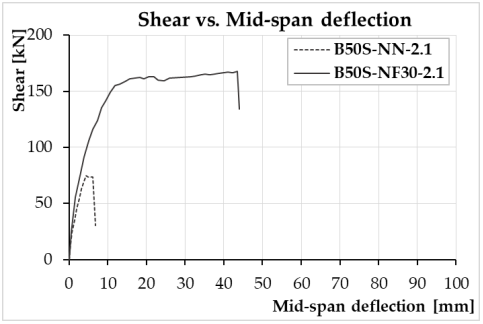

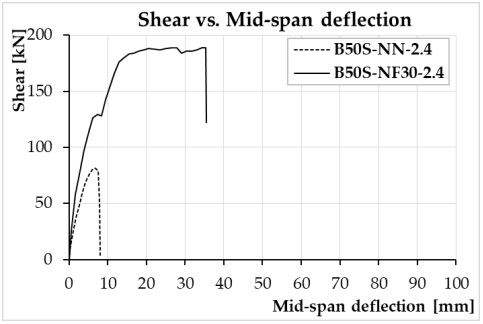

	P_{max} [kN]	V_{FEA} [kN]	M_{max} [kNm]	M_{max}/M_{fl} [-]	δ_u [mm]
B50S-NN-0.9	131.1	65.6	42.0	0.98	13.0
B50S-NF30-0.9	175.2	87.6	56.1	1.00	95.2
B50S-NN-1.6	151.0	75.5	48.3	0.66	9.5
B50S-NF30-1.6	271.3	135.6	51.5	1.00	67.9
B50S-NN-2.1	152.9	76.4	48.9	0.51	6.8
B50S-NF30-2.1	336.1	168.0	107.5	1.00	44.0
B50S-NN-2.4	164.9	82.5	52.8	0.48	8.1
B50S-NF30-2.4	380.4	190.2	121.7	1.00	34.6

a/d=2.5
f_c= 70 MPa
ρ= 0.9%, 1.6%, 2.1%, 2.4%
s_f=30 mm

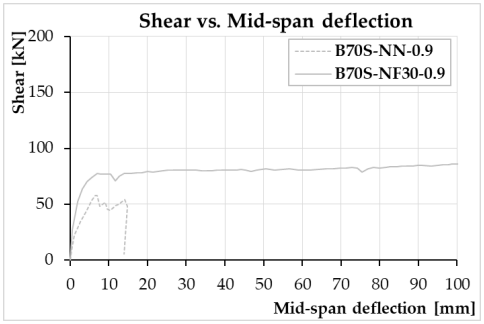

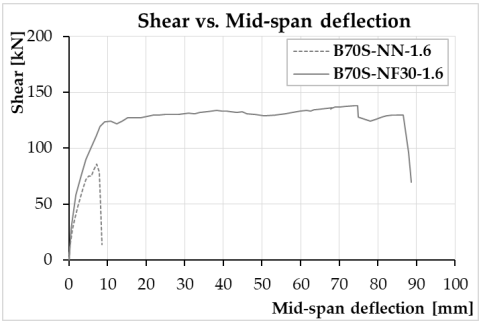

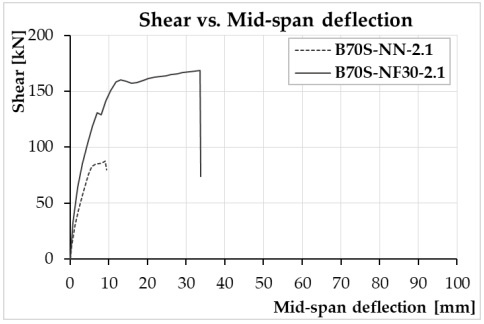

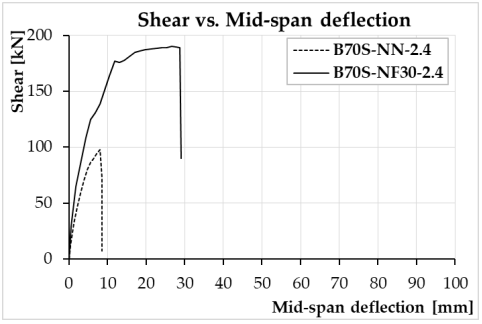

	P_{max} [kN]	V_{FEA} [kN]	M_{max} [kNm]	M_{max}/M_{fl} [-]	δ_u [mm]
B70S-NN-0.9	118.0	59.0	37.8	1.00	13.9
B70S-NF30-0.9	173.6	86.8	55.5	1.00	131.5
B70S-NN-1.6	173.9	86.9	55.6	0.74	8.6
B70S-NF30-1.6	276.4	138.2	88.5	1.00	88.6
B70S-NN-2.1	177.8	88.9	56.8	0.58	9.5
B70S-NF30-2.1	337.6	168.8	108.0	1.00	33.6
B70S-NN-2.4	199.8	99.9	63.9	0.56	8.6
B70S-NF30-2.4	381.3	190.6	122.0	1.00	28.8

a/d=3
f_c= 25 MPa
ρ= 0.9%, 1.6%, 2.1%, 2.4%
s_f=30, 40 mm

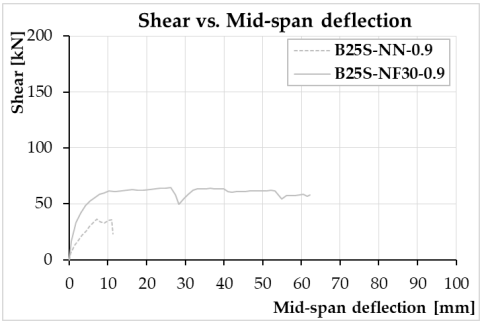

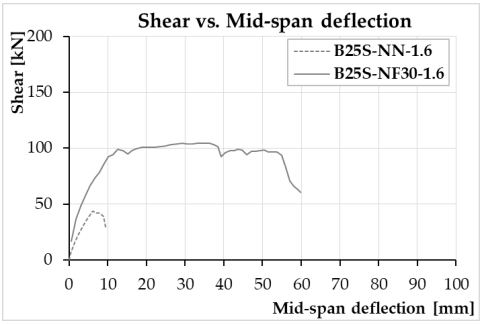

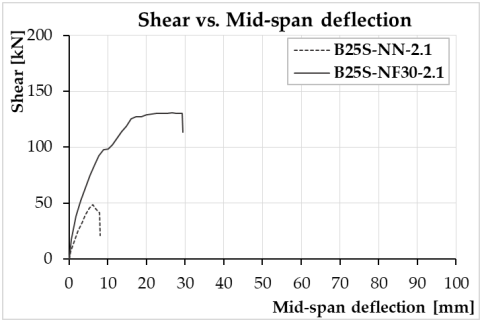

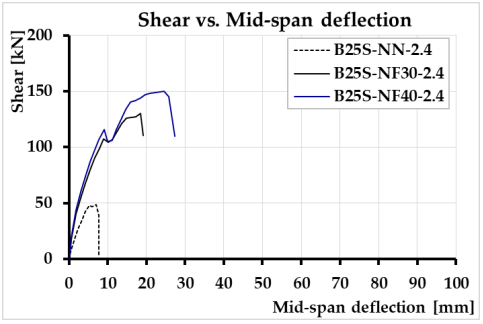

	P_{max} [kN]	V_{FEA} [kN]	M_{max} [kNm]	M_{max}/M_{fl} [-]	δ_u [mm]
B25S-NN-0.9	74.8	37.4	29.2	0.71	11.3
B25S-NF30-0.9	129.3	64.3	50.4	1.00	62.3
B25S-NN-1.6	90.6	45.3	35.4	0.52	9.4
B25S-NF30-1.6	209.8	104.9	81.8	1.00	59.8
B25S-NN-2.1	100.3	50.1	39.1	0.46	8.1
B25S-NF30-2.1	262.3	131.2	102.3	1.00	31.0
B25S-NN-2.4	99.4	49.7	38.8	0.41	7.7
B25S-NF30-2.4	262.5	131.2	102.4	0.82	19.2
B25S-NF40-2.4	300.9	150.5	117.4	1.00	27.3

a/d=3
f_c= 50 MPa
ρ= 0.9%, 1.6%, 2.1%, 2.4%
s_l=30 mm

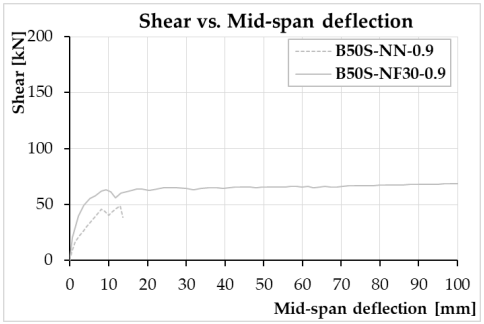

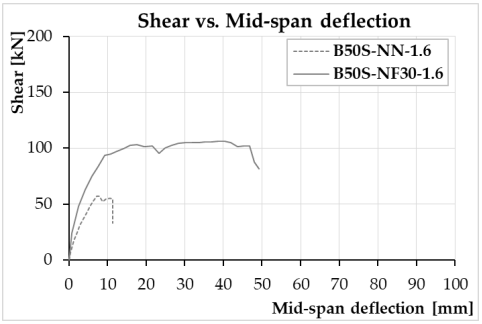

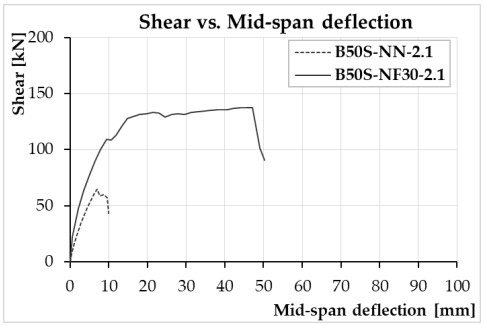

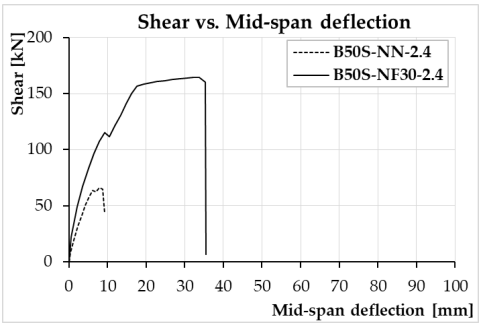

	P_{max} [kN]	V_{FEA} [kN]	M_{max} [kNm]	M_{max}/M_{fl} [-]	δ_u [mm]
B50S-NN-0.9	99.5	49.8	38.8	0.90	13.6
B50S-NF30-0.9	140.9	70.4	54.9	1.00	134.9
B50S-NN-1.6	118.5	59.3	46.2	0.63	11.4
B50S-NF30-1.6	213.9	107.0	83.4	1.00	49.2
B50S-NN-2.1	131.7	65.9	51.4	0.54	10.0
B50S-NF30-2.1	275.7	137.8	107.5	1.00	50.3
B50S-NN-2.4	134.5	67.3	52.5	0.48	9.2
B50S-NF30-2.4	330.3	165.1	128.8	1.00	33.5

a/d=3
f_c= 70 MPa
ρ= 0.9%, 1.6%, 2.1%, 2.4%
s_f=30 mm

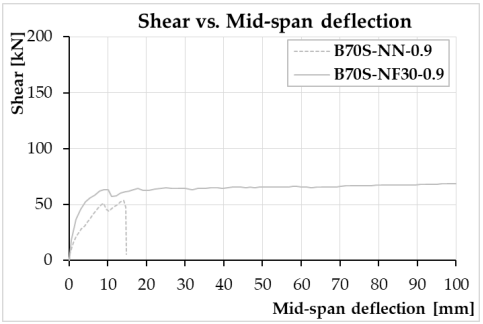

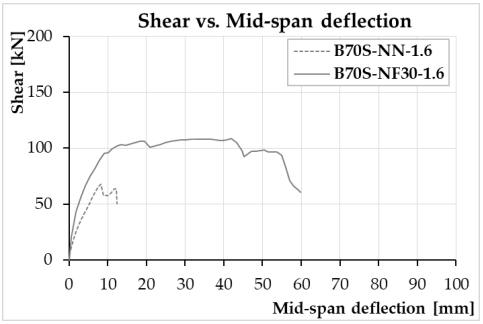

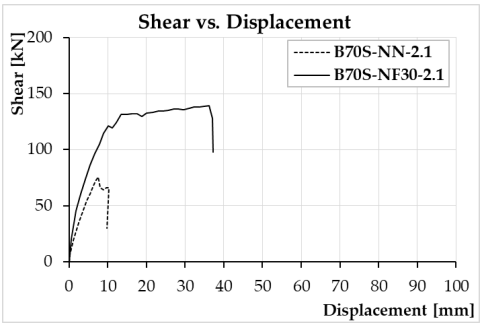

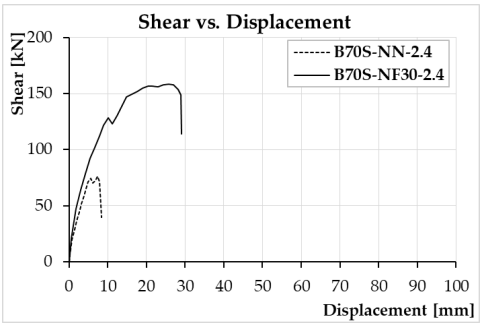

	P_{max} [kN]	V_{FEA} [kN]	M_{max} [kNm]	M_{max}/M_{fl} [-]	δ_u [mm]
B70S-NN-0.9	108.6	54.3	42.4	1.00	14.7
B70S-NF30-0.9	140.9	70.4	54.9	1.00	135.3
B70S-NN-1.6	137.4	68.7	53.6	0.71	12.5
B70S-NF30-1.6	217.8	108.9	84.9	1.00	59.8
B70S-NN-2.1	152.8	76.4	59.6	0.60	10.2
B70S-NF30-2.1	278.9	139.4	108.8	1.00	37.0
B70S-NN-2.4	154.3	77.2	60.2	0.53	8.5
B70S-NF30-2.4	318.1	159.0	124.0	1.00	28.8

a/d=3.5
f_c= 25 MPa
ρ= 0.9%, 1.6%, 2.1%, 2.4%
s_f=30, 40, 50 mm

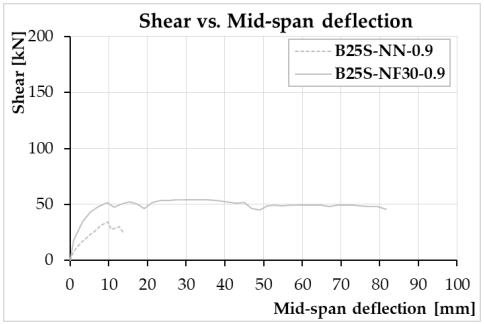

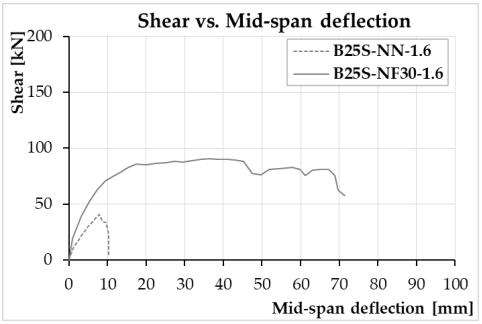

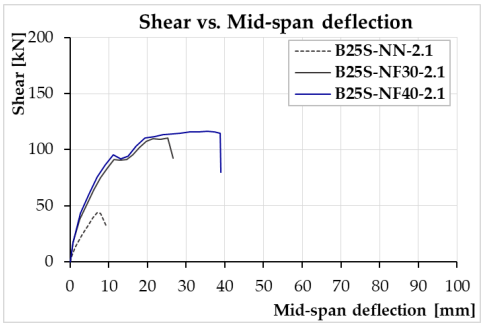

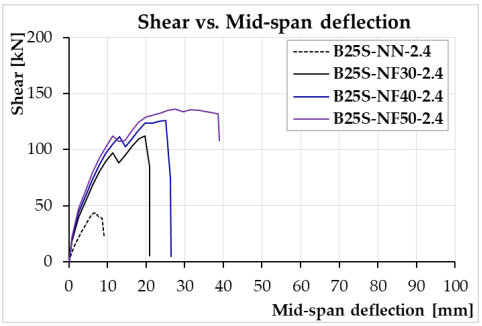

	P_{max} [kN]	V_{FEA} [kN]	M_{max} [kNm]	M_{max}/M_{fl} [-]	δ_u [mm]
B25S-NN-0.9	70.4	35.2	31.7	0.77	13.9
B25S-NF30-0.9	118.0	59.0	53.1	1.00	81.6
B25S-NN-1.6	82.9	41.4	37.3	0.55	10.4
B25S-NF30-1.6	195.7	97.9	88.1	1.00	71.5
B25S-NN-2.1	93.4	46.7	42.0	0.50	9.5
B25S-NF30-2.1	221.2	110.6	99.5	1.00	26.6
B25S-NF40-2.1	234.4	117.2	105.5	1.00	38.7
B25S-NN-2.4	91.7	45.9	41.3	0.44	9.0
B25S-NF30-2.4	226.5	113.2	101.9	0.81	20.8
B25S-NF40-2.4	253.7	126.8	114.2	1.00	26.4
B25S-NF50-2.4	273.8	136.9	123.2	1.00	38.7

a/d=3.5
f_c= 50 MPa
ρ= 0.9%, 1.6%, 2.1%, 2.4%
s_l=30, 40 mm

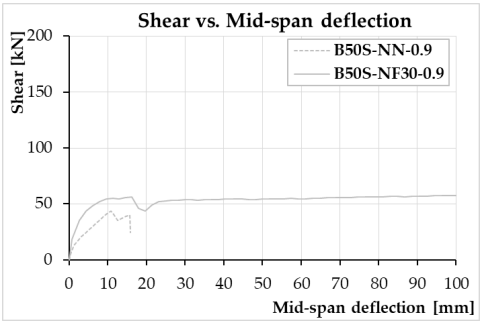

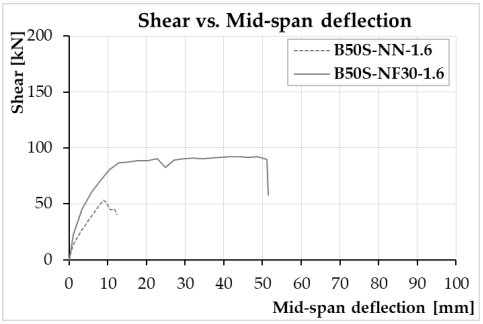

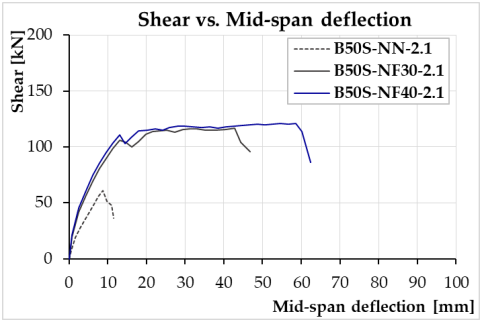

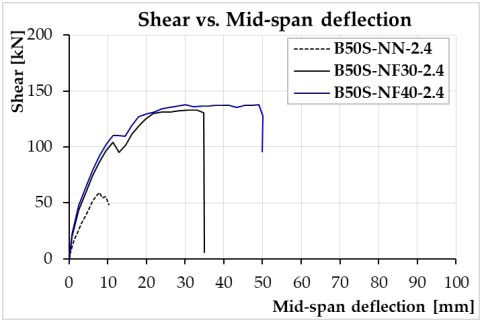

	P_{max} [kN]	V_{FEA} [kN]	M_{max} [kNm]	M_{max}/M_{fl} [-]	δ_u [mm]
B50S-NN-0.9	89.8	44.9	40.4	0.94	15.9
B50S-NF30-0.9	120.2	60.1	54.1	1.00	162.9
B50S-NN-1.6	109.9	55.0	49.5	0.67	12.5
B50S-NF30-1.6	185.1	92.6	83.6	1.00	51.1
B50S-NN-2.1	124.1	62.0	55.8	0.59	11.6
B50S-NF30-2.1	233.4	116.7	105.0	1.00	46.9
B50S-NF40-2.1	242.9	121.5	109.3	1.00	62.5
B50S-NN-2.4	120.4	60.2	54.2	1.00	10.4
B50S-NF30-2.4	267.8	133.9	120.5	0.49	33.0
B50S-NF40-2.4	276.4	138.2	124.4	1.00	50.0

a/d=3.5
f_c= 70 MPa
ρ= 0.9%, 1.6%, 2.1%, 2.4%
s_f=30 mm

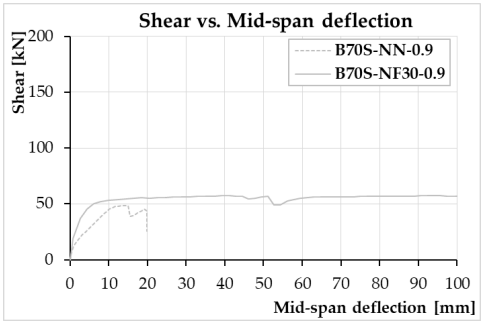

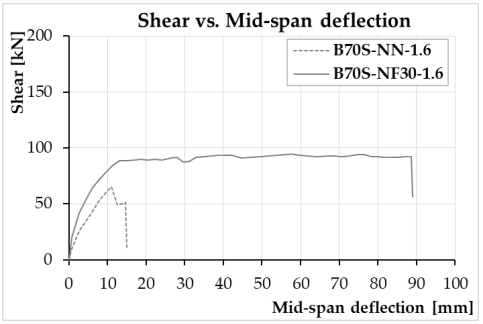

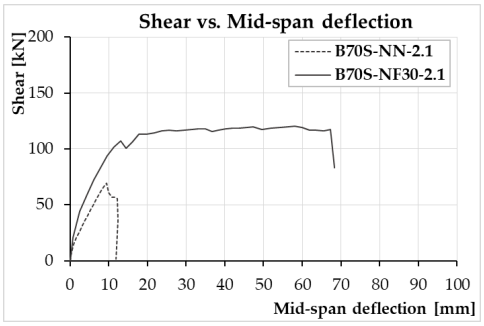

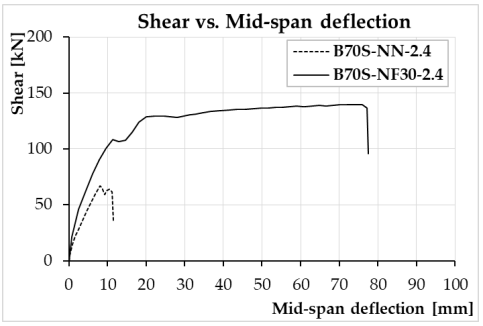

	P_{max} [kN]	V_{FEA} [kN]	M_{max} [kNm]	M_{max}/M_{fl} [-]	δ_u [mm]
B70S-NN-0.9	97.4	48.7	43.8	1.00	19.8
B70S-NF30-0.9	119.6	59.8	53.8	1.00	139.8
B70S-NN-1.6	132.5	66.3	59.6	0.79	14.0
B70S-NF30-1.6	189.5	94.8	85.3	1.00	88.6
B70S-NN-2.1	140.4	70.2	63.2	0.64	12.4
B70S-NF30-2.1	241.7	120.9	108.8	1.00	72.8
B70S-NN-2.4	136.8	68.4	43.8	0.54	11.6
B70S-NF30-2.4	280.3	140.2	126.2	1.00	77.2

a/d=4
f_c= 25 MPa
ρ= 0.9%, 1.6%, 2.1%, 2.4%
s_f=30, 40, 50 mm

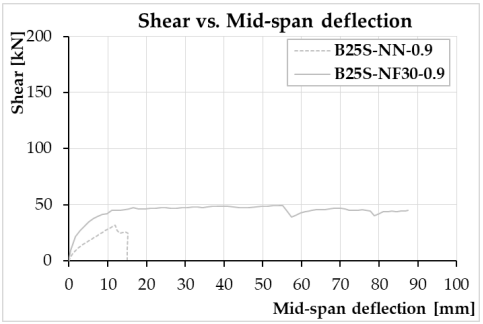

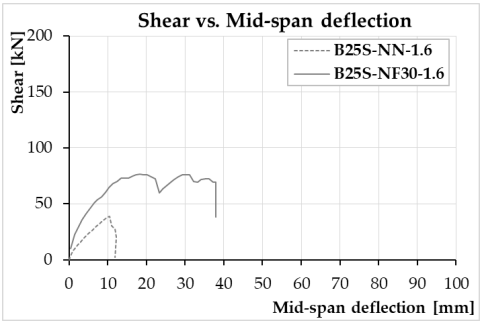

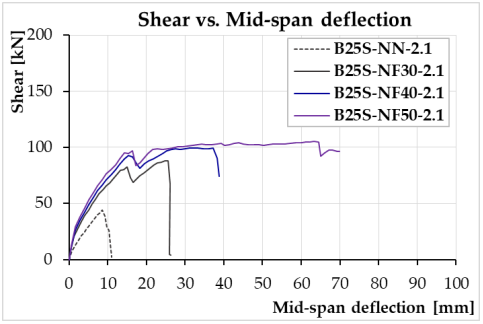

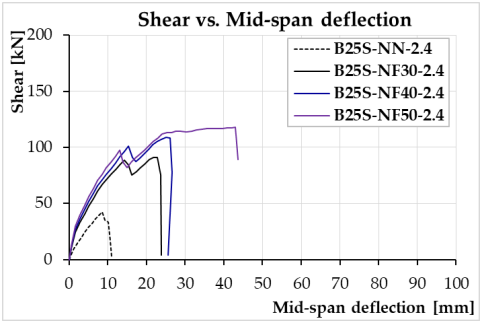

	P_{max} [kN]	V_{FEA} [kN]	M_{max} [kNm]	M_{max}/M_{fl} [-]	δ_u [mm]
B25S-NN-0.9	64.2	32.1	33.4	0.81	14.9
B25S-NF30-0.9	98.4	49.2	51.2	1.00	87.5
B25S-NN-1.6	79.0	39.5	41.1	0.61	11.9
B25S-NF30-1.6	153.3	76.7	79.7	1.00	37.9
B25S-NN-2.1	89.4	44.7	46.5	0.55	11.0
B25S-NF30-2.1	176.6	88.3	91.8	0.83	26.2
B25S-NF40-2.1	199.4	99.7	103.7	1.00	38.8
B25S-NF50-2.1	211.3	105.6	109.9	1.00	69.9
B25S-NN-2.4	86.1	43.0	44.8	0.48	10.9
B25S-NF30-2.4	182.9	91.5	95.1	0.76	23.9
B25S-NF40-2.4	218.6	109.3	113.6	0.87	25.6
B25S-NF50-2.4	236.1	118.0	122.8	1.00	43.6

a/d=4
f_c= 50 MPa
ρ= 0.9%, 1.6%, 2.1%, 2.4%
s_f=30, 40, 50 mm

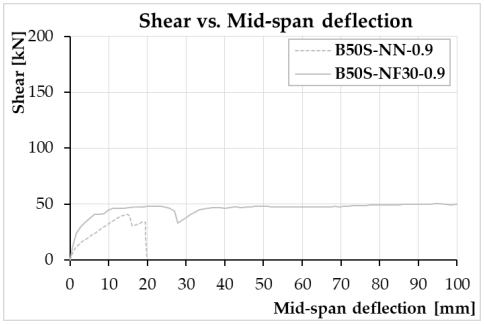

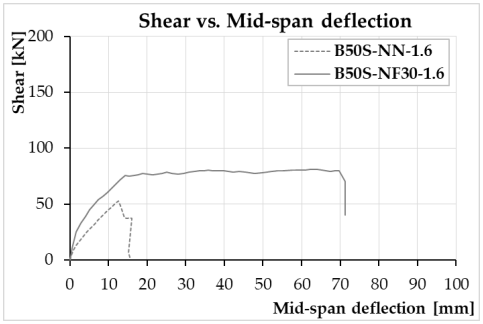

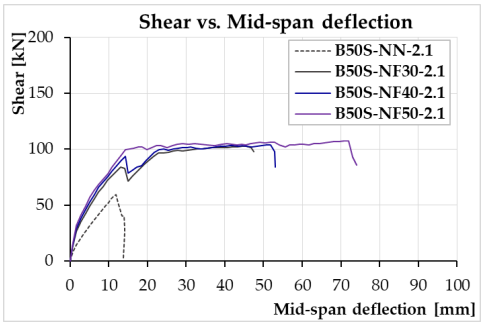

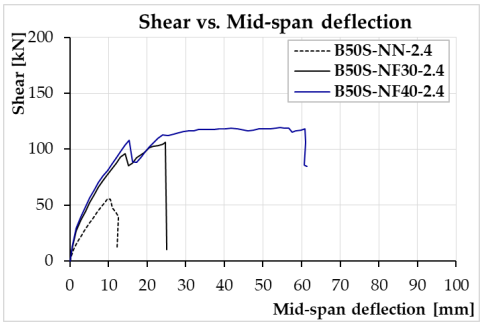

	P_{max} [kN]	V_{FEA} [kN]	M_{max} [kNm]	M_{max}/M_{fl} [-]	δ_u [mm]
B50S-NN-0.9	81.5	40.7	42.4	0.99	19.9
B50S-NF30-0.9	106.0	53.0	55.1	1.00	180.8
B50S-NN-1.6	107.6	53.8	56.0	0.76	15.5
B50S-NF30-1.6	162.5	81.3	84.5	1.00	71.2
B50S-NN-2.1	120.3	60.2	62.6	0.66	13.7
B50S-NF30-2.1	206.0	103.0	107.1	1.00	47.4
B50S-NN-2.4	114.9	57.5	59.8	0.55	12.2
B50S-NF30-2.4	212.4	106.2	110.5	0.85	25.0
B50S-NF40-2.4	239.0	119.5	124.3	1.00	61.3

a/d=4
f_c= 70 MPa
ρ= 0.9%, 1.6%, 2.1%, 2.4%
s_l=30, 40 mm

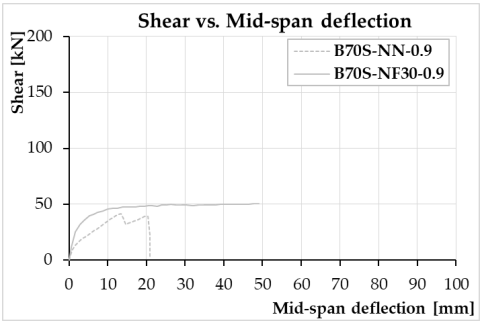

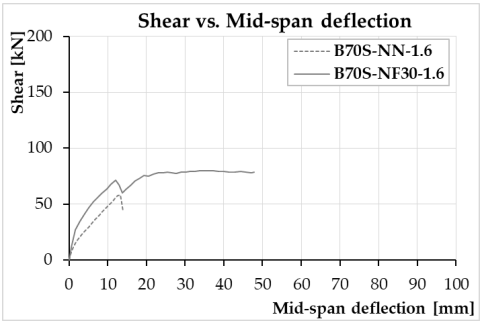

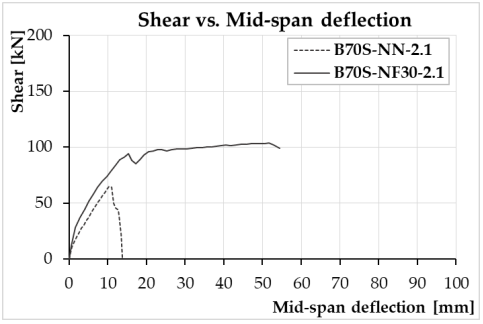

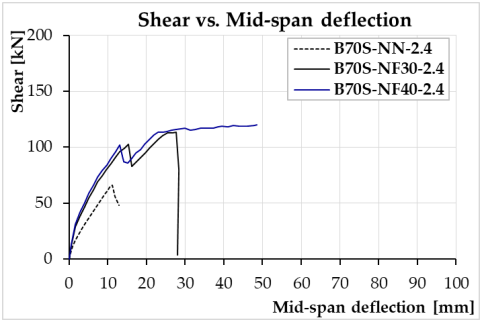

	P_{max} [kN]	V_{FEA} [kN]	M_{max} [kNm]	M_{max}/M_{fl} [-]	δ_u [mm]
B70S-NN-0.9	84.1	42.1	43.7	1.00	20.9
B70S-NF30-0.9	101.0	50.5	52.5	1.00	49.1
B70S-NN-1.6	118.3	59.2	61.5	0.81	13.9
B70S-NF30-1.6	160.1	62.4	83.3	1.00	47.9
B70S-NN-2.1	132.8	66.4	69.1	0.70	13.8
B70S-NF30-2.1	207.7	103.8	108.0	1.00	54.4
B70S-NN-2.4	132.8	66.4	69.1	0.61	12.9
B70S-NF30-2.4	228.3	114.2	118.7	1.00	28.1
B70S-NF40-2.4	239.7	119.9	124.7	1.00	48.5

a/d=4.5
f_c= 25 MPa
ρ= 0.9%, 1.6%, 2.1%, 2.4%
s_f=30, 40, 50 mm

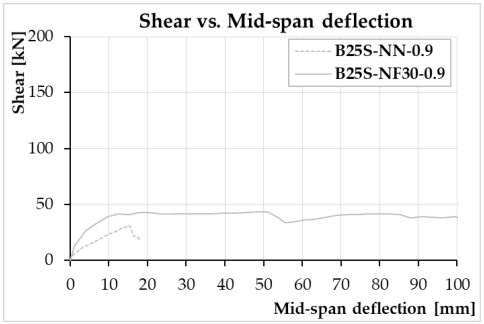

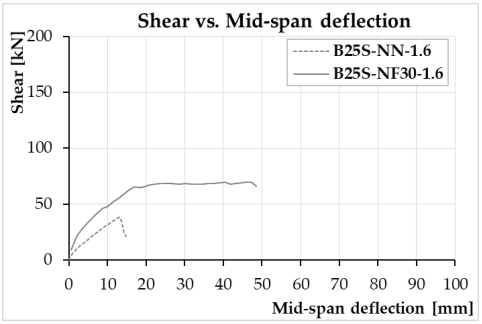

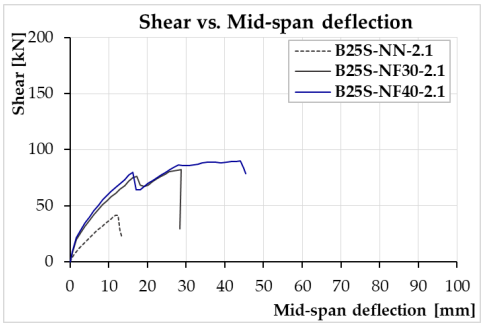

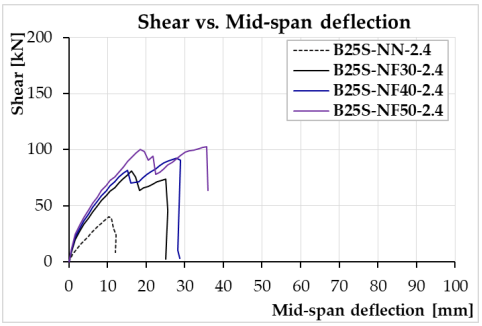

	P_{max} [kN]	V_{FEA} [kN]	M_{max} [kNm]	M_{max}/M_{fl} [-]	δ_u [mm]
B25S-NN-0.9	63.2	31.6	36.7	0.89	18.0
B25S-NF30-0.9	87.3	43.6	50.6	1.00	101.1
B25S-NN-1.6	77.8	38.9	45.1	0.67	14.9
B25S-NF30-1.6	140.0	70.0	81.2	1.00	48.5
B25S-NN-2.1	85.0	42.5	49.3	0.59	13.5
B25S-NF30-2.1	164.7	82.3	95.5	0.86	28.4
B25S-NF40-2.1	180.7	90.3	104.8	1.00	45.4
B25S-NN-2.4	82.9	41.5	48.1	0.51	12.1
B25S-NF30-2.4	165.1	82.5	95.7	0.77	25.1
B25S-NF40-2.4	185.8	92.8	107	0.83	28.7
B25S-NF50-2.4	205.5	102.7	119.2	1.00	36.1

a/d=4.5
f_c= 50 MPa
ρ= 0.9%, 1.6%, 2.1%, 2.4%
s_f=30, 40, 50 mm

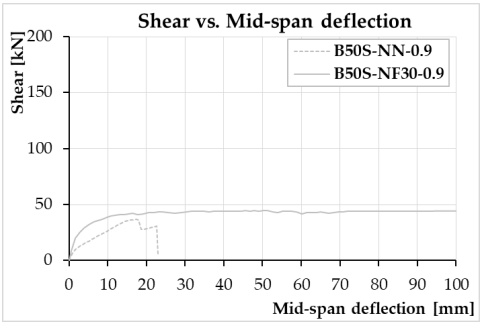

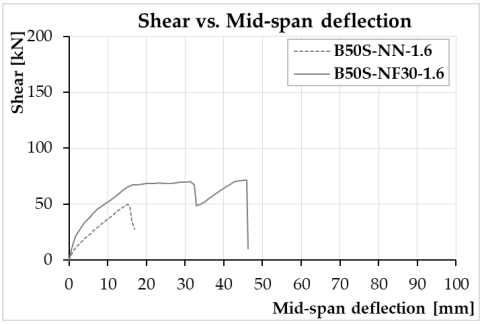

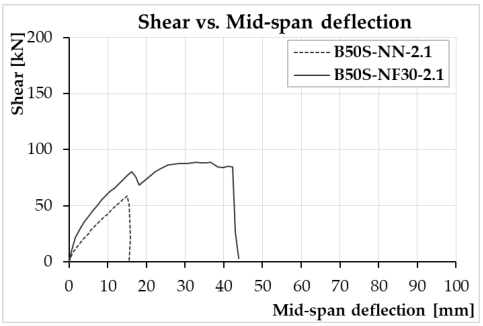

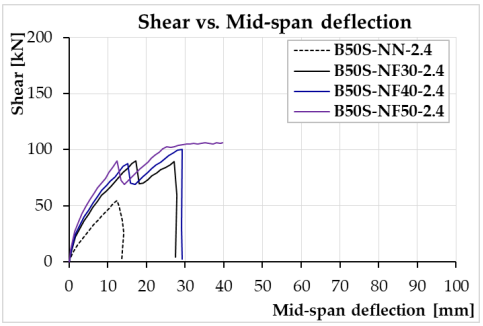

	P_{max} [kN]	V_{FEA} [kN]	M_{max} [kNm]	M_{max}/M_{fl} [-]	δ_u [mm]
B50S-NN-0.9	74.3	37.2	43.1	1.00	23.0
B50S-NF30-0.9	90.5	45.3	52.5	1.00	187.6
B50S-NN-1.6	102.1	51.1	59.2	0.80	17.0
B50S-NF30-1.6	143.8	71.9	83.4	1.00	46.3
B50S-NN-2.1	119.0	59.5	69.0	0.72	15.5
B50S-NF30-2.1	178.4	89.2	103.5	1.00	43.9
B50S-NF40-2.1	110.4	55.2	64.0	0.58	13.7
B50S-NN-2.4	184.9	92.5	107.2	0.83	27.2
B50S-NF30-2.4	202.0	101.0	117.1	0.78	29.3
B50S-NF40-2.4	213.0	106.5	123.5	1.00	39.7

a/d=4.5
f_c= 70 MPa
ρ= 0.9%, 1.6%, 2.1%, 2.4%
s_f=30, 40 mm

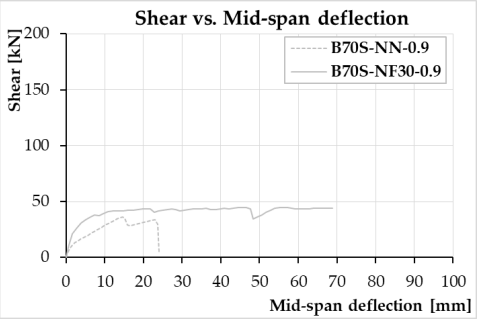

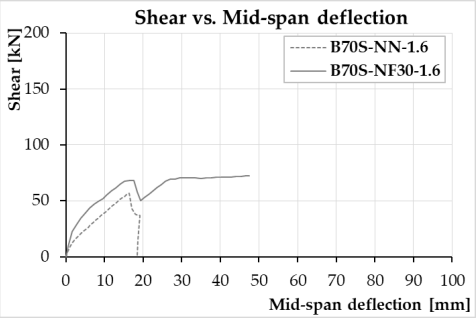

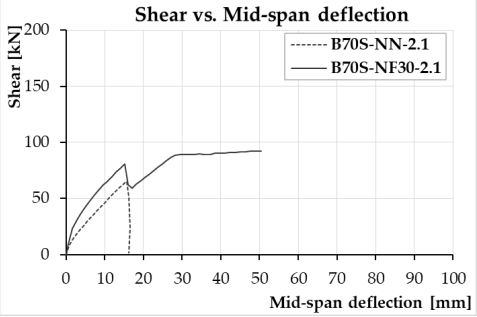

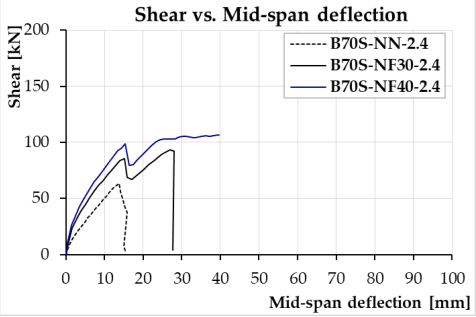

	P_{max} [kN]	V_{FEA} [kN]	M_{max} [kNm]	M_{max}/M_{fl} [-]	δ_u [mm]
B70S-NN-0.9	74.0	37.0	42.9	0.98	24.0
B70S-NF30-0.9	89.6	44.8	52.0	1.00	68.9
B70S-NN-1.6	113.9	57.0	51.3	0.88	18.5
B70S-NF30-1.6	144.5	72.2	83.8	1.00	47.4
B70S-NN-2.1	131.6	65.8	76.3	0.77	16.1
B70S-NF30-2.1	185.0	92.5	107.3	1.00	50.4
B70S-NN-2.4	128.0	64.0	74.2	0.65	15.5
B70S-NF30-2.4	187.4	93.7	108.7	0.82	27.6
B70S-NF40-2.4	213.1	106.6	123.6	1.0	39.7

D.2. Size M

a/d=2.5
f_c= 25 MPa
ρ= 0.9%, 1.6%, 2.1%, 2.4%
s_f=30, 40, 50 mm

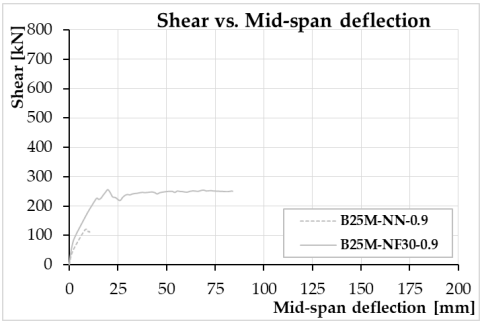

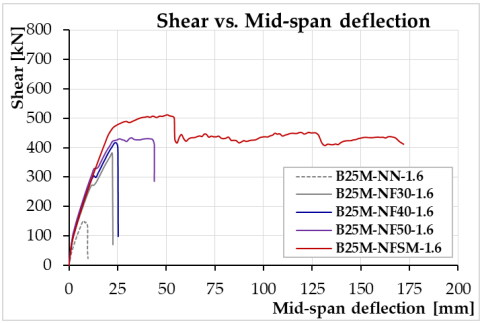

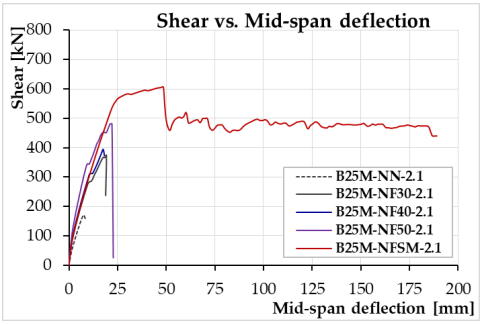

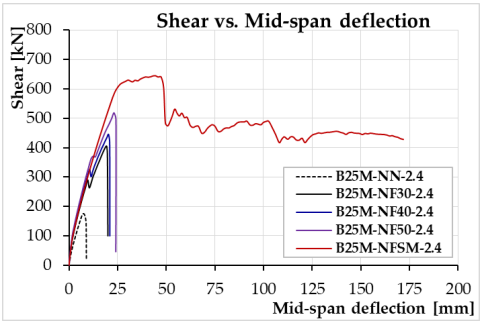

	P_{max} [kN]	V_{FEA} [kN]	M_{max} [kNm]	M_{max}/M_{fl} [-]	δ_u [mm]
B25M-NN-0.9	243.5	121.7	160.7	0.53	10.9
B25M-NF30-0.9	518.5	259.2	342.2	1.00	84.0
B25M-NN-1.6	309.3	154.7	204.1	0.40	9.8
B25M-NF30-1.6	771.8	385.9	509.4	0.85	22.4
B25M-NF40-1.6	839.1	419.6	553.8	1.00	25.1
B25M-NF50-1.6	870.2	435.1	547.3	1.00	42.6
B25M-NN-2.1	348.5	174.3	230.0	0.38	8.8
B25M-NF30-2.1	755.3	377.6	498.5	0.68	18.8
B25M-NF40-2.1	812.9	406.4	536.5	0.71	18.2
B25M-NF50-2.1	993.9	497.0	656.0	0.85	22.7
B25M-NN-2.4	360.3	180.2	237.8	0.36	8.9
B25M-NF30-2.4	818.6	409.3	540.3	0.68	20.0
B25M-NF40-2.4	915.9	458.0	604.5	0.74	21.0
B25M-NF50-2.4	1045.0	522.5	689.7	0.82	22.1

a/d=2.5
f_c= 50 MPa
ρ= 0.9%, 1.6%, 2.1%, 2.4%
s_l=30, 40, 50 mm

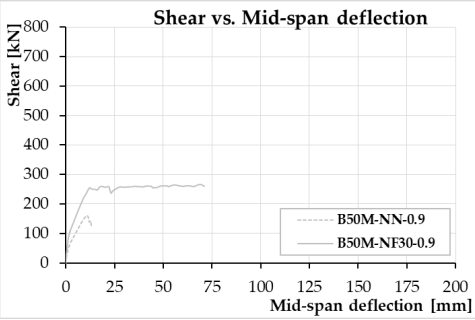

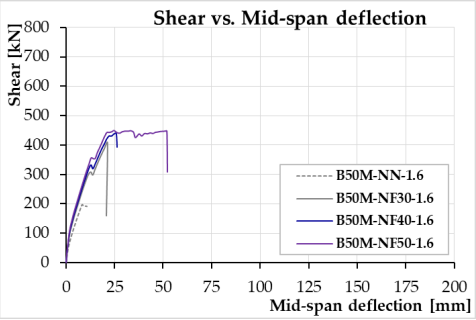

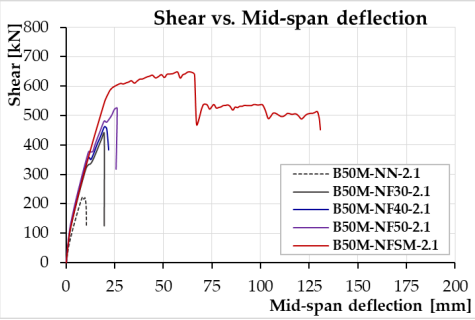

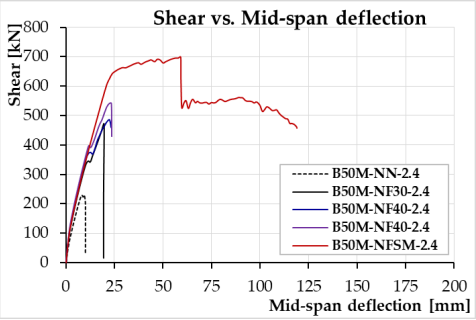

	P_{max} [kN]	V_{FEA} [kN]	M_{max} [kNm]	M_{max}/M_{fl} [-]	δ_u [mm]
B50M-NN-0.9	322.5	161.2	212.8	0.67	13.0
B50M-NF30-0.9	532.1	266.1	351.2	1.00	71.0
B50M-NN-1.6	400.6	200.3	264.4	0.47	11.0
B50M-NF30-1.6	833.4	416.7	550.0	1.00	20.8
B50M-NF40-1.6	887.2	443.6	585.6	1.00	26.3
B50M-NF50-1.6	902.1	451.1	595.4	1.00	52.0
B50M-NN-2.1	449.5	224.8	296.7	0.43	10.4
B50M-NF30-2.1	890.0	445.0	587.4	0.77	19.8
B50M-NF40-2.1	947.5	473.7	625.3	1.00	21.8
B50M-NF50-2.1	1058.2	529.1	698.4	1.00	25.8
B50M-NN-2.4	466.5	233.2	307.9	0.40	10.2
B50M-NF30-2.4	966.2	483.1	637.7	0.76	19.5
B50M-NF40-2.4	978.4	489.2	645.7	0.76	23.2
B50M-NF50-2.4	1101.1	550.5	726.7	0.83	23.5

a/d=2.5
f_c= 70 MPa
ρ= 0.9%, 1.6%, 2.1%, 2.4%
s_l=30, 40, 50 mm

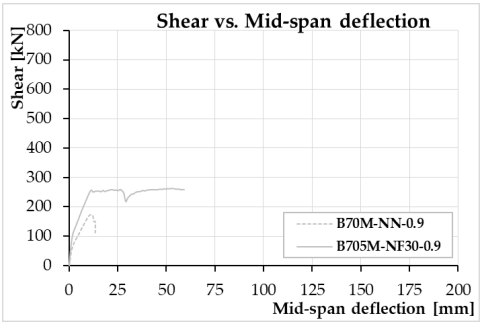

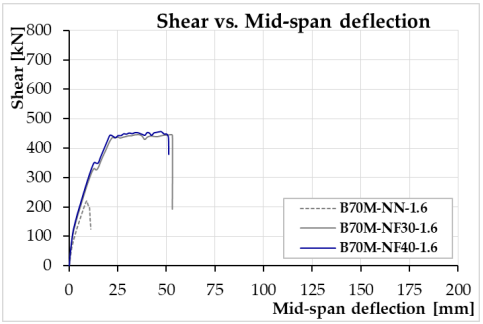

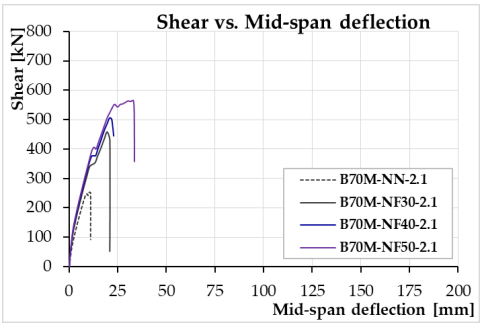

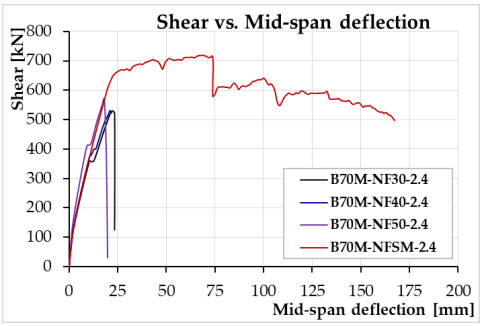

	P_{max} [kN]	V_{FEA} [kN]	M_{max} [kNm]	M_{max}/M_{fl} [-]	δ_u [mm]
B70M-NN-0.9	346.5	173.2	228.7	0.66	13.3
B70M-NF30-0.9	526.6	263.3	347.5	1.00	59.1
B70M-NN-1.6	448.4	224.2	295.9	0.46	11.1
B70M-NF30-1.6	892.5	446.2	589.0	1.00	53.2
B70M-NN-2.1	516.9	258.5	341.2		11.1
B70M-NF30-2.1	952.8	476.4	628.8	0.41	20.8
B70M-NF40-2.1	1044.3	522.1	689.2	0.75	23.1
B70M-NF50-2.1	1135.1	567.6	749.2	0.87	33.4
B70M-NN-2.4	524.7	262.4	346.3	1.00	10.8
B70M-NF30-2.4	1063.4	531.7	701.8	0.39	23.3
B70M-NF40-2.4	1074.2	537.1	709.0	0.74	21.9
B70M-NF50-2.4	1160.9	580.4	766.2	0.81	19.9

a/d=3
f_c= 25 MPa
ρ= 0.9%, 1.6%, 2.1%, 2.4%
s_l=30, 40, 50 mm

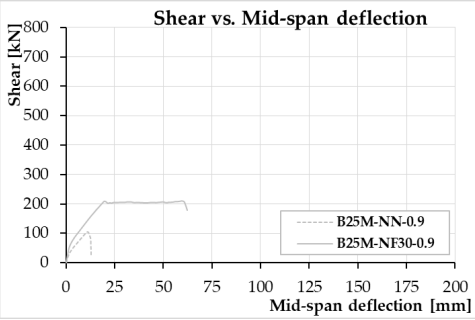

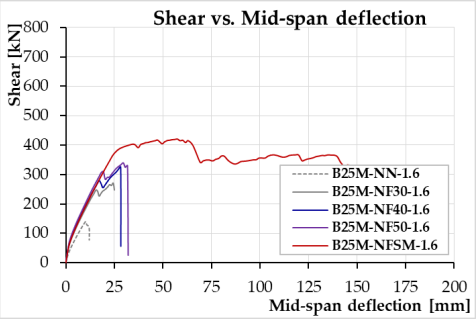

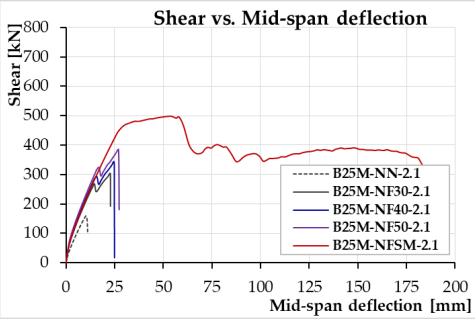

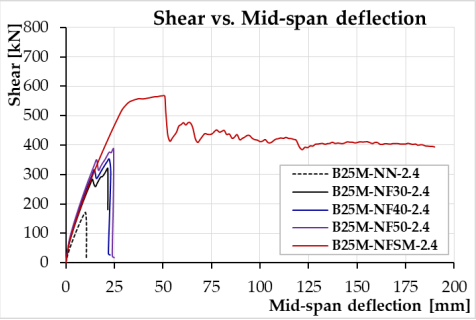

	P_{max} [kN]	V_{FEA} [kN]	M_{max} [kNm]	M_{max}/M_{fl} [-]	δ_u [mm]
B25M-NN-0.9	213.3	106.6	170.6	0.57	13.0
B25M-NF30-0.9	424.3	212.1	339.4	1.00	62.2
B25M-NN-1.6	282.4	141.2	225.9	0.45	12.0
B25M-NF30-1.6	553.7	276.8	442.9	0.74	25.0
B25M-NF40-1.6	655.6	327.8	524.5	0.85	28.3
B25M-NF50-1.6	682.9	341.5	546.3	1.00	32.1
B25M-NN-2.1	323.2	161.6	258.6	0.42	11.1
B25M-NF30-2.1	611.0	305.5	488.8	0.67	22.8
B25M-NF40-2.1	697.7	348.9	558.2	0.74	24.9
B25M-NF50-2.1	777.6	388.8	622.1	0.81	27.3
B25M-NN-2.4	347.2	173.6	277.8	0.42	10.6
B25M-NF30-2.4	646.7	323.4	517.4	0.65	21.6
B25M-NF40-2.4	724.8	362.4	579.9	0.71	22.8
B25M-NF50-2.4	782.1	391.0	625.7	0.75	24.9

a/d=3
f_c= 50 MPa
ρ= 0.9%, 1.6%, 2.1%, 2.4%
s_l=30, 40, 50 mm

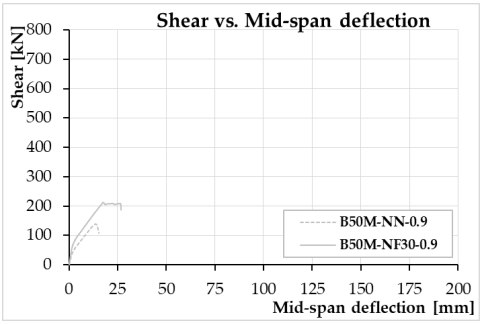

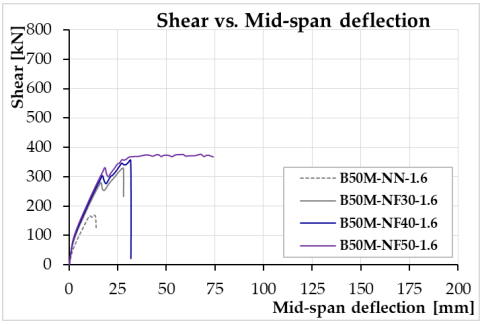

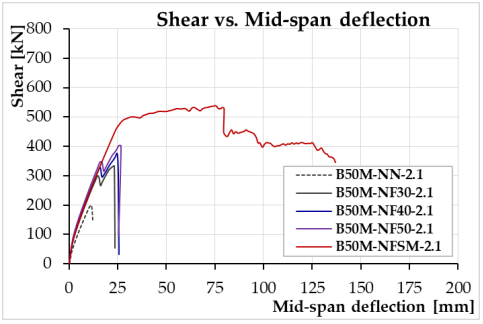

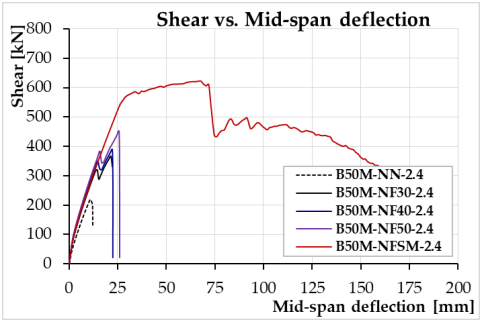

	P_{max} [kN]	V_{FEA} [kN]	M_{max} [kNm]	M_{max}/M_{fl} [-]	δ_u [mm]
B50M-NN-0.9	281.6	140.8	225.3	0.71	15.3
B50M-NF30-0.9	426.7	213.4	341.4	1.00	32.2
B50M-NN-1.6	343.1	171.6	274.5	0.49	13.9
B50M-NF30-1.6	665.3	332.7	532.3	0.86	28.1
B50M-NF40-1.6	717.5	358.8	574.0	0.90	31.8
B50M-NF50-1.6	757.4	378.7	605.9	1.00	73.9
B50M-NN-2.1	405.8	202.9	324.6	0.47	12.3
B50M-NF30-2.1	673.2	336.6	538.6	0.70	23.7
B50M-NF40-2.1	766.9	383.4	613.5	0.78	25.5
B50M-NF50-2.1	820.4	410.2	656.3	0.81	25.6
B50M-NN-2.4	447.6	223.8	358.1	0.47	12.3
B50M-NF30-2.4	747.2	373.6	597.7	0.71	22.3
B50M-NF40-2.4	785.6	392.8	628.5	0.73	22.6
B50M-NF50-2.4	921.2	460.6	736.9	0.84	26.2

a/d=3
f_c= 70 MPa
ρ= 0.9%, 1.6%, 2.1%, 2.4%
s_f=30, 40, 50 mm

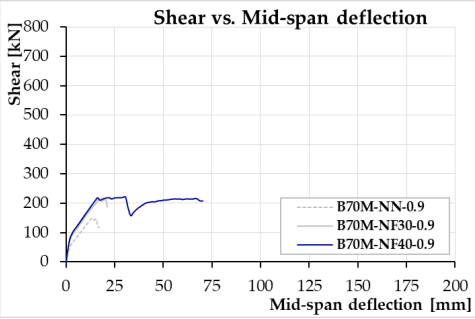

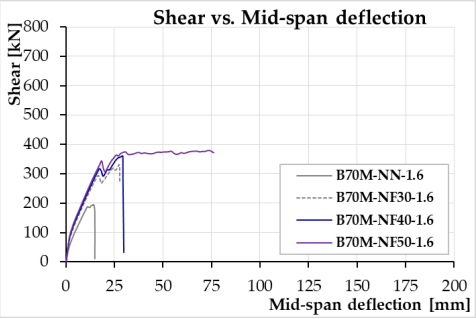

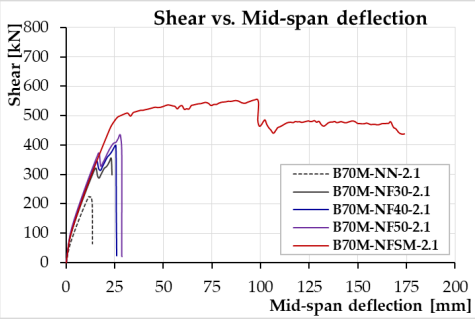

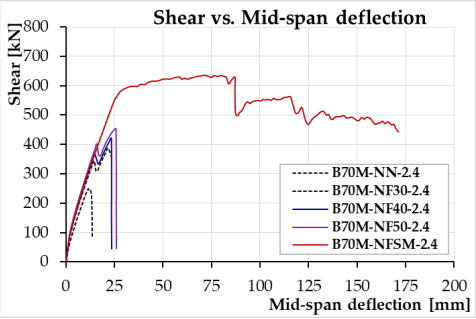

	P_{max} [kN]	V_{FEA} [kN]	M_{max} [kNm]	M_{max}/M_{fl} [-]	δ_u [mm]
B70M-NN-0.9	301.1	150.5	240.9	0.70	17.0
B70M-NF30-0.9	432.6	216.3	346.1	1.00	21.1
B70M-NF40-0.9	442.4	221.2	353.9	1.00	70.5
B70M-NN-1.6	392.9	196.4	314.3	0.48	14.9
B70M-NF30-1.6	672.8	336.4	538.2	0.84	27.6
B70M-NF40-1.6	729.9	364.9	583.9	0.91	29.8
B70M-NF50-1.6	760.5	380.2	608.4	1.00	76.2
B70M-NN-2.1	454.2	227.1	363.4	0.45	13.6
B70M-NF30-2.1	720.5	360.3	576.4	0.69	23.8
B70M-NF40-2.1	806.9	403.5	646.6	0.81	26.2
B70M-NF50-2.1	885.4	442.7	708.3	0.84	29.0
B70M-NN-2.4	500.3	250.1	400.2	0.45	13.8
B70M-NF30-2.4	803.6	401.8	642.8	0.70	23.9
B70M-NF40-2.4	845.6	422.8	676.5	0.78	23.7
B70M-NF50-2.4	918.4	459.2	734.7	0.80	26.0

a/d=3.5
f_c= 25 MPa
ρ= 0.9%, 1.6%, 2.1%, 2.4%
s_l=30, 40, 50 mm

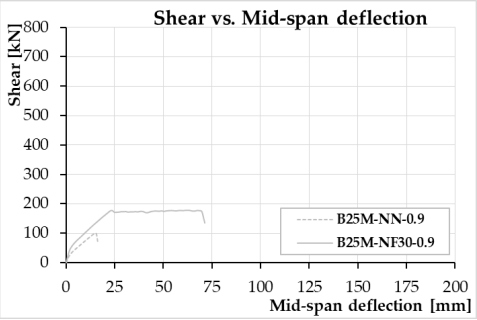

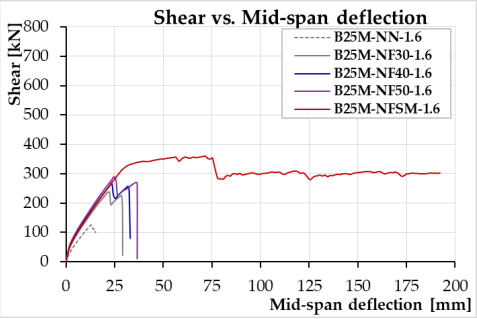

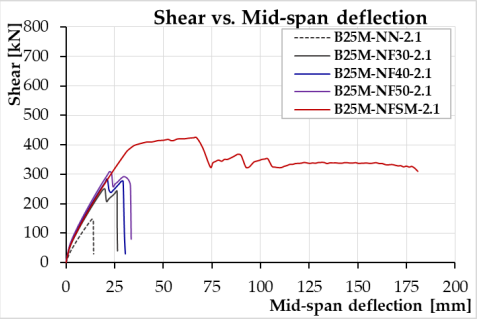

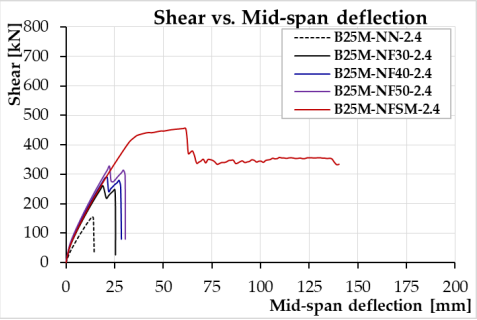

	P_{max} [kN]	V_{FEA} [kN]	M_{max} [kNm]	M_{max}/M_{fl} [-]	δ_u [mm]
B25M-NN-0.9	200.8	100.4	188.7	0.63	16.2
B25M-NF30-0.9	362.3	181.1	340.5	1.00	73.2
B25M-NN-1.6	256.7	128.3	241.3	0.48	15.2
B25M-NF30-1.6	488.9	244.4	459.5	0.77	29.1
B25M-NF40-1.6	540.3	270.2	507.9	0.82	33.0
B25M-NF50-1.6	595.5	297.8	559.8	1.00	36.6
B25M-NN-2.1	299.5	149.8	281.5	0.46	14.2
B25M-NF30-2.1	516.2	258.1	485.3	0.66	26.5
B25M-NF40-2.1	578.4	289.2	543.7	0.72	30.5
B25M-NF50-2.1	642.3	321.2	603.8	0.80	33.5
B25M-NN-2.4	317.3	158.6	298.2	0.45	14.5
B25M-NF30-2.4	536.8	268.4	504.6	0.64	25.5
B25M-NF40-2.4	600.6	300.3	564.5	0.69	28.5
B25M-NF50-2.4	663.8	331.9	624.0	0.75	30.5

a/d=3.5
f_c= 50 MPa
ρ= 0.9%, 1.6%, 2.1%, 2.4%
s_f=30, 40, 50 mm

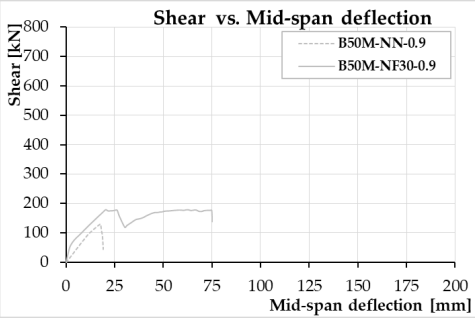

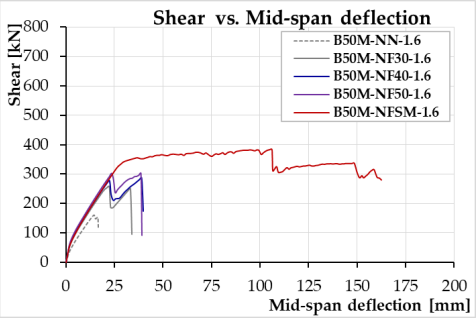

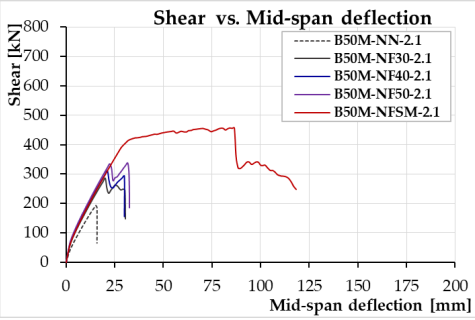

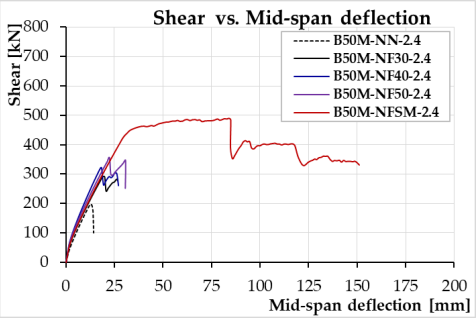

	P_{max} [kN]	V_{FEA} [kN]	M_{max} [kNm]	M_{max}/M_{fl} [-]	δ_u [mm]
B50M-NN-0.9	259.6	129.8	173.9	0.77	19.0
B50M-NF30-0.9	363.2	181.6	341.4	1.00	74.8
B50M-NN-1.6	323.3	161.6	303.9	0.54	16.9
B50M-NF30-1.6	525.9	263.0	494.4	0.77	34.0
B50M-NF40-1.6	580.1	290.0	545.2	1.00	39.8
B50M-NF50-1.6	613.1	306.5	576.3	1.00	39.2
B50M-NN-2.1	391.4	195.7	367.9	0.53	16.0
B50M-NF30-2.1	582.5	291.2	547.5	0.71	30.2
B50M-NF40-2.1	633.7	316.9	595.7	0.76	30.0
B50M-NF50-2.1	690.4	345.2	649.0	0.83	32.4
B50M-NN-2.4	396.7	198.3	372.9	0.49	14.3
B50M-NF30-2.4	603.4	301.7	567.2	0.68	26.8
B50M-NF40-2.4	660.6	330.3	621.0	0.73	27.1
B50M-NF50-2.4	718.9	359.4	675.7	0.77	30.5

a/d=3.5
f_c= 70 MPa
ρ= 0.9%, 1.6%, 2.1%, 2.4%
s_l=30, 40, 50 mm

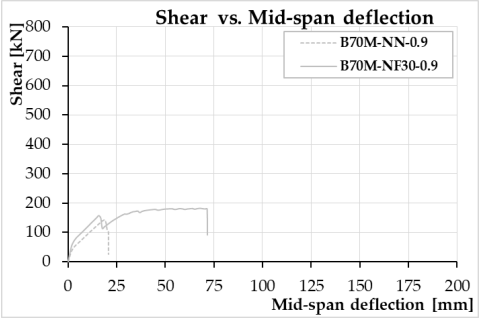

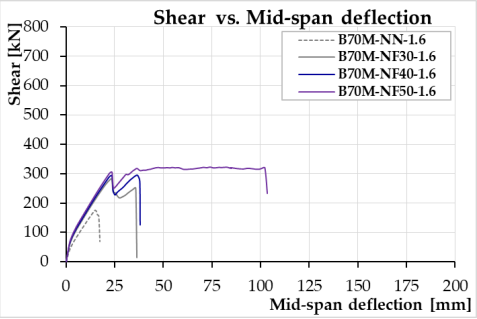

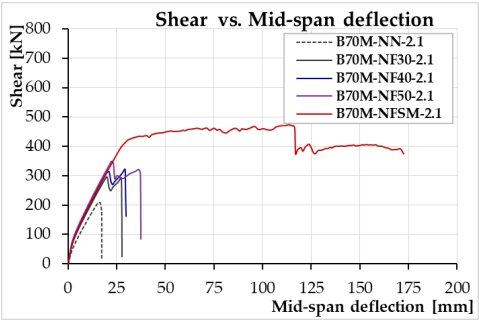

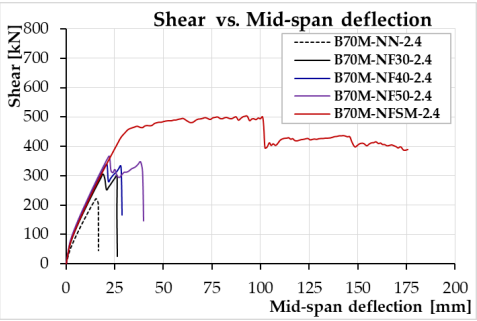

	P_{max} [kN]	V_{FEA} [kN]	M_{max} [kNm]	M_{max}/M_{fl} [-]	δ_u [mm]
B70M-NN-0.9	286.5	143.2	269.3	0.76	20.8
B70M-NF30-0.9	367.3	183.7	345.3	1.00	71.4
B70M-NN-1.6	357.1	178.6	335.7	0.53	17.3
B70M-NF30-1.6	566.4	283.2	532.4	0.78	36.4
B70M-NF40-1.6	593.1	296.5	557.5	1.00	37.8
B70M-NF50-1.6	646.8	323.4	608.0	1.00	103.3
B70M-NN-2.1	422.9	211.4	397.5	0.51	17.3
B70M-NF30-2.1	598.5	299.3	562.6	0.70	27.7
B70M-NF40-2.1	650.6	325.3	611.6	0.77	29.7
B70M-NF50-2.1	720.5	360.3	677.3	0.85	37.3
B70M-NN-2.4	447.2	223.6	420.3	0.47	16.8
B70M-NF30-2.4	620.4	310.2	583.2	0.66	26.4
B70M-NF40-2.4	691.3	345.6	649.8	0.75	28.7
B70M-NF50-2.4	742.0	371.0	697.5	0.76	39.5

a/d=4
f_c= 25 MPa
ρ= 0.9%, 1.6%, 2.1%, 2.4%
s_f=30, 40, 50 mm

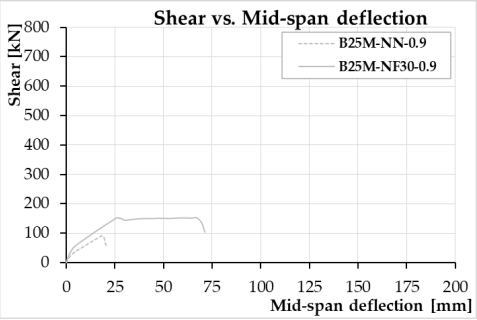

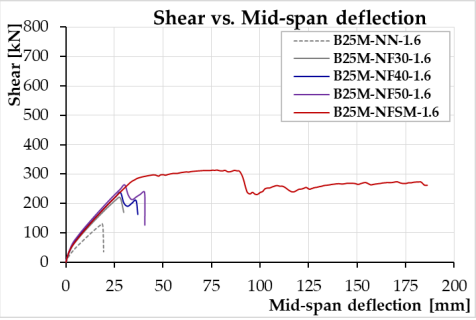

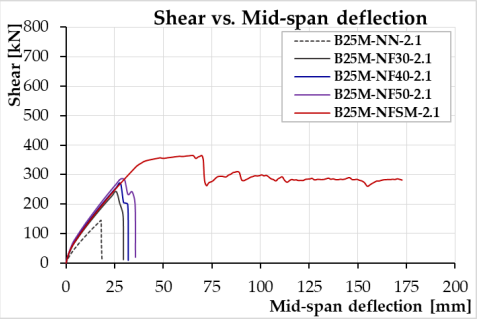

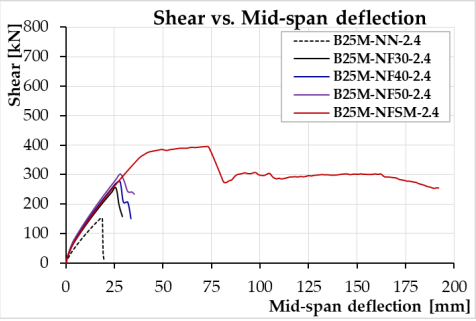

	P_{max} [kN]	V_{FEA} [kN]	M_{max} [kNm]	M_{max}/M_{fl} [-]	δ_u [mm]
B25M-NN-0.9	188.0	94.0	203.0	0.67	21.0
B25M-NF30-0.9	314.3	157.1	339.4	1.00	71.4
B25M-NN-1.6	263.8	131.9	284.9	0.56	18.4
B25M-NF30-1.6	449.9	225.0	485.9	0.81	29.8
B25M-NF40-1.6	485.9	242.9	524.8	0.85	37.0
B25M-NF50-1.6	540.2	270.1	583.4	1.00	40.4
B25M-NN-2.1	290.2	145.1	313.4	0.51	17.8
B25M-NF30-2.1	501.5	250.8	541.7	0.74	28.5
B25M-NF40-2.1	551.8	275.9	595.9	0.72	30.7
B25M-NF50-2.1	604.7	302.4	653.1	0.77	34.5
B25M-NN-2.4	314.0	157.0	339.2	0.51	18.6
B25M-NF30-2.4	520.4	260.2	562.1	0.71	29.1
B25M-NF40-2.4	578.8	289.4	625.1	0.76	33.5
B25M-NF50-2.4	632.1	316.0	682.6	0.82	35.2

a/d=4
f_c= 50 MPa
ρ= 0.9%, 1.6%, 2.1%, 2.4%
s_l=30, 40, 50 mm

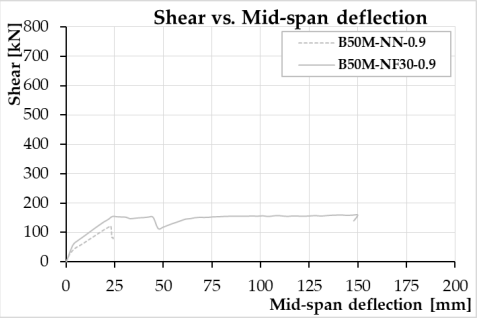

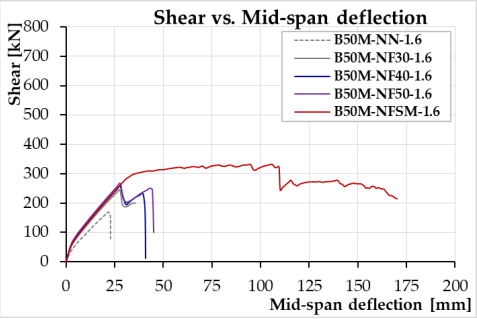

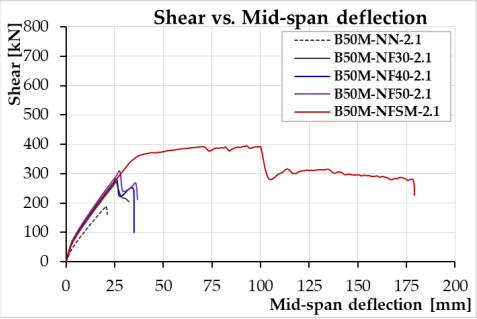

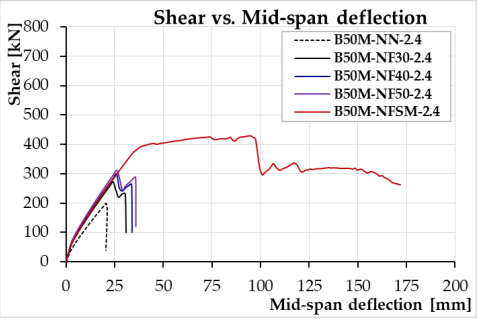

	P_{max} [kN]	V_{FEA} [kN]	M_{max} [kNm]	M_{max}/M_{fl} [-]	δ_u [mm]
B50M-NN-0.9	245.0	122.5	264.6	0.83	24.2
B50M-NF30-0.9	320.2	160.1	345.8	1.00	147.8
B50M-NN-1.6	345.8	172.9	373.4	0.67	22.8
B50M-NF30-1.6	488.3	244.2	527.4	1.00	35.8
B50M-NF40-1.6	519.8	259.9	561.4	1.00	41.0
B50M-NF50-1.6	534.4	267.2	577.1	1.00	45.0
B50M-NN-2.1	379.8	189.9	410.1	0.59	21.1
B50M-NF30-2.1	547.7	273.9	591.6	0.77	32.0
B50M-NF40-2.1	566.2	283.1	611.5	0.76	35.0
B50M-NF50-2.1	620.1	310.0	669.7	0.75	36.9
B50M-NN-2.4	403.5	201.8	435.8	0.57	20.4
B50M-NF30-2.4	558.5	279.3	603.2	0.72	31.0
B50M-NF40-2.4	608.5	304.3	657.2	0.77	34.0
B50M-NF50-2.4	640.2	320.1	691.5	0.79	36.0

a/d=4
f_c= 70 MPa
ρ= 0.9%, 1.6%, 2.1%, 2.4%
s_f=30, 40, 50 mm

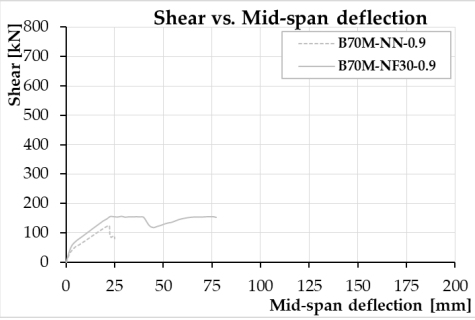

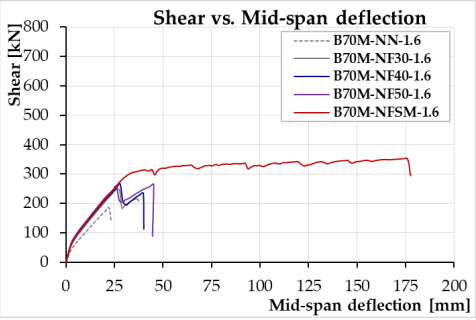

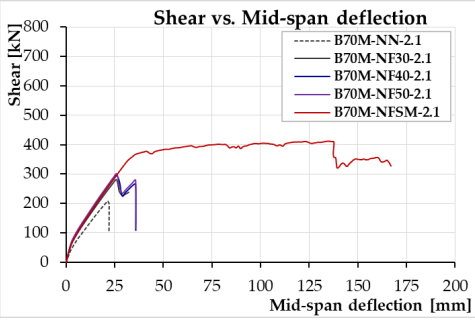

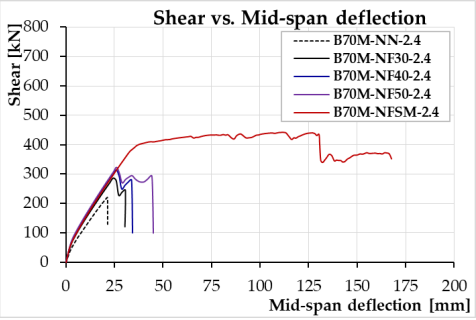

	P_{max} [kN]	V_{FEA} [kN]	M_{max} [kNm]	M_{max}/M_{fl} [-]	δ_u [mm]
B70M-NN-0.9	249.5	124.8	269.5	0.82	24.9
B70M-NF30-0.9	321.0	160.5	346.6	1.00	77.3
B70M-NN-1.6	376.6	188.2	406.6	0.65	23.5
B70M-NF30-1.6	504.3	252.1	544.6	0.84	37.6
B70M-NF40-1.6	538.3	269.2	581.4	1.00	40.1
B70M-NF50-1.6	532.6	266.3	575.2	1.00	44.7
B70M-NN-2.1	424.7	212.4	458.7	0.57	22.1
B70M-NF30-2.1	564.5	282.2	609.6	0.76	32.2
B70M-NF40-2.1	606.3	303.1	654.8	0.77	36.0
B70M-NF50-2.1	604.8	302.4	653.2	0.77	35.7
B70M-NN-2.4	440.9	220.5	476.2	0.55	21.5
B70M-NF30-2.4	592.5	296.2	639.9	0.70	30.3
B70M-NF40-2.4	646.7	323.3	698.4	0.80	34.5
B70M-NF50-2.4	664.4	332.2	717.5	0.79	45.0

a/d=4.5
f_c= 25 MPa
ρ= 0.9%, 1.6%, 2.1%, 2.4%
s_l=30, 40, 50 mm

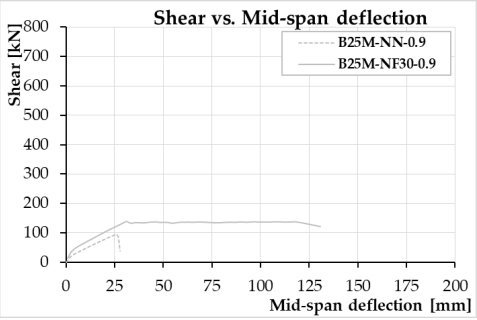

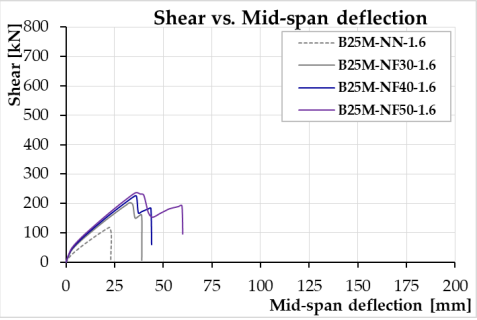

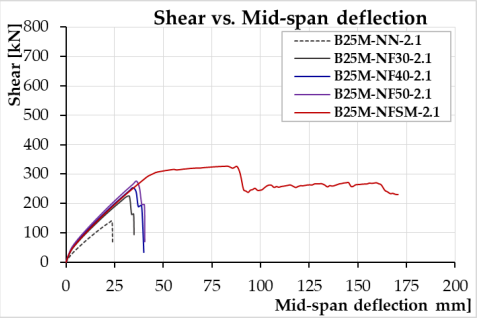

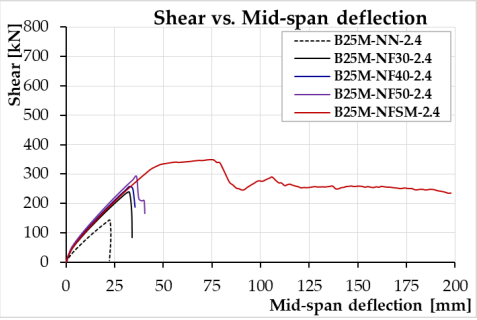

	P_{max} [kN]	V_{FEA} [kN]	M_{max} [kNm]	M_{max}/M_{fl} [-]	δ_u [mm]
B25M-NN-0.9	188.5	94.3	230.0	0.76	27.9
B25M-NF30-0.9	280.3	140.1	341.9	1.00	130.8
B25M-NN-1.6	239.0	119.5	291.6	0.57	23.4
B25M-NF30-1.6	415.8	207.9	507.3	0.85	39.0
B25M-NF40-1.6	458.3	229.2	559.1	0.91	43.6
B25M-NF50-1.6	479.7	239.9	585.2	1.00	59.6
B25M-NN-2.1	280.9	104.5	342.7	0.56	23.9
B25M-NF30-2.1	463.7	231.8	565.7	0.78	34.8
B25M-NF40-2.1	524.0	262.0	693.3	0.75	40.0
B25M-NF50-2.1	568.1	284.1	693.1	1.00	40.3
B25M-NN-2.4	288.0	144.0	351.4	0.53	22.3
B25M-NF30-2.4	490.3	245.2	598.2	0.75	33.8
B25M-NF40-2.4	535.2	267.6	653.0	0.80	35.5
B25M-NF50-2.4	590.0	295.5	720.9	0.86	40.1

a/d=4.5
f_c= 50 MPa
ρ= 0.9%, 1.6%, 2.1%, 2.4%
s_f=30, 40, 50 mm

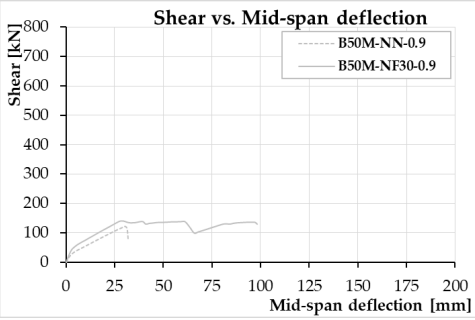

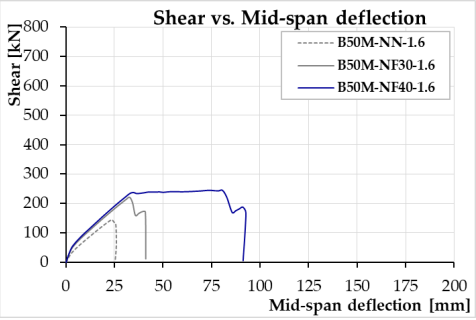

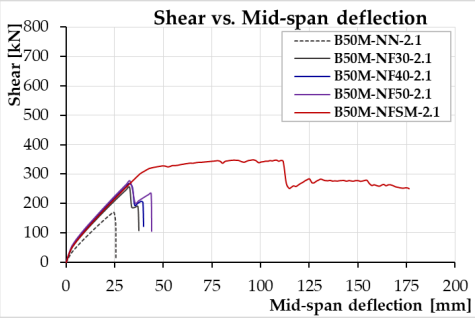

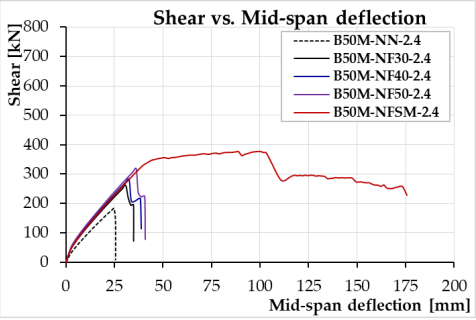

	P_{max} [kN]	V_{FEA} [kN]	M_{max} [kNm]	M_{max}/M_{fl} [-]	δ_u [mm]
B50M-NN-0.9	243.8	121.9	297.4	0.94	31.9
B50M-NF30-0.9	285.3	142.6	348.0	1.00	98.2
B50M-NN-1.6	289.6	144.8	353.3	0.63	25.5
B50M-NF30-1.6	447.4	223.7	545.8	0.88	41.0
B50M-NF40-1.6	489.1	244.5	596.7	1.00	91.5
B50M-NN-2.1	342.5	171.3	417.9	0.60	25.7
B50M-NF30-2.1	516.5	258.3	630.2	0.82	37.0
B50M-NF40-2.1	553.9	276.9	675.8	0.86	39.6
B50M-NF50-2.1	565.3	282.7	689.7	0.85	43.6
B50M-NN-2.4	366.0	183.0	446.5	0.59	25.6
B50M-NF30-2.4	529.7	264.8	646.2	0.77	34.9
B50M-NF40-2.4	569.4	284.7	694.7	0.81	38.5
B50M-NF50-2.4	644.6	322.3	786.4	0.89	40.6

a/d=4.5
f_c= 70 MPa
ρ= 0.9%, 1.6%, 2.1%, 2.4%
s_l=30, 40, 50 mm

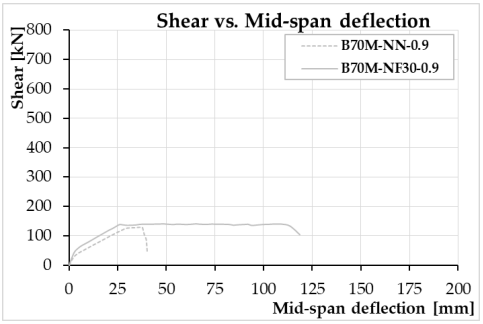

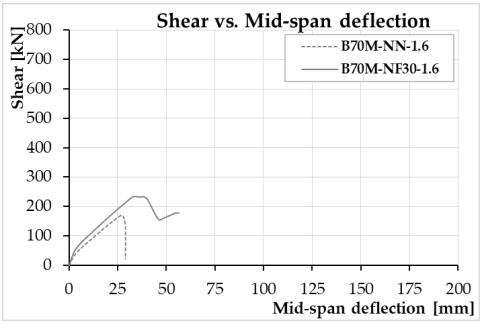

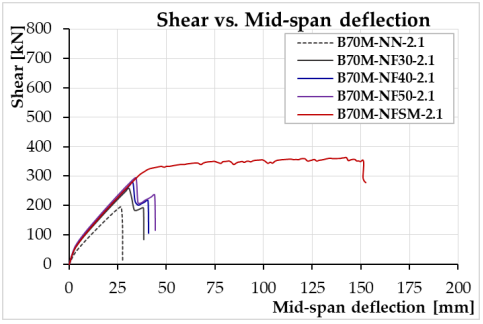

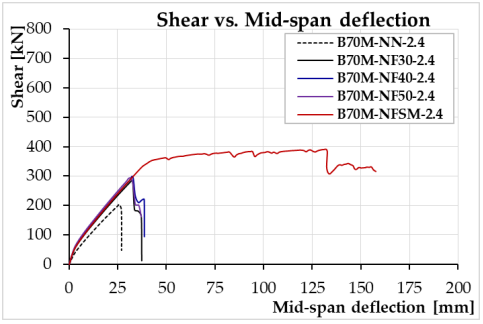

	P_{max} [kN]	V_{FEA} [kN]	M_{max} [kNm]	M_{max}/M_{fl} [-]	δ_u [mm]
B70M-NN-0.9	257.3	128.7	313.9	0.93	40.2
B70M-NF30-0.9	282.8	141.4	345.0	1.00	118.6
B70M-NN-1.6	344.4	172.2	420.2	0.62	29.0
B70M-NF30-1.6	476.4	238.2	581.2	0.86	56.5
B70M-NN-2.1	392.1	196.1	478.4	1.00	28.3
B70M-NF30-2.1	520.9	260.4	635.4	0.58	38.4
B70M-NF40-2.1	561.3	280.6	684.7	0.81	40.5
B70M-NF50-2.1	597.2	298.6	728.5	0.86	44.0
B70M-NN-2.4	409.6	204.8	499.7	0.86	27.0
B70M-NF30-2.4	568.3	284.2	693.3	0.56	37.4
B70M-NF40-2.4	604.8	302.4	737.9	0.75	38.5
B70M-NF50-2.4	608.1	304.0	741.8	0.85	38.5

D.3. Size L

a/d=2.5
f_c= 25 MPa
ρ= 0.9%, 1.6%, 2.1%, 2.4%
s_f=30, 40, 50 mm

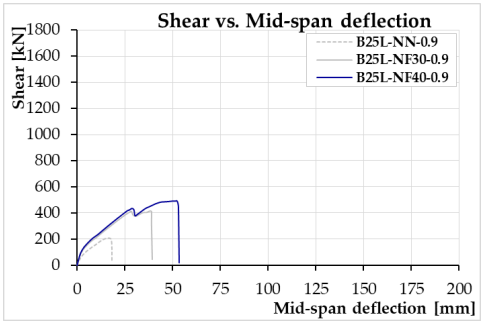

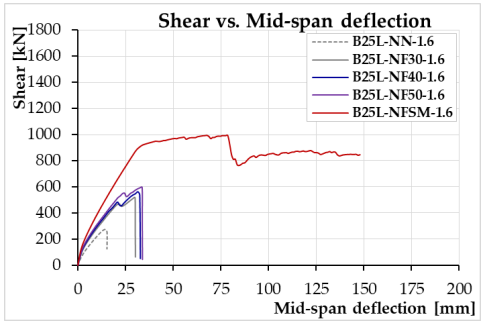

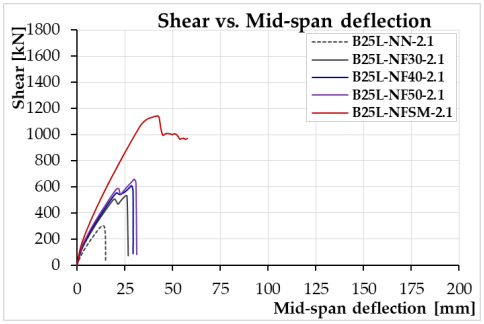

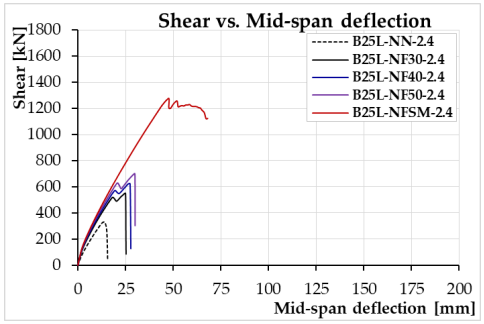

	P_{max} [kN]	V_{FEA} [kN]	M_{max} [kNm]	M_{max}/M_{fl} [-]	δ_u [mm]
B25L-NN-0.9	413.3	206.7	471.2	0.46	18.2
B25L-NF30-0.9	831.8	415.9	948.2	0.78	39.5
B25L-NF40-0.9	984.7	492.3	1122.5	1.00	53.4
B25L-NN-1.6	547.3	273.7	624.0	0.36	15.3
B25L-NF30-1.6	1039.7	519.9	1185.3	0.59	30.2
B25L-NF40-1.6	1131.3	565.3	1289.6	0.64	32.8
B25L-NF50-1.6	1200.1	600.0	1368.1	0.67	33.9
B25L-NN-2.1	603.6	301.8	688.1	0.33	15.0
B25L-NF30-2.1	1074.4	537.2	1224.9	0.49	26.8
B25L-NF40-2.1	1223.3	611.7	1394.6	0.56	29.4
B25L-NF50-2.1	1324.4	622.2	1509.8	0.61	31.3
B25L-NN-2.4	661.2	330.6	753.7	0.32	15.6
B25L-NF30-2.4	1103.0	551.5	1257.4	0.45	25.3
B25L-NF40-2.4	1267.6	633.8	1445.1	0.51	27.8
B25L-NF50-2.4	1403.3	701.6	1599.7	0.57	30.0

a/d=2.5
f_c= 50 MPa
ρ= 0.9%, 1.6%, 2.1%, 2.4%
s_l=30, 40, 50 mm

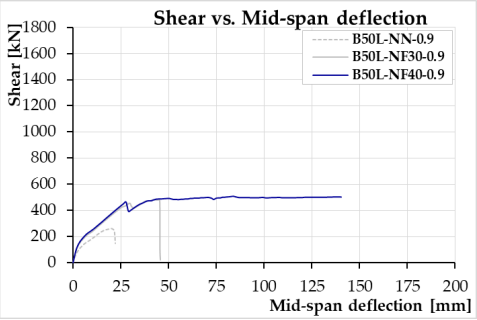

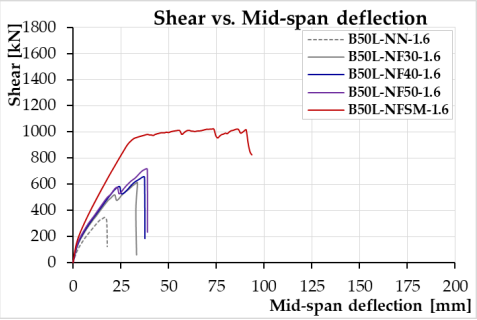

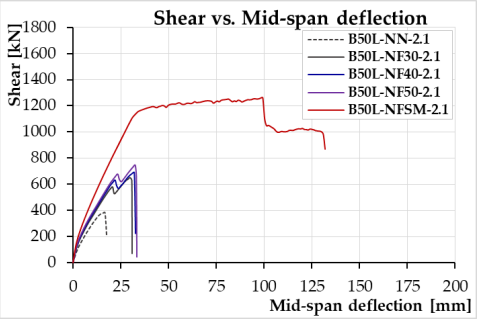

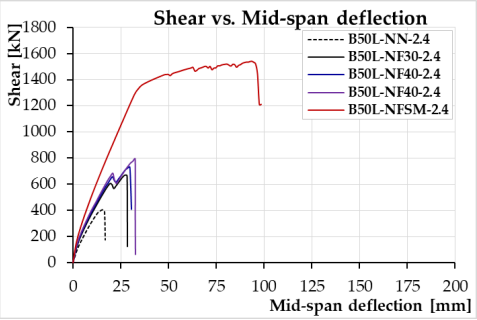

	P_{max} [kN]	V_{FEA} [kN]	M_{max} [kNm]	M_{max}/M_{fl} [-]	δ_u [mm]
B50L-NN-0.9	529.4	264.7	603.6	0.56	22.1
B50L-NF30-0.9	964.7	482.3	1099.7	0.89	45.8
B50L-NF40-0.9	1021.2	510.6	1164.2	1.00	140.5
B50L-NN-1.6	697.4	348.7	795.1	0.44	18.1
B50L-NF30-1.6	1225.5	612.7	1397.1	0.67	33.3
B50L-NF40-1.6	1312.5	656.3	1496.3	0.72	37.7
B50L-NF50-1.6	1447.4	723.7	1650.0	0.79	39.1
B50L-NN-2.1	771.7	385.8	879.7	0.39	17.5
B50L-NF30-2.1	1318.4	659.2	1503.0	0.58	31.0
B50L-NF40-2.1	1384.8	692.4	1578.7	0.61	32.8
B50L-NF50-2.1	1498.9	749.4	1708.7	0.66	33.3
B50L-NN-2.4	816.8	408.4	931.2	0.36	16.9
B50L-NF30-2.4	1344.3	672.1	1532.5	0.52	28.6
B50L-NF40-2.4	1470.6	735.3	1676.5	0.57	30.8
B50L-NF50-2.4	1591.0	795.5	1813.8	0.61	32.6

a/d=2.5
f_c= 70 MPa
ρ= 0.9%, 1.6%, 2.1%, 2.4%
s_f=30, 40, 50 mm

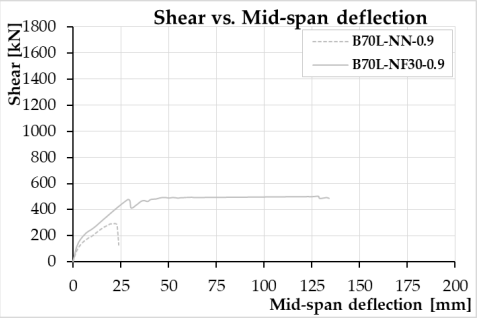

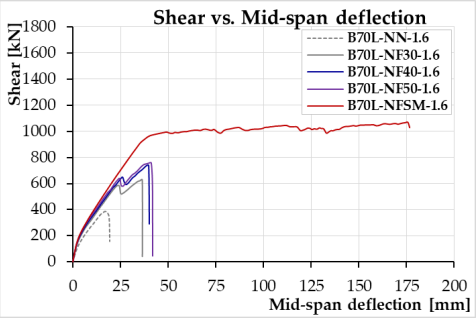

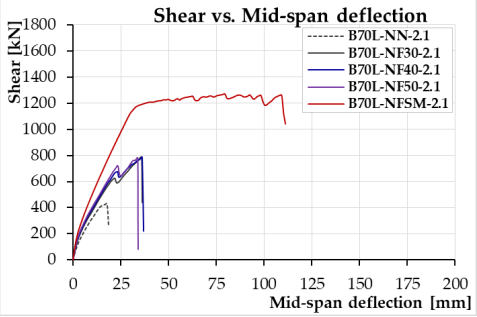

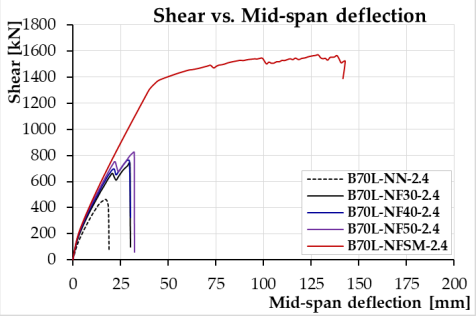

	P_{max} [kN]	V_{FEA} [kN]	M_{max} [kNm]	M_{max}/M_{fl} [-]	δ_u [mm]
B70L-NN-0.9	597.9	299.0	681.6	0.62	23.8
B70L-NF30-0.9	1009.0	504.5	1150.2	1.00	134.1
B70L-NN-1.6	770.5	385.3	878.4	0.45	19.3
B70L-NF30-1.6	1263.6	631.8	1440.5	0.68	36.6
B70L-NF40-1.6	1481.5	740.8	1688.9	0.80	40.0
B70L-NF50-1.6	1515.2	757.6	1727.4	0.81	42.0
B70L-NN-2.1	867.6	433.8	989.1	0.40	18.8
B70L-NF30-2.1	1577.1	788.5	1797.9	0.68	36.4
B70L-NF40-2.1	1577.6	788.8	1798.5	0.68	36.5
B70L-NF50-2.1	1564.3	782.1	1783.3	0.67	34.0
B70L-NN-2.4	940.4	470.2	1072.0	0.38	18.9
B70L-NF30-2.4	1498.4	749.2	1708.1	0.57	30.2
B70L-NF40-2.4	1530.2	765.1	1744.5	0.58	30.4
B70L-NF50-2.4	1653.5	826.8	1885.0	0.62	32.4

a/d=3
f_c= 25 MPa
ρ= 0.9%, 1.6%, 2.1%, 2.4%
s_l=30, 40, 50 mm

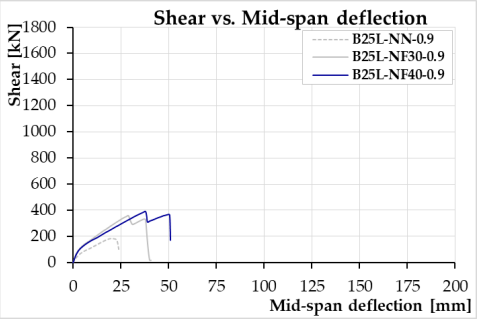

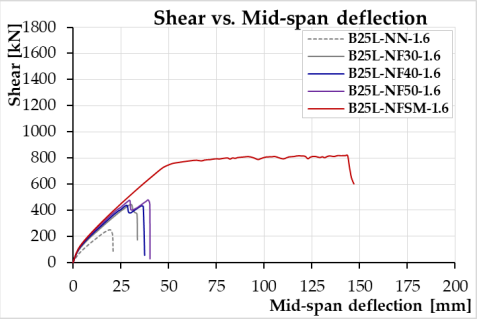

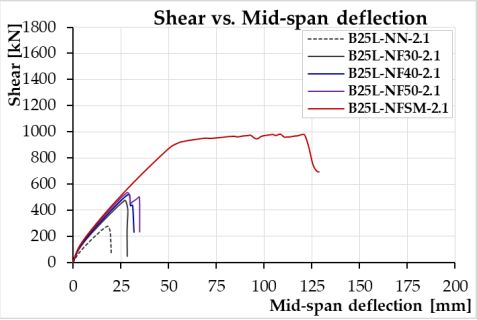

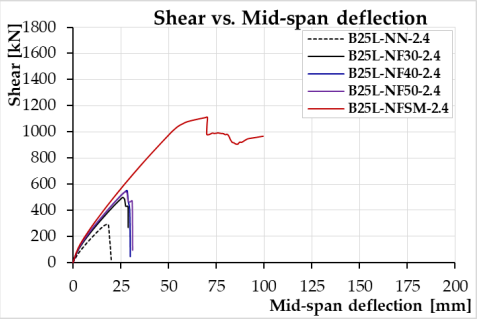

	P_{max} [kN]	V_{FEA} [kN]	M_{max} [kNm]	M_{max}/M_{fl} [-]	δ_u [mm]
B25L-NN-0.9	364.9	182.5	503.6	0.49	23.8
B25L-NF30-0.9	719.4	359.7	992.8	0.82	40.9
B25L-NF40-0.9	782.6	391.3	1080.0	1.00	51.0
B25L-NN-1.6	499.0	249.5	688.7	0.40	21.0
B25L-NF30-1.6	892.8	446.4	1232.1	0.61	33.7
B25L-NF40-1.6	880.2	440.1	1214.7	0.60	37.5
B25L-NF50-1.6	962.4	481.2	1328.2	0.65	40.3
B25L-NN-2.1	554.2	277.1	764.8	0.37	20.0
B25L-NF30-2.1	957.0	478.5	1320.7	0.53	28.4
B25L-NF40-2.1	1042.5	521.2	1438.6	0.58	32.0
B25L-NF50-2.1	1082.5	541.3	1493.9	0.60	34.9
B25L-NN-2.4	584.8	292.4	807.0	0.35	20.0
B25L-NF30-2.4	1004.3	502.2	1386.0	0.49	28.9
B25L-NF40-2.4	1099.4	549.7	1517.2	0.54	30.0
B25L-NF50-2.4	1094.2	547.1	1509.9	0.53	31.2

a/d=3
f_c= 50 MPa
ρ= 0.9%, 1.6%, 2.1%, 2.4%
s_l=30, 40, 50 mm

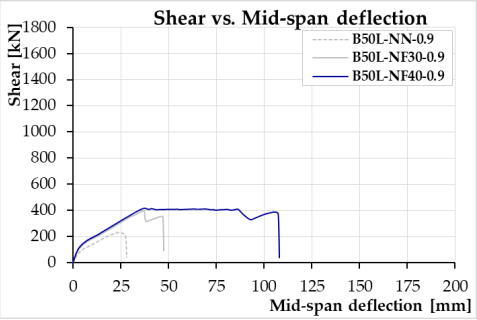

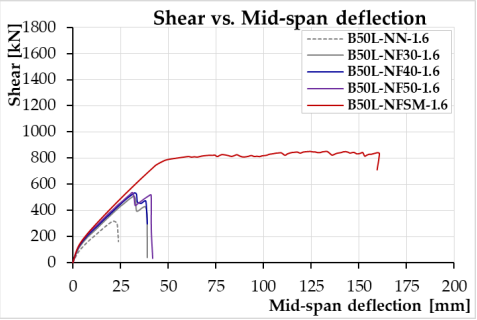

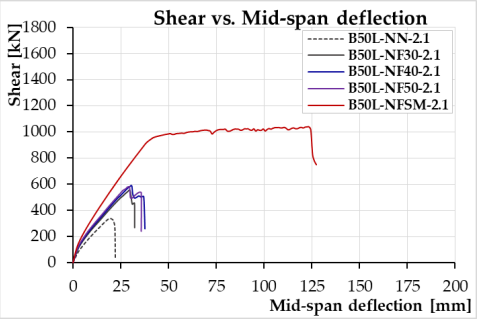

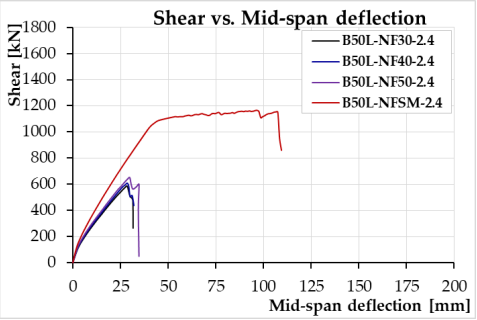

	P_{max} [kN]	V_{FEA} [kN]	M_{max} [kNm]	M_{max}/M_{fl} [-]	δ_u [mm]
B50L-NN-0.9	465.8	232.9	642.8	0.59	28.0
B50L-NF30-0.9	801.4	400.7	1105.9	0.89	47.5
B50L-NF40-0.9	832.9	416.4	1149.4	1.00	108.0
B50L-NN-1.6	635.9	317.9	877.5	0.46	23.8
B50L-NF30-1.6	1022.7	511.3	1411.3	0.68	39.1
B50L-NF40-1.6	1075.7	537.9	1484.5	0.71	38.9
B50L-NF50-1.6	1083.9	542.0	1495.8	0.71	41.7
B50L-NN-2.1	677.3	338.6	934.7	0.39	22.0
B50L-NF30-2.1	1114.4	557.2	1537.9	0.59	32.2
B50L-NF40-2.1	1178.3	589.2	1626.1	0.63	37.8
B50L-NF50-2.1	1179.2	589.6	1627.3	0.62	35.7
B50L-NN-2.4	734.0	367.0	1013.0	0.37	21.7
B50L-NF30-2.4	1174.7	587.3	1621.0	0.55	31.5
B50L-NF40-2.4	1223.9	612.0	1689.0	0.57	31.9
B50L-NF50-2.4	1302.7	651.4	1797.8	0.60	34.5

a/d=3
f_c= 70 MPa
ρ= 0.9%, 1.6%, 2.1%, 2.4%
s_l=30, 40, 50 mm

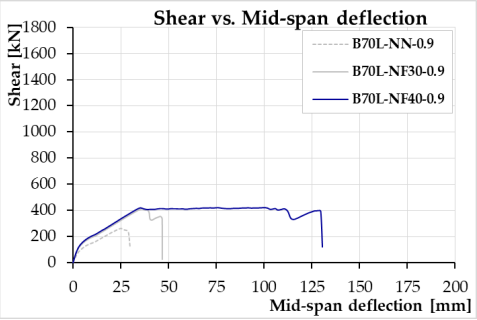

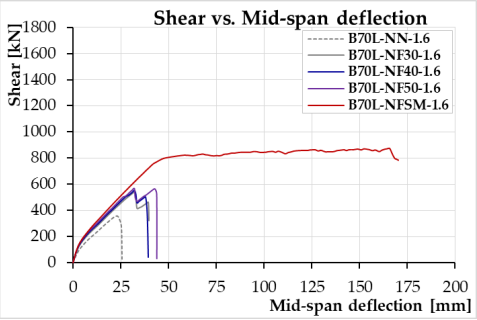

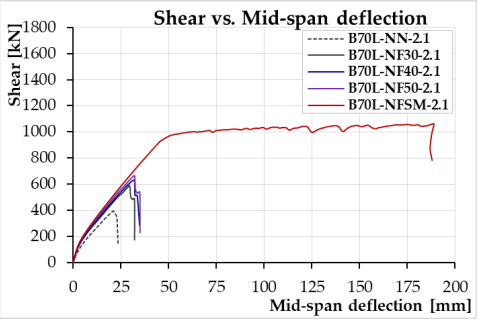

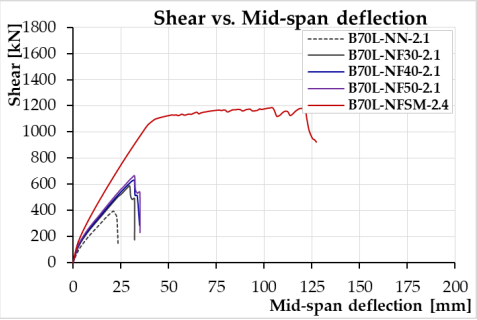

	P_{max} [kN]	V_{FEA} [kN]	M_{max} [kNm]	M_{max}/M_{fl} [-]	δ_u [mm]
B70L-NN-0.9	527.5	263.8	728.0	0.66	29.8
B70L-NF30-0.9	820.1	410.1	1131.8	0.90	46.6
B70L-NF40-0.9	838.4	419.2	1157.0	1.00	130.4
B70L-NN-1.6	716.7	358.4	989.1	0.51	25.8
B70L-NF30-1.6	1084.2	542.1	1496.2	0.71	39.8
B70L-NF40-1.6	1113.9	556.9	1537.1	0.73	39.5
B70L-NF50-1.6	1135.0	567.5	1566.3	0.74	44.0
B70L-NN-2.1	794.2	397.1	1096.0	0.45	23.6
B70L-NF30-2.1	1173.5	586.7	1619.4	0.62	32.2
B70L-NF40-2.1	1274.8	637.4	1759.2	0.67	34.7
B70L-NF50-2.1	1324.9	662.4	1828.3	0.69	35.0
B70L-NN-2.4	824.6	412.3	1138.0	0.40	23.5
B70L-NF30-2.4	1231.0	615.5	1698.8	0.56	31.3
B70L-NF40-2.4	1348.8	674.4	1861.4	0.61	34.0
B70L-NF50-2.4	1387.4	693.7	1914.6	0.63	34.8

a/d=3.5
f_c= 25 MPa
ρ= 0.9%, 1.6%, 2.1%, 2.4%
s_f=30, 40, 50 mm

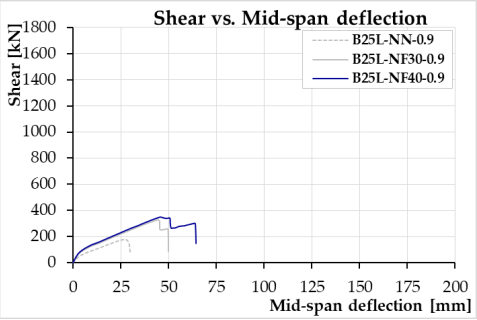

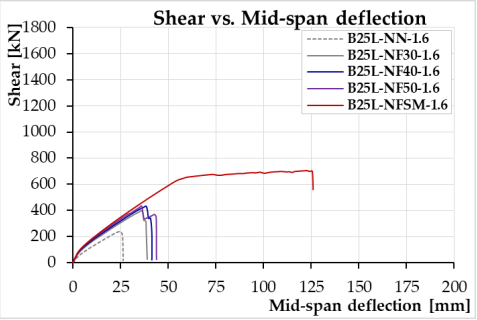

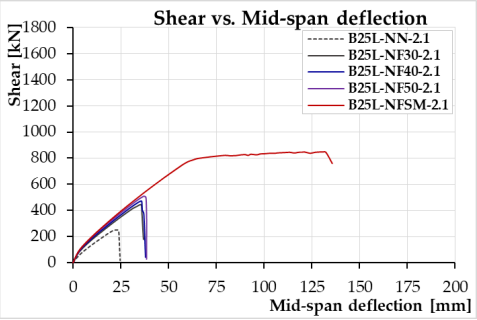

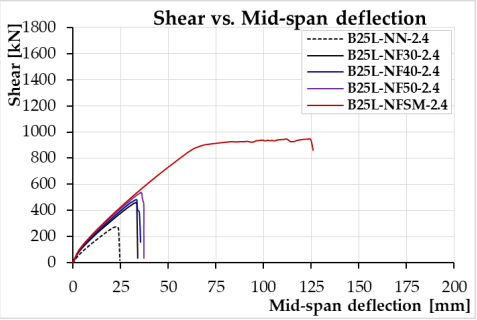

	P_{max} [kN]	V_{FEA} [kN]	M_{max} [kNm]	M_{max}/M_{fl} [-]	δ_u [mm]
B25L-NN-0.9	359.7	179.9	575.5	0.56	30.0
B25L-NF30-0.9	659.6	329.8	1055.3	0.87	50.0
B25L-NF40-0.9	705.8	352.9	1129.2	1.00	64.5
B25L-NN-1.6	480.1	240.0	768.1	0.45	26.4
B25L-NF30-1.6	798.1	399.0	1277.0	0.64	39.0
B25L-NF40-1.6	869.5	434.7	1391.1	0.69	41.5
B25L-NF50-1.6	869.9	435.0	1391.9	0.69	43.9
B25L-NN-2.1	505.1	252.5	808.1	0.39	24.7
B25L-NF30-2.1	895.9	448.0	1433.5	0.58	36.9
B25L-NF40-2.1	946.3	473.2	1514.1	0.61	38.0
B25L-NF50-2.1	1024.7	512.4	1639.6	0.66	38.5
B25L-NN-2.4	550.1	275.0	880.1	0.38	24.6
B25L-NF30-2.4	922.2	461.1	1475.4	0.53	34.0
B25L-NF40-2.4	969.3	484.6	1550.8	0.55	35.5
B25L-NF50-2.4	1075.9	538.0	1721.4	0.61	37.3

a/d=3.5
f_c= 50 MPa
ρ= 0.9%, 1.6%, 2.1%, 2.4%
s_f=30, 40, 50 mm

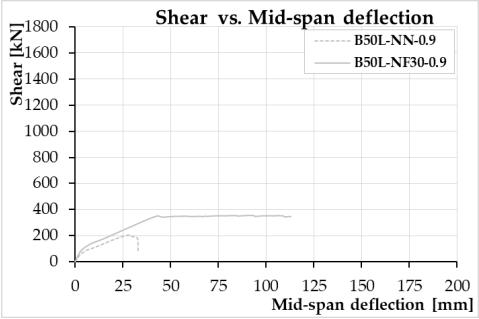

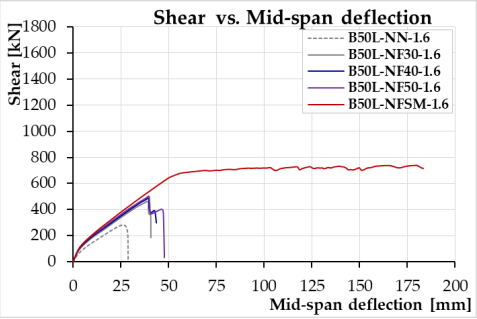

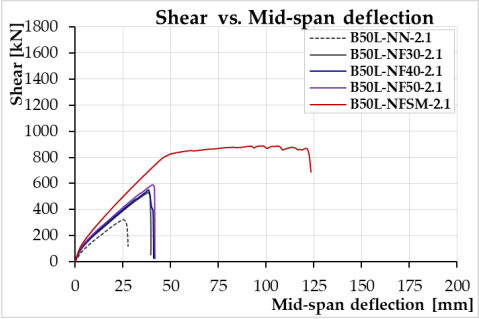

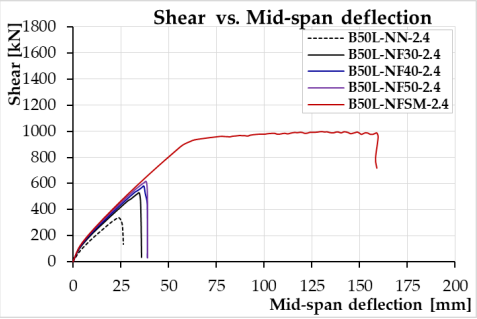

	P_{max} [kN]	V_{FEA} [kN]	M_{max} [kNm]	M_{max}/M_{fl} [-]	δ_u [mm]
B50L-NN-0.9	411.1	205.6	657.8	0.61	32.9
B50L-NF30-0.9	708.6	354.3	1133.7	1.00	112.9
B50L-NN-1.6	571.7	285.9	914.8	0.48	29.0
B50L-NF30-1.6	922.7	461.3	1476.3	0.71	40.9
B50L-NF40-1.6	968.6	484.3	1549.8	0.74	43.6
B50L-NF50-1.6	1003.3	501.7	1605.3	0.76	47.7
B50L-NN-2.1	648.9	324.4	1038.2	0.44	27.7
B50L-NF30-2.1	1060.2	530.1	1696.3	0.66	39.8
B50L-NF40-2.1	1106.4	553.2	1770.3	0.68	41.0
B50L-NF50-2.1	1192.1	596.0	1907.3	0.73	41.9
B50L-NN-2.4	678.7	339.3	1085.9	0.40	26.6
B50L-NF30-2.4	1060.9	530.5	1697.5	0.57	35.9
B50L-NF40-2.4	1162.6	581.3	1860.2	0.63	38.9
B50L-NF50-2.4	1233.2	616.6	1973.1	0.66	39.0

a/d=3.5
f_c= 70 MPa
ρ= 0.9%, 1.6%, 2.1%, 2.4%
s_f=30, 40, 50 mm

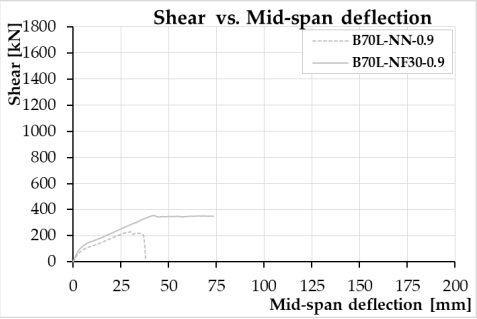

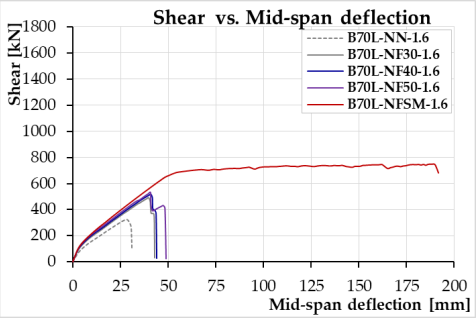

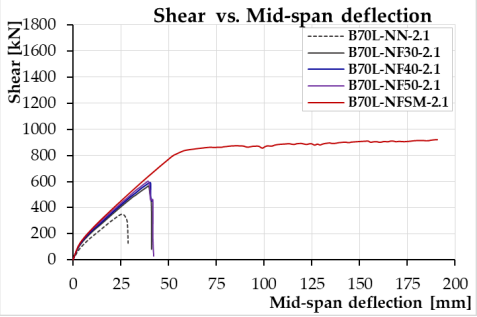

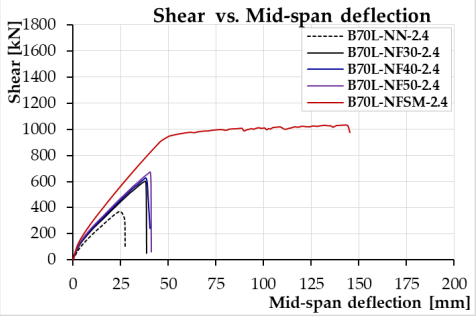

	P_{max} [kN]	V_{FEA} [kN]	M_{max} [kNm]	M_{max}/M_{fl} [-]	δ_u [mm]
B70L-NN-0.9	460.6	230.3	737.0	0.67	37.9
B70L-NF30-0.9	711.8	355.9	1138.9	1.00	73.5
B70L-NN-1.6	648.6	324.3	1037.8	0.54	31.0
B70L-NF30-1.6	987.6	493.8	1580.2	0.75	42.8
B70L-NF40-1.6	1039.4	519.7	1663.0	0.78	44.0
B70L-NF50-1.6	1070.2	535.1	1712.3	0.80	49.1
B70L-NN-2.1	706.6	353.3	1130.6	0.46	28.9
B70L-NF30-2.1	1137.3	568.7	1819.7	0.69	41.0
B70L-NF40-2.1	1190.5	595.3	1904.9	0.72	41.6
B70L-NF50-2.1	1210.6	605.3	1936.9	0.73	42.4
B70L-NN-2.4	741.6	370.8	1186.5	0.42	27.3
B70L-NF30-2.4	1204.4	602.2	1927.0	0.64	38.7
B70L-NF40-2.4	1257.6	628.8	2012.1	0.66	40.4
B70L-NF50-2.4	1346.1	673.1	2153.8	0.71	41.2

a/d=4
f_c= 25 MPa
ρ= 0.9%, 1.6%, 2.1%, 2.4%
s_l=30, 40, 50 mm

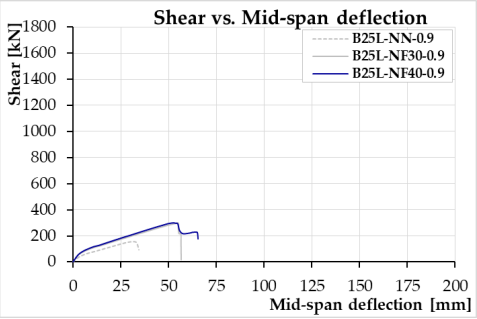

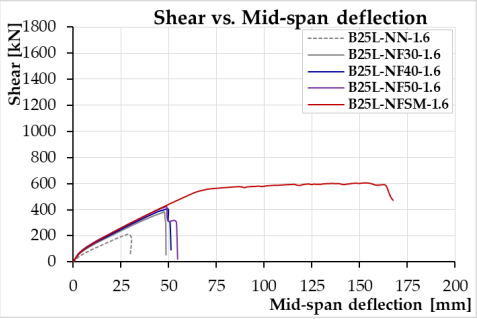

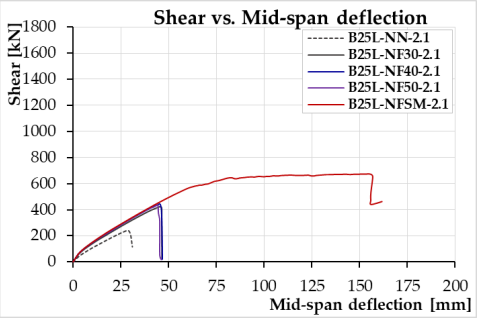

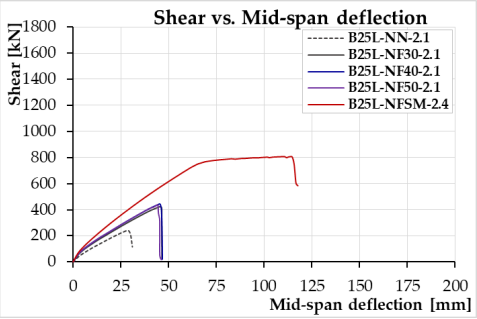

	P_{max} [kN]	V_{FEA} [kN]	M_{max} [kNm]	M_{max}/M_{fl} [-]	δ_u [mm]
B25L-NN-0.9	307.6	153.8	566.0	0.55	34.4
B25L-NF30-0.9	598.0	299.0	1100.4	0.90	56.6
B25L-NF40-0.9	602.2	301.1	1108.0	1.00	65.4
B25L-NN-1.6	425.1	212.6	782.2	0.45	29.9
B25L-NF30-1.6	765.0	382.5	1407.6	0.70	48.7
B25L-NF40-1.6	813.8	406.9	1497.5	0.74	51.3
B25L-NF50-1.6	847.5	423.8	1559.4	0.77	54.8
B25L-NN-2.1	480.3	240.1	883.7	0.42	31.1
B25L-NF30-2.1	847.3	423.6	1559.0	0.63	46.5
B25L-NF40-2.1	887.8	443.9	1633.6	0.66	46.8
B25L-NF50-2.1	873.0	436.5	1606.3	0.64	46.2
B25L-NN-2.4	514.3	275.2	946.4	0.41	29.7
B25L-NF30-2.4	872.1	436.0	1604.6	0.57	43.0
B25L-NF40-2.4	942.3	471.2	1733.9	0.62	45.1
B25L-NF50-2.4	1012.9	506.5	1863.8	0.66	47.1

a/d=4
f_c= 50 MPa
ρ= 0.9%, 1.6%, 2.1%, 2.4%
s_f=30, 40, 50 mm

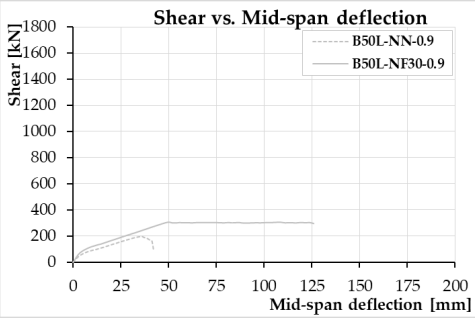

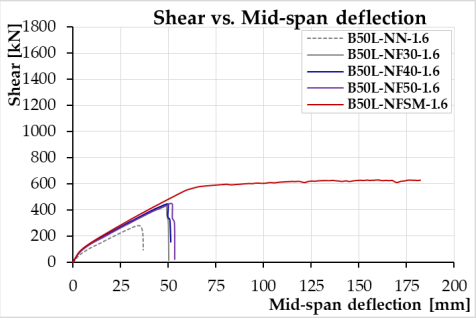

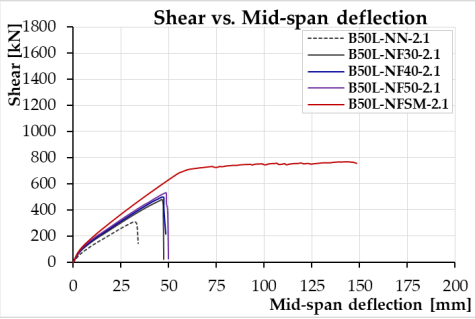

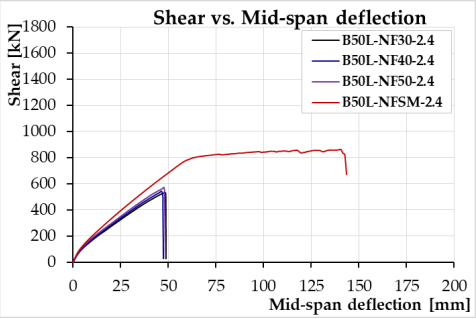

	P_{max} [kN]	V_{FEA} [kN]	M_{max} [kNm]	M_{max}/M_{fl} [-]	δ_u [mm]
B50L-NN-0.9	392.5	196.3	722.3	0.67	42.4
B50L-NF30-0.9	612.0	306.0	1126.1	1.00	125.9
B50L-NN-1.6	554.6	277.3	1020.4	0.54	36.9
B50L-NF30-1.6	862.7	431.3	1587.4	0.76	50.2
B50L-NF40-1.6	893.1	446.5	1643.3	0.79	51.4
B50L-NF50-1.6	897.4	448.7	1651.2	0.79	53.5
B50L-NN-2.1	615.5	307.7	1132.5	0.48	34.2
B50L-NF30-2.1	958.7	479.3	1763.9	0.68	47.5
B50L-NF40-2.1	997.6	498.8	1835.6	0.71	48.7
B50L-NF50-2.1	1055.7	527.9	1942.6	0.75	50.1
B50L-NN-2.4	641.1	320.6	1179.7	0.44	33.2
B50L-NF30-2.4	1064.2	532.1	1958.2	0.66	49.0
B50L-NF40-2.4	1086.9	543.4	1999.9	0.67	47.5
B50L-NF50-2.4	1138.7	569.4	2095.2	0.70	48.5

a/d=4
f_c= 70 MPa
ρ= 0.9%, 1.6%, 2.1%, 2.4%
s_l=30, 40, 50 mm

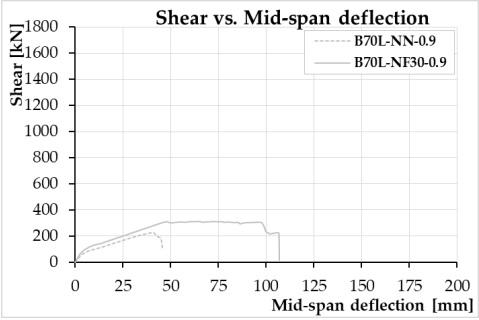

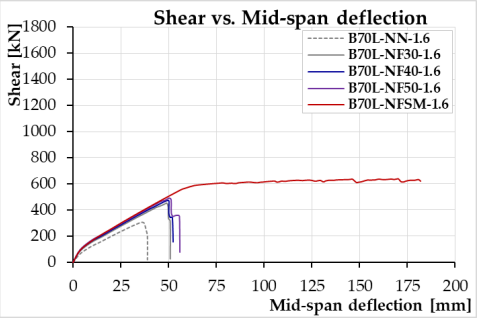

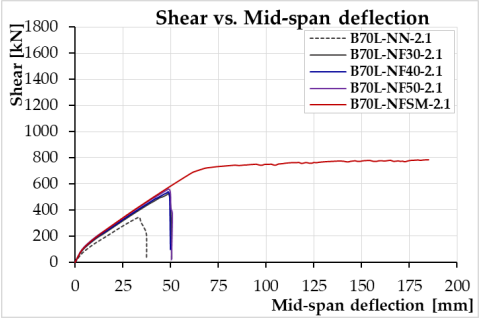

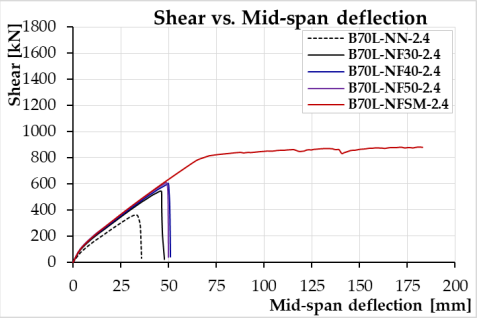

	P_{max} [kN]	V_{FEA} [kN]	M_{max} [kNm]	M_{max}/M_{fl} [-]	δ_u [mm]
B70L-NN-0.9	450.7	225.3	829.3	0.76	45.6
B70L-NF30-0.9	618.2	309.1	1137.4	1.00	106.9
B70L-NN-1.6	615.8	307.9	1133.1	0.58	38.8
B70L-NF30-1.6	906.2	453.1	1667.5	0.79	51.0
B70L-NF40-1.6	938.9	469.4	1727.6	0.82	52.4
B70L-NF50-1.6	976.7	488.4	1797.1	0.84	55.8
B70L-NN-2.1	681.1	340.5	1253.2	0.51	37.5
B70L-NF30-2.1	1043.7	521.8	1920.4	0.73	50.7
B70L-NF40-2.1	1079.6	539.8	1986.4	0.75	50.0
B70L-NF50-2.1	1119.0	559.5	2059.9	0.78	50.4
B70L-NN-2.4	721.7	360.9	1328.0	0.47	35.9
B70L-NF30-2.4	1080.1	540.1	1987.4	0.66	48.0
B70L-NF40-2.4	1200.7	600.3	2209.2	0.73	51.1
B70L-NF50-2.4	1220.9	610.5	2246.5	0.74	50.0

a/d=4.5
f_c= 25 MPa
ρ= 0.9%, 1.6%, 2.1%, 2.4%
s_f=30, 40, 50 mm

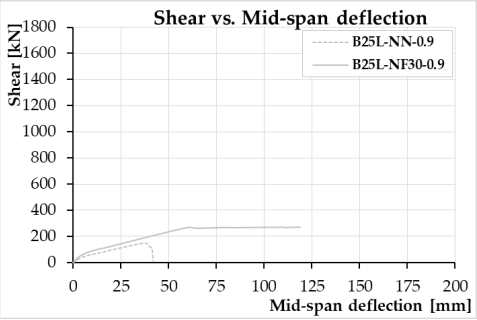

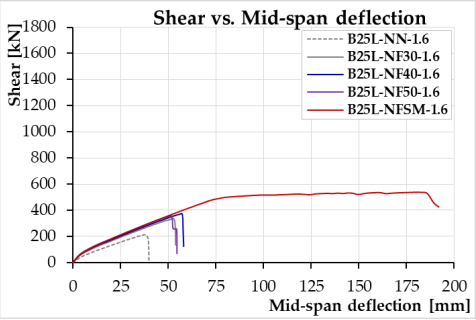

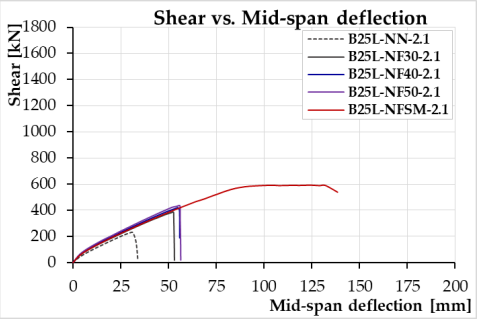

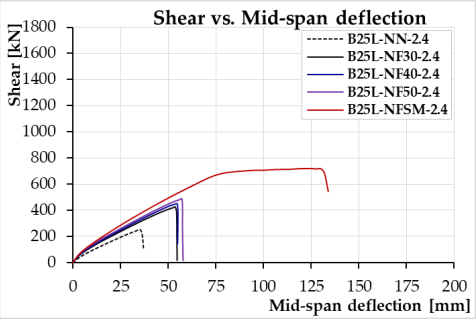

	P_{max} [kN]	V_{FEA} [kN]	M_{max} [kNm]	M_{max}/M_{fl} [-]	δ_u [mm]
B25L-NN-0.9	290.8	145.4	599.1	0.58	41.8
B25L-NF30-0.9	537.5	268.8	1107.3	1.00	118.8
B25L-NN-1.6	425.9	212.9	877.3	0.51	39.9
B25L-NF30-1.6	677.3	338.7	1395.3	0.69	53.9
B25L-NF40-1.6	747.6	373.8	1540.0	0.76	58.1
B25L-NF50-1.6	722.2	361.1	1487.7	0.73	54.6
B25L-NN-2.1	461.4	230.7	950.6	0.45	33.9
B25L-NF30-2.1	769.3	384.6	1584.7	0.64	53.1
B25L-NF40-2.1	841.1	420.5	1732.6	0.70	55.8
B25L-NF50-2.1	874.4	437.2	1801.3	0.72	56.4
B25L-NN-2.4	502.2	251.1	1034.5	0.44	37.1
B25L-NF30-2.4	850.9	425.5	1752.9	0.62	54.7
B25L-NF40-2.4	901.4	450.7	1856.8	0.66	55.0
B25L-NF50-2.4	975.2	487.6	2008.9	0.71	57.8

a/d=4.5
f_c= 50 MPa
ρ= 0.9%, 1.6%, 2.1%, 2.4%
s_l=30, 40, 50 mm

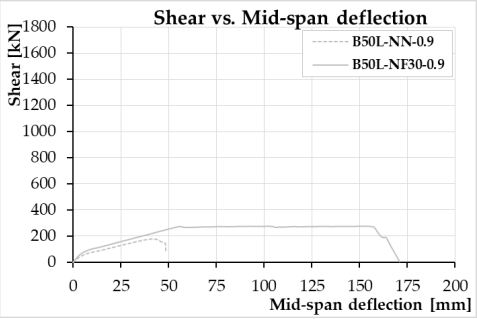

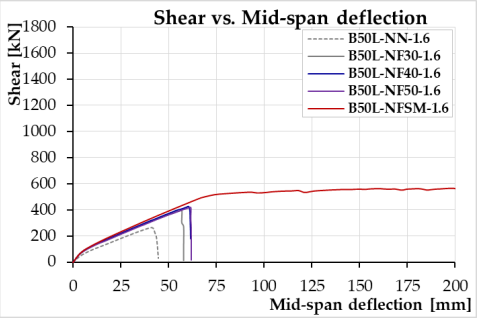

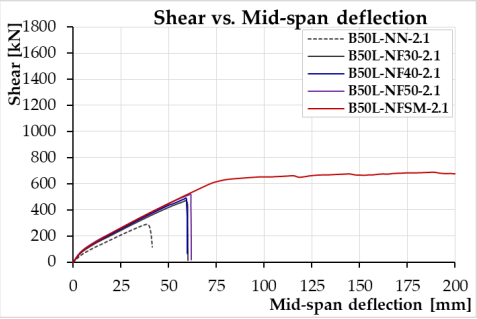

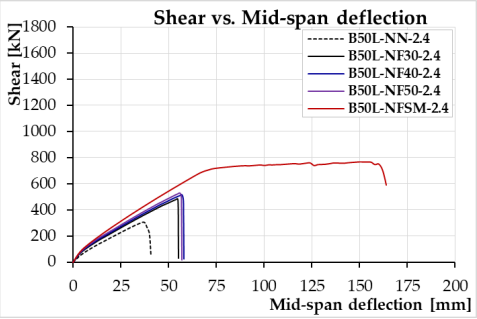

	P_{max} [kN]	V_{FEA} [kN]	M_{max} [kNm]	M_{max}/M_{fl} [-]	δ_u [mm]
B50L-NN-0.9	352.1	176.0	725.3	0.67	48.5
B50L-NF30-0.9	548.3	274.2	1129.5	1.00	171.1
B50L-NN-1.6	524.8	262.4	1081.1	0.57	44.8
B50L-NF30-1.6	788.6	394.3	1624.6	0.78	58.1
B50L-NF40-1.6	857.3	428.6	1766.0	0.85	61.8
B50L-NF50-1.6	837.3	418.7	1724.9	0.82	62.0
B50L-NN-2.1	576.9	288.4	1188.3	0.50	41.5
B50L-NF30-2.1	948.5	474.2	1953.8	0.76	60.3
B50L-NF40-2.1	975.7	487.8	2009.9	0.77	59.9
B50L-NF50-2.1	1036.5	518.3	2135.3	0.82	62.0
B50L-NN-2.4	607.6	303.8	1251.7	0.46	40.8
B50L-NF30-2.4	971.4	485.7	2001.1	0.68	55.3
B50L-NF40-2.4	1037.9	519.0	2138.2	0.72	58.2
B50L-NF50-2.4	1060.0	530.0	2183.5	0.73	57.2

a/d=4.5
f_c= 70 MPa
ρ= 0.9%, 1.6%, 2.1%, 2.4%
s_f=30, 40, 50 mm

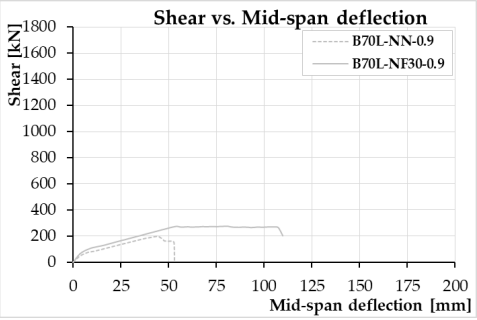

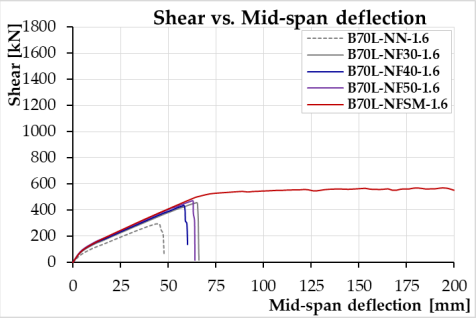

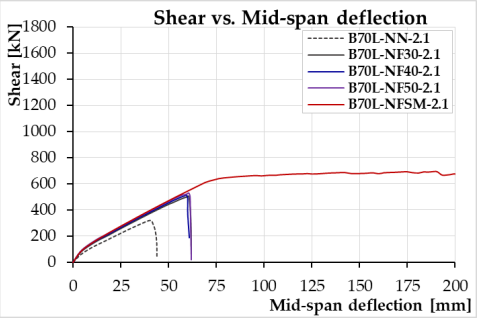

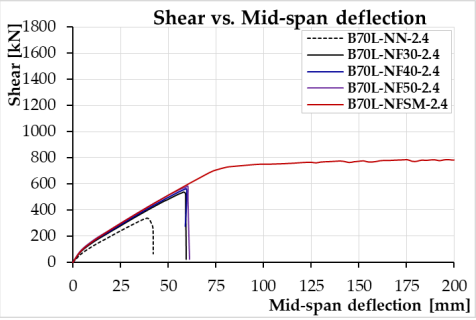

	P_{max} [kN]	V_{FEA} [kN]	M_{max} [kNm]	M_{max}/M_{fl} [-]	δ_u [mm]
B70L-NN-0.9	394.6	197.3	812.9	0.74	53.1
B70L-NF30-0.9	551.5	275.8	1136.1	1.00	109.8
B70L-NN-1.6	589.9	295.0	1215.2	0.63	48.0
B70L-NF30-1.6	903.9	452.0	1862.1	0.88	66.0
B70L-NF40-1.6	870.4	435.2	1793.1	0.85	60.3
B70L-NF50-1.6	935.2	467.6	1926.4	0.90	64.0
B70L-NN-2.1	644.4	322.2	1327.4	0.54	44.0
B70L-NF30-2.1	1007.9	504.0	2076.3	0.79	62.0
B70L-NF40-2.1	1028.3	514.1	2118.2	0.80	61.0
B70L-NF50-2.1	1064.8	532.4	2193.4	0.83	62.0
B70L-NN-2.4	678.6	339.3	1397.9	0.50	42.0
B70L-NF30-2.4	1074.1	537.1	2212.7	0.73	59.5
B70L-NF40-2.4	1120.1	560.0	2307.3	0.76	58.8
B70L-NF50-2.4	1160.8	580.4	2391.3	0.79	61.4

APPENDIX E: PREDICTION OF BEAM SHEAR STRENGTH

The shear strength for the composite beams in the numerical program and the strength predictions are list below.

	Beam type	V_{FEA} [kN]	V_1 [kN]	V_2 [kN]	V_3 [kN]	V_{FEA}/V_1 -	V_{FEA}/V_2 -	V_{FEA}/V_3 -
S a/d=3	**B25S-NF30-2.4**	131.2	115.3	88.8	134.3	1.14	1.48	0.98
S a/d=3.5	**B25S-NF30-2.1**	110.6	112.7	84.3	133.6	0.98	1.31	0.83
	B25S-NF30-2.4	113.2	115.3	88.8	133.6	0.98	1.28	0.85
	B25S-NF40-2.4	126.8	136.6	101.2	169.0	0.93	1.25	0.75
	B50S-NF30-2.1	116.7	125.4	97.0	144.9	0.93	1.20	0.81
	B50S-NF40-2.1	121.5	146.6	108.7	180.3	0.83	1.12	0.67
	B50S-NF30-2.4	133.9	128.8	102.3	144.9	1.04	1.31	0.92
S a/d=4	**B25S-NF30-2.1**	88.3	112.7	84.3	133.6	0.78	1.05	0.66
	B25S-NF30-2.4	91.5	115.3	88.8	133.6	0.79	1.03	0.68
	B25S-NF40-2.4	109.3	136.6	101.2	169.0	0.80	1.08	0.65
	B50S-NF30-2.4	106.2	128.8	114.6	144.9	0.82	0.93	0.73
S a/d=4.5	**B25S-NF30-2.1**	82.3	112.7	84.3	133.6	0.73	0.98	0.62
	B25S-NF30-2.4	82.5	115.3	88.8	133.6	0.72	0.93	0.62
	B25S-NF40-2.4	92.9	136.6	101.2	169.0	0.68	0.92	0.55
	B50S-NF30-2.4	92.5	128.8	102.3	144.92	0.72	0.90	0.64
	B50S-NF40-2.4	101.0	150.0	114.6	180.33	0.67	0.88	0.56
	B70S-NF30-2.4	93.7	136.5	110.0	152.0	0.69	0.85	0.62
M a/d=2.5	**B25M-NF30-1.6**	386.6	254.5	191.0	297.7	1.52	2.02	1.30
	B25M-NF40-1.6	419.6	294.5	209.7	347.6	1.42	2.00	1.21
	B25M-NF30-2.1	377.6	266.0	207.2	315.9	1.42	1.82	1.20
	B25M-NF40-2.1	406.4	306.0	227.6	369.1	1.33	1.79	1.10
	B25M-NF50-2.1	497.0	345.9	247.9	420.3	1.44	2.00	1.18
	B25M-NF30-2.4	409.3	271.2	214.6	323.7	1.51	1.91	1.26
	B25M-NF40-2.4	458.0	311.2	235.7	378.4	1.47	1.94	1.21
	B25M-NF50-2.4	522.5	351.1	256.8	431.0	1.49	2.03	1.21
	B50M-NF30-1.6	416.7	289.6	226.0	325.8	1.44	1.84	1.28
	B50M-NF40-1.6	443.6	329.5	244.7	373.4	1.35	1.81	1.19
	B50M-NF30-2.1	445.0	304.0	245.2	347.4	1.46	1.81	1.28
	B50M-NF40-2.1	473.7	344.0	265.6	398.3	1.38	1.78	1.19
	B50M-NF50-2.1	529.1	383.9	285.9	447.5	1.38	1.85	1.18
	B50M-NF30-2.4	483.1	310.6	254.0	356.8	1.56	1.90	1.35
	B50M-NF40-2.4	489.2	350.5	275.1	409.0	1.40	1.78	1.20
	B50M-NF50-2.4	550.5	390.5	296.1	459.6	1.41	1.86	1.20
	B70M-NF30-2.1	476.4	325.9	267.1	366.0	1.46	1.78	1.30
	B70M-NF40-2.1	522.1	365.8	287.4	415.6	1.43	1.82	1.26
	B70M-NF50-2.1	567.6	405.8	307.8	463.8	1.40	1.84	1.22
	B70M-NF30-2.4	531.7	333.3	276.6	376.3	1.60	1.92	1.41
	B70M-NF40-2.4	537.1	373.2	297.7	427.3	1.44	1.80	1.26
	B70M-NF50-2.4	580.4	413.1	318.8	476.8	1.40	1.82	1.22

M a/d=3	**B25M-NF30-1.6**	276.8	254.5	191.0	284.5	1.09	1.45	0.97
	B25M-NF40-1.6	327.8	294.5	209.7	334.6	1.11	1.56	0.98
	B25M-NF50-1.6	341.5	294.5	209.7	398.0	1.16	1.63	0.86
	B25M-NF30-2.1	305.5	266.0	207.2	302.9	1.15	1.47	1.01
	B25M-NF40-2.1	348.9	306.0	227.6	353.5	1.14	1.53	0.99
	B25M-NF50-2.1	388.8	345.9	247.9	402.0	1.12	1.57	0.97
	B25M-NF30-2.4	323.4	271.2	214.6	310.8	1.19	1.51	1.04
	B25M-NF40-2.4	362.4	311.2	235.7	362.9	1.16	1.54	1.00
	B25M-NF50-2.4	391.0	351.1	256.8	412.9	1.11	1.52	0.95
	B50M-NF30-1.6	332.7	289.6	226.0	310.1	1.15	1.47	1.07
	B50M-NF40-1.6	358.8	329.5	244.7	368.2	1.09	1.47	0.97
	B50M-NF30-2.1	336.6	304.0	245.2	331.8	1.11	1.37	1.01
	B50M-NF40-2.1	383.4	344.0	265.6	380.1	1.11	1.44	1.01
	B50M-NF50-2.1	410.2	383.9	285.9	390.9	1.07	1.43	1.05
	B50M-NF30-2.4	373.6	310.6	254.0	341.2	1.20	1.47	1.09
	B50M-NF40-2.4	392.8	350.5	275.1	390.9	1.12	1.43	1.00
	B50M-NF50-2.4	460.6	390.5	296.1	438.9	1.18	1.56	1.05
	B70M-NF30-1.6	336.4	309.7	246.1	325.9	1.09	1.37	1.03
	B70M-NF40-1.6	364.9	349.6	264.9	389.3	1.04	1.38	0.94
	B70M-NF30-2.1	360.3	389.6	267.1	348.9	0.92	1.35	1.03
	B70M-NF40-2.1	403.5	365.8	287.4	396.0	1.10	1.40	1.02
	B70M-NF50-2.1	442.7	405.8	307.8	452.6	1.09	1.44	0.98
	B70M-NF30-2.4	401.8	333.3	276.6	359.2	1.21	1.45	1.12
	B70M-NF40-2.4	422.8	373.2	297.7	407.6	1.13	1.42	1.04
	B70M-NF50-2.4	459.2	413.1	318.8	454.5	1.11	1.44	1.01
M a/d=3.5	**B25M-NF30-1.6**	244.4	254.5	191.0	273.0	0.96	1.28	0.90
	B25M-NF40-1.6	270.2	294.5	209.7	334.6	0.92	1.29	0.81
	B25M-NF50-1.6	297.8	334.4	228.4	398.0	0.89	1.30	0.75
	B25M-NF30-2.1	258.1	266.0	207.2	291.6	0.97	1.25	0.89
	B25M-NF40-2.1	289.2	306.0	227.6	339.9	0.95	1.27	0.85
	B25M-NF50-2.1	321.2	345.9	247.9	398.0	0.93	1.30	0.81
	B25M-NF30-2.4	268.4	271.2	214.6	299.6	0.99	1.25	0.90
	B25M-NF40-2.4	300.3	311.2	235.7	352.2	0.96	1.27	0.85
	B25M-NF50-2.4	331.9	351.1	256.8	398.0	0.95	1.29	0.83
	B50M-NF30-1.6	263.0	289.6	226.0	304.9	0.91	1.16	0.86
	B50M-NF40-1.6	290.0	329.5	244.7	368.2	0.88	1.19	0.79
	B50M-NF50-1.6	306.5	369.4	263.5	431.6	0.83	1.16	0.71
	B50M-NF30-2.1	291.2	304.0	245.2	318.4	0.96	1.19	0.91
	B50M-NF30-2.1	316.9	344.0	265.6	368.2	0.92	1.19	0.86
	B50M-NF30-2.1	345.2	383.9	285.9	431.6	0.90	1.21	0.80
	B50M-NF30-2.4	301.7	310.6	254.0	327.8	0.97	1.19	0.92
	B50M-NF40-2.4	330.3	350.5	275.1	378.5	0.94	1.20	0.87
	B50M-NF50-2.4	359.4	390.5	296.1	431.6	0.92	1.21	0.83
	B70M-NF30-1.6	283.2	309.7	246.1	325.9	0.91	1.15	0.87
	B70M-NF40-1.6	296.5	349.6	264.9	389.3	0.85	1.12	0.76
	B70M-NF30-2.1	299.3	325.9	267.1	334.2	0.92	1.12	0.90
	B70M-NF40-2.1	325.3	365.8	287.4	389.3	0.89	1.13	0.84
	B70M-NF50-2.1	360.3	405.8	307.8	452.6	0.89	1.17	0.80
	B70M-NF30-2.4	310.2	333.3	276.6	344.4	0.93	1.12	0.90

	B70M-NF40-2.4	345.6	373.2	297.7	394.1	0.93	1.16	0.88
	B70M-NF40-2.4	371.0	413.1	318.8	452.6	0.90	1.16	0.82
M a/d=4	**B25M-NF30-1.6**	219.1	254.5	191.0	271.2	0.86	1.15	0.81
	B25M-NF40-1.6	237.7	294.5	209.7	334.6	0.81	1.13	0.71
	B25M-NF50-1.6	263.2	334.4	228.4	398.0	0.79	1.15	0.66
	B25M-NF30-2.1	242.7	266.0	207.2	281.6	0.91	1.17	0.86
	B25M-NF40-2.1	269.8	306.0	227.6	334.6	0.88	1.19	0.81
	B25M-NF50-2.1	285.4	345.9	247.9	398.0	0.83	1.15	0.72
	B25M-NF30-2.4	254.9	271.2	214.6	289.7	0.94	1.19	0.88
	B25M-NF40-2.4	275.2	311.2	235.7	334.6	0.88	1.17	0.82
	B25M-NF50-2.4	302.0	351.1	256.8	398.0	0.86	1.18	0.76
	B50M-NF30-1.6	243.0	289.6	226.0	304.9	0.84	1.08	0.80
	B50M-NF40-1.6	257.0	329.5	244.7	368.2	0.78	1.05	0.70
	B50M-NF50-1.6	264.8	369.4	263.5	431.6	0.72	1.01	0.61
	B50M-NF30-2.1	270.2	304.0	245.2	306.6	0.89	1.10	0.88
	B50M-NF30-2.1	280.1	344.0	265.6	368.2	0.81	1.05	0.76
	B50M-NF30-2.1	306.5	383.9	285.9	431.6	0.80	1.07	0.71
	B50M-NF30-2.4	272.2	310.6	254.0	316.0	0.88	1.07	0.86
	B50M-NF40-2.4	298.9	350.5	275.1	368.2	0.85	1.09	0.81
	B50M-NF50-2.4	310.7	390.5	296.1	431.6	0.80	1.05	0.72
	B70M-NF30-1.6	246.5	309.7	246.1	325.9	0.80	1.00	0.76
	B70M-NF40-1.6	266.0	349.6	264.9	389.3	0.76	1.00	0.68
	B70M-NF50-1.6	264.8	389.6	283.6	452.6	0.68	0.93	0.58
	B70M-NF30-2.1	280.3	325.9	267.1	325.9	0.86	1.05	0.86
	B70M-NF40-2.1	295.0	365.8	287.4	389.3	0.81	1.03	0.76
	B70M-NF50-2.1	300.1	405.8	307.8	452.6	0.74	0.98	0.66
	B70M-NF30-2.4	286.7	333.3	276.6	331.5	0.86	1.04	0.86
	B70M-NF40-2.4	313.0	373.2	297.7	389.3	0.84	1.05	0.80
	B70M-NF40-2.4	323.9	413.1	318.8	452.6	0.78	1.02	0.72
M a/d=4.5	**B25M-NF30-1.6**	207.9	254.5	191.0	271.2	0.82	1.09	0.77
	B25M-NF40-1.6	229.2	294.5	209.7	334.6	0.78	1.09	0.68
	B25M-NF30-2.1	231.8	266.0	207.2	279.0	0.87	1.12	0.83
	B25M-NF40-2.1	262.0	306.0	227.6	334.6	0.86	1.15	0.78
	B25M-NF50-2.1	284.1	345.9	247.9	398.0	0.82	1.15	0.71
	B25M-NF30-2.4	245.2	271.2	214.6	287.0	0.90	1.14	0.85
	B25M-NF40-2.4	267.6	311.2	235.7	334.6	0.86	1.14	0.80
	B25M-NF50-2.4	295.5	351.1	256.8	398.0	0.84	1.15	0.74
	B50M-NF30-1.6	223.7	289.6	226.0	304.9	0.77	0.99	0.73
	B50M-NF30-2.1	258.3	304.0	245.2	304.9	0.85	1.05	0.85
	B50M-NF40-2.1	276.9	344.0	265.6	368.2	0.81	1.04	0.75
	B50M-NF50-2.1	282.7	383.9	285.9	431.6	0.74	0.99	0.65
	B50M-NF30-2.4	264.8	310.6	254.0	312.9	0.85	1.04	0.85
	B50M-NF40-2.4	284.7	350.5	275.1	368.2	0.81	1.04	0.77
	B50M-NF50-2.4	322.3	390.5	296.1	431.6	0.83	1.09	0.75
	B70M-NF30-2.1	260.4	325.9	267.1	325.9	0.80	0.98	0.80
	B70M-NF40-2.1	280.6	365.8	287.4	389.3	0.77	0.98	0.72
	B70M-NF50-2.1	298.6	405.8	307.8	452.6	0.74	0.97	0.66
	B70M-NF30-2.4	284.2	333.3	276.6	328.2	0.85	1.03	0.87
	B70M-NF40-2.4	302.4	373.2	297.7	389.3	0.81	1.02	0.78

	B70M-NF50-2.4	304.0	413.1	318.8	452.6	0.74	0.95	0.67
L a/d=2.5	**B25L-NF30-1.6**	519.9	443.4	333.3	502.2	1.17	1.56	1.04
	B25L-NF40-1.6	565.6	508.3	361.5	623.7	1.11	1.56	0.91
	B25L-NF50-1.6	600.0	573.2	389.7	662.7	1.05	1.54	0.91
	B25L-NF30-2.1	537.2	465.2	362.5	532.3	1.15	1.48	1.01
	B25L-NF40-2.1	611.7	530.1	393.1	667.8	1.15	1.56	0.92
	B25L-NF50-2.1	662.2	595.0	423.8	703.4	1.11	1.56	0.94
	B25L-NF30-2.4	551.5	479.4	381.6	550.6	1.15	1.45	1.00
	B25L-NF40-2.4	633.8	544.3	413.8	640.6	1.16	1.53	0.99
	B25L-NF50-2.4	701.6	609.2	446.1	728.1	1.15	1.57	0.96
	B50L-NF30-1.6	612.7	508.1	398.0	554.8	1.21	1.54	1.10
	B50L-NF40-1.6	656.3	573.0	426.2	632.7	1.15	1.54	1.04
	B50L-NF50-1.6	723.7	637.9	454.4	708.3	1.13	1.59	1.02
	B50L-NF30-2.1	659.2	535.5	432.8	591.3	1.23	1.52	1.11
	B50L-NF40-2.1	692.4	600.4	463.4	674.2	1.15	1.49	1.03
	B50L-NF50-2.1	749.4	665.3	494.1	755.0	1.13	1.52	0.99
	B50L-NF30-2.4	672.1	553.4	455.6	613.8	1.21	1.48	1.10
	B50L-NF40-2.4	735.3	618.3	487.9	699.7	1.19	1.51	1.05
	B50L-NF50-2.4	795.5	683.2	520.1	783.6	1.16	1.53	1.02
	B70L-NF30-1.6	631.8	545.3	435.2	585.8	1.16	1.45	1.08
	B70L-NF40-1.6	740.8	610.2	463.4	661.7	1.21	1.60	1.12
	B70L-NF50-1.6	757.6	675.1	491.6	735.5	1.12	1.54	1.03
	B70L-NF30-2.1	788.5	575.9	473.2	626.0	1.37	1.67	1.26
	B70L-NF40-2.1	788.8	640.8	503.9	706.9	1.23	1.57	1.12
	B70L-NF50-2.1	782.1	705.7	534.5	785.8	1.11	1.46	1.00
	B70L-NF30-2.4	749.2	596.0	498.2	650.9	1.26	1.50	1.15
	B70L-NF40-2.4	765.1	660.9	530.4	734.8	1.16	1.44	1.04
	B70L-NF50-2.4	826.8	725.8	562.7	816.7	1.14	1.47	1.01
L a/d=3	**B25L-NF30-1.6**	446.4	443.4	333.3	481.2	1.01	1.34	0.93
	B25L-NF40-1.6	440.1	508.3	361.5	558.9	0.87	1.22	0.79
	B25L-NF50-1.6	481.2	573.2	389.7	633.4	0.84	1.23	0.76
	B25L-NF30-2.1	478.5	465.2	362.5	511.8	1.03	1.32	0.93
	B25L-NF40-2.1	521.2	530.1	393.1	594.8	0.98	1.33	0.88
	B25L-NF50-2.1	541.3	595.0	423.8	674.9	0.91	1.28	0.80
	B25L-NF30-2.4	502.2	479.4	381.6	530.4	1.05	1.32	0.95
	B25L-NF40-2.4	549.7	544.3	413.8	616.7	1.01	1.33	0.89
	B25L-NF50-2.4	547.1	609.2	446.1	700.2	0.90	1.23	0.78
	B50L-NF30-1.6	511.3	508.1	398.0	529.4	1.01	1.28	0.97
	B50L-NF40-1.6	537.9	573.0	426.2	603.4	0.94	1.26	0.89
	B50L-NF50-1.6	542.0	637.9	454.4	690.1	0.85	1.19	0.79
	B50L-NF30-2.1	557.2	535.5	432.8	566.1	1.04	1.29	0.98
	B50L-NF40-2.1	589.2	600.4	463.4	645.3	0.98	1.27	0.91
	B50L-NF50-2.1	589.6	665.3	494.1	671.1	0.89	1.19	0.88
	B50L-NF30-2.4	587.3	553.4	455.6	588.8	1.06	1.29	1.00
	B50L-NF40-2.4	612.0	618.3	487.9	671.1	0.99	1.25	0.91
	B50L-NF50-2.4	651.4	683.2	520.1	751.0	0.95	1.25	0.87
	B70L-NF30-1.6	542.1	545.3	435.2	557.8	0.99	1.25	0.97
	B70L-NF40-1.6	556.9	610.2	463.4	629.9	0.91	1.20	0.88
	B70L-NF50-1.6	567.5	675.1	491.6	726.2	0.84	1.15	0.78

	B70L-NF30-2.1	586.7	575.9	473.2	598.1	1.02	1.24	0.98
	B70L-NF40-2.1	637.4	640.8	503.9	675.2	0.99	1.26	0.94
	B70L-NF50-2.1	662.4	705.7	534.5	750.1	0.94	1.24	0.88
	B70L-NF30-2.4	615.5	596.0	498.2	623.1	1.03	1.24	0.99
	B70L-NF40-2.4	674.4	660.9	530.4	703.3	1.02	1.27	0.96
	B70L-NF50-2.4	693.7	725.8	562.7	781.4	0.96	1.23	0.89
L a/d=3.5	**B25L-NF30-1.6**	399.0	443.4	333.3	464.4	0.90	1.20	0.86
	B25L-NF40-1.6	434.7	508.3	361.5	538.8	0.86	1.20	0.81
	B25L-NF50-1.6	435.0	573.2	389.7	541.4	0.76	1.12	0.80
	B25L-NF30-2.1	448.0	465.2	362.5	495.2	0.96	1.24	0.90
	B25L-NF40-2.1	473.2	530.1	393.1	575.2	0.89	1.20	0.82
	B25L-NF50-2.1	512.4	595.0	423.8	652.0	0.86	1.21	0.79
	B25L-NF30-2.4	461.1	479.4	381.6	514.1	0.96	1.21	0.90
	B25L-NF40-2.4	484.6	544.3	413.8	600.7	0.89	1.17	0.81
	B25L-NF50-2.4	538.0	609.2	446.1	677.6	0.88	1.21	0.79
	B50L-NF30-1.6	461.3	508.1	398.0	509.3	0.91	1.16	0.91
	B50L-NF40-1.6	484.3	573.0	426.2	591.4	0.85	1.14	0.82
	B50L-NF50-1.6	501.7	637.9	454.4	690.1	0.79	1.10	0.73
	B50L-NF30-2.1	530.1	535.5	432.8	546.1	0.99	1.22	0.97
	B50L-NF40-2.1	553.2	600.4	463.4	622.1	0.92	1.19	0.89
	B50L-NF50-2.1	596.0	665.3	494.1	695.7	0.90	1.21	0.86
	B50L-NF30-2.4	530.5	553.4	455.6	568.8	0.96	1.16	0.93
	B50L-NF40-2.4	581.3	618.3	487.9	652.1	0.94	1.19	0.89
	B50L-NF50-2.4	616.6	683.2	520.1	724.9	0.90	1.19	0.85
	B70L-NF30-1.6	493.8	545.3	435.2	535.7	0.91	1.13	0.92
	B70L-NF40-1.6	519.7	610.2	463.4	627.5	0.85	1.12	0.83
	B70L-NF50-1.6	535.1	675.1	491.6	726.2	0.79	1.09	0.74
	B70L-NF30-2.1	568.7	575.9	473.2	575.9	0.99	1.20	0.99
	B70L-NF40-2.1	595.3	640.8	503.9	650.0	0.93	1.18	0.92
	B70L-NF50-2.1	605.3	705.7	534.5	726.2	0.86	1.13	0.83
	B70L-NF30-2.4	602.2	596.0	498.2	600.9	1.01	1.21	1.00
	B70L-NF40-2.4	628.8	660.9	530.4	682.5	0.95	1.19	0.92
	B70L-NF50-2.4	673.1	725.8	562.7	753.1	0.93	1.20	0.89
L a/d=4	**B25L-NF30-1.6**	382.49	443.4	333.3	448.1	0.86	1.15	0.85
	B25L-NF40-1.6	406.92	508.3	361.5	533.8	0.80	1.13	0.76
	B25L-NF50-1.6	423.76	573.2	389.7	632.5	0.74	1.09	0.67
	B25L-NF30-2.1	423.64	465.2	362.5	479.2	0.91	1.17	0.88
	B25L-NF40-2.1	443.92	530.1	393.1	556.0	0.84	1.13	0.80
	B25L-NF50-2.1	436.49	595.0	423.8	632.5	0.73	1.03	0.69
	B25L-NF30-2.4	436.03	479.4	381.6	498.2	0.91	1.14	0.88
	B25L-NF40-2.4	471.16	544.3	413.8	578.5	0.87	1.14	0.81
	B25L-NF50-2.4	506.47	609.2	446.1	655.6	0.83	1.14	0.77
	B50L-NF30-1.6	431.35	508.1	398.0	492.7	0.85	1.08	0.88
	B50L-NF40-1.6	446.55	573.0	426.2	591.4	0.78	1.05	0.76
	B50L-NF50-1.6	448.70	637.9	454.4	690.1	0.70	0.99	0.65
	B50L-NF30-2.1	479.33	535.5	432.8	526.7	0.90	1.11	0.91
	B50L-NF40-2.1	498.80	600.4	463.4	599.8	0.83	1.08	0.83
	B50L-NF50-2.1	527.87	665.3	494.1	690.1	0.79	1.07	0.76
	B50L-NF30-2.4	532.12	553.4	455.6	549.5	0.96	1.17	0.97

	B50L-NF40-2.4	543.44	618.3	487.9	625.9	0.88	1.11	0.87
	B50L-NF50-2.4	569.36	683.2	520.1	699.6	0.83	1.09	0.81
	B70L-NF30-1.6	453.12	545.3	435.2	528.8	0.83	1.04	0.86
	B70L-NF40-1.6	469.45	610.2	463.4	627.5	0.77	1.01	0.75
	B70L-NF50-1.6	488.35	675.1	491.6	726.2	0.72	0.99	0.67
	B70L-NF30-2.1	521.84	575.9	473.2	554.7	0.91	1.10	0.94
	B70L-NF40-2.1	539.78	640.8	503.9	627.5	0.84	1.07	0.86
	B70L-NF50-2.1	559.50	705.7	534.5	726.2	0.79	1.05	0.77
	B70L-NF30-2.4	540.07	596.0	498.2	579.6	0.91	1.08	0.93
	B70L-NF40-2.4	600.34	660.9	530.4	653.9	0.91	1.13	0.92
	B70L-NF50-2.4	610.47	725.8	562.7	726.2	0.84	1.08	0.84
L a/d=4.5	**B25L-NF30-1.6**	338.7	443.4	333.3	435.1	0.76	1.02	0.78
	B25L-NF40-1.6	373.8	508.3	361.5	533.8	0.74	1.03	0.70
	B25L-NF50-1.6	361.1	573.2	389.7	632.5	0.63	0.93	0.57
	B25L-NF30-2.1	384.6	465.2	362.5	465.9	0.83	1.06	0.83
	B25L-NF40-2.1	420.5	530.1	393.1	540.3	0.79	1.07	0.78
	B25L-NF50-2.1	437.2	595.0	423.8	632.5	0.73	1.03	0.69
	B25L-NF30-2.4	425.5	479.4	381.6	485.1	0.89	1.12	0.88
	B25L-NF40-2.4	450.7	544.3	413.8	562.9	0.83	1.09	0.80
	B25L-NF50-2.4	487.6	609.2	446.1	637.3	0.80	1.09	0.77
	B50L-NF30-1.6	394.3	508.1	398.0	492.7	0.78	0.99	0.80
	B50L-NF40-1.6	428.6	573.0	426.2	591.4	0.75	1.01	0.72
	B50L-NF50-1.6	418.7	637.9	454.4	690.1	0.66	0.92	0.61
	B50L-NF30-2.1	474.2	535.5	432.8	510.9	0.89	1.10	0.93
	B50L-NF40-2.1	487.8	600.4	463.4	591.4	0.81	1.05	0.82
	B50L-NF50-2.1	518.3	665.3	494.1	690.1	0.78	1.05	0.75
	B50L-NF30-2.4	485.7	553.4	455.6	533.7	0.88	1.07	0.91
	B50L-NF40-2.4	519.0	618.3	487.9	607.6	0.84	1.06	0.85
	B50L-NF50-2.4	530.0	683.2	520.1	690.1	0.78	1.02	0.77
	B70L-NF30-1.6	452.0	545.3	435.2	528.8	0.83	1.04	0.85
	B70L-NF40-1.6	435.2	610.2	463.4	627.5	0.71	0.94	0.69
	B70L-NF50-1.6	467.6	675.1	491.6	726.2	0.69	0.95	0.64
	B70L-NF30-2.1	504.0	575.9	473.2	537.3	0.88	1.06	0.94
	B70L-NF40-2.1	514.1	640.8	503.9	627.5	0.80	1.02	0.82
	B70L-NF50-2.1	532.4	705.7	534.5	726.2	0.75	1.00	0.73
	B70L-NF30-2.4	537.1	596.0	498.2	562.2	0.90	1.08	0.96
	B70L-NF40-2.4	560.0	660.9	530.4	634.1	0.85	1.06	0.88
	B70L-NF50-2.4	580.4	725.8	562.7	726.2	0.80	1.03	0.80

Below are shown the relationship between numerical beam shear strengths (V_{FEA}) and the shear strengths predicted using the three approaches proposed (V_1, V_2, and V_3) for each size and a/d.

If a data point is above the continuous line, the predicted shear strength is greater than the measured shear strength; and vice versa. The dashed lines show the boundary of 20% offset from the measured shear strength.

Approach 1

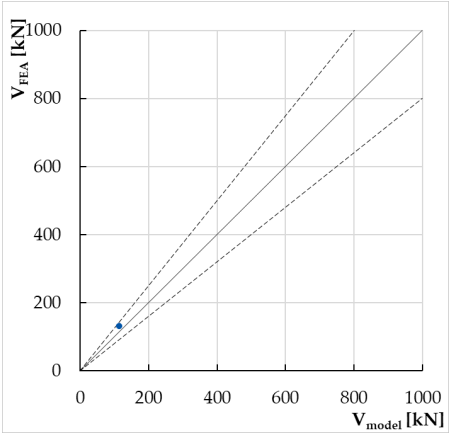

Beam S, a/d=3

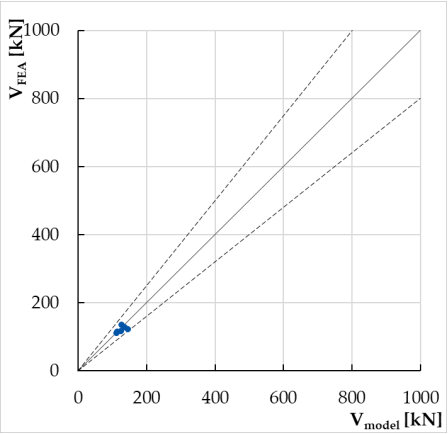

Beam S, a/d=3.5

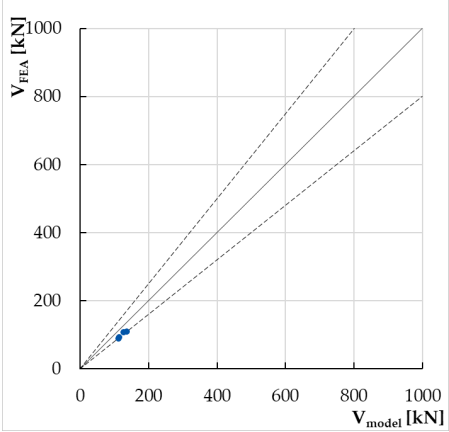

Beam S, a/d=4

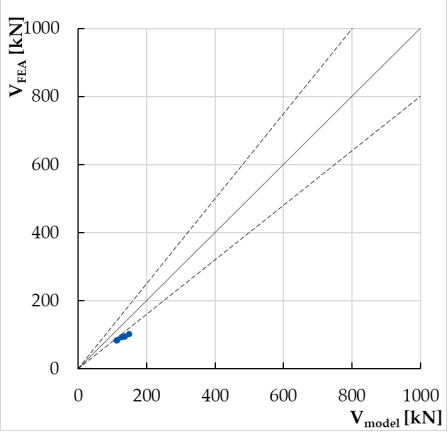

Beam S, a/d=4.5

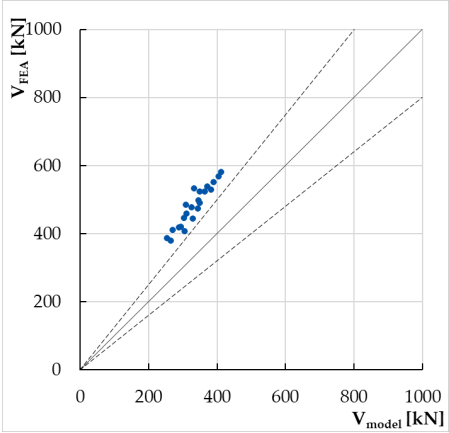

Beam M, a/d=2.5

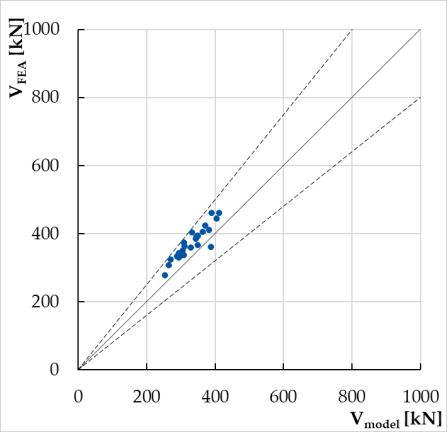

Beam M, a/d=3

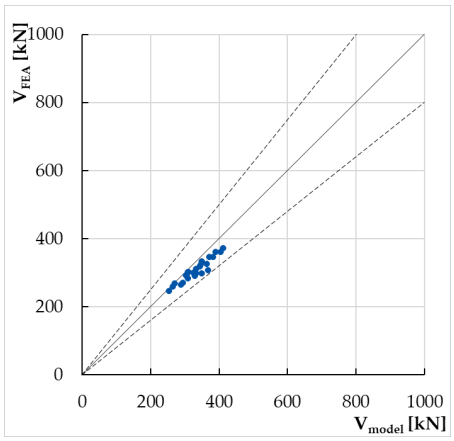

Beam M, a/d=3.5

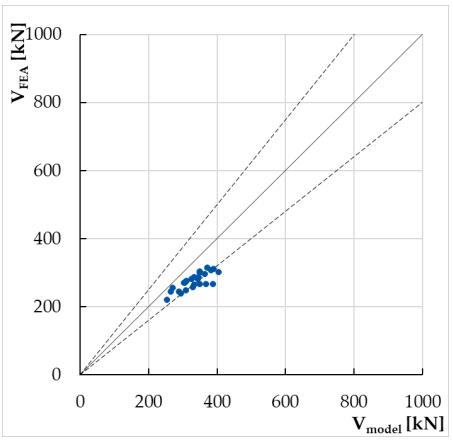

Beam M, a/d=4

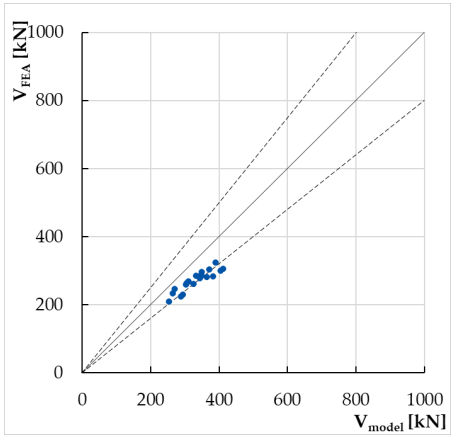

Beam M, a/d=4.5

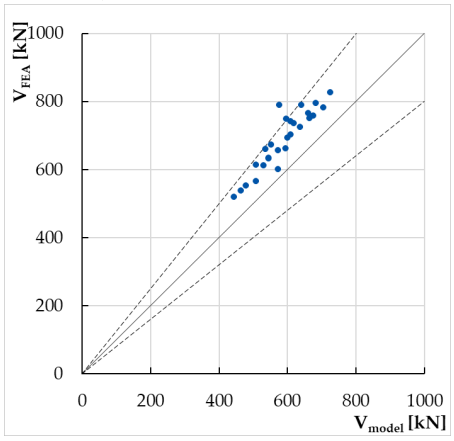

Beam L, a/d=2.5

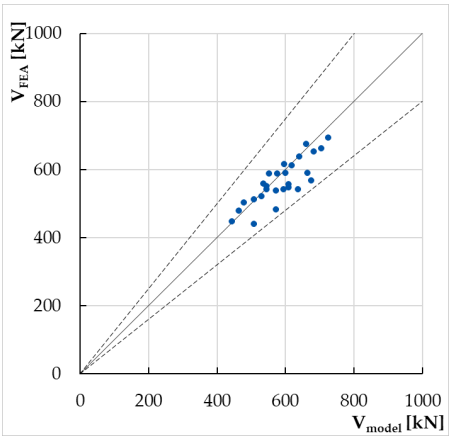

Beam L, a/d=3

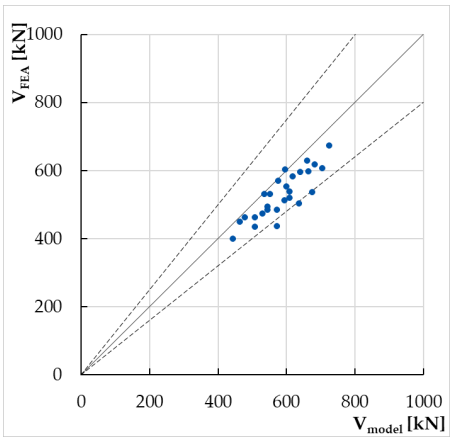

Beam L, a/d=3.5

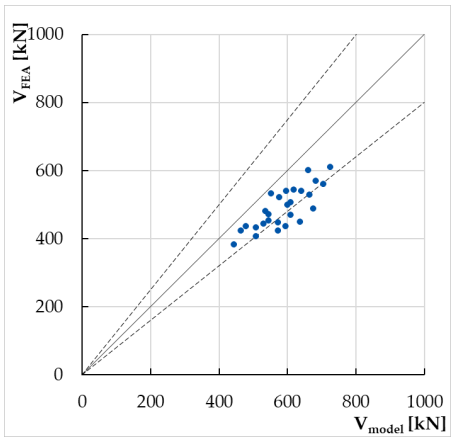

Beam L, a/d=4

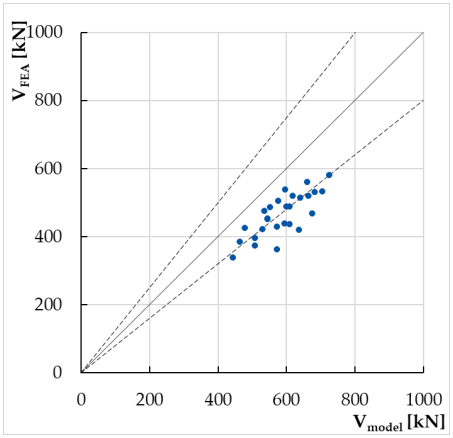

Beam L, a/d=4.5

Approach 2

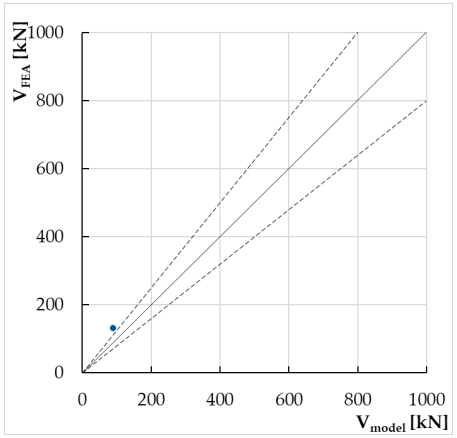

Beam S, a/d=3

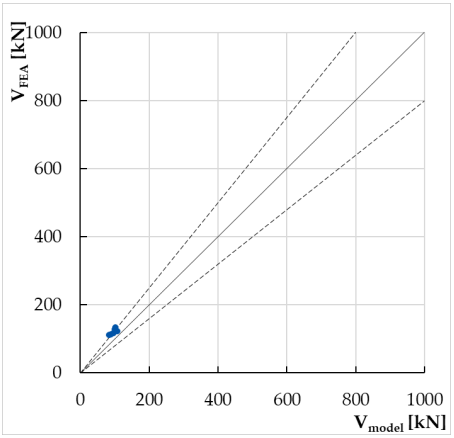

Beam S, a/d=3.5

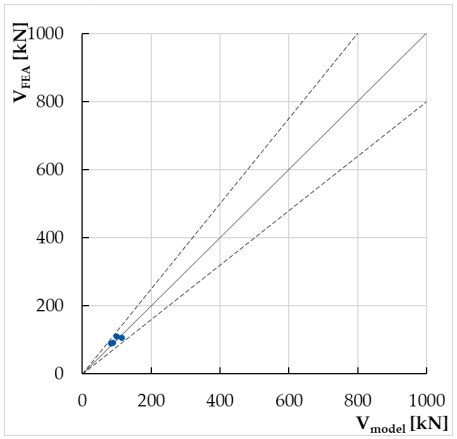

Beam S, a/d=4

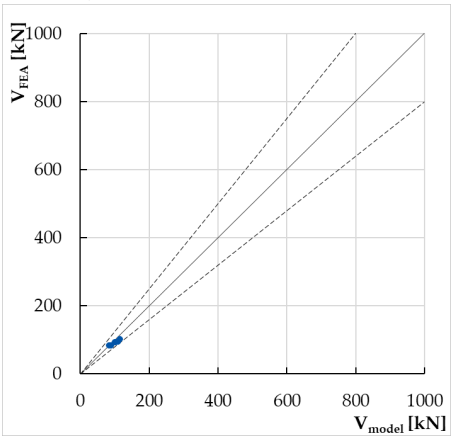

Beam S, a/d=4.5

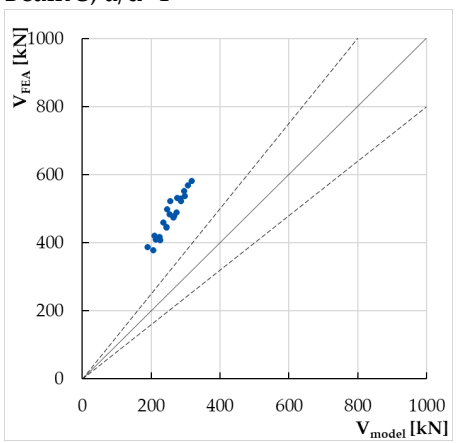

Beam M, a/d=2.5

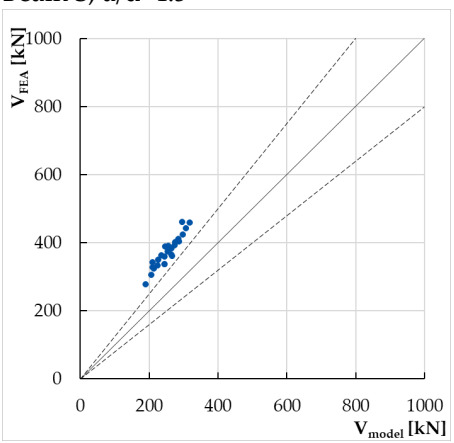

Beam M, a/d=3

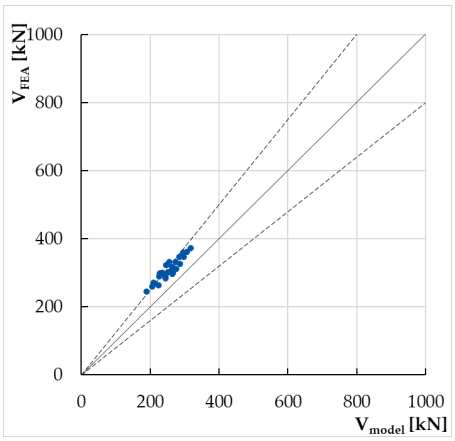

Beam M, a/d=3.5

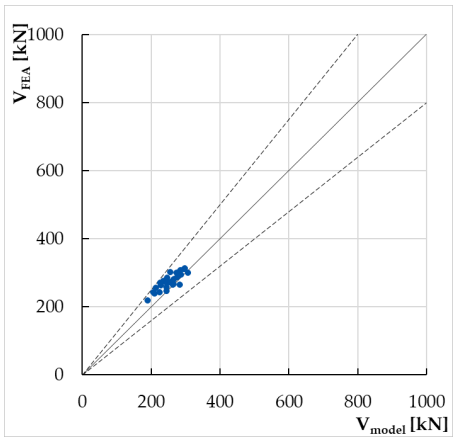

Beam M, a/d=4

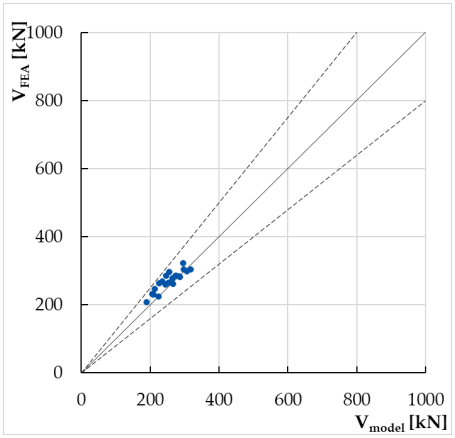

Beam M, a/d=4.5

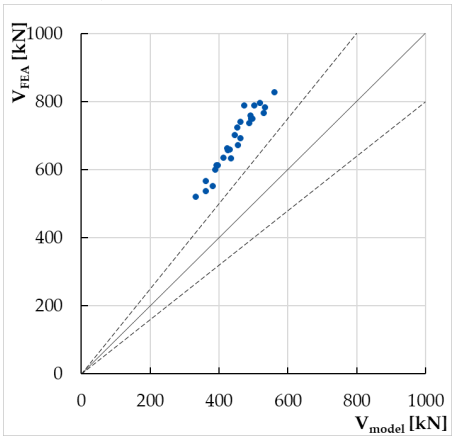

Beam L, a/d=2.5

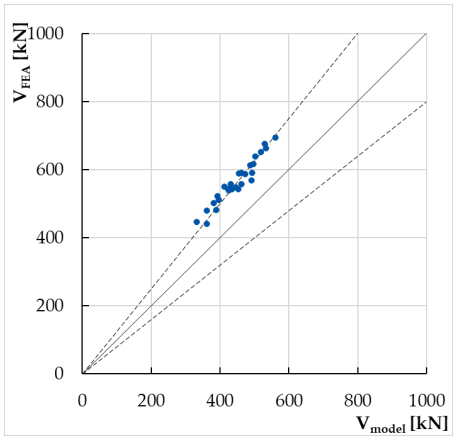

Beam L, a/d=3

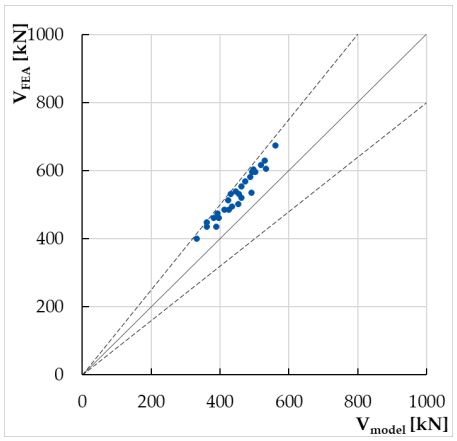

Beam L, a/d=3.5

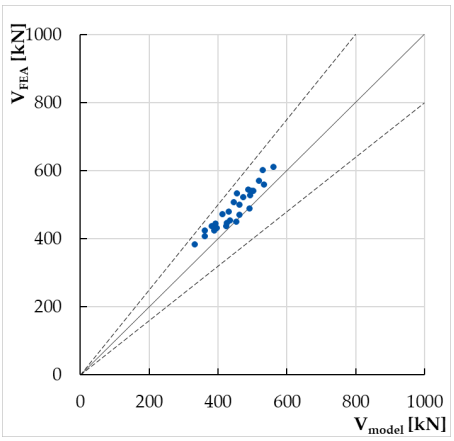

Beam L, a/d=4

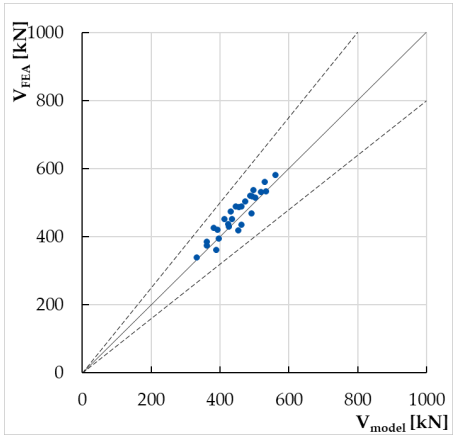

Beam L, a/d=4.5

Approach 3

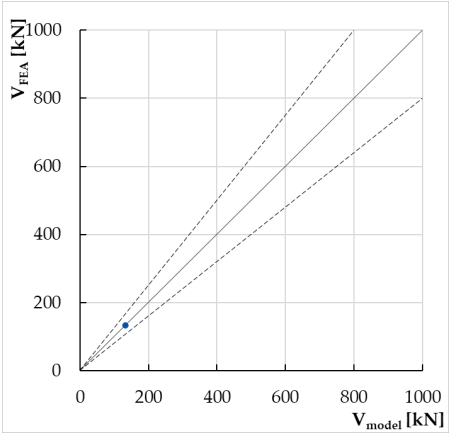

Beam S, a/d=3

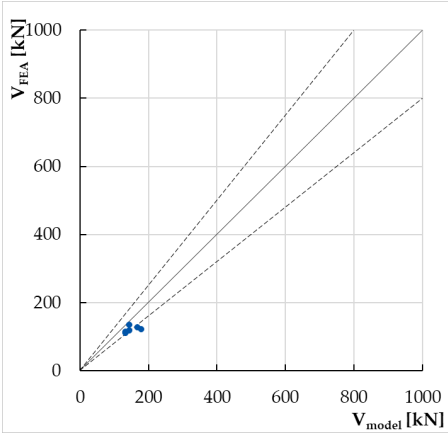

Beam S, a/d=3.5

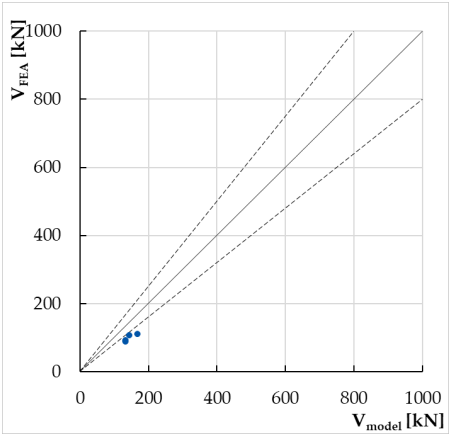

Beam S, a/d=4

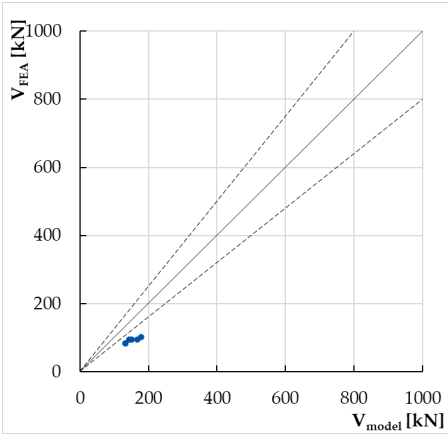

Beam S, a/d=4.5

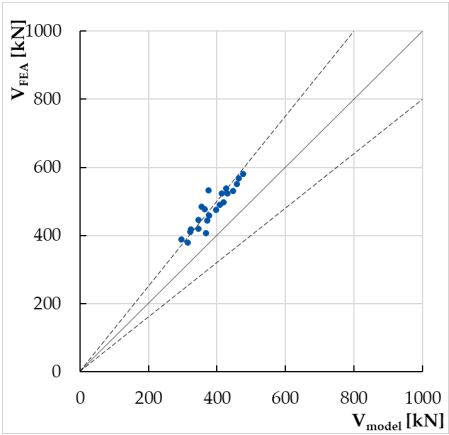

Beam M, a/d=2.5

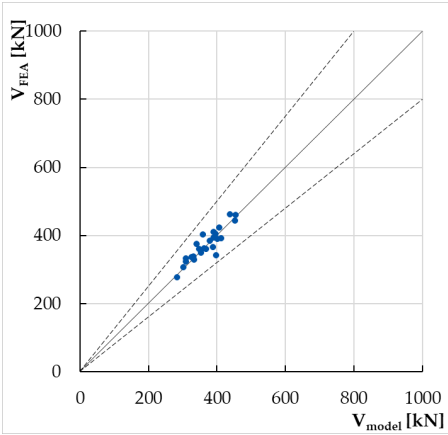

Beam M, a/d=3

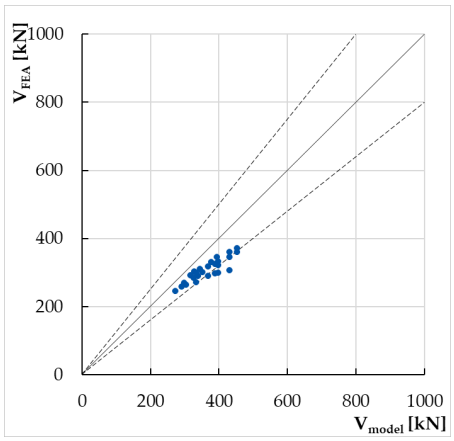

Beam M, a/d=3.5

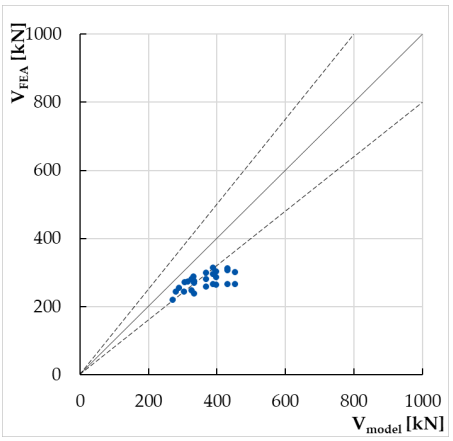

Beam M, a/d=4

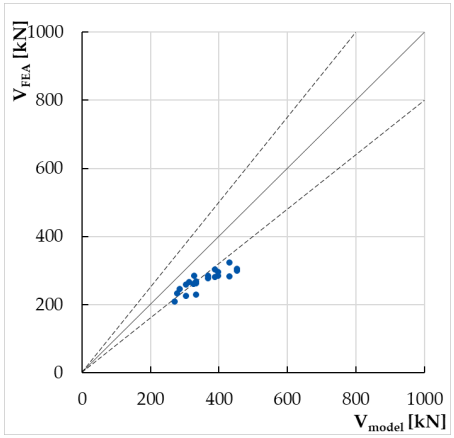

Beam M, a/d=4.5

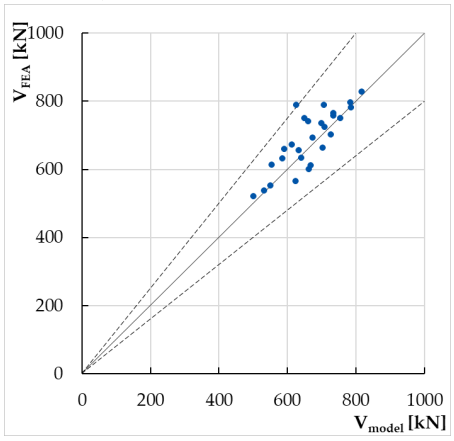

Beam L, a/d=2.5

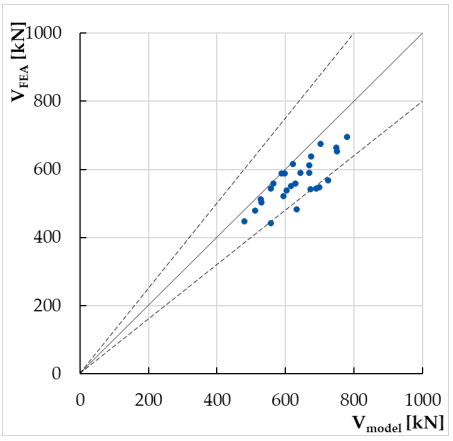

Beam L, a/d=3

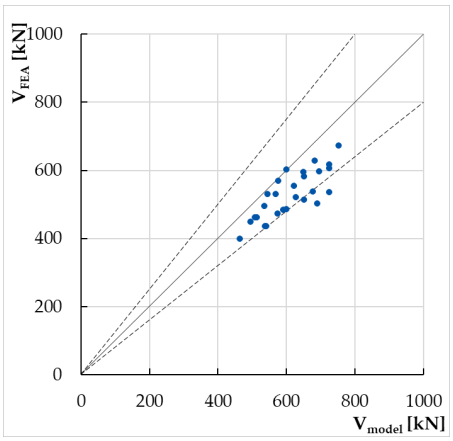

Beam L, a/d=3.5

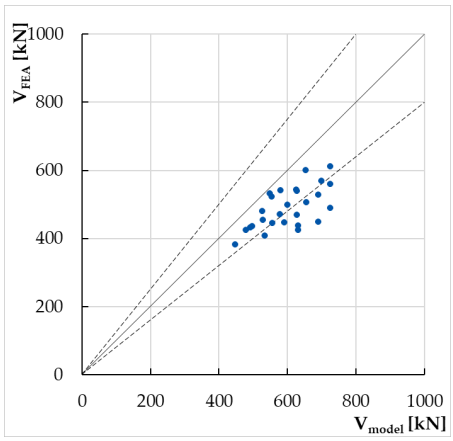

Beam L, a/d=4

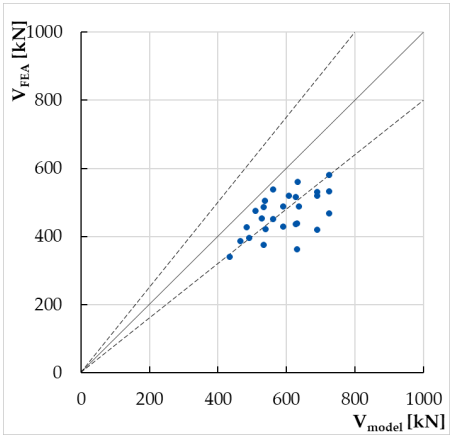

Beam L, a/d=4.5